

Copyrighted Material

# Fundamentals of Liquid Crystal Devices

Deng-Ke Yang  
Shin-Tson Wu

 WILEY

 SID

Series in **Display Technology**

Copyrighted Material

# **Fundamentals of Liquid Crystal Devices**

## **Wiley-SID Series in Display Technology**

Series Editor:

**Anthony C. Lowe**

Consultant Editor:

**Michael A. Kriss**

---

Display Systems:

Design and Applications

**Lindsay W. Macdonald** and **Anthony C. Lowe (Eds)**

Electronic Display Measurement:

Concepts, Techniques and Instrumentation

**Peter A. Keller**

Projection Displays

**Edward H. Stupp** and **Matthew S. Brennesholz**

Liquid Crystal Displays:

Addressing Schemes and Electro-Optical Effects

**Ernst Lueder**

Reflective Liquid Crystal Displays

**Shin-Tson Wu** and **Deng-Ke Yang**

Colour Engineering:

Achieving Device Independent Colour

**Phil Green** and **Lindsay MacDonald (Eds)**

Display Interfaces:

Fundamentals and Standards

**Robert L. Myers**

Digital Image Display:

Algorithms and Implementation

**Gheorghe Berbecel**

Flexible Flat Panel Displays

**Gregory Crawford (Ed.)**

Polarization Engineering for LCD Projection

**Michel G. Robinson, Jianmin Chen, and Gary D. Sharp**

Fundamentals of Liquid Crystal Devices

**Deng-Ke Yang** and **Shin-Tson Wu**

# Fundamentals of Liquid Crystal Devices

**Deng-Ke Yang**

*Kent State University, Ohio, USA*

**Shin-Tson Wu**

*University of Central Florida, Florida, USA*



John Wiley & Sons, Ltd

Copyright © 2006 John Wiley & Sons Ltd, The Atrium, Southern Gate, Chichester,  
West Sussex PO19 8SQ, England  
Telephone (+44) 1243 779777

Email (for orders and customer service enquiries): [cs-books@wiley.co.uk](mailto:cs-books@wiley.co.uk)  
Visit our Home Page on [www.wiley.com](http://www.wiley.com)

All Rights Reserved. No part of this publication may be reproduced, stored in a retrieval system or transmitted in any form or by any means, electronic, mechanical, photocopying, recording, scanning or otherwise, except under the terms of the Copyright, Designs and Patents Act 1988 or under the terms of a licence issued by the Copyright Licensing Agency Ltd, 90 Tottenham Court Road, London W1T 4LP, UK, without the permission in writing of the Publisher. Requests to the Publisher should be addressed to the Permissions Department, John Wiley & Sons Ltd, The Atrium, Southern Gate, Chichester, West Sussex PO19 8SQ, England, or emailed to [permreq@wiley.co.uk](mailto:permreq@wiley.co.uk), or faxed to (+44) 1243 770620.

Designations used by companies to distinguish their products are often claimed as trademarks. All brand names and product names used in this book are trade names, service marks, trademarks or registered trademarks of their respective owners. The Publisher is not associated with any product or vendor mentioned in this book.

This publication is designed to provide accurate and authoritative information in regard to the subject matter covered. It is sold on the understanding that the Publisher is not engaged in rendering professional services. If professional advice or other expert assistance is required, the services of a competent professional should be sought.

#### ***Other Wiley Editorial Offices***

John Wiley & Sons Inc., 111 River Street, Hoboken, NJ 07030, USA

Jossey-Bass, 989 Market Street, San Francisco, CA 94103-1741, USA

Wiley-VCH Verlag GmbH, Boschstr. 12, D-69469 Weinheim, Germany

John Wiley & Sons Australia Ltd, 42 McDougall Street, Milton, Queensland 4064, Australia

John Wiley & Sons (Asia) Pte Ltd, 2 Clementi Loop #02-01, Jin Xing Distripark, Singapore 129809

John Wiley & Sons Canada Ltd, 6045 Freemont Blvd, Mississauga, Ontario, L5R 4J3, Canada

Wiley also publishes its books in a variety of electronic formats. Some content that appears in print may not be available in electronic books.

#### ***Library of Congress Cataloging-in-Publication Data***

Yang, Deng-Ke.

Fundamentals of liquid crystal devices / Deng-Ke Yang, Shin-Tson Wu.

p. cm.

Includes bibliographical references and index.

ISBN 0-470-01542-X (cloth : alk. paper)

1. Liquid crystal devices—Textbooks. 2. Liquid crystal displays—Textbooks. 3. Liquid crystals—Textbooks.

I. Wu, Shin-Tson. II. Title.

TS518.Y36 2006

621.381'422--dc22

2006011247

#### ***British Library Cataloguing in Publication Data***

A catalogue record for this book is available from the British Library

ISBN-13 978-0-470-01542-1 (HB)

ISBN-10 0-470-01542-X (HB)

Typeset in 9/11pt Times by Thomson Digital Noida.

Printed and bound in Great Britain by Antony Rowe Ltd, Chippenham, Wiltshire

This book is printed on acid-free paper responsibly manufactured from sustainable forestry in which at least two trees are planted for each one used for paper production.

# Contents

<b>Foreword</b>	<b>xi</b>
<b>Series Editor's Foreword</b>	<b>xiii</b>
<b>Preface</b>	<b>xv</b>
<b>1 Liquid Crystal Physics</b>	<b>1</b>
1.1 Introduction	1
1.2 Thermodynamics and Statistical Physics	4
1.2.1 Thermodynamic laws	4
1.2.2 Boltzmann distribution	5
1.2.3 Thermodynamic quantities	7
1.2.4 Criteria for thermodynamic equilibrium	9
1.3 Orientational Order	10
1.3.1 Orientational order parameter	10
1.3.2 Landau–de Gennes theory of orientational order in the nematic phase	12
1.3.3 Maier–Saupe theory	16
1.4 Elastic Properties of Liquid Crystals	18
1.4.1 Elastic properties of nematic liquid crystals	18
1.4.2 Elastic properties of cholesteric liquid crystals	21
1.4.3 Elastic properties of smectic liquid crystals	22
1.5 Response of Liquid Crystals to Electromagnetic Fields	24
1.5.1 Magnetic susceptibility	24
1.5.2 Dielectric permittivity and refractive index	25
1.6 Anchoring Effects of Nematic Liquid Crystals at Surfaces	33
1.6.1 Anchoring energy	33
1.6.2 Alignment layers	34
Homework Problems	35
References	37

<b>2 Propagation of Light in Anisotropic Optical Media</b>	<b>39</b>
2.1 Electromagnetic Waves	39
2.2 Polarization	42
2.2.1 Monochromatic plane waves and their polarization states	42
2.2.2 Linear polarization states	42
2.2.3 Circular polarization states	43
2.2.4 Elliptical polarization states	43
2.3 Propagation of Light in Uniform Anisotropic Optical Media	45
2.3.1 Eigenmodes	47
2.3.2 Orthogonality of eigenmodes	51
2.3.3 Energy flux	52
2.3.4 Special cases	53
2.3.5 Polarizers	55
2.4 Propagation of Light in Cholesteric Liquid Crystals	57
2.4.1 Eigenmodes	57
2.4.2 Reflection of cholesteric liquid crystals	66
2.4.3 Lasing in cholesteric liquid crystals	68
Homework Problems	69
References	71
<b>3 Optical Modeling Methods</b>	<b>73</b>
3.1 Jones Matrix Method	73
3.1.1 Jones vector	73
3.1.2 Jones matrix	74
3.1.3 Jones matrix of non-uniform birefringent film	76
3.1.4 Optical properties of twisted nematic liquid crystals	77
3.2 Mueller Matrix Method	82
3.2.1 Partially polarized and unpolarized light	82
3.2.2 Measurement of the Stokes parameters	84
3.2.3 Mueller matrix	86
3.2.4 Poincaré sphere	88
3.2.5 Evolution of the polarization states on the Poincaré sphere	90
3.2.6 Mueller matrix of TN liquid crystals	92
3.2.7 Mueller matrix of non-uniform birefringent film	94
3.3 Berreman $4 \times 4$ method	95
Homework Problems	104
References	105
<b>4 Effects of Electric Field on Liquid Crystals</b>	<b>107</b>
4.1 Dielectric Interaction	107
4.1.1 Reorientation under dielectric interaction	107
4.1.2 Field-induced orientational order	108
4.2 Flexoelectric Effect	112
4.2.1 Flexoelectric effect in nematic liquid crystals	112
4.2.2 Flexoelectric effect in cholesteric liquid crystals	116
4.3 Ferroelectric Liquid Crystals	117
4.3.1 Symmetry and polarization	117
4.3.2 Tilt angle and polarization	119

4.3.3	Surface-stabilized ferroelectric liquid crystals	120
4.3.4	Electroclinic effect in chiral smectic- liquid crystals	122
	Homework Problems	124
	References	124
<b>5</b>	<b>Freedericksz Transition</b>	<b>127</b>
5.1	Calculus of Variations	127
5.1.1	One dimension and one variable	127
5.1.2	One dimension and multiple variables	130
5.1.3	Three dimensions	130
5.2	Freedericksz Transition: Statics	131
5.2.1	Splay geometry	131
5.2.2	Bend geometry	135
5.2.3	Twist geometry	137
5.2.4	Twisted nematic cell	138
5.2.5	Splay geometry with weak anchoring	140
5.2.6	Splay geometry with pretilt angle	142
5.3	Freedericksz Transition: Dynamics	143
5.3.1	Dynamics of the Freedericksz transition in twist geometry	144
5.3.2	Hydrodynamics	145
5.3.3	Backflow	150
	Homework Problems	155
	References	155
<b>6</b>	<b>Liquid Crystal Materials</b>	<b>157</b>
6.1	Introduction	157
6.2	Refractive Indices	157
6.2.1	Extended Cauchy equations	158
6.2.2	Three-band model	159
6.2.3	Temperature effect	161
6.2.4	Temperature gradient	164
6.2.5	Molecular polarizabilities	165
6.3	Dielectric Constants	166
6.3.1	Positive $\Delta\epsilon$ LCs active matrix LC displays	167
6.3.2	Negative $\Delta\epsilon$ LCs	167
6.3.3	Dual-frequency LCs	168
6.4	Rotational Viscosity	169
6.5	Elastic Constants	169
6.6	Figure-of-merit (FoM)	170
6.7	Index matching between LCs and Polymers	171
6.7.1	Refractive index of polymers	171
6.7.2	Matching refractive index	172
	Homework Problems	174
	References	175
<b>7</b>	<b>Modeling Liquid Crystal Director Configuration</b>	<b>179</b>
7.1	Electric Energy of Liquid Crystals	179
7.1.1	Constant charge	180
7.1.2	Constant voltage	181
7.1.3	Constant electric field	183



**viii CONTENTS**

7.2	Modeling the Electric Field	184
7.3	Simulation of Liquid Crystal Director Configuration	186
7.3.1	Angle representation	186
7.3.2	Vector representation	190
7.3.3	Tensor representation	193
	Homework Problems	196
	References	196
<b>8</b>	<b>Transmissive Liquid Crystal Displays</b>	<b>199</b>
8.1	Introduction	199
8.2	Twisted Nematic Cells	200
8.2.1	Voltage-dependent transmittance	200
8.2.2	Film-compensated TN cells	202
8.2.3	Viewing angle	204
8.3	IPS Mode	204
8.3.1	Voltage-dependent transmittance	204
8.3.2	Response time	206
8.3.3	Viewing angle	207
8.3.4	Classification of compensation films	208
8.3.5	Phase retardation of uniaxial media at oblique angles	209
8.3.6	Poincaré sphere representation	210
8.3.7	Light leakage of crossed polarizers at oblique view	211
8.3.8	IPS with a positive $a$ and a positive $c$ film	216
8.3.9	IPS with a positive $a$ and a negative $a$ film	220
8.3.10	Color shift	222
8.4	VA Mode	222
8.4.1	Voltage-dependent transmittance	223
8.4.2	Optical response time	224
8.4.3	Overdrive and undershoot voltage method	224
8.5	MVA Cells	225
8.5.1	MVA with a positive $a$ and a negative $c$ film	227
8.5.2	MVA with a positive $a$ , a negative $a$ , and a negative $c$ film	231
8.6	Optically Compensated Bend (OCB) Cell	235
8.6.1	Voltage-dependent transmittance	235
8.6.2	Compensation films for OCB	236
	Homework Problems	237
	References	239
<b>9</b>	<b>Reflective and Transflective Liquid Crystal Displays</b>	<b>243</b>
9.1	Introduction	243
9.2	Reflective LCDs	244
9.2.1	Film-compensated homogeneous cell	245
9.2.2	MTN cell	246
9.3	Transflector	247
9.3.1	Openings-on-metal transflector	248
9.3.2	Half-mirror metal transflector	249
9.3.3	Multilayer dielectric film transflector	249
9.3.4	Orthogonal polarization transfectors	249

9.4	Classification of Transflective LCDs	250
9.4.1	Absorption-type transflective LCDs	251
9.4.2	Scattering-type transflective LCDs	253
9.4.3	Scattering- and absorption-type transflective LCDs	254
9.4.4	Reflection-type transflective LCDs	255
9.4.5	Phase retardation type	257
9.5	Dual-cell-gap Transflective LCDs	265
9.6	Single-cell-gap Transflective LCDs	267
9.7	Performance of Transflective LCDs	267
9.7.1	Color balance	268
9.7.2	Image brightness	268
9.7.3	Viewing angle	268
	Homework Problems	269
	References	269

**10 Liquid Crystal Display Matrices, Drive Schemes, and Bistable Displays 273**

10.1	Segmented Displays	273
10.2	Passive Matrix Displays and Drive Scheme	274
10.3	Active Matrix Displays	278
10.3.1	TFT structure	279
10.3.2	TFT operating principles	280
10.4	Bistable Ferroelectric LCDs and Drive Scheme	281
10.5	Bistable Nematic Displays	283
10.5.1	Introduction	283
10.5.2	Twisted–untwisted bistable nematic LCDs	283
10.5.3	Surface-stabilized nematic LCDs	288
10.6	Bistable Cholesteric Reflective Displays	290
10.6.1	Introduction	290
10.6.2	Optical properties of bistable Ch reflective displays	291
10.6.3	Encapsulated Ch LCDs	293
10.6.4	Transition between Ch states	294
10.6.5	Drive schemes for bistable Ch displays	300
	Homework Problems	303
	References	303

**11 Liquid Crystal/Polymer Composites 307**

11.1	Introduction	307
11.2	Phase Separation	307
11.2.1	Binary mixture	309
11.2.2	Phase diagram and thermally induced phase separation	312
11.2.3	Polymerization-induced phase separation	314
11.2.4	Solvent-induced phase separation	317
11.2.5	Encapsulation	319
11.3	Scattering Properties of LCPCs	319
11.3.1	Rayleigh–Gans scattering theory	319
11.3.2	Anomalous diffraction scattering theory	324
11.4	PDLCs	324
11.4.1	Liquid crystal droplet configurations in PDLCs	325
11.4.2	Switching PDLCs	327

**x CONTENTS**

11.4.3	Scattering PDLC devices	330
11.4.4	Dichroic dye-doped PDLCs	332
11.4.5	Holographic PDLCs	333
11.5	PSLCs	335
11.5.1	Preparation of PSLCs	335
11.5.2	Working modes of PSLCs	336
11.6	Displays from LCPCs	340
11.6.1	Reflective displays	340
11.6.2	Projection displays	341
11.6.3	Transmissive direct-view displays	342
	Homework Problems	343
	References	344

**12 Tunable Liquid Crystal Photonic Devices 347**

12.1	Introduction	347
12.2	Laser Beam Steering	348
12.2.1	Optical phased array	349
12.2.2	Prism-based beam steering	350
12.3	VOAs	352
12.4	Tunable-focus Lenses	355
12.4.1	Tunable-focus spherical lens	356
12.4.2	Tunable-focus cylindrical lens	358
12.4.3	Switchable positive and negative microlens	361
12.4.4	Hermaphroditic LC microlens	364
12.5	Polarization-independent LC Devices	366
12.5.1	Double-layered homogeneous LC cells	366
12.5.2	Double-layered LC gels	368
	Homework Problems	370
	References	371

**Index 375**

# Foreword

I was first exposed to liquid crystal displays in 1972 when I joined Westinghouse R&D Center as a research engineer. Later, I was assigned the task of developing a  $5'' \times 5''100 \times 100$  pixels TFT-LCD panel for the US Air Force. At that time, the LCD fabrication processes were very primitive. The LC alignment was an obliquely evaporated SiOx film. The cell spacing was done by mylar strips for the second minimum cell gap around 8 microns. The filling of LC was in a vacuum chamber with a hypodermic syringe holding the LC and a needle glued by Epoxy to the covering glass through a hole drilled at the corner of the monochrome ITO covering glass. The LC filling could take half a day. What giant progress the LC fabrication processes have made over the past 30 years. The sizes of the glass substrates can reach almost 4 square meters. The uniform cell gap of LC first minimum around 3–4 microns is maintained by photopatterned spacers. Using the one-drop-fill technique the LC filling can be done in just a few minutes for a 42''-diagonal panel.

During the last 30 some years, the applications of LCDs have expanded tremendously. Starting from watches and calculators in the 1970s with direct-drive TNs, the portable PC terminals utilized monochrome simple-matrix-addressed TNs in the early 1980s, which were followed by monochrome STNs. In the 1990s, dual-scan and multiline addressed STN color panels for notebook PCs appeared. In the early 1990s, the mass-produced color TFT-LCD TN notebook PC panels started the unlimited developmental changes by TFT-LCD panels for increasingly larger panels for notebook PCs, monitors and eventually TV applications. Today, TFT-LCD TV panels have been sold in the market with sizes up to 50'' and performances comparable to CRTs. TFT-LCDs have established their position as the dominating flat panel display technology. Nevertheless, along the long developmental paths, there have been numerous challengers such as thin film EL, vacuum fluorescence, electrochromics, PDP and FED. Each time, LCDs have been able to sustain the challenges and emerge victoriously. Now, it looks certain that TFT-LCDs will replace the ultimate king, CRT, in the home's living room as the primary video display.

The LCD technologies have amazing resources and versatility. For each new application, LCD engineers have been able to expand the LCD capabilities to meet the new demands in performance. Taking the latest TV application as an example, the LCD engineers have been able to solve issues such as wide viewing angle, fast response, color shift versus gray levels and viewing angles.

What will be the next major application beyond TV? We don't know yet. However, we are certain that LCD engineers will be able to rise above the challenges and bring the technology to the next level. The LCD technologies will be the dominating flat panel display for many years to come.

**xii FOREWORD**

There have been many books related to LCD technologies. This book authored by Professor Yang and Professor Wu is the most extensive textbook on LCD which covers the physics, materials and driving methods of many types of LCD modes. I'm sure this book will provide students entering the LCD field with a thorough understanding of the devices.

**Fan Luo  
Vice President and CTO  
AU Optronics  
Science-Based Industrial Park  
Hsinchu  
Taiwan**

# Series Editor's Foreword

Since its inception, the purpose of this series has been to provide works for practising scientists and engineers in the field of display technology. This book will most certainly fulfil that purpose, but it will also mark a new departure for the series as it has been written primarily as a text for postgraduate and senior undergraduate students. This broadening of the aims of the series is welcome since it acknowledges the need to provide works in the display field not only to those already working in the profession but also to those who are about to enter it.

Liquid crystal display technology has developed enormously over the past 35 years. It is already dominating many display markets such as hand held PDA and phone products, notebook computer displays and desktop monitors. In those markets where it does not have total domination, such as flat TV, it has a very healthy and increasing market share. Moreover, although twisted and supertwisted nematic technologies were for many years ubiquitous, as performance requirements have become more stringent, other effects such as in-plane switching and vertically aligned nematics have come to the fore and new effects continue to be invented. For the very lowest power reflective displays, cholesteric and a variety of bistable nematic effects are used. And so far, I have only discussed direct view displays! LC projection displays, which can use only a single polarizer, require extremely innovative twist effects. With so many different liquid crystal effects being used so widely in industry, the addition of this latest book to the series is very timely.

Designed to be self-contained, the first chapters cover the basic physics of liquid crystals, their interaction with light and electric fields and the means by which they can be modelled. Next are described the majority of ways in which liquid crystals can be used in displays and a final chapter deals with photonic devices such as beam steerers, tunable focus lenses and polarisation-independent devices.

Because it is intended to be used as a textbook, another innovation has been introduced for the first time in the series. Each chapter concludes with a set of problems, the answers to which may be found on the Wiley web site.

Written by two academics of world standing in their fields – Deng-Ke Yang is a specialist in cholesterics and polymer stabilised systems and Shin-Tson Wu has made major contributions in twist systems for reflective displays and in many other areas – this latest book is a most welcome addition to the series.

**Anthony C. Lowe**  
**Braishfield, UK 2006**

# Preface

Liquid crystal displays have become the leading technology in the information display industry. They are used in small-sized displays such as calculators, cellular phones, digital cameras, and head-mounted displays; in medium-sized displays such as laptop and desktop computers; and in large-sized displays such as direct-view TVs and projection TVs. They have the advantages of high resolution and high brightness, and, being flat paneled, are lightweight, energy saving, and even flexible in some cases. They can be operated in transmissive and reflective modes. Liquid crystals have also been used in photonic devices such as laser beam steering, variable optical attenuators, and tunable-focus lenses. There is no doubt that liquid crystals will continue to play an important role in the era of information technology.

There are many books on the physics and chemistry of liquid crystals or on liquid crystal devices. There are, however, only few books covering both the basics and applications of liquid crystals. The main goal of this book is to provide a textbook for senior undergraduate and graduate students. The book can be used for a one- or two-semester course. The instructors can selectively choose the chapters and sections according to the length of the course and the interest of the students. The book can also be used as a reference book by scientists and engineers who are interested in liquid crystal displays and photonics.

The book is organized in such a way that the first few chapters cover the basics of liquid crystals and the necessary techniques to study and design liquid crystal devices. The later chapters cover the principles, design, operation, and performance of liquid crystal devices. Because of limited space, we cannot cover every aspect of liquid crystal chemistry and physics and all liquid crystal devices, but we hope this book can introduce readers to liquid crystals and provide them with the basic knowledge and techniques for their careers in liquid crystals.

We are greatly indebted to Dr. A. Lowe for his encouragement. We are also grateful to the reviewers of our book proposal for their useful suggestions and comments. Deng-Ke Yang would like to thank Ms. E. Landry and Prof. J. Kelly for patiently proof-reading his manuscript. He would also like to thank Dr. Q. Li for providing drawings. Shin-Tson Wu would like to thank his research group members for generating the new knowledge included in this book, especially Drs. Xinyu Zhu, Hongwen Ren, Yun-Hsing Fan, and Yi-Hsin Lin, and Mr. Zhibing Ge for kind help during manuscript preparation. He is also indebted to Dr. Terry Dorschner of Raytheon, Dr. Paul McManamon of the Air Force Research Lab, and Dr. Hiroyuki Mori of Fuji Photo Film for sharing their latest results. We would like to thank our colleagues and friends for useful discussions and drawings and our funding

**xvi    PREFACE**

agencies (DARPA, AFOSR, AFRL, and Toppoly) for providing financial support. Finally, we also would like to thank our families (Xiaojiang Li, Kevin Yang, Steven Yang, Cho-Yan Wu, Janet Wu, and Benjamin Wu) for their spiritual support, understanding, and constant encouragement.

**Deng-Ke Yang  
Shin-Tson Wu**



# 1

# Liquid Crystal Physics

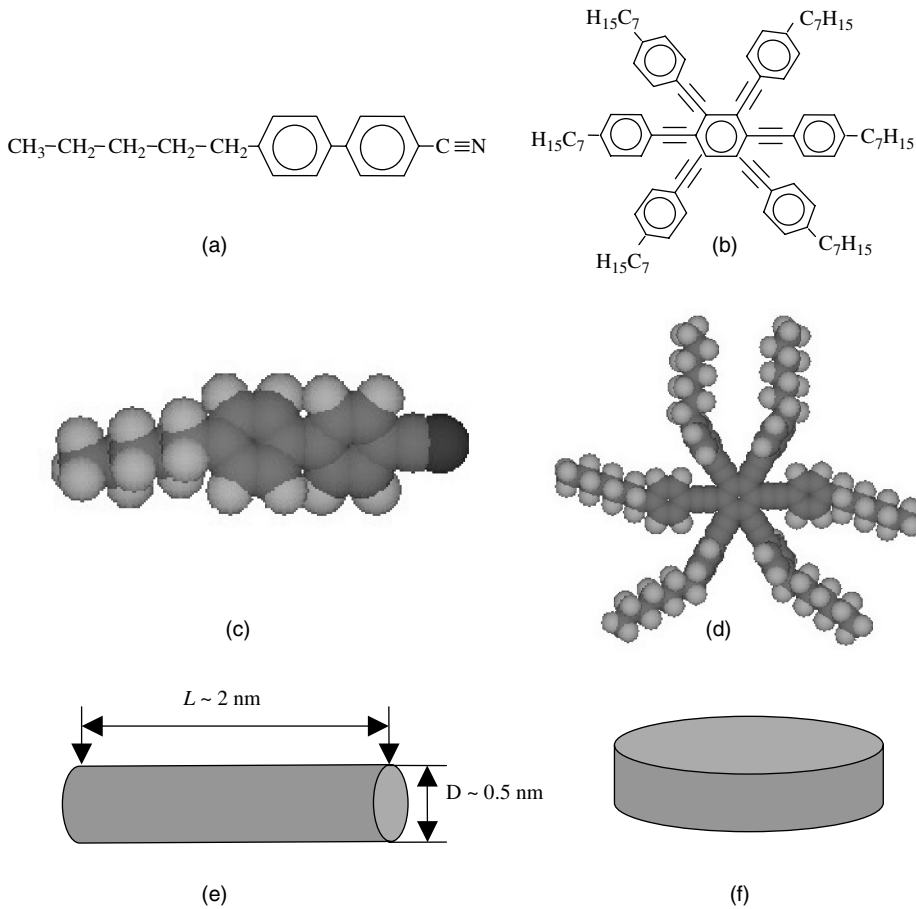
## 1.1 Introduction

Liquid crystals are mesophases between crystalline solids and isotropic liquids [1–3]. The constituents are elongated rod-like (calamitic) or disk-like (discotic) organic molecules as shown in Figure 1.1. The size of the molecules is typically a few nanometers (nm). The ratio between the length and the diameter of the rod-like molecules or the ratio between the diameter and the thickness of the disk-like molecules is about 5 or larger. Because the molecules are non-spherical, besides positional order, they may also possess orientational order.

Figure 1.1(a) shows a typical *calamitic* liquid crystal molecule. Its chemical name is 4'-*n*-pentyl-4-cyano-biphenyl and is abbreviated as 5CB [4,5]. It consists of a biphenyl, which is the rigid core, and a hydrocarbon chain, which is the flexible tail. The space-filling model of the molecule is shown in Figure 1.1(c). Although the molecule itself is not cylindrical, it can be regarded as a cylinder, as shown in Figure 1.1(e), in considering its physical behavior because of the fast rotation (on the order of  $10^{-9}$  s) around the long molecular axis due to thermal motion. The distance between two carbon atoms is about 1.5 Å; therefore the length and the diameter of the molecule are about 2 nm and 0.5 nm, respectively. The molecule shown has a permanent dipole moment (from the CN head); however, it can still be represented by a cylinder whose head and tail are the same, because in non-ferroelectric liquid crystal phases, the dipole has equal probability of pointing up or down. It is necessary for a liquid crystal molecule to have a rigid core(s) and flexible tail(s). If the molecule is completely flexible, it will not have orientational order. If it is completely rigid, it will transform directly from the isotropic liquid phase at high temperature to the crystalline solid phase at low temperature. The rigid part favors both orientational and positional order while the flexible part does not. With balanced rigid and flexible parts, the molecule exhibits liquid crystal phases.

Figure 1.1(b) shows a typical *discotic* liquid crystal molecule [6]. It also has a rigid core and flexible tails. The branches are approximately on one plane. The space-filling model of the molecule is shown in Figure 1.1(d). If there is no permanent dipole moment perpendicular to the plane of the molecule, it can be regarded as a disk in considering its physical behavior as shown in Figure 1.1(f), because of the fast rotation around the axis which is at the center of the molecule and perpendicular to the plane of the molecule. If there is a permanent dipole moment perpendicular to the plane of the molecule, it is better to

## 2 LIQUID CRYSTAL PHYSICS

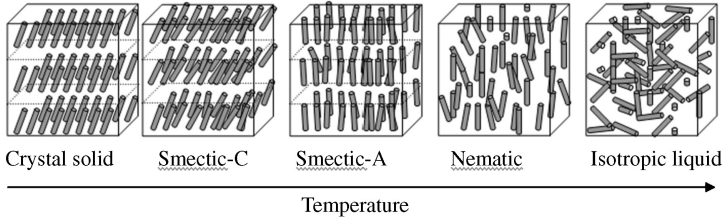


**Figure 1.1** Calamitic liquid crystal: (a) chemical structure, (c) space-filling model, (e) physical model. Discotic liquid crystal: (b) chemical structure, (d) space-filling mode, (f) physical model

visualize the molecule as a bowl, because the reflection symmetry is broken and all the permanent dipoles may point in the same direction and spontaneous polarization occurs. The flexible tails are also necessary, otherwise the molecules form the crystal phase where there is positional order.

The variety of phases that may be exhibited by rod-like molecules are shown in Figure 1.2. At high temperature, the molecules are in the isotropic liquid state where they do not have either positional or orientational order. The molecules can easily move around and the material can flow like water. The translational viscosity is comparable to that of water. Both the long and short axes of the molecules can point in any direction.

When the temperature is decreased, the material transforms into the *nematic* phase, which is the most common and simplest liquid crystal phase, where the molecules have orientational order but still no positional order. The molecules can still diffuse around and the translational viscosity does not change much from that of the isotropic liquid state. The long axis of the molecules has preferred direction. Although the molecules still swivel due to thermal motion, the time-averaged direction of the long axis of a molecule is well defined and is the same for all the molecules at the macroscopic scale. The average



**Figure 1.2** Schematic representation of the phases of rod-like molecules

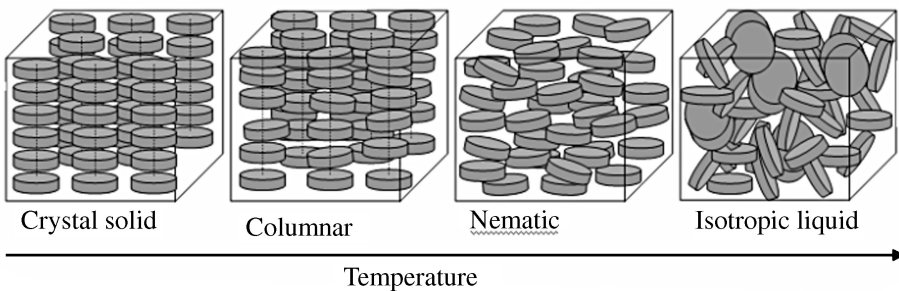
direction of the long molecular axis is denoted by  $\vec{n}$  which is a unit vector and called the liquid crystal director. The short axes of the molecules have no orientational order in a uniaxial nematic liquid crystal.

When the temperature is decreased further, the material may transform into the *smectic-A* phase where, besides the orientational order, the molecules have partial positional order, i.e., the molecules form a layered structure. The liquid crystal director is perpendicular to the layers. Smectic-A is a one-dimensional crystal where the molecules have positional order in the normal direction of the layer. The diagram shown in Figure 1.2 is schematic. In reality, the separation between neighboring layers is not as well defined as that shown in the figure. The molecular number density exhibits an undulation with the wavelength about the molecular length. Within a layer, it is a two-dimensional liquid in which there is no positional order and the molecules can move around. For a material in poly-domain smectic-A, the translational viscosity is significantly higher, and it behaves like a grease. When the temperature is decreased still further, the material may transform into the *smectic-C* phase where the liquid crystal director is no longer perpendicular to the layer but tilted.

At low temperature, the material is in the crystal solid phase where there are both positional and orientational orders. The translational viscosity become infinite and the molecules (almost) no longer diffuse.

Liquid crystals get the ‘crystal’ part of their name because they exhibit optical birefringence like crystalline solids. They get the ‘liquid’ part of their name because they can flow and do not support shearing like regular liquids. Liquid crystal molecules are elongated and have different molecular polarizabilities along their long and short axes. Once the long axes of the molecules orient along a common direction, the refractive indices along and perpendicular to the common direction are different. It should be noted that not all rod-like molecules exhibit all the liquid crystal phases, but just some of them.

Some of the liquid crystal phases of disk-like molecules are shown in Figure 1.3. At high temperature, they are in the isotropic liquid state where there are no positional and orientational orders. The material behaves in the same way as a regular liquid. When the temperature is decreased, the material transforms



**Figure 1.3** Schematic representation of the phases of disk-like molecules

## 4 LIQUID CRYSTAL PHYSICS

into the nematic phase which has orientational order but not positional order. The average direction of the short axis perpendicular to the disk is oriented along a preferred direction which is also called the liquid crystal director and denoted by a unit vector  $\vec{n}$ . The molecules have different polarizabilities along a direction in the plane of the disk and along the short axis. Thus the discotic nematic phase also exhibits birefringence as crystals.

When the temperature is decreased further, the material transforms into the columnar phase where, besides orientational order, there is partial positional order. The molecules stack up to form columns. Within a column, the columnar phase is a liquid where the molecules have no positional order. The columns, however, are arranged periodically in the plane perpendicular to the columns. Hence the columnar phase is a two-dimensional crystal. At low temperature, the material transforms into the crystalline solid phase where the positional order along the columns is developed.

The liquid crystal phases discussed so far are called thermotropic liquid crystals and the transitions from one phase to another phase are driven by varying temperature. There is another type of liquid crystallinity, called lyotropic, exhibited by molecules when they are mixed with a solvent of some kind. The phase transitions from one phase to another phase are driven by varying the solvent concentration. Lyotropic liquid crystals usually consist of amphiphilic molecules which have a hydrophobic group at one end and a hydrophilic group at the other end, with water as the solvent. The common lyotropic liquid crystal phases are micelle phase and lamellar phase. Lyotropic liquid crystals are important in biology. They will not be discussed in this book because its scope concerns displays and photonic devices.

Liquid crystals have a history of more than 100 years. It is believed that the person who discovered liquid crystals was Friedrich Reinitzer, an Austrian botanist [7]. The liquid crystal phase observed by him in 1888 was a cholesteric phase. Since then liquid crystals have come a long way and become a major branch of interdisciplinary science. Scientifically, liquid crystals are important because of the richness of their structures and transitions. Technologically, they have gained tremendous success in display and photonic applications [8–10].

### 1.2 Thermodynamics and Statistical Physics

Liquid crystal physics is an interdisciplinary science, involving thermodynamics, statistical physics, electrostatics, and optics. Here we give a brief introduction to thermodynamics and statistical physics.

#### 1.2.1 Thermodynamic laws

One of the important quantities in thermodynamics is entropy. From the microscopic point of view, entropy is a measure of the number of quantum states accessible to a system. In order to define entropy quantitatively, we first consider the fundamental logical assumption that *for a closed system (in which no energy and particles exchange with other systems), quantum states are either accessible or inaccessible to the system, and the system is equally likely to be in any one of the accessible states as in any other accessible state* [11]. For a macroscopic system, the number of accessible quantum states  $g$  is a huge number ( $\sim 10^{23}$ ). It is easier to deal with  $\ln g$ , which is defined as the *entropy*  $\sigma$ :

$$\sigma = \ln g \tag{1.1}$$

If a closed system consists of subsystem 1 and subsystem 2, the numbers of accessible states of the subsystems are  $g_1$  and  $g_2$ , respectively. The number of accessible quantum states of the whole system is  $g = g_1 g_2$  and the entropy is  $\sigma = \ln g = \ln (g_1 g_2) = \ln g_1 + \ln g_2 = \sigma_1 + \sigma_2$ .

Entropy is a function of the energy  $u$  of the system  $\sigma = \sigma(u)$ . The second law of thermodynamics states that *for a closed system, the equilibrium state has maximum entropy*. Let us consider a closed system which contains two subsystems. When two subsystems are brought into thermal contact the

energy exchange between them is allowed, the energy is allocated to maximize the number of accessible states; that is, the entropy is maximized. Subsystem 1 has energy  $u_1$  and entropy  $\sigma_1$ ; subsystem 2 has energy  $u_2$  and entropy  $\sigma_2$ . For the whole system,  $u = u_1 + u_2$  and  $\sigma = \sigma_1 + \sigma_2$ . The first law of thermodynamics states that *energy is conserved*, i.e.,  $u = u_1 + u_2 = \text{constant}$ . For any process inside the closed system,  $\delta u = \delta u_1 + \delta u_2 = 0$ . From the second law of thermodynamics, for any process we have  $\delta\sigma = \delta\sigma_1 + \delta\sigma_2 \geq 0$ . When the two subsystems are brought into thermal contact, at the beginning energy flows. For example, an amount of energy  $|\delta u_1|$  flows from subsystem 1 to subsystem 2,  $\delta u_1 < 0$  and  $\delta u_2 = -\delta u_1 > 0$ , and

$$\frac{\partial\sigma}{\partial u_2} = \frac{\partial\sigma_1}{\partial u_2} + \frac{\partial\sigma_2}{\partial u_2} = \frac{\partial\sigma_1}{\partial u_1} \frac{\partial u_1}{\partial u_2} + \frac{\partial\sigma_2}{\partial u_2} = -\frac{\partial\sigma_1}{\partial u_1} + \frac{\partial\sigma_2}{\partial u_2} \geq 0$$

When equilibrium is reached, the entropy is maximized and

$$\frac{\partial\sigma_1}{\partial u_1} - \frac{\partial\sigma_2}{\partial u_2} = 0 \quad \text{or} \quad \frac{\partial\sigma_1}{\partial u_1} = \frac{\partial\sigma_2}{\partial u_2}$$

We know that when two systems reach equilibrium, they have the same temperature. Accordingly the *fundamental temperature*  $\tau$  is defined by

$$1/\tau = (\partial\sigma/\partial u)_{N,V} \quad (1.2)$$

where  $N$  is the number of particles and  $V$  the volume. Energy flows from a high temperature system to a low-temperature system. The *conventional temperature* (Kelvin temperature) is defined by

$$T = \tau/k_B \quad (1.3)$$

where  $k_B = 1.81 \times 10^{-23}$  joules/kelvin is the Boltzmann constant. *Conventional entropy*  $S$  is defined by

$$1/T = \partial S/\partial u \quad (1.4)$$

Hence

$$S = k_B\sigma \quad (1.5)$$

### 1.2.2 Boltzmann distribution

Now we consider the thermodynamics of a system at a constant temperature, i.e., in thermal contact with a thermal reservoir. The temperature of the thermal reservoir (named B) is  $\tau$ . The system under consideration (named A) has two states with energy 0 and  $\varepsilon$ , respectively. A and B form a closed system, and its total energy  $u = u_A + u_B = u_o = \text{constant}$ . When A is in the state with energy 0, B has energy  $u_o$ , and the number of accessible states is  $g_1 = g_A \times g_B = 1 \times g_B(u_o) = g_B(u_o)$ . When A has energy  $\varepsilon$ , B has energy  $u_o - \varepsilon$ , and the number of accessible states is  $g_2 = g_A \times g_B = 1 \times g_B(u_o - \varepsilon) = g_B(u_o - \varepsilon)$ . For the whole system, the total number of accessible states is

$$G = g_1 + g_2 = g_B(u_o) + g_B(u_o - \varepsilon) \quad (1.6)$$

(A + B) is a closed system, and the probability in any of the  $G$  states is the same. When the whole system is in one of the  $g_1$  states, A has energy 0. When the whole system is in one of the  $g_2$  states, A has

## 6 LIQUID CRYSTAL PHYSICS

energy  $\varepsilon$ . Therefore the probability that A is in the state with energy 0 is

$$P(0) = \frac{g_1}{g_1 + g_2} = \frac{g_B(u_0)}{g_B(u_0) + g_B(u_0 - \varepsilon)}$$

The probability that A is in the state energy  $\varepsilon$  is

$$P(\varepsilon) = \frac{g_2}{g_1 + g_2} = \frac{g_B(u_0 - \varepsilon)}{g_B(u_0) + g_B(u_0 - \varepsilon)}$$

From the definition of entropy, we have  $g_B(u_0) = e^{\sigma_B(u_0)}$  and  $g_B(u_0 - \varepsilon) = e^{\sigma_B(u_0 - \varepsilon)}$ . Because  $\varepsilon \ll u_0$ ,

$$\sigma_B(u_0 - \varepsilon) \approx \sigma_B(u_0) - \frac{\partial \sigma_B}{\partial u_B} \varepsilon = \sigma_B(u_0) - \frac{1}{\tau} \varepsilon$$

Therefore we have

$$P(0) = \frac{e^{\sigma_B(u_0)}}{e^{\sigma_B(u_0)} + e^{\sigma_B(u_0) - \varepsilon/\tau}} = \frac{1}{1 + e^{-\varepsilon/\tau}} = \frac{1}{1 + e^{-\varepsilon/k_B T}} \quad (1.7)$$

$$P(\varepsilon) = \frac{e^{\sigma_B(u_0) - \varepsilon/\tau}}{e^{\sigma_B(u_0)} + e^{\sigma_B(u_0) - \varepsilon/\tau}} = \frac{e^{-\varepsilon/\tau}}{1 + e^{-\varepsilon/\tau}} = \frac{e^{-\varepsilon/k_B T}}{1 + e^{-\varepsilon/k_B T}} \quad (1.8)$$

$$\equiv \frac{P(\varepsilon)}{P(0)} = e^{-\varepsilon/k_B T} \quad (1.9)$$

For a system having  $N$  states with energies  $\varepsilon_1, \varepsilon_2, \dots, \varepsilon_i, \dots, \varepsilon_{i+1}, \dots, \varepsilon_N$ , the probability for the system in the state with energy  $\varepsilon_i$  is

$$P(\varepsilon_i) = e^{-\varepsilon_i/\tau} / \sum_{j=1}^N e^{-\varepsilon_j/k_B T} \quad (1.10)$$

The *partition function* of the system is defined as

$$Z = \sum_i e^{-\varepsilon_i/k_B T} \quad (1.11)$$

The *internal energy* (average energy) of the system is given by

$$U = \langle \varepsilon \rangle = \sum_i \varepsilon_i P(\varepsilon_i) = \frac{1}{Z} \sum_i \varepsilon_i e^{-\varepsilon_i/k_B T} \quad (1.12)$$

Because

$$\frac{\partial Z}{\partial T} = \sum_i \left( \frac{\varepsilon_i}{k_B T^2} \right) e^{-\varepsilon_i/k_B T} = \frac{1}{k_B T^2} \sum_i \varepsilon_i e^{-\varepsilon_i/k_B T}$$

then

$$U = \frac{k_B T^2}{Z} \frac{\partial Z}{\partial T} = k_B T^2 \frac{\partial (\ln Z)}{\partial T} \quad (1.13)$$

### 1.2.3 Thermodynamic quantities

As energy is conserved, the change of the internal energy  $U$  of a system equals the heat  $dQ$  absorbed and the mechanical work  $dW$  done to the system,  $dU = dQ + dW$ . When the volume of the system changes by  $dV$  under the pressure  $P$ , the mechanical work done to the system is given by

$$dW = -PdV \quad (1.14)$$

When there is no mechanical work, the heat absorbed equals the change of internal energy. From the definition of temperature  $1/T = (\partial S/\partial U)_V$ , the heat absorbed in a reversible process at constant volume is

$$dU = dQ = TdS \quad (1.15)$$

When the volume is not constant, then

$$dU = TdS - PdV \quad (1.16)$$

The derivatives are

$$T = \left( \frac{\partial U}{\partial S} \right)_V \quad (1.17)$$

$$P = - \left( \frac{\partial U}{\partial V} \right)_S \quad (1.18)$$

The internal energy  $U$ , entropy  $S$ , and volume  $V$  are extensive quantities, while temperature  $T$  and pressure  $P$  are intensive quantities. The *enthalpy*  $H$  of the system is defined by

$$H = U + PV \quad (1.19)$$

Its variation in a reversible process is given by

$$dH = dU + d(PV) = (TdS - PdV) + (PdV + VdP) = TdS + VdP \quad (1.20)$$

From this equation, it can be seen that the physical meaning of enthalpy is that in a process at constant pressure ( $dP = 0$ ), the change of enthalpy  $dH$  is equal to the heat absorbed  $dQ (= TdS)$ . The derivatives of the enthalpy are

$$T = \left( \frac{\partial H}{\partial S} \right)_P \quad (1.21)$$

$$V = \left( \frac{\partial H}{\partial P} \right)_S \quad (1.22)$$

The *Helmholtz free energy*  $F$  of the system is defined by

$$F = U - TS \quad (1.23)$$

## 8 LIQUID CRYSTAL PHYSICS

Its variation in a reversible process is given by

$$dF = dU - d(TS) = (TdS - PdV) - (TdS + SdT) = SdT - PdV \quad (1.24)$$

The physical meaning of Helmholtz free energy is that in a process at constant temperature, the change of Helmholtz free energy is equal to the work done to the system. The derivatives are

$$S = -\left(\frac{\partial F}{\partial T}\right)_V \quad (1.25)$$

$$P = -\left(\frac{\partial F}{\partial V}\right)_T \quad (1.26)$$

The *Gibbs free energy*  $G$  of the system is defined by

$$G = U - TS + PV \quad (1.27)$$

The variation in a reversible process is given by

$$dG = dU - d(TS) - d(PV) = -SdT + VdP \quad (1.28)$$

In a process at constant temperature and pressure, the Gibbs free energy does not change. The derivatives are

$$S = -\left(\frac{\partial G}{\partial T}\right)_P \quad (1.29)$$

$$V = \left(\frac{\partial G}{\partial P}\right)_T \quad (1.30)$$

The Helmholtz free energy can be derived from the partition function. From Equations (1.13) and (1.25),

$$F = U - TS = K_B T^2 \frac{\partial(\ln Z)}{\partial T} + T \left(\frac{\partial F}{\partial T}\right)_V$$

$$F - T \left(\frac{\partial F}{\partial T}\right)_V = -T^2 \left\{ \frac{1}{T} \left(\frac{\partial F}{\partial T}\right)_V + F \left[\frac{\partial(1/T)}{\partial T}\right]_V \right\} = -T^2 \left[\frac{\partial(F/T)}{\partial T}\right]_V = K_B T^2 \frac{\partial(\ln Z)}{\partial T}$$

Hence

$$F = -k_B T \ln Z = -k_B T \ln \left( \sum_i e^{-\epsilon_i/k_B T} \right) \quad (1.31)$$

From Equations (1.11), (1.25), and (1.31), the entropy of a system at constant temperature can be calculated as

$$S = -k_B \langle \ln \rho \rangle = -k_B \sum_i \rho_i \ln \rho_i \quad (1.32)$$



### 1.2.4 Criteria for thermodynamic equilibrium

Now we consider the criteria which can be used to judge whether a system is in its equilibrium state under given conditions. We already know that for a closed system, as it changes from a non-equilibrium state to the equilibrium state, the entropy increases:

$$\delta S \geq 0 \quad (1.33)$$

It can be stated differently that, for a closed system, the entropy is maximized in the equilibrium state.

In considering the equilibrium state of a system at constant temperature and volume, we construct a closed system which consists of the system (subsystem 1) under consideration and a thermal reservoir (subsystem 2) with temperature  $T$ . When the two systems are brought into thermal contact, energy is exchanged between subsystem 1 and subsystem 2. Because the whole system is a closed system,  $\delta S = \delta S_1 + \delta S_2 \geq 0$ . For system 2,  $1/T = (\partial S_2 / \partial U_2)_V$ , and therefore  $\delta S_2 = \delta U_2 / T$  (this is true when the volume of the subsystem is fixed, which also means the volume of subsystem 1 is fixed). Because of energy conservation,  $\delta U_2 = -\delta U_1$ . Hence  $\delta S = \delta S_1 + \delta S_2 = \delta S_1 + \delta U_2 / T = \delta S_1 - \delta U_1 / T \geq 0$ . Because the temperature and volume are constant for subsystem 1,  $\delta S_1 - \delta U_1 / T = (1/T)\delta(TS_1 - U) \geq 0$ , and therefore

$$\delta(U_1 - TS_1) = \delta F_1 \leq 0 \quad (1.34)$$

At constant temperature and volume, the equilibrium state has minimum Helmholtz free energy.

Again, as above, in considering the equilibrium state of a system at constant temperature and pressure, we construct a closed system which consists of the system (subsystem 1) under consideration and a thermal reservoir (subsystem 2) with temperature  $T$ . When the two systems are brought into thermal contact, energy is exchanged between subsystem 1 and subsystem 2. Because the whole system is a closed system,  $\delta S = \delta S_1 + \delta S_2 \geq 0$ . But now, for system 2, because the volume is not fixed, and mechanical work is involved,  $\delta U_2 = T\delta S_2 - P\delta V_2$ , i.e.,  $\delta S_2 = (\delta U_2 + P\delta V_2) / T$ . Because  $\delta U_2 = -\delta U_1$  and  $\delta V_2 = -\delta V_1$ , then  $\delta S = \delta S_1 + (\delta U_2 + P\delta V_2) / T = \delta S_1 - (\delta U_1 + P\delta V_1) / T = (1/T)\delta(TS_1 - U_2 - PV_1) \geq 0$ . Therefore

$$\delta(U_1 + PV_1 - TS_1) = \delta G_1 \leq 0 \quad (1.35)$$

At constant temperature and pressure, the equilibrium state has minimum Gibbs free energy. If electric energy is involved, then we have to consider the electric work done to the system by external sources such as a battery. In a thermodynamic process, if the electric work done to the system is  $dW_e$ , then

$$\delta S \geq \frac{dQ}{T} = \frac{dU - dW_m - dW_e}{T} = \frac{dU + PdV - dW_e}{T}$$

Therefore at constant temperature and pressure

$$\delta(U - W_e + PV - TS) = \delta(G - W_e) \leq 0 \quad (1.36)$$

In the equilibrium state,  $G - W_e$  is minimized.

### 1.3 Orientational Order

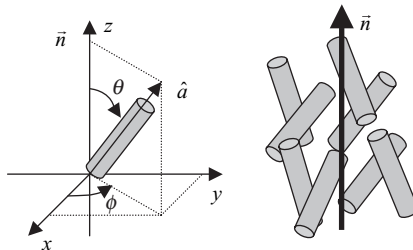
Orientational order is the most important feature of liquid crystals. The average directions of the long axes of the rod-like molecules are parallel to each other. Because of the orientational order, liquid crystals possess anisotropic physical properties; that is, in different directions, they have different responses to external fields such as an electric field, a magnetic field, and shear. In this section, we will discuss how to quantitatively specify orientational order and why rod-like molecules tend to be parallel to each other.

For a rigid elongated liquid crystal molecule, three axes can be attached to it to describe its orientation. One is the long molecular axis and the other two are perpendicular to the long molecular axis. Usually the molecule rotates rapidly around the long molecular axis. Although the molecule is not cylindrical, if there is no hindrance to the rotation in the nematic phase, the rapid rotation around the long molecular axis makes it behave like a cylinder. There is no preferred direction for the short axes and thus the nematic liquid crystal is usually uniaxial. If there is hindrance to the rotation, the liquid crystal is biaxial. A biaxial nematic liquid crystal is a long sought for material. The lyotropic biaxial nematic phase has been observed [12]. The existence of a thermotropic biaxial nematic phase is still under debate, and it may exist in bent-core molecules [13,14]. Here our discussion is on bulk liquid crystals. The rotational symmetry around the long molecular axis can be broken by confinement. In this book, we will deal with uniaxial liquid crystals consisting of rod-like molecules unless otherwise stated.

#### 1.3.1 Orientational order parameter

In uniaxial liquid crystals, we have only to consider the orientation of the long molecular axis. The orientation of a rod-like molecule can be represented by a unit vector  $\hat{a}$  which is attached to the molecule and parallel to the long molecular axis. In the nematic phase, the average directions of the long molecular axes are along a common direction: namely, the liquid crystal director denoted by the unit vector  $\vec{n}$ . The 3-D orientation of  $\hat{a}$  can be specified by the polar angle  $\theta$  and the azimuthal angle  $\phi$  where the  $z$  axis is chosen parallel to  $\vec{n}$  as shown in Figure 1.4. In general the orientational order of  $\hat{a}$  is specified by an orientational distribution function  $f(\theta, \phi)$ .  $f(\theta, \phi)d\Omega$  ( $d\Omega = \sin\theta d\theta d\phi$ ) is the probability that  $\hat{a}$  is oriented along the direction specified by  $\theta$  and  $\phi$  within the solid angle  $d\Omega$ . In the isotropic phase,  $\hat{a}$  has equal probability of pointing in any direction and therefore  $f(\theta, \phi) = \text{constant}$ . For uniaxial liquid crystals, there is no preferred orientation in the azimuthal direction, and then  $f = f(\theta)$  which depends only on the polar angle  $\theta$ .

Rod-like liquid crystal molecules may have permanent dipole moments. If the dipole moment is perpendicular to the long molecular axis, the dipole has equal probability of pointing along any direction because of the rapid rotation around the long molecular axis in uniaxial liquid crystal phases. The dipoles of the molecules cannot generate spontaneous polarization. If the permanent dipole moment is along the



**Figure 1.4** Schematic diagram showing the orientation of rod-like molecules

long molecular axis, the flip of the long molecular axis is much slower (of the order of  $10^{-5}$  s), so the above argument does not hold. In order to see the orientation of the dipoles in this case, we consider the interaction between two dipoles [15]. When one dipole is on top of the other, if they are parallel, the interaction energy is low and thus parallel orientation is preferred. When two dipoles are side by side, if they are anti-parallel, the interaction energy is low and thus anti-parallel orientation is preferred. As we know, the molecules cannot penetrate each other. For elongated molecules, the distance between two dipoles when they are on top of each other is farther than that when they are side by side. The interaction energy between two dipoles is inversely proportional to the cubic power of the distance between them. Therefore anti-parallel orientation of dipoles is dominant in rod-like molecules. There are the same number of dipoles aligned parallel to the liquid crystal director  $\vec{n}$  as there are aligned anti-parallel to  $\vec{n}$ . The permanent dipole along the long molecular axis cannot generate spontaneous polarization. Thus, even when the molecules have a permanent dipole moment along the long molecular axes, they can be regarded as cylinders whose top and bottom are the same. It can also be concluded that  $\vec{n}$  and  $-\vec{n}$  are equivalent.

An order parameter must be defined in order to quantitatively specify the orientational order. The order parameter is usually defined in such a way that it is zero in the high-temperature unordered phase and non-zero in the low-temperature ordered phase. By analogy with ferromagnetism, we may consider the average value of the projection of  $\hat{a}$  along the director  $\vec{n}$ , i.e.,

$$\langle \cos \theta \rangle = \frac{\int_0^\pi \cos \theta f(\theta) \sin \theta d\theta}{\int_0^\pi f(\theta) \sin \theta d\theta} \quad (1.37)$$

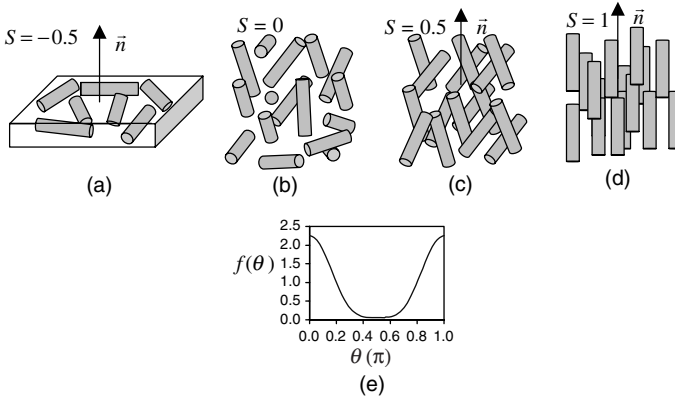
where  $\langle \rangle$  indicate the average (the temporal and spatial averages are the same) and  $\cos \theta$  is the first-order Legendre polynomial. In the isotropic phase, the molecules are randomly oriented and  $\langle \cos \theta \rangle = 0$ . We also know that in the nematic phase the probability that a molecule will orient at angles  $\theta$  and  $\pi - \theta$  is the same, i.e.,  $f(\theta) = f(\pi - \theta)$ ; therefore  $\langle \cos \theta \rangle = 0$ , and so  $\langle \cos \theta \rangle$  provides no information about the orientational order parameter. Next, let us consider the average value of the second-order Legendre polynomial for the order parameter:

$$S = \langle P_2(\cos \theta) \rangle = \left\langle \frac{1}{2}(3 \cos^2 \theta - 1) \right\rangle = \frac{\int_0^\pi \frac{1}{2}(3 \cos^2 \theta - 1) f(\theta) \sin \theta d\theta}{\int_0^\pi f(\theta) \sin \theta d\theta} \quad (1.38)$$

In the isotropic phase as shown in Figure 1.5(b),  $f(\theta) = c$ , a constant, and

$$\int_0^\pi \frac{1}{2}(3 \cos^2 \theta - 1) f(\theta) \sin \theta d\theta = \int_0^\pi \frac{1}{2}(3 \cos^2 \theta - 1) c \sin \theta d\theta = 0$$

In the nematic phase,  $f(\theta)$  depends on  $\theta$ . For a perfectly ordered nematic phase as shown in Figure 1.5(d),  $f(\theta) = \delta(\theta)$ , where  $\sin \theta \delta(\theta) = \infty$  when  $\theta = 0$ ,  $\sin \theta \delta(\theta) = 0$  when  $\theta \neq 0$ , and  $\int_0^\pi \delta(\theta) \sin \theta d\theta = 1$ , and the order parameter is  $S = \frac{1}{2}(3 \cos^2 \theta - 1) = 1$ . It should be pointed out that the order parameter can be positive or negative. Two order parameters with the same absolute value but different signs correspond to different states. When the molecules all lie in a plane but are randomly oriented in the plane as shown in Figure 1.5(a), the distribution function is  $f(\theta) = \delta(\theta - \pi/2)$ , where  $\delta(\theta - \pi/2) = \infty$  when  $\theta = \pi/2$ ,  $\delta(\theta - \pi/2) = 0$  when  $\theta \neq \pi/2$ , and  $\int_0^\pi \delta(\theta - \pi/2) \sin \theta d\theta = 1$ , and the order parameter is  $S = \frac{1}{2}[3 \cos^2(\pi/2) - 1]/1 = -0.5$ . In this case, the average direction of the molecules



**Figure 1.5** Schematic diagram showing the states with different orientational order parameters

is not well defined. The director  $\vec{n}$  is defined by the direction of the uniaxial axis of the material. Figure 1.5(c) shows the state with the distribution function  $f(\theta) = (35/16)[\cos^4\theta + (1/35)]$ , which is plotted vs.  $\theta$  in Figure 1.5(e). The order parameter is  $S = 0.5$ . Many anisotropies of physical properties are related to the order parameter and will be discussed later.

### 1.3.2 Landau–de Gennes theory of orientational order in the nematic phase

Landau developed a theory for second-order phase transitions [16], such as those from the diamagnetic phase to the ferromagnetic phase, in which the order parameter increases continuously from zero as the temperature is decreased across the transition temperature  $T_c$  from the high-temperature disordered phase to the low temperature ordered phase. For a temperature near  $T_c$ , the order is very small. The free energy of the system can be expanded in terms of the order parameter.

The transition from water to ice at 1 atmosphere pressure is a first-order transition and the latent heat is about 100 J/g. The isotropic–nematic transition is a weak first-order transition because the order parameter changes discontinuously across the transition but the latent heat is only about 10 J/g. De Gennes extended Landau’s theory to the isotropic–nematic transition because it is a weak first-order transition [1, 17]. The free energy density  $f$  of the material can be expressed in terms of the order parameter  $S$  as

$$f = \frac{1}{2}a(T - T^*)S^2 - \frac{1}{3}bS^3 + \frac{1}{4}cS^4 + \frac{1}{2}L(\nabla S)^2 \quad (1.39)$$

where  $a, b, c$  and  $L$  are constants and  $T^*$  is the virtual second-order phase transition temperature. The last term is the energy cost when there is a variation of the order parameter in space, but here we will consider only the uniform order parameter case. There is no linear term of  $S$ , which would result in a non-zero order parameter at any temperature;  $a$  is positive, otherwise  $S$  will never be zero and the isotropic phase will not be stable at any temperature. A significant difference between the free energy here and that of a magnetic system is the cubic term. In a magnetic system, the magnetization  $m$  is the order parameter. For a given value of  $|m|$ , there is only one state, and the sign of  $m$  is decided by the choice of the coordinate. The free energy must be the same for a positive  $m$  and a negative  $m$ , and therefore the coefficient of the cubic term must be zero. For nematic liquid crystals, positive and negative values of the order parameter  $S$  correspond to two different states and the corresponding free energies can be different, and therefore  $b$  is not zero;  $b$  must be positive because at sufficiently low temperatures positive order parameters have

global minimum free energies. We also know that the maximum value of  $S$  is 1. The quadratic term with a positive  $c$  prevents  $S$  from exploding. The values of the coefficients can be estimated in the following way: the energy of the intermolecular interaction between the molecules associated with orientation is about 0.1 eV and the molecular size is about 1 nm,  $f$  is the energy per unit volume, and therefore  $Ta$  (or  $b$  or  $c$ )  $\sim 0.1$  eV/volume of 1 molecule  $\sim 0.1 \times 10^{-19}$  joules/ $(10^{-9} \text{ m})^3 \sim 10^7$  J/m<sup>3</sup>. For a given temperature, the order parameter  $S$  is found by minimizing  $f$ :

$$\frac{\partial f}{\partial S} = a(T - T^*)S - bS^2 + cS^3 = [a(T - T^*) - bS + cS^2]S = 0 \quad (1.40)$$

There are three solutions:

$$\begin{aligned} S_1 &= 0 \\ S_2 &= \frac{1}{2c} \left[ b + \sqrt{b^2 - 4ac(T - T^*)} \right] \\ S_3 &= \frac{1}{2c} \left[ b - \sqrt{b^2 - 4ac(T - T^*)} \right] \end{aligned}$$

$S_1 = 0$  corresponds to the isotropic phase and the free energy is  $f_1 = 0$ . The isotropic phase has global minimum free energy at a high temperature. It will be shown that at a low temperature  $S_2$  has global minimum free energy

$$f_2 = \frac{1}{2}a(T - T^*)S_2^2 - \frac{1}{3}bS_2^3 + \frac{1}{4}cS_2^4$$

$S_3$  has a local minimum free energy. At the nematic–isotropic phase transition temperature  $T_{NI}$ , the order parameter is  $S_c = S_{2c}$ , and  $f_2(S_2 = S_c) = f_1 = 0$ ; that is,

$$\frac{1}{2}a(T_{NI} - T^*)S_c^2 - \frac{1}{3}bS_c^3 + \frac{1}{4}cS_c^4 = 0 \quad (1.41)$$

From Equation (1.40), at this temperature, we also have

$$a(T_{NI} - T^*) - bS_c + cS_c^2 = 0 \quad (1.42)$$

From these two equations, we can obtain

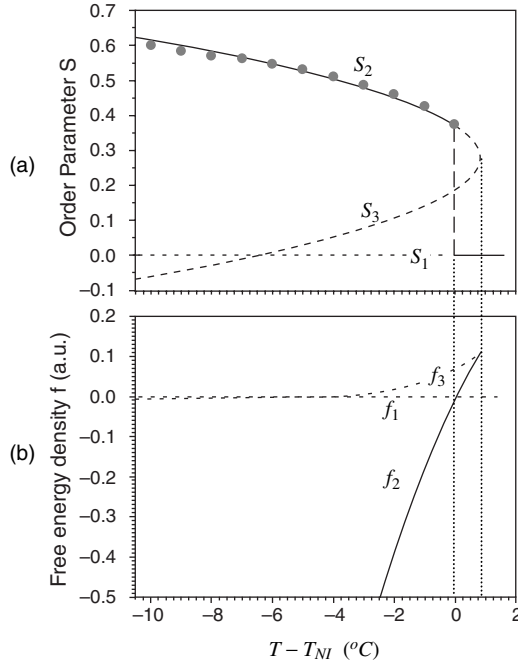
$$a(T_{NI} - T^*) - \frac{1}{3}bS_c = 0$$

Therefore

$$S_c = \frac{3a}{b}(T_{NI} - T^*) \quad (1.43)$$

Substituting Equation (1.43) into Equation (1.42), we get the transition temperature

$$T_{NI} = T^* + \frac{2b^2}{9ac} \quad (1.44)$$



**Figure 1.6** (a) The three solutions of order parameter as a function of temperature; (b) the corresponding free energies as a function of temperature, in Landau-de Gennes theory

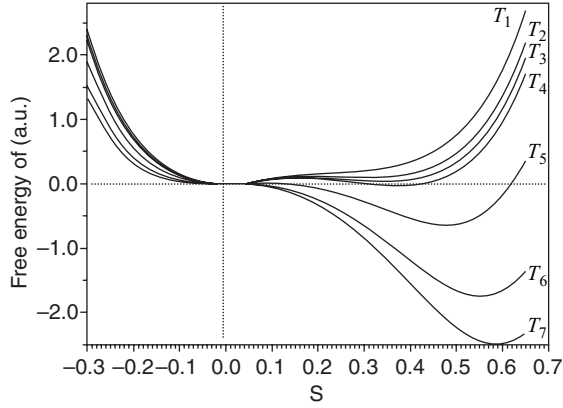
and the order parameter at the transition temperature

$$S_c = \frac{2b}{3c} \tag{1.45}$$

For liquid crystal 5CB, the experimentally measured order parameter is shown by the solid circles in Figure 1.6(a) [6]. In fitting the data, the following parameters were used:  $a = 0.023\sigma \text{ J/Km}^3$ ,  $b = 1.2\sigma \text{ J/m}^3$ , and  $c = 2.2\sigma \text{ J/m}^3$ , where  $\sigma$  is a constant which has to be determined by the latent heat of the nematic–isotropic transition.

Because  $S$  is a real number in the region from  $-0.5$  to  $1.0$ , when  $T - T^* > b^2/4ac$ , i.e., when  $T - T_{NI} > b^2/4ac - 2b^2/9ac = b^2/36ac$ ,  $S_2$  and  $S_3$  are not real. The only real solution is  $S = S_1 = 0$ , corresponding to the isotropic phase. When  $T - T_{NI} < b^2/36ac$ , there are three solutions. However, when  $0 < T - T_{NI} \leq b^2/36ac$ , the isotropic phase is the stable state because its free energy is still the global minimum as shown in Figure 1.6(b). When  $T - T_{NI} \leq 0$ , the nematic phase with order parameter  $S = S_2 = \left[ b + \sqrt{b^2 - 4ac(T - T^*)} \right] / 2c$  is the stable state because its free energy is the global minimum.

In order to see the physical meaning clearly, let us plot  $f$  vs.  $S$  at various temperatures as shown in Figure 1.7. At temperature  $T_1 = T_{NI} + b^2/36ac + 1.0^\circ\text{C}$ , the curve has only one minimum at  $S = 0$ , which means that  $S_1 = 0$  is the only solution and the corresponding isotropic phase is the stable state. At temperature  $T_3 = T_{NI} + b^2/36ac - 0.5^\circ\text{C}$ , there are two local minima and one local maximum, where there are three solutions:  $S_1 = 0$ ,  $S_2 > 0$ , and  $S_3 > 0$ .  $S_1 = 0$  corresponds to the global minimum free energy and the isotropic phase is still the stable state. At  $T_4 = T_{NI}$ , the free energies of the isotropic phase with order parameter  $S_1$  and the nematic phase with order parameter  $S_2$  become the same; phase



**Figure 1.7** Free energy vs. order parameter at various temperatures in Landau-de Gennes theory

transition takes place and the order parameter changes discontinuously from 0 to  $S_c = 2b/3c$ . This is a first-order transition. It can be seen from the figure that at this temperature there is an energy barrier between  $S_1$  and  $S_2$ . If the system is initially in the isotropic phase and there are no means to overcome the energy barrier, it will remain in the isotropic phase at this temperature. As the temperature is decreased, the energy barrier is lowered. At  $T_5 = T_{NI} - 3^\circ\text{C}$ , the energy barrier is low. At  $T_6 = T^*$ , the second-order derivative of  $f$  with respect to  $S$  at  $S_1 = 0$  is

$$\left. \frac{\partial^2 f}{\partial S^2} \right|_{S=0} = a(T - T^*) - 2bS + 3cS^2 \Big|_{S=0} = a(T - T^*) = 0$$

$S_1$  is no longer a local minimum, and the energy barrier disappears.  $T^*$  is therefore the supercooling temperature below which the isotropic phase becomes absolutely unstable. At this temperature,  $S_1 = S_3$ . At  $T_7 = T^* - 2^\circ\text{C}$ , there are two minima located at  $S_2 (> 0)$  and  $S_3 (< 0)$  (the minimum value is slightly below zero), and a maximum at  $S_1 = 0$ .

If initially the system is in the nematic phase, it will remain in this phase even at temperatures higher than  $T_{NI}$  and its free energy is higher than that of the isotropic phase because there is an energy barrier preventing the system from transforming from the nematic phase to the isotropic phase. The temperature  $T_2$  (superheating temperature) at which the nematic phase becomes absolutely unstable can be found from

$$\left. \frac{\partial^2 f}{\partial S^2} \right|_{S_2} = a(T_2 - T^*) - 2bS_2 + 3cS_2^2 = 0 \quad (1.46)$$

Using  $S_2 = (1/2c)[b + \sqrt{b^2 - 4ac(T_2 - T^*)}]$ , we can get  $T_2 = T_{NI} + b^2/36ac$ .

In reality, there are usually irregularities, such as impurities and defects, which can reduce the energy barrier of nematic–isotropic transition. The phase transition takes place before the thermodynamic instability limits (the supercooling or superheating temperature). Under an optical microscope, it is usually observed that with decreasing temperature nematic ‘islands’ are initiated by irregularities and grow out of the isotropic ‘sea’, and with increasing temperature isotropic ‘lakes’ are produced by irregularities and grow on the nematic ‘land’. The irregularities are called nucleation seeds and the transition is a nucleation process. In summary, nematic–isotropic transition is a first-order transition and the order parameter changes discontinuously, there is an energy barrier in the transition, and the

transition is a nucleation process; superheating and supercooling occur. In a second-order transition, there is no energy barrier and the transition occurs simultaneously everywhere at the transition temperature (the critical temperature).

There are a few points worth mentioning in Landau–de Gennes theory. First, the theory works well at temperatures near the transition temperature. At temperatures far below the transition temperature, however, the order parameter increases without limit with decreasing temperature, and the theory does not work well because the maximum order parameter should be 1. In Figure 1.6, the parameters are chosen in such a way that the fitting is good for a relatively wide temperatures region,  $T_{NI} - T^* = 2b^2/9ac = 6.3^\circ\text{C}$ , which is much larger than the value ( $\sim 1^\circ\text{C}$ ) measured by light-scattering experiments in the isotropic phase [18]. There are fluctuations in orientational order in the isotropic phase, which results in a variation of refractive index in space and causes light scattering. The intensity of the scattered light is proportional to  $1/(T - T^*)$ .

### 1.3.3 Maier–Saupe theory

In the nematic phase, there are interactions, such as the van der Waals interaction, between the liquid crystal molecules. Because the molecular polarizability along the long molecular axis is larger than along the short transverse molecular axis, the interaction is anisotropic and results in the parallel alignment of the rod-like molecules. In the spirit of the mean field approximation, Maier and Saupe introduced an effective single molecule potential  $V$  to describe the intermolecular interaction [19, 20]. The potential has the following properties. (1) It must be a minimum when the molecule orients along the liquid crystal director (the average direction of the long molecular axis of the molecules). (2) Its strength is proportional to the order parameter  $S = \langle P_2(\cos \theta) \rangle$  because the potential well is deep when the molecules are highly orientationally ordered and vanishes when the molecules are disordered. (3) It assures that the probabilities for the molecules pointing up and down are the same. The potential in Maier–Saupe theory is given by

$$V(\theta) = -\nu S \left( \frac{3}{2} \cos^2 \theta - \frac{1}{2} \right) \quad (1.47)$$

where  $\nu$  is the orientational interaction constant of the order of 0.1 eV and  $\theta$  is the angle between the long molecular axis and the liquid crystal director as shown in Figure 1.4. The probability  $f$  of the molecule orienting along the direction with polar angle  $\theta$  is governed by the Boltzmann distribution:

$$f(\theta) = \frac{e^{-V(\theta)/k_B T}}{\int_0^\pi e^{-V(\theta)/k_B T} \sin \theta d\theta} \quad (1.48)$$

The single molecule partition function is

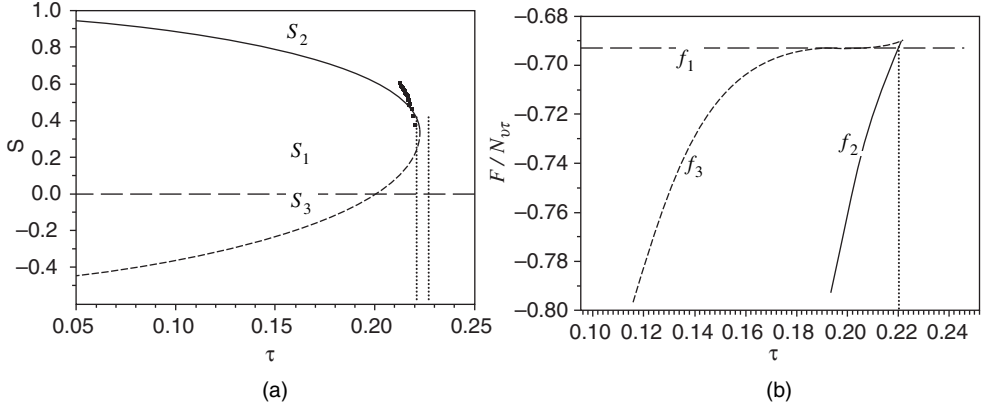
$$Z = \int_0^\pi e^{-V(\theta)/k_B T} \sin \theta d\theta \quad (1.49)$$

From the orientational distribution function we can calculate the order parameter:

$$S = \frac{1}{Z} \int_0^\pi P_2(\cos \theta) e^{-V(\theta)/k_B T} \sin \theta d\theta = \frac{1}{Z} \int_0^\pi P_2(\cos \theta) e^{\nu S P_2(\theta)/k_B T} \sin \theta d\theta \quad (1.50)$$

We introduce a normalized temperature  $\tau = k_B T/\nu$ . For a given value of  $\tau$ , the order parameter  $S$  can be found by numerically solving Equation (1.50). An iteration method can be used for the numerical calculation of the order parameter: (1) choose an initial value for the order parameter, (2) substitute it





**Figure 1.8** (a) The three solutions of order parameter as a function of the normalized temperature in Maier–Saupe theory. The solid circles represent the experimental data. (b) The normalized free energies of the three solutions of the order parameter

into the right hand side of Equation (1.50), and (3) calculate the order parameter. Use the newly obtained order parameter to repeat the above process until a stable value is obtained. As shown in Figure 1.8(a), there are three solutions:  $S_1$ ,  $S_2$ , and  $S_3$ . In order to determine which is the actual solution, we have to examine the corresponding free energies. The free energy  $F$  has two parts,  $F = U - TE_n$ , where  $U$  is the intermolecular interaction energy and  $E_n$  is the entropy. The single molecular potential describes the interaction energy between one liquid crystal molecule and the remaining molecules of the system. The interaction energy of the system with  $N$  molecules is given by

$$U = \frac{1}{2}N\langle V \rangle = \frac{N}{2Z} \int_0^\pi V(\theta) e^{-V(\theta)/k_B T} \sin \theta d\theta \quad (1.51)$$

where the factor  $\frac{1}{2}$  avoids counting the intermolecular interaction twice. The entropy is calculated by using Equation (1.32):

$$En = -Nk_B \langle \ln f \rangle = -\frac{Nk_B}{Z} \int_0^\pi \ln[f(\theta)] e^{-V(\theta)/k_B T} \sin \theta d\theta \quad (1.52)$$

From Equation (1.48) we have  $\ln[f(\theta)] = -V(\theta)/k_B T - \ln Z$ ; therefore  $En = (N/T)\langle V \rangle + Nk_B \ln Z$  and the free energy is

$$F = U - TE_n = -Nk_B T \ln Z - \frac{1}{2}N\langle V \rangle \quad (1.53)$$

From Equation (1.47) we have  $\langle V \rangle = -vS^2$  and therefore

$$F = U - TE_n = -Nk_B T \ln Z + \frac{1}{2}NvS^2 \quad (1.54)$$

Although the second term in this equation looks abnormal, this equation is correct and can be checked by calculating the derivative of  $F$  with respect to  $S$ :

$$\frac{\partial F}{\partial S} = -Nk_B T \frac{\partial \ln Z}{\partial S} - \frac{1}{2}N \frac{\partial \langle V \rangle}{\partial S} = -\frac{Nk_B T}{Z} \frac{\partial Z}{\partial S} + NvS$$

Letting  $\partial F/\partial S = 0$ , we have

$$S = \frac{k_B T}{vZ} \frac{\partial Z}{\partial S} = \frac{k_B T}{vZ} \int_0^\pi \frac{-1}{k_B T} \frac{\partial V}{\partial S} e^{-V(\theta)/k_B T} \sin \theta d\theta = \frac{1}{Z} \int_0^\pi P_2(\cos \theta) e^{vSP_2(\theta)/k_B T} \sin \theta d\theta$$

which is consistent with Equation (1.50). The free energies corresponding to the solutions are shown in Figure 1.8(b). The nematic–isotropic phase transition temperature is  $\tau_{NI} = 0.22019$ . For temperatures higher than  $\tau_{NI}$ , the isotropic phase with order parameter  $S = S_1 = 0$  has a lower free energy and thus is stable. For temperatures lower than  $\tau_{NI}$ , the nematic phase with order parameter  $S = S_2$  has a lower free energy and thus is stable. The order parameter jumps from 0 to  $S_c = 0.4289$  at the transition.

In the Maier–Saupe theory there are no fitting parameters. The predicted order parameter as a function of temperature is universal, and agrees qualitatively, but not quantitatively, with experimental data. This indicates that higher order terms are needed in the single molecule potential, i.e.,

$$V(\theta) = \sum_i [-v_i \langle P_i(\cos \theta) \rangle P_i(\cos \theta)] \quad (1.55)$$

where  $P_i(\cos \theta)$  ( $i = 2, 4, 6, \dots$ ) are the  $i$ th-order Legendre polynomials. The fitting parameters are  $v_i$ . With higher order terms, better agreement with experimental results can be achieved.

Maier–Saupe theory is very useful in considering liquid crystal systems consisting of more than one type of molecule, such as mixtures of nematic liquid crystals and dichroic dyes. The interactions between different molecules are different and the constituent molecules have different order parameters.

All the theories discussed above do not predict well the orientational order parameter for temperatures far below  $T_{NI}$ . The order parameter as a function of temperature is better described by the empirical formula [21]

$$S = \left( 1 - \frac{0.98TV^2}{T_{NI}V_{NI}^2} \right)^{0.22} \quad (1.56)$$

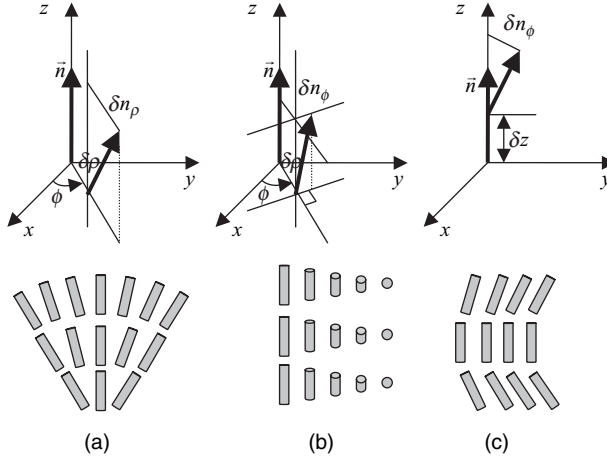
where  $V$  and  $V_{NI}$  are the molar volumes at  $T$  and  $T_{NI}$ , respectively.

## 1.4 Elastic Properties of Liquid Crystals

In the nematic phase, the liquid crystal director  $\vec{n}$  is uniform in space in the ground state. In reality, the liquid crystal director  $\vec{n}$  may vary spatially because of confinement or external fields. This spatial variation of the director, called the deformation of the director, costs energy. When the variation occurs over a distance much larger than the molecular size, the orientational order parameter does not change and the deformation can be described by a continuum theory analogous to the classic elastic theory of a solid. The elastic energy is proportional to the square of the spatial variation rate.

### 1.4.1 Elastic properties of nematic liquid crystals

There are three possible deformation modes of the liquid crystal director as shown in Figure 1.9. We choose the cylindrical coordinate such that the  $z$  axis is parallel to the director at the origin of the coordinate:  $\vec{n}(0) = \hat{z}$ . Consider the variation of the director at an infinitely small distance from the origin. When moving in the radial direction, there are two possible modes of variation: (1) the director tilts toward the radial direction  $\hat{\rho}$  as shown in Figure 1.9(a), and (2) the director tilts toward the azimuthal



**Figure 1.9** The three possible deformations of the liquid crystal director: (a) splay; (b) twist; and (c) bend

direction  $\hat{\phi}$  as shown in Figure 1.9(b). The first mode is called splay, where the director at  $(\delta\rho, \phi, z = 0)$  is

$$\vec{n}(\delta\rho, z = 0) = \delta n_\rho(\delta\rho)\hat{\rho} + [1 + \delta n_z(\delta\rho)]\hat{z} \quad (1.57)$$

where  $\delta n_\rho \ll 1$  and  $\delta n_z \ll 1$ . Because  $|\vec{n}|^2 = n_\rho^2 + n_\phi^2 + n_z^2 = (\delta n_\rho)^2 + (1 + \delta n_z)^2 = 1$ , then  $\delta n_z = -(\delta n_\rho)^2/2$ , where  $\delta n_z$  is a higher order term and can be neglected. The spatial variation rate is  $\partial n_\rho/\partial\rho$  and the corresponding elastic energy is

$$f_{\text{splay}} = (1/2)K_{11}(\partial n_\rho/\partial\rho)^2 \quad (1.58)$$

where  $K_{11}$  is the splay elastic constant.

The second mode is called twist, where the director at  $(\delta\rho, \phi, z = 0)$  is

$$\vec{n}(\delta\rho, \phi, z = 0) = \delta n_\phi(\delta\rho)\hat{\phi} + [1 + \delta n_z(\delta\rho)]\hat{z} \quad (1.59)$$

where  $\delta n_\phi \ll 1$  and  $\delta n_z = -(\delta n_\phi)^2/2$ , a higher order term which can be neglected. The spatial variation rate is  $\partial n_\phi/\partial\rho$  and the corresponding elastic energy is

$$f_{\text{twist}} = (1/2)K_{22}(\partial n_\phi/\partial\rho)^2 \quad (1.60)$$

where  $K_{22}$  is the twist elastic constant.

When moving in the  $z$  direction, there is only one possible mode of variation, as shown in Figure 1.9(c), which is called bend. The director at  $(\rho = 0, \phi, \delta z)$  is

$$\vec{n}(\rho = 0, \phi, \delta z) = \delta n_\rho(\delta z)\hat{\rho} + [1 + \delta n_z(\delta z)]\hat{z} \quad (1.61)$$

where  $\delta n_\rho \ll 1$  and  $\delta n_z = -(\delta n_\rho)^2/2$ , a higher order term which can be neglected.

Note that when  $\rho = 0$ , the azimuthal angle is not well defined and we can choose the coordinate such that the director tilts toward the radial direction. The corresponding elastic energy is

$$f_{bend} = (1/2)K_{33}(\partial n_\rho/\partial z)^2 \quad (1.62)$$

where  $K_{33}$  is the bend elastic constant. Because  $\delta n_z$  is a higher order term,  $\partial n_z/\partial z \approx 0$  and  $\partial n_z/\partial \rho \approx 0$ . Recall that  $\nabla \cdot \vec{n}|_{\rho=0, z=0} = (1/\rho)\partial(\rho n_\rho)/\partial \rho + (1/\rho)\partial n_\phi/\partial \phi + \partial n_z/\partial z = \partial n_\rho/\partial \rho + \delta n_\rho$ . Because  $\partial n_\rho/\partial \rho$  is finite and  $\delta n_\rho \ll 1$ ,  $\nabla \cdot \vec{n}|_{\rho=0, z=0} = \partial n_\rho/\partial \rho$ . The splay elastic energy can be expressed as  $f_{splay} = (1/2)K_{11}(\nabla \cdot \vec{n})^2$ . Because  $\vec{n} = \hat{z}$ , at the origin  $\vec{n} \cdot \nabla \times \vec{n}|_{\rho=0, z=0} = (\nabla \times \vec{n})_z = \partial n_\phi/\partial \rho$ . The twist elastic energy can be expressed as  $f_{twist} = (1/2)K_{22}(\vec{n} \cdot \nabla \times \vec{n})^2$ . Because  $\vec{n} \times \nabla \times \vec{n}|_{\rho=0, z=0} = (\nabla \times \vec{n})_\rho - (\nabla \times \vec{n})_\phi = \partial n_\rho/\partial z$ , the bend elastic energy can be expressed as  $f_{bend} = (1/2)K_{33}(\vec{n} \times \nabla \times \vec{n})^2$ . Putting all the three terms together, we obtain the elastic energy density:

$$f_{ela} = \frac{1}{2}K_{11}(\nabla \cdot \vec{n})^2 + \frac{1}{2}K_{22}(\vec{n} \cdot \nabla \times \vec{n})^2 + \frac{1}{2}K_{33}(\vec{n} \times \nabla \times \vec{n})^2 \quad (1.63)$$

This elastic energy is often referred to as the *Oseen–Frank energy* and  $K_{11}$ ,  $K_{22}$ , and  $K_{33}$  are referred to as the Frank elastic constants because of his pioneering work on the elastic continuum theory of liquid crystals [22]. The value of the elastic constants can be estimated in the following way. When a significant variation of the director occurs in a length  $L$ , the angle between the average directions of the long molecular axes of two neighboring molecules is  $(a/L)$ , where  $a$  is the molecular size. When the average directions of the long molecular axes of two neighboring molecules are parallel, the intermolecular interaction energy between them is a minimum. When the average direction of their long molecular axes makes an angle of  $(a/L)$ , the intermolecular interaction energy increases to  $(a/L)^2 u$ , where  $u$  is the intermolecular interaction energy associated with orientation and is about 0.1 eV. The increase of the interaction energy is the elastic energy, i.e.,

$$\left(\frac{a}{L}\right)^2 u = K_{ii}(\nabla \vec{n})^2 \times \text{molecular volume} = K_{ii} \left(\frac{1}{L}\right)^2 a^3$$

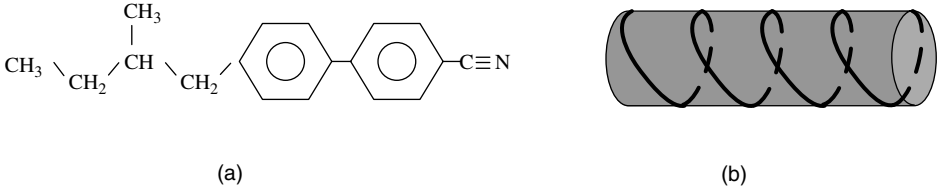
Therefore

$$K_{ii} = \frac{u}{a} \sim 0.1 \times 10^{-19} \frac{\text{J}}{1 \text{ nm}} = 10^{-11} \text{ N}$$

Experiments show that usually the bend elastic constant  $K_{33}$  is the largest and the twist elastic constant  $K_{22}$  is the smallest. As an example, at room temperature the liquid crystal 5CB has these elastic constants:  $K_{11} = 0.64 \times 10^{-11} \text{ N}$ ,  $K_{22} = 0.3 \times 10^{-11} \text{ N}$ , and  $K_{33} = 1 \times 10^{-11} \text{ N}$ .

The elastic constants are temperature dependent. As shown in Maier–Saue theory, the intermolecular interaction energy  $u$  (the averaged value of the potential given by Equation (1.47) is proportional to the square of the orientational order parameter  $S$ . Therefore the elastic constants are proportional to  $S^2$ .

It is usually sufficient to consider the splay, twist, and bend deformations of the liquid crystal director in determining the configuration of the director, except in some cases where the surface to volume ratio is high and another two terms, called divergence terms (or surface terms), may have to be considered. The elastic energy density of these terms is given by  $f_{13} = K_{13}\nabla \cdot (\vec{n}\nabla \cdot \vec{n})$  and  $f_{24} = -K_{24}\nabla \cdot (\vec{n}\nabla \cdot \vec{n} + \vec{n} \times \nabla \times \vec{n})$ , respectively [23]. The volume integral of these two terms can be changed to a surface integral because of the Gauss theorem.



**Figure 1.10** (a) Chemical structure of a typical chiral liquid crystal molecule; (b) physical model of a chiral liquid crystal molecule

#### 1.4.2 Elastic properties of cholesteric liquid crystals

So far we have considered liquid crystals consisting of molecules with reflectional symmetry. The molecules are the same as their mirror images, and are called *achiral* molecules. The liquid crystal 5CB shown in Figure 1.1(a) is an example of an achiral molecule. Now we consider liquid crystals consisting of molecules without reflectional symmetry. The molecules are different from their mirror images and are called *chiral* molecules. Such an example is CB15 shown in Figure 1.10(a). It can be regarded as a screw, instead of a rod, in considering its physical properties. After considering the symmetry where  $\vec{n}$  and  $-\vec{n}$  are equivalent, the generalized elastic energy density is

$$f_{ela} = \frac{1}{2}K_{11}(\nabla \cdot \vec{n})^2 + \frac{1}{2}K_{22}(\vec{n} \cdot \nabla \times \vec{n} + q_o)^2 + \frac{1}{2}K_{33}(\vec{n} \times \nabla \times \vec{n})^2 \quad (1.64)$$

where  $q_o$  is the *chirality* and its physical meaning will be discussed in a moment. Note that  $\nabla \times \vec{n}$  is a pseudo-vector which does not change sign under reflectional symmetry while  $\vec{n} \cdot \nabla \times \vec{n}$  is a pseudo-scalar which changes sign under reflectional symmetry operation. Under reflectional symmetry operation, the elastic energy changes to

$$f'_{ela} = \frac{1}{2}K_{11}(\nabla \cdot \vec{n})^2 + \frac{1}{2}K_{22}(-\vec{n} \cdot \nabla \times \vec{n} + q_o)^2 + \frac{1}{2}K_{33}(-\vec{n} \times \nabla \times \vec{n})^2 \quad (1.65)$$

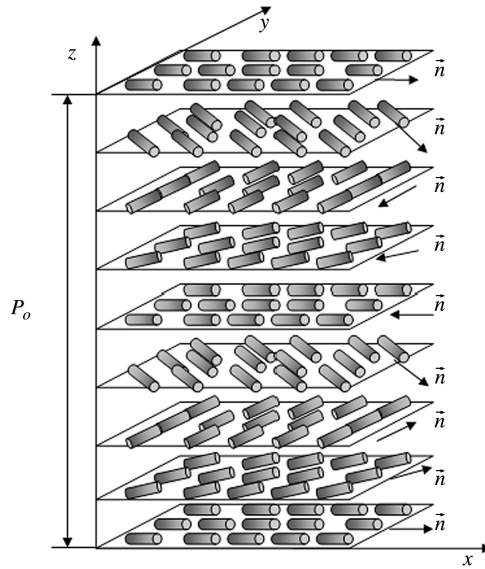
If the liquid crystal molecule is achiral and thus has reflectional symmetry, the system does not change and the elastic energy does not change under reflectional symmetry operation. It is required that  $f_{ela} = f'_{ela}$ ; then  $q_o = 0$ . When the liquid crystal is in the ground state with minimum free energy,  $f_{ela} = 0$ , which requires that  $\nabla \cdot \vec{n} = 0$ ,  $\vec{n} \cdot \nabla \times \vec{n} = 0$ , and  $\vec{n} \times \nabla \times \vec{n} = 0$ . This means that in the ground state, the liquid crystal director  $\vec{n}$  is uniformly aligned along one direction.

If the liquid crystal molecule is chiral and thus has no reflectional symmetry, the system changes under reflectional symmetry operation. The elastic energy may change. It is no longer required that  $f_{ela} = f'_{ela}$ , and thus  $q_o$  may not be zero. When the liquid crystal is in the ground state with minimum free energy,  $f_{ela} = 0$ , which requires that  $\nabla \cdot \vec{n} = 0$ ,  $\vec{n} \cdot \nabla \times \vec{n} = -q_o$ , and  $\vec{n} \times \nabla \times \vec{n} = 0$ . A director configuration which satisfies the above conditions is

$$n_x = \cos(q_o z), \quad n_y = \sin(q_o z), \quad n_z = 0 \quad (1.66)$$

and is schematically shown in Figure 1.11. The liquid crystal director twists in space. This type of liquid crystal is called a *cholesteric* liquid crystal. The axis around which the director twists is called the *helical axis* and is chosen to be parallel to  $z$  here. The distance  $P_o$  over which the director twists by  $360^\circ$  is called the *pitch* and is related to the chirality by

$$P_o = \frac{2\pi}{q_o} \quad (1.67)$$



**Figure 1.11** Schematic diagram of the director configuration of the cholesteric liquid crystal

Depending on the chemical structure, the pitch of a cholesteric liquid crystal could take any value in the region from a few tenths of a micron to infinitely long. The periodicity of a cholesteric liquid crystal with pitch  $P_o$  is  $P_o/2$  because  $\vec{n}$  and  $-\vec{n}$  are equivalent. Cholesteric liquid crystals are also called *chiral nematic* liquid crystals and denoted as  $N^*$ . Nematic liquid crystals can be considered as a special case of cholesteric liquid crystals with an infinitely long pitch.

In practice, a cholesteric liquid crystal is usually obtained by mixing a nematic host with a chiral dopant. The pitch of the mixture is given by

$$P = \frac{1}{(HTP) \cdot x} \tag{1.68}$$

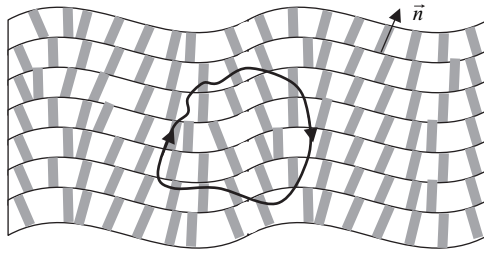
where  $x$  is the concentration of the chiral dopant and  $(HTP)$  is the *helical twisting power* of the chiral dopant, which is mainly determined by the chemical structure of the chiral dopant and depends only slightly on the nematic host.

### 1.4.3 Elastic properties of smectic liquid crystals

Smectic liquid crystals possess partial positional orders besides the orientational order exhibited in nematic and cholesteric liquid crystals. Here we only consider the simplest case: smectic-A. The elastic energy of the deformation of the liquid crystal director in smectic-A is the same as in the nematic liquid crystal. In addition, the dilatation (compression) of the smectic layer also costs energy which is given by [24]

$$f_{layer} = \frac{1}{2} B \left( \frac{d - d_o}{d_o} \right)^2 \tag{1.69}$$

where  $B$  is the elastic constant for the dilatation of the layer and is referred as to the Young modulus,  $d_o$  and  $d$  are the equilibrium layer thickness (the periodicity of the density undulation) and the actual layer



**Figure 1.12** Schematic diagram showing the deformation of the liquid crystal director and the smectic layer in the smectic-A liquid crystal

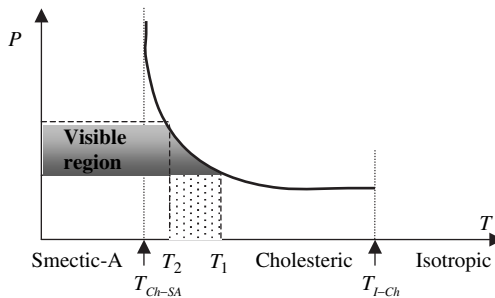
thickness of the smectic layer, respectively. Typical values of  $B$  are about  $10^6 - 10^7 \text{ J/m}^3$ , which are  $10^3$  to  $10^4$  smaller than those in a solid. In a slightly deformed smectic-A liquid crystal, we consider a closed loop as shown in Figure 1.12. The total number of layers traversed by the loop is zero, which can be mathematically expressed as  $\oint \vec{n} \cdot d\vec{l} = 0$ . Using the Stokes theorem, we have  $\int \nabla \times \vec{n} \cdot d\vec{s} = \oint \vec{n} \cdot d\vec{l} = 0$ . Therefore in smectic-A we have

$$\nabla \times \vec{n} = 0 \tag{1.70}$$

which assures that  $\vec{n} \cdot \nabla \times \vec{n} = 0$  and  $\vec{n} \times \nabla \times \vec{n} = 0$ . The consequence is that twist and bend deformations of the director are not allowed (because they change the layer thickness and cost too much energy). The elastic energy in a smectic-A liquid crystal is

$$f_{elas} = \frac{1}{2} K_{11} (\nabla \cdot \vec{n})^2 + \frac{1}{2} B \left( \frac{d - d_0}{d_0} \right)^2 \tag{1.71}$$

Some chiral liquid crystals, as the temperature is decreased, exhibit the mesophases isotropic  $\rightarrow$  cholesteric  $\rightarrow$  smectic-A. Because of the property shown by Equation (1.70), there is no spontaneous twist in smectic-A. Expressed another way, the pitch in smectic-A is infinitely long. In the cholesteric phase, as the temperature is decreased toward the cholesteric–smectic-A transition, there is a pretransitional phenomenon where the smectic-A order forms in short space-scale and time-scale due to thermal fluctuations. This effect causes the pitch of the cholesteric liquid crystal to increase with decreasing temperature and diverge at the transition temperature as shown in Figure 1.13. As will be discussed later, a cholesteric liquid crystal with pitch  $P$  exhibits Bragg reflection at the wavelength  $\lambda = \bar{n}P$ , where  $\bar{n}$  is the average refractive index of the material. If  $\lambda = \bar{n}P$  is in the visible light region,



**Figure 1.13** Schematic diagram showing how the pitch of a thermochromic cholesteric liquid crystal changes

the liquid crystal reflects colored light. When the temperature is varied, the color of the liquid crystal changes. These types of cholesteric liquid crystals are known as thermochromic cholesteric liquid crystals [24]. As shown in Figure 1.13, the reflected light is in the visible region for temperatures in the region from  $T_1$  to  $T_2$ . There are liquid crystals with  $\Delta T = T_1 - T_2 = 1^\circ$ . If there are two thermochromic cholesteric liquid crystals with different cholesteric–smectic-A transition temperatures, mixtures with different concentrations of the two components will exhibit color reflections at different temperatures. This is how thermochromic cholesteric liquid crystals are used to make thermometers.

## 1.5 Response of Liquid Crystals to Electromagnetic Fields

Liquid crystals are anisotropic dielectric and diamagnetic media [1,25]. Their resistivities are very high ( $\sim 10^{10} \Omega \text{ cm}$ ). Dipole moments are induced in them by external fields. They have different dielectric permittivities and magnetic susceptibilities along the directions parallel and perpendicular to the liquid crystal director.

### 1.5.1 Magnetic susceptibility

We first consider magnetic susceptibility. Because the magnetic interaction between the molecules is weak, the local magnetic field of the molecules is approximately the same as the externally applied magnetic field. For a uniaxial liquid crystal, a molecule can be regarded as a cylinder. When a magnetic field  $\vec{H}$  is applied to the liquid crystal, it has different responses to the applied field, depending on the angle between the long molecular axis  $\vec{a}$  and the field  $\vec{H}$ . The magnetic field can be decomposed into a parallel component and a perpendicular component as shown in Figure 1.14. The magnetization  $\vec{M}$  is given by

$$\begin{aligned}\vec{M} &= N\kappa_{\parallel}(\vec{a} \cdot \vec{H})\vec{a} + N\kappa_{\perp}[\vec{H} - (\vec{a} \cdot \vec{H})\vec{a}] \\ &= N\kappa_{\perp}\vec{H} + N\Delta\kappa(\vec{a} \cdot \vec{H})\vec{a} \\ &= N\kappa_{\perp}\vec{H} + N\Delta\kappa(\vec{a}\vec{a}) \cdot \vec{H}\end{aligned}\quad (1.72)$$

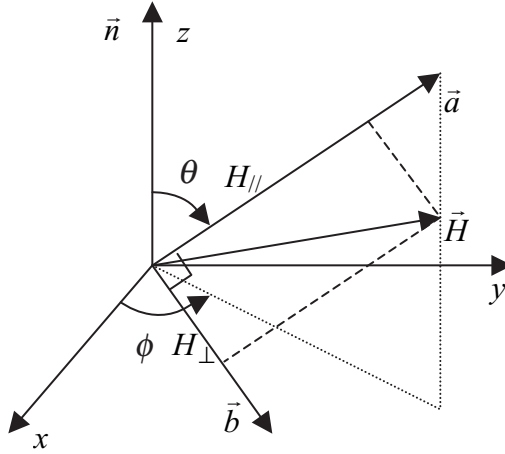
where  $N$  is the molecular number density,  $\kappa_{\parallel}$  and  $\kappa_{\perp}$  are molecular magnetic polarizabilities parallel and perpendicular to the long molecular axis, respectively, and  $\Delta\kappa = \kappa_{\parallel} - \kappa_{\perp}$ . Expressed in matrix form, Equation (1.72) becomes

$$\vec{M} = N \begin{pmatrix} \kappa_{\perp} + \Delta\kappa a_x a_x & \Delta\kappa a_x a_y & \Delta\kappa a_x a_z \\ \Delta\kappa a_y a_x & \kappa_{\perp} + \Delta\kappa a_y a_y & \Delta\kappa a_y a_z \\ \Delta\kappa a_z a_x & \Delta\kappa a_z a_y & \kappa_{\perp} + \Delta\kappa a_z a_z \end{pmatrix} \cdot \vec{H} = N \overleftrightarrow{\kappa} \cdot \vec{H} \quad (1.73)$$

where  $a_i$  ( $i = x, y, z$ ) are the projections of  $\vec{a}$  in the  $x$ ,  $y$ , and  $z$  directions in the lab frame whose  $z$  axis is parallel to the liquid crystal director:  $a_z = \cos\theta$ ,  $a_x = \sin\theta \cos\phi$ , and  $a_y = \sin\theta \sin\phi$ . The molecule swivels because of thermal motion. The averaged magnetization is  $\vec{M} = N \langle \overleftrightarrow{\kappa} \rangle \cdot \vec{H}$ . For a uniaxial liquid crystal, recall that  $\langle \cos^2\theta \rangle = (2S + 1)/3$ ,  $\langle \sin^2\theta \rangle = (2 - 2S)/3$ ,  $\langle \sin^2\phi \rangle = \langle \cos^2\phi \rangle = 1/2$ , and  $\langle \sin\phi \cos\phi \rangle = 0$ . Therefore

$$\langle \overleftrightarrow{\kappa} \rangle = \begin{pmatrix} \kappa_{\perp} + \frac{1}{3}(1 - S)\Delta\kappa & 0 & 0 \\ 0 & \kappa_{\perp} + \frac{1}{3}(1 - S)\Delta\kappa & 0 \\ 0 & 0 & \kappa_{\perp} + \frac{1}{3}(2S + 1)\Delta\kappa \end{pmatrix} \quad (1.74)$$





**Figure 1.14** Schematic diagram showing the field decomposed into components parallel and perpendicular to the long molecular axis:  $\vec{a}$ , unit vector parallel to the long molecular axis;  $\vec{b}$ , unit vector perpendicular to the long molecular axis

Because  $\vec{M} = \vec{\chi} \cdot \vec{H}$ , the magnetic susceptibility tensor is

$$\vec{\chi} = \begin{pmatrix} \chi_{\perp} & 0 & 0 \\ 0 & \chi_{\perp} & 0 \\ 0 & 0 & \chi_{\parallel} \end{pmatrix} = N \begin{pmatrix} \kappa_{\perp} + \frac{1}{3}(1-S)\Delta\kappa & 0 & 0 \\ 0 & \kappa_{\perp} + \frac{1}{3}(1-S)\Delta\kappa & 0 \\ 0 & 0 & \kappa_{\perp} + \frac{1}{3}(2S+1)\Delta\kappa \end{pmatrix} \quad (1.75)$$

The anisotropy is

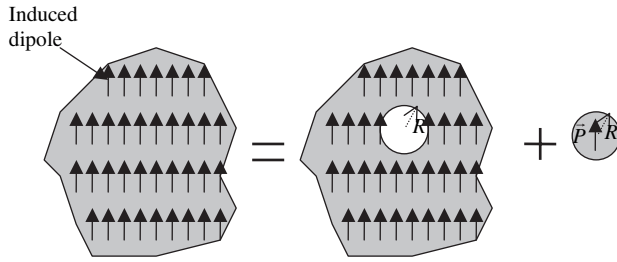
$$\Delta\chi = \chi_{\parallel} - \chi_{\perp} = N\Delta\kappa S \quad (1.76)$$

where  $\chi_{\parallel}$  and  $\chi_{\perp}$  are negative and small ( $\sim 10^{-5}$  in SI units) and  $\Delta\chi$  is usually positive. From Equation (1.75) it can be seen that  $(2\chi_{\perp} + \chi_{\parallel})/3 = N(3\kappa_{\perp} + \Delta\kappa)/3 = N(2\kappa_{\perp} + \kappa_{\parallel})/3$ , which is independent of the order parameter. The quantity  $(2\chi_{\perp} + \chi_{\parallel})/3N$  does not change discontinuously when crossing the nematic–isotropic transition.

### 1.5.2 Dielectric permittivity and refractive index

When an electric field is applied to a liquid crystal, it will induce dipole moments in the liquid crystal. For a uniaxial liquid crystal, the molecule can be regarded as a cylinder, and it has different molecular polarizabilities parallel and perpendicular to the long molecular axis  $\vec{a}$ . Similar to the magnetic case, when a local electric field  $\vec{E}_{loc}$  (also called an internal field) is applied to the liquid crystal, the polarization (dipole moment per unit volume) is given by

$$\begin{aligned} \vec{P} &= N\alpha_{\parallel}(\vec{a} \cdot \vec{E}_{loc})\vec{a} + N\alpha_{\perp}[\vec{E}_{loc} - (\vec{a} \cdot \vec{E}_{loc})\vec{a}] \\ &= N\alpha_{\perp}\vec{E}_{loc} + N\Delta\alpha(\vec{a} \cdot \vec{E}_{loc})\vec{a} \\ &= N\alpha_{\perp}\vec{E}_{loc} + N\Delta\alpha(\vec{a}\vec{a}) \cdot \vec{E}_{loc} \end{aligned} \quad (1.77)$$



**Figure 1.15** Schematic diagram showing how a macroscopic field is produced in a medium

where  $N$  is the molecular density,  $\alpha_{\parallel}$  and  $\alpha_{\perp}$  are the molecular polarizabilities parallel and perpendicular to the long molecular axis, respectively, and  $\Delta\alpha = \alpha_{\parallel} - \alpha_{\perp}$ . Different from the magnetic case, the dipole–dipole interactions between the molecules are strong, or, stated in another way, the local electric field on a molecule is the sum of the externally applied electric field and the electric field produced by the dipole moments of other molecules. We can approach this problem in the following way. Imagine a cavity created by removing the molecule under consideration, as shown in Figure 1.15. The macroscopic field  $\vec{E}$  is the sum of the field  $\vec{E}_{self}$  produced by the molecule itself and the field  $\vec{E}_{else}$ , which is the local field  $\vec{E}_{local}$  produced by the external source and the rest of the molecules of the system:

$$\vec{E} = \vec{E}_{self} + \vec{E}_{else} = \vec{E}_{self} + \vec{E}_{local} \quad (1.78)$$

In order to illustrate the principle, let us first consider an isotropic medium. The cavity can be regarded as a sphere. The field  $\vec{E}_{self}$  is produced by the dipole moment inside the sphere, which can be calculated in the following way. In the calculation of the field, the dipole moment can be replaced by the surface charge produced by the dipole moment on the surface of the sphere. The surface charge density is  $\sigma = \vec{P} \cdot \vec{m}$ . The field produced by the surface charge is  $\vec{E}_{self} = -\vec{P}/3\epsilon_0$ . The local field is  $\vec{E}_{local} = \vec{E} + \vec{P}/3\epsilon_0$ . Hence the polarizability is

$$\vec{P} = N\alpha\vec{E}_{loc} = N\alpha(\vec{E} + \vec{P}/3\epsilon_0) \quad (1.79)$$

$$\vec{P} = \frac{N\alpha\vec{E}}{1 - N\alpha/3\epsilon_0} \quad (1.80)$$

The electric displacement  $\vec{D} = \epsilon_0\epsilon\vec{E} = \epsilon_0\vec{E} + \vec{P}$ , where  $\epsilon_0 = 8.85 \times 10^{12} \text{ N/V}^2$  is the permittivity of vacuum, and  $\epsilon$  is the (relative) dielectric constant which is given by

$$\epsilon = 1 + \frac{\vec{P}}{\epsilon_0\vec{E}} = 1 + \frac{N\alpha/\epsilon_0}{1 - N\alpha/3\epsilon_0} \quad (1.81)$$

$$\frac{\epsilon - 1}{\epsilon + 2} = \frac{1}{3\epsilon_0}N\alpha \quad (1.82)$$

which is called the Clausius–Mossotti relation. At optical frequencies, the refractive index  $n$  is given by  $n^2 = \epsilon$ , and therefore

$$\frac{n^2 - 1}{n^2 + 2} = \frac{1}{3\epsilon_0} N\alpha \quad (1.83)$$

which is called the Lorentz–Lorenz relation. The local field is related to the macroscopic field by

$$\vec{E}_{local} = \vec{E} + \vec{P}/3\epsilon_0 = \vec{E} + \frac{N\alpha/3\epsilon_0}{1 - N\alpha/3\epsilon_0} \vec{E} = \frac{1}{1 - N\alpha/3\epsilon_0} \vec{E} = K\vec{E} \quad (1.84)$$

where the defined  $K = 1/(1 - N\alpha/3\epsilon_0)$  is called the internal field constant.

Liquid crystals are anisotropic. The local field  $\vec{E}_{local}$  in them depends on the macroscopic field  $\vec{E}$  as well as the angles between  $\vec{E}$  and the long molecular axis  $\vec{a}$  and the liquid crystal director  $\vec{n}$ . They are related to each other by

$$\vec{E}_{local} = \vec{K} \cdot \vec{E} \quad (1.85)$$

where  $\vec{K}$  is the internal field tensor which is a second-rank tensor. Taking account of the internal field tensor and the thermal motion of the molecules, the polarization is

$$\vec{P} = N\alpha_{\perp} \langle \vec{K} \rangle \cdot \vec{E} + N\Delta\alpha \langle [\vec{K} \cdot (\vec{a}\vec{a})] \rangle \cdot \vec{E} \quad (1.86)$$

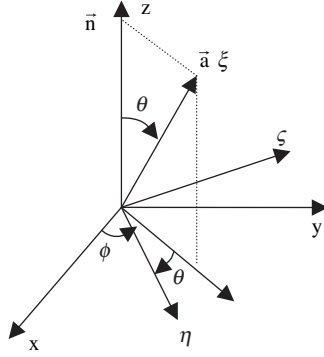
The macroscopic dielectric tensor is

$$\vec{\epsilon} = \vec{I} + \frac{N}{\epsilon_0} [\alpha_{\perp} \langle \vec{K} \rangle + \Delta\alpha \langle \vec{K} \cdot (\vec{a}\vec{a}) \rangle] \quad (1.87)$$

In a material consisting of non-polar molecules, the induced polarization consist of two parts: (1) the electronic polarization  $P_{electronic}$  which comes from the deformation of the electron clouds of the constituting atoms of the molecule, and (2) the ionic polarization  $P_{ionic}$  which comes from the relative displacement of the atoms constituting the molecule. For a material consisting of polar molecules, there is a third contribution, namely the dipolar polarization  $P_{dipolar}$ , which comes from the reorientation of the dipole. These contributions to the molecular polarizability depend on the frequency of the applied field. The rotation of the molecule is slow and therefore the dipole-orientation polarization can only contribute up to a frequency of megahertz. The vibration of atoms in molecules is faster and the ionic polarization can contribute up to the frequency of infrared light. The motion of electrons is the fastest and the electronic polarization can contribute up to the frequency of ultraviolet light. In relation to the magnitudes, the order is  $P_{electronic} < P_{ionic} < P_{dipolar}$ .

At optical frequencies, only the electronic polarization contributes to the molecular polarizability, which is small, and the electric field is usually low. De Jeu and Bordewijk showed experimentally that (1)  $(2\epsilon_{\perp} + \epsilon_{\parallel})/3\rho$  is a constant through the nematic and isotropic phases [25, 26], where  $\rho$  is the mass density, and (2) the dielectric anisotropy  $\Delta\epsilon = \epsilon_{\parallel} - \epsilon_{\perp}$  is directly proportional to the anisotropy of the magnetic susceptibility. Based on these results, it was concluded that  $\vec{K}$  is a molecular tensor independent of the macroscopic dielectric anisotropy. In the molecular principal frame  $\eta\zeta\zeta$  with the  $\zeta$  axis parallel to the long molecular axis  $\vec{a}$ ,  $\vec{K}$  has the form

$$\vec{K} = \begin{pmatrix} K_{\perp} & 0 & 0 \\ 0 & K_{\perp} & 0 \\ 0 & 0 & K_{\parallel} \end{pmatrix} \quad (1.88)$$



**Figure 1.16** Schematic diagram showing the transformation between the molecular principal frame  $\eta\zeta\xi$  and the lab frame  $xyz$

Next we need to find the form of  $\vec{K}$  in the lab frame  $xyz$  with the  $z$  axis parallel to the liquid crystal director  $\vec{n}$ . Because of the axial symmetry around  $\vec{a}$ , we only need to consider the transformation of the matrix between the two frames as shown in Figure 1.16. The frame  $\eta\zeta\xi$  is achieved by first rotating the frame  $xyz$  around the  $z$  axis through the angle  $\phi$  and then rotating the frame around the  $\zeta$  axis through the angle  $\theta$ . The rotation matrix is

$$\vec{R} = \begin{pmatrix} \cos \theta \cos \phi & -\sin \phi & \sin \theta \cos \phi \\ \cos \theta \sin \phi & \cos \phi & \sin \theta \sin \phi \\ -\sin \theta & 0 & \cos \theta \end{pmatrix} \quad (1.89)$$

and the reverse rotation matrix is

$$\vec{R}^{-1} = \begin{pmatrix} \cos \theta \cos \phi & \cos \theta \sin \phi & -\sin \theta \\ -\sin \phi & \cos \phi & 0 \\ \sin \theta \cos \phi & \sin \theta \sin \phi & \cos \theta \end{pmatrix} \quad (1.90)$$

In the lab frame  $\vec{K}$  has the form

$$\begin{aligned} \vec{K} &= \vec{R} \cdot \begin{pmatrix} K_{\perp} & 0 & 0 \\ 0 & K_{\perp} & 0 \\ 0 & 0 & K_{//} \end{pmatrix} \cdot \vec{R}^{-1} \\ &= \begin{pmatrix} K_{\perp} + \Delta K \sin^2 \theta \cos^2 \phi & \Delta K \sin^2 \theta \sin \phi \cos \phi & \Delta K \sin \theta \cos \theta \cos \phi \\ \Delta K \sin^2 \theta \sin \phi \cos \phi & K_{\perp} + \Delta K \sin^2 \theta \sin^2 \phi & \Delta K \sin \theta \cos \theta \sin \phi \\ \Delta K \sin \theta \cos \theta \cos \phi & \Delta K \sin \theta \cos \theta \sin \phi & K_{\perp} + \Delta K \cos^2 \theta \end{pmatrix} \end{aligned} \quad (1.91)$$

where  $\Delta K = K_{\parallel} - K_{\perp}$ , and  $\vec{a}\vec{a}$  has the form

$$\begin{aligned} \vec{a}\vec{a} &= \begin{pmatrix} \sin \theta \cos \phi \\ \sin \theta \sin \phi \\ \cos \theta \end{pmatrix} \begin{pmatrix} \sin \theta \cos \phi & \sin \theta \sin \phi & \cos \theta \end{pmatrix} \\ &= \begin{pmatrix} \sin^2 \theta \cos^2 \phi & \sin^2 \theta \sin \phi \cos \phi & \sin \theta \cos \theta \cos \phi \\ \sin^2 \theta \sin \phi \cos \phi & \sin^2 \theta \sin^2 \phi & \sin \theta \cos \theta \sin \phi \\ \sin \theta \cos \theta \cos \phi & \sin \theta \cos \theta \sin \phi & \cos^2 \theta \end{pmatrix} \end{aligned} \quad (1.92)$$

and  $\vec{a}\vec{a} \cdot \vec{K}$  has the form

$$\vec{a}\vec{a} \cdot \vec{K} = \begin{pmatrix} K_{\parallel} \sin^2 \theta \cos^2 \phi & K_{\parallel} \sin^2 \theta \sin \phi \cos \phi & K_{\parallel} \sin \theta \cos \theta \cos \phi \\ K_{\parallel} \sin^2 \theta \sin \phi \cos \phi & K_{\parallel} \sin^2 \theta \sin^2 \phi & K_{\parallel} \sin \theta \cos \theta \sin \phi \\ K_{\parallel} \sin \theta \cos \theta \cos \phi & K_{\parallel} \sin \theta \cos \theta \sin \phi & K_{\parallel} \cos^2 \theta \end{pmatrix} \quad (1.93)$$

Recall that  $\langle \cos^2 \theta \rangle = (2S + 1)/3$ ,  $\langle \sin^2 \theta \rangle = (2 - 2S)/3$ ,  $\langle \sin^2 \phi \rangle = \langle \cos^2 \phi \rangle = 1/2$ , and  $\langle \cos \theta \rangle = \langle \sin \phi \rangle = \langle \cos \phi \rangle = \langle \sin \phi \cos \phi \rangle = 0$ ; therefore their averaged values are

$$\langle \vec{K} \rangle = \begin{pmatrix} K_{\perp} + \Delta K(1 - S)/3 & 0 & 0 \\ 0 & K_{\perp} + \Delta K(1 - S)/3 & 0 \\ 0 & 0 & K_{\perp} + \Delta K(2S + 1)/3 \end{pmatrix} \quad (1.94)$$

$$\langle \vec{a}\vec{a} \cdot \vec{K} \rangle = \begin{pmatrix} K_{\parallel}(1 - S)/3 & 0 & 0 \\ 0 & K_{\parallel}(1 - S)/3 & 0 \\ 0 & 0 & K_{\parallel}(2S + 1)/3 \end{pmatrix} \quad (1.95)$$

$$\vec{\varepsilon} = \vec{I} + \frac{N}{\varepsilon_0} [\alpha_{\perp} \langle \vec{K} \rangle + \Delta \alpha \langle \vec{K} \cdot (\vec{a}\vec{a}) \rangle]$$

Therefore

$$\vec{\varepsilon} = \begin{pmatrix} 1 + \frac{N}{3\varepsilon_0} [\alpha_{\perp} K_{\perp} (2 + S) + \alpha_{\parallel} K_{\parallel} (1 - S)] & 0 & 0 \\ 0 & 1 + \frac{N}{3\varepsilon_0} [\alpha_{\perp} K_{\perp} (2 + S) + \alpha_{\parallel} K_{\parallel} (1 - S)] & 0 \\ 0 & 0 & 1 + \frac{N}{3\varepsilon_0} [\alpha_{\perp} K_{\perp} (2 - 2S) + \alpha_{\parallel} K_{\parallel} (1 + 2S)] \end{pmatrix} \quad (1.96)$$

### 30 LIQUID CRYSTAL PHYSICS

The anisotropy is

$$\Delta\varepsilon = \varepsilon_{\parallel} - \varepsilon_{\perp} = \frac{N}{\varepsilon_0}(\alpha_{\parallel}K_{\parallel} - \alpha_{\perp}K_{\perp})S \quad (1.97)$$

which is linearly proportional to the order parameter  $S$ . In terms of the refractive indices, Equation (1.97) becomes

$$n_{\parallel}^2 - n_{\perp}^2 = 2\bar{n}\Delta n = \frac{N}{\varepsilon_0}(\alpha_{\parallel}K_{\parallel} - \alpha_{\perp}K_{\perp})S$$

where  $\bar{n} = (n_{\parallel} + n_{\perp})/2$  and  $\Delta n = (n_{\parallel} - n_{\perp})$ . Approximately, the birefringence  $\Delta n$  is linearly proportional to the order parameter. For most liquid crystals,  $\bar{n} \sim 1.5-2.0$  and  $\Delta n \sim 0.05-0.3$ .

The electronic polarization may be treated by using classical mechanics where the system is regarded as a simple harmonic oscillator. There are three forces acting on the electron: (1) the elastic restoring force  $-Kx$ , where  $K$  is the elastic constant and  $x$  is the displacement of the electron from its equilibrium position; (2) the viscosity force  $-\gamma\partial x/\partial t$ ; and (3) the electric force  $-eE_0e^{i\omega t}$ , where  $E_0$  and  $\omega$  are the amplitude and frequency of the applied electric field, respectively. The dynamic equation is

$$m \frac{d^2x}{dt^2} = -kx - eE_0e^{i\omega t} - \gamma \frac{\partial x}{\partial t} \quad (1.98)$$

The solution is  $x = x_0e^{i\omega t}$  and the amplitude of the oscillation is

$$x_0 = \frac{-eE_0}{m(\omega^2 - \omega_0^2) + i\gamma\omega} \quad (1.99)$$

where  $\omega_0 = \sqrt{k/m}$  is the frequency of the oscillator (the frequency of the transition dipole moment in quantum mechanics). The induced dipole moment is  $p = -ex_0$ . The molecule polarizability is

$$\alpha = p/E_{loc} = \frac{e^2}{m} \frac{(\omega_0^2 - \omega^2)}{(\omega_0^2 - \omega^2)^2 + (\gamma\omega/m)^2} - i \frac{e^2}{m} \frac{\gamma\omega/m}{(\omega_0^2 - \omega^2)^2 + (\gamma\omega/m)^2} \quad (1.100)$$

which is a complex number and the imaginary part corresponds to absorption. When the frequency of the light is far from the absorption frequency  $\omega_0$  or the viscosity is small, the absorption is negligible,  $\alpha = p/E_{loc} = (e^2/m)/(\omega_0^2 - \omega^2)$ . The refractive index is

$$n^2 \propto \alpha \propto \frac{1}{(\omega_0^2 - \omega^2)} = \frac{1}{[(2\pi/C\lambda_0)^2 - (2\pi/C\lambda)^2]} = \frac{C^2\lambda_0^2}{4\pi^2} \frac{\lambda^2}{\lambda^2 - \lambda_0^2}$$

as expressed in Sellmeier's equation

$$n^2 = 1 + \frac{H\lambda^2}{\lambda^2 - \lambda_0^2} \quad (1.101)$$

where  $H$  is a constant. When  $\lambda$  is much longer than  $\lambda_0$ , expanding the above equation we have

$$n \approx A + \frac{B}{\lambda^2} + \frac{C}{\lambda^4} \quad (1.102)$$

This is Cauchy's equation. The refractive index increases with decreasing wavelength. For liquid crystals, along different directions with respect to the long molecular axis, the molecular polarizabilities are different. Also along different directions, the frequencies of the transition dipole

moments are different, which results in *dichroic absorption*: that is, when the electric field is parallel to the transition dipole moment, the light is absorbed; when the electric field is perpendicular to the transition moment, the light is not absorbed. Positive dichroic dyes have transition dipole moments parallel to the long molecular axis, while negative dichroic dyes have transition dipole moments perpendicular to the long molecular axis.

Under DC or low-frequency applied electric fields, for liquid crystals of polar molecules, the dipolar polarization is dominant. For a liquid crystal with a permanent dipole moment  $\vec{p}$ , the polarization is given by

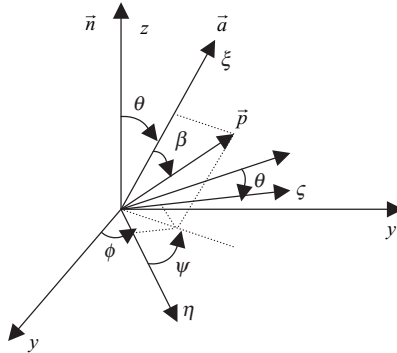
$$\vec{P} = N\alpha_{\perp} \langle \vec{K} \rangle \cdot \vec{E} + N\Delta\alpha \langle [\vec{K} \cdot (\vec{a}\vec{a})] \rangle \cdot \vec{E} + N\langle \vec{p} \rangle \quad (1.103)$$

The macroscopic dielectric tensor is

$$\vec{\epsilon} = \vec{I} + \frac{N}{\epsilon_0} [\alpha_{\perp} \langle \vec{K} \rangle + \Delta\alpha \langle \vec{K} \cdot (\vec{a}\vec{a}) \rangle + \langle \vec{p} \rangle \vec{E}/E^2] \quad (1.104)$$

The energy of the dipole in the directing electric field  $\vec{E}_d$  is  $u = -\vec{p} \cdot \vec{E}_d$ . The directing field  $\vec{E}_d$  is different from the local field  $\vec{E}_{loc}$  because the dipole polarizes its surroundings, which in turn results in a reaction field  $\vec{E}_r$  at the position of the dipole. As  $\vec{E}_r$  is always parallel to the dipole, it cannot affect the orientation of the dipole. As an approximation, it is assumed that  $\vec{E}_d = d \cdot \vec{E}$ , where  $d$  is a constant. Usually the dipole moment  $p$  is about  $1e \times 1A^{\circ} = 1.6 \times 10^{-19} \text{ C} \times 10^{-10} \text{ m} = 1.6 \times 10^{-29} \text{ mC}$ . At room temperature ( $T \sim 300 \text{ K}$ ) and under the normal strength field  $E \sim 1 \text{ V}/\mu\text{m} = 10^6 \text{ V/m}$ ,  $pE/3k_B T \ll 1$ . Consider a liquid crystal molecule with a permanent dipole moment making an angle  $\beta$  with the long molecular axis. In the molecular frame  $\eta\zeta\xi$ , the components of  $\vec{p}$  are  $(p \sin \beta \cos \psi, p \sin \beta \sin \psi, p \cos \beta)$ , as shown in Figure 1.17. Using the rotation matrix given by Equation (1.90), we can calculate the components of  $\vec{p}$  in the lab frame  $xyz$ :

$$\begin{aligned} \vec{p} &= \begin{pmatrix} \cos \phi & -\cos \theta \sin \phi & -\sin \theta \sin \phi \\ \sin \phi & \cos \theta \cos \phi & \sin \theta \cos \phi \\ 0 & -\sin \theta & \cos \theta \end{pmatrix} \cdot p \begin{pmatrix} \sin \beta \cos \psi \\ \sin \beta \sin \psi \\ \cos \beta \end{pmatrix} \\ &= p \begin{pmatrix} \sin \beta \cos \psi \cos \phi - \sin \beta \sin \psi \cos \theta \sin \phi - \cos \beta \sin \theta \sin \phi \\ \sin \beta \sin \psi \sin \phi + \sin \beta \sin \psi \cos \theta \cos \phi + \cos \beta \sin \theta \cos \phi \\ -\sin \theta \sin \beta \sin \psi + \cos \theta \cos \beta \end{pmatrix} \end{aligned} \quad (1.105)$$



**Figure 1.17** Schematic diagram showing the orientation of the dipole  $\vec{p}$  in the molecular principal frame  $\eta\zeta\xi$  and the lab frame  $xyz$

### 32 LIQUID CRYSTAL PHYSICS

When the applied field is parallel to  $\vec{n}$ ,  $\vec{E} = E_{\parallel}\vec{z}$ , the projection of the dipole along the applied field is

$$p_{\parallel} = -p(\sin\beta\sin\psi\sin\theta + \cos\beta\cos\theta) \quad (1.106)$$

and the energy is

$$u = -dp(\cos\beta\cos\theta - \sin\beta\sin\psi\sin\theta)E_{\parallel} \quad (1.107)$$

The average value of the projection is

$$\langle p_{\parallel} \rangle = \frac{\int (p\cos\beta\cos\theta - p\sin\beta\sin\psi\sin\theta)e^{-u/k_B T - V(\theta)/k_B T} \sin\theta d\theta d\phi d\psi}{\int e^{-u/k_B T - V(\theta)/k_B T} \sin\theta d\theta d\phi d\psi} \quad (1.108)$$

Because  $-u \ll k_B T$ ,  $e^{-u/k_B T} \approx (1 - u/k_B T)$ , then

$$\begin{aligned} \langle p_{\parallel} \rangle &= \frac{dE_{\parallel}}{k_B T} \frac{\int (p\cos\beta\cos\theta - p\sin\beta\sin\psi\sin\theta)^2 e^{-V(\theta)/k_B T} \sin\theta d\theta d\phi d\psi}{\int e^{-V(\theta)/k_B T} \sin\theta d\theta d\phi d\psi} \\ &= \frac{dE_{\parallel} p^2}{k_B T} \langle (\cos^2\beta\cos^2\theta + \sin^2\beta\sin^2\theta\sin^2\psi - \sin\beta\cos\beta\sin\theta\cos\theta\sin\psi) \rangle \end{aligned}$$

Because  $\langle \sin^2\psi \rangle = 1/2$ ,  $\langle \sin\psi \rangle = 0$ ,  $\langle \cos^2\theta \rangle = (2S + 1)/3$ , and  $\langle \sin^2\theta \rangle = (2 - 2S)/3$ ,

$$\langle p_{\parallel} \rangle = \frac{dE_{\parallel} p^2}{3k_B T} [\cos^2\beta(2S + 1) + \sin^2\beta(1 - S)] = \frac{dE_{\parallel} p^2}{3k_B T} [1 - (1 - 3\cos^2\beta)S] \quad (1.109)$$

From Equations (1.96), (1.104), and (1.109), we have

$$\varepsilon_{\parallel} = 1 + \frac{N}{3\varepsilon_0} \{ \alpha_{\perp} K_{\perp} (2 - 2S) + \alpha_{\parallel} K_{\parallel} (1 + 2S) + \frac{dp^2}{k_B T} [1 - (1 - 3\cos^2\beta)S] \} \quad (1.110)$$

Note that  $\alpha_{\parallel}$  and  $\alpha_{\perp}$  are the molecular polarizabilities contributed by the electronic and ionic polarizations.

When the applied field is perpendicular to  $\vec{n}$ , say  $\vec{E} = E_{\perp}\hat{x}$ , the projection of the dipole along the applied field is

$$p_{\perp} = p(\sin\beta\cos\psi\cos\phi - \sin\beta\sin\psi\cos\theta\sin\phi - \cos\beta\sin\theta\sin\phi) \quad (1.111)$$

and the energy is

$$u = -dp(\sin\beta\cos\psi\cos\phi - \sin\beta\sin\psi\cos\theta\sin\phi - \cos\beta\sin\theta\sin\phi)E_{\perp} \quad (1.112)$$

The average value of the projection is

$$\begin{aligned} \langle p_{\perp} \rangle &= \frac{dE_{\perp} p^2}{k_B T} \left[ \frac{1}{4}\sin^2\beta + \frac{1}{4}\sin^2\beta\frac{(2S+1)}{3} + \cos^2\beta\frac{(1-S)}{3} \right] \\ &= \frac{dE_{\perp} p^2}{3k_B T} \left[ 1 + \frac{1}{2}(1 - 3\cos^2\beta)S \right] \end{aligned}$$



From Equations (1.96), (1.104), and (1.112), we have

$$\varepsilon_{\perp} = 1 + \frac{N}{3\varepsilon_0} \left\{ \alpha_{\perp} K_{\perp} (2 + S) + \alpha_{\parallel} K_{\parallel} (1 - S) + \frac{dp^2}{k_B T} \left[ 1 + \frac{1}{2} (1 - 3 \cos^2 \beta) S \right] \right\} \quad (1.113)$$

The dielectric anisotropy is

$$\Delta\varepsilon = \varepsilon_{\parallel} - \varepsilon_{\perp} = \frac{N}{\varepsilon_0} \left[ (\alpha_{\parallel} K_{\parallel} - \alpha_{\perp} K_{\perp}) - \frac{dp^2}{2k_B T} (1 - 3 \cos^2 \beta) \right] S \quad (1.114)$$

which is proportional to the order parameter  $S$ . The contribution of induced polarization (electronic and ionic polarizations) changes with temperature like  $S$ , while the contribution of the orientation polarization changes with temperature like  $S/T$ . When the angle between the permanent dipole and the long molecular axis is  $\beta = 55^\circ$ ,  $(1 - 3 \cos^2 \beta) = 0$ , the orientation polarization of the permanent dipole does not contribute to  $\Delta\varepsilon$ .

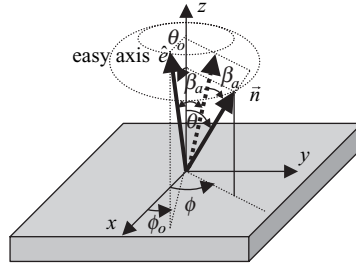
The permanent dipole moment is fixed on the molecule. Thus the molecule has to reorient in order to contribute to the dielectric constants. Qualitatively speaking, only when the frequency of the applied field is lower than a characteristic frequency  $\omega_c$  can the molecule rotate to follow the oscillation of the applied field and therefore to contribute to the dielectric constants. For rod-like liquid crystal molecules, it is easier to spin around the long molecular axis than to rotate around a short molecular axis. Therefore the characteristic frequency  $\omega_{\perp c}$  for  $\varepsilon_{\perp}$  is higher than the characteristic frequency  $\omega_{\parallel c}$  for  $\varepsilon_{\parallel}$ . For molecules for which the angle  $\beta$  between the permanent dipole and the long molecular axis is very small,  $\Delta\varepsilon$  is always positive at all frequencies. For molecules with large permanent dipole moment  $p$  and large  $\beta$ ,  $\Delta\varepsilon$  is negative at low frequencies. For molecules with large permanent dipole moment  $p$  and intermediate  $\beta$ ,  $\Delta\varepsilon$  is positive at low frequencies, then changes to negative when the frequency is increased above a crossover frequency  $\omega_o$ . The cross over frequency is in the region from a few kilohertz to a few tens of kilohertz. At infrared light or higher frequencies, the dipolar polarization no longer contributes, and  $\Delta\varepsilon$  is always positive.

## 1.6 Anchoring Effects of Nematic Liquid Crystals at Surfaces

In most liquid crystal devices, the liquid crystals are sandwiched between two substrates coated with alignment layers. In the absence of externally applied fields, the orientation of the liquid crystal in the cell is determined by the anchoring condition of the alignment layer [26–28].

### 1.6.1 Anchoring energy

Consider an interface between a liquid crystal ( $z > 0$ ) and an alignment layer ( $z < 0$ ) as shown in Figure 1.18. For a liquid crystal molecule on the interface, some of the surrounding molecules are liquid crystal molecules and other surrounding molecules are alignment layer molecules. The potential for the molecule's orientation is different from that of the liquid crystal in the bulk, where all the surrounding molecules are liquid crystal molecules. At the interface, the orientational and positional orders may be different from those in the bulk. Here we only discuss the anisotropic part of the interaction between the liquid crystal molecule and the alignment layer molecule. The liquid crystal is anisotropic. If the alignment layer is also anisotropic, then there is a preferred direction, referred to as the easy axis, for the liquid crystal director at the interface, as shown in Figure 1.18. The interaction energy is a minimum when the liquid crystal director is along the easy axis. The  $z$  axis is perpendicular to the interface and pointing toward the liquid crystal side. The polar angle and the azimuthal angle of the easy axis are  $\theta_o$  and  $\phi_o$ , respectively. If  $\theta_o = 0^\circ$ , the anchoring is referred to as homeotropic. If  $\theta_o = 90^\circ$  and  $\phi_o$  is well



**Figure 1.18** Schematic diagram showing the easy axis of the anchoring and the liquid crystal director

defined, the anchoring is termed homogeneous. If  $\theta_o = 90^\circ$  and there is no preferred azimuthal angle, the anchoring is called planar. If  $0 < \theta_o < 90^\circ$ , the anchoring is referred to as tilted.

When the liquid crystal director  $\vec{n}$  is aligned along the direction specified by the polar angle  $\theta$  and the azimuthal angle  $\phi$ , the anisotropic part of the surface energy, referred to as the anchoring energy function, of the liquid crystal is  $f_s = f_s(\theta, \phi)$ . When  $\theta = \theta_o$  and  $\phi = \phi_o$ ,  $f_s$  has a minimum value of 0, and thus  $\partial f_s / \partial \theta|_{\theta=\theta_o} = 0$  and  $\partial f_s / \partial \phi|_{\phi=\phi_o} = 0$ . The materials above and below the interface are different and there is no reflectional symmetry about the interface. If  $\theta_o \neq 0$ , the anchoring energy does not have azimuthal rotational symmetry around the easy direction. Therefore the anchoring energies are different for deviations in polar angle and azimuthal angle. For small deviations, in the Rapini–Papoular model [29,30], the anchoring energy function can be expressed as

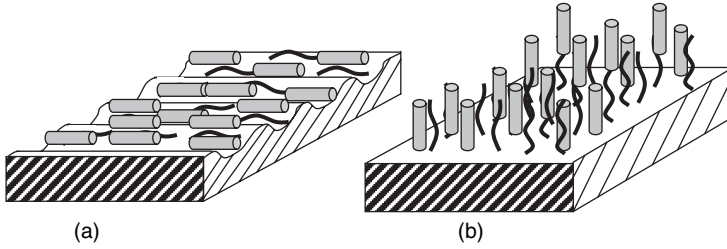
$$f_s = \frac{1}{2} W_p \sin^2 \beta_p + \frac{1}{2} W_a \sin^2 \beta_a \quad (1.115)$$

where  $\beta_p$  and  $\beta_a$  are the angles between  $\vec{n}$  and the easy axis when  $\vec{n}$  deviates from the easy axis in the polar angle direction and azimuthal angle direction, respectively;  $W_p$  and  $W_a$  are the polar and azimuthal anchoring strengths, respectively. For small  $\theta - \theta_o$  and  $\phi - \phi_o$ , we have the approximations  $\sin^2 \beta_p = \sin^2(\theta - \theta_o)$  and  $\sin^2 \beta_a = \sin^2(\phi - \phi_o) \sin^2 \theta_o$ . Therefore the anchoring energy function is

$$f_s = \frac{1}{2} W_p \sin^2(\theta - \theta_o) + \frac{1}{2} W_a \sin^2 \theta_o \sin^2(\phi - \phi_o) \quad (1.116)$$

### 1.6.2 Alignment layers

Homogeneous anchoring can be achieved by mechanically rubbing the surface of the substrate, such as glass, of the liquid crystal cell with a cotton ball or cloth. The rubbing creates micro-grooves along the rubbing direction in the form of ridges and troughs, as shown in Figure 1.19(a). When the liquid crystal is aligned parallel to the grooves, there is no orientational deformation. If the liquid crystal were perpendicular to the grooves, there would be orientational deformation, which costs elastic energy. Therefore the liquid crystal will be homogeneously aligned along the grooves (the rubbing direction). The problem with alignment created in this way is that the anchoring strength ( $\sim 10^{-5} \text{ J/m}^2$ ) is weak. Widely used for the homogeneous alignment layer are rubbed polyimides. The rubbing not only creates the micro-grooves but also aligns the polymer chains. The intermolecular interaction between the liquid crystal and the aligned polymer chains also favors parallel alignment and thus increases the anchoring energy. The anchoring strength can become as high as  $10^{-3} \text{ J/m}^2$ . Furthermore, pretilt angles of a few



**Figure 1.19** (a) Schematic diagram showing the liquid crystal aligned parallel to the grooves, (b)

degrees can be generated. Homogeneous anchoring can also be achieved by using obliquely evaporated SiO film.

Homeotropic anchoring can be achieved using monolayer surfactants such as lecithin and silane. The polar head of the surfactant is chemically attached to the glass substrate and the hydrocarbon tail points out and perpendicular to the surface, as shown in Figure 1.19(b). The intermolecular interaction between the surfactant and the liquid crystal promotes the homeotropic alignment.

## Homework Problems

- 1.1 Consider a nematic liquid crystal. The molecule can be regarded as a cylinder with a length of 2 nm and diameter of 0.5 nm. The molecule has a permanent dipole moment of  $10^{-29}$  mC at the center of the molecule. The interaction between the molecules comes from the interactions between the permanent dipoles. Calculate the interaction between two molecules in the following cases: (1) one molecule is on top of the other molecule and the dipoles are parallel, (2) one molecule is on top of the other molecule and the dipoles are anti-parallel, (3) the molecules are side by side and the dipoles are parallel, and (4) the molecules are side by side and the dipoles are anti-parallel.
- 1.2 Using Equations (1.11), (1.25), and (1.31), prove that the entropy of a system at a constant temperature is

$$S = -k_B \langle \ln \rho \rangle = -k_B \sum_i \rho_i \ln \rho_i$$

- 1.3 Calculate the orientational order parameter in the following two cases. (1) The orientational distribution function is  $f(\theta) = \cos^2 \theta$ . (2) The orientational distribution function is  $f(\theta) = \sin^2 \theta$ .  $\theta$  is the angle between the long molecular axis and the liquid crystal director.
- 1.4 *Landau-de Gennes theory*. For a liquid crystal with parameters  $a = 0.1319 \times 10^5$  J/Km<sup>3</sup>,  $b = -1.836 \times 10^5$  J/m<sup>3</sup>, and  $c = 4.05 \times 10^5$  J/m<sup>3</sup>, numerically calculate the free energy as a function of the order parameter and identify the order parameters corresponding to the maximum and minimum free energy at the following temperatures: (1)  $T - T^* = 4.0^\circ\text{C}$ , (2)  $T - T^* = 3.0^\circ\text{C}$ , (3)  $T - T^* = 2.0^\circ\text{C}$ , (4)  $T - T^* = 1.0^\circ\text{C}$ , (5)  $T - T^* = 0.0^\circ\text{C}$ , (6)  $T - T^* = -10.0^\circ\text{C}$ .
- 1.5 *Maier-Saupe theory*. Use Equation (1.50) to numerically calculate all the possible order parameters as a function of the normalized temperature  $\tau = k_B T / v$ , and use Equation (1.54) to calculate the corresponding free energy.
- 1.6 Use Maier-Saupe theory to study the isotropic–nematic phase transition of a binary mixture consisting of two components A and B. For molecule A, when its long molecular axis makes an angle  $\theta_A$  with respect to the liquid crystal director, the single molecular potential is

$$V_A(\theta) = -v_{AA}(1-x)S_A \left( \frac{3}{2} \cos^2 \theta_A - \frac{1}{2} \right) - v_{AB}xS_B \left( \frac{3}{2} \cos^2 \theta_A - \frac{1}{2} \right)$$

For molecule B, when its long molecular axis makes an angle  $\theta_B$  with respect to the liquid crystal director, the single molecular potential is

$$V_B(\theta) = -v_{AB}(1-x)S_A \left( \frac{3}{2} \cos^2 \theta_B - \frac{1}{2} \right) - v_{BB}xS_B \left( \frac{3}{2} \cos^2 \theta_B - \frac{1}{2} \right)$$

where  $x$  is the molar fraction of component B. The interaction constants are  $v_{BB} = 1.05v_{AA}$  and  $v_{AB} = 0.95v_{AA}$ . Express the normalized temperature by  $\tau = k_B T / v_{AA}$ . Assume that the two components are miscible at any fraction. Numerically calculate the transition temperature as a function of the molar fraction  $x$ .

- 1.7 Consider a nematic liquid crystal cell with a thickness of  $10 \mu\text{m}$ . On the bottom surface the liquid crystal is aligned parallel to the cell surface, and on top of the top surface the liquid crystal is aligned perpendicular to the cell surface. Assume the tilt angle of the liquid crystal director changes linearly with the coordinate  $z$  which is in the cell normal direction. Calculate the total elastic energy per unit area. The elastic constants of the liquid crystal are  $K_{11} = 6 \times 10^{-12} \text{ N}$ ,  $K_{22} = 3 \times 10^{-12} \text{ N}$ , and  $K_{33} = 10 \times 10^{-12} \text{ N}$ .
- 1.8 The Cano-wedge method is an experimental technique to measure the pitch of cholesteric liquid crystals. It consists of a flat substrate and a hemisphere with a cholesteric liquid crystal sandwiched between them as shown Figure 1.20(a). At the center, the spherical surface touches the flat surface. On both the flat and spherical surfaces there is a homogeneous alignment layer. The intrinsic pitch of the liquid crystal is  $P_o$ . Because of the boundary condition, the pitch of the liquid crystal is quantized to match the boundary condition. In region  $n$ ,  $h = n(P/2)$ . In each region, on the inner side, the pitch is compressed, i.e.,  $P < P_o$  while on the outer side, the pitch is stretched, i.e.,  $P > P_o$ . Between region  $(n - 1)$  and region  $n$  there is a disclination ring as shown in Figure 1.20(b). Find the square of the radius of the  $n$ th disclination ring  $r_n^2$  as a function of the intrinsic pitch  $P_o$ , the radius  $R$  of the hemisphere, and the ring number  $n$ .  $R \gg P_o$  and for small  $r$  only twist elastic energy has to be considered. Hint:  $r_n^2$  vs.  $n$  is a straight line with a slope dependent on  $P_o$  and  $R$ .
- 1.9 Consider a sphere of radius  $R$ . The polarization inside the sphere is  $\vec{P}$ . Calculate the electric field at the center of the sphere produced by the polarization. Hint: the polarization can be replaced by a surface charge whose density is given by  $\vec{P} \cdot \vec{n}$ , where  $\vec{n}$  is the unit vector along the surface normal direction.
- 1.10 Using Equations (1.87), (1.91), and (1.93), calculate the dielectric tensor  $\vec{\epsilon}$  in terms of the order parameter  $S$ .

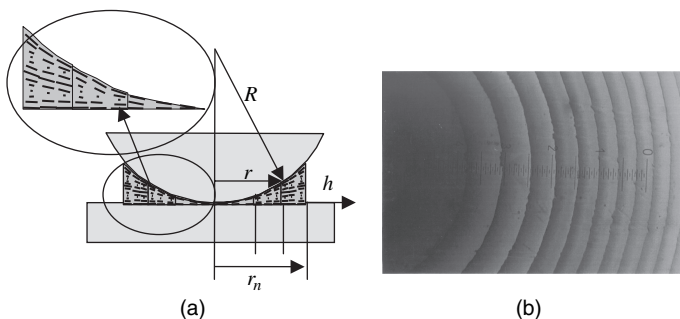


Figure 1.20

## References

- 1 P. G. deGennes and J. Prost, *The physics of liquid crystals* (Oxford University Press, New York, 1993).
- 2 S. Chandrasekhar *Liquid crystals*, 2nd edn (Cambridge University Press, New York, 1997).
- 3 L. M. Blinov and V. G. Chigrinov, *Electrooptical effects in liquid crystal materials* (Springer-Verlag, New York, 1994).
- 4 G. W. Gray, K. J. Harrison, and J. A. Nash, 'New family of nematic liquid crystals for displays', *Electron. Lett.*, **9**, 130 (1973).
- 5 K. J. Toyne, 'Liquid crystal behavior in relation to molecular structure', in *Thermotropic liquid crystals*, ed. G. W. Gray (John Wiley & Sons, Ltd, Chichester, 1987).
- 6 P. J. Collings and M. Hird, *Introduction to liquid crystals, chemistry and physics* (Taylor & Francis, London, 1997).
- 7 F. Reinitzer, *Monatschr. Chem.*, **9**, 421 (1898).
- 8 B. Bahadur (ed.), *Liquid crystals: applications and uses*, Vols. 1, 2, and 3 (Singapore, World Scientific, 1990).
- 9 E. Lueder, *Liquid crystal displays: addressing schemes and electro-optical effects* (John Wiley & Sons, Ltd, Chichester, 2001).
- 10 S.-T. Wu and D.-K. Yang, *Reactive liquid crystal displays* (John Wiley & Sons, Ltd., Chichester, 2001).
- 11 C. Kittel and H. Kroemer, *Thermal physics* 2nd edn (W. H. Freeman, San Francisco, 1980).
- 12 L. J. Lu and A. Saupe, 'Observation of a biaxial nematic phase in potassium laurate-1-decanol-water mixtures', *Phys. Rev. Lett.*, **45**, 1000 (1980).
- 13 L. A. Madsen, T. J. Dingemans, M. Nakata, and E. T. Samulski, 'Thermotropic biaxial nematic liquid crystals', *Phys. Rev. Lett.*, **92**, 145505 (2004).
- 14 B. R. Acharya, A. Primak, and S. Kumar, 'Biaxial nematic phase in bent-core thermotropic mesogens', *Phys. Rev. Lett.*, **92**, 145505 (2004).
- 15 P. Palffy-Muhoray, M. A. Lee, and R. G. Petschek, 'Ferroelectric nematic liquid crystals: realizability and molecular constraints', *Phys. Rev. Lett.*, **60**, 2303 (1988).
- 16 L. D. Landau and E. M. Lifshitz, *Statistical Physics*, Part I, 3rd edn (Pergamon, Oxford, 1980).
- 17 P. G. deGennes, *Mol. Cryst. Liq. Cryst.*, **12**, 193 (1971).
- 18 T. W. Stinson and J. D. Litster, 'Pretransitional phenomena in the isotropic phase of a nematic liquid crystal', *Phys. Rev. Lett.*, **25**, 503 (1970).
- 19 W. Maier and A. Saupe, *Z. Naturforsch.*, **13a**, 564 (1958).
- 20 E. B. Priestley, P. J. Wojtoicz, and P. Sheng, *Introduction to liquid crystals* (Plenum, New York, 1979).
- 21 I. C. Khoo, *Liquid crystals, physical properties and nonlinear optical phenomena* (John Wiley & Sons, Inc., New York, 1995).
- 22 F. C. Frank, 'Liquid crystals. On the theory of liquid crystals', *Discuss Faraday*, **25**, 19 (1958).
- 23 M. Kleman and O. D. Lavrentovich, *Soft matter physics: Introduction* (Springer-Verlag, New York, 2003).
- 24 I. Sage, 'Thermochromic liquid crystal devices', in *Liquid crystals—applications and uses*, Vol. 3, ed. B. Bahadur (World Scientific, Singapore, 1990).
- 25 W. H. de Jeu, 'Physical properties of liquid crystal materials', *Liquid crystal monographs*, vol. 1, ed. G. W. Gray (Gordon and Breach, London, 1980).
- 26 W. H. de Jeu and P. Bordewijk, 'Physical studies of nematic azoxybenzenes. II. Refractive indices and the internal field', *J. Chem. Phys.*, **68**, 109 (1978).
- 27 A. A. Sonin, *The surface physics of liquid crystals* (Gordon and Breach, Luxembourg, 1995).
- 28 T. Uchida, 'Surface alignment of liquid crystals', in *Liquid crystals—applications and uses*, Vol. 3, ed. B. Bahadur (World Scientific, Singapore, 1990).
- 29 S. Faetti, 'Anchoring effects in nematic liquid crystals', in *Liquid crystal materials*, ed. I. C. Khoo (Gordon and Breach, Amsterdam, 1991).
- 30 A. Rapini and M. Papoular, 'Distortion d'une lamelle nematique sous champ magnetique conditions d'ancrage aux parois', *J. Phys. Colloq.* **30**, C-4 (1969).

# 2

## Propagation of Light in Anisotropic Optical Media

### 2.1 Electromagnetic Waves

In wave theory, light is composed of electromagnetic waves propagating in space [1–3]. There are four fundamental quantities in electromagnetic waves: *electric field*  $\vec{E}$ , *electric displacement*  $\vec{D}$ , *magnetic field*  $\vec{H}$ , and *magnetic induction*  $\vec{B}$ . These quantities are vectors. In the SI system, the unit of electric field is *volt/meter*; the unit of electric displacement is *coulomb/meter<sup>2</sup>*, which equals *newton/volt meter*; the unit of magnetic field is *ampere/meter*, which equals *newton/volt second*; and the unit of magnetic induction is *tesla*, which equals *volt second/meter<sup>2</sup>*. In a medium, the electric displacement is related to the electric field by

$$\vec{D} = \epsilon_o \vec{\epsilon} \cdot \vec{E} \quad (2.1)$$

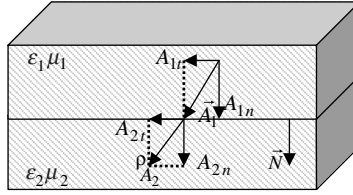
where  $\epsilon_o = 8.85 \times 10^{-12}$  *farad/meter* =  $8.85 \times 10^{-12}$  *newton/volt<sup>2</sup>* and  $\vec{\epsilon}$  is the (relative) dielectric tensor of the medium. The magnetic induction is related to the magnetic field by

$$\vec{B} = \mu_o \vec{\mu} \cdot \vec{H} \quad (2.2)$$

where  $\mu_o = 4\pi \times 10^{-7}$  *henry/meter* =  $4\pi \times 10^{-7}$  *volt<sup>2</sup> second<sup>2</sup>/newton meter<sup>2</sup>* is the permeability of vacuum and  $\vec{\mu}$  is the (relative) permeability tensor of the medium. Liquid crystals are non-magnetic media, with permeability close to 1, and approximately we have  $\vec{\mu} = \vec{I}$ , where  $\vec{I}$  is the identity tensor. In a medium without free charge, electromagnetic waves are governed by the Maxwell equations:

$$\nabla \cdot \vec{D} = 0 \quad (2.3)$$

$$\nabla \cdot \vec{B} = 0 \quad (2.4)$$



**Figure 2.1** Schematic diagram showing the electromagnetic fields at the boundary between two media.  $\vec{A}$  represents  $\vec{E}$ ,  $\vec{D}$ ,  $\vec{H}$ , and  $\vec{B}$ .  $\vec{N}$  is a unit vector along the normal direction of the interface.  $n$ , normal component;  $t$ , tangential component

$$\nabla \times \vec{E} = -\frac{\partial \vec{B}}{\partial t} \tag{2.5}$$

$$\nabla \times \vec{H} = \frac{\partial \vec{D}}{\partial t} \tag{2.6}$$

When light propagates through more than one medium, at the boundary between two media (Figure 2.1) the boundary conditions are

$$D_{2n} - D_{1n} = 0 \tag{2.7}$$

$$B_{2n} - B_{1n} = 0 \tag{2.8}$$

$$E_{2t} - E_{1t} = 0 \tag{2.9}$$

$$H_{2t} - H_{1t} = 0 \tag{2.10}$$

At the boundary, the normal components of  $\vec{D}$  and  $\vec{B}$  and the tangential components of  $\vec{E}$  and  $\vec{H}$  are continuous. These boundary condition equations are derived from the Maxwell equations.

We first consider light propagating in an isotropic uniform medium where  $\vec{D} = \epsilon_o \epsilon \vec{E}$  and  $\vec{B} = \mu_o \mu \vec{H}$ . The Maxwell equations become

$$\nabla \cdot \vec{D} = \nabla \cdot (\epsilon_o \epsilon \vec{E}) = \epsilon_o \epsilon \nabla \cdot \vec{E} = 0 \tag{2.11}$$

$$\nabla \cdot \vec{B} = \nabla \cdot (\mu_o \mu \vec{H}) = \mu_o \mu \nabla \cdot \vec{H} = 0 \tag{2.12}$$

$$\nabla \times \vec{E} = -\frac{\partial \vec{B}}{\partial t} = -\mu_o \mu \frac{\partial \vec{H}}{\partial t} \tag{2.13}$$

$$\nabla \times \vec{H} = \frac{\partial \vec{D}}{\partial t} = \epsilon_o \epsilon \frac{\partial \vec{E}}{\partial t} \tag{2.14}$$

From Equations (2.13) and (2.14), we have

$$\begin{aligned} \nabla \times (\nabla \times \vec{E}) &= \nabla(\nabla \cdot \vec{E}) - \nabla^2 \vec{E} = -\nabla^2 \vec{E} = -\mu_o \mu \nabla \times \left( \frac{\partial \vec{H}}{\partial t} \right) \\ &= -\mu_o \mu \frac{\partial(\nabla \times \vec{H})}{\partial t} = -\epsilon_o \epsilon \mu_o \mu \frac{\partial^2 \vec{E}}{\partial t^2} \end{aligned}$$

that is,

$$\nabla^2 \vec{E} = \epsilon_o \epsilon \mu_o \mu \frac{\partial^2 \vec{E}}{\partial t^2} \quad (2.15)$$

This is a wave equation. In a complex function formulism, the solution for a monochromatic wave is

$$\vec{E}(\vec{r}, t) = \vec{E}_o e^{i(\omega t - \vec{k} \cdot \vec{r})} \quad (2.16)$$

where  $\omega$  is the angular frequency and  $k = 2\pi/\lambda$  ( $\lambda$  is the wavelength in the medium) is the wavevector. The real part of the electric field vector in Equation (2.16) is the actual electric field of the light. Substituting Equation (2.16) into Equation (2.15), we have

$$\omega^2/k^2 = 1/\epsilon_o \mu_o \epsilon \mu \quad (2.17)$$

The propagation velocity of the wave is

$$V = \frac{\omega}{k} = \sqrt{\frac{1}{\epsilon_o \mu_o \epsilon \mu}} \quad (2.18)$$

In a vacuum,  $\epsilon = 1$  and  $\mu = 1$ ,  $V = c = [1/(8.85 \times 10^{-12} \times 4\pi \times 10^{-7})]^{1/2} = 3 \times 10^8$  m/s. In a non-magnetic medium,  $V = c/\sqrt{\epsilon} = c/n$ , where  $n = \sqrt{\epsilon}$  is the refractive index. Here  $\epsilon$  is the dielectric constant that is usually frequency dependent. The wavevector is

$$k = \frac{\omega}{V} = \frac{\omega}{c/n} = \frac{2\pi n}{\lambda_o} \quad (2.19)$$

where  $\lambda_o$  is the wavelength in vacuum. From Equation (2.3), we have

$$\nabla \cdot \vec{D} = -i\vec{k} \cdot \vec{D}_o e^{i(\omega t - \vec{k} \cdot \vec{r})} = 0 \quad (2.20)$$

The electric displacement vector is perpendicular to the propagation direction (the direction of the wavevector), which is true even in anisotropic media. Therefore light is a transverse wave. The electric field vector is perpendicular to the wavevector in isotropic media, but not in anisotropic media.

When light propagates in a homogeneous isotropic medium, all the fields have the same form as Equation (2.16). The amplitudes do not change with time and position. Because of the wave form of the fields, as shown by Equation (2.16), we have

$$\frac{\partial}{\partial t} = i\omega \quad (2.21)$$

$$\nabla = -i\vec{k} \quad (2.22)$$

From Equation (2.13), we can get

$$\vec{B} = \frac{\vec{k} \times \vec{E}}{\omega} \quad (2.23)$$



## 42 PROPAGATION OF LIGHT IN ANISOTROPIC OPTICAL MEDIA

Therefore  $\vec{B}$  and  $\vec{E}$  are orthogonal to each other. Their magnitudes are related by  $|\vec{B}| = (n/c)|\vec{E}|$ . The energy density of the electromagnetic wave is

$$u = \frac{1}{2}(\vec{E} \cdot \vec{D} + \vec{H} \cdot \vec{B}) \quad (2.24)$$

The *Poynting vector* (energy flux) is

$$\vec{S} = \vec{E} \times \vec{H} \quad (2.25)$$

and the magnitude of  $\vec{S}$  is

$$S = \frac{n}{\mu_0 C} E^2 \quad (2.26)$$

## 2.2 Polarization

### 2.2.1 Monochromatic plane waves and their polarization states

When a monochromatic plane light wave is propagating in a homogeneous isotropic medium, only the electric field is needed to characterize it, because the other quantities can be calculated from the electric field. The electric field is a vector and generally has the form

$$\vec{E} = \vec{A}e^{i(\omega t - \vec{k} \cdot \vec{r})} \quad (2.27)$$

where  $\vec{A}$  is a constant. It is understood that the real part of this equation represents the actual electric field. This representation is called the *analytic representation*. The polarization state of a light beam is specified by the electric field vector. In many liquid crystal devices, the liquid crystal is used to manipulate the polarization state of the light.

When the propagation direction is along the  $z$  axis, the real electric field has two components (along the  $x$  and  $y$  axes) [3, 4]:

$$E_x = A_x \cos(\omega t - kz + \delta_x) \quad (2.28)$$

$$E_y = A_y \cos(\omega t - kz + \delta_y) \quad (2.29)$$

$A_x$  and  $A_y$  are positive numbers representing the amplitudes;  $\delta_x$  and  $\delta_y$  are the phases and are defined in the range  $-\pi < \delta_i \leq \pi$  ( $i = 1, 2$ ). The important quantity is the phase difference defined by

$$\delta = \delta_y - \delta_x \quad (2.30)$$

$\delta$  is also defined in the range  $-\pi < \delta \leq \pi$ . We will show that only two parameters are needed to specify the polarization state of a beam. One of the ways to specify a polarization state is the ratio  $A_y/A_x$  and phase difference  $\delta$ .

### 2.2.2 Linear polarization states

Let us consider the time evolution of the electric field vector at a given position ( $z$  is fixed). If the electric field vibrates in a constant direction (in the  $x$ - $y$  plane), the light is said to be *linearly polarized*. This

occurs when  $\delta = 0$  or  $\delta = \pi$ . The angle  $\phi$  of the electric field with respect to the  $x$  axis is given by  $\tan \phi = A_y/A_x$  for  $\delta = 0$  or  $\tan \phi = -A_y/A_x$  for  $\delta = \pi$ . If we examine the spatial evolution of the electric field vector at a fixed time (say,  $t = 0$ ), for linearly polarized light, the curve traced by the electric field in space is confined in a plane. For this reason linearly polarized light is also called *plane polarized* light.

### 2.2.3 Circular polarization states

If the amplitudes in the  $x$  and  $y$  directions are the same and the phase difference is  $\delta = \pi/2$ ,

$$E_x = A \cos(\omega t - kz) \quad (2.31)$$

$$E_y = A \cos(\omega t - kz + \pi/2) = -A \sin(\omega t - kz) \quad (2.32)$$

At a fixed position, say  $z = 0$ ,  $E_x = A \cos(\omega t)$  and  $E_y = -A \sin(\omega t)$ . The endpoint of the electric field vector will trace out a circle clockwise on the  $x$ - $y$  plane (the light is coming toward the observer). At a given time, say  $t = 0$ ,  $E_x = A \cos(kz)$  and  $E_y = A \sin(kz)$ . The endpoint of the electric vector along a line in the propagation direction traces out a right-handed helix in space. The polarization is referred to as *right-handed circular polarization*. If  $\delta = -\pi/2$ , at given time, the endpoint of the electric vector will trace out a left-handed helix in space, and is referred to as *left-handed circular polarization*.

### 2.2.4 Elliptical polarization states

Generally, the amplitudes in the  $x$  and  $y$  directions are not the same and the phase difference is neither 0 nor  $\pi$ . For the purpose of simplicity, let  $\delta_x = 0$ . From Equations (2.28) and (2.29), we have

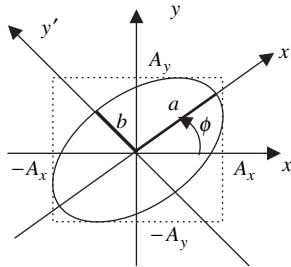
$$E_x/A_x = \cos(\omega t - kz)$$

$$E_y/A_y = \cos(\omega t - kz + \delta) = \cos(\omega t - kz)\cos \delta - \sin(\omega t - kz)\sin \delta$$

By eliminating  $\sin(\omega t - kz)$  and  $\cos(\omega t - kz)$ , we get

$$\left(\frac{E_x}{A_x}\right)^2 + \left(\frac{E_y}{A_y}\right)^2 - 2\left(\frac{E_x}{A_x}\right)\left(\frac{E_y}{A_y}\right)\cos \delta = \sin^2 \delta \quad (2.33)$$

This is an elliptical equation. At a given position, the endpoint of the electric vector traces out an ellipse on the  $x$ - $y$  plane as shown in Figure 2.2. For this reason, the light is said to be *elliptically polarized*. In the  $x'$   $y'$  frame where the coordinate axes are along the major axes of the ellipse, the components,  $E'_x$  and  $E'_y$ ,



**Figure 2.2** The polarization ellipse

#### 44 PROPAGATION OF LIGHT IN ANISOTROPIC OPTICAL MEDIA

of the electric vector satisfy the equation

$$\left(\frac{E'_x}{a}\right)^2 + \left(\frac{E'_y}{b}\right)^2 = 1 \quad (2.34)$$

where  $a$  and  $b$  are the lengths of the principal semi-axes of the ellipse.  $\phi$  is the *azimuthal angle* of the major axis  $x'$  with respect to the  $x$  axis. The transformation of the components of the electric vector between the two frames is given by

$$E_x = E'_x \cos \phi - E'_y \sin \phi \quad (2.35)$$

$$E_y = E'_x \sin \phi + E'_y \cos \phi \quad (2.36)$$

Substituting Equations (2.35) and (2.36) into Equation (2.33), we have

$$\begin{aligned} & \left[ \left(\frac{\cos \phi}{A_x}\right)^2 + \left(\frac{\sin \phi}{A_y}\right)^2 - \frac{\sin 2\phi \cos \delta}{A_x A_y} \right] E_x'^2 + \left[ \left(\frac{\sin \phi}{A_x}\right)^2 + \left(\frac{\cos \phi}{A_y}\right)^2 + \frac{\sin 2\phi \cos \delta}{A_x A_y} \right] E_y'^2 \\ & - \left[ \frac{\sin 2\phi}{A_x^2} - \frac{\sin 2\phi}{A_y^2} + \frac{2 \cos 2\phi}{A_x A_y} \cos \delta \right] E'_x E'_y = \sin^2 \delta \end{aligned} \quad (2.37)$$

Comparing Equation (2.37) to Equation (2.34), we have

$$\left(\frac{\cos \phi}{A_x}\right)^2 + \left(\frac{\sin \phi}{A_y}\right)^2 - \frac{\sin 2\phi \cos \delta}{A_x A_y} = \frac{\sin^2 \delta}{a^2} \quad (2.38)$$

$$\left(\frac{\sin \phi}{A_x}\right)^2 + \left(\frac{\cos \phi}{A_y}\right)^2 + \frac{\sin 2\phi \cos \delta}{A_x A_y} = \frac{\sin^2 \delta}{b^2} \quad (2.39)$$

$$\frac{\sin 2\phi}{A_x^2} - \frac{\sin 2\phi}{A_y^2} + \frac{2 \cos 2\phi}{A_x A_y} \cos \delta = 0 \quad (2.40)$$

The azimuthal angle,  $\phi$ , can be calculated from Equation (2.40) as

$$\tan 2\phi = \frac{A_x A_y \cos \delta}{(A_x^2 - A_y^2)} \quad (2.41)$$

Note that if  $\phi$  is a solution, then  $\phi + \pi/2$  is also a solution. From Equations (2.38) and (2.39) we have

$$\left(\frac{A_x A_y \sin \delta}{a}\right)^2 = A_x^2 \cos^2 \phi + A_y^2 \sin^2 \phi - A_x A_y \sin 2\phi \cos \delta \quad (2.42)$$

$$\left(\frac{A_x A_y \sin \delta}{b}\right)^2 = A_x^2 \sin^2 \phi + A_y^2 \cos^2 \phi + A_x A_y \sin 2\phi \cos \delta \quad (2.43)$$

Adding these two equations together we have

$$(a^2 + b^2) \left(\frac{\sin \delta A_x A_y}{ab}\right)^2 = A_x^2 + A_y^2$$

Because the light intensity does not change upon a transformation between two frames,  $a^2 + b^2 = A_x^2 + A_y^2$ , and therefore

$$(A_x A_y \sin \delta)^2 = (ab)^2 \quad (2.44)$$

From Equations (2.43) and (2.44) we have

$$a^2 = A_x^2 \sin^2 \phi + A_y^2 \cos^2 \phi + A_x A_y \sin 2\phi \cos \delta \quad (2.45)$$

From Equations (2.42) and (2.44) we have

$$b^2 = A_x^2 \cos^2 \phi + A_y^2 \sin^2 \phi - A_x A_y \sin 2\phi \cos \delta \quad (2.46)$$

The lengths of the principal semi-major axes can be calculated from these two equations. The sense of the revolution of an elliptical polarization is determined by the sign of  $\sin \delta$ . If  $\sin \delta > 0$ , the endpoint of the electric vector revolves clockwise (the light is coming toward the observer); if  $\sin \delta < 0$ , the endpoint of the electric vector revolves counterclockwise. The *ellipticity* of the polarization ellipse is defined by

$$e = \pm \frac{b}{a} \quad (2.47)$$

The positive sign is used for right-handed circular polarization while the negative sign is used for left-handed circular polarization. The *ellipticity angle*  $v$  is defined by

$$\tan v = e \quad (2.48)$$

We can also use the azimuthal angle,  $\phi$ , of the major axis and the ellipticity angle,  $v$ , to represent the polarization state. The values of  $\phi$  and  $v$  of various polarization states are listed in Table 2.1.

### 2.3 Propagation of Light in Uniform Anisotropic Optical Media




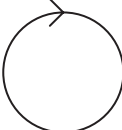
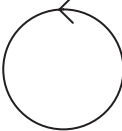


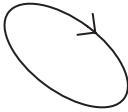
Now we consider the propagation of light in uniform non-magnetic anisotropic media [3, 5]. The speed of light in the medium and thus the phase variation in space depend on the direction of the electric field with respect to the optic axis of the medium. The optical properties of an anisotropic medium are described by the dielectric tensor  $\vec{\epsilon}$ :

$$\vec{\epsilon} = \begin{pmatrix} \epsilon_{11} & \epsilon_{12} & \epsilon_{13} \\ \epsilon_{21} & \epsilon_{22} & \epsilon_{23} \\ \epsilon_{31} & \epsilon_{32} & \epsilon_{33} \end{pmatrix} \quad (2.49)$$

If the medium is non-absorbing, the dielectric tensor is real and symmetric ( $\epsilon_{ij} = \epsilon_{ji}$ ). The values of the elements depend on the choice of the coordinate axes. Because the tensor is symmetric, it is always possible to choose a frame (the principal frame) with three orthogonal axes such that only the diagonal elements of the dielectric tensor are not zero. If the  $xyz$  frame is the *principal frame*, the dielectric tensor has the form

$$\vec{\epsilon} = \begin{pmatrix} \epsilon_x & 0 & 0 \\ 0 & \epsilon_y & 0 \\ 0 & 0 & \epsilon_z \end{pmatrix} \quad (2.50)$$

**Table 2.1** Polarization states in the three representations

Polarization ellipse	$(\phi, \nu)$	Jones vector	Stokes vector
	$(0, 0)$	$\begin{pmatrix} 1 \\ 0 \end{pmatrix}$	$\begin{pmatrix} 1 \\ 1 \\ 0 \\ 0 \end{pmatrix}$
	$(\pi/2, 0)$	$\begin{pmatrix} 0 \\ 1 \end{pmatrix}$	$\begin{pmatrix} 1 \\ -1 \\ 0 \\ 0 \end{pmatrix}$
	$(\pi/4, 0)$	$\frac{1}{\sqrt{2}} \begin{pmatrix} 1 \\ 1 \end{pmatrix}$	$\begin{pmatrix} 1 \\ 0 \\ 1 \\ 0 \end{pmatrix}$
	$(-\pi/4, 0)$	$\frac{1}{\sqrt{2}} \begin{pmatrix} 1 \\ -1 \end{pmatrix}$	$\begin{pmatrix} 1 \\ 0 \\ -1 \\ 0 \end{pmatrix}$
	$(0, \pi/4)$	$\frac{1}{\sqrt{2}} \begin{pmatrix} 1 \\ i \end{pmatrix}$	$\begin{pmatrix} 1 \\ 0 \\ 0 \\ 1 \end{pmatrix}$
	$(0, -\pi/4)$	$\frac{1}{\sqrt{2}} \begin{pmatrix} 1 \\ -i \end{pmatrix}$	$\begin{pmatrix} 1 \\ 0 \\ 0 \\ -1 \end{pmatrix}$
	$[\pi/2, \tan^{-1}(\frac{1}{2})]$	$\frac{1}{\sqrt{5}} \begin{pmatrix} 1 \\ 2i \end{pmatrix}$	$\begin{pmatrix} 1 \\ -3/5 \\ 0 \\ 4/5 \end{pmatrix}$
	$[0, \tan^{-1}(\frac{1}{2})]$	$\frac{1}{\sqrt{5}} \begin{pmatrix} 2 \\ i \end{pmatrix}$	$\begin{pmatrix} 1 \\ 3/5 \\ 0 \\ 4/5 \end{pmatrix}$
	$[\pi/4, \tan^{-1}(\frac{1}{2})]$	$\frac{1}{\sqrt{10}} \begin{pmatrix} 2+i \\ 2-i \end{pmatrix}$	$\begin{pmatrix} 1 \\ 0 \\ 3/5 \\ 4/5 \end{pmatrix}$

In the following discussion in this section, the reference frame used is the principal frame. From the Maxwell equations we get

$$\nabla \times (\nabla \times \vec{E}) = \nabla(\nabla \cdot \vec{E}) - \nabla^2 \vec{E} = -\mu_o \frac{\partial^2 \vec{D}}{\partial t^2} = -\epsilon_o \mu_o \vec{e} \cdot \frac{\partial^2 \vec{E}}{\partial t^2} \quad (2.51)$$

Note that  $\nabla \cdot \vec{D} = \nabla \cdot (\epsilon_o \vec{e} \cdot \vec{E}) = 0$  only assures that  $\vec{D}$ , but not  $\vec{E}$ , is perpendicular to the propagation direction.

### 2.3.1 Eigenmodes

Generally speaking, when light is propagating in a uniform anisotropic medium, the direction of the electric field and therefore the polarization state will vary in space. Only when the electric field is in some special direction, known as the *eigenmode*, will its direction remain invariant in space, which will be proved to be true in this section. In the eigenmode, the electric field has the form

$$\vec{E} = \vec{E}_o e^{i(\omega t - \vec{k} \cdot \vec{r})} \quad (2.52)$$

where  $\vec{E}_o$  is a constant vector known as the *eigenvector*; the corresponding refractive index is called the *eigenvalue*. The wavevector is

$$\vec{k} = \frac{2\pi}{\lambda_o} n \hat{s} = k_o n \hat{s} = k_o n (s_x \hat{x} + s_y \hat{y} + s_z \hat{z}) = k_x \hat{x} + k_y \hat{y} + k_z \hat{z} \quad (2.53)$$

where  $\hat{s} = s_x \hat{x} + s_y \hat{y} + s_z \hat{z}$  is a unit vector along the propagation direction, and  $n$  is the refractive index which depends on the directions of the electric field and the propagation.  $k_o = 2\pi/\lambda_o$  is the wavevector in vacuum. Because of the form of the electric field shown in Equation (2.52), for the monochromatic plane wave we have

$$\frac{\partial}{\partial t} = i\omega \quad (2.54)$$

$$\nabla = -i\vec{k} \quad (2.55)$$

The wave equation (2.51) becomes

$$(\vec{k} \cdot \vec{E}) \vec{k} - k^2 \vec{E} = -\epsilon_o \mu_o \omega^2 \vec{e} \cdot \vec{E} = -k_o^2 \vec{e} \cdot \vec{E} \quad (2.56)$$

In the principal frame, in component form, Equation (2.56) becomes

$$\begin{pmatrix} k_o^2 \epsilon_x - k_y^2 - k_z^2 & k_x k_y & k_x k_z \\ k_y k_x & k_o^2 \epsilon_y - k_x^2 - k_z^2 & k_y k_z \\ k_z k_x & k_z k_y & k_o^2 \epsilon_z - k_x^2 - k_y^2 \end{pmatrix} \cdot \begin{pmatrix} E_x \\ E_y \\ E_z \end{pmatrix} = 0 \quad (2.57)$$

In order to have non-zero solution, the determinant must be zero:

$$\det = \begin{vmatrix} k_o^2 \epsilon_x - k_y^2 - k_z^2 & k_x k_y & k_x k_z \\ k_y k_x & k_o^2 \epsilon_y - k_x^2 - k_z^2 & k_y k_z \\ k_z k_x & k_z k_y & k_o^2 \epsilon_z - k_x^2 - k_y^2 \end{vmatrix} = 0 \quad (2.58)$$

## 48 PROPAGATION OF LIGHT IN ANISOTROPIC OPTICAL MEDIA

This equation is also called the eigenequation. We define

$$n_x^2 = \varepsilon_x, n_y^2 = \varepsilon_y, n_z^2 = \varepsilon_z \quad (2.59)$$

$$a_x = (k_x/k_o)^2 = (ns_x)^2, a_y = (k_y/k_o)^2 = (ns_y)^2, a_z = (k_z/k_o)^2 = (ns_z)^2 \quad (2.60)$$

$$a = a_x + a_y + a_z = n^2 \quad (2.61)$$

Then Equation (2.58) becomes

$$\det = \begin{vmatrix} n_x^2 - a_y - a_z & \sqrt{a_x a_y} & \sqrt{a_x a_z} \\ \sqrt{a_x a_y} & n_y^2 - a_x - a_z & \sqrt{a_y a_z} \\ \sqrt{a_x a_z} & \sqrt{a_y a_z} & n_z^2 - a_x - a_y \end{vmatrix} = 0$$

After some manipulation we obtain

$$(n^2 - n_x^2)(n^2 - n_y^2)(n^2 - n_z^2) = s_x^2 n^2 (n^2 - n_y^2)(n^2 - n_z^2) + s_y^2 n^2 (n^2 - n_x^2)(n^2 - n_z^2) + s_z^2 n^2 (n^2 - n_x^2)(n^2 - n_y^2) \quad (2.62)$$

If  $(n^2 - n_x^2) \neq 0$ ,  $(n^2 - n_y^2) \neq 0$ , and  $(n^2 - n_z^2) \neq 0$ , then this equation can be put into the form

$$\frac{s_x^2}{(n^2 - n_x^2)} + \frac{s_y^2}{(n^2 - n_y^2)} + \frac{s_z^2}{(n^2 - n_z^2)} = \frac{1}{n^2} \quad (2.63)$$

Equation (2.63) looks simpler than Equation (2.62), and is popularly used; it is referred to as *Fresnel's equation of wavenormals*. However, one must be careful in using Equation (2.63) to calculate the refractive index, because an erroneous value may be obtained if  $(n^2 - n_i^2) = 0$  ( $i = x, y, z$ ). For a given propagation direction, the eigenvalue refractive index of the eigenmode can be calculated by using Equation (2.62). On the right hand side of this equation, the coefficient of the term containing  $(n^2)^3$  is 1; on the left hand side, the coefficient of the term containing  $(n^2)^3$  is  $(s_x^2 + s_y^2 + s_z^2)$  which is also 1. Therefore Equation (2.62) is a quadratic in  $n^2$ . For a given propagation direction, there are two solutions of  $n^2$ , and thus there are also two solutions of  $n$ , because  $n > 0$ .

Now we consider the eigenmodes, also referred to as normal modes. In component form Equation (2.57) can be rewritten as three equations:

$$(k_o^2 n_x^2 - k_y^2 - k_z^2)E_x + k_x k_y E_y + k_x k_z E_z = 0 \quad (2.64)$$

$$k_x k_y E_x + (k_o^2 n_y^2 - k_x^2 - k_z^2)E_y + k_y k_z E_z = 0 \quad (2.65)$$

$$k_x k_z E_x + k_y k_z E_z + (k_o^2 n_z^2 - k_x^2 - k_y^2)E_y = 0 \quad (2.66)$$

By eliminating  $E_z$  from Equations (2.64) and (2.65), we get

$$(k_o^2 n_x^2 - k^2)k_y E_x = (k_o^2 n_y^2 - k^2)k_x E_y \quad (2.67)$$

If  $s_x \neq 0$  and  $s_y \neq 0$ , this can be put into the form

$$\frac{(n_x^2 - n^2)E_x}{s_x} = \frac{(n_y^2 - n^2)E_y}{s_y} \quad (2.68)$$

In the same way we can get

$$(k_0^2 n_x^2 - k^2)k_z E_x = (k_0^2 n_z^2 - k^2)k_x E_z \tag{2.69}$$

If  $s_x \neq 0$  and  $s_z \neq 0$ , this can be put into the form

$$\frac{(n_x^2 - n^2)E_x}{s_x} = \frac{(n_z^2 - n^2)E_z}{s_z} \tag{2.70}$$

Therefore the eigenfield is

$$\vec{E} = \begin{pmatrix} s_x / (n_x^2 - n^2) \\ s_y / (n_y^2 - n^2) \\ s_z / (n_z^2 - n^2) \end{pmatrix} \tag{2.71}$$

which is linearly polarized in uniform anisotropic media. The physical meaning of the eigenmode is that for a given propagation direction, if the initial polarization of the light corresponds to an eigenmode when it propagates through the medium, its polarization remains *invariant* and it propagates at the speed  $c/n$  where the refractive index  $n$  is the corresponding eigenvalue. If the initial polarization is not along the eigenmodes, its electric field can be decomposed into two components along the two eigenmodes, respectively. These two components retain their directions, but propagate with different speeds. The resultant polarization changes in space.

It may be easier to visualize the eigenmode refractive indices and the electric field eigenvectors using the *refractive index ellipsoid* [5]. The major axes of the refractive index ellipsoid are parallel to the  $x$ ,  $y$ , and  $z$  axes of the principal frame and have lengths  $2n_x$ ,  $2n_y$ , and  $2n_z$ , respectively, as shown in Figure 2.3. The ellipsoid is described by the equation

$$\frac{x^2}{n_x^2} + \frac{y^2}{n_y^2} + \frac{z^2}{n_z^2} = 1 \tag{2.72}$$

If we draw a straight line through the origin and parallel to  $\hat{s}$  and then cut a plane through the origin, which is perpendicular to  $\hat{s}$ , this plane is described by

$$\hat{s} \cdot (x\hat{x} + y\hat{y} + z\hat{z}) = s_x x + s_y y + s_z z = 0 \tag{2.73}$$

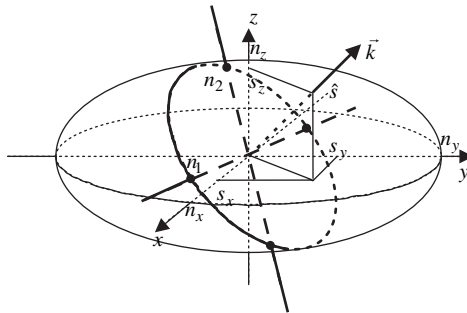


Figure 2.3 The refractive index ellipsoid



## 50 PROPAGATION OF LIGHT IN ANISOTROPIC OPTICAL MEDIA

The intersection of this plane and the ellipsoid is an ellipse. Any point  $(x, y, z)$  on the ellipse must satisfy both Equations (2.72) and (2.73), and its distance from the origin is given by

$$n = (x^2 + y^2 + z^2)^{1/2} \quad (2.74)$$

The maximum and minimum values of  $n$  are, respectively, half the lengths of the major axes of the ellipse. Now we maximize (or minimize)  $n^2$  under the constraints given by Equations (2.72) and (2.73). Using the Lagrange multipliers, we maximize (or minimize)

$$g = (x^2 + y^2 + z^2) - \lambda_1 \left( \frac{x^2}{n_x^2} + \frac{y^2}{n_y^2} + \frac{z^2}{n_z^2} \right) - \lambda_2 (s_x x + s_y y + s_z z) \quad (2.75)$$

where  $\lambda_1$  and  $\lambda_2$  are the Lagrange multipliers. From  $\partial g / \partial x = 0$ ,  $\partial g / \partial y = 0$ , and  $\partial g / \partial z = 0$ , we get

$$x_m = \frac{\lambda_2 s_x n_x^2}{2(n_x^2 - \lambda_1)}, \quad y_m = \frac{\lambda_2 s_y n_y^2}{2(n_y^2 - \lambda_1)}, \quad z_m = \frac{\lambda_2 s_z n_z^2}{2(n_z^2 - \lambda_1)} \quad (2.76)$$

$$n_m^2 = x_m^2 + y_m^2 + z_m^2 = \frac{\lambda_2^2}{4} \left[ \left( \frac{s_x n_x^2}{n_x^2 - \lambda_1} \right)^2 + \left( \frac{s_y n_y^2}{n_y^2 - \lambda_1} \right)^2 + \left( \frac{s_z n_z^2}{n_z^2 - \lambda_1} \right)^2 \right] \quad (2.77)$$

$$\frac{\lambda_2^2}{4} \left[ \frac{n_x^2}{n_m^2} \left( \frac{s_x n_x}{n_x^2 - \lambda_1} \right)^2 + \frac{n_y^2}{n_m^2} \left( \frac{s_y n_y}{n_y^2 - \lambda_1} \right)^2 + \frac{n_z^2}{n_m^2} \left( \frac{s_z n_z}{n_z^2 - \lambda_1} \right)^2 \right] = 1 \quad (2.78)$$

From Equations (2.72) and (2.76), we have

$$\frac{\lambda_2^2}{4} \left[ \left( \frac{s_x n_x}{n_x^2 - \lambda_1} \right)^2 + \left( \frac{s_y n_y}{n_y^2 - \lambda_1} \right)^2 + \left( \frac{s_z n_z}{n_z^2 - \lambda_1} \right)^2 \right] = 1 \quad (2.79)$$

From Equations (2.78) and (2.79), we have

$$\frac{s_x^2 n_x^2}{(n_x^2 - \lambda_1)} \frac{(n_x^2 - n_m^2)}{(n_x^2 - \lambda_1)} + \frac{s_y^2 n_y^2}{(n_y^2 - \lambda_1)} \frac{(n_y^2 - n_m^2)}{(n_y^2 - \lambda_1)} + \frac{s_z^2 n_z^2}{(n_z^2 - \lambda_1)^2} \frac{(n_z^2 - n_m^2)}{(n_z^2 - \lambda_1)} = 0 \quad (2.80)$$

From Equations (2.74) and (2.76), we have

$$\frac{s_x^2 n_x^2}{n_x^2 - \lambda_1} + \frac{s_y^2 n_y^2}{n_y^2 - \lambda_1} + \frac{s_z^2 n_z^2}{n_z^2 - \lambda_1} = 0 \quad (2.81)$$

Comparing these two equations we have

$$\lambda_1 = n_m^2 \quad (2.82)$$

From Equations (2.81) and (2.82), we have

$$\left( \frac{s_x^2}{n_x^2 - n_m^2} + \frac{s_x^2}{n_m^2} \right) + \left( \frac{s_y^2}{n_y^2 - n_m^2} + \frac{s_y^2}{n_m^2} \right) + \left( \frac{s_z^2}{n_z^2 - n_m^2} + \frac{s_z^2}{n_m^2} \right) = 0$$

that is,

$$\frac{s_x^2}{(n_m^2 - n_x^2)} + \frac{s_y^2}{(n_m^2 - n_y^2)} + \frac{s_z^2}{(n_m^2 - n_z^2)} = \frac{s_x^2}{n_m^2} + \frac{s_y^2}{n_m^2} + \frac{s_z^2}{n_m^2} = \frac{1}{n_m^2} \quad (2.83)$$

This equation is the same as Equation (2.63). Therefore half the lengths of the major axes of the ellipse are the two eigenmode refractive indices. The vectors along the major axes of the ellipse are

$$\vec{r} = \begin{bmatrix} s_x n_x^2 / (n_x^2 - n_m^2) \\ s_y n_y^2 / (n_y^2 - n_m^2) \\ s_z n_z^2 / (n_z^2 - n_m^2) \end{bmatrix} \quad (2.84)$$

Comparing Equation (2.84) to Equation (2.71), it can be seen that the eigenmode electric displacements are along the major axes of the ellipse.

### 2.3.2 Orthogonality of eigenmodes

When light propagates in a uniform anisotropic medium, there are two eigenmodes, represented by  $\vec{E}_1$  and  $\vec{E}_2$ , which are linearly polarized and invariant in space. The corresponding eigenmode refractive indices are  $n_1$  and  $n_2$ . Here we discuss some of the basic properties of the eigenmodes.

- (1) *The electric displacement of the eigenmodes,  $\vec{D}_i$  ( $i = 1, 2$ ), is perpendicular to the propagation direction. From Equations (2.3) and (2.55) we have*

$$\hat{s} \cdot \vec{D}_i = 0 \quad (2.85)$$

Therefore the propagation direction  $\hat{s}$  and the electric displacement  $\vec{D}_i$  are orthogonal to each other.

- (2)  $\hat{s}$ ,  $\vec{E}_i$ , and  $\vec{D}_i$  are on the same plane. From Equations (2.51), (2.54), and (2.55) we have the electric displacement of the eigenmodes:

$$\vec{D}_i = \frac{n^2}{c^2 \mu_0} [\vec{E}_i - (\hat{s} \cdot \vec{E}_i) \hat{s}], \quad i = 1, 2 \quad (2.86)$$

Therefore  $\hat{s}$ ,  $\vec{E}_i$ , and  $\vec{D}_i$  lie in the same plane.

- (3)  $\vec{D}_1 \perp \vec{D}_2$ ,  $\vec{D}_1 \perp \vec{E}_2$ , and  $\vec{D}_2 \perp \vec{E}_1$ . Equation (2.59) can be rewritten as

$$k(\hat{s}\hat{s} - \vec{I}) \cdot \vec{E} = -k_o^2 \vec{e} \cdot \vec{E} \quad (2.87)$$

where  $\vec{I}$  is the identity matrix and

$$\hat{s}\hat{s} = \begin{pmatrix} s_x \\ s_y \\ s_z \end{pmatrix} (s_x \quad s_y \quad s_z) = \begin{pmatrix} s_x^2 & s_x s_y & s_x s_z \\ s_x s_y & s_y^2 & s_y s_z \\ s_x s_z & s_y s_z & s_z^2 \end{pmatrix}$$

## 52 PROPAGATION OF LIGHT IN ANISOTROPIC OPTICAL MEDIA

Because  $\vec{E}_1$  is the eigenmode 1 with the eigenvector  $k_1$  and  $\vec{E}_2$  is the eigenmode 2 with the eigenvector  $k_2$ ,

$$k_1(\hat{s}\hat{s} - \vec{I}) \cdot \vec{E}_1 = -k_o^2 \vec{\epsilon} \cdot \vec{E}_1 \quad (2.88)$$

$$k_2(\hat{s}\hat{s} - \vec{I}) \cdot \vec{E}_2 = -k_o^2 \vec{\epsilon} \cdot \vec{E}_2 \quad (2.89)$$

From there two equations, we can get

$$k_1 \vec{E}_2 \cdot (\hat{s}\hat{s} - \vec{I}) \cdot \vec{E}_1 - k_2 \vec{E}_1 \cdot (\hat{s}\hat{s} - \vec{I}) \cdot \vec{E}_2 = -k_o^2 (\vec{E}_2 \cdot \vec{\epsilon} \cdot \vec{E}_1 - \vec{E}_1 \cdot \vec{\epsilon} \cdot \vec{E}_2) = 0 \quad (2.90)$$

Because  $\hat{s}\hat{s}$  is a symmetric matrix,  $\vec{E}_1 \cdot (\hat{s}\hat{s}) \cdot \vec{E}_2 = (\hat{s} \cdot \vec{E}_1)(\hat{s} \cdot \vec{E}_2)$ . The above equation is

$$(k_1 - k_2)[\vec{E}_1 \cdot \vec{E}_2 - (\hat{s} \cdot \vec{E}_1)(\hat{s} \cdot \vec{E}_2)] = 0$$

Because  $k_1 \neq k_2$ , we must have

$$\vec{E}_1 \cdot \vec{E}_2 - (\hat{s} \cdot \vec{E}_1)(\hat{s} \cdot \vec{E}_2) = 0 \quad (2.91)$$

On the other hand,

$$\vec{D}_1 = \frac{n_1^2}{C^2 \mu_o} [\vec{E}_1 - (\hat{s} \cdot \vec{E}_1)\hat{s}] \quad \text{and} \quad \vec{D}_2 = \frac{n_2^2}{C^2 \mu_o} [\vec{E}_2 - (\hat{s} \cdot \vec{E}_2)\hat{s}]$$

Therefore

$$\vec{D}_1 \cdot \vec{D}_2 = \frac{n_1^2 n_2^2}{C^2 \mu_o} [\vec{E}_1 \cdot \vec{E}_2 - (\hat{s} \cdot \vec{E}_1)(\hat{s} \cdot \vec{E}_2)] = 0$$

That is,  $\vec{D}_1$  and  $\vec{D}_2$  are orthogonal to each other. We also have

$$\vec{D}_1 \cdot \vec{E}_2 = \frac{n_1^2}{C^2 \mu_o} [\vec{E}_1 \cdot \vec{E}_2 - (\hat{s} \cdot \vec{E}_1)(\hat{s} \cdot \vec{E}_2)] = 0$$

$$\vec{D}_2 \cdot \vec{E}_1 = \frac{n_2^2}{C^2 \mu_o} [\vec{E}_2 \cdot \vec{E}_1 - (\hat{s} \cdot \vec{E}_2)(\hat{s} \cdot \vec{E}_1)] = 0$$

Generally  $\vec{E}_1$  and  $\vec{E}_2$  are not perpendicular to  $\hat{s}$ . From Equation (2.91) we have  $\vec{E}_1 \cdot \vec{E}_2 = (\hat{s} \cdot \vec{E}_1)(\hat{s} \cdot \vec{E}_2)$ . If both  $\vec{E}_1$  and  $\vec{E}_2$  are not perpendicular to  $\hat{s}$ , then  $\vec{E}_1 \cdot \vec{E}_2 \neq 0$ . If at least one of the eigenmode electric fields is perpendicular to  $\hat{s}$ , then  $\vec{E}_1 \cdot \vec{E}_2 = 0$ .

### 2.3.3 Energy flux

The energy flux in a uniform anisotropic medium is still given by the Poynting vector  $\vec{S} = \vec{E} \times \vec{H}$ . From Equations (2.13), (2.54), and (2.55), for an eigenmode  $\vec{E}_i (i = 1, 2)$ , we have the magnetic field

$$\vec{H}_i = \frac{n_i}{\mu_o C} \hat{s} \times \vec{E}_i \quad (2.92)$$

$$\vec{S}_i = \frac{n_i}{\mu_o C} \vec{E}_i \times (\hat{s} \times \vec{E}_i) = \frac{n_i}{\mu_o C} [E_i^2 \hat{s} - (\hat{s} \cdot \vec{E}_i)\vec{E}_i] \quad (2.93)$$

Because in general  $\vec{E}_i$  is not perpendicular to  $\hat{s}$ ,  $\vec{S}_i$  is not parallel to  $\hat{s}$ . For a light beam, if the initial polarization is not an eigenmode, then the electric field can be decomposed into two eigenmodes:

$$\vec{E} = c_1 \vec{E}_1 + c_2 \vec{E}_2 \quad (2.94)$$

where  $c_1$  and  $c_2$  are constants. The magnetic field is given by

$$\vec{H} = c_1 \vec{H}_1 + c_2 \vec{H}_2 = c_1 \frac{n_1}{\mu_0 C} \hat{s} \times \vec{E}_1 + c_2 \frac{n_2}{\mu_0 C} \hat{s} \times \vec{E}_2 \quad (2.95)$$

The Poynting vector is

$$\begin{aligned} \vec{S} &= (c_1 \vec{E}_1 + c_2 \vec{E}_2) \times (c_1 \vec{H}_1 + c_2 \vec{H}_2) = (c_1 \vec{E}_1 + c_2 \vec{E}_2) \\ &\times \left( \frac{n_1}{\mu_0 C} \hat{s} \times \vec{E}_1 + \frac{n_2}{\mu_0 C} \hat{s} \times \vec{E}_2 \right) \end{aligned} \quad (2.96)$$

which is not equal to  $c_1^2 \vec{S}_1 + c_2^2 \vec{S}_2$ ; that is, the total energy flux is not equal to the sum of the energy fluxes of the two eigenmodes because of the cross-terms between the two eigenmodes. Now let us consider the projections of the cross-terms in the propagation direction. From Equation (2.91), for  $i \neq j$  ( $i, j = 1, 2$ ),

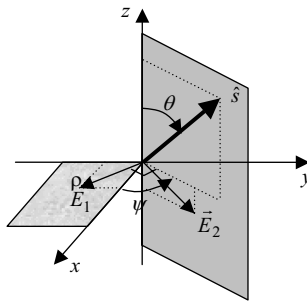
$$\hat{s} \cdot (\vec{E}_i \times \vec{H}_j) = \vec{H}_i = \frac{n_j}{\mu_0 C} \hat{s} \cdot [\vec{E}_i \times \hat{s} \times \vec{E}_j] = \frac{n_j}{\mu_0 C} [\vec{E}_i \cdot \vec{E}_j - (\hat{s} \cdot \vec{E}_i)(\hat{s} \cdot \vec{E}_j)] = 0 \quad (2.97)$$

Hence  $\hat{s} \cdot \vec{S} = \hat{s} \cdot (c_1^2 \vec{S}_1) + \hat{s} \cdot (c_2^2 \vec{S}_2)$ , indicating that the total energy flux in the propagation direction is equal to the sum of the energy fluxes of the two eigenmodes. This is known as the *power orthogonal theorem*.

### 2.3.4 Special cases

First we consider a uniaxial medium whose dielectric constants along the principal frame axes are  $\epsilon_x = \epsilon_y = n_o^2 \neq \epsilon_z = n_e^2$ , where  $n_o$  and  $n_e$  are the ordinary and extraordinary refractive index, respectively. When the propagation direction is along  $\hat{s} = \sin \theta \cos \psi \hat{x} + \sin \theta \sin \psi \hat{y} + \cos \theta \hat{z}$ , as shown in Figure 2.4, Equation (2.62) becomes

$$(n^2 - n_o^2)^2 (n^2 - n_e^2) = \sin^2 \theta n^2 (n^2 - n_o^2) (n^2 - n_e^2) + \cos^2 \theta n^2 (n^2 - n_o^2)^2$$



**Figure 2.4** Diagram showing the propagation direction and the corresponding eigenmodes

## 54 PROPAGATION OF LIGHT IN ANISOTROPIC OPTICAL MEDIA

*Solution 1:*  $(n^2 - n_o^2) = 0$ , namely,

$$n = n_1 = n_o \quad (2.98)$$

From Equation (2.69) we have  $k_o^2(n_e^2 - n_o^2)k_x E_z = 0$ , and therefore  $E_z = 0$ . In this case, Equation (2.71) does not provide any information on the eigenvector. In order to get the eigenvector corresponding to the refractive index  $n_o$ , we use the condition  $\vec{k} \cdot \vec{\varepsilon} \cdot \vec{E} = 0$  because  $\nabla \cdot \vec{D} = \nabla \cdot (\vec{\varepsilon} \cdot \vec{E}) = 0$  and  $\nabla = ik$ . Thus,

$$\vec{k} \cdot \vec{\varepsilon} \cdot \vec{E} = k(\sin \theta \cos \psi, \sin \theta \sin \psi, \cos \theta) \begin{pmatrix} n_o^2 & 0 & 0 \\ 0 & n_o^2 & 0 \\ 0 & 0 & n_e^2 \end{pmatrix} \begin{pmatrix} E_x \\ E_y \\ 0 \end{pmatrix} = 0$$

which gives  $\cos \psi E_x + \sin \psi E_y = 0$ . Hence the eigenmode is

$$\vec{E}_1 = \begin{pmatrix} \sin \psi \\ -\cos \psi \\ 0 \end{pmatrix} \quad (2.99)$$

which is in the  $x$ - $y$  plane and perpendicular to the projection direction  $\hat{k}_{xy}$  of  $\vec{k}$  on the  $x$ - $y$  plane. This eigenmode is sometimes referred to as the *ordinary wave* or simply *O wave*.

*Solution 2:*  $(n^2 - n_o^2)(n^2 - n_e^2) = \sin^2 \theta n^2(n^2 - n_e^2) + \cos^2 \theta n^2(n^2 - n_o^2)$ , namely

$$n = n_2 = \frac{n_o n_e}{(n_e^2 \cos^2 \theta + n_o^2 \sin^2 \theta)^{1/2}} \quad (2.100)$$

From Equation (2.71) we have the eigenmode

$$\vec{E}_2 = \begin{pmatrix} \frac{s_x}{(n_x^2 - n^2)} \\ \frac{s_y}{(n_y^2 - n^2)} \\ \frac{s_z}{(n_z^2 - n^2)} \end{pmatrix} = \begin{pmatrix} \frac{\cos \psi}{n_o^2 \sin \theta} \\ \frac{\sin \psi}{n_o^2 \sin \theta} \\ \frac{-1}{n_e^2 \cos \theta} \end{pmatrix} = \frac{1}{n_o^2 n_e^2 \sin \theta \cos \theta} \begin{pmatrix} n_e^2 \cos \psi \cos \theta \\ n_e^2 \sin \psi \cos \theta \\ -n_o^2 \sin \theta \end{pmatrix} \quad (2.101)$$

which is on the  $z$ - $k_{xy}$  plane. This eigenmode is sometimes referred to as the *extraordinary wave* or simply *E wave*. It can be shown that  $\hat{s}$  is perpendicular to  $\vec{E}_1$  but not to  $\vec{E}_2$ .

When  $\psi = \pi/2$ , the light wave propagates in the  $y$ - $z$  plane. Eigenmode 1 is  $\vec{E}_1^T = (1, 0, 0)$ , where  $T$  stands for the transpose, which is along the  $x$  axis, and the corresponding eigenvalue is  $n_o$ . Eigenmode 2 is  $\vec{E}_2^T = (0, n_e^2 \cos \theta, -n_o^2 \sin \theta)$ , which is in the  $y$ - $z$  plane, and the corresponding eigenvalue is  $n = n_e n_o / (n_e^2 \cos^2 \theta + n_o^2 \sin^2 \theta)^{1/2}$ . Note that the angle between  $\vec{E}_2$  and the  $z$  axis is  $\tan^{-1}(n_e^2 \cos \theta / n_o^2 \sin \theta) \neq \pi/2 - \theta$ .  $\vec{D}_2^T = \vec{\varepsilon} \cdot \vec{E}_2 = n_e^2 n_o^2 (0, \cos \theta, -\sin \theta)$ . The angle between  $\vec{D}_2$  and the  $z$  axis is  $\pi/2 - \theta$ .

When  $\theta = \pi/2$ , the light is propagating in the  $x$ - $y$  plane. The eigenmode 1 is  $\vec{E}_1^T = (\sin \psi, -\cos \psi, 0)$ , and the corresponding eigenvalue is  $n_o$ . The eigenmode 2 is  $\vec{E}_2^T = (0, 0, 1)$ , which is along the  $z$  axis, and the corresponding eigenvalue is  $n_e$ .

2.3.5 Polarizers

Polarizers are an essential component of many liquid crystal devices. Most sheet polarizers are uniaxially anisotropic in their absorption. One way to make a sheet polarizer is to embed elongated absorbing molecules (or tiny rod-like crystals), which exhibit strong absorption for light polarized along their long axis, in a polymer film, and stretch the polymer, which produces a unidirectional alignment of the embedded molecules. Small needle-like crystals of herapathite in polyvinyl alcohol is such an example. The refractive indices of a uniaxial polarizer can be written as

$$n'_o = n_o - ia_o \tag{2.102}$$

$$n'_e = n_e - ia_e \tag{2.103}$$

where the imaginary parts  $a_o, a_e$  are referred to as the extinction coefficients and are responsible for the absorption.  $n'_e$  and  $n'_o$  are the refractive indices, respectively, parallel and perpendicular to the uniaxial axis. Sometimes polarizers are divided into two types: the *O-type polarizer* where  $a_e \gg a_o \approx 0$  and the *E-type polarizer* where  $a_o \gg a_e \approx 0$ . The transmittances of the polarizer for light polarized parallel and perpendicular to its transmission axis are, respectively,

$$T_1 = e^{-2(2\pi a_{\min}/\lambda)h} \tag{2.104}$$

$$T_2 = e^{-2(2\pi a_{\max}/\lambda)h} \tag{2.105}$$

where  $h$  is the optical path inside the polarizer,  $a_{\max}$  the bigger of  $(a_o, a_e)$ , and  $a_{\min}$  the smaller of  $(a_o, a_e)$ . An ideal polarizer would have  $T_1 = 1$  and  $T_2 = 0$ . For a real polarizer  $T_1 < 1$  and  $T_2 > 0$ . The extinction ratio of a polarizer is defined by  $T_1/T_2$ . When unpolarized light is incident on one polarizer, the transmittance is  $(T_1 + T_2)/2$ . When an unpolarized light beam is incident on two parallel polarizers, the transmittance is  $(T_1^2 + T_2^2)/2$ . When an unpolarized light beam is incident on two crossed polarizers, the transmittance is  $T_1 T_2/2$ .

For oblique incident light, some light will leak through a set of two crossed polarizers even if the polarizers are ideal [4]. We consider the leakage of two crossed ideal O-type polarizers as shown in Figure 2.5. The normal of the polarizer films is in the  $z$  direction in the lab frame. The propagation direction is specified by the polar angle  $\theta$  and the azimuthal angle  $\psi$ . For polarizer 1, the transmission axis is parallel to the  $x$  axis in the lab frame. In the local frame  $x'y'z'$ , the transmission axis is parallel to

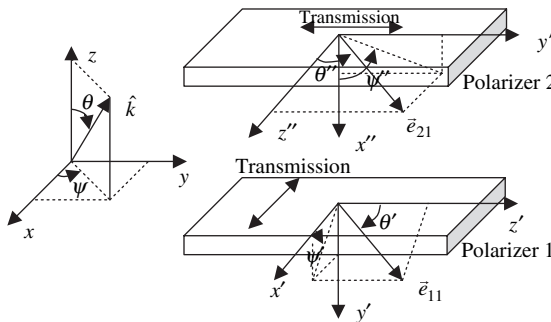


Figure 2.5 Schematic diagram of two crossed polarizers

## 56 PROPAGATION OF LIGHT IN ANISOTROPIC OPTICAL MEDIA

the  $x'$  axis and the uniaxial axis is parallel to the  $z'$  axis. In this local frame, the formulas derived in the last section can be used. The eigenmode 1 has the non-absorbing refractive index  $n_o$  and thus can pass polarizer 1. The direction of the electric field eigenvector is along the direction  $\vec{e}'_{11}$  which in the local frame is given by

$$\vec{e}'_{11} = \begin{pmatrix} \sin \psi' \\ -\cos \psi' \\ 0 \end{pmatrix} \quad (2.106)$$

In the lab frame  $xyz$ , this vector is given by

$$\vec{e}_{11} = \begin{pmatrix} \sin \psi' \\ 0 \\ \cos \psi' \end{pmatrix} \quad (2.107)$$

The relationships between the propagation angles in these frames are  $\cos \theta = -\sin \theta' \sin \psi'$ ,  $\sin \theta \cos \psi = \sin \theta' \cos \psi'$ , and  $\sin \theta \sin \psi = \cos \theta'$ . Therefore we have

$$\vec{e}_{11} = \frac{1}{\sqrt{1 - \sin^2 \theta \sin^2 \psi}} \begin{pmatrix} -\cos \theta \\ 0 \\ \sin \theta \cos \psi \end{pmatrix} \quad (2.108)$$

For polarizer 2, the transmission axis is parallel to the  $y$  axis in the lab frame. In the local frame  $x''y''z''$ , the transmission axis is parallel to the  $x''$  axis and the uniaxial axis is parallel to the  $z''$  axis. For the eigenmode that has the non-absorbing refractive index  $n_o$  and can pass polarizer 2, the direction of the electric field eigenvector is along the direction  $\vec{e}''_{21}$ , which in the local frame is given by

$$\vec{e}''_{21} = \begin{pmatrix} \sin \psi'' \\ -\cos \psi'' \\ 0 \end{pmatrix} \quad (2.109)$$

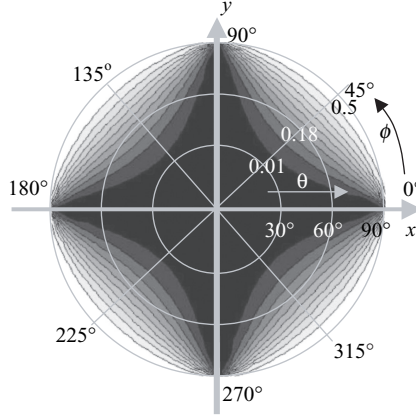
In the lab frame, this vector is given by

$$\vec{e}_{21} = \begin{pmatrix} 0 \\ -\cos \psi'' \\ \sin \psi'' \end{pmatrix} \quad (2.110)$$

The relationships between the propagation angles in the lab frame  $xyz$  and the local frame  $x''y''z''$  are  $\cos \theta = -\sin \theta'' \cos \psi''$ ,  $\sin \theta \cos \psi = \cos \theta''$ , and  $\sin \theta \sin \psi = \sin \theta'' \sin \psi''$ . Therefore we have

$$\vec{e}_{21} = \frac{1}{\sqrt{1 - \sin^2 \theta \cos^2 \psi}} \begin{pmatrix} 0 \\ \cos \theta \\ \sin \theta \sin \psi \end{pmatrix} \quad (2.111)$$

The light (eigenmode  $\vec{e}_{11}$ ) coming out of polarizer 1 can be decomposed into two components in the eigenvector directions of polarizer 2. The component along the eigenmode  $\vec{e}_{11}$  passes polarizer 2



**Figure 2.6** Iso-transmittance diagram of the crossed polarizers: black, low transmittance; white, high transmittance

without absorption. The leakage of unpolarized light through the two crossed polarizers is given by

$$T_{leakage} = \frac{1}{2} (\vec{e}_{11} \cdot \vec{e}_{21})^2 = \frac{\sin^4 \theta \sin^2 \psi \cos^2 \psi}{2(1 - \sin^2 \theta \sin^2 \psi)(1 - \sin^2 \theta \cos^2 \psi)} \quad (2.112)$$

Note that the angle  $\theta$  here is the polar angle of the propagation direction inside the polarizers. This leakage, if not compensated, will limit the viewing angle of liquid crystal displays. The iso-transmittance (leakage) diagram of the crossed polarizers as a function of the polar and azimuthal angles is shown in Figure 2.6. It resembles the appearance of crossed polarizers under isotropic incident light when viewed at various polar and azimuthal angles. Black indicates low transmittance (leakage) and white indicates high transmittance (leakage). At the azimuthal angle of  $45^\circ$ , when the polar angle is  $30^\circ$ ,  $60^\circ$ , and  $90^\circ$ , the transmittance is 0.01, 0.18, and 0.5, respectively. The leakage of the crossed polarizers can be reduced by using compensation films [6].

## 2.4 Propagation of Light in Cholesteric Liquid Crystals

### 2.4.1 Eigenmodes

We showed in the previous section that in a uniform anisotropic medium, for each propagation direction, there are two eigenmodes which are linearly polarized. The polarization state of the eigenmodes is invariant in space. In this section we discuss the propagation of light in the special case of a non-uniform anisotropic medium: a cholesteric liquid crystal which locally is optically uniaxial, but the optic axis twists uniformly in space [6, 7]. We choose the  $z$  axis of the lab frame to be parallel to the helical axis of the cholesteric liquid crystal. The pitch  $P$  of the liquid crystal is the distance over which the liquid crystal director twists  $2\pi$ . The components of the liquid crystal director of a right-handed cholesteric liquid crystal ( $q > 0$ ) are given by

$$n_x = \cos(qz), n_y = \sin(qz), n_z = 0 \quad (2.113)$$

where the twisting rate (chirality)  $q$  is related to the pitch by  $q = 2\pi/P$ . We consider light propagating in the  $z$  direction,  $\vec{E}(z, t) = \vec{A}(z)e^{i\omega t}$ , and therefore  $\nabla = \hat{z}\partial/\partial z$  and  $\partial/\partial t = i\omega$ . From Equation (2.51)



we have

$$\frac{\partial^2 \vec{A}(z)}{\partial z^2} = -k_o^2 \vec{\varepsilon}(z) \cdot \vec{A}(z) \quad (2.114)$$

where  $k_o = \omega/c = 2\pi/\lambda$  ( $\lambda$  is the wavelength in vacuum). The dielectric constants of the liquid crystal for light polarized parallel and perpendicular to the liquid crystal director are  $\varepsilon_{\parallel} = n_o^2$  and  $\varepsilon_{\perp} = n_e^2$ , respectively. The dielectric tensor in the  $x$ - $y$  plane in the lab frame is

$$\vec{\varepsilon}(z) = \varepsilon_{\perp} \vec{I} + \delta \vec{n}\vec{n} = \begin{pmatrix} \varepsilon_{\perp} + 2\delta n_x^2 & 2\delta n_x n_y \\ 2\delta n_y n_x & \varepsilon_{\perp} + 2\delta n_y^2 \end{pmatrix} = \begin{pmatrix} \bar{\varepsilon} + \delta \cos(2qz) & \delta \sin(2qz) \\ \delta \sin(2qz) & \bar{\varepsilon} - \delta \cos(2qz) \end{pmatrix} \quad (2.115)$$

where  $\delta = (\varepsilon_{\parallel} - \varepsilon_{\perp})/2$  and  $\bar{\varepsilon} = (\varepsilon_{\parallel} + \varepsilon_{\perp})/2$ . As we will show, there is no mode whose polarization state is invariant in space in the lab frame; consequently we employ the local frame whose  $x'$  axis is parallel to the liquid crystal director. The angle between the  $x'$  axis and the  $x$  axis is  $\phi = qz$ . The relation between the two frames is

$$\hat{x}' = \cos(qz)\hat{x} + \sin(qz)\hat{y} \quad (2.116)$$

$$\hat{y}' = -\sin(qz)\hat{x} + \cos(qz)\hat{y} \quad (2.117)$$

In the  $x'y'$  frame, the electric field is

$$\vec{A}' = \begin{pmatrix} A'_x \\ A'_y \end{pmatrix} = \begin{pmatrix} \cos \phi & \sin \phi \\ -\sin \phi & \cos \phi \end{pmatrix} \begin{pmatrix} A_x \\ A_y \end{pmatrix} \equiv \vec{S}^{-1}(\phi) \vec{A} \quad (2.118)$$

where  $\vec{S}$  is the transformation matrix. The dielectric tensor in the local frame is

$$\begin{aligned} \vec{\varepsilon}' &= \vec{S}^{-1} \vec{\varepsilon} \vec{S} = \begin{pmatrix} \cos \phi & \sin \phi \\ -\sin \phi & \cos \phi \end{pmatrix} \begin{pmatrix} \bar{\varepsilon} + \delta \cos(2\phi) & \delta \sin(2\phi) \\ \delta \sin(2\phi) & \bar{\varepsilon} - \delta \cos(2\phi) \end{pmatrix} \begin{pmatrix} \cos \phi & -\sin \phi \\ \sin \phi & \cos \phi \end{pmatrix} \\ &= \begin{pmatrix} \varepsilon_{\parallel} & 0 \\ 0 & \varepsilon_{\perp} \end{pmatrix} \end{aligned} \quad (2.119)$$

Because the dielectric tensor in the local frame is a constant tensor, we presume that the polarization of the eigenmodes is invariant in space in this frame [4, 8], which will be proved true:

$$\vec{A}'(z) = \vec{A}'_o e^{-ikz} = (A'_{ox} \hat{x}' + A'_{oy} \hat{y}') e^{-ikz} \quad (2.120)$$

where  $A'_{ox}$  and  $A'_{oy}$  are constants. In the lab frame, the electric field is

$$\begin{aligned} \vec{A}(z) &= \vec{S}(qz) \cdot \vec{A}'(z) \\ &= [A'_{ox} \cos(qz) - A'_{oy} \sin(qz)] e^{-ikz} \hat{x} + [A'_{ox} \sin(qz) + A'_{oy} \cos(qz)] e^{-ikz} \hat{y} \\ &= (A'_{ox} \hat{x} + A'_{oy} \hat{y}) \cos(qz) e^{-ikz} + (-A'_{oy} \hat{x} + A'_{ox} \hat{y}) \sin(qz) e^{-ikz} \end{aligned} \quad (2.121)$$

$$\begin{aligned} \frac{\partial \vec{A}}{\partial z} &= (-ik)(A'_{ox} \hat{x} + A'_{oy} \hat{y}) \cos(qz) e^{-ikz} + (-ik)(-A'_{oy} \hat{x} + A'_{ox} \hat{y}) \sin(qz) e^{-ikz} \\ &\quad + (-q)(A'_{ox} \hat{x} + A'_{oy} \hat{y}) \sin(qz) e^{-ikz} + (q)(-A'_{oy} \hat{x} + A'_{ox} \hat{y}) \cos(qz) e^{-ikz} \end{aligned}$$

$$\frac{\partial^2 \vec{A}}{\partial z^2} = (-k^2 - q^2) \vec{A} + (i2kq) \vec{B} \quad (2.122)$$

where

$$\vec{B} = \{[A'_{ox} \sin(qz) + A'_{oy} \cos(qz)]\hat{x} - [A'_{ox} \cos(qz) - A'_{oy} \sin(qz)]\hat{y}\} e^{-ikz} \quad (2.123)$$

Equation (2.114) becomes

$$-(k^2 + q^2)\vec{A}(z) + (i2kq)\vec{B} = -k_o^2 \vec{\epsilon}(z) \cdot \vec{A}(z) \quad (2.124)$$

Multiplying both sides by the transformation matrix, we get

$$\begin{aligned} -(k^2 + q^2)\vec{S}^{-1} \cdot \vec{A}(z) + (i2kq)\vec{S}^{-1} \cdot \vec{B} &= -k_o^2 \vec{S}^{-1} \vec{\epsilon}(z) \cdot \vec{S} \cdot \vec{S}^{-1} \cdot \vec{A}(z) \\ -(k^2 + q^2)\vec{A}'(z) + (i2kq)\vec{S}^{-1} \cdot \vec{B} &= -k_o^2 \vec{\epsilon}'(z) \cdot \vec{A}'(z) \end{aligned}$$

Because

$$\vec{S}^{-1} \cdot \vec{B} = \begin{pmatrix} \cos \phi & \sin \phi \\ -\sin \phi & \cos \phi \end{pmatrix} \begin{pmatrix} A'_{ox} \sin \phi + A'_{oy} \cos \phi \\ -A'_{ox} \cos \phi + A'_{oy} \sin \phi \end{pmatrix} = \begin{pmatrix} A'_{oy} \\ -A'_{ox} \end{pmatrix}$$

Equation (2.124) can be put into the form

$$\begin{pmatrix} n_e^2 k_o^2 - k^2 - q^2 & i2qk \\ -i2qk & n_o^2 k_o^2 - k^2 - q^2 \end{pmatrix} \begin{pmatrix} A'_{ox} \\ A'_{oy} \end{pmatrix} = 0 \quad (2.125)$$

For non-zero solutions, it is required that

$$\begin{vmatrix} n_e^2 k_o^2 - k^2 - q^2 & i2qk \\ -i2qk & n_o^2 k_o^2 - k^2 - q^2 \end{vmatrix} = 0 \quad (2.126)$$

We define  $k = nk_o$  and  $\alpha = q/k_o = \lambda/P$ . Equation (2.126) becomes

$$\begin{aligned} n^4 - (2\alpha^2 + n_e^2 + n_o^2)n^2 + (\alpha^2 - n_e^2)(\alpha^2 - n_o^2) &= 0 \\ n_1^2 = \alpha^2 + \bar{\epsilon} + (4\alpha^2 \bar{\epsilon} + \delta^2)^{1/2} \end{aligned} \quad (2.127)$$

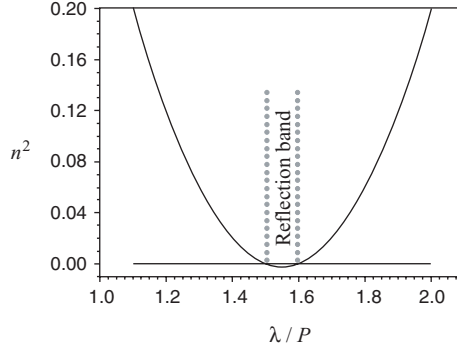
$$n_2^2 = \alpha^2 + \bar{\epsilon} - (4\alpha^2 \bar{\epsilon} + \delta^2)^{1/2} \quad (2.128)$$

$n_1^2$  is always positive.  $n_2^2$  can be either positive or negative depending on the ratio between the wavelength and the pitch, as shown in Figure 2.7.

The eigenvalues are

$$n_{1\pm} = \pm[\alpha^2 + \bar{\epsilon} + (4\alpha^2 \bar{\epsilon} + \delta^2)^{1/2}]^{1/2} = \pm\{(\lambda/P)^2 + \bar{\epsilon} + [4(\lambda/P)^2 \bar{\epsilon} + \delta^2]^{1/2}\}^{1/2} \quad (2.129)$$

$$n_{2\pm} = \pm[\alpha^2 + \bar{\epsilon} - (4\alpha^2 \bar{\epsilon} + \delta^2)^{1/2}]^{1/2} = \pm\{(\lambda/P)^2 + \bar{\epsilon} - [4(\lambda/P)^2 \bar{\epsilon} + \delta^2]^{1/2}\}^{1/2} \quad (2.130)$$



**Figure 2.7**  $n^2$  vs.  $\lambda/P$  curve.  $n_e = 1.6$  and  $n_o = 1.5$  are used in the calculation

For each eigenvalue, there is an eigenmode. All together there are four eigenmodes. Two of the eigenmodes propagate in the  $+z$  direction, and the other two eigenmodes propagate in the  $-z$  direction. For the positive case, the corresponding eigenmode is not necessarily propagating in the  $+z$  direction. From Equation (2.125) we can calculate the polarization of the eigenmodes:

$$\vec{A}'_{o1\pm} = a \begin{pmatrix} 1 \\ i[n_e^2 - n_{1\pm}^2 - \alpha^2]/2\alpha n_{1\pm} \end{pmatrix} \quad (2.131)$$

$$\vec{A}'_{o2\pm} = b \begin{pmatrix} 1 \\ i[n_e^2 - n_{2\pm}^2 - \alpha^2]/2\alpha n_{2\pm} \end{pmatrix} \quad (2.132)$$

where  $a$  and  $b$  are normalization constants. Generally they are elliptically polarized because of the  $\pi/2$  phase difference between  $A'_{ox}$  and  $A'_{oy}$ .  $n_{1\pm}$  is always real for any frequency  $\omega$ ;  $n_{2\pm}$  can be real or imaginary depending on the frequency  $\omega$ .

We now consider some special cases.

(1)  $P \gg \lambda$

In this case,  $\alpha = \lambda/P \ll 1$ . Using the approximation  $\bar{\epsilon} \approx \bar{n}^2$  and the assumption  $\Delta n \ll 1$ , from Equation (2.129) we have

$$\begin{aligned} n_1 &= \{\alpha^2 + \bar{n}^2 + 2\bar{n}[\alpha^2 + (\Delta n/2)^2]^{1/2}\}^{1/2} \\ &= \bar{n} + \sqrt{\alpha^2 + (\Delta n/2)^2} = \bar{n} + \alpha\sqrt{1+u^2} \end{aligned} \quad (2.133)$$

where  $u = \Delta n/2\alpha = \Delta n P/2\lambda$ . The corresponding eigenmode has the polarization

$$\vec{A}'_{o1} \approx a \begin{pmatrix} 1 \\ i[n_e^2 - \bar{n}^2 - (2+u^2)\alpha^2 - 2\bar{n}\alpha\sqrt{1+u^2}]/(2\alpha\bar{n}) \end{pmatrix} \approx \begin{pmatrix} 1 \\ i(u - \sqrt{1+u^2}) \end{pmatrix} \quad (2.134)$$

which is elliptically polarized in the local frame. From Equation (2.130) we have

$$\begin{aligned} n_2 &= \{\alpha^2 + \bar{n}^2 - 2\bar{n}[\alpha^2 + (\Delta n/2)^2]^{1/2}\}^{1/2} \\ &= \bar{n} - \sqrt{\alpha^2 + (\Delta n/2)^2} = \bar{n} - \alpha\sqrt{1+u^2} \end{aligned} \quad (2.135)$$

The corresponding eigenmode has the polarization

$$\vec{A}'_{o2} \approx a \begin{pmatrix} 1 \\ i[n_e^2 - \bar{n}^2 - (2+u^2)\alpha^2 + 2\bar{n}\alpha\sqrt{1+u^2}]/(2\alpha\bar{n}) \end{pmatrix} \approx \begin{pmatrix} 1 \\ i(u + \sqrt{1+u^2}) \end{pmatrix} \quad (2.136)$$

which is also elliptically polarized in the local frame. We consider light propagating in the  $+z$  direction. At the entrance plane the electric field vector is  $\vec{E}'_{in} = (E_{xi}, E_{yi})$ ; the local frame is the same as the lab frame. If the amplitudes of the two eigenmodes are  $u_i$  and  $v_i$ , we have

$$\begin{aligned} \begin{pmatrix} E_{xi} \\ E_{yi} \end{pmatrix} &= u_i \begin{pmatrix} 1 \\ i(u - \sqrt{1+u^2}) \end{pmatrix} + v_i \begin{pmatrix} 1 \\ i(u + \sqrt{1+u^2}) \end{pmatrix} \\ &= \begin{pmatrix} 1 & 1 \\ i(u - \sqrt{1+u^2}) & i(u + \sqrt{1+u^2}) \end{pmatrix} \begin{pmatrix} u_i \\ v_i \end{pmatrix} \end{aligned} \quad (2.137)$$

From the above equation we can get

$$\begin{pmatrix} u_i \\ v_i \end{pmatrix} = \frac{1}{2\sqrt{1+u^2}} \begin{pmatrix} u + \sqrt{1+u^2} & i \\ -u + \sqrt{1+u^2} & -i \end{pmatrix} \begin{pmatrix} E_{xi} \\ E_{yi} \end{pmatrix} \quad (2.138)$$

After the light propagates a distance  $h$  along the  $+z$  direction, in the local frame the amplitude of the eigenmodes becomes

$$\begin{aligned} \begin{pmatrix} u_o \\ v_o \end{pmatrix} &= \begin{pmatrix} e^{-i2\pi h(\bar{n} + \alpha\sqrt{1+u^2})/\lambda} & 0 \\ 0 & e^{-i2\pi h(\bar{n} - \alpha\sqrt{1+u^2})/\lambda} \end{pmatrix} \begin{pmatrix} u_{in} \\ v_{in} \end{pmatrix} \\ &= e^{-i2\pi h\bar{n}/\lambda} \begin{pmatrix} e^{-i\Theta} & 0 \\ 0 & e^{i\Theta} \end{pmatrix} \begin{pmatrix} u_{in} \\ v_{in} \end{pmatrix} \end{aligned} \quad (2.139)$$

where  $\Theta = 2\pi h\alpha\sqrt{1+u^2}/\lambda$ . The electric field in the local frame becomes

$$\begin{aligned} \begin{pmatrix} E'_{xo} \\ E'_{yo} \end{pmatrix} &= u_o \begin{pmatrix} 1 \\ i(u - \sqrt{1+u^2}) \end{pmatrix} + v_o \begin{pmatrix} 1 \\ i(u + \sqrt{1+u^2}) \end{pmatrix} \\ &= \begin{pmatrix} 1 & 1 \\ i(u - \sqrt{1+u^2}) & i(u + \sqrt{1+u^2}) \end{pmatrix} \begin{pmatrix} u_o \\ v_o \end{pmatrix} \end{aligned} \quad (2.140)$$

## 62 PROPAGATION OF LIGHT IN ANISOTROPIC OPTICAL MEDIA

Substituting Equations (2.138) and (2.139) into Equation (2.140) we get

$$\begin{aligned}
 \begin{pmatrix} E'_{xo} \\ E'_{yo} \end{pmatrix} &= \frac{e^{-i2\pi h\bar{n}/\lambda}}{2\sqrt{1+u^2}} \begin{pmatrix} 1 & 1 \\ i(u - \sqrt{1+u^2}) & i(u + \sqrt{1+u^2}) \end{pmatrix} \begin{pmatrix} e^{-i\Theta} & 0 \\ 0 & e^{i\Theta} \end{pmatrix} \\
 &\quad \begin{pmatrix} u + \sqrt{1+u^2} & i \\ -u + \sqrt{1+u^2} & -i \end{pmatrix} \begin{pmatrix} E_{xi} \\ E_{yi} \end{pmatrix} \\
 &= \frac{e^{-i2\pi h\bar{n}/\lambda}}{2\sqrt{1+u^2}} \begin{pmatrix} 2\sqrt{1+u^2}\cos\Theta - i2u\sin\Theta & 2\sin\Theta \\ -2\sin\Theta & 2\sqrt{1+u^2}\cos\Theta + i2u\sin\Theta \end{pmatrix} \\
 \begin{pmatrix} E_{xi} \\ E_{yi} \end{pmatrix} &= e^{-i2\pi h\bar{n}/\lambda} \begin{pmatrix} \cos\Theta - i\frac{u}{\sqrt{1+u^2}}\sin\Theta & \frac{1}{\sqrt{1+u^2}}\sin\Theta \\ -\frac{1}{\sqrt{1+u^2}}\sin\Theta & \cos\Theta + i\frac{u}{\sqrt{1+u^2}}\sin\Theta \end{pmatrix} \begin{pmatrix} E_{xi} \\ E_{yi} \end{pmatrix} \quad (2.141)
 \end{aligned}$$

Defining the total twist angle  $\Phi = 2\pi h/P$  and total retardation angle  $\Gamma = 2\pi\Delta n h/\lambda$ , then

$$\begin{aligned}
 \Theta &= 2\pi h \frac{\lambda}{P} \sqrt{1 + (\Delta n P/2\lambda)^2} / \lambda = \left[ \left( \frac{2\pi h}{P} \right)^2 + \left( \frac{2\pi h}{2\lambda} \right)^2 \right]^{1/2} = [\Phi^2 + (\Gamma/2)^2]^{1/2} \\
 \frac{u}{\sqrt{1+u^2}} &= \frac{(\Gamma/2)}{\Theta}
 \end{aligned}$$

and

$$\frac{1}{\sqrt{1+u^2}} = \frac{\Phi}{\Theta}$$

Equation (2.141) becomes

$$\begin{pmatrix} E'_{xo} \\ E'_{yo} \end{pmatrix} = e^{-i2\pi h\bar{n}/\lambda} \begin{pmatrix} \cos\Theta - i\frac{(\Gamma/2)}{\Theta}\sin\Theta & \frac{\Phi}{\Theta}\sin\Theta \\ -\frac{\Phi}{\Theta}\sin\Theta & \cos\Theta + i\frac{(\Gamma/2)}{\Theta}\sin\Theta \end{pmatrix} \begin{pmatrix} E_{xi} \\ E_{yi} \end{pmatrix} \quad (2.142)$$

The factor  $e^{-i2\pi h\bar{n}/\lambda}$  can be omitted. In the lab frame we have

$$\begin{aligned}
 \begin{pmatrix} E_{xo} \\ E_{yo} \end{pmatrix} &= \begin{pmatrix} \cos\Phi & -\sin\Phi \\ \sin\Phi & \cos\Phi \end{pmatrix} \begin{pmatrix} \cos\Theta - i\frac{(\Gamma/2)}{\Theta}\sin\Theta & \frac{\Phi}{\Theta}\sin\Theta \\ -\frac{\Phi}{\Theta}\sin\Theta & \cos\Theta + i\frac{(\Gamma/2)}{\Theta}\sin\Theta \end{pmatrix} \\
 \begin{pmatrix} E_{xi} \\ E_{yi} \end{pmatrix} & \quad (2.143)
 \end{aligned}$$

Under the Mauguin condition  $\Delta n P \gg \lambda$  [9],  $u = \Delta n/2\alpha = \Delta n P/2\lambda \gg 1$ , Equation (2.133) becomes

$$n_1 = \bar{n} + \alpha\sqrt{1+u^2} \approx \bar{n} + \alpha u = \bar{n} + \frac{\lambda}{P} \frac{\Delta n P}{2\lambda} = \bar{n} + \frac{\Delta n}{2} = n_e \quad (2.144)$$

The corresponding eigenmode has the polarization

$$\vec{A}'_{o1} = \begin{pmatrix} 1 \\ i(u - \sqrt{1+u^2}) \end{pmatrix} = \begin{pmatrix} 1 \\ -i/2u \end{pmatrix} \approx \begin{pmatrix} 1 \\ 0 \end{pmatrix} \quad (2.145)$$

which is linearly polarized along the liquid crystal director. Equation (2.150) becomes

$$n_2 = \bar{n} - \alpha\sqrt{1+u^2} = \bar{n} - \alpha u = \bar{n} - \frac{\lambda}{P} \frac{\Delta n P}{2\lambda} = \bar{n} - \frac{\Delta n}{2} = n_o \quad (2.146)$$

The corresponding eigenmode has the polarization

$$\vec{A}'_{o2} = b \begin{pmatrix} 1 \\ i(u + \sqrt{1+u^2}) \end{pmatrix} = b \begin{pmatrix} 1 \\ 2iu \end{pmatrix} = \begin{pmatrix} 0 \\ 1 \end{pmatrix} \quad (2.147)$$

which is linearly polarized perpendicular to the liquid crystal director. In this regime, for the eigenmodes, the polarization twists in phase with the liquid crystal director in space. This is the 'waveguide' regime.

(2)  $\Delta n P \ll \lambda$

In this case,  $4\alpha^2\bar{\epsilon} \gg \delta^2$ . From Equation (2.129) we have

$$n_{1\pm} \approx \pm \left( \alpha^2 + \bar{\epsilon} + 2\alpha\sqrt{\bar{\epsilon}} + \frac{\delta^2}{4\alpha\sqrt{\bar{\epsilon}}} \right)^{1/2} \approx \pm \left[ \alpha + \sqrt{\bar{\epsilon}} + \frac{\delta^2}{8\alpha(\alpha + \sqrt{\bar{\epsilon}})\sqrt{\bar{\epsilon}}} \right] \quad (2.148)$$

The corresponding eigenmodes have the polarization

$$\vec{A}'_{o1\pm} \approx a \begin{pmatrix} \left[ n_e^2 - \left( \alpha^2 + \bar{\epsilon} + 2\alpha\sqrt{\bar{\epsilon}} + \frac{\delta^2}{4\alpha\sqrt{\bar{\epsilon}}} \right) - \alpha^2 \right] \\ 2\alpha \left[ \pm \left( \alpha + \sqrt{\bar{\epsilon}} + \frac{\delta^2}{8\alpha(\alpha + \sqrt{\bar{\epsilon}})\sqrt{\bar{\epsilon}}} \right) \right] \end{pmatrix} \approx \begin{pmatrix} -i[2\alpha^2 + 2\alpha\sqrt{\bar{\epsilon}}] \\ 2\alpha[\pm(\alpha + \sqrt{\bar{\epsilon}})] \end{pmatrix} \approx \begin{pmatrix} 1 \\ \mp i \end{pmatrix}$$

In the lab frame, the polarization is

$$\begin{aligned} A_{o1\pm x} &= [\cos(qz) \pm i \sin(qz)] e^{-ik_o n_{1\pm} z} = e^{i(\pm q - k_o n_{1\pm})z} \\ A_{o1\pm y} &= [\sin(qz) \mp i \cos(qz)] e^{-ik_o n_{1\pm} z} = (\mp i) e^{i(\pm q - k_o n_{1\pm})z} \end{aligned}$$

Because

$$\pm q - k_o n_{1\pm} = \pm k_o \alpha \mp k_o \left[ \alpha + \sqrt{\bar{\epsilon}} + \frac{\delta^2}{8\alpha(\alpha + \sqrt{\bar{\epsilon}})\sqrt{\bar{\epsilon}}} \right] = \mp k_o \left[ \sqrt{\bar{\epsilon}} + \frac{\delta^2}{8\alpha(\alpha + \sqrt{\bar{\epsilon}})\sqrt{\bar{\epsilon}}} \right]$$

## 64 PROPAGATION OF LIGHT IN ANISOTROPIC OPTICAL MEDIA

we have

$$\vec{A}_{1\pm} = \begin{pmatrix} 1 \\ \mp i \end{pmatrix} e^{-i(\pm k_o) \left[ \sqrt{\bar{\epsilon}} + \frac{\delta^2}{8\alpha(\alpha + \sqrt{\bar{\epsilon}})\sqrt{\bar{\epsilon}}} \right] z} \quad (2.149)$$

Eigenmode 1 is left-handed circularly polarized and propagates in the  $+z$  direction with refractive index

$$n_1 = \sqrt{\bar{\epsilon}} + \delta^2 / [8\alpha(\alpha + \sqrt{\bar{\epsilon}})\sqrt{\bar{\epsilon}}] \quad (2.150)$$

Eigenmode 2 is also left-handed circularly polarized but propagates in the  $-z$  direction with the same refractive index.

From Equation (2.130) we have

$$n_{2\pm} \approx \pm \left[ \alpha^2 + \bar{\epsilon} - 2\alpha\sqrt{\bar{\epsilon}} - \frac{\delta^2}{4\alpha\sqrt{\bar{\epsilon}}} \right]^{1/2} \approx \pm \left[ \alpha - \sqrt{\bar{\epsilon}} - \frac{\delta^2}{8\alpha(\alpha - \sqrt{\bar{\epsilon}})\sqrt{\bar{\epsilon}}} \right] \quad (2.151)$$

The corresponding eigenmodes have the polarization

$$\vec{A}'_{o2\pm} \approx a \begin{pmatrix} 1 \\ \left[ \frac{n_e^2 - \left( \alpha^2 + \bar{\epsilon} - 2\alpha\sqrt{\bar{\epsilon}} + \frac{\delta^2}{4\alpha\sqrt{\bar{\epsilon}}} \right) - \alpha^2}{2\alpha \left[ \pm \left( \alpha - \sqrt{\bar{\epsilon}} + \frac{\delta^2}{8\alpha(\alpha - \sqrt{\bar{\epsilon}})\sqrt{\bar{\epsilon}}} \right) \right]} \right] \end{pmatrix} \approx \begin{pmatrix} -i[2\alpha^2 - 2\alpha\sqrt{\bar{\epsilon}}] \\ 2\alpha[\pm(\alpha - \sqrt{\bar{\epsilon}})] \end{pmatrix} \approx \begin{pmatrix} 1 \\ \mp i \end{pmatrix}$$

In the lab frame, the polarization is

$$\begin{aligned} A_{2\pm x} &= [\cos(qz) \pm i \sin(qz)] e^{-ik_o n_{2\pm} z} = e^{i(\pm q - k_o n_{2\pm})z} \\ A_{2\pm y} &= [\sin(qz) \mp i \cos(qz)] e^{-ik_o n_{2\pm} z} = (\mp i) e^{i(\pm q - k_o n_{2\pm})z} \end{aligned}$$

Because

$$\pm q - k_o n_{2\pm} = \pm k_o \alpha \mp k_o \left[ \alpha - \sqrt{\bar{\epsilon}} - \frac{\delta^2}{8\alpha(\alpha - \sqrt{\bar{\epsilon}})\sqrt{\bar{\epsilon}}} \right] = \pm k_o \left[ \sqrt{\bar{\epsilon}} + \frac{\delta^2}{8\alpha(\alpha - \sqrt{\bar{\epsilon}})\sqrt{\bar{\epsilon}}} \right]$$

we have

$$\vec{A}_{2\pm} = \begin{pmatrix} 1 \\ \mp i \end{pmatrix} e^{-i(\mp k_o) \left[ \sqrt{\bar{\epsilon}} + \frac{\delta^2}{8\alpha(\alpha - \sqrt{\bar{\epsilon}})\sqrt{\bar{\epsilon}}} \right] z} \quad (2.152)$$

Eigenmode 3 is right-handed circularly polarized and propagates in the  $-z$  direction with refractive index

$$n_2 = \sqrt{\bar{\epsilon}} + \delta^2 / [8\alpha(\alpha - \sqrt{\bar{\epsilon}})\sqrt{\bar{\epsilon}}] \quad (2.153)$$

Eigenmode 4 is also right-handed circularly polarized but propagates in the  $+z$  direction with the same refractive index. In the above calculation, the higher order terms  $\delta^2/[8\alpha(\alpha + \sqrt{\bar{\epsilon}})\sqrt{\bar{\epsilon}}]$  and  $\delta^2/[8\alpha(\alpha - \sqrt{\bar{\epsilon}})\sqrt{\bar{\epsilon}}]$  are kept because they are important in calculating the optical rotatory power of the cholesteric liquid crystal.

$$(3) \sqrt{\bar{\epsilon}}P \sim \lambda \text{ and } \delta/\bar{\epsilon} \ll 1$$

In this case  $\alpha = q/k_o = \lambda/P \sim \sqrt{\bar{\epsilon}}$ . From Equation (2.129) we have

$$n_{1\pm} = \pm[\bar{\epsilon} + \bar{\epsilon} + 2\bar{\epsilon}]^{1/2} = \pm 2\sqrt{\bar{\epsilon}} \quad (2.154)$$

The corresponding eigenmodes have the polarization

$$\vec{A}'_{o1\pm} = a \begin{pmatrix} 1 \\ i[n_e^2 - 4\bar{\epsilon} - \bar{\epsilon}]/2\bar{\epsilon}(\pm 2\bar{\epsilon}) \end{pmatrix} = \begin{pmatrix} 1 \\ \mp i \end{pmatrix} \quad (2.155)$$

In the lab frame, the polarization is

$$\begin{aligned} A_{1\pm x} &= [\cos(qz) \pm i\sin(qz)]e^{-ik_o n_{1\pm} z} = e^{i(\pm q - k_o n_{1\pm})z} \\ A_{1\pm y} &= [\sin(qz) \mp i\cos(qz)]e^{-ik_o n_{1\pm} z} = (\mp i)e^{i(\pm q - k_o n_{1\pm})z} \end{aligned}$$

Because

$$\pm q - k_o n_{1\pm} = \pm k_o \sqrt{\bar{\epsilon}} \mp k_o 2\sqrt{\bar{\epsilon}} = \mp k_o \sqrt{\bar{\epsilon}},$$

we have

$$\vec{A}_{1\pm} = \begin{pmatrix} 1 \\ \mp i \end{pmatrix} e^{-i(\pm k_o)\sqrt{\bar{\epsilon}}z} \quad (2.156)$$

Eigenmode 1 is left-handed circularly polarized and propagates in the  $+z$  direction with a speed of  $c/\sqrt{\bar{\epsilon}}$ . Eigenmode 2 is also left-handed circularly polarized but propagates in the  $-z$  direction with a speed of  $c/\sqrt{\bar{\epsilon}}$ . The instantaneous electric field pattern is of the opposite sense to the cholesteric helix which is right-handed.

From Equation (2.130) we have

$$n_{2\pm} = \pm \left[ \bar{\epsilon} + \bar{\epsilon} - (4\bar{\epsilon}^2 + \delta^2)^{1/2} \right]^{1/2} = \pm i \frac{\delta}{2\sqrt{\bar{\epsilon}}} \quad (2.157)$$

which is imaginary. The corresponding polarization is

$$\vec{A}'_{o2\pm} \approx a \begin{pmatrix} 1 \\ i \left[ n_e^2 + \frac{\delta^2}{4\bar{\epsilon}} - \bar{\epsilon} \right] / \left[ 2\sqrt{\bar{\epsilon}} (\pm i\delta/2\sqrt{\bar{\epsilon}}) \right] \end{pmatrix} = a \begin{pmatrix} 1 \\ \pm \left[ 1 + \frac{\delta}{4\bar{\epsilon}} \right] \end{pmatrix} \approx \frac{1}{\sqrt{2}} \begin{pmatrix} 1 \\ \pm 1 \end{pmatrix} \quad (2.158)$$



which makes an angle of  $\pm 45^\circ$  with the  $x'$  axis. In the lab frame, the polarization is

$$\begin{aligned} A_{2\pm x} &= [\cos(qz) \mp \sin(qz)]e^{-ik_o n_{2\pm} z} = [\cos(qz) \mp \sin(qz)]e^{\pm k_o \delta z / (2\sqrt{\bar{\epsilon}})} \\ A_{2\pm y} &= [\sin(qz) \pm \cos(qz)]e^{-ik_o n_{2\pm} z} = [\sin(qz) \pm \cos(qz)]e^{\pm k_o \delta z / (2\sqrt{\bar{\epsilon}})} \\ \vec{A}_{2\pm} &= \begin{pmatrix} \cos(qz) \mp \sin(qz) \\ \sin(qz) \pm \cos(qz) \end{pmatrix} e^{\pm k_o \delta z / (2\sqrt{\bar{\epsilon}})} \end{aligned} \quad (2.159)$$

Because the refractive index is imaginary, these eigenmodes are non-propagating waves. The instantaneous electric field pattern of these eigenmodes varies in space in the same way as the cholesteric helix. The light intensity decays as these eigenmodes propagate into the liquid crystal. This means that the cholesteric liquid crystal reflects circularly polarized light with the same handedness and the same periodicity. The reflection band can be calculated from the equation  $\alpha^2 + \bar{\epsilon} - (4\alpha^2 \bar{\epsilon} + \delta^2)^{1/2} = 0$ , which gives

$$\lambda_1 = \sqrt{\bar{\epsilon}_{\parallel}} P = n_e P \quad (2.160)$$

$$\lambda_2 = \sqrt{\bar{\epsilon}_{\perp}} P = n_o P \quad (2.161)$$

When  $n_o P < \lambda < n_e P$ , the refractive index is imaginary. The width of this region is

$$\Delta\lambda = \lambda_1 - \lambda_2 = (n_e - n_o)P = \Delta n P \quad (2.162)$$

At  $\lambda_2$ ,  $\alpha = n_o$ ,  $n_2 = 0$ , the polarization of the eigenmodes is  $\vec{A}_2^T = (0, 1)$  (i.e., linearly polarized perpendicular to the liquid crystal director). At  $\lambda_1$ ,  $\alpha = n_e$ ,  $n_2 = 0$ , the polarization of the eigenmodes is  $\vec{A}_2^T = (1, 0)$  (i.e., linearly polarized parallel to the liquid crystal director). When the wavelength changes from  $\lambda_1$  to  $\lambda_2$ , the angle  $\chi$  between the electric vector and the liquid crystal director changes from  $0^\circ$  to  $90^\circ$ . For light having a wavelength in the region from  $\lambda_2$  to  $\lambda_1$  (in a vacuum),  $\chi$  varies in such a way that the wavelength of the light inside the cholesteric liquid crystal is equal to the helical pitch.

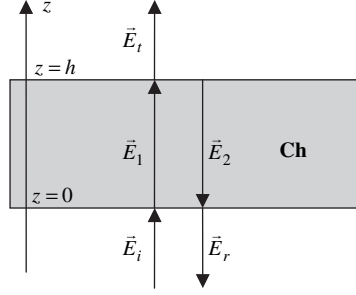
#### 2.4.2 Reflection of cholesteric liquid crystals

Now we consider the reflection of the cholesteric liquid crystal [10]. In the wavelength region from  $\lambda_2 (= n_o P)$  to  $\lambda_1 (= n_e P)$ , for light which is circularly polarized with the same helical sense as the helix of the liquid crystal, the angle between the electric vector of the light and the liquid crystal director is fixed as the light propagates along the helical axis. Light reflected from different positions is always in phase, and they interfere constructively and result in strong reflection. We calculate the reflection from a cholesteric film in a simple case in which media below and above this film are isotropic and have refractive index  $\bar{n} = (n_e + n_o)/2$ , as shown in Figure 2.8. The film thickness is  $h = mp$ , where  $m$  is an integer. The incident light is right-handed circularly polarized and has field amplitude  $u$ . The electric field is

$$\vec{E}_i = \frac{u}{\sqrt{2}} \begin{pmatrix} 1 \\ i \end{pmatrix} e^{-ik_o \bar{n} z} \quad (2.163)$$

The reflected light is also right-handed circularly polarized and has amplitude  $r$ . The field is

$$\vec{E}_r = \frac{r}{\sqrt{2}} \begin{pmatrix} 1 \\ -i \end{pmatrix} e^{ik_o \bar{n} z} \quad (2.164)$$



**Figure 2.8** Schematic diagram showing the reflection of the cholesteric (Ch) film

Generally speaking, there are four eigenmodes inside the cholesteric film. Two of the eigenmodes (eigenmodes 1 and 2) are left-handed circularly polarized (one propagating in the  $+z$  direction and the other propagating in the  $-z$  direction). The other two eigenmodes (eigenmodes 3 and 4) are right-handed circularly polarized (one propagating in the  $+z$  direction and the other propagating in the  $-z$  direction). The amplitudes of the left-handed circularly polarized eigenmodes are zero. For the right-handed eigenmodes (in the cholesteric liquid crystal),

$$\vec{B} = \frac{1}{i\omega} \nabla \times \vec{E} = \frac{-q}{i\omega} \vec{E}$$

For the incident, reflected, and transmitted right-handed circularly polarized light (outside the liquid crystal),

$$\vec{B} = \frac{1}{i\omega} \nabla \times \vec{E} = \frac{-k_o \bar{n}}{i\omega} \vec{E}$$

In and near the reflection band,  $k_o \bar{n} \approx q$ . If the boundary conditions for the electric field are satisfied, the boundary conditions for the magnetic field are also satisfied. Therefore we do not need to consider the boundary conditions for the magnetic field. The electric field in the cholesteric film is

$$\vec{E}_{ch} = \frac{v_1}{\sqrt{2}} \begin{pmatrix} 1 \\ w \end{pmatrix} e^{-ik_o n_2 z} + \frac{v_2}{\sqrt{2}} \begin{pmatrix} 1 \\ -w \end{pmatrix} e^{+ik_o n_2 z} \quad (2.165)$$

where

$$w = i(n_e^2 - n_o^2 - \alpha^2)/2\alpha n_2 \quad (2.166)$$

and  $v_1$  and  $v_2$  are the electric field amplitudes of eigenmodes 3 and 4. Note that the local frame is the same as the lab frame at the bottom and top surface of the cholesteric film because the film has  $m$  pitches, and thus the rotation matrix is omitted in Equation (2.165). Above the cholesteric film, there is only light propagating in the  $+z$  direction, which is the transmitted light that is right circularly polarized and has the field

$$\vec{E}_t = \frac{t}{\sqrt{2}} \begin{pmatrix} 1 \\ i \end{pmatrix} e^{-ik_o \bar{n} z} \quad (2.167)$$

where  $t$  is the amplitude of the wave. The relations between  $u$ ,  $r$ ,  $v_1$ ,  $v_2$ , and  $t$  can be found by using the boundary conditions at the surface of the cholesteric film. At the interfaces, the tangential components of the electric field are continuous. We consider a cholesteric film with  $h/P$  an integer. The boundary

conditions at  $z = h$  are

$$te^{-ik_o\bar{n}h} = v_1e^{-ik_on_2h} + v_2e^{ik_on_2h} \quad (2.168)$$

$$ite^{-ik_o\bar{n}h} = v_1we^{-ik_on_2h} - v_2we^{ik_on_2h} \quad (2.169)$$

From these two equations we get

$$v_1 = \frac{t}{2}e^{-ik_o\bar{n}h}(w + i)e^{ik_on_2h} \quad (2.170)$$

$$v_2 = \frac{t}{2}e^{-ik_o\bar{n}h}(w - i)e^{-ik_on_2h} \quad (2.171)$$

The boundary conditions at  $z = 0$  are

$$u + r = v_1 + v_2 \quad (2.172)$$

$$u - r = -i\omega v_1 + i\omega v_2 \quad (2.173)$$

From these two equations we get

$$u = \frac{1}{2}(1 - i\omega)v_1 + \frac{1}{2}(1 + i\omega)v_2 \quad (2.174)$$

$$r = \frac{1}{2}(1 + i\omega)v_1 + \frac{1}{2}(1 - i\omega)v_2 \quad (2.175)$$

The reflectance is given by [11]

$$R = \left| \frac{r}{u} \right|^2 = \left| \frac{(1 + wi) + (1 - wi)(v_2/v_1)}{(1 - wi) + (1 + wi)(v_2/v_1)} \right|^2 = \left| \frac{(w^2 + 1)(1 - e^{-i2k_on_2h})}{2w(1 + e^{-i2k_on_2h}) - i(w^2 - 1)(1 - e^{-i2k_on_2h})} \right|^2 \quad (2.176)$$

The calculated reflection spectra of cholesteric films with a few film thicknesses are shown in Figure 2.9 [12, 13]. For a sufficiently thick cholesteric film, within the reflection band,  $e^{-i2k_on_2h} \approx 0$ ,

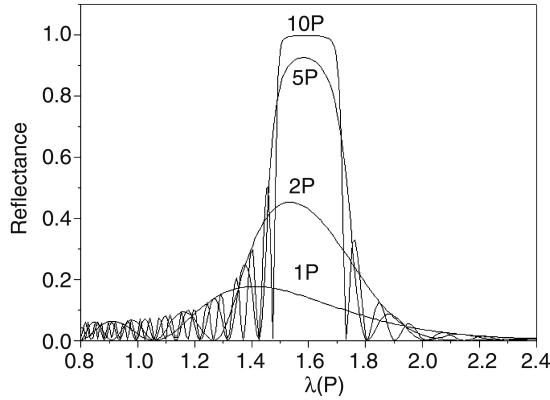
$$R \approx \left| \frac{(w^2 + 1)}{2w - i(w^2 - 1)} \right|^2 = 1$$

The thickness dependence of the reflectance can be estimated in the following way. At the center of the reflection band,  $\lambda = \sqrt{\bar{\epsilon}}P$ ,  $w = 1$ , and  $n_2 = -i\delta/(2\sqrt{\bar{\epsilon}}) \approx -i\Delta n/2$ . The reflectance is given by

$$R = \left( \frac{1 - \exp(-2\Delta n\pi h/\bar{n}P)}{1 + \exp(-2\Delta n\pi h/\bar{n}P)} \right)^2 \quad (2.177)$$

### 2.4.3 Lasing in cholesteric liquid crystals

Cholesteric liquid crystals are periodic optical media. When doped with fluorescent dyes, they can be used to make cavity-free lasers [14, 15]. In lasers, one of the important properties is the spontaneous



**Figure 2.9** Reflection spectra of cholesteric films with various film thicknesses. The refractive indices used are 1.7 and 1.5

emission rate  $W$ , which is proportional to the density of states  $\rho$ , as pointed out by Purcell [16]. The density of states function is given by

$$\rho = \frac{dk}{d\omega} = \frac{d(nk_o)}{d(2\pi C/\lambda)} = \frac{d(2\pi n/\lambda)}{d(2\pi C/\lambda)} = \frac{1}{C} \left( n - \lambda \frac{dn}{d\lambda} \right) \tag{2.178}$$

For the eigenmodes corresponding to the refractive index

$$n_2 = \left\{ (\lambda/P)^2 + \bar{\epsilon} - \left[ 4(\lambda/P)^2 \bar{\epsilon} + \delta^2 \right]^{1/2} \right\}^{1/2}$$

the density of states function has the term

$$\frac{dn_2}{d\lambda} = \frac{1}{2n_2} \frac{dg}{d\lambda}$$

where

$$g = (\lambda/P)^2 + \bar{\epsilon} - \left[ 4(\lambda/P)^2 \bar{\epsilon} + \delta^2 \right]^{1/2}$$

At the edges of the reflection band of the cholesteric liquid crystal, the density of states is very large because  $n_2 = 0$ . Therefore lasing can occur at the edges of the reflection band.

## Homework Problems

- 2.1 Calculate and draw the endpoint of the electric field vector at a fixed position in space as a function of time for all the polarization states listed in Table 2.1.
- 2.2 Consider a homogeneously aligned nematic film of thickness  $h$  shown in Figure 2.10. The ordinary and extraordinary refractive indices of the liquid crystal are  $n_o$  and  $n_e$ . Light with wavelength  $\lambda$  is

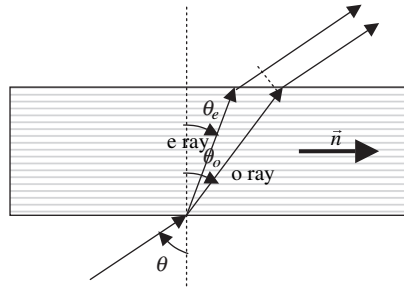


Figure 2.10

incident on the film at an angle  $\theta$ . The refractive angles of the ordinary and extraordinary rays are  $\theta_e$  and  $\theta_o$ , respectively. Prove that the phase difference between the extraordinary ray and ordinary ray when they come out of the film is

$$\Gamma = \frac{2\pi h}{\lambda} (n_{eff} \cos \theta_e - n_o \cos \theta_o) = h(k_{ez} - k_{oz})$$

where  $\sin \theta = n_o \sin \theta_o$ ,  $\sin \theta = n_{eff} \sin \theta_e = n_o n_e \sin \theta_e / (n_o^2 \cos^2 \theta_e + n_e^2 \sin^2 \theta_e)^{1/2}$ , and  $k_{ez}$  and  $k_{oz}$  are the projections in the film normal direction of the wavevectors of the extraordinary and ordinary rays, respectively.

- 2.3 What is the transmittance of a stack of three ideal polarizers? The angle between the transmission axes of the first and third polarizers is  $90^\circ$ . The transmission axis of the second polarizer is  $45^\circ$  with respect to the transmission axes of the other polarizers.
- 2.4 Linearly polarized light is normally incident on a uniformly aligned nematic liquid crystal cell that has a pretilt angle of  $45^\circ$ . The refractive indices of the liquid crystal are  $n_o = 1.5$  and  $n_e = 1.7$ . If the polarization is in the plane defined by the director and the wavevector, determine the angle that the Poynting vector makes to the wavevector.
- 2.5 A wedge cell is filled with a homogeneously aligned nematic liquid crystal whose director is aligned along the wedge direction. The angle of the wedge is  $3^\circ$ . The wedge is sandwiched between two crossed polarizers with the entrance polarizer placed at  $45^\circ$  to the director. When the cell is illuminated at normal incidence with light at a wavelength of 620 nm and viewed in transmission with a microscope, dark fringes are observed at intervals of 100 microns along the wedge. What is the birefringence of the liquid crystal?
- 2.6 *Crossed polarizer with compensation films.* Consider two crossed O-type polarizers. A uniaxial  $a$  plate and a uniaxial  $c$  plate are sandwiched between the two polarizers. The  $a$  plate has its optic axis parallel to the transmission axis of the first polarizer and has a retardation of  $\lambda/4$  ( $(\Delta nd)_a = \lambda/4$ ). The  $c$  plate has a retardation of  $2\lambda/9$  ( $(\Delta nd)_c = 2\lambda/9$ ). Calculate the transmission of the system at the azimuthal angle of  $45^\circ$  as a function of the polar angle  $\theta$ .
- 2.7 A liquid crystal optical switch based on total internal reflection is shown in Figure 2.11. It consists of two thick glass plates with a thin layer of liquid crystal sandwiched between them. On the left side, the liquid crystal is aligned homeotropically by a homeotropic alignment layer and serves as a beam splitter. On the right side, the liquid crystal is aligned homogeneously (in the direction perpendicular to the plane of the paper) by a homogeneous alignment layer and serves as a switch. The refractive index of the glass is 1.7. The refractive indices of the liquid crystal are  $n_o = 1.5$  and  $n_e = 1.7$ , respectively. The incident light is unpolarized. When the liquid crystal on the right side is in the field-off state, light is switched to Exit 1. When the liquid crystal on the right side is switched into

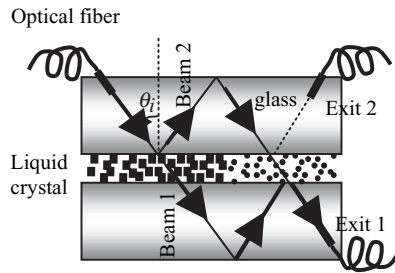


Figure 2.11

the homeotropic state by an external field applied across the cell, light is switched to Exit 2. What are the polarization states of Beams 1 and 2? Also, explain how the switch works.

## References

- 1 J. D. Jackson, *Classical electrodynamics*, 3rd edn. (John Wiley & Sons, Inc., New York, 1998).
- 2 M. Born and E. Wolf, *Principles of optics: electromagnetic theory of propagation, interference and diffraction of light* 7th edn (Cambridge University Press, Cambridge, 1999).
- 3 R. D. Guenther, *Modern optics* (John Wiley & Sons, Inc., New York, 1990).
- 4 P. Yeh and C. Gu, *Optics of liquid crystal displays* (John Wiley & Sons, Inc., New York, 1999).
- 5 A. Yariv and P. Yeh, *Optical waves in crystals* (John Wiley & Sons, Inc., New York, 1984).
- 6 J. Chen, K.-H. Kim, J.-J. Jyu, J. H. Souk, J. R. Kelly, and P. J. Bos, 'Optimum film compensation modes for TN and VA LCDs', *SID Symp. Dig. Tech. Pap.*, **29**, 315 (1998).
- 7 E. B. Priestley, P. J. Wojtoicz, and P. Sheng, *Introduction to liquid crystals* (Plenum, New York, 1979).
- 8 P. Palffy-Mohoray's lecture note.
- 9 C. Mauguin, 'Sur les cristaux liquides de Lehman', *Bull. Soc. Fr. Mineral*, **34**, 71 (1911).
- 10 W. Cao, 'Fluorescence and lasing in liquid crystalline photonic bandgap materials', *Dissertation* (Kent State University, 2005).
- 11 S. Chandrasekhar *Liquid crystals*, 2nd edn (Cambridge University Press, New York, 1997).
- 12 S.-T. Wu and D.-K. Yang, *Reflective liquid crystal displays* (John Wiley & Sons, Ltd, chichester, 2001).
- 13 M. Xu, F. D. Xu, and D.-K. Yang, 'Effects of cell structure on the reflection of cholesteric liquid crystal display', *J. Appl. Phys.*, **83**, 1938 (1998).
- 14 V. I. Kopp, B. Fan, H. K. M. Vithana, and A. Z. Genack, 'Low threshold lasing at the edge of a photonic stop band in cholesteric liquid crystals', *Opt. Lett.*, **23**, 1707 (1998).
- 15 A. Muñoz, P. Palffy-Muhoray, and B. Taheri, 'Ultraviolet lasing in cholesteric liquid crystals', *Opt. Lett.*, **26**, 804 (2001).
- 16 E. M. Purcell, *Phys. Rev.*, **69**, 181 (1946).

# 3

## Optical Modeling Methods

For many liquid crystal devices, their optical properties cannot be calculated analytically because their refractive indices vary in space. In this chapter we will discuss methods which can be used to numerically calculate the optical properties of liquid crystal devices.

### 3.1 Jones Matrix Method

#### 3.1.1 Jones vector

For a light beam with frequency  $\omega$  propagating in a uniform medium, the electric field vector is sufficient to specify the beam. In this chapter, the coordinate frame is always chosen in such a way that the propagation direction is the  $z$  direction except when otherwise specified. In this section, we only consider the case where the light propagation direction is parallel to the normal direction of the optical film, i.e., normal incident light. As discussed in Chapter 2, light is a transverse wave. If the medium under consideration is isotropic, the electric field vector lies in the  $x$ - $y$  plane. If the medium is uniaxial and its optic axis is in the  $x$ - $y$  plane or parallel to the  $z$  axis, the electric field vector is also in the  $x$ - $y$  plane. In these cases, the only quantities needed to specify a light beam are its electric field components,  $E_x$  and  $E_y$ , in the  $x$  and  $y$  directions. Thus the wave can be represented by the Jones vector defined by [1, 2]

$$\vec{E} = \begin{pmatrix} E_x \\ E_y \end{pmatrix} \quad (3.1)$$

If we are interested only in the polarization state of the wave, it is convenient to use the normalized *Jones vector*, which satisfies

$$\vec{E}^* \cdot \vec{E} = 1 \quad (3.2)$$

where  $\vec{E}^*$  is the complex conjugate. For light linearly polarized along a direction making an angle  $\phi$  with respect to the  $x$  axis, the Jones vector is

$$\vec{L}(\phi) = \begin{pmatrix} \cos \phi \\ \sin \phi \end{pmatrix} \quad (3.3)$$

The Jones vectors for right- and left-handed circularly polarized light are

$$\vec{C}_R = \frac{1}{\sqrt{2}} \begin{pmatrix} 1 \\ i \end{pmatrix} \quad (3.4)$$

$$\vec{C}_L = \frac{1}{\sqrt{2}} \begin{pmatrix} 1 \\ -i \end{pmatrix} \quad (3.5)$$

respectively. The Jones vector of various polarization states is listed in Table 2.1.

### 3.1.2 Jones matrix

In the Jones representation, the effect of an optical element can be represented by a  $2 \times 2$  matrix known as the Jones matrix. We first consider the Jones matrix of a uniaxial birefringent film with ordinary and extraordinary refractive indices  $n_o$  and  $n_e$ , respectively. A uniformly aligned nematic liquid crystal is such an example. As discussed in Chapter 2, in the uniaxial birefringence film there are two eigenmodes whose electric field eigenvectors do not change in space. If the optic axis (the uniaxis, also called the  $c$  axis) is along the  $x$  axis of the lab frame, one of the eigenmodes has its eigenvector along the  $x$  axis and propagates at speed  $c/n_e$ ; the other eigenmode has its eigenvector along the  $y$  axis and propagates at speed  $c/n_o$ . If  $n_e > n_o$ , the  $x$  axis is called the slow axis and the  $y$  axis is called the fast axis. If the incident light on the film has the Jones vector  $\vec{E}_i^T = (E_{xi}, E_{yi})$ , when the component of the electric vector along the  $x$  axis propagates through the film, its amplitude remains as  $E_{xi}$  and its phase changes according to  $e^{-2\pi n_e z/\lambda}$ . When the component of the electric vector along the  $y$  axis propagates through the film, its amplitude remains as  $E_{yi}$  and its phase changes according to  $e^{-2\pi n_o z/\lambda}$ . Therefore the Jones vector  $\vec{E}_o^T = (E_{xo}, E_{yo})$  of outgoing light will be

$$\vec{E}_o = \begin{pmatrix} E_{xo} \\ E_{yo} \end{pmatrix} = e^{-i[\pi(n_e+n_o)h/\lambda]} \begin{pmatrix} e^{-i\Gamma/2} & 0 \\ 0 & e^{i\Gamma/2} \end{pmatrix} \begin{pmatrix} E_{xi} \\ E_{yi} \end{pmatrix} \quad (3.6)$$

where  $\Gamma$  is the phase retardation and is given by  $\Gamma = 2\pi(n_e - n_o)h/\lambda$ , where  $h$  is the thickness of the film and  $\lambda$  is the wavelength of the light in vacuum. Uniform birefringent films are also called retardation films or wave plates. If  $\Gamma = \pi/2$ , the film is called a quarter-wave plate. If  $\Gamma = \pi$ , the film is called a half-wave plate. The phase factor  $e^{-i[\pi(n_e+n_o)h/\lambda]}$  can be neglected when the absolute phase is not important. Defining the Jones matrix of retardation as

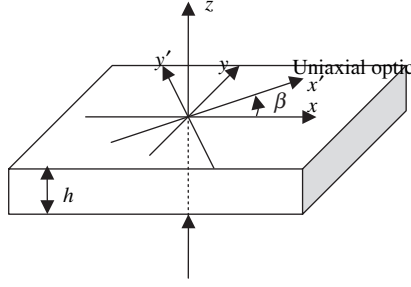
$$\vec{G}(\Gamma) = \begin{pmatrix} e^{-i\Gamma/2} & 0 \\ 0 & e^{i\Gamma/2} \end{pmatrix} \quad (3.7)$$

Equation (3.6) becomes

$$\vec{E}_o = \vec{G} \cdot \vec{E}_i \quad (3.8)$$

If the optic axis makes an angle  $\beta$  with the  $x$  axis of the lab frame, as shown in Figure 3.1, the eigenvectors are no longer in the  $x$  and  $y$  directions. For incident light not polarized along the optic axis,





**Figure 3.1** Schematic diagram showing a light beam propagating through a uniaxial birefringent film

its polarization will vary in space when propagating through the film. In this case, we have to use the principal frame  $x'y'$  whose  $x'$  is parallel to the optic axis of the film. In the principal frame, Equation (3.6) is valid. The Jones vector  $\vec{E}'_i$  of the incident light in the principal frame is related to the Jones vector  $\vec{E}_i$  in the lab frame by

$$\vec{E}'_i = \begin{pmatrix} E'_{xi} \\ E'_{yi} \end{pmatrix} = \begin{pmatrix} \cos \beta & \sin \beta \\ -\sin \beta & \cos \beta \end{pmatrix} \begin{pmatrix} E_x \\ E_y \end{pmatrix} = \begin{pmatrix} \cos \beta & \sin \beta \\ -\sin \beta & \cos \beta \end{pmatrix} \vec{E}_i \quad (3.9)$$

We define the matrix for the rotation of the frame as

$$\vec{R}(\beta) = \begin{pmatrix} \cos \beta & -\sin \beta \\ \sin \beta & \cos \beta \end{pmatrix} \quad (3.10)$$

Note that  $\vec{R}^{-1}(\beta) = \vec{R}(-\beta)$ . Then

$$\vec{E}'_i = \vec{R}^{-1}(\beta) \cdot \vec{E}_i \quad (3.11)$$

In the principal frame, the amplitudes of the electric fields in the  $x'$  and  $y'$  directions do not change with position  $z$ , but propagate with different speeds given by  $c/n_e$  and  $c/n_o$ , respectively, and thus their phase delays are different. The outgoing light in the principal frame is given by

$$\vec{E}'_o = \begin{pmatrix} E'_{xo} \\ E'_{yo} \end{pmatrix} = \begin{pmatrix} e^{-i\Gamma/2} & 0 \\ 0 & e^{i\Gamma/2} \end{pmatrix} \begin{pmatrix} E'_{xi} \\ E'_{yi} \end{pmatrix} = \vec{G}(\Gamma) \cdot \vec{E}'_i \quad (3.12)$$

The Jones vector of the outgoing light in the lab frame is

$$\vec{E}_o = \begin{pmatrix} E_{xo} \\ E_{yo} \end{pmatrix} = \begin{pmatrix} \cos \beta & -\sin \beta \\ \sin \beta & \cos \beta \end{pmatrix} \begin{pmatrix} E'_{xo} \\ E'_{yo} \end{pmatrix} = \vec{R}(\beta) \cdot \vec{G}(\Gamma) \cdot \vec{R}^{-1}(\beta) \vec{E}_i \quad (3.13)$$

From Equations (3.10) and (3.12) we have

$$\vec{E}_o = \begin{pmatrix} \cos^2 \beta e^{-i\Gamma/2} + \sin^2 \beta e^{i\Gamma/2} & \sin \beta \cos \beta (e^{-i\Gamma/2} - e^{i\Gamma/2}) \\ \sin \beta \cos \beta (e^{-i\Gamma/2} - e^{i\Gamma/2}) & \sin^2 \beta e^{-i\Gamma/2} + \cos^2 \beta e^{i\Gamma/2} \end{pmatrix} \vec{E}_i \quad (3.14)$$

The polarization of a light beam can be changed into any other polarization state by using a proper birefringent film. If the incident light is linearly polarized along the  $x$  axis and the uniaxial birefringent film is a quarter-wave plate with its slow axis (the uniaxial axis) at  $45^\circ$  with respect to the  $x$  axis,  $\vec{E}_o^T = (1/\sqrt{2})(1, -i)$ , and the outgoing light is left-handed circularly polarized. If the slow axis is at  $-45^\circ$  with respect to the  $x$  axis,  $\vec{E}_o^T = (1/\sqrt{2})(1, i)$ , and the outgoing light is right-handed circularly polarized. If the film is a half-wave plate and the slow axis is at  $45^\circ$ ,  $\vec{E}_o^T = (-i)(0, 1)$ , and the outgoing light is linearly polarized along the  $y$  axis.

If the birefringent film is sandwiched between two polarizers with the transmission axis of the (bottom) polarizer along the  $x$  axis, then  $\vec{E}_i^T = (1, 0)$ . The polarization of the outgoing light is

$$\begin{aligned}\vec{E}_o &= \begin{pmatrix} \cos^2\beta e^{-i\Gamma/2} + \sin^2\beta e^{i\Gamma/2} & \sin\beta \cos\beta(e^{-i\Gamma/2} - e^{i\Gamma/2}) \\ \sin\beta \cos\beta(e^{-i\Gamma/2} - e^{i\Gamma/2}) & \cos^2\beta e^{-i\Gamma/2} + \sin^2\beta e^{i\Gamma/2} \end{pmatrix} \begin{pmatrix} 1 \\ 0 \end{pmatrix} \\ &= \begin{pmatrix} \cos^2\beta e^{-i\Gamma/2} + \sin^2\beta e^{i\Gamma/2} \\ \sin\beta \cos\beta(e^{-i\Gamma/2} - e^{i\Gamma/2}) \end{pmatrix}\end{aligned}\quad (3.15)$$

If the transmission axis of the analyzer (top polarizer) is along the  $y$  axis, only the  $y$  component of the outgoing light can pass the analyzer, and the transmittance is

$$T = |E_{yo}|^2 = |\sin\beta \cos\beta(e^{-i\Gamma/2} - e^{i\Gamma/2})|^2 = \sin^2(2\beta)\sin^2(\Gamma/2)\quad (3.16)$$

When  $\beta = \pi/4$  and  $\Gamma = \pi$ , the maximum transmittance  $T = 1$  is obtained.

Birefringent films are used as compensation films to improve the viewing angle of liquid crystal displays. They can be divided into three groups according to the orientation of the uniaxis ( $c$  axis) with respect to the normal of the film:

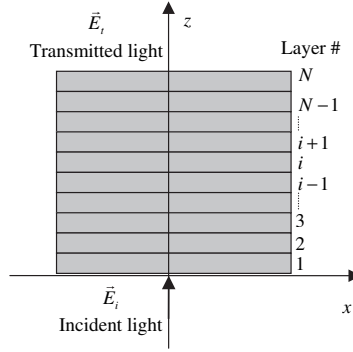
- (1)  $a$  plate: the  $c$  axis is perpendicular to the film normal.
- (2)  $c$  plate: the  $c$  axis is parallel to the film normal.
- (3)  $o$  plate: the  $c$  axis makes an angle  $\alpha$  ( $\neq 0^\circ, \neq 90^\circ$ ) with respect to the film normal.

### 3.1.3 Jones matrix of non-uniform birefringent film

When light propagates through films in which the slow and fast axes as well as the refractive indices are a function of position  $z$ , the Jones matrix method can still be used as an approximation method as long as the refractive indices do not change much in one wavelength distance. We divide the film into  $N$  slabs as shown in Figure 3.2. When the thickness  $\Delta h = h/N$  of the slabs is sufficiently small, then within each slab, the slow axis can be considered fixed.

For layer  $j$ , the angle of the slow axis with respect to the  $x$  axis is  $\beta_j$  and the phase retardation is  $\Gamma_j = 2\pi[n_e(z = j\Delta h) - n_o(z = j\Delta h)]\Delta h/\lambda$ . In the lab frame, the Jones vector of the incident light on the layer is  $\vec{E}_{ji}$ , which is the same as the Jones vector,  $\vec{E}_{(j-1)o}$ , of the light exiting layer  $(j-1)$ , and the Jones vector of the outgoing light is  $\vec{E}_{jo}$  [3]:

$$\vec{E}_{jo} = \vec{R}(\beta_j) \cdot \vec{G}(\Gamma_j) \cdot \vec{R}^{-1}(\beta_j)\vec{E}_{ji} = \vec{R}(\beta_j) \cdot \vec{G}(\Gamma_j) \cdot \vec{R}^{-1}(\beta_j) \cdot \vec{E}_{(j-1)o}\quad (3.17)$$



**Figure 3.2** Schematic diagram showing the propagation of light through a birefringent film with varying slow axis

The Jones vector,  $\vec{E}_o$ , of the outgoing light is related to the Jones vector,  $\vec{E}_i$ , of the incident light by

$$\begin{aligned}
 \vec{E}_o &= [\vec{R}(\beta_N) \cdot \vec{G}(\Gamma_N) \cdot \vec{R}^{-1}(\beta_N)] \cdot \\
 &\quad [\vec{R}(\beta_{N-1}) \cdot \vec{G}(\Gamma_{N-1}) \cdot \vec{R}^{-1}(\beta_{N-1})] \cdot \\
 &\quad \dots \cdot \\
 &\quad [\vec{R}(\beta_1) \cdot \vec{G}(\Gamma_1) \cdot \vec{R}^{-1}(\beta_1)] \cdot \vec{E}_i \\
 &= \prod_{j=1}^N [\vec{R}(\beta_j) \cdot \vec{G}(\Gamma_j) \cdot \vec{R}^{-1}(\beta_j)] \cdot \vec{E}_i
 \end{aligned} \tag{3.18}$$

Usually the multiplication of the matrices is carried out numerically. Analytical solutions can be obtained in some special cases.

The Jones matrix method has the limitation that it only works well for normally incident and paraxial rays. It neglects reflection and refraction from the interface between two optic media whose refractive indices are different. The extended Jones matrix method takes into account the reflection and refraction, but still neglects multiple reflection, and can be used to calculate the optical properties of media for obliquely incident light [4–7].

### 3.1.4 Optical properties of twisted nematic liquid crystals

Nematic liquid crystals are usually uniaxial. Twisted nematic (TN) liquid crystals have been used in many applications, especially in flat-panel displays [8]. A TN cell consists of two parallel substrates with a nematic liquid crystal sandwiched between them. The inner surfaces of the cell are coated with homogeneous anchoring alignment layers. At the surface, the liquid crystal director is aligned along the alignment direction. The alignment directions of the bottom and top alignment layers are different. The angle between the alignment directions is  $\Phi$  which is referred to as the total twist angle. The liquid crystal director twists at a constant rate from the bottom to the top to match the boundary condition. The twist rate is  $\tau = \Phi/h$ , where  $h$  is the thickness.

In the calculation of the optical properties, the TN film is divided into  $N$  thin slabs of thickness  $\Delta h = h/N$ . Within each slab, the liquid crystal director can be approximately considered uniform. If the alignment direction of the liquid crystal director at the entrance plane is along the  $x$  axis, the rotation matrix of the  $i$ th layer is

$$\vec{S}_i(\beta_i) = \begin{pmatrix} \cos\beta_i & -\sin\beta_i \\ \sin\beta_i & \cos\beta_i \end{pmatrix} = \begin{pmatrix} \cos[i\Delta\beta] & -\sin[i\Delta\beta] \\ \sin[i\Delta\beta] & \cos[i\Delta\beta] \end{pmatrix} \equiv \vec{S}(i\Delta\beta) \tag{3.19}$$

## 78 OPTICAL MODELING METHODS

where  $\Delta\beta = (\Delta h/h)\Phi = \Phi/N$ . The Jones matrix of the  $i$ th layer in the principal frame is

$$\vec{G}_i(\Gamma_i) = \begin{pmatrix} e^{-i\Delta\Gamma/2} & 0 \\ 0 & e^{i\Delta\Gamma/2} \end{pmatrix} \equiv \vec{G}(\Delta\Gamma) \quad (3.20)$$

where  $\Delta\Gamma = 2\pi(n_e - n_o)\Delta h/\lambda = 2\pi\Delta n\Delta h/\lambda$ . The Jones vector of the outgoing light is related to that of the incident light by

$$\vec{E}_o = \prod_{i=1}^N [\vec{S}_i(\beta_i) \cdot \vec{G}_i(\Gamma_i) \cdot \vec{S}_i^{-1}(\beta_i)] \cdot \vec{E}_i = \prod_{i=1}^N [\vec{S}(i\Delta\beta) \cdot \vec{G}(\Delta\Gamma) \cdot \vec{S}^{-1}(\Delta\beta)] \cdot \vec{E}_i$$

Note that

$$\vec{S}_i^{-1}(\beta_i)\vec{S}_{(i-1)}(\beta_{(i-1)}) = \begin{pmatrix} \cos[\Delta\beta] & \sin[\Delta\beta] \\ -\sin[\Delta\beta] & \cos[\Delta\beta] \end{pmatrix} \equiv \vec{S}(\Delta\beta)$$

Therefore

$$\vec{E}_o = \vec{S}(N\Delta\beta) \cdot \left[ \vec{G}(\gamma) \cdot \vec{S}^{-1}(\Delta\beta) \right]^N \cdot \vec{E}_i \quad (3.21)$$

We define a new matrix  $\vec{A}$ :

$$\vec{A} = \vec{G}(\Delta\Gamma) \cdot \vec{S}^{-1}(\Delta\beta) = \begin{pmatrix} e^{-i\Gamma/2}\cos\Delta\beta & -e^{-i\Gamma/2}\sin\Delta\beta \\ e^{i\Gamma/2}\sin\Delta\beta & e^{i\Gamma/2}\cos\Delta\beta \end{pmatrix} \quad (3.22)$$

Because  $\vec{A}$  is a  $2 \times 2$  matrix, from Cayley–Hamilton theory [9],  $\vec{A}^N$  can be expanded as

$$\vec{A}^N = \lambda_1 \vec{I} + \lambda_2 \vec{A} \quad (3.23)$$

where  $\lambda_1$  and  $\lambda_2$  are found from the equations

$$q_1^N = \lambda_1 + \lambda_2 A q_1 \quad (3.24)$$

$$q_2^N = \lambda_1 + \lambda_2 A q_2 \quad (3.25)$$

where  $q_1$  and  $q_2$  are the eigenvalues of  $\vec{A}$  and can be calculated from the following equation:

$$\begin{vmatrix} e^{-i\Gamma/2}\cos\Delta\beta - q & -e^{-i\Gamma/2}\sin\Delta\beta \\ e^{i\Gamma/2}\sin\Delta\beta & e^{i\Gamma/2}\cos\Delta\beta - q \end{vmatrix} = 0$$

which is

$$1 - 2q \cos(\Delta\beta)\cos(\Delta\Gamma/2) + q^2 = 0 \quad (3.26)$$

Defining angle  $\theta$  by

$$\cos\theta = \cos(\Delta\beta)\cos(\Delta\Gamma/2) \quad (3.27)$$

Equation (3.26) becomes  $(q - \cos\theta)^2 = -\sin^2\theta$ , and therefore the solutions are

$$q = \cos\theta \pm i\sin\theta = e^{\pm i\theta} \quad (3.28)$$

Equations (3.24) and (3.25) become  $e^{iN\theta} = \lambda_1 + \lambda_2 e^{i\theta}$  and  $e^{-iN\theta} = \lambda_1 + \lambda_2 e^{-i\theta}$ , and the solutions are  $\lambda_1 = -\sin(N-1)\theta/\sin\theta$  and  $\lambda_2 = \sin N\theta/\sin\theta$ . From Equation (3.23) we have

$$\begin{aligned} \vec{A}^N &= -\frac{\sin(N-1)\theta}{\sin\theta} \vec{I} + \frac{\sin N\theta}{\sin\theta} \vec{A} \\ &= \begin{pmatrix} \frac{\sin N\theta}{\sin\theta} \cos\Delta\beta e^{-i\Delta\Gamma/2} - \frac{\sin(N-1)\theta}{\sin\theta} & \frac{\sin N\theta}{\sin\theta} \sin\Delta\beta e^{-i\Gamma/2} \\ -\frac{\sin N\theta}{\sin\theta} \sin\Delta\beta e^{i\Gamma/2} & \frac{\sin N\theta}{\sin\theta} \cos\Delta\beta e^{i\Gamma/2} - \frac{\sin(N-1)\theta}{\sin\theta} \end{pmatrix} \end{aligned} \quad (3.29)$$

We also have

$$\vec{S}(N\Delta\beta) = \begin{pmatrix} \cos[N\Delta\beta] & -\sin[N\Delta\beta] \\ \sin[N\Delta\beta] & \cos[N\Delta\beta] \end{pmatrix} = \begin{pmatrix} \cos\Phi & -\sin\Phi \\ \sin\Phi & \cos\Phi \end{pmatrix} \quad (3.30)$$

The total phase retardation is

$$\Gamma = N\Delta\Gamma = \frac{2\pi}{\lambda}(n_e - n_o)h \quad (3.31)$$

When  $N \rightarrow \infty$ ,  $\Delta\beta \rightarrow 0$ , and  $\Gamma \rightarrow 0$ , we have  $\sin\Delta\beta = \Delta\beta$ ,  $\cos\Delta\beta = 1$  and  $\sin(\Gamma/2) = \Gamma/2$ ,  $\cos(\Gamma/2) = 1$ . Also from Equation (3.27) we have

$$\theta = [(\Delta\beta)^2 + (\Delta\Gamma/2)^2]^{1/2} \quad (3.32)$$

$$N\theta = [\Phi^2 + (\Gamma/2)^2]^{1/2} \equiv \Theta \quad (3.33)$$

$$\begin{aligned} (\vec{A}^N)_{11} &= \frac{\sin N\theta}{\sin\theta} \cos\Delta\beta \left[ \cos\left(\frac{\Delta\Gamma}{2}\right) - i \sin\left(\frac{\Delta\Gamma}{2}\right) \right] - \frac{\sin N\theta \cos\theta - \sin\theta \cos N\theta}{\sin\theta} \\ &= \frac{\sin N\theta}{\sin\theta} \cos\Delta\beta \cos\left(\frac{\Delta\Gamma}{2}\right) - i \frac{\sin N\theta}{\sin\theta} \cos\Delta\beta \sin\left(\frac{\Delta\Gamma}{2}\right) - \frac{\sin N\theta \cos\theta - \sin\theta \cos N\theta}{\sin\theta} \\ &\approx \frac{\sin N\theta}{\sin\theta} \cos\theta - i \frac{\sin N\theta}{\theta} \cdot 1 \cdot \left(\frac{\Delta\Gamma}{2}\right) - \frac{\sin N\theta \cos\theta - \sin\theta \cos N\theta}{\sin\theta} \\ &= \cos\Theta - i \frac{\Delta\Gamma}{2\theta} \sin\Theta \\ &= \cos\Theta - i \frac{\Gamma}{2\Theta} \sin\Theta \\ (\vec{A}^N)_{12} &= \frac{\sin N\theta}{\sin\theta} \sin\Delta\beta e^{-i\Gamma/2} = \frac{\Delta\beta}{\theta} \sin\Theta = \frac{\Phi}{\Theta} \sin\Theta \\ (\vec{A}^N)_{21} &= -\frac{\Phi}{\Theta} \sin\Theta \\ (\vec{A}^N)_{22} &= \cos\Theta + i \frac{\Gamma}{2\Theta} \sin\Theta \end{aligned}$$

Equation (3.21) becomes

$$\vec{E}_o = \begin{pmatrix} \cos \Phi & -\sin \Phi \\ \sin \Phi & \cos \Phi \end{pmatrix} \begin{pmatrix} \cos \Theta - i \frac{(\Gamma/2)}{\Theta} \sin \Theta & \frac{\Phi}{\Theta} \sin \Theta \\ -\frac{\Phi}{\Theta} \sin \Theta & \cos \Theta + i \frac{(\Gamma/2)}{\Theta} \sin \Theta \end{pmatrix} \cdot \vec{E}_i \quad (3.34)$$

A TN liquid crystal is the same as a cholesteric liquid crystal. The pitch  $P$  is related to the film thickness  $h$  and the total twist angle  $\Phi$  by  $P = h/(\Phi/2\pi)$ . It should be noted that in the derivation of Equation (3.34), reflection and interference effects have not been considered, which are important when the wavelength is comparable to the pitch.

We consider the optical properties of a TN liquid crystal film in a few special cases.

(1)  $\Delta nP \gg \lambda$

The twisting rate is  $\tau = \Phi/h$ . The retardation angle per unit length is  $2\pi\Delta n/\lambda$ . When  $\Delta nP \gg \lambda$  (the *Mauguin* condition) [10],  $\tau/(2\pi\Delta n/\lambda) = \lambda/[\Delta n \cdot h/(\Phi/2\pi)] = \lambda/\Delta nP \ll 1$ . In this case, the twisting rate is low:  $\Delta\beta/(\Delta\Gamma/2) = (\Phi/N)/(\pi\Delta nh/N\lambda) = (\Phi/\pi)(\lambda/\Delta nh) \ll 1$ . Therefore  $\Phi/\Theta \ll 1$ ,  $\Gamma/2\Theta \approx 1$ , and Equation (3.34) becomes

$$\vec{E}_o = \begin{pmatrix} \cos \Phi & -\sin \Phi \\ \sin \Phi & \cos \Phi \end{pmatrix} \begin{pmatrix} e^{-i\Gamma/2} & 0 \\ 0 & e^{i\Gamma/2} \end{pmatrix} \vec{E}_i = \begin{pmatrix} \cos \Phi e^{-i\Gamma/2} & -\sin \Phi e^{i\Gamma/2} \\ \sin \Phi e^{-i\Gamma/2} & \cos \Phi e^{i\Gamma/2} \end{pmatrix} \vec{E}_i \quad (3.35)$$

When the incident light is linearly polarized along the liquid crystal director at the entrance plane (the *E mode*), namely  $\vec{E}_i^T = (1, 0)$ , then  $\vec{E}_o^T = (\cos \Phi, \sin \Phi)e^{-i\Gamma/2}$ . This indicates that the polarization remains parallel to the liquid crystal director as the light propagates through the TN liquid crystal and the propagating speed is  $c/n_e$ . When the incident light is linearly polarized perpendicular to the liquid crystal director at the entrance plane (the *O mode*), namely  $\vec{E}_i^T = (0, 1)$ , then  $\vec{E}_o^T = (-\sin \Phi, \cos \Phi)e^{i\Gamma/2}$ . This indicates that the polarization remains perpendicular to the liquid crystal director as the light propagates through the TN liquid crystal and the propagating speed is  $c/n_o$ . This result is the same as that obtained by solving the Maxwell equation in Section 2.4.

(2)  $\Delta nP \ll \lambda$

The twisting rate is very high (much larger than the retardation angle per unit length  $2\pi\Delta n/\lambda$ ):  $\Gamma/\Phi = (2\pi\Delta nh/\lambda)/\Phi = \Delta nP/\lambda = \Delta n/\alpha \ll 1$ , where  $\alpha = \lambda/P$ , and

$$\Theta = \left[ \Phi^2 + \left( \frac{\Gamma}{2} \right)^2 \right]^{1/2} \approx \Phi + \frac{\Delta n^2}{8\alpha^2} \Phi = \Phi + \frac{\Delta n^2}{8\alpha} \left( \frac{2\pi h}{\lambda} \right) \quad (3.36)$$

Equation (3.34) becomes

$$\vec{E}_o = \begin{pmatrix} \cos \Phi & -\sin \Phi \\ \sin \Phi & \cos \Phi \end{pmatrix} \begin{pmatrix} \cos \Theta & \sin \Theta \\ -\sin \Theta & \cos \Theta \end{pmatrix} \vec{E}_i \quad (3.37)$$

If the incident light is right-handed circularly polarized, namely

$$\vec{E}_i = \frac{1}{\sqrt{2}} \begin{pmatrix} 1 \\ i \end{pmatrix}$$

the outgoing light is

$$\vec{E}_o = \frac{1}{\sqrt{2}} \begin{pmatrix} \cos \Phi & -\sin \Phi \\ \sin \Phi & \cos \Phi \end{pmatrix} \begin{pmatrix} \cos \Theta & \sin \Theta \\ -\sin \Theta & \cos \Theta \end{pmatrix} \begin{pmatrix} 1 \\ i \end{pmatrix} = \frac{1}{\sqrt{2}} \begin{pmatrix} 1 \\ i \end{pmatrix} e^{i(\Theta - \Phi)} \quad (3.38)$$

which is still right-handed circularly polarized. Therefore right-handed circular polarization is an eigenmode. Recall the omitted factor  $e^{-i2\pi\bar{n}h/\lambda}$ . Then the total phase angle is

$$\Theta - \Phi - \frac{2\pi\bar{n}h}{\lambda} = -\frac{2\pi\bar{n}h}{\lambda} + \frac{\Delta n^2}{8\alpha} \left( \frac{2\pi h}{\lambda} \right) \equiv -\frac{2\pi n_1 h}{\lambda} \quad (3.39)$$

and the corresponding refractive index is

$$n_1 = \bar{n} - \frac{\Delta n^2}{8\alpha} \quad (3.40)$$

This result is the same as Equation (2.131) when  $\alpha \ll \bar{n}$ .

If the incident light is left-handed circularly polarized, namely

$$\vec{E}_i = \frac{1}{\sqrt{2}} \begin{pmatrix} 1 \\ -i \end{pmatrix}$$

the outgoing light is

$$\vec{E}_o = \frac{1}{\sqrt{2}} \begin{pmatrix} \cos \Phi & -\sin \Phi \\ \sin \Phi & \cos \Phi \end{pmatrix} \begin{pmatrix} \cos \Theta & \sin \Theta \\ -\sin \Theta & \cos \Theta \end{pmatrix} \begin{pmatrix} 1 \\ -i \end{pmatrix} = \frac{1}{\sqrt{2}} \begin{pmatrix} 1 \\ -i \end{pmatrix} e^{i(\Phi - \Theta)} \quad (3.41)$$

which is still left-handed circularly polarized. Therefore left-handed circular polarization is another eigenmode. The total phase angle is

$$\Phi - \Theta - \frac{2\pi\bar{n}h}{\lambda} = -\frac{2\pi\bar{n}h}{\lambda} - \frac{\Delta n^2}{8\alpha} \left( \frac{2\pi h}{\lambda} \right) \equiv -\frac{2\pi n_2 h}{\lambda} \quad (3.42)$$

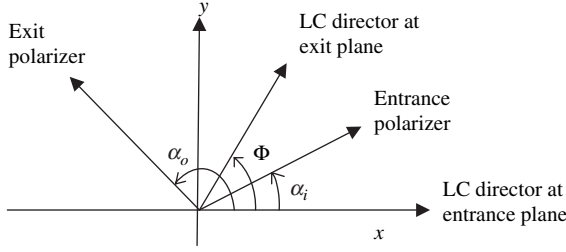
and the corresponding refractive index is

$$n_2 = \bar{n} + \frac{\Delta n^2}{8\alpha} \quad (3.43)$$

This result is the same as Equation (2.128) when  $\alpha \ll \bar{n}$ .

Now we consider a TN display whose geometry is shown in Figure 3.3 [11,12]. The TN liquid crystal is sandwiched between two polarizers. The  $x$  axis of the lab frame is chosen parallel to the liquid crystal director at the entrance plane. The angles of the entrance and exit polarizers are  $\alpha_i$  and  $\alpha_o$ , respectively. The Jones vector of the incident light is  $\vec{E}_i^T = (\cos \alpha_i, \sin \alpha_i)$ . The Jones vector of the existing light is given by

$$\vec{E}_o = \begin{pmatrix} \cos \Phi & -\sin \Phi \\ \sin \Phi & \cos \Phi \end{pmatrix} \begin{pmatrix} \cos \Theta - i \frac{(\Gamma/2)}{\Theta} \sin \Theta & \frac{\Phi}{\Theta} \sin \Theta \\ -\frac{\Phi}{\Theta} \sin \Theta & \cos \Theta + i \frac{(\Gamma/2)}{\Theta} \sin \Theta \end{pmatrix} \begin{pmatrix} \cos \alpha_i \\ \sin \alpha_i \end{pmatrix}$$



**Figure 3.3** Geometry of the TN display

The exit polarizer is along the direction represented by the unit vector  $\vec{P}_{exit}^T = (\cos \alpha_o, \sin \alpha_o)$ . The electric field of the light which can pass through the exit polarizer is given by

$$\begin{aligned}
 E_{exit} &= \vec{P}_{exit} \cdot \vec{E}_o \\
 &= (\cos \alpha_o, \sin \alpha_o) \begin{pmatrix} \cos \Phi & -\sin \Phi \\ \sin \Phi & \cos \Phi \end{pmatrix} \begin{pmatrix} \cos \Theta - i \frac{(\Gamma/2)}{\Theta} \sin \Theta & \frac{\Phi}{\Theta} \sin \Theta \\ -\frac{\Phi}{\Theta} \sin \Theta & \cos \Theta + i \frac{(\Gamma/2)}{\Theta} \sin \Theta \end{pmatrix} \begin{pmatrix} \cos \alpha_i \\ \sin \alpha_i \end{pmatrix} \\
 &= \cos \Theta \cos(\alpha_o - \alpha_i - \Phi) - \frac{\Phi}{\Theta} \sin \Theta \sin(\alpha_o - \alpha_i - \Phi) - i \frac{(\Gamma/2)}{\Theta} \sin \Theta \cos(\alpha_o + \alpha_i - \Phi)
 \end{aligned} \quad (3.44)$$

The intensity of the light is

$$\begin{aligned}
 I_o &= |E_{exit}|^2 = \cos^2(\alpha_o - \alpha_i - \Phi) - \sin^2 \Theta \sin[2(\alpha_o - \Phi)] \sin(2\alpha_i) \\
 &\quad - \frac{\Phi^2}{\Theta^2} \sin^2 \Theta \cos[2(\alpha_o - \Phi)] \cos(2\alpha_i) - \frac{\Phi}{2\Theta} \sin(2\Theta) \sin[2(\alpha_o - \alpha_i - \Phi)]
 \end{aligned} \quad (3.45)$$

For a normal-black  $90^\circ$  TN display where the transmission axes of the two polarizers are parallel to the liquid crystal director,  $\Phi = \pi/2$ ,  $\alpha_i = \alpha_o = 0$ ,  $\Theta = [(\pi/2)^2 + (\Gamma/2)^2]^{1/2} = (\pi/2)[1 + (2\Delta nh/\lambda)^2]^{1/2}$ , and the transmittance of the TN cell (normalized to the light intensity before the entrance polarizer) is given by

$$T = \frac{1}{2} \frac{\Phi^2}{\Theta^2} \sin^2 \Theta = \frac{\sin^2 \left[ (\pi/2) \sqrt{1 + (2\Delta nh/\lambda)^2} \right]}{2[1 + (2\Delta nh/\lambda)^2]} \quad (3.46)$$

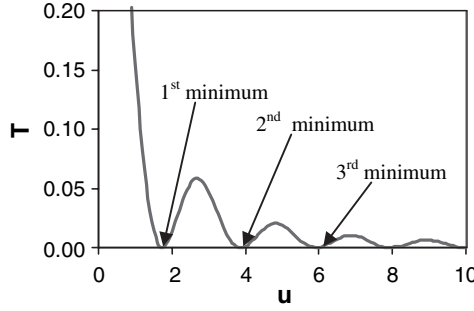
The transmittance  $T$  vs. the retardation  $u = 2\Delta nh/\lambda$  is shown in Figure 3.4. Generally the transmittance of the display is not zero except when  $\sqrt{1 + u^2} = 2i$  ( $i = 1, 2, 3, \dots$ ), namely  $u = \sqrt{3}, \sqrt{15}, \dots$ . These values are known as the first, second, etc., minimum conditions, respectively. When  $u \gg 1$ , the case where the polarization rotates with the liquid crystal director, the denominator becomes very large and the transmittance becomes very small.

## 3.2 Mueller Matrix Method

### 3.2.1 Partially polarized and unpolarized light

If light is not absolutely monochromatic, the amplitudes and relative phase between the  $x$  and  $y$  components can both vary with time. As a result, the polarization state of a polychromatic plane wave





**Figure 3.4** Transmittance of normal-black  $90^\circ$  TN vs. retardation

may be constantly changing. If the polarization state changes more rapidly than the speed of observation, the light is *partially polarized* or *unpolarized* depending on the time-averaged behavior of the polarization state. In optics, one often deals with light with an oscillation frequency of about  $10^{14} \text{ s}^{-1}$ , whereas the polarization state may change in a time period of about  $10^{-8} \text{ s}$ . In order to describe unpolarized and partially polarized light, the *Stokes vector* is introduced.

A quasimonochromatic wave, whose frequency spectrum is confined to a narrow bandwidth  $\Delta\lambda (\Delta\lambda \ll \lambda)$ , can still be described by

$$\vec{E} = [A_x(t)\hat{x} + A_y(t)e^{i\delta}\hat{y}]e^{i(\omega t - kz)} \quad (3.47)$$

where the wave is propagating in the  $z$  direction;  $A_x$  and  $A_y$  are positive numbers which may be time dependent. At a given position, the components of the Stokes vector are defined as follows [13]:

$$S_0 = \langle E_x E_x^* + E_y E_y^* \rangle = \langle A_x^2 + A_y^2 \rangle \quad (3.48)$$

which describes the light intensity;

$$S_1 = \langle E_x E_x^* - E_y E_y^* \rangle = \langle A_x^2 - A_y^2 \rangle \quad (3.49)$$

which describes the difference in intensity between components along the  $x$  and  $y$  axes;

$$S_2 = \langle E_x E_y^* + E_y E_x^* \rangle = 2\langle A_x A_y \cos\delta \rangle \quad (3.50)$$

which describes the component along the direction at  $\pm 45^\circ$ ; and

$$S_3 = \langle i(E_x E_y^* - E_y E_x^*) \rangle = 2\langle A_x A_y \sin\delta \rangle \quad (3.51)$$

which describes the circular polarization.  $\langle \rangle$  denote the average performed over a time interval  $\tau_D$  that is the characteristic time constant of the detection process.  $S_0$  specifies the intensity of the light beam. By considering the following cases, the rationale of defining the parameters will be shown:

(1) *Unpolarized light*. The average amplitudes of the electric field components in the  $x$  and  $y$  directions are the same, but the phase difference between them is completely random, i.e.,  $\langle A_x^2 \rangle = \langle A_y^2 \rangle$ ,  $\langle \cos\delta \rangle = \langle \sin\delta \rangle = 0$ , and therefore the normalized Stokes vector is

$$\vec{S}^T = (1, 0, 0, 0) \quad (3.52)$$

(2) *Linearly polarized light along a direction which makes an angle  $\psi$  with respect to the  $x$  axis.* The amplitudes of the electric field components in the  $x$  and  $y$  directions are  $A_x = \cos\psi$  and  $A_y = \sin\psi$ , respectively. The phase difference is  $\delta = 0$ . The Stokes vector is

$$\vec{S}^T = [1, \cos(2\psi), \sin(2\psi), 0] \tag{3.53}$$

When the light is linearly polarized along the  $x$  axis,  $\vec{S}^T = (1, 1, 0, 0)$ ; when it is linearly polarized along the  $y$  axis,  $\vec{S}^T = (1, -1, 0, 0)$ ; when it is linearly polarized along the direction at  $45^\circ$ ,  $\vec{S}^T = (1, 0, 1, 0)$ ; and when it is linearly polarized along the direction at  $-45^\circ$ ,  $\vec{S}^T = (1, 0, -1, 0)$ .

(3) *Circularly polarized.* The amplitudes of the electric field components in the  $x$  and  $y$  directions are the same, i.e.,  $A_x = A_y = 1/\sqrt{2}$ , and the phase difference is  $\delta$ . The Stokes vector is

$$\vec{S}^T = (1, 0, 0, \sin \delta) \tag{3.54}$$

For right-handed circular polarization, the phase difference is  $\delta = \pi/2$ , and  $\vec{S}^T = (1, 0, 0, 1)$ ; while for left-handed circular polarization,  $\delta = -\pi/2$ , and  $\vec{S}^T = (1, 0, 0, -1)$ .

If there were only two parameters  $S_0$  and  $S_1$ , when  $S_1 = 0$ , there are three possibilities: (i) unpolarized, (ii) linearly polarized along the direction at  $\pm 45^\circ$ , and (iii) circularly polarized. Therefore more parameters are needed to differentiate them. If there were only three parameters  $S_0$ ,  $S_1$ , and  $S_3$ , when  $S_1 = 0$  and  $S_3 = 0$ , there are two possibilities: (i) unpolarized and (ii) linearly polarized along the direction at  $\pm 45^\circ$ . Therefore one more parameter is needed to differentiate them. The four parameters are necessary and also sufficient to describe the polarization of a light beam. The Stokes vectors of various polarizations are listed in Table 2.1.

When a light beam is completely polarized,  $S_1 + S_2 + S_3 = S_0 = 1$ . When a light beam is unpolarized,  $S_1 + S_2 + S_3 = 0$ . The degree of polarization can be described by

$$\gamma = \frac{S_1 + S_2 + S_3}{S_0} \tag{3.55}$$

For partially polarized light,  $0 < \gamma < 1$ .

### 3.2.2 Measurement of the Stokes parameters

The light beam to be studied is incident on a combination of a quarter-wave plate and a polarizer as shown in Figure 3.5. The slow optic axis of the wave plate is along the  $y$  axis and the retardation angle is  $\beta = 90^\circ$ . The transmission axis of the polarizer is at an angle  $\alpha$ .

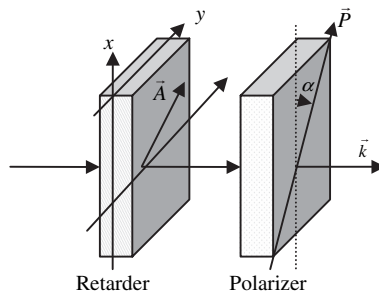


Figure 3.5 Schematic diagram of the setup which is used to measure the Stokes parameters

The electric field (in Jones vector form) of the incident light (before the quarter-wave plate) is

$$\vec{E} = \begin{pmatrix} A_x \\ A_y e^{i\delta} \end{pmatrix} \quad (3.56)$$

where  $A_x$  and  $A_y$  are positive numbers which may be time dependent. After the quarter-wave plate, the field is

$$\vec{E}_1 = \begin{pmatrix} A_x \\ A_y e^{i(\delta+\beta)} \end{pmatrix} \quad (3.57)$$

At the polarizer, the electric field along the transmission axis is

$$E = A_x \cos \alpha + A_y e^{i(\delta+\beta)} \sin \alpha \quad (3.58)$$

The intensity of the outgoing light is

$$\begin{aligned} I &= \langle |E|^2 \rangle = \langle (A_x \cos \alpha + A_y e^{i(\delta+\beta)} \sin \alpha)(A_x \cos \alpha + A_y e^{-i(\delta+\beta)} \sin \alpha) \rangle \\ &= \langle A_x^2 \rangle \cos^2 \alpha + \langle A_y^2 \rangle \sin^2 \alpha + \sin(2\alpha) (\langle A_x A_y \cos \delta \rangle \cos \beta + \langle A_x A_y \sin \delta \rangle \sin \beta) \\ &= \frac{1}{2}(S_o + S_1) \cos^2 \alpha + \frac{1}{2}(S_o - S_1) \sin^2 \alpha + \sin(2\alpha) \left( \frac{1}{2} S_2 \cos \beta + \frac{1}{2} S_3 \sin \beta \right) \\ &= \frac{1}{2} [S_o + S_1 \cos(2\alpha) + \sin(2\alpha) (S_2 \cos \beta + S_3 \sin \beta)] \end{aligned} \quad (3.59)$$

In the first step of the measurement, the quarter-wave plate is removed, which is equivalent to  $\beta = 0$ . The light intensity is measured when the polarizer is at the following positions:

$$I(\beta = 0, \alpha = 0) = \frac{1}{2}(S_o + S_1) \quad (3.60)$$

$$I(\beta = 0, \alpha = 45^\circ) = \frac{1}{2}(S_o + S_2) \quad (3.61)$$

$$I(\beta = 0, \alpha = 90^\circ) = \frac{1}{2}(S_o - S_1) \quad (3.62)$$

When the quarter-wave plate is inserted and the polarizer is at  $45^\circ$ , the measured light intensity will be

$$I(\beta = 90^\circ, \alpha = 45^\circ) = \frac{1}{2}(S_o + S_3) \quad (3.63)$$

From these four equations, the Stokes parameters can be calculated.

It is impossible by means of any instrument to distinguish between various incoherent superpositions of wave fields, having the same frequency, that may together form a beam with the same Stokes parameters. This is known as the *principle of optical equivalence*.

The Stokes vectors of incoherent beams can be composed and decomposed. For example, an unpolarized beam can be decomposed into two opposite elliptically polarized light beams (with the same ellipticity but opposite handedness and orthogonal major axes), i.e.,

$$I_o \begin{pmatrix} 1 \\ 0 \\ 0 \\ 0 \end{pmatrix} = \frac{I_o}{2} \begin{pmatrix} 1 \\ \cos(2\nu)\cos(2\phi) \\ \cos(2\nu)\sin(2\phi) \\ \sin(2\nu) \end{pmatrix} + \frac{I_o}{2} \begin{pmatrix} 1 \\ \cos(-2\nu)\cos[2(\phi + \pi/2)] \\ \cos(-2\nu)\sin[2(\phi + \pi/2)] \\ \sin(-2\nu) \end{pmatrix} \quad (3.64)$$

where  $\nu$  and  $\phi$  are the ellipticity angle and azimuthal angle of the polarization ellipse, respectively (see Sections 2.2.4 and 3.3.4 for details).

A partially polarized beam can be decomposed into a completely polarized beam and an unpolarized beam:

$$\begin{pmatrix} S_o \\ S_1 \\ S_2 \\ S_3 \end{pmatrix} = (1 - \gamma) \begin{pmatrix} S_o \\ 0 \\ 0 \\ 0 \end{pmatrix} + \begin{pmatrix} \gamma S_o \\ S_1 \\ S_2 \\ S_1 \end{pmatrix} \quad (3.65)$$

where

$$\gamma = \frac{\sqrt{S_1^2 + S_2^2 + S_3^2}}{S_o}$$

A partially polarized beam can also be decomposed into two oppositely polarized beams:

$$\begin{pmatrix} S_o \\ S_1 \\ S_2 \\ S_3 \end{pmatrix} = \frac{(1 + \gamma)}{2\gamma} \begin{pmatrix} \gamma S_o \\ S_1 \\ S_2 \\ S_3 \end{pmatrix} + \frac{(1 - \gamma)}{2\gamma} \begin{pmatrix} \gamma S_o \\ -S_1 \\ -S_2 \\ -S_1 \end{pmatrix} \quad (3.66)$$

### 3.2.3 Mueller matrix

When the polarization state of a light beam is represented by the Stokes vector, the effect of an optical element can be represented by the Mueller matrix  $\vec{M}$  which operates on the Stokes vector,  $\vec{S}_i$ , of the incident light to generate the Stokes vector,  $\vec{S}_o$ , of the outgoing light:

$$\vec{S}_o = \vec{M} \cdot \vec{S}_i \quad (3.67)$$

The Mueller matrix  $\vec{M}$  has the form

$$\vec{M} = \begin{pmatrix} m_{00} & m_{01} & m_{02} & m_{03} \\ m_{10} & m_{11} & m_{12} & m_{13} \\ m_{20} & m_{21} & m_{22} & m_{23} \\ m_{30} & m_{31} & m_{32} & m_{33} \end{pmatrix} \quad (3.68)$$

If the Jones matrix of the optical element is

$$\vec{G} = \begin{pmatrix} g_{11} & g_{12} \\ g_{21} & g_{22} \end{pmatrix} \quad (3.69)$$

the Mueller matrix of the element is

$$\vec{M} = \frac{1}{2} \begin{pmatrix} 1 & 0 & 0 & 1 \\ 1 & 0 & 0 & -1 \\ 0 & 1 & 1 & 0 \\ 0 & i & -i & 0 \end{pmatrix} \begin{pmatrix} g_{11}g_{11}^* & g_{11}g_{12}^* & g_{12}g_{11}^* & g_{12}g_{12}^* \\ g_{11}g_{21}^* & g_{11}g_{22}^* & g_{12}g_{21}^* & g_{12}g_{22}^* \\ g_{21}g_{11}^* & g_{21}g_{12}^* & g_{22}g_{11}^* & g_{22}g_{12}^* \\ g_{21}g_{21}^* & g_{21}g_{22}^* & g_{22}g_{21}^* & g_{22}g_{22}^* \end{pmatrix} \begin{pmatrix} 1 & 1 & 0 & 0 \\ 0 & 0 & 1 & -i \\ 0 & 0 & 1 & i \\ 1 & -1 & 0 & 0 \end{pmatrix} \quad (3.70)$$

We first consider the Mueller matrix of an absorber. The transmission coefficients along the  $x$  and  $y$  axes are  $p_x$  and  $p_y$ , respectively, namely

$$\begin{pmatrix} E'_x \\ E'_y \end{pmatrix} = \begin{pmatrix} p_x & 0 \\ 0 & p_y \end{pmatrix} \begin{pmatrix} E_x \\ E_y \end{pmatrix} \quad (3.71)$$

If  $p_x = p_y = p$ , the absorber is a neutral density filter. If  $p_x = 0$  and  $p_y = p = 1$ , it is a vertical polarizer (transmission axis parallel to the  $y$  axis). If  $p_x = p = 1$  and  $p_y = 0$ , it is a horizontal polarizer. The Mueller matrix of the absorber is

$$\vec{M}_P = \frac{1}{2} \begin{pmatrix} p_x^2 + p_y^2 & p_x^2 - p_y^2 & 0 & 0 \\ p_x^2 - p_y^2 & p_x^2 + p_y^2 & 0 & 0 \\ 0 & 0 & 2p_x p_y & 0 \\ 0 & 0 & 0 & 2p_x p_y \end{pmatrix} \quad (3.72)$$

We now consider the Mueller matrix of a rotator. In the  $xy$  frame, the electric field vector is  $\vec{E} = E_x \hat{x} + E_y \hat{y}$ . In another frame  $x'y'$ , which is in the same plane but the  $x'$  axis makes an angle  $\phi$  with the  $x$  axis, the electric vector is  $\vec{E}' = E'_x \hat{x}' + E'_y \hat{y}'$ . The components of the electric field in the two frames are transformed according to Equation (3.9). The Mueller matrix that transform the Stokes vector in the  $xy$  frame into the Stokes vector in the  $x'y'$  frame is

$$\vec{M}_R(\phi) = \begin{pmatrix} 1 & 0 & 0 & 0 \\ 0 & \cos(2\phi) & \sin(2\phi) & 0 \\ 0 & -\sin(2\phi) & \cos(2\phi) & 0 \\ 0 & 0 & 0 & 1 \end{pmatrix} \quad (3.73)$$

The Mueller matrix of an ideal polarizer at the angle  $\phi$  is

$$\begin{aligned} \vec{M}_P(\phi) &= \vec{M}_R(-\phi) \cdot \vec{M}_P(0) \cdot \vec{M}_R(\phi) \\ &= \frac{1}{2} \begin{pmatrix} 1 & \cos(2\phi) & \sin(2\phi) & 0 \\ \cos(2\phi) & \cos^2(2\phi) & \sin(2\phi)\cos(2\phi) & 0 \\ \sin(2\phi) & \sin(2\phi)\cos(2\phi) & \sin^2(2\phi) & 0 \\ 0 & 0 & 0 & 0 \end{pmatrix} \end{aligned} \quad (3.74)$$

For a retarder with retardation angle  $\Gamma = 2\pi\Delta nh/\lambda$  and the slow axis along the  $x$  axis,

$$\begin{pmatrix} E'_x \\ E'_y \end{pmatrix} = \begin{pmatrix} e^{i\Gamma/2} & 0 \\ 0 & e^{-i\Gamma/2} \end{pmatrix} \begin{pmatrix} E_x \\ E_y \end{pmatrix} \quad (3.75)$$

the corresponding Mueller matrix is

$$\vec{M}_{retarder}(\Gamma, 0) = \begin{pmatrix} 1 & 0 & 0 & 0 \\ 0 & 1 & 0 & 0 \\ 0 & 0 & \cos\Gamma & -\sin\Gamma \\ 0 & 0 & \sin\Gamma & \cos\Gamma \end{pmatrix} \quad (3.76)$$

The Mueller matrix of a retarder, whose slow axis makes an angle  $\phi$  with the  $x$  axis, is

$$\begin{aligned} \vec{M}_{retarder}(\Gamma, \phi) &= \vec{M}_R(-\phi) \cdot \vec{M}_{retarder}(\Gamma, 0) \cdot \vec{M}_R(\phi) \\ &= \begin{pmatrix} 1 & 0 & 0 & 0 \\ 0 & \cos^2(2\phi) + \sin^2(2\phi)\cos\Gamma & \sin(2\phi)\cos(2\phi)(1 - \cos\Gamma) & \sin(2\phi)\sin\Gamma \\ 0 & \sin(2\phi)\cos(2\phi)(1 - \cos\Gamma) & \sin^2(2\phi) + \cos^2(2\phi)\cos\Gamma & -\cos(2\phi)\sin\Gamma \\ 0 & -\sin(2\phi)\sin\Gamma & \cos(2\phi)\sin\Gamma & \cos\Gamma \end{pmatrix} \end{aligned} \quad (3.77)$$

If there is no absorption element involved, we need to consider the three-component vector  $\vec{S}^T = (S_1, S_2, S_3)$ . The function of optical elements is described by  $3 \times 3$  matrices.

$$\vec{M} = \begin{pmatrix} m_{11} & m_{12} & m_{13} \\ m_{21} & m_{22} & m_{23} \\ m_{31} & m_{32} & m_{33} \end{pmatrix} \quad (3.78)$$

### 3.2.4 Poincaré sphere

For completely polarized light, the normalized Stokes parameters satisfy the condition  $S_1^2 + S_2^2 + S_3^2 = S_0^2 = 1$ . Therefore a point with coordinates  $(S_1, S_2, S_3)$  is on the surface of a unit sphere in 3-D space. This sphere is known as the *Poincaré sphere* and is shown in Figure 3.6.

For completely polarized light, whose Jones vector is

$$\vec{E} = \begin{pmatrix} A_x \\ A_y e^{i\delta} \end{pmatrix} \quad (3.79)$$

where  $A_x$  and  $A_y$  are time-independent positive numbers and  $\delta$  is a time-independent number. Generally, it is elliptically polarized. The azimuthal angle  $\phi$  of the polarization ellipse is given by (Equation (2.41))

$$\tan 2\phi = \frac{A_x A_y \cos \delta}{(A_x^2 - A_y^2)} \quad (3.80)$$

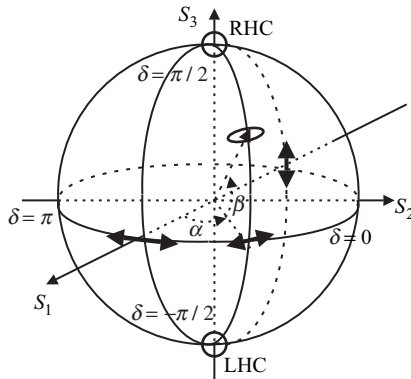


Figure 3.6 Poincaré sphere

The ellipticity angle  $v$  is given by (Equation (2.48))

$$\sin 2v = \frac{2 \tan v}{1 + \tan^2 v} = \frac{2b/a}{1 + (b/a)^2} = \frac{2ab}{a^2 + b^2} \quad (3.81)$$

where  $a$  and  $b$  are the lengths of the principal semi-axes of the polarization ellipse. From Equations (2.45) and (2.46) we have

$$\sin 2v = \frac{2A_x A_y \sin \delta}{A_x^2 + A_y^2} \quad (3.82)$$

The Stokes parameters are given by

$$S_1 = (A_x^2 - A_y^2)/(A_x^2 + A_y^2) \quad (3.83)$$

$$S_2 = 2A_x A_y \cos \delta / (A_x^2 + A_y^2) \quad (3.84)$$

$$S_3 = 2A_x A_y \sin \delta / (A_x^2 + A_y^2) \quad (3.85)$$

The longitudinal angle  $\alpha$  of the point representing the polarization on the Poincaré sphere is given by

$$\tan \alpha = \frac{S_2}{S_1} = \frac{2A_x A_y \cos \delta}{A_x^2 - A_y^2} = \tan 2\phi \quad (3.86)$$

Therefore  $\alpha = 2\phi$ . The latitude angle  $\beta$  is given by

$$\sin \beta = S_3 = 2A_x A_y \sin \delta / (A_x^2 + A_y^2) = \sin 2v \quad (3.87)$$

Therefore  $\beta = 2v$ . If we know the azimuthal angle  $\phi$  and the ellipticity angle  $v$  of the polarization ellipse, the Stokes vector is

$$\vec{S} = \begin{pmatrix} \cos(2v)\cos(2\phi) \\ \cos(2v)\sin(2\phi) \\ \sin(2v) \end{pmatrix} \quad (3.88)$$

If we know the angle  $\chi = \tan^{-1}(A_x/A_y)$  and the phase difference  $\delta$ , then the Stokes vector is

$$\vec{S} = \begin{pmatrix} \cos(2\chi) \\ \sin(2\chi)\cos\delta \\ \sin(2\chi)\sin\delta \end{pmatrix} \quad (3.89)$$

The points corresponding to some special polarization states are as follows:

North pole (0,0,1):	right-handed polarized
South pole (0,0,-1):	left-handed polarized
A point on the equator:	linearly polarized
(1,0,0):	linearly polarized along the $x$ axis
(-1,0,0):	linearly polarized along the $y$ axis
(0,1,0):	linearly polarized along $45^\circ$

*Features of the Poincaré sphere*

- (1) Two diametrically opposed points on the sphere correspond to states with orthogonal polarization.
- (2) For any point on a half circle connecting the north and south poles (fixed longitude), the inclination angle  $\phi$  of the polarization ellipse is the same, because  $S_2/S_1 = \text{constant}$ .
- (3) For any point on a circle with fixed  $S_3$  (fixed latitude) on the sphere, the ellipticity is the same.

**3.2.5 Evolution of the polarization states on the Poincaré sphere**

We consider how the three-component Stokes vector  $\vec{S}$  evolves on the Poincaré sphere under the action of retardation films. The Mueller matrix of a uniform uniaxial retarder with the retardation angle  $\Gamma$  and the slow axis making an angle  $\phi$  with the  $x$  axis is given by (from Equations (3.77) and (3.78))

$$\vec{M}(\Gamma, \psi) = \begin{pmatrix} \cos^2(2\phi) + \sin^2(2\phi)\cos\Gamma & \sin(2\phi)\cos(2\phi)(1 - \cos\Gamma) & \sin(2\phi)\sin\Gamma \\ \sin(2\phi)\cos(2\phi)(1 - \cos\Gamma) & \sin^2(2\phi) + \cos^2(2\phi)\cos\Gamma & -\cos(2\phi)\sin\Gamma \\ -\sin(2\phi)\sin\Gamma & \cos(2\phi)\sin\Gamma & \cos\Gamma \end{pmatrix} \quad (3.90)$$

For a thin retardation film with thickness  $dz \rightarrow 0$ , and retardation angle  $d\Gamma = (2\pi\Delta n/\lambda)dz = k_o\Delta ndz \rightarrow 0$ , we have the approximations that  $\cos d\Gamma = 1$  and  $\sin d\Gamma = d\Gamma$ , and the Mueller matrix becomes

$$\vec{M}(d\Gamma, \phi) = \begin{pmatrix} 1 & 0 & \sin(2\phi)d\Gamma \\ 0 & 1 & -\cos(2\phi)d\Gamma \\ -\sin(2\phi)d\Gamma & \cos(2\phi)d\Gamma & 1 \end{pmatrix} \quad (3.91)$$

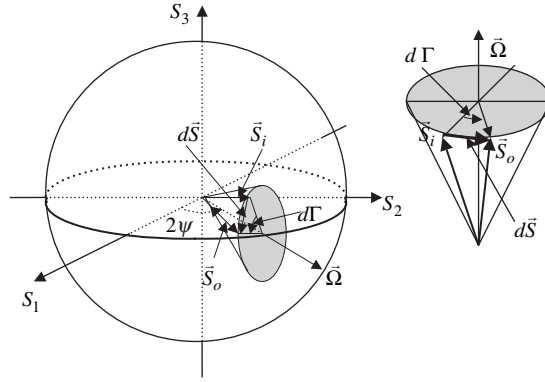
If the Stokes vector of the incident light is  $\vec{S}_i$ , the Stokes vector of the outgoing light is  $\vec{S}_o = \vec{M}(\Gamma, \psi) \cdot \vec{S}_i$ . The change in the Stokes vector caused by the retardation film is

$$d\vec{S} = \vec{S}_o - \vec{S}_i = \vec{M}(d\Gamma, \psi) \cdot \vec{S}_i - \vec{S}_i = d\Gamma \begin{pmatrix} 0 & 0 & \sin(2\phi) \\ 0 & 0 & -\cos(2\phi) \\ -\sin(2\phi) & \cos(2\phi) & 0 \end{pmatrix} \cdot \vec{S}_i \quad (3.92)$$

This can be rewritten as

$$d\vec{S} = d\Gamma \vec{\Omega} \times \vec{S}_i \quad (3.93)$$





**Figure 3.7** Schematic diagram showing the rotation of the Stokes vector under the action of the retardation film

where  $\vec{\Omega}$  is a unit vector and has the form

$$\vec{\Omega} = \begin{pmatrix} \cos(2\phi) \\ \sin(2\phi) \\ 0 \end{pmatrix} \quad (3.94)$$

From Equation (3.93), we can see that the effect of the retarder is to rotate  $\vec{S}$  around the axis represented by  $\vec{\Omega}$  with the rotation angle of  $d\Gamma$  as shown in Figure 3.7. From Equation (3.94), it can be seen that the rotation axis is on the equator and makes an angle of  $2\phi$  with the  $S_1$  axis, which is twice the angle of the slow axis (with respect to the  $x$  axis) of the retarder (in the  $xy$  frame).

For a uniform retardation film with retardation angle  $\Gamma$ , even if its thickness is not small, the Stokes vector of the outgoing light can be derived from Equation (3.93) and is

$$\vec{S}_o = \vec{S}_i + \Gamma \vec{\Omega} \times \vec{S}_i \quad (3.95)$$

One of the reasons for using the Poincaré sphere is that the effect of retardation films and the evolution of the polarization state can be easily visualized. We consider polarization conversion in the following special cases.

#### (1) Polarization conversion using quarter-wave plates

An elliptical polarization state (with inclination angle  $\phi$  and ellipticity angle  $v$ ) can be converted into a circular polarization state by using two quarter-wave plates [4]. This can be done in two steps. First, use a quarter wave-plate with the  $c$  axis parallel to the major axis of the polarization ellipse. The rotation axis is at  $2\phi$  and the cone angle of the rotation cone is  $2 \times 2v$ . The rotation angle is  $\pi/2$ . After this quarter-wave plate, the Stokes vector is on the equator and the longitudinal angle is  $2\phi - 2v$  on the Poincaré sphere, i.e., the light is linearly polarized at an angle  $(2\phi - 2v)/2 = (\phi - v)$  with respect to the  $x$  axis in the  $xy$  frame. In order to convert the linear polarization into right-handed circular polarization, the rotation axis should be at  $\phi - v - \pi/2$  and the rotation angle should be  $\pi/2$  on the Poincaré sphere. Therefore the  $c$  axis of the second quarter-wave plate should be at an angle  $(\phi - v - \pi/2)/2$  with respect to the  $x$  axis in the  $xy$  frame. By reversing this procedure, circularly polarized light can be converted into elliptically polarized light by using two quarter-wave plates. By combining the above two procedures, any

elliptically polarized light can be converted into any other elliptically polarized light by using four properly oriented quarter-wave plates.

(2) *Polarization conversion using two quarter-wave plates and one half-wave plate*

Elliptically polarized light at  $(\phi_1, \nu_1)$  can be converted into elliptically polarized light at  $(\phi_2, \nu_2)$  [4] as follows. First, use a quarter-wave plate with its  $c$  axis at an angle  $\phi_1$  in the  $xy$  frame. The rotation axis is at an angle  $2\phi_1$ , the cone angle is  $2 \times 2\nu_1$ , and the rotation angle is  $\pi/2$  on the Poincaré sphere. After this quarter-wave plate, the light becomes linearly polarized at the angle  $2\phi_1 - 2\nu_2$  on the Poincaré sphere. Secondly, use a half-wave plate whose rotation axis is at an angle  $[(2\phi_2 - 2\nu_2) + (2\phi_1 - 2\nu_1)]/2 = \phi_2 - \nu_2 + \phi_1 - \nu_1$ , which will convert the linear polarization into another linear polarization at the angle  $(2\phi_1 - 2\nu_1) + 2[(\phi_2 - \nu_2 + \phi_1 - \nu_1) - (2\phi_1 - 2\nu_1)] = 2\phi_2 - 2\nu_2$  on the Poincaré sphere. In the  $xy$  frame, the  $c$  axis of the half-wave plate is at an angle  $(\phi_2 - \nu_2 + \phi_1 - \nu_1)/2$  with respect to the  $x$  axis. Thirdly, use another quarter-wave plate whose  $c$  axis is at an angle  $\phi_2$  with respect to the  $x$  axis, which will convert the linear polarization into elliptical polarization at  $(\phi_2, \nu_2)$ .

### 3.2.6 Mueller matrix of TN liquid crystals

We now consider the Mueller matrix of a uniform TN (or cholesteric) liquid crystal. The problem can be simplified if we consider the Stokes vector and Mueller matrix in the local frame  $x'y'$  in which the liquid crystal director lies along the  $x'$  axis. We divide the liquid crystal film into  $N$  thin slabs. The thickness of each slab is  $dz = h/N$ , where  $h$  is the thickness of the liquid crystal film. The angle between the liquid crystal director of two neighboring slabs is  $d\psi = qdz$ , where  $q$  is the twisting rate. The retardation angle of a slab is  $d\Gamma = k_o\Delta ndz$ . If the Stokes vector (in the local frame) of the light incident on a slab is  $\vec{S}'$ , then the Stokes vector of the light incident on the next slab is (from Equations (3.73) and (3.76))

$$\vec{S}' + d\vec{S}' = \begin{pmatrix} 1 & 2qdz & 0 \\ -2qdz & 1 & 0 \\ 0 & 0 & 1 \end{pmatrix} \begin{pmatrix} 1 & 0 & 0 \\ 0 & 1 & -k_o\Delta ndz \\ 0 & k_o\Delta ndz & 1 \end{pmatrix} \vec{S}' = \begin{pmatrix} 1 & 2qdz & 0 \\ -2qdz & 1 & -k_o\Delta ndz \\ 0 & k_o\Delta ndz & 1 \end{pmatrix} \vec{S}' \quad (3.96)$$

In deriving the above equation, only first order terms are kept when  $dz \rightarrow 0$ . In component form we have

$$\frac{dS'_1}{dz} = 2qS'_2 \quad (3.97)$$

$$\frac{dS'_2}{dz} = -2qS'_1 - k_o\Delta nS'_3 \quad (3.98)$$

$$\frac{dS'_3}{dz} = k_o\Delta nS'_2 \quad (3.99)$$

From Equation (3.98) we get

$$\frac{d^2S'_2}{dz^2} = -2q\frac{dS'_1}{dz} - k_o\Delta n\frac{dS'_3}{dz} = -[(2q)^2 + (k_o\Delta n)^2]S'_2 \quad (3.100)$$

We define

$$\chi = [(2q)^2 + (k_o\Delta n)^2]^{1/2} = 2[\Phi^2 + (\Gamma/2)^2]^{1/2}/h \quad (3.101)$$

where  $\Phi$  and  $\Gamma$  are the total twist angle and retardation angle of the liquid crystal film, respectively. The solution of Equation (3.100) is

$$S'_2 = A_{21}\sin(\chi z) + A_{22}\cos(\chi z) \quad (3.102)$$

From Equation (3.97) we get

$$S'_1 = \frac{2q}{\chi} [-A_{21}\cos(\chi z) + A_{22}\sin(\chi z)] + A_{11} \quad (3.103)$$

From Equation (3.99) we get

$$S'_3 = \frac{k_o\Delta n}{\chi} [-A_{21}\cos(\chi z) + A_{22}\sin(\chi z)] + A_{33} \quad (3.104)$$

If the Stokes vector of the light incident on the liquid crystal film is  $\vec{S}'_i = (S'_{10} \ S'_{20} \ S'_{30})$ , then we have the boundary condition equations ( $z = 0$ )

$$A_{22} = S'_{20} \quad (3.105)$$

$$-\frac{2q}{\chi}A_{21} + A_{11} = S'_{10} \quad (3.106)$$

$$-\frac{k_o\Delta n}{\chi}A_{21} + A_{33} = S'_{30} \quad (3.107)$$

Also from Equation (3.98) we get

$$-2qA_{11} - k_o\Delta nA_{33} = 0 \quad (3.108)$$

From the above four equations we can find the four coefficients. The final results are

$$S'_1 = \left[ 1 - 2\left(\frac{2q}{\chi}\right)^2 \sin^2\left(\frac{\chi}{2}z\right) \right] S'_{10} + \frac{2q}{\chi} \sin(\chi z) S'_{20} - \frac{4qk_o\Delta n}{\chi^2} \sin^2\left(\frac{\chi}{2}z\right) S'_{30} \quad (3.109)$$

$$S'_2 = -\frac{2q}{\chi} S'_{10} \sin(\chi z) + S'_{20} \cos(\chi z) - \frac{k_o\Delta n}{\chi} S'_{30} \sin(\chi z) \quad (3.110)$$

$$S'_3 = -\frac{4qk_o\Delta n}{\chi^2} \sin^2\left(\frac{\chi}{2}z\right) S'_{10} + \frac{k_o\Delta n}{\chi} \sin(\chi z) S'_{20} + \left[ 1 - 2\left(\frac{2q}{\chi}\right)^2 \sin^2\left(\frac{\chi}{2}z\right) \right] S'_{30} \quad (3.111)$$

Therefore the Stokes vector  $\vec{S}'_o$  after the TN film is related to the Stokes vector  $\vec{S}'_i$  before the film by

$$\vec{S}'_o = \begin{pmatrix} 1 - 2\frac{\Phi^2}{X^2} \sin^2 X & \frac{\Phi}{X} \sin(2X) & -2\frac{\Phi(\Gamma/2)}{X^2} \sin^2 X \\ -\frac{\Phi}{X} \sin(2X) & \cos(2X) & -\frac{(\Gamma/2)}{X} \sin(2X) \\ -2\frac{\Phi(\Gamma/2)}{X^2} \sin^2 X & \frac{(\Gamma/2)}{X} \sin(2X) & 1 - 2\frac{(\Gamma/2)^2}{X^2} \sin^2 X \end{pmatrix} \cdot \vec{S}'_i \quad (3.112)$$

where

$$X = [\Phi^2 + (\Gamma/2)^2]^{1/2} \quad (3.113)$$

We know that at the exiting plane the local frame makes an angle  $\Phi$  with the lab frame, and at the entrance plane the  $x'$  axis is parallel to the  $x$  axis and therefore  $\vec{S}'_i = \vec{S}_i$ . Therefore in the lab frame we have

$$\vec{S}_o = \begin{pmatrix} \cos(2\Phi) & -\sin(2\Phi) & 0 \\ \sin(2\Phi) & \cos(2\Phi) & 0 \\ 0 & 0 & 1 \end{pmatrix} \cdot \begin{pmatrix} 1 - 2\frac{\Phi^2}{X^2}\sin^2X & \frac{\Phi}{X}\sin(2X) & -2\frac{\Phi(\Gamma/2)}{X^2}\sin^2X \\ -\frac{\Phi}{X}\sin(2X) & \cos(2X) & -\frac{(\Gamma/2)}{X}\sin(2X) \\ -2\frac{\Phi(\Gamma/2)}{X^2}\sin^2X & \frac{(\Gamma/2)}{X}\sin(2X) & 1 - 2\frac{(\Gamma/2)^2}{X^2}\sin^2X \end{pmatrix} \cdot \vec{S}_i \quad (3.114)$$

This equation can also be obtained from Equations (3.34) and (3.70).

For example, for the normal-black  $90^\circ$  TN liquid crystal where the two polarizers are parallel to each other,  $\Phi = \pi/2$  and  $\vec{S}'_i = (1, 0, 0)$ , so

$$\begin{aligned} \vec{S}_o &= \begin{pmatrix} -1 & 0 & 0 \\ 0 & -1 & 0 \\ 0 & 0 & 1 \end{pmatrix} \begin{pmatrix} 1 - 2\frac{\Phi^2}{X^2}\sin^2X & \frac{\Phi}{X}\sin(2X) & -2\frac{\Phi(\Gamma/2)}{X^2}\sin^2X \\ -\frac{\Phi}{X}\sin(2X) & \cos(2X) & -\frac{(\Gamma/2)}{X}\sin(2X) \\ -2\frac{\Phi(\Gamma/2)}{X^2}\sin^2X & \frac{(\Gamma/2)}{X}\sin(2X) & 1 - 2\frac{(\Gamma/2)^2}{X^2}\sin^2X \end{pmatrix} \begin{pmatrix} 1 \\ 0 \\ 0 \end{pmatrix} \\ &= \begin{pmatrix} -1 + 2\frac{\Phi^2}{X^2}\sin^2X \\ \frac{\Phi}{X}\sin(2X) \\ 2\frac{\Phi(\Gamma/2)}{X^2}\sin^2X \end{pmatrix} \end{aligned}$$

The polarizer after the TN liquid crystal is also along the  $x$  axis. From the definition of the Stokes vector we can get the transmittance

$$T = (1 + S_{o1})/2 = \left(\frac{\Phi}{X}\right)^2 \sin^2X$$

which is the same as that given by Equation (3.46).

### 3.2.7 Mueller matrix of non-uniform birefringent film

In the same way that the Jones matrix can be used to numerically calculate the optical properties of non-uniform birefringent films, the Mueller matrix can also be used to numerically calculate the optical properties of a non-uniform birefringent film. We divide the film into  $N$  slabs as shown in Figure 3.2. When the thickness  $\Delta h = h/N$  of the slabs is sufficiently small, within each slab, the slow axis can be considered fixed. For layer  $i$ , the angle of the slow axis with respect the  $x$  axis is  $\beta_i$  and the phase retardation is  $\Gamma_i = 2\pi[n_e(z = i\Delta h) - n_o(z = i\Delta h)]\Delta h/\lambda$ . In the lab frame, the Stokes vector of the incident light on the layer is  $\vec{S}_{ii}$ , which is the same as the Stokes vector,  $\vec{S}'_{(i-1)o}$ , of the light exiting the layer  $(i-1)$ , and the Stokes vector of the light coming out of layer  $i$  is  $S_{io}$  [9]

$$\begin{aligned} \vec{S}_{io} &= \vec{M}_{rotator}(\beta_i) \cdot \vec{M}_{retardar}(\Gamma_i) \cdot \vec{M}_{rotator}^{-1}(\beta_i) \cdot \vec{S}_{ii} \\ &= \vec{M}_{rotator}(\beta_i) \cdot \vec{M}_{retardar}(\Gamma_i) \cdot \vec{M}_{rotator}^{-1}(\beta_i) \cdot \vec{S}'_{(i-1)o} \end{aligned} \quad (3.115)$$

The Stokes vector,  $\vec{S}_o$ , of the outgoing light is related to the Stokes vector,  $\vec{S}_i$ , of the incident light by

$$\begin{aligned}\vec{S}_o &= [\vec{M}_{rotator}(\beta_N) \cdot \vec{M}_{retarder}(\Gamma_N) \cdot \vec{M}_{rotator}^{-1}(\beta_N)] \cdot \\ &\quad [\vec{M}_{rotator}(\beta_{N-1}) \cdot \vec{M}_{retarder}(\Gamma_{N-1}) \cdot \vec{M}_{rotator}^{-1}(\beta_{N-1})] \cdot \\ &\quad \dots \cdot \\ &\quad [\vec{M}_{rotator}(\beta_1) \cdot \vec{M}_{retarder}(\Gamma_1) \cdot \vec{M}_{rotator}^{-1}(\beta_1)] \cdot \vec{S}_i \\ &= \prod_{i=1}^N [\vec{M}_{rotator}(\beta_i) \cdot \vec{M}_{retarder}(\Gamma_i) \cdot \vec{M}_{rotator}^{-1}(\beta_i)] \cdot \vec{S}_i\end{aligned}\quad (3.116)$$

Usually the multiplication of the matrices is carried out numerically.

### 3.3 Berreman 4 x 4 Method

For stratified optical media (whose refractive indices are only a function of the coordinate normal to the film), Berreman introduced a  $4 \times 4$  matrix method (now known as the Berreman  $4 \times 4$  method) [14–18], in which the electric field and magnetic field (the sum of the fields of the light beam propagating in forward and backward directions) are considered. When the film is divided into slabs, the reflection at the interface between the slabs is taken into account. The Berreman  $4 \times 4$  method works well for both normal and obliquely incident light. Consider an optical film, such as a cholesteric liquid crystal in the planar texture (TN), whose dielectric tensor is only a function of the coordinate  $z$ , which is perpendicular to the film:

$$\vec{\epsilon}(z) = \begin{pmatrix} \epsilon_{11}(z) & \epsilon_{12}(z) & \epsilon_{13}(z) \\ \epsilon_{21}(z) & \epsilon_{22}(z) & \epsilon_{23}(z) \\ \epsilon_{31}(z) & \epsilon_{32}(z) & \epsilon_{33}(z) \end{pmatrix}\quad (3.117)$$

For light incident in the  $x$ - $z$  plane with incident angle  $\alpha$  with respect to the  $z$  axis (see Figure 3.8), the fields of the optical wave are

$$\vec{E} = \vec{E}(z)e^{-ik_x x + i\omega t}\quad (3.118)$$

$$\vec{H} = \vec{H}(z)e^{-ik_x x + i\omega t}\quad (3.119)$$

The Maxwell equations for the optical wave are

$$\nabla \cdot \vec{D} = \nabla \cdot (\epsilon_o \vec{\epsilon} \cdot \vec{E}) = 0\quad (3.120)$$

$$\nabla \cdot \vec{B} = \nabla \cdot (\mu_o \vec{H}) = 0\quad (3.121)$$

$$\nabla \times \vec{E} = -\frac{\partial \vec{B}}{\partial t} = -i\mu_o \omega \vec{H}\quad (3.122)$$

$$\nabla \times \vec{H} = \frac{\partial \vec{D}}{\partial t} = i\epsilon_o \omega \vec{\epsilon} \cdot \vec{E}\quad (3.123)$$

Because of Equation (3.120), it is required that

$$k_x = k_o \sin \alpha = \frac{2\pi}{\lambda} \sin \alpha = \text{constant}\quad (3.124)$$

Therefore

$$\frac{\partial}{\partial x} = -ik_x \quad (3.125)$$

Because the light is propagating in the  $x$ - $z$  plane,

$$\frac{\partial}{\partial y} = 0 \quad (3.126)$$

From Equation (3.122) we have

$$\begin{aligned} \nabla \times \vec{E} &= \left( \frac{\partial E_z}{\partial y} - \frac{\partial E_y}{\partial z} \right) \hat{x} + \left( \frac{\partial E_x}{\partial z} - \frac{\partial E_z}{\partial x} \right) \hat{y} + \left( \frac{\partial E_y}{\partial x} - \frac{\partial E_x}{\partial y} \right) \hat{z} \\ &= \left( -\frac{\partial E_y}{\partial z} \right) \hat{x} + \left( \frac{\partial E_x}{\partial z} + ik_x E_z \right) \hat{y} + (-ik_x E_y) \hat{z} \\ &= -i\mu_o \omega \vec{H} = -i\mu_o \omega (H_x \hat{x} + H_y \hat{y} + H_z \hat{z}) \end{aligned} \quad (3.127)$$

In terms of components, we have

$$\frac{\partial E_y}{\partial z} = i\mu_o \omega H_x \quad (3.128)$$

$$\frac{\partial E_x}{\partial z} = -ik_x E_z - i\mu_o \omega H_y \quad (3.129)$$

$$E_y = \frac{\mu_o \omega}{k_x} H_z \quad (3.130)$$

From Equation (3.123) we get

$$\begin{aligned} \nabla \times \vec{H} &= \left( \frac{\partial H_z}{\partial y} - \frac{\partial H_y}{\partial z} \right) \hat{x} + \left( \frac{\partial H_x}{\partial z} - \frac{\partial H_z}{\partial x} \right) \hat{y} + \left( \frac{\partial H_y}{\partial x} - \frac{\partial H_x}{\partial y} \right) \hat{z} \\ &= \left( -\frac{\partial H_y}{\partial z} \right) \hat{x} + \left( \frac{\partial H_x}{\partial z} + ik_x H_z \right) \hat{y} + (-ik_x H_y) \hat{z} \\ &= i\epsilon_o \omega \vec{E} \cdot \vec{E} \end{aligned}$$

In components we have

$$\frac{\partial H_y}{\partial z} = -i\epsilon_o \omega (\epsilon_{11} E_x + \epsilon_{12} E_y + \epsilon_{13} E_z) \quad (3.132)$$

$$\frac{\partial H_x}{\partial z} = -ik_x H_z + i\epsilon_o \omega (\epsilon_{21} E_x + \epsilon_{22} E_y + \epsilon_{23} E_z) \quad (3.133)$$

$$H_y = -\frac{\mu_o \omega}{k_x} (\epsilon_{31} E_x + \epsilon_{32} E_y + \epsilon_{33} E_z) \quad (3.134)$$

From Equation (3.130) we have

$$H_z = \frac{k_x}{\mu_o \omega} E_y = \frac{k_x}{k_o} \frac{k_o}{\mu_o \omega} E_y = \frac{k_x}{k_o} \frac{\sqrt{\epsilon_o \mu_o}}{\mu_o} E_y = \frac{k_x}{k_o} \frac{1}{\sqrt{\mu_o / \epsilon_o}} E_y = \frac{k_x}{k_o} \frac{1}{\eta_o} E_y \quad (3.135)$$

where  $\eta_o = \sqrt{\mu_o/\epsilon_o} = 376.98 \Omega$  is known as the resistance of vacuum. Equation (3.135) can be used to replace  $H_z$  in Equation (3.133). From Equation (3.134) we can find

$$E_z = \frac{-1}{\epsilon_{33}} [(k_x/\mu_o\omega)H_y + \epsilon_{31}E_x + \epsilon_{32}E_y] = \frac{-1}{\epsilon_{33}} [(\eta_o k_x/k_o)H_y + \epsilon_{31}E_x + \epsilon_{32}E_y] \quad (3.136)$$

which can be used to replace  $E_z$  in Equation (3.129). Therefore only four components of the electric and magnetic fields are needed to specify the light. We define the Berreman vector

$$\vec{\psi}^T = (E_x, \eta_o H_y, E_y, -\eta_o H_x) \quad (3.137)$$

Then we have

$$\frac{\partial \vec{\psi}}{\partial z} = -ik_o \begin{pmatrix} -\chi \frac{\epsilon_{31}}{\epsilon_{33}} & -\chi^2 \frac{1}{\epsilon_{33}} + 1 & -\chi \frac{\epsilon_{32}}{\epsilon_{33}} & 0 \\ -\frac{\epsilon_{13}\epsilon_{31}}{\epsilon_{33}} + \epsilon_{11} & -\chi \frac{\epsilon_{13}}{\epsilon_{33}} & -\frac{\epsilon_{13}\epsilon_{32}}{\epsilon_{33}} + \epsilon_{12} & 0 \\ 0 & 0 & 0 & 1 \\ -\frac{\epsilon_{23}\epsilon_{31}}{\epsilon_{33}} + \epsilon_{21} & -\chi \frac{\epsilon_{23}}{\epsilon_{33}} & -\chi^2 - \frac{\epsilon_{23}\epsilon_{32}}{\epsilon_{33}} + \epsilon_{22} & 0 \end{pmatrix} \vec{\psi} \equiv -ik_o \vec{Q} \cdot \vec{\psi} \quad (3.138)$$

where  $\chi = k_x/k_o$ . Note that  $Q_{13} = Q_{42}$ ,  $Q_{11} = Q_{22}$ , and  $Q_{41} = Q_{23}$  because the dielectric tensor is symmetric. Equation (3.138) is known as the Berreman equation. If the dielectric tensor does not change in the region from  $z$  to  $z + \Delta z$ , then  $\vec{Q}(z)$  does not change in this region and the solution to Equation (3.138) is

$$\vec{\psi}(z + \Delta z) = e^{-ik_o \vec{Q}(z)\Delta z} \cdot \vec{\psi}(z) \equiv \vec{P}(z) \cdot \vec{\psi}(z) \quad (3.139)$$

This equation can be used to calculate the Berreman vector in the optical film. In the calculation, the film is divided into  $N$  slabs as shown in Figure 3.8. If the Berreman vector of the incident light is  $\vec{\psi}_i$ , the

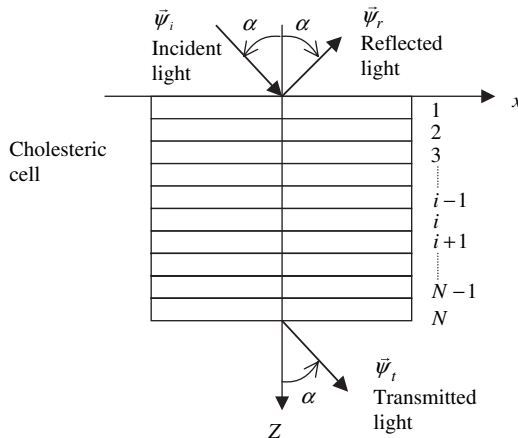


Figure 3.8 The coordinate system used to describe light propagation in the Berreman  $4 \times 4$  method

Berreman vector  $\vec{\psi}_o$  of the outgoing light can be numerically calculated by

$$\vec{\psi}_o = \prod_{i=1}^N \vec{P}(i\Delta z) \cdot \vec{\psi}_i \quad (3.140)$$

In this method, in order to obtain accurate results, the thickness of the slabs must be much thinner than  $\lambda/2\pi$  and thus the computational time is long. The number of slabs can be dramatically reduced and therefore the computation is much faster if the fast Berreman method is used [19, 20]. The fast Berreman method utilizes the Cayley–Hamilton theory that states  $\vec{P}$  can be expanded as

$$\vec{P} = e^{-ik_o \vec{Q} \Delta z} = \gamma_o \vec{I} + \gamma_1 (-ik_o \vec{Q} \Delta z) + \gamma_2 (-ik_o \vec{Q} \Delta z)^2 + \gamma_3 (-ik_o \vec{Q} \Delta z)^3 \quad (3.141)$$

where  $\vec{I}$  is the identity matrix and  $\gamma_i (i = 0, 1, 2, 3)$  are the solutions of the following equations:

$$\gamma_o + \gamma_1 (-ik_o \Delta z q_i) + \gamma_2 (-ik_o \Delta z q_i)^2 + \gamma_3 (-ik_o \Delta z q_i)^3 = e^{(-ik_o \Delta z q_i)} \quad i = 1, 2, 3, 4 \quad (3.142)$$

where  $q_i (i = 1, 2, 3, 4)$  are the eigenvalues of the Berreman matrix  $\vec{Q}$ . That is, they are solutions of the equation

$$|\vec{Q} - q \vec{I}| = q^4 - 2Q_{11}q^3 - (Q_{43} - Q_{11}^2 + Q_{12}Q_{21})q^2 - 2(Q_{13}Q_{23} - Q_{43}Q_{11})q - (Q_{11}^2Q_{43} + Q_{21}Q_{13}^2 + Q_{12}Q_{23}^2 - 2Q_{11}Q_{13}Q_{23} - Q_{12}Q_{21}Q_{43}) = 0 \quad (3.143)$$

For a uniaxial liquid crystal with ordinary and extraordinary refractive indices  $n_e$  and  $n_o$ , respectively, when the liquid crystal director is  $\vec{n} = (n_x, n_y, n_z)$ , the dielectric tensor is

$$\vec{\varepsilon} = \begin{pmatrix} \varepsilon_{\perp} + \Delta\varepsilon n_x^2 & \Delta\varepsilon n_x n_y & \Delta\varepsilon n_x n_z \\ \Delta\varepsilon n_x n_y & \varepsilon_{\perp} + \Delta\varepsilon n_y^2 & \Delta\varepsilon n_y n_z \\ \Delta\varepsilon n_x n_z & \Delta\varepsilon n_y n_z & \varepsilon_{\perp} + \Delta\varepsilon n_z^2 \end{pmatrix} \quad (3.144)$$

where  $\varepsilon_{\perp} = n_o^2$  and  $\Delta\varepsilon = \varepsilon_{\parallel} - \varepsilon_{\perp} = n_e^2 - n_o^2$ . The Berreman matrix is given by

$$\vec{Q} = \frac{1}{(\varepsilon_{\perp} + \Delta\varepsilon n_z^2)} \begin{pmatrix} -\chi \Delta\varepsilon n_x n_z & (\varepsilon_{\perp} + \Delta\varepsilon n_z^2) - \chi^2 & -\chi \Delta\varepsilon n_y n_z & 0 \\ \varepsilon_{\perp} [\varepsilon_{\perp} + \Delta\varepsilon (n_x^2 + n_z^2)] & -\chi \Delta\varepsilon n_x n_z & \varepsilon_{\perp} \Delta\varepsilon n_x n_y & 0 \\ 0 & 0 & 0 & 1 \\ \varepsilon_{\perp} \Delta\varepsilon n_x n_y & -\chi \Delta\varepsilon n_y n_z & (\varepsilon_{\perp} - \chi^2)(\varepsilon_{\perp} + \Delta\varepsilon n_z^2) + \varepsilon_{\perp} \Delta\varepsilon n_y^2 & 0 \end{pmatrix} \quad (3.145)$$



The solutions of Equation (3.143) are

$$q_{1/2} = \pm(Q_{43} - Q_{13}Q_{23}/Q_{11})^{1/2} = \pm[\varepsilon_{\perp} - \chi^2]^{1/2} \quad (3.146)$$

$$q_{3/4} = Q_{11} \pm (Q_{12}Q_{21} + Q_{13}Q_{23}/Q_{11})^{1/2} \\ = \frac{-\chi\Delta\varepsilon n_x n_z}{\varepsilon_{\perp} + \Delta\varepsilon n_z^2} \pm \frac{(\varepsilon_{\parallel}\varepsilon_{\perp})^{1/2}}{\varepsilon_{\perp} + \Delta\varepsilon n_z^2} \left[ \varepsilon_{33} - \chi^2 \left( 1 - \frac{\Delta\varepsilon}{\varepsilon_{\parallel}} n_y^2 \right) \right]^{1/2} \quad (3.147)$$

Note that when  $n_z \rightarrow 0$ ,  $Q_{11} \rightarrow 0$  and  $Q_{13} \rightarrow 0$ , but not  $Q_{13}/Q_{11}$ . It can be derived that [16]

$$(-ik_o\Delta z)^0 \gamma_o = -\frac{q_2 q_3 q_4 e^{-ik_o\Delta z q_1}}{(q_1 - q_2)(q_1 - q_3)(q_1 - q_4)} - \frac{q_1 q_3 q_4 e^{-ik_o\Delta z q_2}}{(q_2 - q_1)(q_2 - q_3)(q_2 - q_4)} \\ - \frac{q_1 q_2 q_4 e^{-ik_o\Delta z q_3}}{(q_3 - q_1)(q_3 - q_2)(q_3 - q_4)} - \frac{q_1 q_2 q_3 e^{-ik_o\Delta z q_4}}{(q_4 - q_1)(q_4 - q_2)(q_4 - q_3)} \quad (3.148)$$

$$(-ik_o\Delta z) \gamma_1 = \frac{(q_2 q_3 + q_2 q_4 + q_3 q_4) e^{-ik_o\Delta z q_1}}{(q_1 - q_2)(q_1 - q_3)(q_1 - q_4)} + \frac{(q_1 q_3 + q_1 q_4 + q_3 q_4) e^{-ik_o\Delta z q_2}}{(q_2 - q_1)(q_2 - q_3)(q_2 - q_4)} \\ + \frac{(q_1 q_2 + q_1 q_4 + q_2 q_4) e^{-ik_o\Delta z q_3}}{(q_3 - q_1)(q_3 - q_2)(q_3 - q_4)} + \frac{(q_1 q_2 + q_1 q_3 + q_2 q_3) e^{-ik_o\Delta z q_4}}{(q_4 - q_1)(q_4 - q_2)(q_4 - q_3)} \quad (3.149)$$

$$(-ik_o\Delta z)^2 \gamma_2 = -\frac{(q_2 + q_3 + q_4) e^{-ik_o\Delta z q_1}}{(q_1 - q_2)(q_1 - q_3)(q_1 - q_4)} - \frac{(q_1 + q_3 + q_4) e^{-ik_o\Delta z q_2}}{(q_2 - q_1)(q_2 - q_3)(q_2 - q_4)} \\ - \frac{(q_1 + q_2 + q_4) e^{-ik_o\Delta z q_3}}{(q_3 - q_1)(q_3 - q_2)(q_3 - q_4)} - \frac{(q_1 + q_2 + q_3) e^{-ik_o\Delta z q_4}}{(q_4 - q_1)(q_4 - q_2)(q_4 - q_3)} \quad (3.150)$$

$$(-ik_o\Delta z)^3 \gamma_3 = \frac{q_1 e^{-ik_o\Delta z q_1}}{(q_1 - q_2)(q_1 - q_3)(q_1 - q_4)} + \frac{q_2 e^{-ik_o\Delta z q_2}}{(q_2 - q_1)(q_2 - q_3)(q_2 - q_4)} \\ + \frac{q_3 e^{-ik_o\Delta z q_3}}{(q_3 - q_1)(q_3 - q_2)(q_3 - q_4)} + \frac{q_4 e^{-ik_o\Delta z q_4}}{(q_4 - q_1)(q_4 - q_2)(q_4 - q_3)} \quad (3.151)$$

We consider some special cases below.

(1) *Isotropic medium*

Consider an isotropic medium of dielectric constant  $\varepsilon = n^2$ , where  $n$  is the refractive index. From Equation (3.138) we have

$$\vec{Q} = \begin{pmatrix} 0 & \frac{-\chi^2}{\varepsilon} + 1 & 0 & 0 \\ \varepsilon & 0 & 0 & 0 \\ 0 & 0 & 0 & 1 \\ 0 & 0 & -\chi^2 + \varepsilon & 0 \end{pmatrix} = \begin{pmatrix} 0 & \frac{k_z^2}{(nk_o)^2} & 0 & 0 \\ n^2 & 0 & 0 & 0 \\ 0 & 0 & 0 & 1 \\ 0 & 0 & \frac{k_z^2}{k_o^2} & 0 \end{pmatrix} \quad (3.152)$$

In the medium the wavevector is  $k = nk_o$ . From Equations (3.146) and (3.147) we have the eigenvalues of the Berreman matrix

$$q_{1,3/2,4} = \pm(n^2 - \chi^2)^{1/2} = \frac{k_z}{k_o} = \pm n \cos \alpha \quad (3.153)$$

The eigenvalues are degenerate and in this case  $e^{-ik_o\vec{Q}\Delta z}$  can be expanded as

$$e^{-ik_o\vec{Q}\Delta z} = \gamma_o\vec{I} + \gamma_1(-ik_o\vec{Q}\Delta z) \quad (3.154)$$

where  $\gamma_i (i = 0, 1)$  are the solutions of the following equations:

$$\gamma_o + \gamma_1(-ik_z\Delta z) = e^{-ik_z\Delta z} \quad (3.155)$$

$$\gamma_o + \gamma_1(+ik_z\Delta z) = e^{+ik_z\Delta z} \quad (3.156)$$

From these two equations we find

$$\gamma_o = \cos(k_z\Delta z) \quad (3.157)$$

$$\gamma_1 = \frac{1}{k_z\Delta z} \sin(k_z\Delta z) \quad (3.158)$$

$$e^{-ik_o\vec{Q}\Delta z} = \cos(k_z\Delta z) \begin{pmatrix} 1 & 0 & 0 & 0 \\ 0 & 1 & 0 & 0 \\ 0 & 0 & 1 & 0 \\ 0 & 0 & 0 & 1 \end{pmatrix} - \frac{ik_o}{k_z} \sin(k_z\Delta z) \begin{pmatrix} 0 & k_z^2/k^2 & 0 & 0 \\ n^2 & 0 & 0 & 0 \\ 0 & 0 & 0 & 1 \\ 0 & 0 & n^2 k_z^2/k^2 & 0 \end{pmatrix} \quad (3.159)$$

$$= \begin{pmatrix} \cos(k_z\Delta z) & -\frac{ik_z}{nk} \sin(k_z\Delta z) & 0 & 0 \\ -\frac{ink}{k_z} \sin(k_z\Delta z) & \cos(k_z\Delta z) & 0 & 0 \\ 0 & 0 & \cos(k_z\Delta z) & -\frac{ik}{nk_z} \sin(k_z\Delta z) \\ 0 & 0 & -\frac{ink_z}{k} \sin(k_z\Delta z) & \cos(k_z\Delta z) \end{pmatrix}$$

We also know that  $E_i(z + \Delta z) = e^{-ik_z\Delta z} E_i(z)$  and  $H_i(z + \Delta z) = e^{-ik_z\Delta z} H_i(z) (i = x, y)$ . From Equation (3.139), in components we have

$$E_x(z + \Delta z) = e^{-ik_z\Delta z} E_x(z) = \cos(k_z\Delta z) E_x(z) - \frac{ik_z}{nk} \sin(k_z\Delta z) \eta_o H_y(z) \quad (3.160)$$

$$\eta_o H_y(z + \Delta z) = e^{-ik_z\Delta z} \eta_o H_y(z) = \cos(k_z\Delta z) \eta_o H_y(z) - \frac{ink}{k_z} \sin(k_z\Delta z) E_x(z) \quad (3.161)$$

$$E_y(z + \Delta z) = e^{-ik_z\Delta z} E_y(z) = \cos(k_z\Delta z) E_y(z) + \frac{ik_z}{nk} \sin(k_z\Delta z) \eta_o H_x(z) \quad (3.162)$$

$$\eta_o H_x(z + \Delta z) = e^{-ik_z\Delta z} \eta_o H_x(z) = \cos(k_z\Delta z) \eta_o H_x(z) + \frac{ink}{k_z} \sin(k_z\Delta z) E_y(z) \quad (3.163)$$

Therefore

$$\eta_o H_y(z) = \frac{nk}{k_z} E_x(z) = \frac{n}{\cos \alpha} E_x(z) \quad (3.164)$$

$$-\eta_o H_x(z) = \frac{nk}{k_z} E_y(z) = n \cos \alpha E_y(z) \quad (3.165)$$

The Berreman vector in the isotropic medium is

$$\vec{\psi}^T = \left( E_x \frac{n}{\cos \alpha} E_x \ E_y \ n \cos \alpha E_y \right) \quad (3.166)$$

From Equation (3.136) we have

$$E_z = \frac{-1}{\varepsilon_{33}} [(\eta_o k_x / k_o) H_y + \varepsilon_{31} E_x + \varepsilon_{32} E_y] = \frac{-1}{\varepsilon} (k_x / k_o) \frac{n}{\cos \alpha} E_x(z) = -\frac{\sin \alpha}{\cos \alpha} E_x(z) \quad (3.167)$$

The intensity of light is

$$I = n \left( |E_p|^2 + |E_s|^2 \right) = n \left[ (|E_x|^2 + |E_z|^2) + |E_y|^2 \right] = n \left( |E_x|^2 / \cos^2 \alpha + n |E_y|^2 \right) \quad (3.168)$$

where  $E_p$  and  $E_s$  are the components of the electric vector in and perpendicular to the incident plane, respectively.

### (2) Cholesteric liquid crystal

For a uniaxial cholesteric liquid crystal that has chirality  $q_o$  and refractive indices  $n_o$  and  $n_e$ , when it is in the planar state,  $n_x = \cos(q_o z)$ ,  $n_y = \sin(q_o z)$ , and  $n_z = 0$ . The dielectric tensor is

$$\overleftrightarrow{\varepsilon} = \begin{pmatrix} \varepsilon_{11} & \varepsilon_{12} & 0 \\ \varepsilon_{12} & \varepsilon_{22} & 0 \\ 0 & 0 & \varepsilon_{33} \end{pmatrix} = \begin{pmatrix} \varepsilon_{\perp} + \Delta\varepsilon \cos^2(q_o z) & \Delta\varepsilon \sin(q_o z) \cos(q_o z) & 0 \\ \Delta\varepsilon \sin(q_o z) \cos(q_o z) & \varepsilon_{\perp} + \Delta\varepsilon \cos^2(q_o z) & 0 \\ 0 & 0 & \varepsilon_{\perp} \end{pmatrix} \quad (3.169)$$

The Berreman matrix is

$$\overleftrightarrow{Q} = \begin{pmatrix} 0 & 1 - \chi^2 / \varepsilon_{\perp} & 0 & 0 \\ \varepsilon_{\perp} + \Delta\varepsilon n_x^2 & 0 & \Delta\varepsilon n_x n_y & 0 \\ 0 & 0 & 0 & 1 \\ \Delta\varepsilon n_x n_y & 0 & (\varepsilon_{\perp} - \chi^2) + \Delta\varepsilon n_y^2 & 0 \end{pmatrix} \quad (3.170)$$

From Equations (3.146) and (3.147) we get the eigenvalues of the Berreman matrix

$$q_{1/2} = \pm [\varepsilon_{\perp} - \chi^2]^{1/2} \quad (3.171)$$

$$q_{3/4} = \pm \left( \frac{\varepsilon_{\parallel}}{\varepsilon_{\perp}} \right)^{1/2} \left[ \varepsilon_{\perp} - \chi^2 \left( 1 - \frac{\Delta\varepsilon}{\varepsilon_{\parallel}} n_y^2 \right) \right]^{1/2} = \pm \left[ \varepsilon_{\parallel} - \chi^2 \frac{1}{\varepsilon_{\perp}} (\varepsilon_{\parallel} - \Delta\varepsilon n_y^2) \right]^{1/2} \quad (3.172)$$

Outside the cholesteric cell, the medium is an isotropic medium with refractive index  $n_g$ . On top of the cholesteric film (incident side), there is incident light and reflected light, and the actual Berreman vector is the sum of the Berreman vectors of the incident light and reflected light. From Equation (3.166) we know that for the incident light, the Berreman vector is

$$\vec{\psi}_i^T = \left( E_{xi} \frac{n}{\cos \alpha} E_{xi} \ E_{yi} \ n_g \cos \alpha E_{yi} \right) \quad (3.173)$$

For the reflected light, because it propagates in the reverse direction, the Berreman vector is

$$\vec{\psi}_r^T = \left( E_{xr} \frac{-n}{\cos \alpha} E_{xr} \ E_{yr} \ -n_g \cos \alpha E_{yr} \right) \quad (3.174)$$

At the bottom of the cholesteric film, there is only the transmitted light whose Berreman vector is

$$\vec{\psi}_t^T = \left( E_{xt} \frac{n}{\cos \alpha} E_{xt} \ E_{yt} \ n_g \cos \alpha E_{yt} \right) \quad (3.175)$$

We divide the cholesteric film into  $N$  slabs with thicknesses  $\Delta z$ . The Berreman vectors at the boundaries between the slabs are

$$\begin{aligned} \vec{\psi}(0) &= \vec{\psi}_i + \vec{\psi}_r \\ \vec{\psi}(1) &= \vec{P}(z_1) \cdot \vec{\psi}(0) \\ \vec{\psi}(2) &= \vec{P}(z_2) \cdot \vec{\psi}(1) = \vec{P}(z_2) \cdot \vec{P}(z_1) \cdot \vec{\psi}(0) \\ &\vdots \\ \vec{\psi}_t = \vec{\psi}(N) &= \prod_{i=1}^N \vec{P}(z_i)(z_N) \cdot \vec{\psi}(0) = \prod_{i=1}^N \vec{P}(z_i)(z_N) \cdot (\vec{\psi}_i + \vec{\psi}_r) \equiv \vec{B} \cdot (\vec{\psi}_i + \vec{\psi}_r) \end{aligned} \quad (3.176)$$

where the  $\vec{P}$  for each slab can be numerically calculated by using the fast Berreman method. In components, Equation (3.176) contains four equations:  $\vec{\psi}_i$  is given;  $\vec{\psi}_r$  and  $\vec{\psi}_t$  have two unknown variables each and can be found by solving equation (3.176). We define a new vector  $\vec{\psi}_{t/r}$ :

$$\vec{\psi}_{t/r}^T = (E_{tx} \ E_{ty} \ E_{rx} \ E_{ry}) \quad (3.177)$$

The Berreman vectors of the transmitted and reflected light are related to  $\vec{\psi}_{t/r}$  by

$$\vec{\psi}_t = \begin{pmatrix} 1 & 0 & 0 & 0 \\ n_g/\cos \alpha & 0 & 0 & 0 \\ 0 & 1 & 0 & 0 \\ 0 & n_g \cos \alpha & 0 & 0 \end{pmatrix} \cdot \vec{\psi}_{t/r} \equiv \vec{A}_t \cdot \vec{\psi}_{t/r} \quad (3.178)$$

$$\vec{\psi}_r = \begin{pmatrix} 0 & 0 & 1 & 0 \\ 0 & 0 & -n_g/\cos \alpha & 0 \\ 0 & 0 & 0 & 1 \\ 0 & 0 & 0 & -n_g \cos \alpha \end{pmatrix} \cdot \vec{\psi}_{t/r} \equiv \vec{A}_r \cdot \vec{\psi}_{t/r} \quad (3.179)$$

From Equation (3.176) we have

$$\vec{A}_t \cdot \vec{\psi}_{t/r} \equiv \vec{B} \cdot (\vec{\psi}_i + \vec{A}_r \cdot \vec{\psi}_{t/r}) \tag{3.180}$$

$$\vec{\psi}_{t/r} \equiv (\vec{A}_t + \vec{B} \cdot \vec{A}_r)^{-1} \cdot \vec{B} \cdot \vec{\psi}_i \tag{3.181}$$

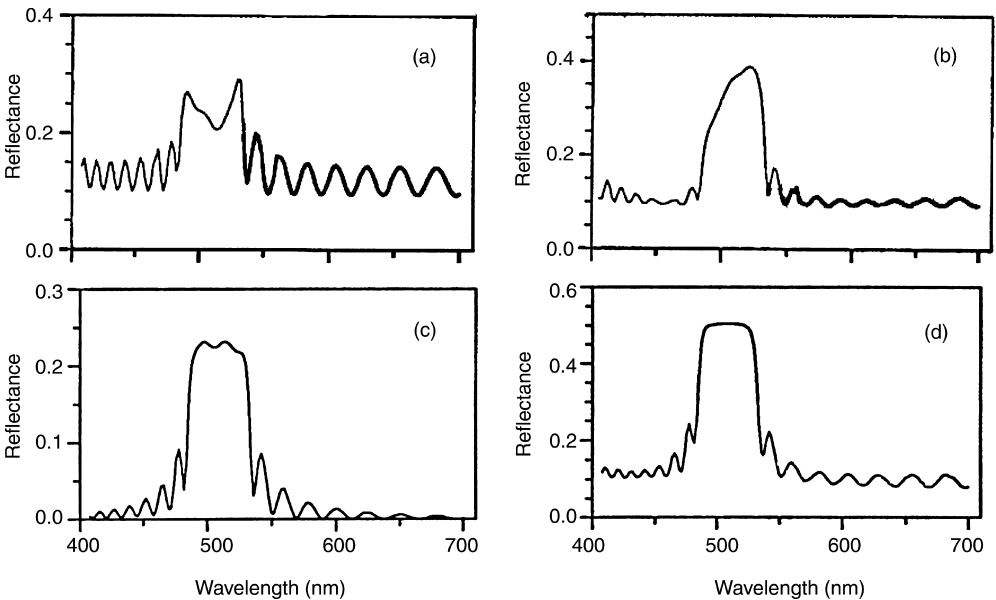
The reflectance can be calculated by

$$R = [(E_{xr}/\cos \alpha)^2 + E_{yr}^2]/[(E_{xi}/\cos \alpha)^2 + E_{yi}^2] \tag{3.182}$$

Therefore the transmittance can be calculated by

$$T = [(E_{xt}/\cos \alpha)^2 + E_{yt}^2]/[(E_{xi}/\cos \alpha)^2 + E_{yi}^2] \tag{3.183}$$

The reflection of a cholesteric liquid crystal in the planar texture depends on the polarization state of the incident light and how the reflected light is measured. As an example, we consider a cholesteric liquid crystal with the following parameters:  $P_o = 338$  nm, cell thickness  $h = 5070$  nm,  $n_o = 1.494$ , and  $n_e = 1.616$ . The incident angle is  $22.5^\circ$ . The refractive index of the glass substrates is 1.5. On the surface of the glass substrates there are an indium–tin–oxide (ITO) conducting film and a polyimide alignment layer. The thickness of the ITO film is 25 nm and its refractive index is  $n(\lambda) = 2.525 - 0.001271\lambda$ , where  $\lambda$  is the wavelength of light in units of nanometers. The thickness of the polyimide is 98 nm and its refractive index is 1.7. The reflection spectra are shown in Figure 3.9 [21]. In Figure 3.9(a) and (b), the



**Figure 3.9** The reflection spectra of the cholesteric liquid crystal. (a) Incident light:  $\sigma$  polarization and parallel to the liquid crystal director on the entrance plane; detection:  $\sigma$  polarization. (b) Incident light:  $\sigma$  polarization and perpendicular to the liquid crystal director on the entrance plane; detection:  $\sigma$  polarization. (c) Incident light:  $\sigma$  polarization; detection:  $\pi$  polarization. (d) Incident light: unpolarized; detection: unpolarized [21]

incident light is linearly polarized perpendicular to the incident plane and the component of the reflected light in the same direction is measured. In Figure 3.9(a), the polarization of the incident light is parallel to the liquid crystal director in the entrance plane, while in Figure 3.9(b) the polarization is perpendicular to the liquid crystal director in the entrance plane. The spectra are very different because of the interference between the light reflected from the liquid crystal and the light reflected from the interfaces between the glass substrate, the ITO electrode, the alignment layer, and the liquid crystal. In Figure 3.9(a) the components interfere destructively and therefore there is a dip in the middle of the reflection band. In Figure 3.9(b) they interfere constructively and therefore the reflection is higher in the middle of the reflection band. In Figure 3.9(c), crossed polarizers are used. The light reflected from the interfaces cannot go through the analyzer and is not detected. The linearly polarized incident light can be decomposed into two circularly polarized components, and one of them is reflected. The reflected circularly polarized light can be decomposed into two linearly polarized components, and one of them passes through the analyzer. Therefore the maximum reflection is 25%. In Figure 3.9(d) the incident light is unpolarized and all the reflected light is detected. The reflection in the band is slightly higher than 50% because of the light reflected from the interfaces. The fringes are due to the finite thickness of the liquid crystal. They exist even when the substrates have a refractive index that matches that of the liquid crystal, but disappear for infinitely thick samples. These simulated results agree very well with experimental results.

## Homework Problems

- 3.1 Use the Jones matrix method to numerically calculate the transmittance of a  $90^\circ$  twisted nematic display in the field-off state as a function of the retardation  $u = 2\Delta nh/\lambda$ . The polarizers are parallel to each other and are also parallel to the liquid crystal director at the entrance plane. Compare your result with Figure 3.4.
- 3.2 Consider a  $90^\circ$  twisted nematic cell sandwiched between two polarizers. Use Equation (3.45) to calculate and plot the transmittance as a function of  $u = 2\Delta nh/\lambda$  in the following case. The polarizers are parallel to each other and the transmission axis of the polarizer at the entrance plane is parallel to the liquid crystal director.
- 3.3 Using the definition of the Stokes vector, derive the Mueller matrix given by Equation (3.70) of an optical element whose Jones matrix is given by Equation (3.69).
- 3.4 Linearly polarized light is normally incident on a homogeneously aligned nematic liquid crystal that acts as a half-wave plate. The polarization is along the  $x$  direction. The liquid crystal director is at an angle of  $22.5^\circ$  with respect to the  $x$  axis. Sketch the polarization trajectory on the Poincaré sphere when the light propagates through the liquid crystal.
- 3.5 Derive the Mueller matrix given by Equation (3.77) of a retarder whose retardation is  $\Gamma$  and its slow axis makes an angle  $\phi$  with respect to the  $x$  axis.
- 3.6 Use Equations (3.34) and (3.70) to derive Equation (3.114).
- 3.7 In the Berreman  $4 \times 4$  method, using  $\nabla \cdot \vec{D} = 0$ , prove that  $k_x = \text{constant}$ .
- 3.8 Using the  $\vec{Q}$  given by Equation (3.145), prove that the  $q$  given by Equations (3.146) and (3.147) are solutions of Equation (3.143).
- 3.9 *Cell thickness dependence of the reflection of a cholesteric liquid crystal in the planar state.* The pitch of the liquid crystal is  $P = 350$  nm. The refractive indices of the liquid crystal are  $n_e = 1.7$  and  $n_o = 1.5$ . The liquid crystal is sandwiched between two glass plates with refractive index  $n_g = 1.6$ . The incident light is circularly polarized with the same helical handedness as the liquid crystal. Neglecting the reflection from the glass-air interface, calculate the reflection spectrum of the liquid crystal with cell thicknesses  $P$ ,  $2P$ ,  $5P$ , and  $10P$  using first the Berreman  $4 \times 4$  method and second a method using Equation (2.176). Compare the results from the two methods.

- 3.10 Use the Berreman  $4 \times 4$  method to calculate the reflection spectra of the cholesteric film under the polarization conditions specified in Figure 3.9. The parameters of the cholesteric liquid crystal are also given in Figure 3.9.
- 3.11 A uniaxial birefringent film is sandwiched between two crossed polarizers. The transmission axis of the polarizer at the entrance plane is along the  $x$  axis. Use the Jones matrix method and the Berreman matrix method separately to calculate the transmittance pattern in the following two cases as a function of the polar and azimuthal angles  $\theta$  and  $\phi$  of the incident light. (1) An  $a$  plate has retardation  $\Delta nd = \lambda$  and its slow axis makes an angle of  $45^\circ$  with respect to the  $x$  axis. (2) A  $c$  plate has retardation  $\Delta nd = \lambda$ . If the results obtained by the two methods are different, explain the difference. Neglect reflection in the Berreman method.

## References

- 1 R. C. Jones, *J. Opt. Soc. Am.*, **31**, 488 (1941).
- 2 I. J. Hodgkinson and Q. H. Wu, *Birefringent thin films and polarizing elements* (World Scientific, Singapore, 1997).
- 3 S. Chandrasekhar, *Liquid crystals*, 2nd edn (Cambridge University Press, New York, 1997).
- 4 P. Yeh and C. Gu, *Optics of liquid crystal displays* (John Wiley & Sons, Inc., New York, 1999).
- 5 P. Yeh, 'Extended Jones matrix method', *J. Opt. Soc. Am.*, **72**, 507 (1982).
- 6 C. Gu and P. Yeh, 'Extended Jones matrix method II', *J. Opt. Soc. Am.*, **A10**, 966 (1993).
- 7 A. Lien, 'The general and simplified Jones matrix representations for the high pretilt twisted nematic cell', *J. Appl. Phys.*, **67**, 2853 (1990).
- 8 T. Scheffer and J. Nehring, 'Twisted nematic and supertwisted nematic mode LCDs', in *Liquid crystals—applications and uses*, Vol. 1, ed. B. Bahadur (World Scientific, Singapore, 1990).
- 9 R. A. Horn and C. R. Johnson, *Matrix analysis* (Cambridge University Press, Cambridge, 1985).
- 10 C. Mauguin, 'Sur les cristaux liquides de Lehman', *Bull. Soc. Fr. Mineral.*, **34**, 71–117 (1911).
- 11 H. L. Ong, 'Optical properties of general twisted nematic liquid-crystal displays', *Appl. Phys. Lett.*, **51**, 1398 (1987).
- 12 H. L. Ong, 'Origin and characteristics of the optical properties of general twisted nematic liquid crystals', *J. Appl. Phys.*, **64**, 614 (1988).
- 13 H. C. van de Hulst, *Light scattering by small particles* (Dover, New York, 1957).
- 14 D. W. Berreman, 'Optics in stratified and anisotropic media:  $4 \times 4$ -matrix formulation', *J. Opt. Soc. Am.*, **62**, 502 (1972).
- 15 D. W. Berreman, 'Optics in smoothly varying anisotropic planar structures: application to liquid-crystal twist cells', *J. Opt. Soc. Am.*, **63**, 1374 (1973).
- 16 H. Wöhler and M. E. Becker, 'The optics of liquid crystals', Seminar Lecture Notes, *EuroDisplay'93*.
- 17 D. W. Berreman and T. J. Scheffer, 'Bragg reflection of light from single-domain cholesteric liquid crystal films', *Phys. Rev. Lett.*, **25**, 577 (1970).
- 18 D. W. Berreman and T. J. Scheffer, 'Reflection and transmission by single-domain cholesteric liquid crystal films: theory and verification', *Mol. Cryst. Liq. Cryst.*, **11**, 395 (1970).
- 19 D. W. Berreman, 'Ultrafast  $4 \times 4$  matrix optics with averaged interference fringes', *SID International Symposium, Seminar and Exhibition*, 101–104, Seattle, USA, 16–21 May (1993).
- 20 H. Wöhler, G. Haas, M. Fritsch, and D. A. Mlynski, 'Faster  $4 \times 4$  method, for uniaxial inhomogeneous media', *J. Opt. Soc. Am.*, **A5**, 1554 (1988).
- 21 M. Xu, F. D. Xu, and D.-K. Yang, 'Effects of cell structure on the reflection of cholesteric liquid crystal display', *J. Appl. Phys.*, **83**, 1938 (1998).

# 4

## Effects of Electric Field on Liquid Crystals

One of the main reasons, if not the only reason, that liquid crystals are of great importance in display applications is their ready response to externally applied electric fields [1, 2]. Their direction can be easily changed by electric fields produced by applications of a few volts across the liquid crystal cells. They are either dielectric or ferroelectric materials with high resistivities and thus consume little energy. When the liquid crystals reorient, their optical properties change dramatically because of their large birefringences. In this chapter, we will first discuss how liquid crystals interact with externally applied electric fields, and then consider their applications.

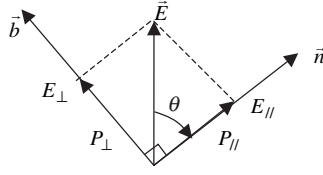
### 4.1 Dielectric Interaction

Uniformly oriented uniaxial nematic liquid crystals of rod-like molecules are non-polar because of the intermolecular interaction and the resulting symmetry of  $D_{\infty h}$  (in Schoenflies notation) [3]. The continuous rotational symmetry axis is parallel to the liquid crystal director  $\vec{n}$ . A uniformly oriented nematic liquid crystal is invariant for a rotation of any angle around  $\vec{n}$ . It is also invariant for the reflectional symmetry operation about the plane perpendicular to  $\vec{n}$ . In the absence of an external electric field, it has non-polar cylindrical symmetry. If the liquid crystal molecules have a permanent dipole along the long molecular axis, the dipole has the same probability of pointing up and pointing down with respect to the liquid crystal director  $\vec{n}$ . If the permanent dipole is perpendicular to the long molecular axis, it has the same probability of pointing in any direction perpendicular to the director. There is no spontaneous polarization and therefore uniformly aligned nematic liquid crystals are dielectrics.

#### 4.1.1 Reorientation under dielectric interaction

When an electric field is applied to a nematic liquid crystal, it induces polarization. As discussed in Chapter 1, the induced polarization depends on the orientation of the liquid crystal director with





**Figure 4.1** Schematic diagram showing the field decomposed into components parallel and perpendicular to the liquid crystal director

respect to the applied field because the permittivity in the direction parallel to  $\vec{n}$  is different from that in the direction perpendicular to  $\vec{n}$ . When the applied field is parallel to  $\vec{n}$ , the permittivity is  $\chi_{\parallel}$ ; when the applied field is perpendicular to  $\vec{n}$ , the permittivity is  $\chi_{\perp}$ . When the applied field is neither parallel nor perpendicular to  $\vec{n}$ , as shown in Figure 4.1, the applied electric field can be decomposed into a component parallel to  $\vec{n}$  and another component perpendicular to  $\vec{n}$ . The induced polarization is given by

$$\vec{P} = \epsilon_o \chi_{\parallel} (\vec{E} \cdot \vec{n}) \vec{n} + \epsilon_o \chi_{\perp} [\vec{E} - (\vec{E} \cdot \vec{n}) \vec{n}] = \epsilon_o [\chi_{\perp} \vec{E} + \Delta\chi (\vec{E} \cdot \vec{n}) \vec{n}] \quad (4.1)$$

The dielectric constants  $\epsilon_{\parallel}$  and  $\epsilon_{\perp}$  are related to the permittivities by  $\epsilon_{\parallel} = 1 + \chi_{\parallel}$  and  $\epsilon_{\perp} = 1 + \chi_{\perp}$ . Therefore  $\Delta\chi = \chi_{\parallel} - \chi_{\perp} = \epsilon_{\parallel} - \epsilon_{\perp} = \Delta\epsilon$ . The electric energy of the liquid crystal per unit volume is approximately given by (a detailed discussion will be presented in Chapter 7)

$$f_{electric} = -\frac{1}{2} \vec{P} \cdot \vec{E} = -\frac{1}{2} \epsilon_o [\chi_{\perp} \vec{E} + \Delta\chi (\vec{E} \cdot \vec{n}) \vec{n}] \cdot \vec{E} = -\frac{1}{2} \epsilon_o \chi_{\perp} E^2 - \frac{1}{2} \epsilon_o \Delta\epsilon (\vec{E} \cdot \vec{n})^2 \quad (4.2)$$

When the applied field is low,  $\Delta\epsilon$  can be approximately considered as a constant independent of the field. The first term on the right hand side of Equation (4.2) is independent of the orientation of the director with respect to the applied field, and thus can be neglected in considering the reorientation of liquid crystals in electric fields. The second term depends on the orientation of the director with respect to the applied field. When  $\vec{n}$  is perpendicular to  $\vec{E}$ ,  $(\vec{E} \cdot \vec{n})^2 = 0$ . When  $\vec{n}$  is parallel or anti-parallel to  $\vec{E}$ ,  $(\vec{E} \cdot \vec{n})^2 = E^2$ . If the liquid crystal has a positive dielectric anisotropy ( $\Delta\epsilon > 0$ ), the electric energy is minimized when the liquid crystal director is parallel or anti-parallel to the applied field; therefore the liquid crystal tends to align parallel (or anti-parallel) to the applied field. Conversely, if the dielectric anisotropy is negative ( $\Delta\epsilon < 0$ ), then the electric energy is low when the liquid crystal director is perpendicular to the applied field; therefore the liquid crystal tends to align perpendicular to the applied field. The dielectric responses of liquid crystals to DC and AC electric fields are the same (except the dielectric constants may be frequency dependent). For most nematic liquid crystals, the dielectric anisotropy is in the region from  $-5$  to  $+30$ . For example, when  $\Delta\epsilon = 10$  and the applied electric field is  $1 \text{ V}/\mu\text{m} = 10^6 \text{ V/m}$ , the electric energy density is  $\frac{1}{2} \epsilon_o \Delta\epsilon E^2 = 44.2 \text{ J/m}^3$ . The reorientation of liquid crystals under dielectric interactions will be discussed in more detail in Chapters 5 and 7.

#### 4.1.2 Field-induced orientational order

Besides aligning liquid crystals, external electric fields can also change the orientational order and thus the electro-optical properties of liquid crystals. When the long molecular axis of a liquid crystal molecule, whose anisotropy of polarizability is positive, is parallel to the applied field, the potential of the molecule is low. Thus the applied field suppresses the thermal fluctuation and increases the order parameter. Now we discuss how the orientational order of a nematic liquid crystal changes with applied fields. Using the Landau–de Gennes theory, the free energy density of a liquid crystal in an electric field

(when the liquid crystal director is parallel to the field) is [4]

$$f = -\frac{1}{2}\varepsilon_o\varepsilon_{\parallel}E^2 + \frac{1}{2}a(T - T^*)S^2 - \frac{1}{3}bS^3 + \frac{1}{4}cS^4 \quad (4.3)$$

As discussed in Section 1.5.2,  $\varepsilon_{\parallel} + 2\varepsilon_{\perp} = \text{constant}$ , i.e.,  $3\varepsilon_{\parallel} - 2\Delta\varepsilon = \text{constant}$  and therefore  $\varepsilon_{\parallel} = (2/3)(\Delta\varepsilon + \text{constant})$ . Equation (1.114) shows that the dielectric anisotropy  $\Delta\varepsilon$  is a linear function of the order parameter  $S$ . At a temperature below the nematic–isotropic transition temperature and under zero applied field, when the order parameter is  $S_o$ , the dielectric anisotropy is  $(\Delta\varepsilon)_o$ . Approximately we have

$$\varepsilon_{\parallel} = \frac{2(\Delta\varepsilon)_o}{3S_o}S + \frac{2}{3} \times \text{constant} \quad (4.4)$$

In the calculation of the order parameter by minimizing the free energy, the constant term can be neglected. The free energy density becomes

$$f = -\frac{1}{2}\varepsilon_o\alpha E^2 S + \frac{1}{2}a(T - T^*)S^2 - \frac{1}{3}bS^3 + \frac{1}{4}cS^4 \quad (4.5)$$

where  $\alpha = 2(\Delta\varepsilon)_o/3S_o$ . The first term on the right hand side of Equation (4.5) is negative and decreases with increasing order parameter, provided the dielectric anisotropy is positive. Therefore the applied field tends to increase the order parameter. Even in the isotropic phase at temperatures above the nematic–isotropic phase transition temperature, nematic order is induced by the applied electric field. This phase with field-induced order parameter is referred to as the *paranematic* phase.

We define the normalized field  $e = \varepsilon_o\alpha E^2/2c$ , the normalized temperature  $t = a(T - T^*)/c$ , and  $\beta = b/c$ . The normalized free energy density becomes

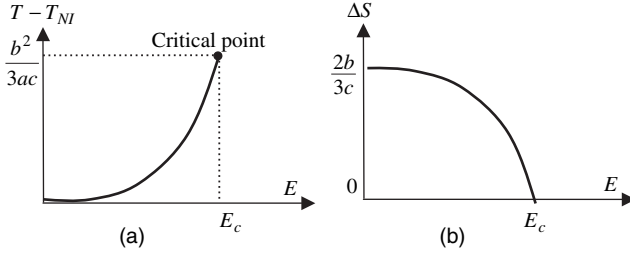
$$\frac{f}{c} = -eS + \frac{1}{2}tS^2 - \frac{1}{3}\beta S^3 + \frac{1}{4}S^4 \quad (4.6)$$

The order parameter  $S$  as a function of the applied field  $E$  can be found by minimizing the free energy:

$$\frac{\partial(f/c)}{\partial S} = -e + tS - \beta S^2 + S^3 \equiv 0 \quad (4.7)$$

There are three solutions to Equation (4.7). At a given temperature, the real order parameter is one that minimizes the free energy. When the applied field is low, the induced order parameter in the paranematic phase is small. When the temperature is lowered, there is a paranematic–nematic phase transition. At the phase transition, the order parameter changes discontinuously. As the applied field is increased, the paranematic–nematic phase transition temperature  $t_{PN}$  increases, as shown in Figure 4.2(a), and the jump in the order parameter at the transition becomes smaller, as shown in Figure 4.2(b). When the applied field is increased above a critical field  $E_c$ , the jump in the order parameter becomes zero. The phase transition temperature, the jump in the order parameter  $\Delta S$  at the transition, and the critical field  $E_c$  can be derived without explicitly calculating the order parameter. Let the order parameter in the paranematic phase be  $S_1$  and the order parameter in the nematic phase be  $S_2$ . At the transition temperature  $t_{PN}$ , we have

$$-e + t_{PN}S_1 - \beta S_1^2 + S_1^3 \equiv 0 \quad (4.8)$$



**Figure 4.2** Schematic diagram showing how the transition temperature changes with the applied field

$$-e + t_{PN}S_2 - \beta S_2^2 + S_2^3 \equiv 0 \quad (4.9)$$

Also at the transition temperature  $t_{PN}$ , the free energies corresponding to these two solutions are the same, namely

$$-eS_1 + \frac{1}{2}t_{PN}S_1^2 - \frac{1}{3}\beta S_1^3 + \frac{1}{4}S_1^4 = -\frac{1}{2}eS_2 + \frac{1}{2}t_{PN}S_2^2 - \frac{1}{3}\beta S_2^3 + \frac{1}{4}S_2^4$$

which gives

$$-4e + 2t_{PN}(S_2 + S_1) - \frac{4}{3}\beta(S_2^2 + S_1S_2 + S_1^2) + (S_2^2 + S_1^2)(S_2 + S_1) = 0 \quad (4.10)$$

In Equations (4.8), (4.9), and (4.10), there are three variables  $S_1$ ,  $S_2$ , and  $t_{PN}$ . By solving these three equations we can find these three variables. For example, we can take the following approach to find them. Subtracting Equation (4.8) from Equation (4.9) give

$$t_{PN}(S_2 - S_1) - \beta(S_2^2 - S_1^2) + (S_2^3 - S_1^3) = 0$$

or

$$t_{PN} - \beta(S_2 + S_1) + (S_2^2 + S_2S_1 + S_1^2) = 0 \quad (4.11)$$

$S_2 \times$  Equation (4.9)  $- S_1 \times$  Equation (4.8) gives

$$-e(S_2 - S_1) + t_{PN}(S_2^2 - S_1^2) - \beta(S_2^3 - S_1^3) + (S_2^4 - S_1^4) = 0$$

or

$$-e + t_{PN}(S_2 + S_1) - \beta(S_2^2 + S_1S_2 + S_1^2) + (S_2^2 + S_1^2)(S_2 + S_1) = 0 \quad (4.12)$$

Equation (4.12)  $-$  Equation (4.10) gives

$$3e - t_{PN}(S_2 + S_1) + \frac{1}{3}\beta(S_2^2 + S_1S_2 + S_1^2) = 0 \quad (4.13)$$

4 × Equation (4.12) – 3 × Equation (4.10) gives

$$8e - 2t_{PN}(S_2 + S_1) + (S_2^2 + S_1^2)(S_2 + S_1) = 0 \quad (4.14)$$

$\beta$  × Equation (4.11) – 3 × Equation (4.13) gives

$$S_2 + S_1 = \frac{\beta t_{PN} - 9e}{\beta^2 - 3t_{PN}} \equiv h \quad (4.15)$$

Substituting Equation (4.15) into Equation (4.11) we have

$$S_2^2 + S_1 S_2 + S_1^2 = \beta h - t_{PN} = \frac{3(t_{PN}^2 - 3e\beta)}{(\beta^2 - 3t_{PN})} \quad (4.16)$$

Substituting Equation (4.15) into Equation (4.14) we have

$$S_2^2 + S_1^2 = 2t_{PN} - \frac{8e}{h} = \frac{2(\beta t_{PN}^2 + 3et_{PN} - 4e\beta^2)}{(\beta t_{PN} - 9e)} \quad (4.17)$$

Because  $2(S_2^2 + S_2 S_1 + S_1^2) - (S_2^2 + S_1^2) = (S_2 + S_1)^2$ , from Equations (4.15), (4.16), and (4.17) we have

$$\frac{6(t_{PN}^2 - 3e\beta)}{(\beta^2 - 3t_{PN})} - \frac{2(\beta t_{PN}^2 + 3et_{PN} - 4e\beta^2)}{(\beta t_{PN} - 9e)} = \frac{(\beta t_{PN} - 9e)^2}{(\beta^2 - 3t_{PN})^2} \quad (4.18)$$

From Equation (4.18) the transition temperature is found to be

$$t_{NP} = \frac{2\beta^2}{9} + \frac{3e}{\beta} \quad (4.19)$$

The unnormalized transition temperature is

$$T_{PN} = T^* + \frac{2b^2}{9ac} + \frac{3c\varepsilon_0\alpha E^2}{2ab} = T_{NI} + \frac{3c\varepsilon_0\alpha E^2}{2ab} \quad (4.20)$$

where  $T_{NI}$  is the nematic–isotropic phase transition temperature under zero field. At the paranematic–nematic transition

$$S_2 + S_1 = \frac{2}{3}\beta = \frac{2b}{3c} \quad (4.21)$$

which is a constant independent of the applied field. The jump in the order parameter at the transition is given by

$$\Delta S = S_2 - S_1 = [2(S_2^2 + S_1^2) - (S_2 + S_1)^2]^{1/2} = \left(\frac{4\beta^2}{9} - \frac{12e}{\beta}\right)^{1/2} \quad (4.22)$$

At the critical field  $e_c$ , the jump in the order parameter becomes zero, i.e.,  $\Delta S = 0$ . Therefore the critical field is

$$e_c = \frac{\beta^3}{27} \tag{4.23}$$

The unnormalized critical field is

$$E_c = \left( \frac{2b^3}{27c^2\epsilon_0\alpha} \right)^{1/2} \tag{4.24}$$

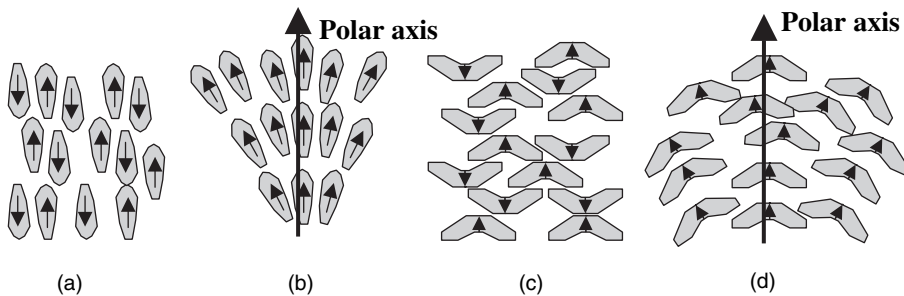
For example, for a liquid crystal with  $b = 1.6 \times 10^6 \text{ J/m}^3$ ,  $c = 3.9 \times 10^6 \text{ J/m}^3$ , and  $\alpha = 10$  (the dielectric anisotropy in the nematic phase at zero field is about 10), the critical field is  $E_c = 15 \text{ V}/\mu\text{m}$ . The induced order parameter at the critical point about is 0.15. This has been confirmed experimentally [5]. At such a high field, attention must be paid to avoiding the heating effect of the field on the liquid crystal cell and the electrical breakdown of the material.

## 4.2 Flexoelectric Effect

### 4.2.1 Flexoelectric effect in nematic liquid crystals

Uniformly oriented uniaxial nematic liquid crystals have non-polar cylindrical symmetry in the absence of an external electric field. If the liquid crystal molecules have a permanent dipole along the long molecular axis, the potential for the orientation of the dipole has reflectional symmetry about the plane perpendicular to the director  $\vec{n}$  and the dipole has the same probability of being parallel and anti-parallel to the director, as shown in Figure 4.3(a). If the permanent dipole is perpendicular to the long molecular axis, the potential for the orientation of the dipole is cylindrically symmetric around the director and the dipole has the same probability of pointing in any direction perpendicular to the director, as shown in Figure 4.3(c).

If the orientation of the liquid crystal is not uniform and the constituent molecules are not cylindrical, the properties discussed in the previous paragraph are no longer true [1, 2]. For pear-shaped molecules, because of the steric interaction, splay deformation of the liquid crystal director will destroy the reflectional symmetry about the plane perpendicular to the director, as shown in Figure 4.3(b). The permanent dipole along the long molecular axis has a higher probability of pointing in one direction than



**Figure 4.3** Schematic diagram showing the deformation of the liquid crystal director and induced spontaneous polarization

the opposite direction, and therefore spontaneous polarization along  $\vec{n}$  becomes possible. For banana-shaped molecules, bend deformation will destroy the rotational symmetry around the director, as shown in Figure 4.3(d). The permanent dipole perpendicular to the long molecular axis has a higher (or lower) probability of pointing in the direction of  $\vec{n} \times \nabla \times \vec{n}$  than in other directions perpendicular to the director  $\vec{n}$ , and spontaneous polarization along the direction of  $\vec{n} \times \nabla \times \vec{n}$  may occur. This director deformation-induced polarization was first pointed out by Meyer and was called the ‘piezoelectric’ effect in analogy to induced polarization in solid crystals by strain under externally applied pressure [6]. Because the director deformations in nematics are usually not produced by pressure, ‘flexoelectric’ is more popularly used in order to avoid confusion.

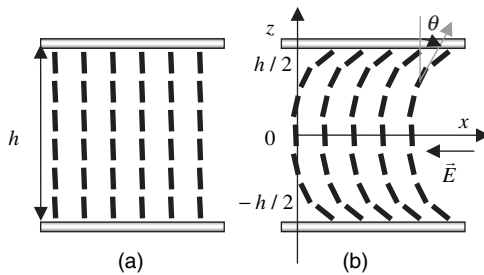
In the case of pear-shaped molecules, the value of the induced polarization is proportional to the splay deformation  $\nabla \cdot \vec{n}$  and its direction is along  $\vec{n}$ . In the case of the banana-shaped molecules, the induced polarization is proportional to the bend deformation  $\vec{n} \times \nabla \times \vec{n}$ . Including both cases, the induced polarization is given by

$$\vec{P}_f = e_s(\vec{n}\nabla \cdot \vec{n}) + e_b(\vec{n} \times \nabla \times \vec{n}) \tag{4.25}$$

where  $e_s$  and  $e_b$  are the flexoelectric coefficients and have the dimension of electric potential (volt). The magnitude of the flexoelectric coefficients depends on the asymmetry of the molecule’s shape and the permanent dipole moment and their sign could be either positive or negative. The energy of the induced polarization in an electric field  $\vec{E}$  is  $-\vec{P}_f \cdot \vec{E}$ .

In liquid crystals with the capability of the flexoelectric effect, in the absence of external electric fields, the state with uniform director configuration, which has no induced polarization, is the ground state and is stable. When an electric field is applied to the liquid crystal, the uniform orientation becomes unstable, because any small orientational deformation produced by thermal fluctuations or boundary conditions will induce a polarization which will interact with the electric field and result in a lower free energy. The torque on the molecules due to the applied field and the induced polarization tends to make the deformation grow. Of course, the deformation costs elastic energy which is against the deformation. The electric energy of the induced polarization, which is linearly proportional to the deformation, dominates in the beginning where the deformation is small. The elastic energy, which is proportional to the square of the deformation, dominates when the deformation is large. In the end, the system reaches the equilibrium state in which the electric torque and the elastic torque balance each other.

Now we consider the experiments which can be used to study the flexoelectric effect and can also be used in electro-optical applications. Figure 4.4 shows the geometry for studying the flexoelectric effect in bend deformation [2, 7]. The substrates are coated with a homeotropic alignment layer with very weak anchoring strength. The liquid crystal used has a small negative dielectric anisotropy  $\Delta\epsilon$ . In the absence of external electric fields, the liquid crystal is in the uniform homeotropic state as shown in Figure 4.4(a). When an electric field is applied along the  $-x$  direction, bend deformation occurs, as



**Figure 4.4** Schematic diagram showing the flexoelectric effect in the bend deformation

## 114 EFFECTS OF ELECTRIC FIELD ON LIQUID CRYSTALS

shown in Figure 4.4(b), due to the flexoelectric effect. The dielectric energy in the field is neglected as an approximation because  $\Delta\epsilon$  is very small. The free energy density is

$$f = \frac{1}{2}K_{33}(\vec{n} \times \vec{n} \times \nabla\vec{n})^2 - \vec{P}_f \cdot \vec{E} = \frac{1}{2}K_{33}(\vec{n} \times \vec{n} \times \nabla\vec{n})^2 - e_b(\vec{n} \times \vec{n} \times \nabla\vec{n}) \cdot \vec{E} \quad (4.26)$$

The components of the liquid crystal director are

$$n_x = \sin\theta(z), \quad n_y = 0, \quad n_z = \cos\theta(z) \quad (4.27)$$

When the applied voltage is low, the deformation is very small and  $\theta$  is very small. The divergence  $\nabla \cdot \vec{n} = -\sin\theta\partial\theta/\partial z$  is a 2<sup>nd</sup> order small quantity and the splay elastic energy is so small as to be negligible. The curl of  $\vec{n}$  is

$$\nabla \times \vec{n} = \cos\theta \frac{\partial\theta}{\partial z} \hat{y} \quad (4.28)$$

and that of the bend is

$$\vec{n} \times \nabla \times \vec{n} = -\cos^2\theta \frac{\partial\theta}{\partial z} \hat{x} + \sin\theta \cos\theta \frac{\partial\theta}{\partial z} \hat{z} \approx -\frac{\partial\theta}{\partial z} \hat{x} \quad (4.29)$$

Equation (4.26) becomes

$$f = \frac{1}{2}K_{33} \left( \frac{\partial\theta}{\partial z} \right)^2 - e_b E \frac{\partial\theta}{\partial z} \quad (4.30)$$

Minimizing the free energy

$$\frac{\delta f}{\delta\theta} = -\frac{d}{dz} \left( \frac{\partial f}{\partial\theta} \right) = -\frac{d}{dz} \left[ K_{33} \left( \frac{\partial\theta}{\partial z} \right) - e_b E \right] = 0 \quad (4.31)$$

Because  $\partial\theta/\partial z = 0$  when  $E = 0$ ,

$$\frac{\partial\theta}{\partial z} = \frac{e_b E}{K_{33}} \quad (4.32)$$

If the anchoring of the liquid crystal at the cell surface is very weak, the solution to Equation (4.32) is

$$\theta = \frac{e_b E}{K_{33}} z \quad (4.33)$$

It is worthwhile pointing out two characteristics of the flexoelectric effect. First, there is no threshold for the applied field, which is different from the Freedericksz transition where there is a threshold below which no deformation occurs. Deformation of the director configuration occurs under any field. Secondly, the direction of the bend depends on the polarity of the applied field, which is also different from the Freedericksz transition where the deformation is independent of the polarity of the applied field.

One of the experimental methods for studying the orientation of the liquid crystal under the flexoelectric effect is to measure the retardation of the liquid crystal cell, which is given by

$$\Delta nd = \int_{-h/2}^{h/2} [n_{eff}(z) - n_o] dz = 2 \int_0^{h/2} [n_{eff}(z) - n_o] dz \quad (4.34)$$

where  $n_{eff}$  is the effective refractive index of the liquid crystal and is given (for normal incident light with linear polarization along the  $x$  direction) by

$$n_{eff} = \frac{n_e n_o}{\sqrt{n_e^2 \cos^2 \theta + n_o^2 \sin^2 \theta}} = \frac{n_e n_o}{\sqrt{n_e^2 - (n_e^2 - n_o^2) \sin^2 \theta}} \quad (4.35)$$

For small  $\theta$  we have the approximation  $n_{eff} = n_o [1 + (1/2)(1 - n_o^2/n_e^2)\theta^2]$ . Thus

$$\begin{aligned} \Delta nd &= \int_0^{h/2} n_o \left(1 - \frac{n_o^2}{n_e^2}\right) \theta^2 dz = n_o \left(1 - \frac{n_o^2}{n_e^2}\right) \int_0^{\theta(z=h/2)} \theta^2 \left(1 / \frac{d\theta}{dz}\right) d\theta \\ &= n_o \left(1 - \frac{n_o^2}{n_e^2}\right) \frac{1}{24} \left(\frac{e_b}{K_{33}}\right)^2 E^2 h^3 \end{aligned} \quad (4.36)$$

In the Freedericksz transition, when the applied field is slightly above the threshold  $E_c$ , the tilt is proportional to  $\sqrt{E - E_c}$  and the retardation is proportional to  $(E - E_c)$  (see Chapter 5 for details).

In the experiment performed by Schmidt *et al.* on the liquid crystal MBBA [8], for a field of  $0.3 \text{ V}/\mu\text{m}$ , the variation rate  $\partial\theta/\partial z$  was about  $1 \times 10^{-4} \mu\text{m}^{-1}$ . The elastic constant was  $K_{33} = 7.5 \times 10^{-12} \text{ N}$ . The flexoelectric coefficient  $e_b$  has a value of about  $2.5 \times 10^{-15} \text{ V}$ .

If  $\Delta\epsilon$  were negative but not very small, the dielectric interaction would prevent the deformation of the director configuration. We estimate the dielectric anisotropy  $\Delta\epsilon$ , which will make the flexoelectric effect disappear, in the following way. The dielectric energy is  $-(1/2)\epsilon_o\Delta\epsilon(\vec{E} \cdot \vec{n})^2 = -(1/2)\epsilon_o\Delta\epsilon E^2 \sin^2 \theta$ , which operates against the deformation. The average tilt angle is  $(\partial\theta/\partial z)(h/4)$ . The average dielectric energy is approximately  $-(1/2)\epsilon_o\Delta\epsilon E^2 [(\partial\theta/\partial z)(h/4)]^2$ . The flexoelectric energy is  $-e_b E(\partial\theta/\partial z)$ , which favors the deformation. If both energies were the same, the deformation would be hindered:  $-(1/2)\epsilon_o\Delta\epsilon E^2 [(\partial\theta/\partial z)(h/4)]^2 = e_b E(\partial\theta/\partial z)$ , which gives  $\Delta\epsilon = -8e_b / [\epsilon_o E(\partial\theta/\partial z)h^2]$ . Using the values in the previous paragraph, we get  $\Delta\epsilon = -0.75$ . Moreover, because the flexoelectric energy is linearly proportional to  $E$  while the dielectric energy is proportional to  $E^2$ , the dielectric effect will become dominant at high fields. Therefore, only when  $|\Delta\epsilon| \ll 0.75$  and at low fields do we have a pure flexoelectric effect. If  $\Delta\epsilon$  were positive and not very small, the liquid crystal would be aligned parallel to the applied field under the weak anchoring condition. Therefore, in order to have the flexoelectric effect described in the previous paragraph under a field of  $0.3 \text{ V}/\mu\text{m}$ , the dielectric anisotropy should be negative and its absolute value should be much smaller than 0.75.

The geometry shown in Figure 4.4 can be used for an electrically controlled birefringence device. For normal incident light with polarization parallel to the  $x$  axis, it encounters the refractive index  $n_o$  in the field-off state. When an electric field is applied along the  $x$  direction, the liquid crystal molecules tilt and the light will encounter the refractive index  $n_{eff}$ . Therefore the retardation of the liquid crystal cell is changed. The flexoelectric effect can also be used in the switching of bistable nematic displays with asymmetrical anchoring conditions [9].

Figure 4.5 shows the geometry for studying the flexoelectric effect in splay deformation [2]. The substrates are coated with a homogeneous alignment layer with very weak anchoring strength. The



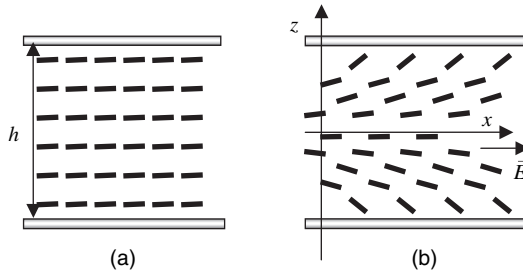


Figure 4.5 Schematic diagram showing the flexoelectric effect in the splay deformation

liquid crystal used has a small positive dielectric anisotropy  $\Delta\epsilon$ . In the absence of external electric fields, the liquid crystal is in the uniform homogeneous state as shown in Figure 4.5(a). When an electric field is applied along the  $x$  direction, a splay deformation occurs due to the flexoelectric effect, as shown in Figure 4.5(b). The director configuration in the equilibrium state can be calculated in a similar way as in the bend case.

4.2.2 Flexoelectric effect in cholesteric liquid crystals

The flexoelectric effect also exists in cholesteric liquid crystals because the orientational order is locally the same as in nematic liquid crystals. Here we consider the cell geometry shown in Figure 4.6 [2, 10–12]. The cholesteric liquid crystal is sandwiched between two parallel substrates with a transparent electrode. A homogeneous alignment layer is coated on the inner surface of the substrates. When the liquid crystal is cooled down from the isotropic phase under an external electric field, the helical axis  $\vec{h}$  of the liquid crystal is parallel to the substrate and uniformly aligned along the  $x$  axis by the alignment layer, as shown in Figure 4.6(a) and (b). The liquid crystal with undistorted helical structure behaves like an optically uniaxial medium (when the pitch is much smaller than the wavelength of light) with uniaxis  $\vec{o}$  coincident with the helical axis. The dielectric anisotropy  $\Delta\epsilon$  is very small and the dielectric interaction is negligible. When an electric field is applied across the cell along the  $z$  axis, the helical structure is preserved and the pitch is unchanged, and the helical axis remains parallel to the substrate. Because the helical structure is incompatible with the planar boundary condition, there are director deformations near the surface and thus there is induced polarization. The applied field interacts with the induced polarization and makes the in-plane component of the liquid crystal director tilt, as shown in Figure 4.6(c). This tilting will produce more distortion and therefore induce more polarization.

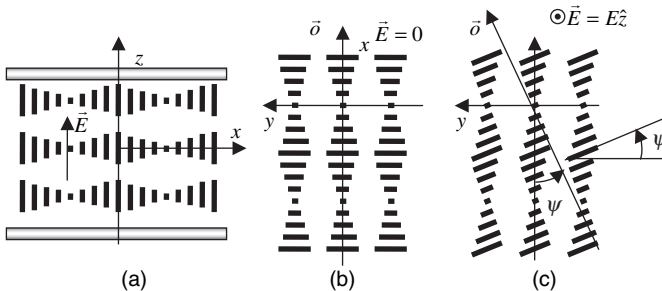


Figure 4.6 Schematic diagram showing the flexoelectric effect in the cholesteric liquid crystal

The components of the liquid crystal director in the distorted state are

$$n_x = \sin\psi \sin(q_o x), n_y = -\cos\psi \sin(q_o x), n_z = \cos(q_o x) \quad (4.37)$$

where  $\psi$  is the tilt angle of the in-plane component of the director. Now the uniaxial optic axis  $\vec{o}$  is also tilted by the same angle. The induced polarization is

$$\begin{aligned} \vec{P}_f &= e_s(\vec{n}\nabla \cdot \vec{n}) + e_b(\vec{n} \times \nabla \times \vec{n}) \\ &= e_s q_o \sin\psi \sin(q_o x) \cos(q_o x) [\sin\psi \hat{x} - \cos\psi \hat{y}] + e_s q_o \sin\psi \cos^2(q_o x) \hat{z} \\ &\quad + e_b q_o \sin\psi \sin(q_o x) \cos(q_o x) [-\sin\psi \hat{x} + \cos\psi \hat{y}] + e_b q_o \sin\psi \sin^2(q_o x) \hat{z} \\ &= e_s q_o \sin\psi \hat{z} \end{aligned} \quad (4.38)$$

where the approximation  $e_s = e_b$  is used. The free energy density is

$$f = \frac{1}{2} K_{11} q_o^2 \sin^2\psi + \frac{1}{2} K_{22} (q_o - q_o \cos\psi)^2 - e_s q_o E \sin\psi \quad (4.39)$$

where the approximation  $K_{11} = K_{33}$  is used. For small  $\psi$ ,  $\sin\psi \approx \psi$ ,  $(1 - \cos\psi) \approx 0$ , and then we have the approximation

$$f = \frac{1}{2} K_{11} q_o^2 \psi^2 - e_s q_o E \psi \quad (4.40)$$

Minimizing  $f$  with respect to  $\psi$ , we get

$$\psi = e_s E / K_{11} q_o \quad (4.41)$$

The tilt angle is linearly proportional to  $E$ . When the polarity of the applied voltage is reversed, the optic axis will be tilted in the opposite direction. In the rotation, the torque due to the elastic and electric energies is balanced by the viscosity torque:

$$\gamma \frac{\partial\psi}{\partial t} = -\frac{\partial f}{\partial\psi} = -K_{11} q_o^2 \psi + e q_o E \quad (4.42)$$

where  $\gamma$  is an effective viscosity coefficient. If the applied field is turned off from a distorted state with tilt angle  $\psi_o$ , the solution to Equation (4.42) is  $\psi = \psi_o e^{-t/\tau}$ . The relaxation time is  $\tau = \gamma / K_{11} q_o^2$ . For short-pitch cholesteric liquid crystals,  $\tau$  can be as small as 100  $\mu\text{s}$  [13]. This flexoelectric effect of the cholesteric liquid crystal can be used to modulate light intensity when the liquid crystal cell is placed between two crossed polarizers because the optic axis can be tilted by applying an electric field.

## 4.3 Ferroelectric Liquid Crystals

### 4.3.1 Symmetry and polarization

We have mentioned that it is impossible for uniformly oriented nematic liquid crystals to have spontaneous polarization because of their  $D_{h\infty}$  symmetry. Now let us consider the possibility of spontaneous polarization in other liquid crystal phases. For rod-like molecules, it is impossible in any

liquid crystal phase to have spontaneous polarization along the liquid crystal director because  $\vec{n}$  and  $-\vec{n}$  are equivalent.

Cholesteric liquid crystals consist of chiral molecules and therefore do not have reflectional symmetry. The symmetry group of cholesteric liquid crystals is  $D_2$  [1,3]. A cholesteric liquid crystal is invariant for the two-fold ( $180^\circ$ ) rotation around  $\vec{n}$ , which rules out the possibility of spontaneous polarization perpendicular to  $\vec{n}$ . It is also invariant for the two-fold rotation around an axis that is perpendicular to the  $\vec{n}-\vec{h}$  (the helical axis) plane, which rules out the possibility of spontaneous polarization parallel to  $\vec{n}$ . Therefore there is no ferroelectricity in the cholesteric phase.

Smectic-A liquid crystals, besides having orientational order as nematics, possess 1-D positional order. They have a layered structure. The liquid crystal director  $\vec{n}$  is perpendicular to the smectic layers. The symmetry of smectic-A crystals is  $D_{\infty h}$  if the constituent molecule is achiral or  $D_\infty$  if the constituent molecule is chiral. It is invariant for any rotation around  $\vec{n}$ . It is also invariant for the two-fold rotation around any axis perpendicular to  $\vec{n}$ . The continuous rotational symmetry is around  $\vec{n}$  and therefore there is no spontaneous polarization in any direction perpendicular to  $\vec{n}$ . Hence it is impossible to have spontaneous polarization in smectic-A crystals even when the constituent molecule is chiral.

Smectic-C liquid crystals are similar to smectic-A liquid crystals except that the liquid crystal director is no longer perpendicular to the layer but tilted. For the convenience of our symmetry discussion, let us introduce a unit vector  $\vec{a}$  which is perpendicular to the layer. The symmetry group is  $C_{2h}$ . The two-fold rotational symmetry is around the axis that is perpendicular to the  $\vec{n}-\vec{a}$  plane (which contains both  $\vec{n}$  and  $\vec{a}$ ). This implies that there is no spontaneous polarization in the  $\vec{n}-\vec{a}$  plane. The reflectional symmetry is about the  $\vec{n}-\vec{a}$  plane, and therefore there is no spontaneous polarization perpendicular to the  $\vec{n}-\vec{a}$  plane either. This rules out the possibility of spontaneous polarization in smectic-C liquid crystals.

As pointed out by Meyer [14], the reflectional symmetry of smectic-C liquid crystals can be removed if the constituent molecules are chiral, and thus it becomes possible to have spontaneous polarization. This phase is called the chiral smectic-C or smectic-C\* phase and its structure is shown in Figure 4.7. Within a layer, the structure is the same as in the smectic-C phase. The liquid crystal

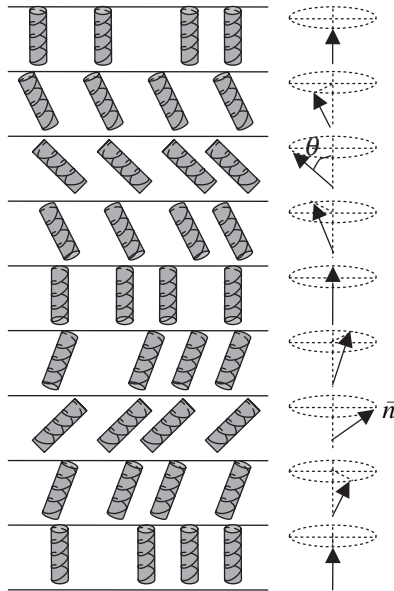
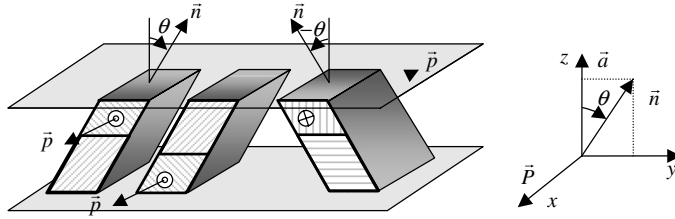


Figure 4.7 Schematic diagram of the structure of chiral smectic-C phase



**Figure 4.8** Schematic diagram showing the spontaneous polarization in smectic-C\* crystals

director  $\vec{n}$  is, however, no longer oriented unidirectionally in space but twists from layer to layer as in the cholesteric phase [15]. The symmetry group is  $C_2$ . The two-fold rotational symmetry axis is perpendicular to both the layer normal  $\vec{a}$  and the director  $\vec{n}$ . Now it is possible to have spontaneous polarization along the two-fold rotational symmetry axis.

In order to illustrate the spontaneous polarization in smectic-C\* liquid crystals, the liquid crystal molecule can be regarded as a parallelepiped with an attached arrow as shown in Figure 4.8. The parallelepiped does not have reflectional symmetry: its top differs from its bottom, its front differs from its back, and its left differs from its right. The arrow represents the lateral permanent dipole and is perpendicular to the director  $\vec{n}$ . Because of the  $C_2$  symmetry, the parallelepiped has equal probability of pointing up (parallel to  $\vec{n}$ ) and down (anti-parallel to  $\vec{n}$ ), but in both cases the dipole points out of the paper. When the dipole points into the paper, it does not belong to the same domain because the tilt angle is  $-\theta$ . If the tilt angle  $\theta$  is zero, as in smectic-A liquid crystals, then the dipole has equal probability of pointing out and pointing in. This explains why it is impossible to have spontaneous polarization in smectic-A crystals even if the constituent molecule is chiral. In smectic-C liquid crystals, when the constituent molecules are a racemic mixture (equal amounts of left- and right-handed molecules), if the left-handed molecule has its permanent dipole pointing out, then the right-handed molecule has its dipole pointing in. They cancel each other and thus there is no spontaneous polarization.

### 4.3.2 Tilt angle and polarization

We first consider the temperature dependence of the tilt angle  $\theta$  of a liquid crystal that exhibits smectic-A and smectic-C phases. In the smectic-A phase, the tilt angle is zero. The transition from smectic-A to smectic-C phase is a second-order transition. Below the transition, the tilt angle increases gradually with increasing temperature. The tilt angle,  $\theta$ , can be used as the order parameter. Near the transition, the free energy density of the system can be expressed in terms of the Landau expansion in powers of  $\theta$  [15]:

$$f = f_o + \frac{1}{2}a(T - T_c)\theta^2 + \frac{1}{4}b\theta^4 \quad (4.43)$$

where  $a$  and  $b$  are temperature-independent positive coefficients, and  $T_c$  is the smectic A–C transition temperature. The equilibrium value of  $\theta$  can be obtained by minimizing the free energy:

$$\frac{\partial f}{\partial \theta} = a(T - T_c)\theta + b\theta^3 = 0$$

The stable solution for temperatures below  $T_c$  is

$$\theta = (a/b)^{1/2}(T_c - T)^{1/2} \quad (4.44)$$

This result is also valid for the smectic-C\* phase.

We now consider the relation between the tilt angle and the spontaneous polarization. In the smectic-A phase, the director  $\vec{n}$  is normal to the smectic layers, and the rotation around the long molecular axis is not biased at zero applied field. If the constituent molecule has a lateral dipole, the dipole has equal probability of pointing in any direction perpendicular to the director, independent of whether the constituent molecule is chiral or not. The average direction of the long molecular axis is along  $\vec{n}$ , and therefore there is no spontaneous polarization perpendicular to  $\vec{n}$ . In the smectic-C phase, the tilt angle is no longer zero, and the rotational symmetry around the long molecular axis is broken. The rotation along the long molecular axis is biased. The molecule, however, has equal probability of pointing up and down with respect to  $\vec{n}$  because of the symmetry that  $\vec{n}$  and  $-\vec{n}$  are equivalent. This rules out the possibility that net polarization adds up in the  $\vec{a}-\vec{n}$  plane. If the constituent molecule is achiral, the lateral dipole has equal probability of pointing out of and into the plane of the paper (the  $\vec{a}-\vec{n}$  plane), therefore no net polarization can add up in the direction perpendicular to the  $\vec{a}-\vec{n}$  plane. When the constituent molecule is chiral, the reflection symmetry about the  $\vec{a}-\vec{n}$  plane is broken; it becomes possible for net polarization to add up in the direction perpendicular to the  $\vec{a}-\vec{n}$  plane. Whether the spontaneous polarization is out of the plane or into the plane is determined by the molecular structure.

When the tilt angle changes from  $\theta$  to  $-\theta$ , which is the same as the rotation of the system around the layer normal by  $180^\circ$ ,  $\vec{P}_s$  points in the opposite direction and the polarization changes sign. Therefore the spontaneous polarization must be an odd function of the tilt angle. For small  $\theta$ , we must have

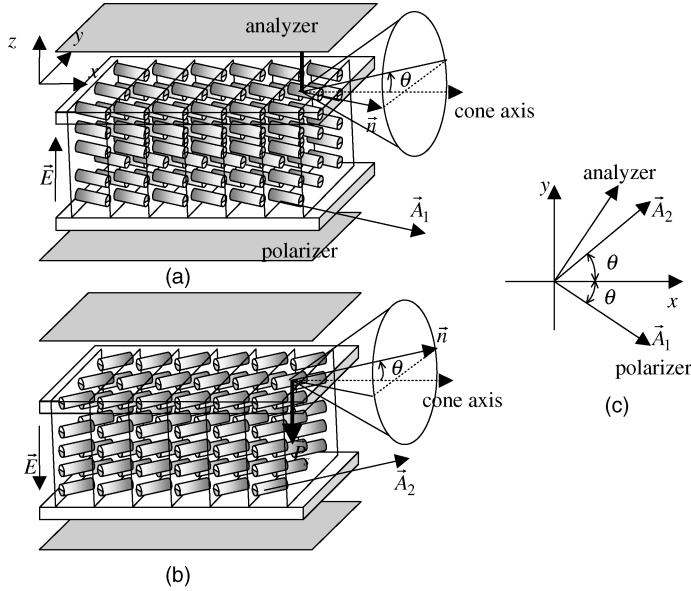
$$P_s = c \cdot \theta \quad (4.45)$$

where  $c$  is a constant. The larger the tilt angle is, the more biased the rotation around the long molecular axis becomes, and therefore the larger the spontaneous polarization is.

### 4.3.3 Surface-stabilized ferroelectric liquid crystals

In electro-optical devices, it is usually required that the liquid crystal director is unidirectionally oriented. In the smectic-C\* phase, however, the liquid crystal director twists from layer to layer. This problem was overcome by Clark and Lagerwall in their invention of the surface-stabilized ferroelectric liquid crystal (SSFLC) device [16], shown in Figure 4.9. The liquid crystal is sandwiched between two parallel substrates with the cell gap,  $h$ , thinner than the helical pitch,  $P$ , of the liquid crystal. The inner surface of the substrates is coated with alignment layers which promote parallel (to the substrate) anchoring of the liquid crystal on the surface of the substrate. The smectic layers are perpendicular to the substrate of the cell while the helical axis is parallel to the substrate. Now the helical twist is suppressed and unwound by the anchoring. There are only two directions,  $\vec{A}_1$  and  $\vec{A}_2$ , on the helical cone, which are compatible with the boundary condition at the substrate surface. The cone angle is  $2\theta$ , and therefore the angle between  $\vec{A}_1$  and  $\vec{A}_2$  is  $2\theta$ . The two orientational states can be further selected by applying a DC electric field across the cell. For example, an electric field in the  $+z$  direction selects the orientational state  $\vec{A}_1$  where the spontaneous polarization,  $\vec{P}_s$ , is pointing up and parallels the field. Then an electric field in the  $-z$  direction will select the orientational state  $\vec{A}_2$  where the spontaneous polarization,  $\vec{P}_s$ , is pointing down. Once the liquid crystal is switched into state  $\vec{A}_1$  (or  $\vec{A}_2$ ) by an externally applied electric field, it will remain in that state after the field is removed, because there is an energy barrier between these two states. Therefore the SSFLC is ideally bistable, which is a very useful property in multiplexed display applications. In reality, it is difficult to make a large-area truly bistable SSFLC display because of surface irregularities.

In the SSFLC display, the polarizer is chosen to be parallel to one of the stable orientational states, say  $\vec{A}_1$ , and the analyzer is perpendicular to the polarizer. When the liquid crystal is in state  $\vec{A}_1$ , the polarization of the incident light is parallel to the liquid crystal director, and remains in this direction when propagating through the cell. When the light comes out of the cell, its polarization is



**Figure 4.9** Schematic diagram of the bookshelf cell structure of the surface-stabilized ferroelectric liquid crystal display. (a) The director is along the direction  $\vec{A}_1$  when the applied field is up. (b) The director is along the direction  $\vec{A}_2$  when the applied field is down. (c) Directions of the polarizer and

perpendicular to the analyzer and therefore the display is black. When the liquid crystal is switched into state  $\vec{A}_2$ , the polarization of the incident light makes the angle  $2\theta$  with respect to the liquid crystal director, and therefore when light propagates through the liquid crystal, its polarization is rotated. The transmittance of the display is

$$T = \sin^2(4\theta) \sin^2\left(\frac{1}{2} \frac{2\pi\Delta nh}{\lambda}\right) \quad (4.46)$$

where  $2\pi\Delta nh/\lambda$  is the retardation angle. The maximum transmittance of 100% can be achieved if  $2\theta = \pi/4$  and  $2\pi\Delta nh/\lambda = \pi$ .

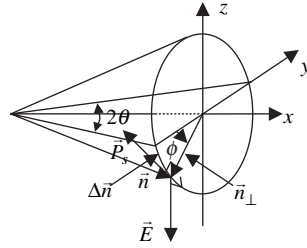
For a ferroelectric liquid crystal with the spontaneous polarization  $\vec{P}_s$ , the electric energy density in an electric field  $\vec{E}$  is  $-\vec{P}_s \cdot \vec{E}$ . A typical value of the spontaneous polarization of ferroelectric liquid crystals is  $100 \text{ nC/cm}^2 = 10^{-3} \text{ C/m}^2$ . When the strength of the applied field is  $1 \text{ V}/\mu\text{m} = 10^6 \text{ V/m}$  and  $\vec{P}_s$  is parallel to  $\vec{E}$ , the electric energy density is  $|\vec{P}_s \cdot \vec{E}| = 10^3 \text{ J/m}^3$ , which is much higher than the electric energy density of the dielectric interaction of non-ferroelectric liquid crystals with the electric field. This is one of the reasons for the fast switching speed of ferroelectric liquid crystal devices.

Now we consider the dynamics of the switching of the SSFLC. We only consider rotation around the cone (Goldstone mode), as shown in Figure 4.10. The electric torque is

$$\vec{\Gamma}_e = \vec{P}_s \times \vec{E} = P_s E \sin \phi \hat{x} \quad (4.47)$$

The viscosity torque is

$$\vec{\Gamma}_v = -\gamma \vec{n}_\perp \times \frac{\Delta \vec{n}}{\Delta t} = -\gamma \sin \theta \frac{\sin \theta \Delta \phi}{\Delta t} \hat{x} = -\gamma \sin^2 \theta \frac{\partial \phi}{\partial t} \hat{x} \quad (4.48)$$



**Figure 4.10** Schematic diagram showing the switching process in the SSFLC

where  $\gamma$  is the rotational viscosity coefficient. These two torques balance each other and the dynamic equation is

$$P_s E \sin\phi - \gamma \sin^2\theta \frac{\partial\phi}{\partial t} = 0 \tag{4.49}$$

The solution is

$$\phi(t) = 2 \tan^{-1}[\tan(\phi_o/2)e^{t/(\gamma \sin^2\theta/P_s E)}] \tag{4.50}$$

The response time is

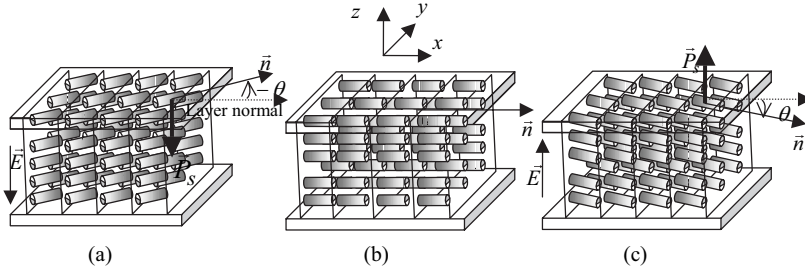
$$\tau = \frac{\gamma \sin^2\theta}{P_s E} \tag{4.51}$$

The rotation around the (small) cone is another reason for the fast switching speed. For  $P_s = 10^2 \text{ nC/cm}^2$ ,  $E = 1 \text{ V}/\mu\text{m}$ ,  $\gamma = 0.1 \text{ poise}$ , and  $\theta = 22.5^\circ$ ,  $\tau \sim 10 \mu\text{s}$ .

The fast switching speed is a merit of ferroelectric liquid crystal devices. Regarding the bistability, on the one hand, it is good because it enables multiplexed displays of the ferroelectric liquid crystal on passive matrices; on the other hand, the bistability is a problem because it makes it difficult to produce gray scales. Another issue with the SSFLC is that it is more challenging to achieve uniform orientation in the SSFLC than in nematic liquid crystals.

### 4.3.4 Electroclinic effect in chiral smectic- liquid crystals

As discussed in Section 3.1, there is no ferroelectricity in chiral smectic-A liquid crystals (smectic-A consisting of chiral molecules, denoted as smectic-A\*). In the cell geometry of smectic-A\* liquid crystals shown in Figure 4.11(b), at zero applied field, the liquid crystal director is perpendicular to the smectic layers. The transverse dipole moment has equal probability of pointing in any direction in the smectic layer plane because of the unbiased rotation of the molecule along its long molecular axis. When the temperature is lowered toward the smectic-A\*-smectic-C\* transition, short length-scale and time-scale domains with smectic-C\* order form because the tilt of the director away from the layer normal direction does not cost much energy. This is known as the pretransition phenomenon, which was experimentally demonstrated and theoretically explained by Garoff and Meyer [17]. Within each domain spontaneous polarization occurs. The macroscopic polarization, however, is still zero because the polarizations of the domains are random through the cell and fluctuate with time. When an electric field is applied across the cell, the temporal domains are stabilized and reorient such that their polarizations become parallel



**Figure 4.11** Schematic diagram showing the electroclinic effect in smectic-A\* crystals

to the applied field. Thus uniform macroscopic smectic-C\* structure is established and the tilt angle becomes non-zero. This effect of field-induced tilt of liquid crystal molecules in the smectic-A\* structure is known as the *electroclinic effect*. Similar to the smectic-C\* case, the spontaneous polarization is perpendicular to the plane formed by the liquid crystal director  $\vec{n}$  and the smectic layer normal  $\vec{a}$ . Therefore in the induced smectic-C\* structure, the  $\vec{n}-\vec{a}$  plane is perpendicular to the applied field. When a DC electric field pointing down is applied, the smectic-C\* structure, say, with positive tilt angle is induced as shown in Figure 4.11(a). When a DC electric field pointing up is applied, the smectic-C structure with negative tilt angle is induced as shown in Figure 4.11(c).

As shown in Section 4.3.2, when the tilt angle is  $\theta$ , the spontaneous polarization  $\vec{P}_s$  is given by Equation (4.45), and the electric energy density is  $-\vec{P}_s \cdot \vec{E} = -cE\theta$ . The free energy density is [15]

$$f = f_0 + \frac{1}{2}a(T - T_c)\theta^2 + \frac{1}{4}b\theta^4 - cE\theta \quad (4.52)$$

The tilt angle as a function of the applied electric field  $E$  can be found by minimizing the free energy:

$$\frac{\partial f}{\partial \theta} = a(T - T_c)\theta + b\theta^3 - cE \equiv 0 \quad (4.53)$$

When the applied field is low, the tilt angle is small, and the cubic term in Equation (4.53) can be neglected. The tilt angle is

$$\theta = \frac{cE}{a(T - T_c)} \quad (4.54)$$

The induced tilt angle is linearly proportional to the applied field. The tilt angle can be larger than  $10^\circ$  at an electric field of  $10 \text{ V}/\mu\text{m}$  for some liquid crystals.

In the tilting of the liquid crystal molecule, the torque produced by the electric field and the elastic force is  $-\partial f / \partial \theta = -a(T - T_c)\theta + cE$ , which is balanced by the viscosity torque  $-\gamma \partial \theta / \partial t$ :

$$-a(T - T_c)\theta + cE - \gamma \partial \theta / \partial t = 0 \quad (4.55)$$

The solution is

$$\theta(t) = \frac{cE}{a(T - T_c)} (1 - 2e^{-t/\tau}) \quad (4.56)$$



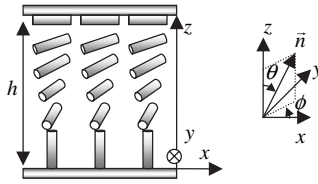


Figure 4.12

where  $\tau = \gamma/a(T - T^*)$  is the response time. It is found by experiment that the response time is fast and on the order of a few tens of microseconds. The advantages of the electroclinic effect of smectic-A\* crystals are that the tilt angle, and thus the electro-optical effect, is a linear function of the applied field and the response time is fast. The disadvantage is that the electro-optical effect is temperature dependent.

### Homework Problems

- 4.1 The electric field-induced orientational order in a nematic liquid crystal is given by Equation (4.7). The liquid crystal has the parameter  $\beta = 0.3$ . Numerically calculate the order parameter  $S$  as a function of the normalized temperature  $t$  in the region from  $-0.1$  to  $0.1$  under various normalized electric fields  $e = 0.0, 0.5(\beta^3/27), 0.8(\beta^3/27), (\beta^3/27),$  and  $1.2(\beta^3/27)$ .
- 4.2 Consider the flexoelectric effect in the splay geometry as shown in Figure 4.5. The cell thickness  $h$  is 5 microns. The splay elastic constant  $K_{11}$  of the liquid crystal is  $10^{-11}$  N. The flexoelectric coefficient  $e_s$  is  $2.0 \times 10^{-15}$  V. Calculate the tilt angle  $\theta$  at the cell surface when the applied field is  $1 \text{ V}/\mu\text{m}$ .
- 4.3 *Flexoelectric effect in hybrid cell.* On the top of the cell ( $z = h$ ) the liquid crystal is aligned homogeneously along the  $x$  direction, while on the bottom ( $z = 0$ ) of the cell the liquid crystal is aligned homeotropically (Figure 4.12). There is an induced polarization  $\vec{P}$  due to the director deformation. When a DC electric field  $\vec{E}$  is applied along the  $y$  direction, the liquid crystal is twisted in the  $y$  direction due to the interaction between  $\vec{E}$  and  $\vec{P}$ . Under the one elastic constant approximation, show that the maximum twist angle (at  $z = 0$ ) is given by  $\phi(0) = -(e_s - e_b)Eh/\pi K$ .

### References

- 1 P. G. de Gennes and J. Prost, *The physics of liquid crystals* (Oxford University Press, New York, 1993).
- 2 L. M. Blinov and V. G. Chigrinov, *Electrooptical effects in liquid crystal materials* (Springer-Verlag, New York, 1994).
- 3 A. J. Leadbetter, 'Structure classification of liquid crystals', in *Thermotropic liquid crystals*, ed. G. W. Gray (John Wiley & Sons, Ltd, Chichester, 1987).
- 4 R. M. Hornreich, 'Landau theory of the isotropic-nematic critical point', *Phys. Lett.*, **109A**, 232 (1985).
- 5 I. Lelidis and G. Durand, 'Electric-field-induced isotropic-nematic phase transition', *Phys. Rev. E*, **48**, 3822 (1993).
- 6 R. B. Meyer, 'Piezoelectric effects in liquid crystals', *Phys. Rev. Lett.*, **22**, 918 (1969).
- 7 A. I. Derzhanski, A. G. Petrov, and M. D. Mitov, 'Liquid-crystalline curvature electricity: the bending mode of MBBA', *J. Physique*, **39**, 273 (1978).
- 8 D. Schmidt, M. Schadt, and W. Z. Helfrich, *Z. Naturforsch.*, **A27**, 277 (1972).
- 9 E. L. Wood, G. P. Bryan-Brown, P. Brett, A. Graham, J. C. Jones, and J. R. Hughes, 'Zenithal bistable device (ZBD) suitable for portable applications', *SID Int. Symp. Dig. Tech. Pap.*, **31**, 124 (2000).

- 10 J. S. Patel and R. Meyer, 'Flexoelectric electro-optics of a cholesteric liquid crystal', *Phys. Rev. Lett.*, **58**, 1538 (1987).
- 11 G. Chilaya, 'Cholesteric liquid crystals: optics, electro-optics, and photo-optics', *Chirality in liquid crystals*, ed. H.-S. Kitzerow and C. Bahar (Springer-Verlag, New York, 2001).
- 12 L. Komitov, S. T. Lagerwall, B. Stenler and A. Strigazzi, 'Sign reversal of the linear electro-optical effect in the chiral nematic phase', *J. Appl. Phys.*, **76**, 3762 (1994).
- 13 J. S. Patel and S.-D. Lee, 'Fast linear electro-optic effect based on cholesteric liquid crystals', *J. Appl. Phys.*, **66**, 1879 (1987).
- 14 R. B. Meyer, L. Liebert, L. Strezelecki, and P. Keller, *J. Physique Lett.*, **36**, L69 (1975).
- 15 J. W. Goodby, R. Blinc, N. A. Clark, S. T. Lagerwall, M. A. Osipov, S. A. Pikin, T. Sakurai, K. Yoshino, and B. Žekš, 'Ferroelectric liquid crystals: principles, properties and applications', *Ferroelectricity and related phenomena*, Vol. 7 (Gordon and Breach, Amsterdam, 1991).
- 16 N. A. Clark and S. T. Lagerwall, 'Submicrosecond bistable electro-optic switching in liquid crystals', *Appl. Phys. Lett.*, **36**, 899 (1980).
- 17 S. Garoff and R. F. Meyer, 'Electroclinic effect at the A-C phase change of a chiral smectic liquid crystal', *Phys. Rev. Lett.*, **38**, 848 (1977); *Phys. Rev. A.*, **19**, 388 (1979).

# 5

## Freedericksz Transition

Liquid crystals reorient in externally applied electric fields because of their dielectric anisotropies. The electric energy, a part of the free energy, of a liquid crystal depends on the orientation of the liquid crystal director in the applied electric field. Under a given electric field, the liquid crystal will be in the equilibrium state where the total free energy is minimized.

### 5.1 Calculus of Variations

In a liquid crystal cell, under a given boundary condition and an externally applied field, the liquid crystal is in a director field configuration  $\vec{n}(\vec{r})$  that minimizes the total free energy of the system. The free energy density has two parts: (1) the elastic energy, which depends on the spatial derivatives of  $\vec{n}$ ; and (2) the dielectric electric energy, which depends on  $\vec{n}$ . The total free energy is given by

$$F = \int f[\vec{n}(\vec{r}), \vec{n}'(\vec{r}), \vec{r}] d^3r \quad (5.1)$$

Mathematically  $F$  is referred to as the functional. In order to search for the director configuration  $\vec{n}(\vec{r})$  that minimizes the total free energy, we need the calculus of variations [1].

#### 5.1.1 One dimension and one variable

##### (1) Fixed boundary condition

We start with the simplest case in which the liquid crystal is sandwiched between two parallel plates located at  $z = 0$  and  $z = h$ , respectively, as shown in Figure 5.1(a). The director  $\vec{n}$  is described by an angle  $\theta$  which is only a function of  $z$ , as shown in Figure 5.1(b). The anchoring of the liquid crystal at the substrate surface is infinitely strong so that the orientation of the liquid crystal at the top and

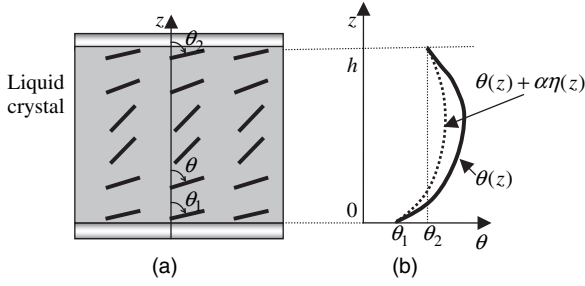


Figure 5.1 Schematic diagram of the 1-D liquid crystal director configuration

bottom surface is fixed. The boundary conditions are

$$\theta = \begin{cases} \theta_1 & \text{at } z = 0 \\ \theta_2 & \text{at } z = h \end{cases} \tag{5.2}$$

In this case, the total free energy (free energy per unit area) is given by

$$F = \int_0^h f(\theta, \theta', z) dz \tag{5.3}$$

If the configuration given by the function  $\theta = \theta(z)$  has the minimum or maximum free energy  $F_m$ , i.e.,  $F$  is stationary under  $\theta = \theta(z)$ , then for a small variation  $\alpha\eta(z)$ , where  $\alpha$  is a constant and infinitely small and  $\eta(z)$  is a function, the change of the free energy is zero to first order of  $\alpha$  [2]. Because of the fixed boundary condition, it is required that  $\eta(z=0) = 0$  and  $\eta(z=h) = 0$ . Thus

$$\begin{aligned} F(\alpha) &= \int_0^h f[\theta + \alpha\eta(z), \theta' + \alpha\eta'(z), z] dz \\ &= \int_0^h \left\{ f(\theta, \theta', z) + \frac{\partial f}{\partial \theta}[\alpha\eta(z)] + \frac{\partial f}{\partial \theta'}[\alpha\eta'(z)] + O(\alpha^2) \right\} dz \\ &= \int_0^h f(\theta, \theta', z) dz + \alpha \int_0^h \left[ \frac{\partial f}{\partial \theta} \eta(z) + \frac{\partial f}{\partial \theta'} \eta'(z) \right] dz + O(\alpha^2) \\ &= F(\alpha = 0) + \alpha \int_0^h \left[ \frac{\partial f}{\partial \theta} \eta(z) + \frac{\partial f}{\partial \theta'} \eta'(z) \right] dz + O(\alpha^2) \end{aligned} \tag{5.4}$$

Therefore it is required that

$$\delta F = F(\alpha) - F(\alpha = 0) = \alpha \int_0^h \left[ \frac{\partial f}{\partial \theta} \eta(z) + \frac{\partial f}{\partial \theta'} \eta'(z) \right] dz = 0$$

Using partial integration, we have

$$\delta F = \alpha \int_0^h \left[ \frac{\partial f}{\partial \theta} \eta(z) + \frac{\partial f}{\partial \theta'} \eta'(z) \right] dz = \alpha \int_0^h \left[ \frac{\partial f}{\partial \theta} - \frac{d}{dz} \left( \frac{\partial f}{\partial \theta'} \right) \right] \eta(z) dz + \alpha \left[ \eta(z) \frac{\partial f}{\partial \theta'} \right]_0^h = 0 \quad (5.5)$$

The last term is zero because of the boundary condition for  $\eta(z)$ . Therefore it is required that

$$\int_0^h \left[ \frac{\partial f}{\partial \theta} - \frac{d}{dz} \left( \frac{\partial f}{\partial \theta'} \right) \right] \eta(z) dz = 0$$

This should hold for any function  $\eta(z)$  which satisfies the boundary condition. Hence it is required that

$$\frac{\delta f}{\delta \theta} \equiv \frac{\partial f}{\partial \theta} - \frac{d}{dz} \left( \frac{\partial f}{\partial \theta'} \right) = 0 \quad (5.6)$$

This is the *Euler–Lagrange equation*. The solution  $\theta(z)$  of this equation minimizes or maximizes the total free energy  $F$ .

Next we consider how to minimize the total free energy  $F$  under a constraint  $G = \int_0^h g(\theta, \theta', z) dz = \sigma$ , where  $\sigma$  is a constant. Now, besides

$$\delta F = \int_0^h \frac{\delta f}{\delta \theta} \delta \theta dz = 0 \quad (5.7)$$

it is also required that

$$\delta G = \int_0^h \frac{\delta g}{\delta \theta} \delta \theta dz = 0 \quad (5.8)$$

because  $G$  is a constant. Therefore  $(\delta f / \delta \theta) / (\delta g / \delta \theta)$  must be a constant  $\lambda$  independent of  $z$ .  $\lambda$  is called the Lagrange multiplier. To minimize  $F$  under the constraint is equivalent to minimizing  $\int_0^h [f(\theta, \theta', z) + \lambda g(\theta, \theta', z)] dz$  without the constraint. The solution found from  $\delta(f + \lambda g) / \delta \theta = 0$  will depend on  $\lambda$ . The value of  $\lambda$  can be found by substituting the solution into  $G = \int_0^h g(\theta, \theta', z) dz = \sigma$ .

## (2) Unfixed boundary condition

If the anchoring of the liquid crystal at the substrate surface is not infinitely strong but weak, the value of  $\theta$  at the boundary is not fixed. The surface energy varies with the director configuration, and therefore must be included in the total free energy of the system:

$$F = \int_0^h f(\theta, \theta', z) dz + f_s[\theta(z=0)] + f_s[\theta(z=h)] \quad (5.9)$$

## 130 FREEDERICKSZ TRANSITION

Under a small variation  $\alpha\eta(z)$ , the variation of the total free energy is

$$\begin{aligned}
 \delta F &= \left\{ \int_0^h f[\theta + \alpha\eta(z), \theta' + \alpha\eta'(z), z] dz + f_s[\theta(z=0) + \alpha\eta(z=0)] + f_s[\theta(z=h) + \alpha\eta(z=h)] \right\} \\
 &\quad - \left\{ \int_0^h f[\theta, \theta', z] dz + f_s[\theta(z=0)] + f_s[\theta(z=h)] \right\} \\
 &= \alpha \int_0^h \left[ \frac{\partial f}{\partial \theta} - \frac{d}{dz} \left( \frac{\partial f}{\partial \theta'} \right) \right] \eta(z) dz + \alpha \left[ \eta(z) \frac{\partial f}{\partial \theta} \right] \Big|_0^h + \alpha \left( \eta \frac{\partial f_s}{\partial \theta} \right) \Big|_{z=0} + \alpha \left( \eta \frac{\partial f_s}{\partial \theta} \right) \Big|_{z=h} = 0 \\
 &= \alpha \int_0^h \left[ \frac{\partial f}{\partial \theta} - \frac{d}{dz} \left( \frac{\partial f}{\partial \theta'} \right) \right] \eta(z) dz + \alpha \eta \left( \frac{\partial f_s}{\partial \theta} - \frac{\partial f}{\partial \theta'} \right) \Big|_{z=0} + \alpha \eta \left( \frac{\partial f_s}{\partial \theta} + \frac{\partial f}{\partial \theta'} \right) \Big|_{z=h} = 0
 \end{aligned} \tag{5.10}$$

If  $F$  is stationary under the director configuration  $\theta(z)$ , then besides Equation (5.6), it is also required that

$$\left( -\frac{\partial f}{\partial \theta'} + \frac{\partial f_s}{\partial \theta} \right) \Big|_{z=0} = 0 \tag{5.11a}$$

$$\left( \frac{\partial f}{\partial \theta'} + \frac{\partial f_s}{\partial \theta} \right) \Big|_{z=h} = 0 \tag{5.11b}$$

### 5.1.2 One dimension and multiple variables

If  $\vec{n}$  is described by two angles  $\theta$  and  $\phi$  which are functions of  $z$ , the total free energy of the system is given by

$$F = \int_0^h f(\theta, \theta', \phi, \phi', z) dz \tag{5.12}$$

When the free energy is minimized or maximized, it is required that

$$\frac{\delta f}{\delta \theta} = \frac{\partial f}{\partial \theta} - \frac{d}{dz} \left( \frac{\partial f}{\partial \theta'} \right) = 0 \tag{5.13a}$$

and

$$\frac{\delta f}{\delta \phi} = \frac{\partial f}{\partial \phi} - \frac{d}{dz} \left( \frac{\partial f}{\partial \phi'} \right) = 0 \tag{5.13b}$$

### 5.1.3 Three dimensions

If  $\vec{n}$  is described by the angle  $\theta$  which is a function of more than one coordinate, say,  $x$ ,  $y$ , and  $z$ , the total free energy is given by

$$F = \int f(\theta, \theta'_x, \theta'_y, \theta'_z, x, y, z) \tag{5.14}$$

When the free energy is minimized or maximized, it is required that

$$\frac{\delta f}{\delta \theta} = \frac{\partial f}{\partial \theta} - \frac{d}{dx} \left( \frac{\partial f}{\partial \theta'_x} \right) - \frac{d}{dy} \left( \frac{\partial f}{\partial \theta'_y} \right) - \frac{d}{dz} \left( \frac{\partial f}{\partial \theta'_z} \right) = 0 \tag{5.15}$$

When  $\vec{n}$  is described by multiple variables which are a function of more than one coordinate, each variable must satisfy the Euler–Lagrange equation as Equation (5.15).

## 5.2 Fredericksz Transition: Statics

When a nematic liquid crystal is confined, such as when it is sandwiched between two parallel substrates with alignment layers, in the absence of external fields, the orientation of the liquid crystal director is determined by the anchoring condition. When an external electric field is applied to the liquid crystal, it will reorient because of the dielectric interaction between the liquid crystal and the applied field. If the dielectric anisotropy is positive ( $\Delta\epsilon > 0$ ), the liquid crystal tends to align parallel to the applied field. If  $\Delta\epsilon < 0$ , it tends to align perpendicular to the field. This field-induced reorientation of the liquid crystal is referred to as the *Fredericksz transition* [3–5].

### 5.2.1 Splay geometry

The cell structure of the bend geometry is shown in Figure 5.2, which is popularly used for electrically controlled birefringent (ECB) devices. The liquid crystal is sandwiched between two parallel plates of cell thickness  $h$ . The easy axis of the anchoring of the top and bottom alignment layers is parallel to the plates (the  $x$  axis). In the absence of fields, the liquid crystal director is uniformly aligned along the  $x$  axis, as shown in Figure 5.2(a). When a sufficiently high electric field is applied across the cell (in the  $z$  direction), the liquid crystal director will be tilted toward the cell normal direction, as shown in Figure 5.2(b). Because of the anchoring at the surface of the plates, the liquid crystal director in the distorted state is not uniform. This costs elastic energy and works against the transition. The liquid crystal director is always in the  $x$ – $z$  plane, provided  $\Delta\epsilon > 0$ , and is given by

$$\vec{n} = \cos \theta(z)\hat{x} + \sin \theta(z)\hat{z} \tag{5.16}$$

The divergence of  $\vec{n}$  is  $\nabla \cdot \vec{n} = \cos \theta \theta'$  and the curl is  $\nabla \times \vec{n} = -\sin \theta \theta' \hat{y}$ , where  $\theta' = \partial \theta / \partial z$ . The elastic energy is positive and given by

$$f_{elastic} = \frac{1}{2} K_{11} \cos^2 \theta \theta'^2 + \frac{1}{2} K_{33} \sin^2 \theta \theta'^2 \tag{5.17}$$

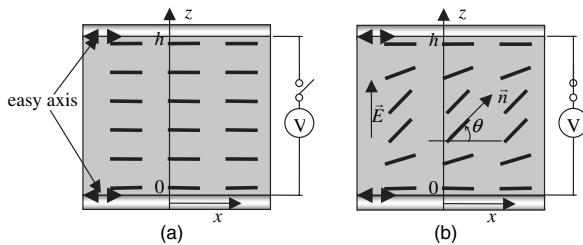


Figure 5.2 Schematic diagram of Fredericksz transition in splay geometry

### 132 FREDERICKSZ TRANSITION

When the tilt angle is small, the splay elastic energy dominates and the cell geometry is called splay geometry. The electric energy is negative and is approximately given by

$$f_{electric} = -\frac{1}{2}\varepsilon_o\Delta\varepsilon(\vec{E} \cdot \vec{n})^2 = -\frac{1}{2}\varepsilon_o\Delta\varepsilon E^2 \sin^2 \theta \quad (5.18)$$

This is a good approximation when  $\theta$  is small. The free energy density is

$$f = \frac{1}{2}(K_{11} \cos^2 \theta + K_{33} \sin^2 \theta)\theta'^2 - \frac{1}{2}\varepsilon_o\Delta\varepsilon E^2 \sin^2 \theta \quad (5.19)$$

The total free energy (per unit area) of the system is

$$F = \int_0^h \left[ \frac{1}{2}(K_{11} \cos^2 \theta + K_{33} \sin^2 \theta)\theta'^2 - \frac{1}{2}\varepsilon_o\Delta\varepsilon E^2 \sin^2 \theta \right] dz \quad (5.20)$$

Using the Euler–Lagrange method to minimize the free energy, we obtain

$$\begin{aligned} \frac{\delta f}{\delta \theta} &= \frac{\partial f}{\partial \theta} - \frac{d}{dz} \left( \frac{\partial f}{\partial \theta'} \right) \\ &= -\varepsilon_o\Delta\varepsilon E^2 \sin \theta \cos \theta - (K_{33} - K_{11}) \sin \theta \cos \theta \theta'^2 - (K_{11} \cos^2 \theta + K_{33} \sin^2 \theta) \theta'' = 0 \end{aligned} \quad (5.21)$$

When  $\theta$  is small, we use the approximations  $\sin \theta = \theta$  and  $\cos \theta = 1$ . Neglecting second-order terms, Equation (5.21) becomes

$$-\varepsilon_o\Delta\varepsilon E^2 \theta - K_{11} \theta'' = 0 \quad (5.22)$$

The general solution is

$$\theta = A \sin \left( \sqrt{\frac{\varepsilon_o\Delta\varepsilon E^2}{K_{11}}} z \right) + B \cos \left( \sqrt{\frac{\varepsilon_o\Delta\varepsilon E^2}{K_{11}}} z \right) \quad (5.23)$$

Now let us look at the boundary condition. Under infinitely strong anchoring, the boundary conditions are  $\theta(z=0) = \theta(z=h) = 0$ . Therefore  $B = 0$  and

$$\sqrt{\frac{\varepsilon_o\Delta\varepsilon E^2}{K_{11}}} h = m\pi, \quad m = 1, 2, 3, \dots \quad (5.24)$$

When the applied field is low, it can only produce distortion with the longest wavelength  $\pi/h$ , and thus the threshold field  $E_c$  can be found using  $\sqrt{\varepsilon_o\Delta\varepsilon E_c^2/K_{11}h} = \pi$ . Therefore

$$E_c = \frac{\pi}{h} \sqrt{\frac{K_{11}}{\varepsilon_o\Delta\varepsilon}} \quad (5.25)$$



which is inversely proportional to the cell thickness, because the elastic energy is higher with thinner cell thickness. The threshold voltage is

$$V_c = hE_c = \pi \sqrt{\frac{K_{11}}{\varepsilon_o \Delta \varepsilon}} \quad (5.26)$$

which is independent of the cell thickness. In order to see the physical meaning of the existence of the threshold, let us consider the free energy when the tilt angle is small. Because of the boundary condition that  $\theta = 0$  at  $z = 0$  and  $z = h$ ,  $\theta = A \sin(\pi z/h)$ . For small amplitude  $A$ , the free energy is approximately given by

$$f = \frac{1}{2} \left( \frac{K_{11} \pi^2}{h^2} - \varepsilon_o \Delta \varepsilon E^2 \right) A^2 \quad (5.27)$$

When

$$E < E_c = \frac{\pi}{h} \sqrt{\frac{K_{11}}{\varepsilon_o \Delta \varepsilon}}$$

in the reorientation of the liquid crystal, the decrease of the electric energy cannot compensate for the increase of the elastic energy. The free energy of the distorted state is positive and higher than the free energy of the undistorted state, which is zero, and therefore the transition cannot occur. When the applied field is increased, the electric energy decreases (becomes more negative). When  $E > E_c$ , the decrease of the electric energy can compensate for the increase of the elastic energy. The free energy of the system decreases as the transition takes place.

In the approximation discussed above, when  $E < E_c$ , the amplitude of the distortion is  $A = 0$ . When  $E > E_c$ ,  $A$  suddenly explodes because larger  $A$  gives lower free energy. This will not happen in reality because it is not consistent with the assumption that  $\theta$  is small. Now we calculate the precise solution. From Equation (5.21) we have

$$(K_{33} - K_{11}) \sin \theta \cos \theta \theta'^2 + (K_{11} \cos^2 \theta + K_{22} \sin^2 \theta) \theta'' = -\varepsilon_o \Delta \varepsilon E^2 \sin \theta \cos \theta$$

Multiplying both sides by  $d\theta/dz$ , we obtain

$$\frac{d}{dz} \left[ \frac{1}{2} (K_{11} \cos^2 \theta + K_{33} \sin^2 \theta) \left( \frac{d\theta}{dz} \right)^2 \right] = -\frac{d}{dz} \left( \frac{1}{2} \varepsilon_o \Delta \varepsilon E^2 \sin^2 \theta \right)$$

Integrating, we get

$$(K_{11} \cos^2 \theta + K_{22} \sin^2 \theta) \left( \frac{d\theta}{dz} \right)^2 = C - \varepsilon_o \Delta \varepsilon E^2 \sin^2 \theta$$

where  $C$  is the integration constant which can be found by considering the fact that the distortion must be symmetric about the middle plane,

$$\frac{d\theta}{dz} (z = h/2) = 0$$

The tilt angle at the middle plane is also the maximum angle  $\theta_m$  [4]. Therefore

$$\left(\frac{d\theta}{dz}\right)^2 = \varepsilon_o \Delta \varepsilon E^2 \frac{\sin^2 \theta_m - \sin^2 \theta}{(K_{11} \cos^2 \theta + K_{33} \sin^2 \theta)} \tag{5.28}$$

$$\sqrt{\varepsilon_o \Delta \varepsilon E^2} dz = \left(\frac{K_{11} \cos^2 \theta + K_{33} \sin^2 \theta}{\sin^2 \theta_m - \sin^2 \theta}\right)^{1/2} d\theta$$

Using Equation (5.25) and integrating Equation (5.28) from 0 to  $z$ , over which  $\theta$  changes from 0 to  $\theta(z)$ , we have

$$\left(\frac{E}{E_c}\right) \left(\frac{z}{h}\right) = \frac{1}{\pi} \int_0^{\theta(z)} \left(\frac{\cos^2 \alpha + (K_{33}/K_{11}) \sin^2 \alpha}{\sin^2 \theta_m - \sin^2 \alpha}\right)^{1/2} d\alpha \tag{5.29}$$

The maximum angle  $\theta_m$  is given by

$$\left(\frac{E}{E_c}\right) \left(\frac{1}{2}\right) = \frac{1}{\pi} \int_0^{\theta_m} \left(\frac{\cos^2 \alpha + (K_{33}/K_{11}) \sin^2 \alpha}{\sin^2 \theta_m - \sin^2 \alpha}\right)^{1/2} d\alpha \tag{5.30}$$

For a given field  $E(>E_c)$ ,  $\theta_m$  can be found by numerically solving this integration equation. In the calculation of  $\theta_m$  as a function of  $E$ , instead of calculating  $\theta_m$  for each given  $E$ , it is much easier to calculate  $E$  for each given  $\theta_m$ . Once  $\theta_m$  is known,  $\theta$  as a function of  $z$  can be calculated by using Equation (5.29). Instead of calculating  $\theta$  for a given  $z$ , it is much easier to calculate  $z$  for a given  $\theta (<\theta_m)$ . The solution is symmetrical about the middle plane,  $\theta(z) = \theta(h-z)$  for  $h/2 \leq z \leq h$ .

We can obtain some information on how the tilt angle depends on the applied field even without numerical calculation. For the purpose of simplicity, we assume that  $K_{11} = K_{33}$ , and then Equation (5.30) becomes

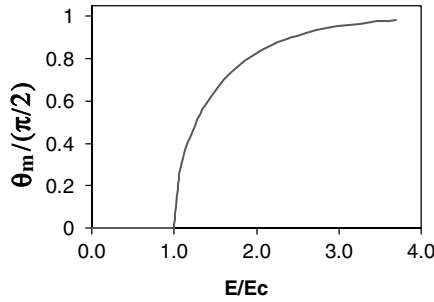
$$\left(\frac{E}{E_c}\right) = \frac{2}{\pi} \int_0^{\theta_m} \left(\frac{1}{\sin^2 \theta_m - \sin^2 \alpha}\right)^{1/2} d\alpha$$

Using a new variable  $\psi$  defined by  $\sin \alpha = \sin \theta_m \sin \psi$ , we have

$$\left(\frac{E}{E_c}\right) = \frac{2}{\pi} \int_0^{\pi/2} \frac{1}{\sqrt{1 - \sin^2 \theta_m - \sin^2 \psi}} d\psi \tag{5.31}$$

When the applied field is not much higher than the threshold, the tilt angle  $\theta_m$  at the middle plane is small, and approximately we have

$$\left(\frac{E}{E_c}\right) \approx \frac{2}{\pi} \int_0^{\pi/2} \left(1 + \frac{1}{2} \sin^2 \theta_m \sin^2 \psi\right) d\psi = 1 + \frac{1}{4} \sin^2 \theta_m \tag{5.32}$$



**Figure 5.3** The tilt angle at the middle plane vs. the applied field in splay geometry.  $K_{11} = 6.4 \times 10^{-12}$  N and  $K_{33} = 10 \times 10^{-11}$  N are used

Therefore

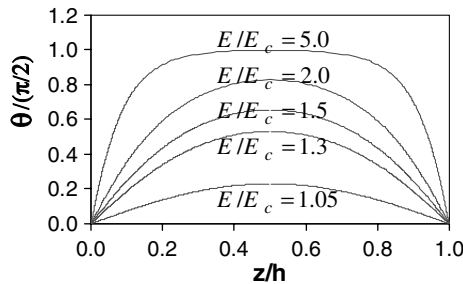
$$\sin \theta_m = 2\sqrt{(E - E_c)/E_c} \tag{5.33}$$

which indicates that when the applied field is increased above the threshold, the increase of the tilt angle with the field is rapid at the beginning, and then slows down. The numerically calculated tilt angle at the middle plane of the cell vs. the normalized field is shown in Figure 5.3. The numerically calculated tilt angle as a function of position at various applied fields is plotted in Figure 5.4.

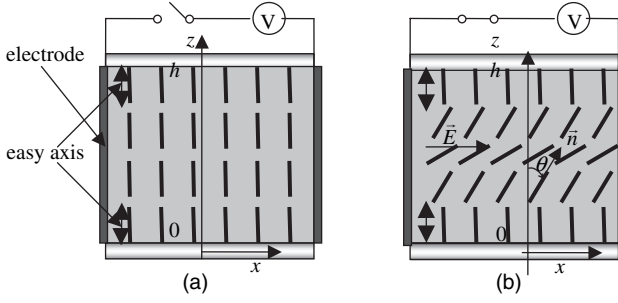
### 5.2.2 Bend geometry

The cell structure for bend geometry is shown in Figure 5.5 where the liquid crystal is sandwiched between two parallel substrates with an homeotropic alignment layer. In the field-off state, the liquid crystal is uniformly aligned perpendicular to the cell substrate because of the homeotropic anchoring condition of the alignment layer, as shown in Figure 5.5(a). When a sufficiently high electric field is applied parallel to the cell (in the  $x$  direction), the liquid crystal (with  $\Delta\epsilon > 0$ ) will be tilted toward the  $x$  direction, as shown in Figure 5.5(b). The liquid crystal director is always in the  $x-z$  plane and is given by

$$\vec{n} = \sin \theta(z)\hat{x} + \cos \theta(z)\hat{z} \tag{5.34}$$



**Figure 5.4** The tilt angle as a function of position at various fields in splay geometry.  $K_{11} = 6.4 \times 10^{-12}$  N and  $K_{33} = 10 \times 10^{-11}$  N are used



**Figure 5.5** Schematic diagram of Fredericksz transition in bend geometry

The elastic energy is given by

$$f_{elastic} = \frac{1}{2}K_{11} \sin^2 \theta \theta^2 + \frac{1}{2}K_{33} \cos^2 \theta \theta^2 \quad (5.35)$$

When the tilt angle is small, the bend elastic energy dominates and the cell geometry is called bend geometry. The electric energy is negative and is approximately given by

$$f_{electric} = -\frac{1}{2}\epsilon_o \Delta\epsilon (\vec{E} \cdot \vec{n})^2 = -\frac{1}{2}\epsilon_o \Delta\epsilon E^2 \sin^2 \theta \quad (5.36)$$

The free energy density is

$$f = \frac{1}{2}(K_{11} \sin^2 \theta + K_{33} \cos^2 \theta)\theta^2 - \frac{1}{2}\epsilon_o \Delta\epsilon E^2 \sin^2 \theta \quad (5.37)$$

In a similar way as in the splay geometry, the threshold can be found to be

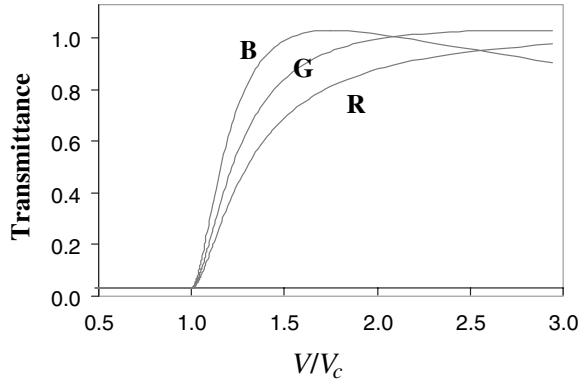
$$E_c = \frac{\pi}{h} \sqrt{\frac{K_{33}}{\epsilon_o \Delta\epsilon}} \quad (5.38)$$

The tilt angle  $\theta$  as a function of  $z$  under an applied field  $E (> E_c)$  can be calculated in a similar way as in the bend geometry.

The same phenomenon occurs if the liquid crystal has a negative dielectric anisotropy and the applied field is along the  $z$  direction (known as the vertical alignment (VA) mode), where the electric energy is

$$f_{electric} = -\frac{1}{2}\epsilon_o (-|\Delta\epsilon|) (\vec{E} \cdot \vec{n})^2 = \frac{1}{2}\epsilon_o |\Delta\epsilon| E^2 \cos^2 \theta = \text{constant} - \frac{1}{2}\epsilon_o |\Delta\epsilon| E^2 \sin^2 \theta$$

The calculated transmittance vs. applied voltage of a VA mode liquid crystal display is shown in Figure 5.6. Light is incident normally on the liquid crystal cell. The parameters of the liquid crystal are  $K_{11} = 6.4 \times 10^{-12} \text{ N}$ ,  $K_{33} = 10 \times 10^{-12} \text{ N}$ ,  $\Delta\epsilon = -3$ ,  $n_e = 1.57$ , and  $n_o = 1.50$ . The thickness of the cell is  $5.0 \mu\text{m}$ . The liquid crystal is sandwiched between two crossed polarizers. In the voltage-activated state, the plane that the liquid crystal director lies in makes an angle of  $45^\circ$  with respect to



**Figure 5.6** Transmittance of the VA mode liquid crystal display: R, 650 nm; G, 550 nm; B, 450 nm

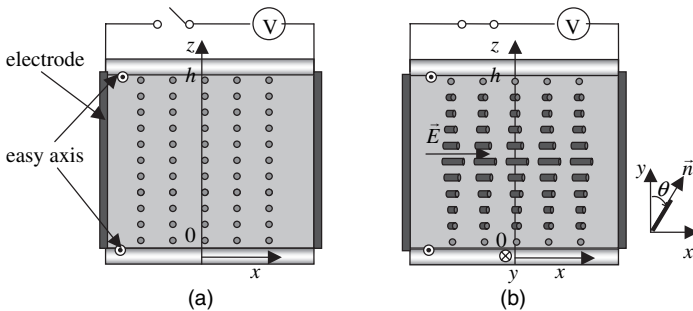
the polarizers. The retardation is

$$\Gamma = \frac{2\pi}{\lambda} \int_0^h \left( \frac{n_e n_o}{\sqrt{n_e^2 \cos^2 \theta(z) + n_o^2 \sin^2 \theta(z)}} - 1 \right) dz$$

The transmittance is  $T = \sin^2(\Gamma/2)$ . In the voltage-off state, the retardation is zero and the transmittance is zero for any wavelength. The retardation of the voltage-activated states is wavelength dependent and therefore the voltages for R, G, and B light to reach maximum transmittance are different.

**5.2.3 Twist geometry**

The twist geometry is shown in Figure 5.7 where the liquid crystal is sandwiched between two parallel plates with a homogeneous alignment layer. In the absence of an external field, the liquid crystal director uniformly orients parallel to the cell surface in the  $y$  direction because of the homogeneous anchoring condition of the alignment layer, as shown in Figure 5.7(a). When a sufficiently high electric field is applied along the  $x$  direction, the liquid crystal (with  $\Delta\epsilon > 0$ ) is tilted toward the field direction, as shown in Figure 5.7(b). The liquid crystal director is in the  $x$ - $y$  plane



**Figure 5.7** Schematic diagram of Freedericksz transition in bend geometry

and is given by

$$\vec{n} = \sin \theta(z) \hat{x} + \cos \theta(z) \hat{y} \tag{5.39}$$

In this geometry, only twist elastic energy is involved and the elastic energy is given by

$$f_{elastic} = \frac{1}{2} K_{22} \theta'^2 \tag{5.40}$$

The electric energy is negative and is approximately given by

$$f_{electric} = -\frac{1}{2} \epsilon_o \Delta \epsilon (\vec{E} \cdot \vec{n})^2 = -\frac{1}{2} \epsilon_o \Delta \epsilon E^2 \sin^2 \theta \tag{5.41}$$

The free energy density is

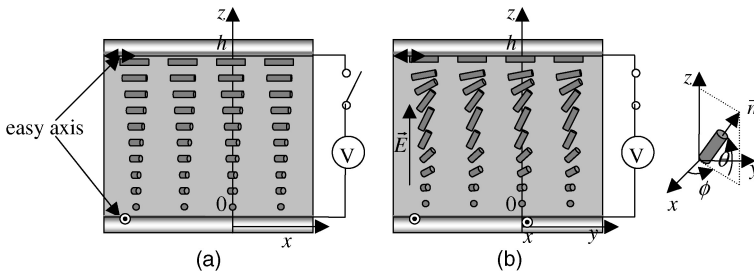
$$f = \frac{1}{2} K_{22} \theta'^2 - \frac{1}{2} \epsilon_o \Delta \epsilon E^2 \sin^2 \theta \tag{5.42}$$

In a similar way as in the splay geometry, the threshold can be found to be

$$E_c = \frac{\pi}{h} \sqrt{\frac{K_{22}}{\epsilon_o \Delta \epsilon}} \tag{5.43}$$

**5.2.4 Twisted nematic cell**

One of the most important liquid crystal displays is the twisted nematic (TN) display shown in Figure 5.8. The liquid crystal is anchored parallel to the cell surface by the alignment layers. The angle between the two alignment directions is  $\Phi$ , referred to as the total twist angle, which can be any value in general. In the particular case shown in Figure 5.8,  $\Phi = 90^\circ$  and the twisting is counter-clockwise when looking down from the top. In the absence of external electric fields, the liquid crystal is in the planar twisted state, where the liquid crystal director twists at a constant rate from the bottom to the top of the cell, as shown in Figure 5.8(a). The boundary conditions can also be satisfied if the director twists the complementary angle to  $\Phi$  in the opposite twisting direction. If the liquid crystal is nematic, domains with the director twisting in both directions coexist in the cell. In order to achieve a single domain, usually a chiral dopant is added to the nematic host to select one



**Figure 5.8** Schematic diagram of Freedericksz transition in the twisted nematic cell

twisting direction. The chirality of the mixture is  $q_o = 2\pi(HTP)x_c$ , where  $(HTP)$  and  $x_c$  are the helical twisting power and concentration of the chiral dopant, respectively. When a sufficiently high electric field is applied across the cell, the liquid crystal ( $\Delta\varepsilon > 0$ ) is tilted toward the field direction as shown in Figure 5.8(b). The liquid crystal director is described by the polar angle  $\theta$  and the azimuthal angle  $\phi$ . Both angles are a function of  $z$ . The components of the director  $\vec{n}$  are given by

$$n_x = \cos\theta(z)\cos\phi(z), \quad n_y = \cos\theta(z)\sin\phi(z), \quad n_z = \sin\theta(z) \quad (5.44)$$

We consider the case where the anchoring is finitely strong and the boundary conditions are

$$\phi(z=0) = \phi_1, \quad \phi(z=h) = \phi_2 \quad (5.45)$$

where  $\phi_2 - \phi_1 = \Phi$ , and

$$\theta(z=0) = 0, \quad \theta(z=h) = 0 \quad (5.46)$$

The divergence of  $\vec{n}$  is

$$\nabla \cdot \vec{n} = \cos\theta\theta' \quad (5.47)$$

where  $\theta' = \partial\theta/\partial z$ . The curl is

$$\nabla \times \vec{n} = (\sin\theta\sin\phi\theta' - \cos\theta\cos\phi\phi')\hat{x} + (-\sin\theta\cos\phi\theta' - \cos\theta\sin\phi\phi')\hat{y} \quad (5.48)$$

The free energy density is

$$f = \frac{1}{2}K_{11}\cos^2\theta\theta'^2 + \frac{1}{2}K_{22}(q_o - \cos^2\theta\phi')^2 + \frac{1}{2}K_{33}\sin^2\theta(\theta' + \cos^2\theta\phi'^2) - \frac{1}{2}\Delta\varepsilon\varepsilon_o E^2 \sin^2\theta \quad (5.49)$$

Using the Euler–Lagrange method to minimize the total free energy,

$$-\frac{\delta f}{\delta\theta} = (K_{11}\cos^2\theta + K_{33}\sin^2\theta)\theta'' + [(K_{33} - K_{11})\theta'^2 + (2K_{22}\cos^2\theta - K_{33}\cos 2\theta)\phi'^2 + \Delta\varepsilon\varepsilon_o E^2 - 2K_{22}q_o\phi']\sin\theta\cos\theta = 0 \quad (5.50)$$

$$-\frac{\delta f}{\delta\phi} = (K_{22}\cos^2\theta + K_{33}\sin^2\theta)\cos^2\theta\phi'' + 2[(-2K_{22}\cos^2\theta + K_{33}\cos 2\theta)\phi' + K_{22}q_o]\theta'\sin\theta\cos\theta = 0 \quad (5.51)$$

When the applied field is slightly above the threshold,  $\theta$  is very small, and we have the approximations  $\sin\theta \approx \theta$  and  $\cos\theta \approx 1$ . Keeping only first order terms, Equation (5.51) becomes  $-\delta f/\delta\phi = K_{22}\phi'' = 0$ , whose solution is

$$\phi = \frac{z\Phi}{h} \quad (5.52)$$

## 140 FREDERICKSZ TRANSITION

Equation (5.50) becomes

$$-\frac{\delta f}{\delta \theta} = K_{11}\theta'' + \left[ (2K_{22} - K_{33})\left(\frac{\Phi}{h}\right)^2 + \Delta\epsilon\epsilon_o E^2 - 2K_{22}q_o\left(\frac{\Phi}{h}\right) \right] \theta = 0 \quad (5.53)$$

Because of the boundary condition given in Equation (5.59), the solution is

$$\theta = A \sin\left(\frac{\pi}{h}z\right) \quad (5.54)$$

The dynamics of the transition is governed by

$$\gamma \frac{\partial \theta}{\partial t} = -\frac{\delta f}{\delta \theta} \quad (5.55a)$$

The physical meaning of this equation is that the viscosity torque, which is the product of the rotational viscosity coefficient  $\gamma$  and the angular speed  $\partial\theta/\partial t$ , is balanced by  $-\delta f/\delta\theta$  which is the sum of the elastic and electric torques. Using Equations (5.53), (5.54), and (5.55a), it can be obtained that

$$\gamma \frac{\partial A}{\partial t} = \left[ (2K_{22} - K_{33})\left(\frac{\Phi}{h}\right)^2 - K_{11}\left(\frac{\pi}{h}\right)^2 + \Delta\epsilon\epsilon_o E^2 - 2K_{22}q_o\left(\frac{\Phi}{h}\right) \right] A = 0 \quad (5.55b)$$

Initially  $\theta = 0$ , and therefore  $A = 0$ . If the applied field is low, the coefficient on the right hand side of Equation (5.55b) is negative, meaning that  $A$  cannot grow and remains at zero. When the applied field is sufficiently high, the coefficient becomes positive, meaning that  $A$  grows and therefore the transition takes place. Hence the field threshold can be found by setting

$$(2K_{22} - K_{33})\left(\frac{\Phi}{h}\right)^2 - K_{11}\left(\frac{\pi}{h}\right)^2 + \Delta\epsilon\epsilon_o E_c^2 - 2K_{22}q_o\left(\frac{\Phi}{h}\right) = 0$$

which gives [6, 7]

$$E_c = \frac{\pi}{h} \sqrt{\frac{K_{11}}{\Delta\epsilon\epsilon_o}} \left[ 1 + \frac{(K_{33} - 2K_{22})}{K_{11}} \left(\frac{\Phi}{\pi}\right)^2 + 2\frac{K_{22}}{K_{11}} \left(\frac{hq_o}{\pi}\right) \left(\frac{\Phi}{\pi}\right) \right]^{1/2} = 0 \quad (5.56)$$

The polar and azimuthal angles as a function of  $z$  under an applied field higher than the threshold can only be numerically calculated and will be discussed in Chapter 7.

### 5.2.5 Splay geometry with weak anchoring

If the anchoring of the liquid crystal at the boundary is not infinitely strong, the tilt angle  $\theta$  at the boundary is no longer fixed but changes with the applied field. Now we must consider the surface energy in determining the equilibrium director configuration. The total free energy of the system is



given by [5, 8]

$$\begin{aligned}
 F &= \int_0^h f dz + f_s|_{z=0} + f_s|_{z=h} \\
 &= \int_0^h \left[ \frac{1}{2} (K_{11} \cos^2 \theta + K_{33} \sin^2 \theta) \theta'^2 - \frac{1}{2} \varepsilon_o \Delta \varepsilon E^2 \sin^2 \theta \right] dz + \frac{1}{2} W \sin^2 \theta_1 + \frac{1}{2} W \sin^2 \theta_2 \quad (5.57)
 \end{aligned}$$

where  $W$  is the anchoring strength, and  $\theta_1$  and  $\theta_2$  are tilt angles at the bottom and top surfaces, respectively. The boundary conditions at the bottom and top surfaces are respectively

$$\left( -\frac{\partial f}{\partial \theta'} + \frac{\partial f_s}{\partial \theta} \right) \Big|_{z=0} = -(K_{11} \cos^2 \theta_1 + K_{33} \sin^2 \theta_1) \theta' + W \sin \theta_1 \cos \theta_1 = 0 \quad (5.58)$$

$$\left( \frac{\partial f}{\partial \theta'} + \frac{\partial f_s}{\partial \theta} \right) \Big|_{z=h} = (K_{11} \cos^2 \theta_2 + K_{33} \sin^2 \theta_2) \theta' + W \sin \theta_2 \cos \theta_2 = 0 \quad (5.59)$$

When the applied field is low, the liquid crystal director is homogeneously aligned along the  $x$  axis and the tilt angle is zero. When the applied field is increased above a threshold, the liquid crystal director begins to tilt. When the applied field is only slightly above the threshold, the tilt angle is small. Approximately we have  $\cos \theta \approx 1$  and  $\sin \theta \approx \theta$ . Equations (5.58) and (5.59) become

$$-K_{11} \theta' \Big|_{z=0} + W \theta_1 = 0 \quad (5.60)$$

$$K_{11} \theta' \Big|_{z=h} + W \theta_2 = 0 \quad (5.61)$$

The Euler–Lagrange equation for the minimization of the total bulk free energy is (Equation (5.22))

$$-\varepsilon_o \Delta \varepsilon E^2 \theta - K_{11} \theta'' = 0 \quad (5.62)$$

We define the surface extrapolation length

$$L = K_{11}/W \quad (5.63)$$

and also the field coherence length

$$\xi = \left( \frac{K_{11}}{\varepsilon_o \Delta \varepsilon E^2} \right)^{1/2} \quad (5.64)$$

whose physical meaning is that the applied field can produce a significant reorientation of the liquid crystal director over the distance  $\xi$ . When  $K_{11} = 10^{-11}$  N,  $\Delta \varepsilon = 10$ , and  $E = 1$  V/ $\mu\text{m}$ , the field coherence length is  $\xi = 0.3$   $\mu\text{m}$ . Because the solution of Equation (5.62) must be symmetric about  $z = h/2$ , the solution is

$$\theta = B \cos \left( \frac{z - h/2}{\xi} \right) \quad (5.65)$$

Note that this is the solution for an applied field slightly above the threshold. The boundary condition (5.60) becomes

$$\frac{B}{\xi} \sin\left(\frac{h}{2\xi}\right) = \frac{B}{L} \cos\left(\frac{h}{2\xi}\right)$$

i.e.,

$$\tan\left(\frac{h}{2\xi}\right) = \frac{\xi}{L} \tag{5.66}$$

When the anchoring is infinitely strong,  $W = \infty$  and thus  $L = 0$ ; the solution of Equation (5.66) is  $h/2\xi = \pi/2$ , which gives the field threshold  $E_c = (\pi/h)\sqrt{K_{11}/\epsilon_o\Delta\epsilon}$ . When the anchoring is weak, e.g.,  $W = 10^{-5} \text{ J/m}^2$ , the surface extrapolation length is  $L = 10^{-11} \text{ N}/(10^{-5} \text{ J/m}^2) = 10^{-1} \mu\text{m}$ . When the applied field is low,  $\xi$  is large and  $\xi/L \gg 1$ . At the field threshold,  $h/2\xi$  is close to  $\pi/2$ , and thus we have the approximation

$$\tan\left(\frac{h}{2\xi}\right) = \tan\left[\frac{\pi}{2} - \left(\frac{\pi}{2} - \frac{h}{2\xi}\right)\right] \approx 1 / \left(\frac{\pi}{2} - \frac{h}{2\xi}\right) = \frac{\xi}{L}$$

which gives  $1/\xi = \pi/(h + 2L)$ . Therefore the field threshold is

$$E_c = \frac{\pi}{(h + 2L)} \sqrt{\frac{K_{11}}{\epsilon_o\Delta\epsilon}} \tag{5.67}$$

This result is the same as the one when the anchoring is infinitely strong and the cell gap is increased from  $h$  to  $h + 2L$ .

### 5.2.6 Splay geometry with pretilt angle

In ECB liquid crystal devices, alignment layers with non-zero pretilt angle are usually used in order to avoid poly-domain structures resulting from opposite tilting of the liquid crystal director under externally applied fields. The rubbing directions of the bottom and top alignment layers are anti-parallel. Now we consider how the pretilt angle affects the reorientation of the liquid crystal under externally applied fields. The Euler–Lagrange equation for the minimization of the total free energy is (Equation (5.21))

$$\begin{aligned} \frac{\delta f}{\delta \theta} &= -\epsilon_o\Delta\epsilon E^2 \sin\theta \cos\theta - (K_{33} - K_{11})\sin\theta \cos\theta \theta'^2 \\ &- (K_{11} \cos^2\theta + K_{33} \sin^2\theta)\theta'' = 0 \end{aligned} \tag{5.68}$$

When the pretilt angle is  $\theta_o$ , we define a new variable  $\beta = \theta - \theta_o$ . When the applied field is low,  $\beta$  is very small, and approximately we have  $\sin(\beta + \theta_o) \approx \beta \cos\theta_o + \sin\theta_o$  and  $\cos(\beta + \theta_o) \approx \cos\theta_o - \beta \sin\theta_o$ ;  $\theta'' = \beta''$ . Neglecting higher order terms, Equation (5.68) becomes

$$-\epsilon_o\Delta\epsilon E^2 \left(\frac{1}{2}\sin 2\theta_o + \beta \cos 2\theta_o\right) - (K_{11} \cos^2\theta_o + K_{33} \sin^2\theta_o)\beta'' = 0 \tag{5.69}$$

The general solution is

$$\beta = B \cos \left[ \sqrt{\frac{\varepsilon_o \Delta \varepsilon E^2 \cos(2\theta_o)}{(K_{11} \cos^2 \theta_o + K_{33} \sin^2 \theta_o)}} \left( z - \frac{h}{2} \right) \right] - \frac{1}{2} \tan(2\theta_o) \quad (5.70)$$

where  $B$  is a constant which can be found from the boundary condition. Under infinitely strong anchoring, the boundary conditions are  $\beta(z=0) = \beta(z=h) = 0$ . Therefore

$$B \cos \left[ \sqrt{\frac{\varepsilon_o \Delta \varepsilon E^2 \cos(2\theta_o)}{(K_{11} \cos^2 \theta_o + K_{33} \sin^2 \theta_o)}} \frac{h}{2} \right] = \frac{1}{2} \tan(2\theta_o)$$

Equation (5.70) becomes

$$\beta = \frac{1}{2} \tan(2\theta_o) \left\{ \frac{\cos \left[ \sqrt{\frac{\varepsilon_o \Delta \varepsilon E^2 \cos(2\theta_o)}{(K_{11} \cos^2 \theta_o + K_{33} \sin^2 \theta_o)}} \left( z - \frac{h}{2} \right) \right]}{\cos \left[ \sqrt{\frac{\varepsilon_o \Delta \varepsilon E^2 \cos(2\theta_o)}{(K_{11} \cos^2 \theta_o + K_{33} \sin^2 \theta_o)}} \frac{h}{2} \right]} - 1 \right\} \quad (5.71)$$

$\beta$  is not zero for any non-zero applied field  $E$ . The pretilt angle breaks the reflection symmetry of the anchoring and eliminates the threshold. When  $E$  is very small, we have

$$\beta = \frac{\varepsilon_o \Delta \varepsilon E^2 \sin(2\theta_o)}{4(K_{11} \cos^2 \theta_o + K_{33} \sin^2 \theta_o)} z(h-z) \quad (5.72)$$

The maximum tilt angle (at the middle plane) is (when  $K_{11} = K_{33}$ )

$$\beta_m = \frac{\varepsilon_o \Delta \varepsilon E^2 \sin(2\theta_o) h^2}{16K_{11}} \quad (5.73)$$

When

$$E = E_c = \frac{\pi}{h} \sqrt{\frac{K_{11}}{\varepsilon_o \Delta \varepsilon}}$$

(the threshold field when the pretilt angle is zero), the maximum tilt angle is  $\beta_m = \beta_{mc} = \sin(2\theta_o)/16$ , which is small for small pretilt angle  $\theta_o$ . For an applied field below  $E_c$ ,  $\beta_m = \beta_{mc}(E/E_c)^2$ . For an applied field slightly above  $E_c$ ,  $\beta_m = \beta_{mc} + 2\sqrt{(E-E_c)/E_c}$ .

### 5.3 Freedericksz Transition: Dynamics

The dynamics of the rotation of liquid crystal molecules is very complicated in general because of the coupling between the rotational motion and the translational motion. A rotation of the liquid crystal molecules may generate a translational motion of the molecules. A gradient of the velocity of the

translational motion produces a torque which in turn affects the rotation of the molecules. In this section we will proceed from some simple cases to complicated ones.

### 5.3.1 Dynamics of the Freedericksz Transition in Twist Geometry

In the twist geometry, the rotation of the liquid crystal director is not coupled to the translational motion of the molecules. The rotation of the liquid crystal director is governed by the overdamped dynamics: the elastic and electric torques are balanced by the rotational viscosity torque and the inertial term can be neglected [4]. Mathematically we have

$$\gamma_r \frac{\partial \theta}{\partial t} = - \frac{\delta f}{\delta \theta} \quad (5.74)$$

where  $\theta$  is the twist angle as discussed in Section 2.3, and  $\gamma_r$  is the rotational viscosity coefficient whose dimension is  $\text{N s/m}^2$ . Using the free energy given by Equation (5.42), we obtain

$$\gamma_r \frac{\partial \theta}{\partial t} = K_{22} \frac{\partial^2 \theta}{\partial z^2} + \epsilon_o \Delta \epsilon E^2 \sin \theta \cos \theta \quad (5.75)$$

We first consider the turn-off time when the applied field is turned off from the distorted state. The anchoring is infinitely strong and the twist angle at the boundary is zero. The initial twist angle can be expanded in terms of all the possible modes:

$$\theta_o(z) = \sum_{m=1}^{\infty} A_m \sin\left(\frac{m\pi z}{h}\right) \quad (5.76)$$

The solution of the dynamic equation is

$$\theta(t) = \sum_{m=1}^{\infty} A_m \sin\left(\frac{m\pi z}{h}\right) e^{-t/\tau_m} \quad (5.77)$$

where  $\tau_m$  is the relaxation time of the  $m$ th mode and is given by

$$\tau_m = \frac{\gamma_r}{K_{22}} \left(\frac{h}{\pi}\right)^2 \frac{1}{m^2} \quad (5.78)$$

The turn-off time  $\tau_{off}$  is approximately equal to the relaxation time  $\tau_1$  of the slowest mode ( $m = 1$ )

$$\tau_{off} = \frac{\gamma_r}{K_{22}} \left(\frac{\pi}{h}\right)^2 \quad (5.79)$$

Now we consider the turn-on time. When the applied field is not much higher than the threshold, the twist angle is small and  $m = 1$  is the only mode excited because it costs the least energy. The solution to the dynamic equation is

$$\theta(t) = A_1 e^{t/\tau} \sin\left(\frac{\pi z}{h}\right) \quad (5.80)$$

Using the approximations  $\sin \theta \approx \theta$  and  $\cos \theta = 1$  and substituting Equation (5.80) into Equation (5.75), we have

$$\frac{\gamma_r}{\tau} = -K_{22} \left(\frac{\pi}{h}\right)^2 + \varepsilon_o \Delta \varepsilon E^2 = K_{22} \left(\frac{\pi}{h}\right)^2 \left[ \left(\frac{E}{E_c}\right)^2 - 1 \right] \quad (5.81)$$

The turn-on time is

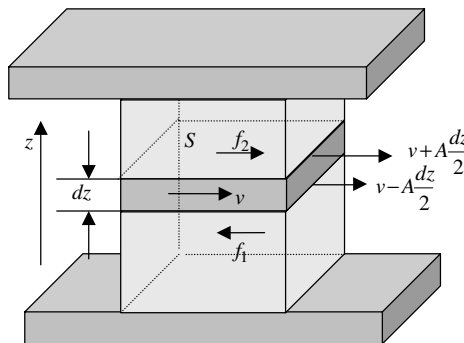
$$\tau_{on} = \frac{\gamma_r}{K_{22}} \left(\frac{h}{\pi}\right)^2 \frac{1}{(E/E_c)^2 - 1} \quad (5.82)$$

Although the dynamics of the Freedericksz transition in splay geometry, bend geometry, and twisted geometry is more complicated, the response time is still on the same order and has the same cell thickness dependence. The rotational viscosity coefficient is of the order  $0.1 \text{ N s/m}^2$ . When the elastic constant is  $10^{-11} \text{ N}$  and the cell thickness is  $10 \mu\text{m}$ , the response time is of the order 100 ms. Faster response times can be achieved by using thinner cell gaps.

### 5.3.2 Hydrodynamics

Now we consider the hydrodynamics of nematic liquid crystals [4, 9, 10]. For most phenomena in liquid crystals, it is reasonable to assume that liquid crystals are incompressible fluids. We first consider viscosity in isotropic fluids. The viscosity of a fluid is the internal friction that hinders neighboring layers of the fluid from sliding with respect to each other. Consider a steady shear whose velocity is only a function of  $z$ , as shown in Figure 5.9. Then consider a fluid element with area  $S$  and thickness  $dz$ . There are particle exchanges between the fluid element and the fluid above and below it. If the velocity is uniform, the net momentum transfer between the fluid element and the fluid above and below it is zero, and thus there is no force acting on it. If the velocity is not uniform but has a gradient, say  $A(z) (= \partial v / \partial z)$ , the particles moving in the fluid above have a smaller momentum than the particles moving from the fluid above into the element, provided  $A > 0$ . The fluid element gains momentum from the fluid above [11]. This momentum gain can be described as a force acting on the surface of the element toward the right side, which is proportional to the area of the element and the velocity gradient (known as a Newtonian fluid):

$$f_2 = \eta A_2 S \quad (5.83)$$



**Figure 5.9** The viscosity is the force acting on the surface of the fluid element due to the velocity gradient

where  $\eta$  is the translational viscosity coefficient, which has the dimension  $\text{N}/[(\text{m s}^{-1}/\text{m})(\text{m}^2)] = [\text{N s}/\text{m}^2]$ . The commonly used unit is *poise* which is equal to  $0.1 \text{ N s}/\text{m}^2$ . The viscosity coefficient of water at room temperature is about  $10^{-3} \text{ N s}/\text{m}^2$ . In the same way, the particles moving into the fluid below have a larger momentum than the particles moving from the fluid below into the element. The fluid element loses momentum to the fluid below. This momentum loss can also be described as a force acting on the surface of the element toward the left side:  $f_1 = \eta A_1 S$ . The net force acting on the fluid element is

$$f = f_2 - f_1 = (A_2 - A_1)\eta S = [A(z + dz/2) - A(z - dz/2)]\eta S = \frac{dA}{dz}\eta S \cdot dz \quad (5.84)$$

If  $dA/dz = 0$ , the net force is zero. The torque acting on the element, however, is not zero and is given by

$$\tau = \eta AS \cdot dz \quad (5.85)$$

This torque plays an important role in the dynamics of liquid crystals. A non-uniform translational motion will cause the liquid crystal to rotate.

Now we consider the hydrodynamics of an incompressible isotropic fluid. The velocity of the fluid is  $\vec{v} = \vec{v}(\vec{r}, t)$ . Applying Newton's law to a unitary volume of the fluid, we have [12]

$$\rho \frac{d\vec{v}}{dt} = \rho \left[ \frac{\partial \vec{v}}{\partial t} + (\vec{v} \cdot \nabla) \vec{v} \right] = -\nabla p + \vec{f}_v \quad (5.86)$$

where  $\rho$  is the mass density,  $p$  is the pressure, and  $\vec{f}_v$  is the viscosity force. Equation (5.86) is known as the *Navier–Stokes equation* and can be rewritten as

$$\rho \left[ \frac{\partial \vec{v}}{\partial t} + (\vec{v} \cdot \nabla) \vec{v} \right] = \nabla \cdot \vec{\sigma} \quad (5.87)$$

where  $\vec{\sigma}$  is the stress tensor defined by

$$\vec{\sigma} = -p\vec{I} + \vec{\sigma}' \quad (5.88)$$

$\vec{\sigma}'$  is the viscous stress tensor which arises from the velocity gradient. In order to find the relation between the viscous stress tensor and the velocity gradient, we consider a special case where the fluid rotates as a whole. When the angular velocity of the rotation is  $\vec{\Omega}$  the velocity is  $\vec{v} = \vec{\Omega} \times \vec{r}$ . We introduce two new tensors: the symmetric part of the velocity gradient tensor  $\vec{A}$  whose components are defined by [9]

$$A_{ij} = \frac{1}{2} \left( \frac{\partial v_j}{\partial x_i} + \frac{\partial v_i}{\partial x_j} \right) \quad (5.89)$$

where  $i, j = 1, 2, 3$ ,  $x_1 = x$ ,  $x_2 = y$ , and  $x_3 = z$ , and the anti-symmetric part of the velocity gradient tensor  $\vec{W}$  whose components are defined by

$$W_{ij} = \frac{1}{2} \left( \frac{\partial v_j}{\partial x_i} - \frac{\partial v_i}{\partial x_j} \right) \quad (5.90)$$

In this special case where the fluid rotates as a whole,  $A_{ij} = 0$ ,  $W_{xy} = \Omega_z$ ,  $W_{yz} = \Omega_x$ , and  $W_{zx} = \Omega_y$ . There should be no viscous stress. Therefore the viscous stress tensor must be proportional to  $\vec{A}$ :

$$\sigma'_{ij} = 2\eta A_{ij} = \eta \left( \frac{\partial v_j}{\partial x_i} + \frac{\partial v_i}{\partial x_j} \right) \tag{5.91}$$

where  $\eta$  is the translational viscosity coefficient. The vorticity of the flow (the angular velocity of the rotation of the fluid as a whole) is related to  $\vec{W}$  by

$$\vec{\omega} = \frac{1}{2} \nabla \times \vec{v} = (W_{yz}, W_{zx}, W_{xy}) \tag{5.92}$$

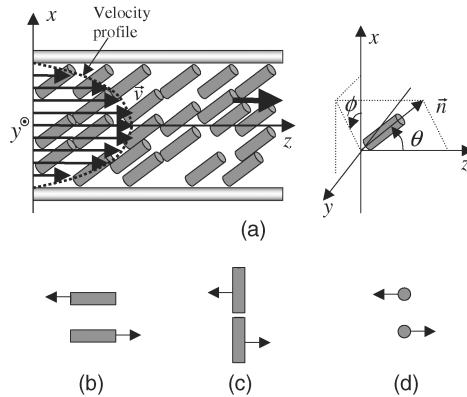
Now we consider the viscous stress tensor of a nematic liquid crystal. The translational viscous stress depends on the orientation of the liquid crystal director, the flow direction, and the gradient direction. First we assume that the liquid crystal director is fixed. Consider a special case of shear flow as shown in Figure 5.10(a). The velocity is along the  $z$  axis and the gradient of the velocity is along the  $x$  direction, namely,  $\vec{v} = u(x)\hat{z}$ . The two non-zero components of the viscous stress are

$$\sigma'_{xz} = \sigma'_{zx} = \eta(\theta, \phi) \frac{\partial u}{\partial x} \tag{5.93}$$

where  $\eta(\theta, \phi)$  is the viscosity coefficient which depends on the orientation of the liquid crystal director and is given by

$$\eta(\theta, \phi) = (\eta_1 + \eta_{12} \cos^2 \theta) \sin^2 \theta \cos^2 \phi + \eta_2 \cos^2 \theta + \eta_3 \sin^2 \theta \sin^2 \phi \tag{5.94}$$

$\eta_2 = \eta(\theta = 0)$  is the smallest viscosity coefficient, corresponding to the geometry shown in Figure 5.10(b).  $\eta_1 = \eta(\theta = 90^\circ, \phi = 0^\circ)$  is the largest viscosity coefficient, corresponding to the geometry shown in Figure 5.10(c).  $\eta_3 = \eta(90^\circ, 90^\circ)$  is the intermediate one, corresponding to the geometry shown in Figure 5.10(d).  $\eta_{12}$  contributes most when  $\theta = 45^\circ$  and  $\phi = 0^\circ$ . At room temperature  $\eta_i (i = 1, 2, 3)$  is about  $10^{-2}$  Ns/m<sup>2</sup>.  $\eta_{12}$  may be very small and can be neglected.



**Figure 5.10** Diagram defining the orientation of the liquid crystal director with respect to the flow of the liquid crystal and special geometries of shear flows

Now we consider the rotational motion of the liquid crystal director. The variation of the director  $\vec{n}$  associated with a fluid element with respect to time is given by

$$\frac{d\vec{n}}{dt} = \frac{\partial\vec{n}}{\partial t} + (\vec{v} \cdot \nabla)\vec{n} \tag{5.95}$$

The second term of this equation is due to the flow of the liquid crystal. As shown in Figure 5.11, the local angular velocity,  $\vec{\Omega}$ , of the director is related to  $d\vec{n}/dt$  by  $\vec{\Omega} dt \times \vec{n} = d\vec{n}$ . Therefore

$$\vec{n} \times (\vec{\Omega} \times \vec{n}) = \vec{\Omega} = \vec{n} \times \frac{d\vec{n}}{dt} \tag{5.96}$$

The dynamic equation of the rotation of the director per unit volume is

$$I \frac{d\vec{\Omega}}{dt} = \vec{\Gamma} \tag{5.97}$$

where  $I$  is the moment of inertia per unit volume and  $\vec{\Gamma}$  is the torque. The torque has three parts:

$$\vec{\Gamma} = \vec{\Gamma}_{mol} + \vec{\Gamma}_{vis} + \vec{\Gamma}_{flow} \tag{5.98}$$

$\vec{\Gamma}_{mol}$  is the molecular torque which is given by

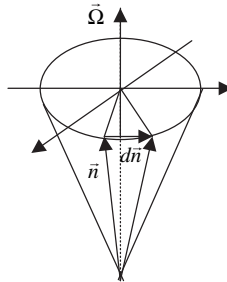
$$\vec{\Gamma}_{mol} = \vec{n} \times \vec{h} = \vec{n} \times \left( -\frac{\delta f}{\delta \vec{n}} \right) \tag{5.99}$$

where  $\vec{h} = -\delta f / \delta \vec{n}$  is the molecular field due to elastic distortion and the applied field.  $\vec{\Gamma}_{vis}$  is the rotational viscosity torque which is given by

$$\vec{\Gamma}_{vis} = -\gamma_1 \vec{n} \times \vec{N} \tag{5.100}$$

where  $\gamma_1$  is the rotational viscosity coefficient and  $\vec{N}$  is the net rotational velocity of the director, which equals the local angular velocity minus the angular velocity,  $\vec{\omega}$ , of the liquid crystal rotating as a whole:

$$\vec{N} = (\vec{\Omega} - \vec{\omega}) \times \vec{n} = \frac{d\vec{n}}{dt} - \vec{\omega} \times \vec{n} \tag{5.101}$$



**Figure 5.11** Schematic diagram showing the rotation of the liquid crystal director



$\vec{\Gamma}_{flow}$  is the torque produced by the viscosity of the translational motion as discussed above. Because only the component of the velocity gradient parallel to the liquid crystal director can produce the torque to cause the director to rotate, therefore

$$\vec{\Gamma}_{flow} = -\gamma_2 \vec{n} \times (\vec{A} \cdot \vec{n}) \tag{5.102}$$

where  $\gamma_2$  is referred to as the second rotational viscosity coefficient.  $\gamma_2$  has a negative value with a magnitude comparable to that of  $\gamma_1$ . In many liquid crystal phenomena, the dynamics is overdamped and the inertia term is negligible. Then the dynamic equation of the rotation of the director becomes

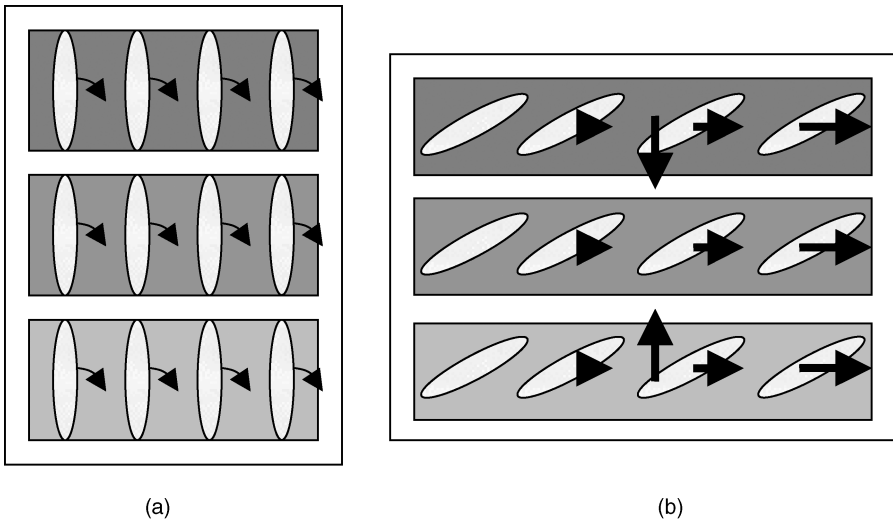
$$\vec{n} \times [\vec{h} - \gamma_1 \vec{N} - \gamma_2 (\vec{A} \cdot \vec{n})] = 0 \tag{5.103}$$

This equation generally means that  $[\vec{h} - \gamma_1 \vec{N} - \gamma_2 (\vec{A} \cdot \vec{n})]$ , not necessarily zero, is parallel to  $\vec{n}$ . The translational motion may induce a rotational motion of the liquid crystal molecules.

Now we consider how a rotational motion of the liquid crystal molecules induces a translational motion. As an example, initially the liquid crystal molecules are aligned vertically as shown in Figure 5.12(a). The average distance between the neighboring molecular centers in the vertical direction is larger than that in the horizontal direction. When the molecules rotate to the horizontal direction, as shown in Figure 5.12(b), the average distance between the neighboring molecular centers in the horizontal direction becomes larger than that in the vertical direction. This means that the molecules move translationally.

In the Ericksen–Leslie theory, the viscous stress tensor is given by

$$\vec{\sigma}' = \alpha_1 (\vec{n}\vec{n}) (\vec{n} \cdot \vec{A} \cdot \vec{n}) + \alpha_2 \vec{n}\vec{N} + \alpha_3 \vec{N}\vec{n} + \alpha_4 \vec{A} + \alpha_5 \vec{n} (\vec{n} \cdot \vec{A}) + \alpha_6 (\vec{n} \cdot \vec{A}) \vec{n} \tag{5.104}$$



**Figure 5.12** Schematic diagram showing how rotation of the liquid crystal molecules induces translational motion

## 150 FREDERICKSZ TRANSITION

The components are

$$\sigma'_{ij} = \alpha_1 n_i n_j n_k n_l A_{kl} + \alpha_2 n_i N_j + \alpha_3 n_j N_i + \alpha_4 A_{ij} + \alpha_5 n_i n_k A_{kj} + \alpha_6 n_j n_k A_{ki} \quad (5.105)$$

where  $\alpha_i$  ( $i = 1, 2, 3, 4, 5, 6$ ) are Leslie viscosity coefficients. The second and third terms describe the effect of director rotation on the translational motion. The relationships between the Leslie coefficients and the translational and rotational viscosity coefficients are [9]

$$\eta_1 = \frac{1}{2}(-\alpha_2 + \alpha_4 + \alpha_5) \quad (5.106)$$

$$\eta_2 = \frac{1}{2}(\alpha_3 + \alpha_4 + \alpha_6) \quad (5.107)$$

$$\eta_3 = \frac{1}{2}\alpha_4 \quad (5.108)$$

$$\eta_{12} = \alpha_1 \quad (5.109)$$

$$\gamma_1 = \alpha_3 - \alpha_2 \quad (5.110)$$

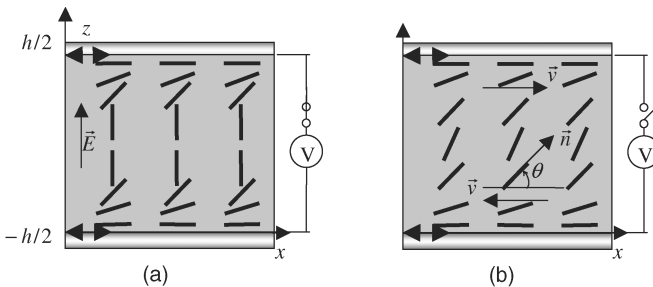
$$\gamma_2 = \alpha_6 - \alpha_5 \quad (5.111)$$

$$\alpha_6 = \alpha_2 + \alpha_3 + \alpha_5 \quad (5.112)$$

### 5.3.3 Backflow

We consider the dynamics of the Freedericksz transition in the splay geometry upon removal of the applied field [13–16]. Initially the liquid crystal director is aligned vertically by the applied field as shown in Figure 5.13(a). When the applied field is removed, the liquid crystal relaxes back to the homogeneous state. The rotation of the molecules induces a macroscopic translational motion known as the *backflow*. The velocity of the flow is

$$\vec{v} = [u(z), 0, 0] \quad (5.113)$$



**Figure 5.13** Schematic diagram showing the relaxation of the liquid crystal in the splay geometry

The  $y$  component of the velocity is zero because of the symmetry of the cell. The  $z$  component is zero because of the mass conservation and incompressibility of the liquid crystal. The boundary condition of the velocity of the translational motion is

$$u(z = -h/2) = u(z = h/2) = 0 \quad (5.114)$$

The liquid crystal director is in the  $x$ - $z$  plane and is given by

$$\vec{n} = n_x \hat{x} + n_z \hat{z} = \cos \theta(z, t) \hat{x} + \sin \theta(z, t) \hat{z} \quad (5.115)$$

The elastic energy density is

$$f = \frac{1}{2} K_{11} \left( \frac{\partial n_z}{\partial z} \right)^2 + \frac{1}{2} K_{33} \left( \frac{\partial n_x}{\partial z} \right)^2 \quad (5.116)$$

The molecular field is

$$\begin{aligned} \vec{h} &= \left[ -\frac{\partial f}{\partial n_x} + \frac{\partial}{\partial z} \left( \frac{\partial f}{\partial (\partial n_x / \partial z)} \right) \right] \hat{x} + \left[ -\frac{\partial f}{\partial n_z} + \frac{\partial}{\partial z} \left( \frac{\partial f}{\partial (\partial n_z / \partial z)} \right) \right] \hat{z} \\ &= K_{33} \frac{\partial^2 n_x}{\partial z^2} \hat{x} + K_{11} \frac{\partial^2 n_z}{\partial z^2} \hat{z} \\ &= -K_{33} \left[ \sin \theta \frac{\partial^2 \theta}{\partial z^2} + \cos \theta \left( \frac{\partial \theta}{\partial z} \right)^2 \right] \hat{x} + K_{11} \left[ \cos \theta \frac{\partial^2 \theta}{\partial z^2} - \sin \theta \left( \frac{\partial \theta}{\partial z} \right)^2 \right] \hat{z} \end{aligned} \quad (5.117)$$

The rate of change of the director is

$$\frac{d\vec{n}}{dt} = \dot{\theta} (-\sin \theta \hat{x} + \cos \theta \hat{z}) \quad (5.118)$$

where  $\dot{\theta} = \partial \theta / \partial t$ . The velocity gradient tensor is

$$\overleftrightarrow{A} = \begin{pmatrix} 0 & 0 & b \\ 0 & 0 & 0 \\ b & 0 & 0 \end{pmatrix} \quad (5.119)$$

where  $b = (1/2) \partial u / \partial z$ . Thus

$$\overleftrightarrow{A} \cdot \vec{n} = \begin{pmatrix} 0 & 0 & b \\ 0 & 0 & 0 \\ b & 0 & 0 \end{pmatrix} \begin{pmatrix} \cos \theta \\ 0 \\ \sin \theta \end{pmatrix} = \begin{pmatrix} b \sin \theta \\ 0 \\ b \cos \theta \end{pmatrix} \quad (5.120)$$

The angular velocity of the liquid crystal rotating as a whole is

$$\vec{\omega} = \frac{1}{2} \nabla \times \vec{v} = (0, b, 0) \quad (5.121)$$

## 152 FREDERICKSZ TRANSITION

The net rotation velocity of the director is

$$\begin{aligned}\vec{N} &= \frac{d\vec{n}}{dt} - \vec{\omega} \times \vec{n} = \dot{\theta}(-\sin\theta\hat{x} + \cos\theta\hat{z}) - b\hat{y} \times (\cos\theta\hat{x} + \sin\theta\hat{z}) \\ &= (\dot{\theta} + b)[- \sin\theta\hat{x} + \cos\theta\hat{z}]\end{aligned}\quad (5.122)$$

The dynamic equation of the rotation of the liquid crystal director is

$$\vec{n} \times [\vec{h} - \gamma_1\vec{N} - \gamma_2(\vec{A} \cdot \vec{n})] = 0 \quad (5.123)$$

Therefore

$$\vec{h} - \gamma_1\vec{N} - \gamma_2(\vec{A} \cdot \vec{n}) = c\vec{n} \quad (5.124)$$

where  $c$  is a constant. In components we have

$$-K_{33} \left[ \sin\theta \frac{\partial^2\theta}{\partial z^2} + \cos\theta \left( \frac{\partial\theta}{\partial z} \right)^2 \right] + \gamma_1(\dot{\theta} + b)\sin\theta - \gamma_2 b \sin\theta = c \cos\theta \quad (5.125)$$

$$K_{11} \left[ \cos\theta \frac{\partial^2\theta}{\partial z^2} - \sin\theta \left( \frac{\partial\theta}{\partial z} \right)^2 \right] - \gamma_1(\dot{\theta} + b)\cos\theta - \gamma_2 b \cos\theta = c \sin\theta \quad (5.126)$$

Under the isotropic elastic constant assumption ( $K_{11} = K_{33} = K$ ), multiplying Equation (5.126) by  $\cos\theta$  and Equation (5.125) by  $\sin\theta$ , and subtracting, we get

$$\gamma_1 \frac{\partial\theta}{\partial t} = K \frac{\partial^2\theta}{\partial z^2} - [\gamma_1 + \gamma_2(\cos^2\theta - \sin^2\theta)]b \quad (5.127)$$

Using Equations (5.110), (5.111), and (5.112), we then have

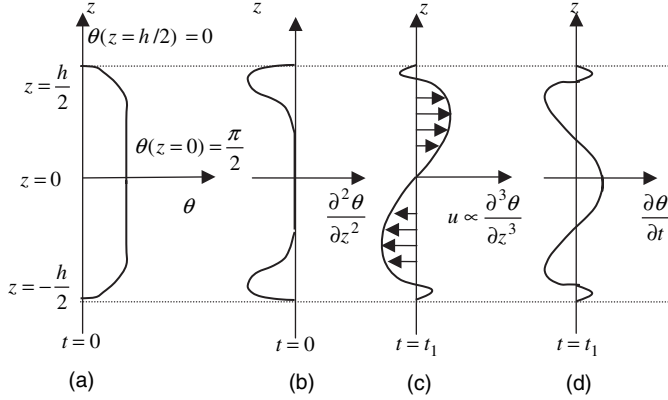
$$\gamma_1 \frac{\partial\theta}{\partial t} = K \frac{\partial^2\theta}{\partial z^2} - 2(\alpha_3 \cos^2\theta - \alpha_2 \sin^2\theta)b \quad (5.128)$$

Comparing Equation (5.127) to Equation (5.75), we can see the extra term which is from the translational motion. For the translational motion, there is only motion in the  $x$  direction. Using the dynamic equation (Equation (5.87)), we have

$$\rho \frac{\partial u}{\partial t} = \frac{\partial}{\partial z} \sigma_{zx} \quad (5.129)$$

When the pressure gradient is small and can be neglected, we have

$$\begin{aligned}\sigma_{zx} &= \alpha_1 n_z n_x (n_x n_z A_{xz} + n_z n_x A_{zx}) + \alpha_2 n_z N_x + \alpha_3 n_x N_z + \alpha_4 A_{zx} + \alpha_5 n_z n_z A_{zx} + \alpha_6 n_x n_x A_{xz} \\ &= [(2\alpha_1 \cos^2\theta - \alpha_2 + \alpha_5)\sin^2\theta + \alpha_4 + (\alpha_6 + \alpha_3)\cos^2\theta]b + (-\alpha_2 \sin^2\theta + \alpha_3 \cos^2\theta) \frac{\partial\theta}{\partial t}\end{aligned}\quad (5.130)$$



**Figure 5.14** The profiles of the liquid crystal director and velocity in the relaxation of the bistable TN liquid crystal

It is difficult to calculate the hydrodynamics involved analytically. We present a qualitative discussion here. If the applied field  $E$  is sufficiently high, the liquid crystal is aligned in the cell normal direction, except very near the cell surfaces. In the equilibrium state under the field, the tilt angle  $\theta$  is  $\pi/2$  in most parts of the cell, as shown in Figure 5.14(a). We also have

$$K_{22} \frac{\partial^2 \theta}{\partial z^2} = -\epsilon_o \Delta \epsilon E^2 \sin \theta \cos \theta$$

which is shown in Figure 5.14(b). Right after the applied high voltage is turned off ( $t=0$ ), there is no flow. The variational rate of  $\theta$  with respect to time is given by

$$\gamma_1 \frac{\partial \theta}{\partial t} = K \frac{\partial^2 \theta}{\partial z^2} < 0 \quad (5.131)$$

The angle decreases with time. The non-zero components of the stress tensor are

$$\sigma_{zx} = \sigma_{xz} = (-\alpha_2 \sin^2 \theta + \alpha_3 \cos^2 \theta) \frac{\partial \theta}{\partial t} = \frac{K}{\gamma_1} (-\alpha_2 \sin^2 \theta + \alpha_3 \cos^2 \theta) \frac{\partial^2 \theta}{\partial z^2} \quad (5.132)$$

From Equation (5.129) we have

$$\rho \frac{\partial u}{\partial t} = \frac{\partial \sigma_{zx}}{\partial z} = \frac{K}{\gamma_1} \frac{\partial}{\partial z} \left[ (-\alpha_2 \sin^2 \theta + \alpha_3 \cos^2 \theta) \frac{\partial^2 \theta}{\partial z^2} \right] \quad (5.133)$$

$$u = \frac{Kt}{\rho \gamma_1} \frac{\partial}{\partial z} \left[ (-\alpha_2 \sin^2 \theta + \alpha_3 \cos^2 \theta) \frac{\partial^2 \theta}{\partial z^2} \right] \propto \frac{\partial^3 \theta}{\partial z^3} \quad (5.134)$$

Consider the case  $\alpha_3 > 0$  (the final result is the same for negative  $\alpha_3$ ). At a time slightly later ( $t = t_1$ ), the profile of the velocity of the developed translational motion is as shown in Figure 5.14(c). In the top half of the cell,  $v_x = u > 0$ , i.e., the flow is in the  $+x$  direction. In the bottom half of the cell,  $v_x = u < 0$ , i.e., the flow is in the  $-x$  direction. The translational motion will affect the rotation of the

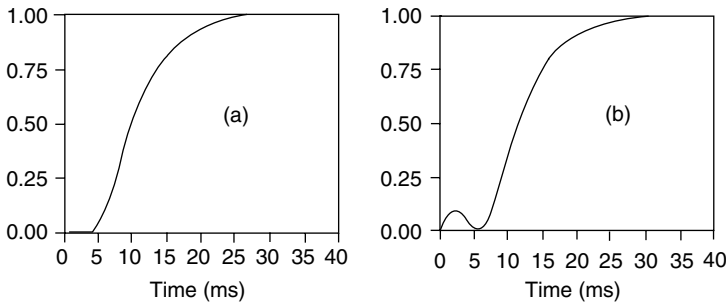
liquid crystal. From Equation (5.128) we have

$$\begin{aligned} \gamma_1 \frac{\partial \theta}{\partial t} &= K \frac{\partial^2 \theta}{\partial z^2} - (\alpha_3 \cos^2 \theta - \alpha_2 \sin^2 \theta) \left\{ \frac{Kt}{\rho \gamma_1} \frac{\partial^2}{\partial z^2} \left[ (-\alpha_2 \sin^2 \theta + \alpha_3 \cos^2 \theta) \frac{\partial^2 \theta}{\partial z^2} \right] \right\} \\ &\approx K \frac{\partial^2 \theta}{\partial z^2} - (\alpha_3 \cos^2 \theta - \alpha_2 \sin^2 \theta)^2 \frac{Kt}{\rho \gamma_1} \frac{\partial^4 \theta}{\partial z^4} \end{aligned} \tag{5.135}$$

The second term on the right hand side of this expression will make the angle increase in the middle of the cell. The translational motion makes the liquid crystal rotate in the opposite direction, which is known as the backflow effect. The strength of the backflow depends on the initial director configuration, which in turn depends on the initially applied field. If the applied field is high, the effect of the backflow is stronger.

In TN and ECB displays, the backflow slows the relaxation of the liquid crystal director from the distorted state under an applied field to the undistorted state at zero field, and may even make the relaxation non-monotonic. The transmittance of a normal-white TN crystal as a function of time is shown in Figure 5.15 after the applied voltage is turned off [16]. When the applied voltage is 5V, the liquid crystal is not well aligned homeotropically. When the applied field is removed, the backflow is not strong and the transmittance increases monotonically as shown in Figure 5.15(a). When the applied voltage is 8V, the liquid crystal is well aligned homeotropically. When the applied field is removed, the backflow is strong and the transmittance does not increase monotonically as shown in Figure 5.15(b). The dip at 6 ms after the removal of the applied voltage is due to the reverse rotation of the liquid crystal caused by the backflow.

Backflow can also be utilized in liquid crystal devices. The bistable TN crystal is such an example [13–15], where the display cell has homogeneous alignment layers. Chiral dopant is added to the liquid crystal in such a way that the intrinsic pitch  $P$  is twice the cell thickness  $h$ . Initially a high voltage is applied across the cell and the liquid crystal is switched to the homeotropic state where there is no twist. If the applied voltage is removed slowly, the tilt angle of the liquid crystal director decreases slowly with time, and the backflow is small. The liquid crystal relaxes to the state where the liquid crystal director is aligned homogeneously, known as the  $0^\circ$  twist state. The free energy of this state is a local minimum and the liquid crystal remains in this state for quite a long period. If the applied voltage is removed quickly, the tilt angle of the liquid crystal director decreases rapidly with time, and the backflow is large. The liquid crystal in the middle of the cell rotates in the direction opposite to the rotation direction of the director near the cell surfaces. The liquid crystal transforms into a state where the director twists  $360^\circ$  from the bottom to the top of the cell. The free energy of this state is also a local minimum and the liquid crystal remains in this state for a long period.



**Figure 5.15** Transmittance vs. time of the normal-white TN crystal after the applied voltage has been removed: (a) 5V; (b) 8V [16]

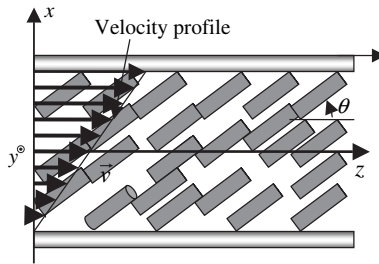


Figure 5.16

## Homework Problems

- 5.1 *Freedericksz in the twist geometry shown in Figure 5.7.* The cell thickness is  $h$ . The free energy is given by Equation (5.42). Use the Euler–Lagrange equation for the minimization of the total free energy to derive the twist angle as a function of the normalized position  $z/h$  when the applied field  $E$  is above the threshold  $E_c$ . The anchoring is infinitely strong and the twist angle at the bottom and top surfaces is zero.
- 5.2 Explain why the voltage threshold in the Freedericksz transition is cell thickness independent.
- 5.3 *Freedericksz in splay geometry.* Use the parameters in Figure 5.3 and Equation (5.30) to calculate and plot the tilt angle at the middle plane as a function of the normalized field  $E/E_c$ .
- 5.4 *Freedericksz in splay geometry.* The cell thickness is  $h$ . Use the parameters in Figure 5.4 to calculate and plot the tilt angle as a function of the normalized position  $z/h$  at the following various fields:  $E/E_c = 1.2$ ,  $E/E_c = 3.0$ , and  $E/E_c = 10$ .
- 5.5 Calculate the transmittance of the VA mode liquid crystal display for R, G, and B light. The parameters of the liquid crystal are  $K_{11} = 6.4 \times 10^{-12} \text{N}$ ,  $K_{33} = 10 \times 10^{-12} \text{N}$ ,  $\Delta\epsilon = -3$ ,  $n_e = 1.57$ , and  $n_o = 1.50$ . The thickness of the cell is  $5.0 \mu\text{m}$ . The wavelengths of the R, G, and B light are  $650 \text{ nm}$ ,  $550 \text{ nm}$ , and  $450 \text{ nm}$ , respectively.
- 5.6 *Flow alignment angle.* Consider a shear as shown in Figure 5.16. The shear rate  $dv/dx = \text{constant}$  and the liquid crystal director is uniformly oriented in the  $x$ – $z$  plane. Show that when  $|\gamma_1/\gamma_2| < 1$ , the tilt angle is given by  $\cos 2\theta = -\gamma_1/\gamma_2$  in the steady state.
- 5.7 Show that in the twist geometry, it is possible to have director motion without any flow.

## References

- 1 J. Mathews and R. L. Walker, *Mathematical methods of physics*, 2nd edn (W. A. Benjamin, Menlo Park, CA, 1970).
- 2 R. Barberi and G. Barbero, ‘Variational calculus and simple applications of continuum theory’, Chapter IX in *Liquid crystal materials*, ed. I. C. Khoo (Gordon and Breach, Amsterdam, 1991).
- 3 P. G. de Gennes and J. Prost, *The physics of liquid crystals* (Oxford University Press, New York, 1993).
- 4 S. Chandrasekhar *Liquid crystals*, 2nd edn (Cambridge University Press, New York, 1997).
- 5 A. Strigazzi, ‘Freedericksz transition’, Chapter X in *Liquid crystal materials*, ed. I. C. Khoo (Gordon and Breach, Amsterdam, 1991).
- 6 T. Scheffer and J. Nehring, ‘Twisted nematic and supertwisted nematic mode LCDs’, in *Liquid crystals—applications and uses*, Vol. 1, ed. B. Bahadur (World Scientific, Singapore, 1990).
- 7 E. P. Raynes, ‘The theory of supertwist transitions’, *Mol. Cryst. Liq. Cryst. Lett.*, **4**, 1 (1986).
- 8 S. Faetti, ‘Anchoring effects in nematic liquid crystals’, Chapter XII in *Liquid crystal materials*, ed. I. C. Khoo (Gordon and Breach, Amsterdam, 1991).

- 9 W. H. de Jeu, 'Physical properties of liquid crystal materials', in *Liquid crystal monographs*, Vol. 1, ed. G. W. Gray (Gordon and Breach, London, 1980).
- 10 P. G. de Gennes and J. Prost, *The physics of liquid crystals* (Oxford University Press, New York, 1993).
- 11 D. Tabor, *Gases, liquids and solids and other states of matter*, 3rd. edn (Cambridge University Press, Cambridge, 1991).
- 12 P. K. Kundu and I. M. Cohen, *Fluid mechanics*, 2nd edn. (Academic Press, San Diego, CA, 2002).
- 13 D. W. Berreman and W. R. Heffner, 'New bistable cholesteric liquid-crystal display', *Appl. Phys. Lett.*, **37**, 109 (1980).
- 14 D. W. Berreman, 'Liquid-crystal twist cell dynamics with backflow', *J. Appl. Phys.*, **46**, 3746 (1975).
- 15 C. Z. van Doorn, 'Dynamic behaviour of twisted nematic', *J. Appl. Phys.*, **46**, 3738 (1975).
- 16 J. Kelly, S. Jamal, and M. Cui, 'Simulation of the dynamics of twisted nematic devices including flow', *J. Appl. Phys.*, **86**, 4091 (1999).



# 6

## Liquid Crystal Materials

### 6.1 Introduction

Liquid crystal (LC) material, although only occupying a small portion in a display or photonic device, makes a decisive contribution to device performance. For instance, the device contrast ratio, response time, viewing angle, and operating voltage are all related to the LC material and how they are aligned. The refractive indices and cell gap determine the phase retardation or phase change of the LC device employed for either amplitude or phase modulation. The dielectric constants and elastic constants jointly determine the threshold voltage. The viscosity, cell gap, and temperature determine the response time.

Absorption is another important factor affecting the physical properties of LC material. Most of the conjugated LC compounds have strong absorption in the ultraviolet (UV) region due to allowed electronic transitions. These UV absorption bands and their corresponding oscillator strengths play important roles in affecting the LC refractive indices and photostability. In the visible region, the electronic absorption tail decays rapidly so that the absorption effect is small and can be ignored. However, molecular vibrations appear in the mid- and long-infrared (IR) regions. The overtones of these vibration bands extend to the near IR ( $\sim 1 \mu\text{m}$ ). The material absorption affects the optical transmittance and especially the power handling capability of a LC-based optical phased array for steering a high-power IR laser beam.

In this chapter, we will first describe the origins of the LC refractive indices and their wavelength and temperature dependencies, and then extend our discussion to dielectric constants, elastic constants, and viscosity.

### 6.2 Refractive Indices

The classic Clausius–Mossotti equation [1] correlates the permittivity ( $\epsilon$ ) of an *isotropic* media with molecular polarizability ( $\alpha$ ) as follows:

$$\frac{\epsilon - 1}{\epsilon + 2} = \frac{4\pi}{3} N\alpha \quad (6.1)$$

In Equation (6.1),  $N$  is the molecular packing density, or number of molecules per unit volume. In the optical frequency regime, we substitute  $\varepsilon = n^2$  and obtain the Lorentz–Lorenz equation [2]:

$$\frac{n^2 - 1}{n^2 + 2} = \frac{4\pi}{3} N\alpha \tag{6.2}$$

For anisotropic LC media, there are two principal refractive indices,  $n_e$  and  $n_o$ , which are the refractive indices for the extraordinary ray and ordinary ray, respectively. In principle, each refractive index is supposedly related to the corresponding molecular polarizabilities,  $\alpha_e$  and  $\alpha_o$ . An earlier approach replaced both  $n^2$  in Equation (6.2) by  $n_{e,o}^2$  and  $\alpha$  by  $\alpha_{e,o}$ . However, this model does not fit the experimental results well. In 1964, Vuks made an assumption that the internal field in a crystal is the same in all directions [3]:

$$E_i = \frac{\langle n^2 \rangle + 2}{3} E \tag{6.3}$$

where  $E_i$  is the internal field, the average field that acts on a molecule, and  $E$  is the macroscopic electric field. With this assumption, Vuks derived the following equation for *anisotropic media*:

$$\frac{n_{e,o}^2 - 1}{\langle n^2 \rangle + 2} = \frac{4\pi}{3} N\alpha_{e,o} \tag{6.4}$$

where

$$\langle n^2 \rangle = (n_e^2 + 2n_o^2)/3 \tag{6.5}$$

Equation (6.4) is different from Equation (6.2) in two aspects: (1) the  $n^2$  term in the denominator of Equation (6.2) is replaced by  $\langle n^2 \rangle$ , while the  $n^2$  term in the numerator is replaced by  $n_{e,o}^2$ ; and (2)  $\alpha$  is replaced by  $\alpha_{e,o}$ . The Vuks equation (6.4) has been validated experimentally using the refractive index data of several LC compounds and mixtures [4].

### 6.2.1 Extended Cauchy equations

In Equation (6.4),  $n_e$  and  $n_o$  are coupled together through the  $\langle n^2 \rangle$  term. By substituting Equation (6.5) into (6.4) and through a series of expansion of the Vuks equation,  $n_e$ ,  $n_o$ , and birefringence  $\Delta n (= n_e - n_o)$  can be expressed as follows [5]:

$$n_e(\lambda, T) \approx n_i(\lambda) + GS \frac{\lambda^2 \lambda^{*2}}{\lambda^2 - \lambda^{*2}} \tag{6.6}$$

$$n_o(\lambda, T) \approx n_i(\lambda) - \frac{GS}{2} \frac{\lambda^2 \lambda^{*2}}{\lambda^2 - \lambda^{*2}} \tag{6.7}$$

$$\Delta n(\lambda, T) \approx \frac{3GS}{2} \frac{\lambda^2 \lambda^{*2}}{\lambda^2 - \lambda^{*2}} \tag{6.8}$$

where  $n_i(\lambda)$  is the LC refractive index in the isotropic phase,  $\langle \alpha \rangle$  is the average molecular polarizability,  $G = (2\sqrt{2}/3) \pi gNZ(f_e^* - f_o^*) / (1 - 4/3 \pi N \langle \alpha \rangle)$  is a proportionality constant, and  $S$

is the order parameter. In the isotropic state,  $n_i(\lambda)$  can be expressed by the traditional Cauchy equation:

$$n_i(\lambda) = A_i + \frac{B_i}{\lambda^2} + \frac{C_i}{\lambda^4} \quad (6.9)$$

where  $A_i$ ,  $B_i$ , and  $C_i$  are the Cauchy coefficients for the isotropic state. The temperature effect of  $N$  (molecular packing density) and  $f_e^* - f_o^*$  (differential oscillator strength) is much smaller than that of  $S$ . Thus, we can assume that  $G$  is insensitive to the temperature. Equation (6.8) is identical to the single band birefringence dispersion model [6].

In the off-resonance region, the terms on the right of Equations (6.6) and (6.7) can be expanded by a power series to the  $\lambda^{-4}$  term and then combined with Equation (6.9) to form the extended Cauchy equations for describing the wavelength-dependent refractive indices of *anisotropic* LCs:

$$n_{e,o} \cong A_{e,o} + \frac{B_{e,o}}{\lambda^2} + \frac{C_{e,o}}{\lambda^4} \quad (6.10)$$

In equation (6.10),  $A_{e,o}$ ,  $B_{e,o}$ , and  $C_{e,o}$  are three Cauchy coefficients. By measuring the refractive indices of a LC material at three wavelengths, these Cauchy coefficients can be determined. Afterward, the refractive indices at any particular wavelength can be extrapolated.

Although the extended Cauchy equation fits the experimental data well [7], its physical origin is not clear. A better physical meaning can be obtained by the three-band model which takes three major electronic transition bands into consideration.

### 6.2.2 Three-band model

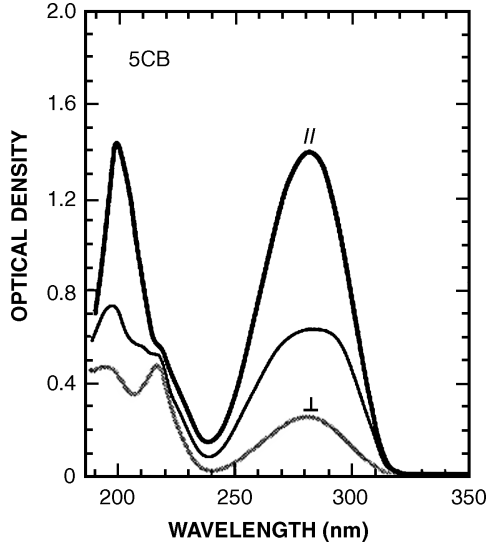
The major absorption of a LC compound occurs in two spectral regions: namely, UV and IR. The  $\sigma \rightarrow \sigma^*$  electronic transitions take place in the vacuum UV (100–180 nm) region whereas the  $\pi \rightarrow \pi^*$  electronic transitions occur in the UV (180–400 nm) region.

Figure 6.1 shows the measured polarized UV absorption spectra of 5CB [8]. To avoid saturation, only 1 wt% of 5CB was dissolved in a UV transparent nematic LC mixture, ZLI-2359. A quartz cell without an indium–tin–oxide (ITO) conductive coating was used. To produce homogeneous alignment, a thin SiO<sub>2</sub> layer was sputtered onto the quartz substrate. The cell gap was controlled at 6  $\mu\text{m}$ . The  $\lambda_1$  band which is centered at  $\sim 200$  nm consists of two closely overlapped bands. The  $\lambda_2$  band shifts to  $\sim 282$  nm. The  $\lambda_0$  band should occur in the vacuum UV region ( $\lambda_0 \sim 120$  nm) which is not shown in Figure 6.1.

If a LC compound had a longer conjugation, its electronic transition wavelength would extend to a longer UV wavelength. In the near-IR region, some overtone molecular vibration bands appear [9]. The fundamental molecular vibration bands, such as CH, CN, and C=C, occur in the mid- and long-IR regions. Typically, the oscillator strength of these vibration bands is about two orders of magnitude weaker than that of the electronic transitions. Thus, the resonant enhancement of these bands to the LC birefringence is localized.

The three-band model takes one  $\sigma \rightarrow \sigma^*$  transition (the  $\lambda_0$  band) and two  $\pi \rightarrow \pi^*$  transitions (the  $\lambda_1$  and  $\lambda_2$  bands) into consideration. In the three-band model, the refractive indices ( $n_e$  and  $n_o$ ) are expressed as follows [10, 11]:

$$n_{e,o} \cong 1 + g_{0e,o} \frac{\lambda^2 \lambda_0^2}{\lambda^2 - \lambda_0^2} + g_{1e,o} \frac{\lambda^2 \lambda_1^2}{\lambda^2 - \lambda_1^2} + g_{2e,o} \frac{\lambda^2 \lambda_2^2}{\lambda^2 - \lambda_2^2} \quad (6.11)$$



**Figure 6.1** Measured polarized UV absorption spectra of 5CB using a homogeneous quartz cell without ITO. || and ⊥ represent the e-ray and o-ray, and the middle curve is for the unpolarized light. Sample: 1 wt% 5CB dissolved in ZLI-2359 (a UV transparent nematic mixture). Cell gap is 6 μm.  $T = 23^\circ\text{C}$ .  $\lambda_1 = 200\text{ nm}$  and  $\lambda_2 = 282\text{ nm}$

In the visible region,  $\lambda > \lambda_0$  ( $\sim 120\text{ nm}$ ) and the  $\lambda_0$  band’s contribution in Equation (6.11) can be approximated by a constant  $n_{0e,o}$  so that Equation (6.11) is simplified as

$$n_{e,o} \cong 1 + n_{0e,o} + g_{1e,o} \frac{\lambda^2 \lambda_1^2}{\lambda^2 - \lambda_1^2} + g_{2e,o} \frac{\lambda^2 \lambda_2^2}{\lambda^2 - \lambda_2^2} \tag{6.12}$$

The three-band model clearly describes the origins of refractive indices of LC compounds. However, a commercial mixture usually consists of several compounds with different molecular structures in order to obtain a wide nematic range. The individual  $\lambda_i$  are therefore different. Under such circumstances, Equation (6.12) would have too many unknowns to describe the refractive indices of a LC mixture.

To model the refractive indices of a LC mixture, we could expand Equation (6.12) into a power series because in the visible and IR spectral regions,  $\lambda > \lambda_2$ . By keeping up to  $\lambda^{-4}$  terms, the above extended Cauchy equation (6.10) is again derived.

Although Equation (6.10) is derived based on a LC compound, it can be extended easily to include eutectic mixtures by taking the superposition of each compound. From Equation (6.10), if we measure the refractive indices at three wavelengths, the three Cauchy coefficients ( $A_{e,o}$ ,  $B_{e,o}$ , and  $C_{e,o}$ ) can be obtained by fitting the experimental results. Once these coefficients are determined, the refractive indices at any wavelength can be calculated. From Equations (6.8) and (6.10), both refractive indices and birefringence decrease as the wavelength increases. In the long-wavelength (IR and millimeter wave) region,  $n_e$  and  $n_o$  are reduced to  $A_e$  and  $A_o$ , respectively. The coefficients  $A_e$  and  $A_o$  are constants; they are independent of wavelength, but dependent on temperature. That means that, in the IR region, the refractive indices are insensitive to wavelength, except for the resonance enhancement effect near the local molecular vibration bands. This prediction is consistent with much experimental evidence [12].

Equation (6.10) applies equally well to both high- and low-birefringence LC materials in the off-resonance region. For low-birefringence ( $\Delta n < 0.12$ ) LC mixtures, the  $\lambda^{-4}$  terms are insignificant and can be omitted. Thus,  $n_e$  and  $n_o$  each have only two fitting parameters. The two-coefficient Cauchy model has the following simple form [13]:

$$n_{e,o} \cong A_{e,o} + \frac{B_{e,o}}{\lambda^2} \quad (6.13)$$

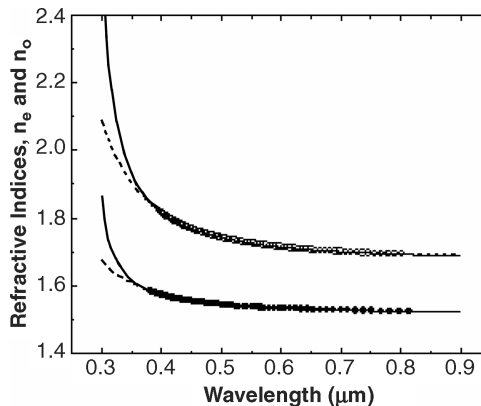
By measuring the refractive indices at two wavelengths, we can determine  $A_{e,o}$  and  $B_{e,o}$ . Once these two parameters are found,  $n_e$  and  $n_o$  can be calculated at any wavelength of interest.

For most LC displays [14], the cell gap is controlled at around  $4 \mu\text{m}$  so that the required birefringence is smaller than 0.12. Thus, Equation (6.13) can be used to describe the wavelength-dependent refractive indices. For IR applications, high-birefringence LC mixtures are required [15]. Under such circumstances, the three-coefficient extended Cauchy model (Equation (6.10)) should be used.

Figure 6.2 shows the fittings of experimental data of 5CB using the three-band model (solid lines) and the extended Cauchy equations (dashed lines). The fitting parameters are listed in Table 6.1. In the visible and near-IR regions, both models give excellent fits to the experimental data. In the UV region, the deviation between these two models becomes more apparent. The three-band model considers the resonance effect, but the extended Cauchy model does not. Thus, in the near-resonance region the results from the three-band model are more accurate.

### 6.2.3 Temperature effect

The temperature effect is particularly important for projection displays [16]. Due to the thermal effect of the lamp, the temperature of the display panel could reach  $50^\circ\text{C}$ . It is important to know beforehand the LC properties at the anticipated operating temperature. The thermal non-linearity of LC refractive indices is also very important for some new photonic applications, such as LC photonic bandgap fibers [17, 18] and thermal solitons [19, 20].



**Figure 6.2** Wavelength-dependent refractive indices of 5CB at  $T = 25.1^\circ\text{C}$ . Open and solid circles are experimental data for  $n_e$  and  $n_o$ , respectively. The solid line represents the three-band model and dashed lines are for the extended Cauchy model. The fitting parameters are listed in Table 6.1. Reprinted with permission from J. Li and S.-T. Wu, 'Extended Cauchy equations for the refractive indices of liquid crystals', *Journal of Applied Physics*, February 1, 2004, Volume 95, Issue 3, pp. 896, Figure 2, © 2004, American Institute of Physics

**Table 6.1** Fitting parameters for the three-band model and the extended Cauchy equations. LC: 5CB at  $T = 25.1^\circ\text{C}$ . The units of Cauchy's  $B$  and  $C$  coefficients are  $\mu\text{m}^2$  and  $\mu\text{m}^4$ , respectively

Model	$n_e$			$n_o$		
	$n_{0e}$	$g_{1e}$	$g_{2e}$	$n_{0o}$	$g_{1o}$	$g_{2o}$
Three-band model	0.4618	2.1042	1.4413	0.4202	1.2286	0.4934
Cauchy model	$A_e$	$B_e$	$C_e$	$A_o$	$B_o$	$C_o$
	1.6795	0.0048	0.0027	1.5187	0.0016	0.0011

Birefringence  $\Delta n$  is defined as the difference between the extraordinary and ordinary refractive indices,  $\Delta n = n_e - n_o$ , and the average refractive index  $\langle n \rangle$  is defined as  $\langle n \rangle = (n_e + 2n_o)/3$ . Based on these two definitions,  $n_e$  and  $n_o$  can be rewritten as follows:

$$n_e = \langle n \rangle + \frac{2}{3}\Delta n \tag{6.14}$$

$$n_o = \langle n \rangle - \frac{1}{3}\Delta n \tag{6.15}$$

To describe the temperature-dependent birefringence, the Haller approximation has been commonly employed when the temperature is not too close to the clearing point [21]:

$$\Delta n(T) = (\Delta n)_o(1 - T/T_c)^\beta \tag{6.16}$$

In Equation (6.16),  $(\Delta n)_o$  is the LC birefringence in the crystalline state (or  $T = 0\text{ K}$ ), the exponent  $\beta$  is a material constant, and  $T_c$  is the clearing temperature of the LC material under investigation. On the other hand, the average refractive index decreases linearly with increasing temperature as [22]:

$$\langle n \rangle = A - BT \tag{6.17}$$

because the LC density decreases with increasing temperature.

Figure 6.3 plots the temperature-dependent density of 5CB [23]. At room temperature, the density of 5CB is around  $1.02\text{ g/cm}^3$ , slightly heavier than that of water because of its higher molecular weight. As the temperature increases, the density decreases almost linearly. Due to the second-order phase transition, a disrupt density change occurs at  $T \sim 35.3^\circ\text{C}$ . In the isotropic state, the 5CB density continues to decrease linearly as the temperature increases.

By substituting Equations (6.16) and (6.17) back into Equations (6.14) and (6.15), the four-parameter model for describing the temperature dependence of the LC refractive indices is derived [24]:

$$n_e(T) \approx A - BT + \frac{2(\Delta n)_o}{3} \left(1 - \frac{T}{T_c}\right)^\beta \tag{6.18}$$

$$n_o(T) \approx A - BT - \frac{(\Delta n)_o}{3} \left(1 - \frac{T}{T_c}\right)^\beta \tag{6.19}$$

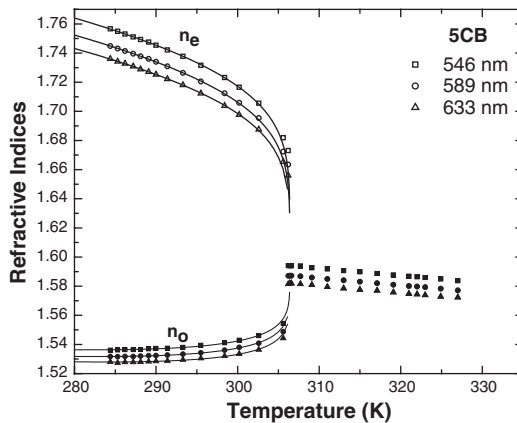
The parameters  $[A, B]$  and  $[(\Delta n)_o, \beta]$  can be obtained respectively by two-stage fittings. To obtain  $[A, B]$ , we fit the average refractive index  $\langle n \rangle = (n_e + 2n_o)/3$  as a function of temperature using

Publisher's Note:  
 Permission to reproduce this image  
 online was not granted by the  
 copyright holder. Readers are kindly  
 requested to refer to the printed version  
 of this chapter.

**Figure 6.3** Temperature-dependent density of 5CB. Reprinted Figure 1 with permission from H. R. Zeller, 'Dielectric relaxation in nematics and Doolittle's law', *Physical Review A*, Volume 26, Issue 3, pp. 1785, February 4, 1982, © 1982 by the American Physical Society

Equation (6.15). To find  $[(\Delta n)_o, \beta]$ , we fit the birefringence data as a function of temperature using Equation (6.14). Therefore, these two sets of parameters can be obtained separately from the same set of refractive indices but in different forms.

Figure 6.4 plots the temperature-dependent refractive indices of 5CB at  $\lambda = 546, 589,$  and  $633\text{nm}$ . As the temperature increases,  $n_e$  decreases, but  $n_o$  gradually increases. In the isotropic state  $n_e = n_o$  and the refractive index decreases linearly with increasing temperature.



**Figure 6.4** Temperature-dependent refractive indices of 5CB at  $\lambda = 546, 589,$  and  $633\text{nm}$ . Squares, circles, and triangles are experimental data for refractive indices measured at  $\lambda = 546, 589,$  and  $633\text{nm}$ , respectively

6.2.4 Temperature gradient

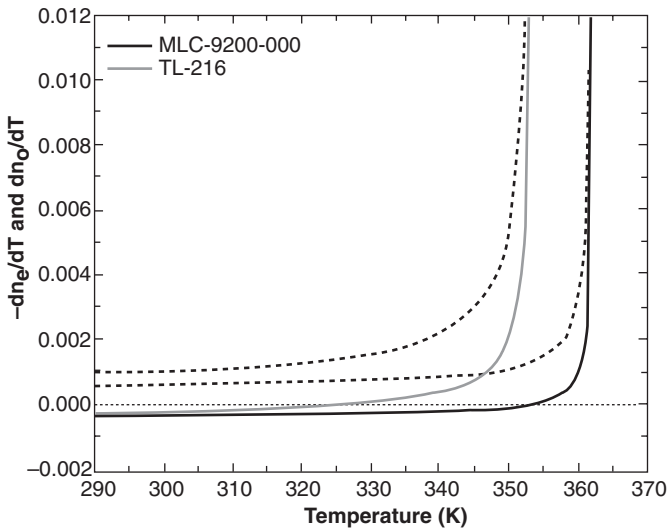
Based on Equations (6.18) and (6.19), we can derive the temperature gradient for  $n_e$  and  $n_o$ , respectively:

$$\frac{dn_e}{dT} = -B - \frac{2\beta(\Delta n)_o}{3T_c(1 - T/T_c)^{1-\beta}} \tag{6.20}$$

$$\frac{dn_o}{dT} = -B + \frac{\beta(\Delta n)_o}{3T_c(1 - T/T_c)^{1-\beta}} \tag{6.21}$$

In Equation (6.20), both terms on the right hand side are negative, independent of temperature. This implies that  $n_e$  decreases as the temperature increases throughout the entire nematic range. However, Equation (6.21) consists of a negative term ( $-B$ ) and a positive term which depends on the temperature. In the low-temperature regime ( $T < T_c$ ), the positive term could be smaller than the negative term resulting in a negative  $dn_o/dT$ . As the temperature increases, the positive term also increases. As  $T$  approaches  $T_c$ ,  $dn_o/dT$  jumps to a large positive number. In the intermediate region, there exists a transition temperature where  $dn_o/dT = 0$ . Let us define this temperature as the crossover temperature  $T_o$  for  $n_o$ . To find  $T_o$ , we simply solve  $dn_o/dT = 0$  from Equation (6.21).

Figure 6.5 depicts the temperature-dependent values of  $-dn_e/dT$  and  $dn_o/dT$  for two Merck LC mixtures, MLC-9200-000 and TL-216. In Figure 6.5, the values of  $-dn_e/dT$  for both LC mixtures remain positive throughout their nematic range. This means that  $n_e$ , the extraordinary refractive index, decreases monotonously as the temperature increases in the entire nematic range. However,  $dn_o/dT$



**Figure 6.5** Temperature gradient for  $n_e$  and  $n_o$  of MLC-9200-000 and TL-216 at  $\lambda = 546$  nm. Black and gray solid lines represent the calculated  $dn_o/dT$  curves for MLC-9200-000 and TL-216, respectively, while the dashed lines represent the calculated  $-dn_e/dT$  curves. The crossover temperatures for MLC-9200-000 and TL-216 are around 80.1 and 52.7 °C, respectively. Reproduced with permission from J. Li *et al.*, ‘High temperature-gradient refractive index liquid crystals’, *Optical Express*, Volume 12, pp. 2002–2010 (May 3, 2004), Figure 6.5, © 2004, Optical Society of America



changes sign at the crossover temperature  $T_o$ . The values of  $dn_o/dT$  are negative when the temperature is below  $T_o$ , but becomes positive when the temperature is beyond  $T_o$ . This implies that  $n_o$ , the ordinary refractive index, decreases as the temperature increases when the temperature is below  $T_o$ , but increases with temperature when the temperature is above  $T_o$ .

### 6.2.5 Molecular polarizabilities

Since the Vuks equation correlates the macroscopic refractive index with the microscopic molecular polarizability, if we know the refractive index, then we can calculate the molecular polarizability, or vice versa. For instance, if we know the  $n_e$  and  $n_o$  data of a LC, then we can calculate its  $\alpha_e$  and  $\alpha_o$  values at different temperatures and wavelengths.

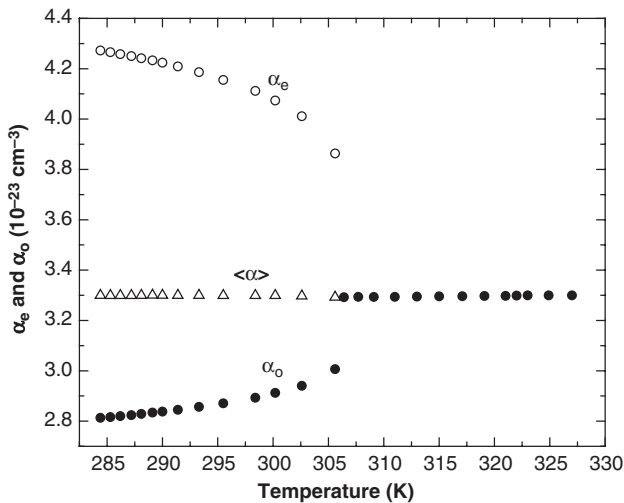
In Equation (6.4), there is still an unknown parameter  $N$ , the number of molecules per unit volume. However,  $N$  is equal to  $\rho N_A/M$ , where  $\rho$  is the LC density,  $M$  is the molecular weight, and  $N_A$  is the Avogadro number. Rearranging Equation (6.4), we find

$$\alpha_e = \frac{3M}{4\pi\rho N_A} \cdot \frac{n_e^2 - 1}{\langle n^2 \rangle + 2} \quad (6.22)$$

$$\alpha_o = \frac{3M}{4\pi\rho N_A} \cdot \frac{n_o^2 - 1}{\langle n^2 \rangle + 2} \quad (6.23)$$

Let us use 5CB (cyano-biphenyl) as an example to calculate the molecular polarizabilities. For 5CB, the molecular weight is  $M = 249.3$  g/mol and the density  $\rho(T)$  is taken from Figure 6.3. Using the measured refractive indices at  $\lambda = 589$  nm, we can calculate the  $\alpha_e$  and  $\alpha_o$  of 5CB from Equations (6.22) and (6.23).

Figure 6.6 plots the temperature-dependent  $\alpha_e$ ,  $\alpha_o$ , and  $\langle\alpha\rangle$  of 5CB at  $\lambda = 589$  nm. In the isotropic state,  $\alpha_e$  and  $\alpha_o$  are equal. From Figure 6.6,  $\alpha_e$  decreases while  $\alpha_o$  increases as the temperature



**Figure 6.6** Temperature-dependent molecular polarizabilities  $\alpha_e$  and  $\alpha_o$  of 5CB at  $\lambda = 589$  nm. Open and filled circles are the results for  $\alpha_e$  and  $\alpha_o$ , respectively. Triangles represent the average polarizability  $\langle\alpha\rangle$ . In the isotropic phase,  $\alpha_e = \alpha_o$

increases. However, the average polarizability  $\langle\alpha\rangle$  is quite insensitive to the temperature. The average polarizability for 5CB at  $\lambda = 589 \text{ nm}$  is found to be  $\langle\alpha\rangle \sim 3.3 \times 10^{-23} \text{ cm}^{-3}$ , which agrees very well with the calculated value ( $\langle\alpha\rangle \sim 3.25 \times 10^{-23} \text{ cm}^{-3}$ ) published by Sarkar *et al.* [25].

### 6.3 Dielectric Constants

The dielectric constants of a LC affect the operation voltage, resistivity, and response time. For example, in a vertical alignment (VA) cell the threshold voltage ( $V_{th}$ ) is related to the dielectric anisotropy ( $\Delta\epsilon = \epsilon_{\parallel} - \epsilon_{\perp}$ ) and bend elastic constant ( $K_{33}$ ) as [26]:

$$V_{th} = \pi\sqrt{\epsilon_o K_{33}/\Delta\epsilon} \quad (6.24)$$

Thus, low threshold voltage can be obtained by either enhancing the dielectric anisotropy, or reducing the elastic constant, or a combination of both. However, a smaller elastic constant slows down the response time because of the weaker restoring torque.

Dielectric constants of a LC are mainly determined by the dipole moment ( $\mu$ ), its orientation angle ( $\theta$ ) with respect to the principal molecular axis, and order parameter ( $S$ ), as described by the Maier and Meier mean field theory [27]:

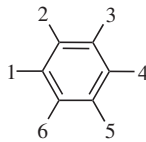
$$\epsilon_{\parallel} = NhF\left\{\langle\alpha_{\parallel}\rangle + (F\mu^2/3kT)[1 - (1 - 3\cos^2\theta)S]\right\} \quad (6.25)$$

$$\epsilon_{\perp} = NhF\left\{\langle\alpha_{\perp}\rangle + (F\mu^2/3kT)[1 + (1 - 3\cos^2\theta)S/2]\right\} \quad (6.26)$$

$$\Delta\epsilon = NhF\left\{(\langle\alpha_{\parallel}\rangle - \langle\alpha_{\perp}\rangle) - (F\mu^2/2kT)(1 - 3\cos^2\theta)S\right\} \quad (6.27)$$

Here,  $N$  stands for the molecular packing density,  $h = 3\epsilon/(2\epsilon + 1)$  is the cavity field factor,  $\epsilon = (\epsilon_{\parallel} + 2\epsilon_{\perp})/3$  is the averaged dielectric constant,  $F$  is the Onsager reaction field, and  $\langle\alpha_{\parallel}\rangle$  and  $\langle\alpha_{\perp}\rangle$  are the principal elements of the molecular polarizability tensor.

From Equation (6.27), for a non-polar compound,  $\mu \sim 0$  and its dielectric anisotropy is very small ( $\Delta\epsilon < 0.5$ ). In this case,  $\Delta\epsilon$  is determined mainly by the differential molecular polarizability, i.e., the first term in Equation (6.27). For a polar compound, the dielectric anisotropy depends on the dipole moment, angle  $\theta$ , temperature ( $T$ ), and applied frequency. If a LC has more than one dipole, then the resultant dipole moment is their vector summation. In a phenyl ring, the position of the dipole is defined as



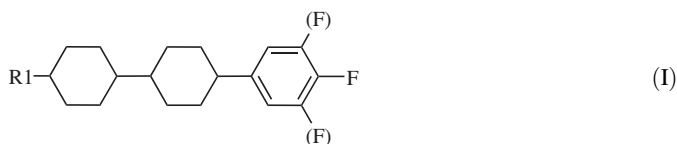
From Equation (6.27), if a polar compound has an effective dipole at  $\theta < 55^\circ$ , then its  $\Delta\epsilon$  will be positive. On the other hand,  $\Delta\epsilon$  becomes negative if  $\theta > 55^\circ$ .

Fluoro (F) [28], cyano (CN) [29], and isothiocyanato (NCS) [30] are the three commonly employed polar groups. Among them, the fluoro group possesses a modest dipole moment ( $\mu \sim 1.5$  debyes), high resistivity, and low viscosity. However, its strong negativity compresses the electron clouds and, subsequently, lowers the compound's birefringence. As a result, the fluorinated compounds are more suitable for visible display applications where the required birefringence is around 0.1.

For IR applications, a higher birefringence ( $\Delta n > 0.3$ ) compound is needed in order to compensate for the longer wavelength. To obtain a higher birefringence, two approaches can be taken to enhance the electron conjugation length: (1) by elongating the core structure, e.g., tolane and terphenyl; and (2) by attaching an electron acceptor polar group, such as CN and NCS. The CN group has a larger dipole moment ( $\mu \sim 3.9$  debyes) than NCS ( $\mu \sim 3.7$  debyes) because of its linear structure. However, due to the very strong polarization of the carbon–nitrogen triple bond, the Huckel charges of carbon and nitrogen are high and well localized. Accordingly, dimers are formed by the strong intermolecular interactions between the nitrile group and phenyl ring. Thus, a relatively high viscosity is observed in the cyano-based LC mixtures. On the other hand, the Huckel charges of nitrogen, carbon, and sulfur are smaller in the NCS group. The predicted intermolecular interactions by the NCS group in the isothiocyanato-benzene systems are smaller than those in the nitrile-based systems. The dimers are not formed and, therefore, the viscosity of such molecular systems is lower than that of nitrile-based ones. Due to the longer  $\pi$ -electron conjugation, the NCS-based LC compounds exhibit a higher birefringence than the corresponding CN compounds.

### 6.3.1 Positive $\Delta\epsilon$ LCs active matrix LC displays

Positive  $\Delta\epsilon$  LCs have been used in twisted nematic (TN) [31] and in-plane switching (IPS) [32, 33] displays, although IPS can also use negative  $\Delta\epsilon$  LCs. For displays based on the thin-film-transistor (TFT), the employed LC material must possess a high resistivity [34]. Fluorinated compounds exhibit a high resistivity and are the natural candidates for TFT LCD applications [35, 36]. A typical fluorinated LC structure is shown below:



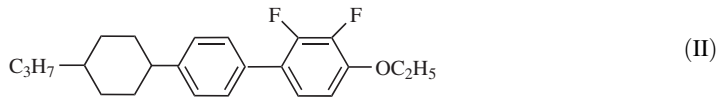
From Equation (6.27), to obtain the largest  $\Delta\epsilon$  for a given dipole, the best position for the fluoro substitution is along the principal molecular axis, i.e., in the 4 position. The single fluoro compound should have  $\Delta\epsilon \sim 5$ . To further increase  $\Delta\epsilon$ , more fluoro groups can be added. For example, compound (I) has two more fluoro groups in the 3 and 5 positions [37]. Its  $\Delta\epsilon$  should increase to  $\sim 10$ , but its birefringence would slightly decrease (because of the lower molecular packing density) and its viscosity increases substantially (because of the higher moment of inertia). Besides fluoro, the  $\text{OCF}_3$  group is found to exhibit a fairly low viscosity. Low-viscosity LC is helpful for improving response times [38].

The birefringence of compound (I) is around 0.07. If a higher birefringence is needed, the middle cyclohexane ring can be replaced by a phenyl ring. The elongated electron cloud will increase the birefringence to about 0.12. The phase transition temperatures of a LC compound are difficult to predict beforehand. In general, the lateral fluoro substitution would lower the melting temperature of the parent compound because the increased molecular separation leads to a weaker intermolecular association. Thus, a smaller thermal energy is able to separate the molecules. That means that the melting point is decreased.

### 6.3.2 Negative $\Delta\epsilon$ LCs

For VA [39], the LC employed should have a negative dielectric anisotropy. From Equation (6.27), in order to obtain a negative dielectric anisotropy, the dipoles should be in the lateral (2, 3) positions. Similarly, in the interests of obtaining high resistivity, the lateral difluoro group is a favorable choice.

A typical negative  $\Delta\epsilon$  LC compound is shown below [40]:

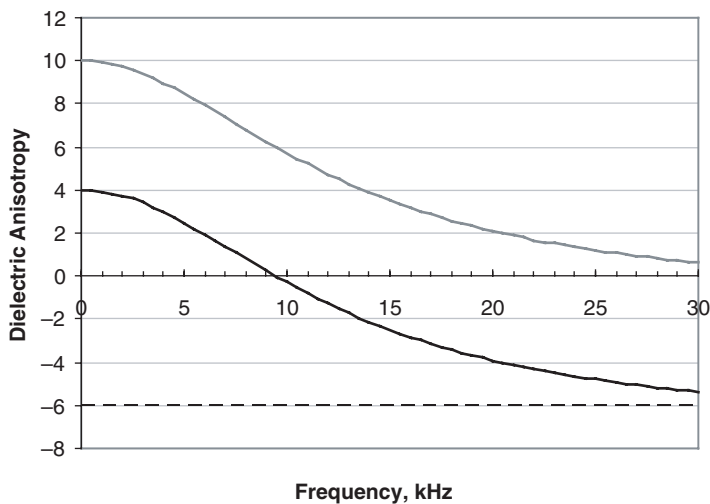


Compound (II) has two lateral fluoro groups. Their dipole components in the horizontal axis are perfectly cancelled. On the other hand, the vertical components add up. As a result,  $\Delta\epsilon$  is negative. The neighboring alkoxy group also contributes to enhance the negative  $\Delta\epsilon$ . However, its viscosity is somewhat larger than that of an alkyl group. The estimated  $\Delta\epsilon$  of compound is about  $-4$ . To further increase  $\Delta\epsilon$ , more fluoro groups need to be substituted. That would increase the viscosity unfavorably. This is a common problem of negative LCs. It is not easy to increase  $\Delta\epsilon$  value without tradeoffs.

### 6.3.3 Dual-frequency LCs

Dual-frequency LC (DFLC) [41, 42] exhibits a unique feature where its  $\Delta\epsilon$  changes from positive at low frequencies to negative as the frequency passes the crossover frequency ( $f_c$ ), as Figure 6.7 shows. The frequency when  $\Delta\epsilon = 0$  is called the crossover frequency. The major attraction of a DFLC device is its fast response time. During the turn-on and turn-off processes, AC voltage bursts with low and high frequencies are applied. As a result, rapid rise and decay times can be achieved [43].

In practice, a DFLC mixture is composed of some positive (with an ester group) and negative  $\Delta\epsilon$  LC compounds and its crossover frequency is around a few kilohertz, depending on the molecular structures and compositions [44]. The  $\Delta\epsilon$  of the ester compounds is frequency dependent, as shown by the top gray line in Figure 6.7. As the frequency increases,  $\Delta\epsilon$  decreases gradually. However,  $\Delta\epsilon$  for the negative components of the DFLC mixture remains fairly flat, as depicted by the bottom dashed line. The resultant  $\Delta\epsilon$  is frequency dependent, as plotted by the middle solid line. In this example, the crossover frequency occurs at about 9.2 kHz.



**Figure 6.7** Frequency-dependent dielectric anisotropy of a positive LC mixture whose  $\Delta\epsilon$  is frequency dependent (top), a negative  $\Delta\epsilon$  LC mixture (bottom), and a DFLC mixture (middle)

## 6.4 Rotational Viscosity

Viscosity, especially rotational viscosity ( $\gamma_1$ ), plays a crucial role in the LCD response time. The response time of a nematic LC device is linearly proportional to  $\gamma_1$  [45]. The rotational viscosity of an aligned LC depends on the detailed molecular constituents, structure, intermolecular association, and temperature. As the temperature increases, viscosity decreases rapidly. Several theories, rigorous or semi-empirical, have been developed in an attempt to account for the origin of the LC viscosity [46, 47]. However, due to the complicated anisotropic attractive and steric repulsive interactions among LC molecules, these theoretical results are not completely satisfactory [48, 49].

A general temperature-dependent rotational viscosity can be expressed as

$$\gamma_1 = bS \cdot \exp(E/kT) \quad (6.28)$$

where  $b$  is a proportionality constant which takes into account the molecular shape, dimension, and moment of inertia,  $S$  is the order parameter,  $E$  is the activation energy of molecular rotation,  $k$  is the Boltzmann constant, and  $T$  is the operating temperature. When the temperature is not too close to the clearing point ( $T_c$ ), the order parameter can be approximated as follows:

$$S = (1 - T/T_c)^\beta \quad (6.29)$$

In Equation (6.29),  $\beta$  is a material parameter. Generally, rotational viscosity is a complicated function of molecular shape, moment of inertia, activation energy, and temperature. Among these factors, activation energy and temperature are the most crucial ones [50]. The activation energy depends on the detailed intermolecular interactions. An empirical rule is that for every 10 degrees of temperature rise, the rotational viscosity drops by about two times.

From the molecular structure standpoint, a linear LC molecule is more likely to have a low viscosity [51]. However, all the other properties need to be taken into account too. For instance, a linear structure may lack flexibility and lead to a higher melting point. Within the same homologues, a longer alkyl chain will in general (except for the even-odd effect) have a lower melting temperature. However, its moment of inertia is increased. As a result, the homologue with a longer chain length is likely to exhibit higher viscosity.

## 6.5 Elastic Constants

There are three basic elastic constants (splay  $K_{11}$ , twist  $K_{22}$ , and bend  $K_{33}$ ) involved in the electro-optics of a LC cell depending on the molecular alignment [52]. Elastic constants affect a LC device through threshold voltage and response time. For example, the threshold voltage of a VA cell is expressed in Equation (6.24). A smaller elastic constant will result in a lower threshold voltage; however, the response time, which is proportional to the visco-elastic coefficient, the ratio of  $\gamma_1/K_{ii}$ , is increased. Therefore, proper balance between threshold voltage and response time should be taken into consideration.

Several molecular theories have been developed for correlating the Frank elastic constants with molecular constituents. The commonly employed one is mean field theory [53, 54]. In the mean field theory, the three elastic constants are expressed as:

$$K_{ii} = a_i S^2 \quad (6.30)$$

where  $a_i$  is a proportionality constant.

For many of the LC compounds and mixtures that have been studied, the magnitude of elastic constants has the following order:  $K_{33} > K_{11} > K_{22}$ . Therefore, LC alignment also plays an essential role in achieving a fast response time. For example, a VA cell ( $K_{33}$  effect) should have a faster response time

than an IPS cell ( $K_{22}$  effect) due to the elastic constant effect, provided that all the other parameters such as cell gap and viscosity remain the same. Usually, the lateral difluoro substitutions increase viscosity to a certain extent because of the increased molecular moment of inertia.

### 6.6 Figure-of-merit (FoM)

To compare the performance of different LC materials, a figure-of-merit (FoM) has been defined as [55]:

$$FoM = K(\Delta n)^2/\gamma_1 \tag{6.31}$$

In Equation (6.31),  $K$  is the elastic constant for a given molecular alignment. For example,  $K = K_{33}$  for a VA cell, and  $K = K_{11}$  for a planar (homogeneous) cell.  $K$ ,  $\Delta n$ , and  $\gamma_1$  are temperature dependent. Using Equations (6.16), (6.28), (6.29), and (6.30) for the corresponding temperature dependency, the FoM is derived as follows:

$$FoM = (a_i/b)(\Delta n_o)^2(1 - T/T_c)^{3\beta} \cdot \exp(-E/kT) \tag{6.32}$$

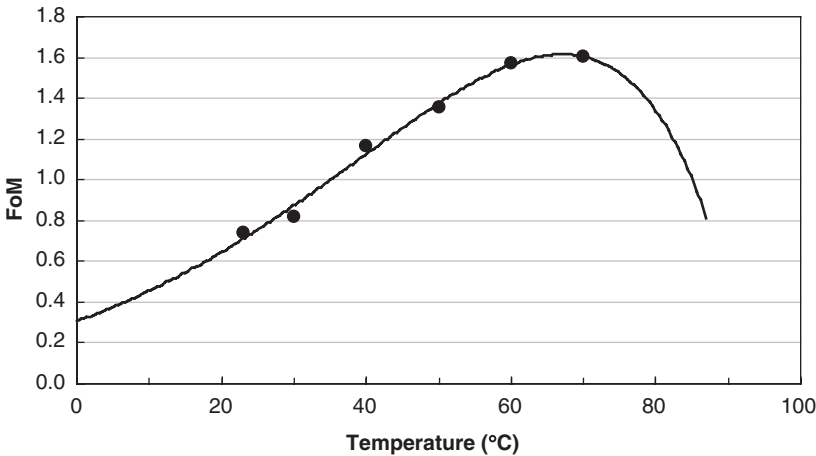
Equation (6.32) has a maximum at an optimal operating temperature  $T_{op}$ :

$$T_{op} = \frac{E}{6\beta k_o}[\sqrt{1 + 12\beta k_o T_c/E} - 1] \tag{6.33}$$

The quantity  $12\beta k_o T_c/E$  in Equation (6.33) is small, and the square root term can be expanded into a power series. Keeping the lowest order terms, we find:

$$T_{op} \sim T_c(1 - 3\beta k_o T_c/E + \dots) \tag{6.34}$$

Figure 6.8 shows the temperature-dependent FoM of Merck MLC-6608, a negative  $\Delta\epsilon$  LC mixture. The results were measured using a He-Ne laser with  $\lambda = 633$  nm. The clearing temperature of



**Figure 6.8** Temperature-dependent FoM of MLC-6608.  $\lambda = 633$  nm. The solid circles are experimental data and the solid line is fitted using Equation (6.32) with  $\beta = 0.272$  and  $E = 325$  meV

MLC-6608 is  $T_c = 92.1^\circ\text{C}$ . From fitting to Equation (6.32),  $\beta = 0.272$  and  $E = 325$  meV are obtained. At room temperature, the FoM is about 0.8. As the temperature increases, the FoM increases gradually and reaches a peak ( $\sim 1.6$ ) at  $T_{op} \sim 70^\circ\text{C}$  and then drops sharply. The optimal operating temperature is about  $20^\circ\text{C}$  below  $T_c$ . For a LCD TV application, about 50% of the backlight is absorbed by the polarizer, which is laminated onto the glass substrates. The absorbed light will be converted to heat. As a result, the LC temperature could reach about  $35\text{--}40^\circ\text{C}$ . From Figure 6.8, the FoM at  $T \sim 40^\circ\text{C}$  is about 60% higher than that at room temperature.

## 6.7 Index Matching Between LCs and Polymers

Polymer-dispersed LC (PDLC) [56] and polymer-stabilized LC have been used for displays [57] and photonic devices [58]. In a PDLC, the refractive index difference between the LC droplets and polymer matrix plays an important role in determining the voltage-off and voltage-on state transmittance. In a normal-mode PDLC, the droplet size is controlled at  $\sim 1\mu\text{m}$ , which is comparable to the wavelength of visible light. In the voltage-off state, the droplets are randomly oriented. The index mismatch between the LC (whose average refractive index is given by  $\langle n \rangle = (n_e + 2n_o)/3$  and polymer matrix ( $n_p$ ) affects the light-scattering capability. For a given droplet size, the larger the index mismatch, the higher the light scattering. Conversely, in the voltage-on state the LC directors inside the droplets are reoriented along the electric field direction so that the refractive index becomes  $n_o$ , the ordinary refractive index. If  $n_o \sim n_p$ , then the PDLC becomes isotropic and will have an excellent transmittance. Therefore, the preferred LC material for PDLC is not only of high birefringence ( $\Delta n = n_e - n_o$ ) but also a good index match between  $n_o$  and  $n_p$ . In a polymer-stabilized LC system, polymer networks help to improve the response time. A good index match would reduce light scattering.

### 6.7.1 Refractive index of polymers

NOA65 (Norland Optical Adhesive 65) is a commonly used photocurable polymer because its refractive index ( $n_p \sim 1.52$ ) is close to the  $n_o$  of many commercial LC mixtures. Before UV curing, NOA65 is a clear and colorless liquid. The measurement of the monomer is fairly simple. However, in a practical device, such as a PDLC, all the monomers are cured to form a polymer matrix. Therefore, it is more meaningful to measure the refractive index of the cured polymers than the monomers.

To prepare a polymer film, the monomer is infiltrated into an empty cell with a 1 mm gap using capillary flow [59]. During the experiment, the cells were placed on a hot plate at a constant temperature ( $T \sim 50^\circ\text{C}$ ) and then illuminated with a uniform UV light ( $I = 14$  mW/cm<sup>2</sup>,  $\lambda \sim 365$  nm) for 40 minutes because of the large cell gap. Afterward, the glass substrates were peeled off and the thick polymer film was removed under a high temperature ( $T \sim 120^\circ\text{C}$ ). The film was kept in a stove at a constant temperature of  $50^\circ\text{C}$  for 12 hours to age completely. The cured polymer film of NOA65 was quite flexible. In order to get an accurate measurement, the films were cut into rectangular parallelepipeds 15 mm long, 9 mm wide, and 1 mm thick. The bottom surface of the samples was polished so that it completely contacted the main prism surface of the Abbe refractometer. First, a small drop of contact liquid (monobromonaphthalene) was placed on the main prism before the sample. It is essential to spread the contact liquid evenly between the sample and the main prism and get rid of any dust or bubbles between the solid sample and the main prism. A lighting glass was used to compensate for the weak light because the samples are thin. Similarly, a small amount of the contact liquid was spread on the top surface of the sample and the lighting glass was placed on top of the contact liquid. The thin contact liquid should be spread evenly between the sample and the lighting glass. At this stage, the contact liquid is sandwiched as films between the main prism and the

**Table 6.2** The measured refractive index ( $n$ ) of cured NOA65 film at  $\lambda = 450, 486, 546, 589, 633,$  and  $656$  nm at different temperatures

$T(^{\circ}\text{C})$	$\lambda$ (nm)					
	450	486	546	589	633	656
20	1.5396	1.5352	1.5301	1.5275	1.5255	1.5243
25	1.5391	1.5347	1.5296	1.5270	1.5250	1.5239
30	1.5386	1.5343	1.5292	1.5266	1.5246	1.5235
35	1.5377	1.5335	1.5282	1.5254	1.5233	1.5225
40	1.5363	1.5324	1.5272	1.5245	1.5222	1.5214
45	1.5352	1.5311	1.5261	1.5235	1.5211	1.5204
50	1.5340	1.5305	1.5248	1.5223	1.5202	1.5192
55	1.5330	1.5298	1.5243	1.5217	1.5194	1.5187

sample, and between the sample and the lighting glass. The incident light entered the sample slightly aslant from the upside.

Table 6.2 lists the measured refractive indices of NOA65 at various wavelengths and temperatures.

The refractive index of NOA65 was also measured in the monomer state. After UV curing, the refractive index of the cured polymers increases by 1.7% for NOA65. This slight refractive index increase originates from the increased density of the polymer after cross-linking.

For a normal-mode PDLC, the light scattering in the voltage-off state depends on the LC birefringence: the higher the birefringence, the higher the scattering efficiency. In the voltage-on state, the transmittance depends on the refractive index match between the LC ( $n_o$ ) and the polymer matrix ( $n_p$ ). If  $n_o \sim n_p$ , then the on-state will be highly transparent. After measuring the  $n_p$  of NOA65, two commercial high-birefringence LC series are selected with their  $n_o$  close to  $n_p$ . The two LC series are the BL-series (BL038, BL006, and BL003) and E-series (E48, E44, and E7). To measure the refractive indices, the LCs are aligned perpendicular to the main and secondary prism surfaces of the Abbe refractometer by coating these two surfaces with a surfactant consisting of 0.294 wt% hexadecyltri-methyle-ammonium bromide (HMAB) in methanol solution.

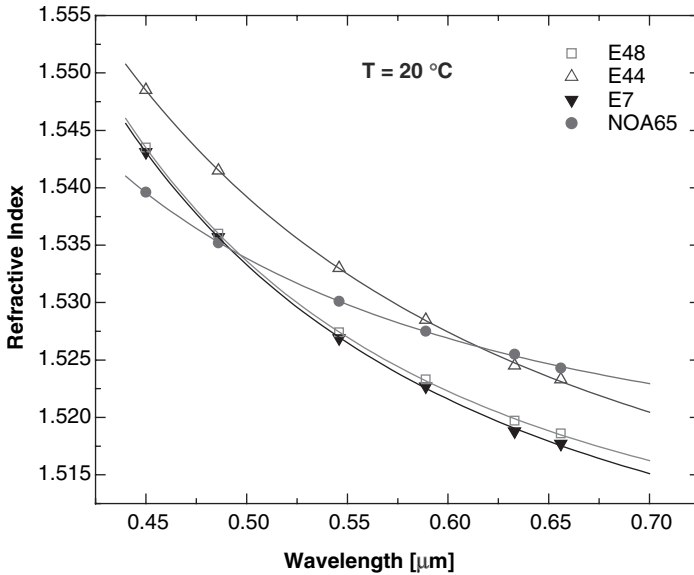
### 6.7.2 Matching refractive index

For a linearly conjugated LC, a high  $n_o$  often leads to a high  $\Delta n$ . Most of the commercially available high-birefringence ( $\Delta n \sim 0.20\text{--}0.28$ ) LCs have  $n_o \sim 1.50\text{--}1.52$ . These are mixtures of cyano-biphenyls and cyano-terphenyls, e.g., the Merck E-series and BL-series. Only a few high-birefringence ( $\Delta n \geq 0.4$ ) LCs have  $n_o > 1.55$ . These are mainly isothiocyanato-tolane mixtures. Thus, let us focus on the index matching phenomena of some Merck E-series (E7, E44, and E48) and BL-series (BL003, BL006, and BL038) LC with NOA65.

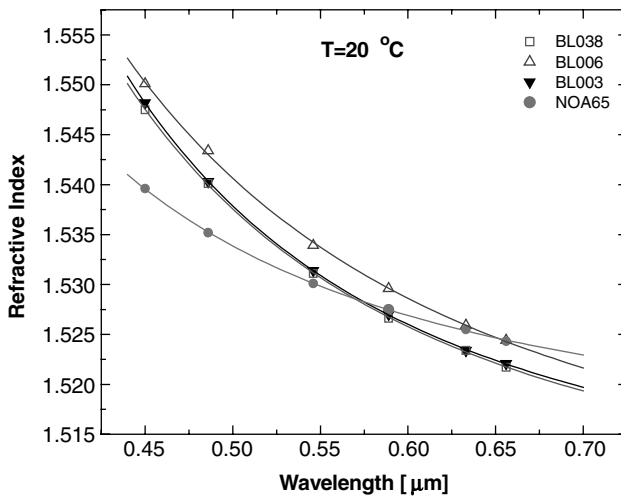
Figure 6.9 shows the measured refractive index of the UV-cured NOA65 and the ordinary refractive index of E48, E44, and E7, as a function of wavelength at  $T = 20^{\circ}\text{C}$ . The fitting parameters  $A$ ,  $B$ , and  $C$  are listed in Table 6.3. From Figure 6.9, E48, E44, and E7 all have a reasonably good index matching with NOA65. The mismatch is within 0.005 at  $\lambda = 550$  nm. More specifically, E44 has the best match in the red spectral region while E7 and E48 have the best match in the blue region. In the green region ( $\lambda = 546$  nm) where the human eye is most sensitive, E44 has a slightly higher index, while E7 and E48 are slightly lower than NOA65, but the difference is in the third decimal.

Figure 6.10 shows the refractive index of the cured NOA65 and the ordinary refractive indices of BL038, BL006, and BL003 as a function of wavelength at  $T = 20^{\circ}\text{C}$ . In Figure 6.10, BL038, BL006, and BL003 have a similar trend in  $n_o(\lambda)$ . The index matching with NOA65 is quite good in the green and red





**Figure 6.9** Wavelength-dependent refractive index of NOA65 and the ordinary refractive indices of E48, E44, and E7 at  $T = 20^\circ\text{C}$ . The open squares and triangles, and the solid circles and triangles, are the measured refractive indices of E48 and E44, and NOA65 and E7, respectively. The solid lines represent the fittings using the extended Cauchy model (Equation (6.10)). The fitting parameters are listed in Table 6.3



**Figure 6.10** Wavelength-dependent refractive index of NOA65 and the ordinary refractive indices of BL038, BL006, and BL003 at  $T = 20^\circ\text{C}$ . The open squares and triangles, and the solid circles and triangles, are the measured refractive indices of BL038 and BL006, and NOA65 and BL003, respectively. The solid lines represent the fittings using the extended Cauchy model (Equation (6.10)). The fitting parameters are listed in Table 6.3

**Table 6.3** The fitting parameters for the refractive index (Equation (6.10)) of NOA65 and the ordinary refractive indices of E48, E44, E7, BL038, BL006, and BL003 at  $T = 20^\circ\text{C}$

Cauchy coefficients	NOA65	E48	E44	E7	BL038	BL006	BL003
A	1.5130	1.5027	1.5018	1.4995	1.5042	1.5034	1.5056
$B$ ( $\mu\text{m}^2$ )	0.0045	0.0055	0.0089	0.0068	0.0065	0.0085	0.0057
$C$ ( $\mu\text{m}^4$ )	$1.8 \times 10^{-4}$	$5.6 \times 10^{-4}$	$1.0 \times 10^{-4}$	$4.1 \times 10^{-4}$	$4.7 \times 10^{-4}$	$1.9 \times 10^{-4}$	$5.9 \times 10^{-4}$

spectral regions. A larger deviation is observed in the blue region, but the difference is still in the third decimal (see Table 6.3).

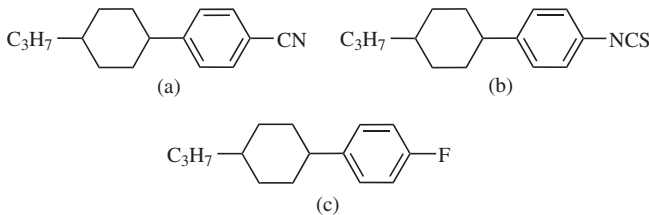
In a PDLC system, good index matching ( $n_o \sim n_p$ ) between the employed polymer and LC helps to improve the transmittance in the voltage-on state. On the other hand, a larger index mismatch ( $n > n_p$ ), i.e., a higher birefringence LC, enhances the light-scattering efficiency in the voltage-off state. However, refractive index match or mismatch is not the only factor deciding the PDLC performance. UV stability of LC and miscibility between polymers and LC also play important roles affecting the PDLC properties. From the above discussion, the E-series and BL-series LC all have a good index match with NOA65. All of them are good candidates for PDLC applications when NOA65 is used. In the visible spectrum, E48 and E7 have very similar ordinary refractive indices at  $T = 20^\circ\text{C}$ , as do BL038 and BL003. However, E48 has a higher birefringence than E7 and BL038 has a higher birefringence than BL003. Therefore, E48 and BL038 are somewhat better choices than E7 and BL003 for NOA65-based PDLC systems.

## Homework Problems

6.1 The following building blocks are given: two alkyl chains  $\text{C}_3\text{H}_7$ ,  $\text{C}_5\text{H}_{11}$ ; three polar groups F, CN, and NCS; a cyclohexane ring; and a phenyl ring. Assuming that each alkyl chain and polar group can be used only once in each compound, except for the rings:

- (1) Construct a two-ring compound with the largest positive dielectric anisotropy.
- (2) Construct a two-ring compound with the largest negative dielectric anisotropy.
- (3) Construct a three-ring compound with  $\Delta n \sim 0.05$  which is suitable for reflective TFT LCDs.

6.2 Compare the physical properties (at the same reduced temperature) of the following compounds:



- (1) Dielectric anisotropy: ( ) > ( ) > ( )
- (2) Birefringence: ( ) > ( ) > ( )
- (3) Rotational viscosity: ( ) > ( ) > ( )

6.3 Prove that the extended Cauchy equations (Equation (6.10)) derived from LC compounds can be applied to LC mixtures. Hint: See Ref. 13.

- 6.4 A TFT LC mixture has  $\Delta n = 0.090$  at  $\lambda = 589 \text{ nm}$  and  $0.085$  at  $\lambda = 633 \text{ nm}$ . What is the extrapolated birefringence at  $\lambda = 550 \text{ nm}$ ?
- 6.5 Prove that  $n_e$ ,  $n_o$ , and  $\Delta n$  reach saturation values beyond the near-IR region.

## References

- 1 J. D. Jackson, *Classical Electrodynamics*, 2nd edn (John Wiley & Sons, Inc., New York, 1962).
- 2 M. Born and E. Wolf, *Principle of Optics*, 6th edn (Pergamon, New York, 1980).
- 3 M. F. Vuks, 'Determination of the optical anisotropy of aromatic molecules from the double refraction of crystals', *Opt. Spektrosk.*, **20**, 644 (1966).
- 4 J. Li and S. T. Wu, 'Self-consistency of Vuks equations for liquid-crystal refractive indices', *J. Appl. Phys.*, **96**, 6253 (2004).
- 5 J. Li and S. T. Wu, 'Extended Cauchy equations for the refractive indices of liquid crystals', *J. Appl. Phys.*, **95**, 896 (2004).
- 6 S. T. Wu, 'Birefringence dispersions of liquid crystals', *Phys. Rev. A*, **33**, 1270 (1986).
- 7 H. Mada and S. Kobayashi, 'Wavelength and voltage dependences of refractive indices of nematic liquid crystals', *Mol. Cryst. Liq. Cryst.*, **33**, 47 (1976).
- 8 S. T. Wu, E. Ramos, and U. Finkenzeller, 'Polarized UV spectroscopy of conjugated liquid crystals', *J. Appl. Phys.*, **68**, 78 (1990).
- 9 S. T. Wu, 'Absorption measurements of liquid crystals in the ultraviolet, visible, and infrared', *J. Appl. Phys.*, **84**, 4462 (1998).
- 10 S. T. Wu, 'A semiempirical model for liquid-crystal refractive index dispersions', *J. Appl. Phys.*, **69**, 2080 (1991).
- 11 S. T. Wu, C. S. Wu, M. Warengem, and M. Ismaili, 'Refractive index dispersions of liquid crystals', *Opt. Eng.*, **32**, 1775 (1993).
- 12 S. T. Wu, U. Efron, and L. D. Hess, 'Infrared birefringence of liquid crystals', *Appl. Phys. Lett.*, **44**, 1033 (1984).
- 13 J. Li and S. T. Wu, 'Two-coefficient Cauchy model for low birefringence liquid crystals', *J. Appl. Phys.*, **96**, 170 (2004).
- 14 S.-T. Wu and D.-K. Yang, *Reflective Liquid Crystal Displays* (John Wiley & Sons, Ltd, Chichester, 2001).
- 15 S. Gauza, H. Wang, C. H. Wen, S. T. Wu, A. Seed, and R. Dabrowski, 'High birefringence isothiocyanato toluene liquid crystals', *Jpn. J. Appl. Phys.*, **42**, 3463 (2003).
- 16 E. H. Stupp and M. S. Brennessoltz, *Projection Displays* (John Wiley & Sons, Inc., New York, 1998).
- 17 T. T. Alkeskjold, A. Bjarklev, D. S. Hermann, and J. Broeng, 'Optical devices based on liquid crystal photonic bandgap fibres', *Opt. Express*, **11**, 2589 (2003).
- 18 T. T. Alkeskjold, J. Lægsgaard, A. Bjarklev, D. S. Hermann, A. Anawati, J. Broeng, J. Li, and S. T. Wu, 'All-optical modulation in dye-doped nematic liquid crystal photonic bandgap fibers', *Opt. Express*, **12**, 5857 (2004).
- 19 M. Warengem, J. F. Henninot, and G. Abbate, 'Non linearly induced self waveguiding structure in dye doped nematic liquid crystals confined in capillaries', *Opt. Express*, **2**, 483 (1998).
- 20 M. Warengem, J. F. Henninot, F. Derrin, and G. Abbate, 'Thermal and orientational spatial optical solitons in dye-doped liquid crystals', *Mol. Cryst. Liq. Cryst.*, **373**, 213 (2002).
- 21 I. Haller, 'Thermodynamic and static properties of liquid crystals', *Prog. Solid State Chem.*, **10**, 103 (1975).
- 22 J. Li, S. Gauza, and S. T. Wu, 'High temperature-gradient refractive index liquid crystals', *Opt. Express*, **12**, 2002 (2004).
- 23 H. R. Zeller, 'Dielectric relaxation in nematics and Doolittle's law', *Phys. Rev. A*, **26**, 1785 (1982).
- 24 J. Li and S. T. Wu, 'Temperature effect on liquid crystal refractive indices', *J. Appl. Phys.*, **96**, 19 (2004).
- 25 P. Sarkar, P. Mandal, S. Paul, and R. Paul, 'X-ray diffraction, optical birefringence, dielectric and phase transition properties of the long homologous series of nematogens 4-(trans-4'-n-alkylcyclohexyl) isothiocyanatobenzenes', *Liq. Cryst.*, **30**, 507 (2003).

- 26 H. J. Deuling, *Liquid Crystals*, ed. L. Liebert, Solid State Phys. Suppl. 14 (Academic Press, New York, 1978).
- 27 W. Maier and G. Meier, 'A simple theory of the dielectric characteristics of homogeneous oriented crystalline-liquid phases of the nematic type', *Z. Naturforsch.*, A **16**, 262 (1961).
- 28 M. Schadt, 'Field-effect liquid-crystal displays and liquid-crystal materials - key technologies of the 1990s', *Displays*, **13**, 11 (1992).
- 29 G. Gray, K. J. Harrison, and J. A. Nash, 'New family of nematic liquid crystals for displays', *Electron. Lett.*, **9**, 130 (1973).
- 30 R. Dabrowski, 'Isothiocyanates and their mixtures with a broad range of nematic phase', *Mol. Cryst. Liq. Cryst.*, **191**, 17 (1990).
- 31 M. Schadt and W. Helfrich, 'Voltage-dependent optical activity of a twisted nematic liquid crystal', *Appl. Phys. Lett.*, **18**, 127 (1971).
- 32 R.A. Soref, 'Transverse field effect in nematic liquid crystals', *Appl. Phys. Lett.*, **22**, 165 (1973).
- 33 M. Oh-e and K. Kondo, 'Electro-optical characteristics and switching behavior of the in-plane switching mode', *Appl. Phys. Lett.*, **67**, 3895 (1995).
- 34 Y. Nakazono, H. Ichinose, A. Sawada, S. Naemura, and K. Tarumi, 'Characterization of LC materials with negative dielectric anisotropy for AMLCDs', *International Display Research Conference*, Toronto, Canada, 65 (1997).
- 35 R. Tarao, H. Saito, S. Sawada, and Y. Goto, 'Advances in liquid crystals for TFT displays', *SID Tech. Dig.*, **25**, 233 (1994).
- 36 T. Geelhaar, K. Tarumi, and H. Hirschmann, 'Trends in LC materials', *SID Tech. Dig.*, **27**, 167 (1996).
- 37 Y. Goto, T. Ogawa, S. Sawada, and S. Sugimori, 'Fluorinated liquid crystals for active matrix displays', *Mol. Cryst. Liq. Cryst.*, **209**, 1 (1991).
- 38 H. Saito, E. Nakagawa, T. Matsushita, F. Takeshita, Y. Kubo, S. Matsui, K. Miyazawa, and Y. Goto, 'Fluorinated liquid crystalline materials for AM-LCD applications', *IEICE Trans. Electron.*, **E79-C**, 1027 (1996).
- 39 M. F. Schiekel and K. Fahrenschon, 'Deformation of nematic liquid crystals with vertical orientation in electric fields', *Appl. Phys. Lett.*, **19**, 391 (1971).
- 40 R. Eidenschink and L. Pohl, US patent 4,415,470 (1983).
- 41 H. K. Bücher, R. T. Klingbiel, and J. P. VanMeter, 'Frequency-addressed liquid crystal field effect', *Appl. Phys. Lett.*, **25**, 186 (1974).
- 42 M. Schadt, 'Low frequency dielectric relaxation in nematic and dual frequency addressing of field effect', *Mol. Cryst. Liq. Cryst.*, **89**, 77 (1982).
- 43 Y. Lu, X. Liang, Y. H. Wu, F. Du, and S. T. Wu, 'Dual-frequency addressed hybrid-aligned nematic liquid crystal', *Appl. Phys. Lett.*, **85**, 3354 (2004).
- 44 C. H. Wen and S. T. Wu, 'Dielectric heating effects of dual-frequency liquid crystals', *Appl. Phys. Lett.*, **86**, 231104 (2005).
- 45 E. Jakeman and E. P. Raynes, 'Electro-optic response times of liquid crystals', *Phys. Lett.*, **A39**, 69 (1972).
- 46 H. Imura and K. Okano, 'Temperature dependence of the viscosity coefficients of liquid crystals', *Jpn. J. Appl. Phys.*, **11**, 1440 (1972).
- 47 A. C. Diogo and A. F. Martins, 'Thermal behavior of the twist viscosity in a series of homologous nematic liquid crystals', *Mol. Cryst. Liq. Cryst.*, **66**, 133 (1981).
- 48 V. V. Belyaev, S. Ivanov, and M. F. Grebenkin, 'Temperature dependence of rotational viscosity of nematic liquid crystals', *Sov. Phys. Crystallogr.*, **30**, 674 (1985).
- 49 S. T. Wu and C. S. Wu, 'Rotational viscosity of nematic liquid crystals', *Liq. Cryst.*, **8**, 171 (1990).
- 50 M. A. Osipov and E. M. Terentjev, 'Rotational diffusion and rheological properties of liquid crystals', *Z. Naturforsch.*, A **44**, 785 (1989).
- 51 S. T. Wu and C. S. Wu, 'Experimental confirmation of Osipov-Terentjev theory on the viscosity of liquid crystals', *Phys. Rev. A*, **42**, 2219 (1990).
- 52 P. G. deGennes, *The Physics of Liquid Crystals* (Clarendon Press, Oxford, 1974).

- 53 W. Maier and A. Saupe, 'A simple molecular statistical theory for nematic liquid crystal phase, Part II', *Z. Naturforsch.*, A **15**, 287 (1960).
- 54 H. Gruler, 'The elastic constants of a nematic liquid crystal', *Z. Naturforsch.*, A **30**, 230 (1975).
- 55 S. T. Wu, A. M. Lackner, and U. Efron, 'Optimal operation temperature of liquid crystal modulators', *Appl. Opt.*, **26**, 3441 (1987).
- 56 P. S. Drzaic, *Liquid Crystal Dispersions* (World Scientific, Singapore, 1995).
- 57 Y. H. Lin, H. W. Ren, and S. T. Wu, 'High contrast polymer-dispersed liquid crystal in a 90° twisted cell', *Appl. Phys. Lett.*, **84**, 4083 (2004).
- 58 H. Ren, Y. H. Lin, Y. H. Fan, and S. T. Wu, 'Polarization-independent phase modulation using a polymer-dispersed liquid crystal', *Appl. Phys. Lett.*, **86**, 141110 (2005).
- 59 J. Li, G. Baird, H. Ren, Y. H. Lin, and S. T. Wu, 'Refractive index matching between liquid crystals and photopolymers', *J. SID*, **13**, 1017 (2005).

# 7

## Modeling Liquid Crystal Director Configuration

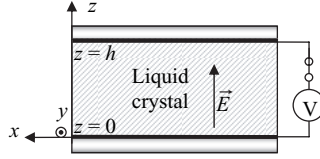
Liquid crystal director configuration and optical modeling methods are well developed and reliable and widely used in the design of liquid crystal devices [1–7]. In the modeling, the equilibrium director configuration is obtained by minimizing the total free energy of the system (elastic energy plus electric energy). The popular numerical methods used in liquid crystal modeling are the *finite-difference method* (FDM) [1, 8] and *finite-element method* (FEM) [7, 9, 10]. FDM is simple and easy to understand while FEM is versatile in modeling arbitrary liquid crystal device structures. We will only discuss FDM in this chapter.

### 7.1 Electric Energy of Liquid Crystals

In order to model the liquid crystal director configuration, we first must know how liquid crystals interact with externally applied electric fields. Many liquid crystal devices make use of uniaxial nematic liquid crystals which are dielectrics. We consider the electric energy of nematic liquid crystals in externally applied electric fields through dielectric interaction. A typical liquid crystal device cell is shown in Figure 7.1, where the liquid crystal is sandwiched between two parallel substrates with transparent electrodes. The electric energy of the liquid crystal is given by [11–13]

$$U_e = \int_V \frac{1}{2} \vec{E} \cdot \vec{D} d^3r \quad (7.1)$$

where the volume integration is over the liquid crystal. The internal energy (including the electric energy) of the system is  $U$ . The change of internal energy  $dU$  in a process is equal to the sum of the heat absorbed  $dQ$ , the mechanical work  $dW_m$  done on the system, and the electric work  $dW_e$  done on the



**Figure 7.1** Schematic diagram of the liquid crystal cell connected to a voltage source

system by external sources:

$$dU = dQ + dW_m + dW_e \tag{7.2}$$

When the liquid crystal undergoes a change in its director configuration, the electric field may change and the electric work  $dW_e$  depends on whether the liquid crystal cell is connected to a voltage source or not. We will consider several cases in the following sections.

**7.1.1 Constant charge**

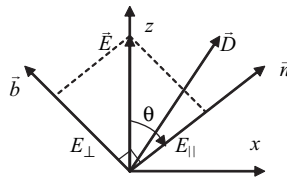
In the first case, the liquid crystal cell is disconnected from the voltage source. The free charge on the interface between the liquid crystal and the electrode is fixed, and this case is called fixed charge. The external voltage source does not do electric work, i.e.,  $dW_e = 0$ . At constant temperature and pressure, the Gibbs free energy

$$G = \int (f_{elastic} + \frac{1}{2} \vec{E} \cdot \vec{D}) d^3r \tag{7.3}$$

is minimized in the equilibrium state. As an example, we consider a 1-D case where the liquid crystal director  $\vec{n}$  is confined in the  $x-z$  plane and is only a function of the coordinate  $z$  that is parallel to the cell normal. Inside the electrode,  $\vec{E} = 0$ . The tangential boundary condition gives  $E_x = E_y = 0$  everywhere. Therefore  $\vec{E} = E(z)\hat{z}$ . From Figure 7.2 the electric displacement is found to be

$$\begin{aligned} \vec{D} &= \epsilon_o \{ \epsilon_{||} (\vec{E} \cdot \vec{n}) \vec{n} + \epsilon_{\perp} [\vec{E} - (\vec{E} \cdot \vec{n}) \vec{n}] \} = \epsilon_o [\epsilon_{\perp} \vec{E} + \Delta\epsilon (\vec{E} \cdot \vec{n}) \vec{n}] \\ &= \epsilon_o [\epsilon_{\perp} \vec{E} + \Delta\epsilon E \cos \theta \vec{n}] \end{aligned} \tag{7.4}$$

The surface free charge density  $\sigma_1 = D_z(z=0) = \sigma$  on the bottom surface and the surface free charge density  $\sigma_2 = -D_z(z=h)$  on the top surface are fixed. In the 1-D case here,  $\vec{D} = \vec{D}(z)$  and



**Figure 7.2** Schematic diagram showing the field decomposed into components parallel and perpendicular to the liquid crystal director, respectively

$\nabla \cdot \vec{D} = \partial D_z / \partial z = 0$ ; therefore  $D_z$  is a constant across the cell:

$$D_z(z) = D_z(z = h) = \epsilon_o \epsilon_{\perp} E + \epsilon_o \Delta \epsilon E \cos^2 \theta = \sigma \quad (7.5)$$

The electric field is given by

$$E = \sigma / [\epsilon_o (\epsilon_{\perp} + \Delta \epsilon \cos^2 \theta)] \quad (7.6)$$

When the liquid crystal undergoes a configurational change,  $\theta$  changes and thus  $E$  changes. The electric energy density is

$$f_{electric} = \frac{1}{2} \vec{E} \cdot \vec{D} = \frac{1}{2} E \cdot D_z = \frac{\sigma^2}{2\epsilon_o (\epsilon_{\perp} + \Delta \epsilon \cos^2 \theta)} \quad (7.7)$$

In the equilibrium state, the Gibbs free energy

$$G = \int \left( f_{elastic} + \frac{1}{2} \vec{E} \cdot \vec{D} \right) dV = \int \left[ f_{elastic} + \frac{\sigma^2}{2\epsilon_o (\epsilon_{\perp} + \Delta \epsilon \cos^2 \theta)} \right] d^3 r \quad (7.8)$$

is minimized. Note that  $\sigma$  is a constant. The voltage across the cell is

$$V = \int_0^h E_z dz = \int_0^h \frac{\sigma}{\epsilon_o (\epsilon_{\perp} + \Delta \epsilon \cos^2 \theta)} dz \quad (7.9)$$

which is not a constant and changes with the director configuration. If  $\Delta \epsilon > 0$ , when  $\vec{n} \parallel \vec{E}$ ,  $\theta = 0$ , the electric energy is minimized; therefore the liquid crystal molecules tend to align parallel to the field. If  $\Delta \epsilon < 0$ , when  $\vec{n} \perp \vec{E}$ ,  $\theta = \pi/2$ , the electric energy is minimized; therefore the liquid crystal molecules tend to align perpendicular to the field.

### 7.1.2 Constant voltage

Next, we consider the second case where the liquid crystal cell is connected to the voltage source such that the voltage  $V$  applied across the cell is fixed. The electric potential in the cell is  $\phi(z)$ . On top of the cell ( $z = h$ ), the potential  $\phi(z = h) = \phi_2$  is low. At the bottom of the cell ( $z = 0$ ), the potential  $\phi(z = 0) = \phi_1$  is high.  $\phi_1 - \phi_2 = V$ . The electric field is in the  $+z$  direction. The free surface charge density on the top surface of the liquid crystal is  $\sigma_2 = -\sigma$ , which is negative. The free surface charge density on the bottom surface of the liquid crystal is  $\sigma_1 = \sigma$ , which is positive. When the liquid crystal undergoes an orientational configuration change,  $\sigma$  may vary. During the reorientation of the liquid crystal, the charge  $dQ = \int_{S_2} (-\delta \sigma_2) dS$  is moved from the top plate to the bottom plate by the voltage source and the electric work done by the voltage source to the liquid crystal is

$$dW_e = V dQ = (\phi_1 - \phi_2) dQ = (\phi_1 - \phi_2) \int_{S_2} (-\delta \sigma_2) dS = \int_{S_2} \phi_2 \delta \sigma_2 dS + \int_{S_1} \phi_1 \delta \sigma_1 dS \quad (7.10)$$



The electric energy of the liquid crystal is

$$\int_{Vol} \frac{1}{2} \vec{D} \cdot \vec{E} d^3 r = \int_{Vol} \frac{1}{2} \vec{D} \cdot (-\nabla \phi) d^3 r = - \int_{Vol} \frac{1}{2} \nabla \cdot (\phi \vec{D}) dV + \int_{Vol} \frac{1}{2} \phi (\nabla \cdot \vec{D}) d^3 r \quad (7.11)$$

The last term is zero because  $\nabla \cdot \vec{D} = 0$ . The surface normal vector points out of the liquid crystal:

$$- \int_V \frac{1}{2} \nabla \cdot (\phi \vec{D}) dV = - \frac{1}{2} \oint_S \phi \vec{D} \cdot d\vec{S} = - \frac{1}{2} \int_{S_2} \phi_2 D_z(z=h) dS - \frac{1}{2} \int_{S_1} \phi_1 D_z(z=0) (-dS)$$

The free surface charge densities are given by  $\sigma_2 = -D_z(z=h)$  and  $\sigma_1 = D_z(z=0)$ . Therefore

$$\int_{Vol} \frac{1}{2} \vec{D} \cdot \vec{E} d^3 r = \frac{1}{2} \left( \int_{S_2} \phi_2 \delta \sigma_2 dS + \int_{S_1} \phi_1 \delta \sigma_1 dS \right) \quad (7.12)$$

Comparing Equations (7.10) and (7.12), we have

$$dW_e = \delta \int_{Vol} \vec{D} \cdot \vec{E} d^3 r \quad (7.13)$$

In a reorientation of the liquid crystal, as discussed in Chapter 1, the change of entropy of the system is given by  $dS \geq dQ/T = (\delta U - dW_m - dW_e)/T = (\delta U + PdV - dW_e)/T$ . At constant temperature and pressure,  $\delta(U - W_e + PV - TS) \leq 0$ , i.e.,

$$\delta \left[ \int (f_{elastic} + f_{electric} - \vec{D} \cdot \vec{E}) d^3 r \right] = \delta \left[ \int \left( f_{elastic} - \frac{1}{2} \vec{D} \cdot \vec{E} \right) d^3 r \right] \leq 0$$

Therefore at the equilibrium state

$$R = \int \left( f_{elastic} - \frac{1}{2} \vec{D} \cdot \vec{E} \right) d^3 r \quad (7.14)$$

is minimized. Using Equation (7.6), we have

$$R = \int \left[ f_{elastic} - \frac{\sigma^2}{2\epsilon_0(\epsilon_{\perp} + \Delta\epsilon \cos^2\theta)} \right] d^3 r \quad (7.15)$$

At first glance, it seems that in order to minimize  $R$ , provided  $\Delta\epsilon > 0$ ,  $\vec{n}$  should be perpendicular to  $\vec{E}$  ( $\theta = \pi/2$ ), in contrast to the result of the constant charge case. The liquid crystal molecules do not know whether the charge is fixed or the voltage is fixed and the liquid crystal ( $\Delta\epsilon > 0$ ) always tends to align parallel to the applied field. This paradox can be resolved by noting that, in Equation (7.15),

$\sigma$  is no longer a constant, because

$$\begin{aligned} V &= \int_0^h E_z dz = \int_0^h \frac{\sigma}{\varepsilon_o(\varepsilon_\perp + \Delta\varepsilon \cos^2\theta)} dz \\ &= \frac{1}{A} \int \frac{\sigma}{\varepsilon_o(\varepsilon_\perp + \Delta\varepsilon \cos^2\theta)} d^3r = \text{a fixed constant} \end{aligned} \quad (7.16)$$

where  $A$  is the surface area of the cell. When  $\theta(z)$  changes,  $\sigma$  must vary in order to keep  $V$  fixed.  $R$  is a functional of  $\theta$  and  $\sigma$ . Equation (7.16) is the constraint under which  $R$  is minimized. The constraint can be removed if we use a Lagrange multiplier [14], and minimize

$$\Omega = \int \left[ f_{\text{elastic}} - \frac{\sigma^2}{2\varepsilon_o(\varepsilon_\perp + \Delta\varepsilon \cos^2\theta)} + \lambda \cdot \frac{\sigma}{\varepsilon_o(\varepsilon_\perp + \Delta\varepsilon \cos^2\theta)} \right] d^3r \quad (7.17)$$

where  $\lambda$  is the Lagrange multiplier. Minimizing  $\Omega$  with respect to  $\sigma$ , we have

$$\frac{\partial \Omega}{\partial \sigma} = -\frac{2\sigma}{2\varepsilon_o(\varepsilon_\perp + \Delta\varepsilon \cos^2\theta)} + \lambda \cdot \frac{1}{\varepsilon_o(\varepsilon_\perp + \Delta\varepsilon \cos^2\theta)} = 0 \quad (7.18)$$

Hence  $\lambda = \sigma$ . We minimize

$$\Omega = G = \int \left[ f_{\text{elastic}} + \frac{\sigma^2}{2\varepsilon_o(\varepsilon_\perp + \Delta\varepsilon \cos^2\theta)} \right] d^3r \quad (7.19)$$

with  $\sigma$  treated as a constant and without the constraint given by Equation (7.16). This is the same as Equation (7.8) for the case of constant charge.

In reality, the voltage is usually fixed and known. We can use the following strategy to calculate the director configuration for a given voltage  $V$ : (1) Assume  $\sigma$  is fixed and has a trial value  $\sigma_t$ . (2) Use the Euler–Lagrange method to minimize the Gibbs free energy given by Equation (7.8) and find the solution  $\theta = \theta(z)$ . (3) Calculate the corresponding voltage

$$V_{\text{try}} = \int_0^h \frac{\sigma_t}{\varepsilon_o(\varepsilon_\perp + \Delta\varepsilon \cos^2\theta)} dz$$

If  $V_{\text{try}} \neq V$ , try a new surface charge density  $\sigma_n = \sigma_t + \alpha(V - V_t)\varepsilon_o\varepsilon_\perp/h$ , where  $\alpha$  is a numerical constant which may be chosen to be 0.5. Repeat the above process until  $|V_t - V|$  is sufficiently small.

### 7.1.3 Constant electric field

When the orientation of the liquid crystal is uniform in space,  $\theta$  is a constant independent of  $z$ . For a fixed  $V$ , the electric field  $E = E_z = V/h$  is a constant independent of the orientation of the liquid crystal. In the equilibrium state,  $R$ , given by Equation (7.14), is minimized:  $-(1/2)\vec{D} \cdot \vec{E} = -(1/2)\varepsilon_o\varepsilon_\perp E^2 - (1/2)\varepsilon_o \Delta\varepsilon (\vec{E} \cdot \vec{n})^2$ . Because  $-(1/2)\varepsilon_o\varepsilon_\perp E^2$  is a constant independent of the orientation of the liquid crystal, Equation (7.14) becomes

$$R = \int \left[ f_{\text{elastic}} - (1/2)\varepsilon_o \Delta\varepsilon (\vec{n} \cdot \vec{E})^2 \right] d^3r \quad (7.20)$$

In the equilibrium state  $R$  is minimized. If  $\Delta\varepsilon > 0$ , when  $\vec{n} \parallel \vec{E}$ ,  $\theta = 0$ , the electric energy is minimized; therefore the liquid crystal molecules tend to align parallel to the field. If  $\Delta\varepsilon < 0$ , when  $\vec{n} \perp \vec{E}$ ,  $\theta = \pi/2$ , the electric energy is minimized; therefore the liquid crystal molecules tend to align perpendicular to the field.

## 7.2 Modeling the Electric Field

Multiplexed displays have many pixels where liquid crystals are sandwiched between two substrates with conducting films. Electric fields are produced by applied electric voltage across the conducting coatings. The pixels are separated by gaps where the conducting coating is etched off. Fringe fields are produced at the edge of the pixels, which may cause serious problems in microdisplays where the gap between pixels is not much smaller than the pixel (linear) size. In this section we will consider how to numerically calculate electric fields in multiplexed displays.

Electric field  $\vec{E}$  is related to electric potential  $\phi$  by  $\vec{E} = -\nabla\phi$ . Liquid crystals are dielectric media and there are usually no free charges inside them. From the Maxwell equations we have

$$\nabla \cdot \vec{D} = \nabla \cdot (\vec{\epsilon} \cdot \vec{E}) = -\nabla \cdot (\vec{\epsilon} \cdot \nabla\phi) = 0 \tag{7.21}$$

We first consider a simple case where the medium is isotropic and uniform. Equation (7.21) becomes

$$\nabla^2\phi = 0 \tag{7.22}$$

which is known as the Laplace equation. Several approaches have been developed to solve the Laplace equation. The simple and dominant method is the *finite-difference method* (FDM) [1, 15, 16].

In the FDM, a regular mesh is used on the region in which a solution is to be found. As an example, the region to be considered is a rectangle with lengths  $L_x$  and  $L_y$  in the  $x$  and  $y$  directions. We superimpose a mesh on the rectangle. The unit cell of the mesh is a square with length  $\Delta$ . At each lattice point of the mesh, the potential is  $\phi(i, j)$ , and the Laplace equation is approximated by

$$\frac{\phi(i+1, j) + \phi(i-1, j) - 2\phi(i, j)}{\Delta^2} + \frac{\phi(i, j+1) + \phi(i, j-1) - 2\phi(i, j)}{\Delta^2} = 0 \tag{7.23}$$

where  $i = 0, 1, 2, \dots, N_x (N_x = L_x/\Delta)$  and  $j = 0, 1, 2, \dots, N_y (N_y = L_y/\Delta)$ . Rearranging Equation (7.23) we have

$$\phi(i, j) = \frac{1}{4}[\phi(i+1, j) + \phi(i-1, j) + \phi(i, j+1) + \phi(i, j-1)] \tag{7.24}$$

Usually the potential at the boundary is given. Assume an initial condition  $\phi_o(i, j)$  that is consistent with the boundary condition. The potential at any mesh point can be calculated from the assumed potentials at its nearest neighbor mesh points by using the above equation. In the calculation the latest available values of the potential are always used on the right hand side of the equation. The solution to the Laplace equation can be calculated iteratively. This process has the shortcoming that it converges quite slowly to the solution of the Laplace equation. The rate of convergence can be improved by using the ‘over-relaxation’ method:

$$\begin{aligned} \phi^{\tau+1}(i, j) = & (1 - \alpha)\phi^\tau(i, j) + \frac{\alpha}{4} \left[ \phi^\tau(i+1, j) + \phi^\tau(i-1, j) \right. \\ & \left. + \phi^\tau(i, j+1) + \phi^\tau(i, j-1) \right] \end{aligned} \tag{7.25}$$

where  $\tau$  is the order of the iteration and  $\alpha$  is the relaxation constant, which should be a positive constant smaller than 1.5 in order to obtain a stable solution. Equation (7.25) can be rewritten as

$$\begin{aligned}\varphi^{\tau+1}(i, j) = & \varphi^{\tau}(i, j) + \frac{\alpha}{4} \left[ \varphi^{\tau}(i+1, j) + \varphi^{\tau}(i-1, j) - 2\varphi^{\tau}(i, j) \right. \\ & \left. + \varphi^{\tau}(i, j+1) + \varphi^{\tau}(i, j-1) - 2\varphi^{\tau}(i, j) \right]\end{aligned}$$

that is,

$$\varphi^{\tau+1}(i, j) = \varphi^{\tau}(i, j) + \frac{\alpha\Delta^2}{4} \left[ \frac{\partial^2 \varphi^{\tau}}{\partial x^2}(i, j) + \frac{\partial^2 \varphi^{\tau}}{\partial y^2}(i, j) \right] \quad (7.26)$$

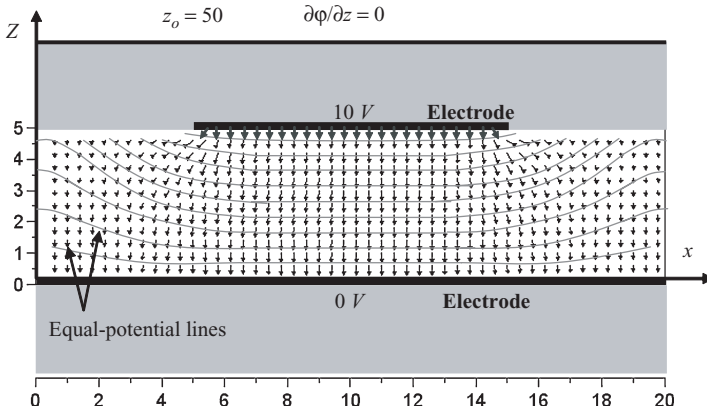
As  $\varphi^{(i,j)}(i, j)$  approaches the actual solution to the Laplace equation, the change  $\Delta\varphi^{\tau}(i, j) = \varphi^{\tau+1}(i, j) - \varphi^{\tau}(i, j)$  becomes smaller and smaller. When  $\varphi^{\tau}(i, j)$  no longer changes, i.e.,

$$\frac{\partial^2 \varphi^{\tau}}{\partial x^2}(i, j) + \frac{\partial^2 \varphi^{\tau}}{\partial y^2}(i, j) = 0$$

the Laplace equation is satisfied. In the numerical calculation, the iteration is stopped when the maximum  $|\Delta\varphi_m|$  of the absolute values of  $\Delta\varphi^{\tau}(i, j)$  at the lattice points on the mesh is smaller than a specified value. For a 3-D non-uniform anisotropic medium, the potential can be numerically calculated by

$$\begin{aligned}\varphi^{\tau+1}(i, j) = & \varphi^{\tau}(i, j, k) + \frac{\alpha\Delta^2}{4} \nabla \cdot (\overset{\leftrightarrow}{\varepsilon} \cdot \nabla \varphi)^{\tau}(i, j, k) \\ = & \varphi^{\tau}(i, j, k) + \frac{\alpha\Delta^2}{4} \left[ \frac{\partial}{\partial x} \left( \varepsilon_{11} \frac{\partial \varphi}{\partial x} \right) + \frac{\partial}{\partial x} \left( \varepsilon_{12} \frac{\partial \varphi}{\partial y} \right) + \frac{\partial}{\partial x} \left( \varepsilon_{13} \frac{\partial \varphi}{\partial z} \right) \right]^{\tau}(i, j, k) \\ & + \frac{\alpha\Delta^2}{4} \left[ \frac{\partial}{\partial y} \left( \varepsilon_{21} \frac{\partial \varphi}{\partial x} \right) + \frac{\partial}{\partial y} \left( \varepsilon_{22} \frac{\partial \varphi}{\partial y} \right) + \frac{\partial}{\partial y} \left( \varepsilon_{23} \frac{\partial \varphi}{\partial z} \right) \right]^{\tau}(i, j, k) \\ & + \frac{\alpha\Delta^2}{4} \left[ \frac{\partial}{\partial z} \left( \varepsilon_{31} \frac{\partial \varphi}{\partial x} \right) + \frac{\partial}{\partial z} \left( \varepsilon_{32} \frac{\partial \varphi}{\partial y} \right) + \frac{\partial}{\partial z} \left( \varepsilon_{33} \frac{\partial \varphi}{\partial z} \right) \right]^{\tau}(i, j, k) \quad (7.27)\end{aligned}$$

As an example, we calculate the electric field in a cell where the stripe electrode is along the  $y$  direction. The widths of the stripe electrode and the gap between the electrodes are both  $10 \mu\text{m}$ . The cell thickness is  $5 \mu\text{m}$  as shown in Figure 7.3. The dielectric constant of the glass substrate is  $\varepsilon_G = 6.5$ . The dielectric constant of the liquid crystal is assumed to be isotropic and equal to  $\varepsilon_{LC} = 10.0$  in the calculation of the electric field. The voltage on the bottom electrode is  $0\text{V}$  and that on the top electrode is  $10\text{V}$ . On the top substrate, in the gap region between the electrodes, the electric potential is unknown, and the electric displacement is continuous because there is no free surface charge. An imagined boundary can be placed far away from the surface of the top substrate. The boundary condition at the imagined boundary can be either  $\varphi = 0$  or  $E_z = \partial\varphi/\partial z = 0$ . To be correct, the imagined boundary should be at  $z = \infty$ . Since the mesh cannot be infinite in the simulation, the imagined boundary is at  $z = z_o = 50 \mu\text{m}$ . If the boundary condition of  $\varphi(z_o) = 0$  is used, the error will



**Figure 7.3** Electric field in the display cell with striped electrodes along the  $y$  direction. The unit of length is the micron

be on the order of  $1/z_0$ . If the boundary condition of  $E_z(z_0) = (\partial\phi/\partial z)(z_0) = 0$  is used, the error will be on the order of  $e^{-z_0}$ . A periodic boundary condition is used in the  $x$  direction.

### 7.3 Simulation of Liquid Crystal Director Configuration

In many liquid crystal devices the liquid crystal director configuration cannot be calculated analytically and must be computed numerically. Under a given external field and boundary condition, when a liquid crystal is in the equilibrium state, the total free energy is minimized. If the system is initially not in the equilibrium state, it will relax into a state with lower free energy. As the liquid crystal director configuration evolves, the free energy decreases. The change of the director configuration stops when the minimum free energy is reached. The dynamic equation for the change of the liquid crystal director can be used to numerically calculate the equilibrium director configuration, which is referred to as the relaxation method.

#### 7.3.1 Angle representation

In some cases, it is simpler to describe the liquid crystal director  $\vec{n}$  in terms of the polar angle  $\theta$  and azimuthal angle  $\phi$ . The angles may vary in one, two, or three dimensions. We first consider a simple case: the Freedericksz transition in the splay geometry. The liquid crystal director is represented by the tilt angle  $\theta$ :  $\vec{n} = \cos\theta(z)\hat{x} + \sin\theta(z)\hat{z}$  where the  $z$  axis is in the cell normal direction. The electric field is applied in the cell normal direction. From Equations (4.17) and (7.8) we have the free energy density

$$f = \frac{1}{2}(K_{11} \cos^2\theta + K_{33} \sin^2\theta) \theta'^2 + \frac{\sigma^2}{2\epsilon_0(\epsilon_{\perp} + \Delta\epsilon \sin^2\theta)} \tag{7.28}$$

where  $\sigma$  is the free surface charge density and  $\theta' = \partial\theta/\partial z$ . Note that here  $\theta$  is the angle between the liquid crystal director and the  $x$  axis. In the equilibrium state, the total free energy  $F = \int_0^h f dz$  is minimized, and the director configuration is  $\theta_{eq}(z)$  which satisfies the Euler-Lagrange

equation:

$$\begin{aligned}
 -\frac{\delta f}{\delta \theta} \Big|_{eq} &= -\left[ \frac{\partial f}{\partial \theta} - \frac{d}{dz} \left( \frac{\partial f}{\partial \theta'} \right) \right] \Big|_{eq} \\
 &= (K_{11} \cos^2 \theta_{eq} + K_{33} \sin^2 \theta_{eq}) \theta''_{eq} + (K_{33} - K_{11}) \sin \theta_{eq} \cos \theta_{eq} \theta_{eq}^2 \\
 &\quad + \frac{\sigma^2 \Delta \varepsilon \sin \theta_{eq} \cos \theta_{eq}}{\varepsilon_o (\varepsilon_{\perp} + \Delta \varepsilon \sin^2 \theta_{eq})^2} \\
 &\equiv u(\theta_{eq}) \theta''_{eq} + w(\theta_{eq}, \theta'_{eq}) = 0
 \end{aligned} \tag{7.29}$$

If initially the system is not in the equilibrium state,  $\theta(z) = \theta_{in}(z)$ . It will relax toward the equilibrium state. The dynamic equation governing the relaxation of the system is given by Equation (4.74):

$$\gamma_r \frac{\partial \theta}{\partial t} = -\frac{\delta f}{\delta \theta} = -\frac{\partial f}{\partial \theta} + \frac{d}{dz} \left( \frac{\partial f}{\partial \theta'} \right) = u(\theta) \theta'' + w(\theta, \theta') \tag{7.30}$$

Using this equation, the angle at time  $t + \Delta t$  can be calculated from the angle at time  $t$

$$\theta^{t+\Delta t} = \theta^t + \frac{\Delta t}{\gamma_r} \left[ u(\theta^t) \theta''^t + w(\theta^t, \theta'^t) \right] \tag{7.31}$$

When the system reaches the equilibrium state, the director configuration no longer changes and  $\partial \theta / \partial t = -\delta f / \delta \theta = 0$ . Equation (7.30) may not describe the actual dynamic process because the hydrodynamic effect is not considered, but the final director configuration obtained is the actual one of the equilibrium state.

In the numerical calculation, the liquid crystal cell is discretized into a 1-D mesh with  $N$  lattice sites. The length of the lattice unit is  $\Delta z = h/N$ . At step  $\tau$ , the tilt angle at the lattice site  $i$  is  $\theta(i)$  ( $i = 0, 1, 2, 3, \dots, N$ ). The derivatives are calculated by

$$\theta'^{\tau}(i) = \frac{\theta^{\tau}(i+1) - \theta^{\tau}(i-1)}{2\Delta z} \tag{7.32}$$

$$\theta''^{\tau}(i) = \frac{\theta^{\tau}(i+1) + \theta^{\tau}(i-1) - 2\theta^{\tau}(i)}{(\Delta z)^2} \tag{7.33}$$

The angle at step  $\tau + 1$  can be calculated by

$$\theta^{\tau+1}(i) = \theta^{\tau}(i) + \Delta \theta^{\tau}(i) \tag{7.34}$$

$$\Delta \theta^{\tau}(i) = \alpha (\Delta z)^2 \{ u[\theta^{\tau}(i)] \theta''^{\tau}(i) + w[\theta^{\tau}(i), \theta'^{\tau}(i)] \} \tag{7.35}$$

where  $\alpha$  is a relaxation constant which must be sufficiently small in order to avoid unstable solutions. In the numerical calculation, if the change  $\Delta \theta^{\tau}(i)$  at all the lattice sites is calculated first using the angles at step  $\tau$ , and then the angles at all the lattice sites are updated,  $\alpha$  must be smaller than  $0.5/u[\theta^{\tau}(i)]$  in order to avoid unstable solutions. If the change  $\Delta \theta^{\tau}(i)$  at each lattice site is calculated

and then the angle at that the lattice site is immediately updated, known as the over-relaxation method, an  $\alpha$  larger than  $1/u[\theta^\tau(i)]$  can be used. In the numerical calculation, the total change of the angle

$$T\theta = \sum_{i=0}^N |\Delta\theta^\tau(i)|$$

in each step must be monitored.  $T\theta$  decreases as the relaxation proceeds and becomes zero when the equilibrium configuration is reached. In reality, in the numerical calculation,  $T\theta$  decreases but will never become exactly zero. When  $T\theta$  becomes sufficiently small, the calculation can be stopped.

If the anchoring of the liquid crystal at the boundaries is infinitely strong, the angle at the boundary is fixed. If the pretilt angles at the boundaries  $z = 0$  and  $z = h$  are  $\theta_1$  and  $\theta_2$ , respectively, the boundary conditions are  $\theta(0) = \theta_1$  and  $\theta(N) = \theta_2$ . If the anchoring is weak with anchoring energy  $W$ , the boundary conditions are  $\theta'(0) = (W/K_{11})\theta(0)$  and  $\theta'(N) = -(W/K_{11})\theta(N)$  (from Equations (5.60) and (5.61)), which give  $\theta(0) = \theta(1)/(1 + \Delta z W/K_{11})$  and  $\theta(N) = \theta(N-1)/(1 - \Delta z W/K_{11})$ .

The angle representation is a valid method when the change of the angle within the cell is less than  $90^\circ$ . Otherwise it must be handled carefully in the case where the liquid crystal directors at two neighboring lattice sites are anti-parallel. The numerical calculation may produce a large elastic energy while the actual elastic energy is zero, because  $\vec{n}$  and  $-\vec{n}$  are equivalent.

If two angles, say  $\theta(z)$  and  $\phi(z)$ , are needed to describe the orientation of the liquid crystal director, the total free energy is given by

$$F = \int_0^h f[\theta, \phi, \theta', \phi', z] dz \quad (7.36)$$

In the numerical relaxation method, the angles at the lattices sites can be calculated by

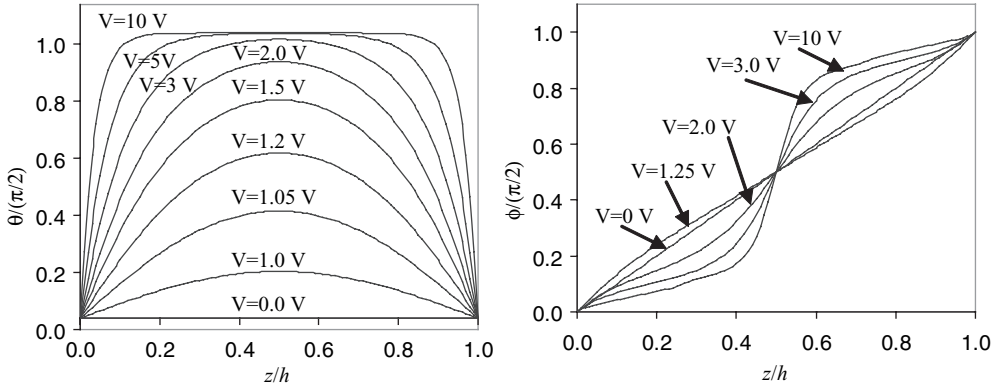
$$\theta^{\tau+1}(i) = \theta^\tau(i) + \alpha(\Delta z)^2 \left[ -\frac{\delta f^\tau}{\delta \theta}(i) \right] \quad (7.37)$$

$$\phi^{\tau+1}(i) = \phi^\tau(i) + \beta(\Delta z)^2 \left[ -\frac{\delta f^\tau}{\delta \phi}(i) \right] \quad (7.38)$$

where  $\alpha$  and  $\beta$  are the relaxation constants.

As an example, we numerically calculate the polar angle  $\theta$  and azimuthal angle  $\Phi$  in the Freedericksz transition in the twisted nematic geometry. The parameters of the liquid crystal are  $K_{11} = 6.4 \times 10^{-12}$  N,  $K_{22} = 3.0 \times 10^{-12}$  N,  $K_{33} = 10.0 \times 10^{-12}$  N, and  $\Delta\varepsilon = 10$ . The thickness  $h$  of the cell is 10 microns. The intrinsic pitch of the liquid crystal is  $P = (2\pi/\Phi)h$ , where  $\Phi$  is the total twist angle. The polar angle is the angle between the liquid crystal director and the  $x$ - $y$  plane. When the twist angle  $\Phi$  is  $90^\circ$ , the polar and azimuthal angles as a function of  $z$  at various applied voltages are as shown in Figure 7.4. The voltage threshold calculated from Equation (5.56) is  $V_{th} = 0.996$  V.

The change of the polar angle as a function of the applied voltage depends on the total twist angle  $\Phi$  as shown in Figure 7.5. The threshold increases with increasing  $\Phi$  for the two reasons. First, in the field-activated states, there is twist elastic energy that increases with  $\Phi$ . Secondly, the bend elastic energy increases with  $\Phi$  when the polar angle is small. The saturation voltage does not increase much with increasing  $\Phi$  because there is no bend deformation in the saturated state. Therefore the transition region (the region between the threshold voltage and the saturation voltage) decreases with increasing  $\Phi$ . When  $\Phi$  is increased above  $270^\circ$ , the polar angle has two different values for a given voltage, i.e., there is a hysteresis in the Freedericksz transition. Twisted nematic cells with twist



**Figure 7.4** The polar and azimuthal angles of the liquid crystal director as functions of  $z$  in the  $90^\circ$  twisted nematic cell under various applied voltages

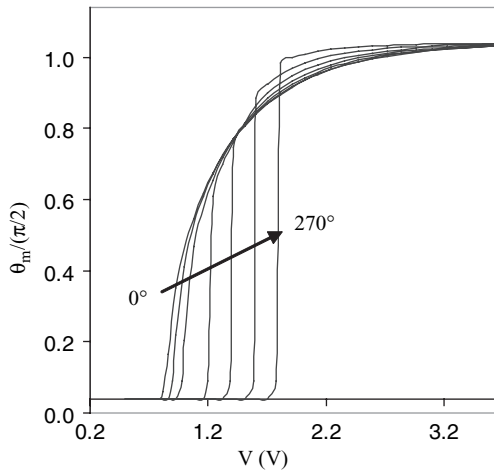
angles larger than  $90^\circ$  are known as *super-twisted nematic* (STN) cells. Because of their steep transition, they are used to make multiplexed displays on passive matrices.

If the angle  $\theta$  of the liquid crystal director varies in three dimensions, i.e.,  $\theta = \theta(x, y, z)$ , the total free energy is given by

$$F = \iiint f(\theta, \theta', x, y, z) dx dy dz \tag{7.39}$$

In the numerical calculation, a 3-D mesh with unit cell size  $(\Delta x)^3$  is used. The angle at the lattice sites  $(i, j, k)$  is calculated by

$$\theta^{\tau+1}(i, j, k) = \theta^\tau(i, j, k) + \alpha(\Delta x)^2 \left[ -\frac{\delta f^\tau}{\delta \theta}(i, j, k) \right] \tag{7.40}$$



**Figure 7.5** The polar angle at the middle plane vs. the applied voltage in twisted nematic cells with the twist angles  $0^\circ, 45^\circ, 90^\circ, 135^\circ, 180^\circ, 225^\circ,$  and  $270^\circ$



The derivatives at step  $\tau$  are calculated by

$$\theta'_x{}^\tau(i, j, k) = \frac{\theta^\tau(i+1, j, k) - \theta^\tau(i-1, j, k)}{2\Delta x} \quad (7.41)$$

$$\theta''_x{}^\tau(i) = \frac{\theta^\tau(i+1, j, k) + \theta^\tau(i-1, j, k) - 2\theta^\tau(i, j, k)}{(\Delta x)^2} \quad (7.42)$$

$$\theta''_{xy}{}^\tau(i) = \frac{\theta^\tau(i+1, j+1, k) + \theta^\tau(i-1, j-1, k) - \theta^\tau(i-1, j+1, k) - \theta^\tau(i+1, j-1, k)}{4\Delta x\Delta y} \quad (7.43)$$

and so on.

### 7.3.2 Vector representation

The liquid crystal director  $\vec{n}$  can also be specified by its three components  $(n_x, n_y, n_z)$ . The free energy density (with constant voltage) is then expressed as a function of the components and their spatial derivatives:

$$f = \frac{1}{2}K_{11}(\nabla \cdot \vec{n})^2 + \frac{1}{2}K_{22}(\vec{n} \cdot \nabla \times \vec{n})^2 + \frac{1}{2}K_{33}(\vec{n} \times \nabla \times \vec{n})^2 + q_0 K_{22} \vec{n} \cdot \nabla \times \vec{n} - \frac{1}{2} \vec{D} \cdot \vec{E} \quad (7.44)$$

In component form, we have

$$\nabla \cdot \vec{n} = \frac{\partial n_i}{\partial x_i} \quad (7.45)$$

where  $i = x, y, z$  and the convention of summing over repeating indices is used. Then

$$(\nabla \cdot \vec{n})^2 = \frac{\partial n_i}{\partial x_i} \cdot \frac{\partial n_j}{\partial x_j} \quad (7.46)$$

$$\nabla \times \vec{n} = e_{ijk} \frac{\partial n_k}{\partial x_j} \hat{x}_i \quad (7.47)$$

where  $e_{ijk}$  is the Levi-Civita symbol ( $e_{xyz} = e_{yzx} = e_{zyx} = -e_{xzy} = -e_{zxy} = -e_{yxz} = 1$  and all other  $e_{ijk} = 0$ ). Thus

$$(\nabla \times \vec{n})^2 = \frac{\partial n_l}{\partial x_k} \frac{\partial n_l}{\partial x_k} - \frac{\partial n_k}{\partial x_l} \frac{\partial n_l}{\partial x_k} \quad (7.48)$$

$$\vec{n} \cdot \nabla \times \vec{n} = e_{ijk} n_i \frac{\partial n_k}{\partial x_j} \quad (7.49)$$

$$\vec{n} \times \nabla \times \vec{n} = e_{lmi} e_{ijk} n_m \frac{\partial n_k}{\partial x_j} \hat{x}_l = \left( n_k \frac{\partial n_k}{\partial x_l} - n_k \frac{\partial n_l}{\partial x_k} \right) \hat{x}_l = -n_k \frac{\partial n_l}{\partial x_k} \hat{x}_l \quad (7.50)$$

Note that

$$n_k \frac{\partial n_k}{\partial x_l} = \frac{1}{2} \frac{\partial (n_k n_k)}{\partial x_l} = \frac{1}{2} \frac{\partial (n_x^2 + n_y^2 + n_z^2)}{\partial x_l} = \frac{1}{2} \frac{\partial (1)}{\partial x_l} = 0$$

$$(\vec{n} \times \nabla \times \vec{n})^2 = \left( -n_k \frac{\partial n_l}{\partial x_k} \right) \left( -n_i \frac{\partial n_l}{\partial x_i} \right) = n_k n_i \frac{\partial n_l}{\partial x_k} \frac{\partial n_l}{\partial x_i} \quad (7.51)$$

$$\begin{aligned} (\vec{n} \cdot \nabla \times \vec{n})^2 &= (\nabla \times \vec{n})^2 - (\vec{n} \times \nabla \times \vec{n})^2 \\ &= \left( \frac{\partial n_l}{\partial x_k} \frac{\partial n_l}{\partial x_k} - \frac{\partial n_k}{\partial x_l} \frac{\partial n_l}{\partial x_k} \right) - n_k n_i \frac{\partial n_l}{\partial x_k} \frac{\partial n_l}{\partial x_i} \end{aligned} \quad (7.52)$$

The electric energy is

$$\begin{aligned} -\frac{1}{2} \vec{E} \cdot \vec{D} &= -\frac{1}{2} \vec{E} \cdot (\vec{e} \cdot \vec{E}) = -\frac{1}{2} \vec{E} \cdot [\epsilon_o \epsilon_{\perp} \vec{E} + \epsilon_o \Delta \epsilon (\vec{E} \cdot \vec{n}) \vec{n}] \\ &= -\frac{1}{2} \epsilon_o \epsilon_{\perp} E^2 - \frac{1}{2} \epsilon_o \Delta \epsilon E_i E_j n_i n_j \end{aligned} \quad (7.53)$$

The first term on the right hand side of Equation (7.52) is a constant independent of  $n_i$  and thus it does not affect the orientation of the liquid crystal and can be omitted. The bulk free energy density becomes

$$\begin{aligned} f &= \frac{1}{2} K_{11} \frac{\partial n_i}{\partial x_i} \frac{\partial n_j}{\partial x_j} + \frac{1}{2} K_{22} \left( \frac{\partial n_j}{\partial x_i} \frac{\partial n_j}{\partial x_i} - \frac{\partial n_i}{\partial x_j} \frac{\partial n_j}{\partial x_i} \right) + \frac{1}{2} (K_{33} - K_{22}) n_i n_j \frac{\partial n_k}{\partial x_i} \frac{\partial n_k}{\partial x_j} \\ &\quad + q_o K_{22} e_{ijk} n_i \frac{\partial n_k}{\partial x_j} - \frac{1}{2} \epsilon_o \Delta \epsilon E_i E_j n_i n_j \end{aligned} \quad (7.54)$$

In the equilibrium state, the total free energy is minimized. The director components  $n_i$  ( $i = x, y, z$ ) in space in the equilibrium state can also be calculated numerically by the relaxation method. At the lattice site  $(l_x, l_y, l_z)$  of the mesh the changes of the director components from step  $\tau$  to step  $(\tau + 1)$  are calculated from the values of the director components at step  $\tau$ :

$$\Delta n_i^{\tau+1}(l_x, l_y, l_z) = \alpha (\Delta x)^2 \left( -\frac{\delta f}{\delta n_i} \right)^{\tau}(l_x, l_y, l_z) \quad (7.55)$$

The variation of the free energy with respect to  $n_i$  is

$$\frac{\delta f}{\delta n_i} = \frac{\partial f}{\partial n_i} - \frac{\partial}{\partial x_j} \left( \frac{\partial f}{\partial n'_{i,j}} \right) \quad (7.56)$$

where  $n'_{i,j} = \partial n_i / \partial x_j$ . Thus

$$\begin{aligned}
 \frac{\partial f}{\partial n_i} &= \frac{\partial}{\partial n_i} \left[ \frac{1}{2} (K_{33} - K_{22}) n_l n_j \frac{\partial n_k}{\partial x_l} \frac{\partial n_k}{\partial x_j} + q_o K_{22} e_{ljk} n_l \frac{\partial n_k}{\partial x_j} - \frac{1}{2} \varepsilon_o \Delta \varepsilon E_l E_j n_l n_j \right] \\
 &= \frac{1}{2} (K_{33} - K_{22}) \left( \delta_{il} n_j \frac{\partial n_k}{\partial x_l} \frac{\partial n_k}{\partial x_j} + \delta_{ij} n_l \frac{\partial n_k}{\partial x_l} \frac{\partial n_k}{\partial x_j} \right) \\
 &\quad + q_o K_{22} \delta_{il} e_{ijk} \frac{\partial n_k}{\partial x_j} - \frac{1}{2} \varepsilon_o \Delta \varepsilon (\delta_{il} E_l E_j n_j + \delta_{ij} E_l E_j n_l) \\
 &= \frac{1}{2} \left( K_{33} - K_{22} \right) \left( n_j \frac{\partial n_k}{\partial x_i} \frac{\partial n_k}{\partial x_j} + n_l \frac{\partial n_k}{\partial x_l} \frac{\partial n_k}{\partial x_i} \right) \\
 &\quad + q_o K_{22} e_{ijk} \frac{\partial n_k}{\partial x_j} - \frac{1}{2} \varepsilon_o \Delta \varepsilon (E_i E_j n_j + E_l E_l n_l) \\
 &= (K_{33} - K_{22}) n_j \frac{\partial n_k}{\partial x_i} \frac{\partial n_k}{\partial x_j} + q_o K_{22} e_{ijk} \frac{\partial n_k}{\partial x_j} - \varepsilon_o \Delta \varepsilon E_i E_j n_j
 \end{aligned} \tag{7.57}$$

$$\begin{aligned}
 \frac{\partial f}{\partial n'_{i,j}} &= \frac{\partial}{\partial n'_{i,j}} \left[ \frac{1}{2} K_{11} \frac{\partial n_l}{\partial x_l} \frac{\partial n_m}{\partial x_m} + \frac{1}{2} K_{22} \left( \frac{\partial n_m}{\partial x_l} \frac{\partial n_m}{\partial x_l} - \frac{\partial n_l}{\partial x_m} \frac{\partial n_m}{\partial x_l} \right) \right. \\
 &\quad \left. + \frac{1}{2} (K_{33} - K_{22}) n_l n_m \frac{\partial n_k}{\partial x_l} \frac{\partial n_k}{\partial x_m} + q_o K_{22} e_{lmk} n_l \frac{\partial n_k}{\partial x_m} \right] \\
 &= K_{11} \delta_{ij} \frac{\partial n_m}{\partial x_m} + K_{22} \left( \frac{\partial n_i}{\partial x_j} - \frac{\partial n_j}{\partial x_i} \right) + (K_{33} - K_{22}) n_j n_m \frac{\partial n_i}{\partial x_m} + q_o K_{22} e_{lji} n_l
 \end{aligned} \tag{7.58}$$

$$\begin{aligned}
 \frac{\partial}{\partial x_j} \left( \frac{\partial f}{\partial n'_{i,j}} \right) &= \frac{\partial}{\partial x_j} \left[ K_{11} \delta_{ij} \frac{\partial n_m}{\partial x_m} + K_{22} \left( \frac{\partial n_i}{\partial x_j} - \frac{\partial n_j}{\partial x_i} \right) + (K_{33} - K_{22}) n_j n_m \frac{\partial n_i}{\partial x_m} + q_o K_{22} e_{lji} n_l \right] \\
 &= K_{11} \frac{\partial^2 n_m}{\partial x_m \partial x_i} + K_{22} \left( \frac{\partial^2 n_i}{\partial x_j^2} - \frac{\partial^2 n_j}{\partial x_j \partial x_i} \right) \\
 &\quad + (K_{33} - K_{22}) \left( n_j n_m \frac{\partial^2 n_i}{\partial x_m \partial x_j} + n_j \frac{\partial n_i}{\partial x_m} \frac{\partial n_m}{\partial x_j} + n_m \frac{\partial n_i}{\partial x_m} \frac{\partial n_j}{\partial x_j} \right) + q_o K_{22} e_{lji} \frac{\partial n_l}{\partial x_j} \\
 - \frac{\delta f}{\delta n_i} &= (K_{11} - K_{22}) \frac{\partial^2 n_j}{\partial x_j \partial x_i} + K_{22} \frac{\partial^2 n_i}{\partial x_j^2} + (K_{33} - K_{22}) n_j n_k \frac{\partial^2 n_i}{\partial x_k \partial x_j} \\
 &\quad + (K_{33} - K_{22}) \left( n_j \frac{\partial n_i}{\partial x_k} \frac{\partial n_k}{\partial x_j} + n_k \frac{\partial n_i}{\partial x_k} \frac{\partial n_j}{\partial x_j} - n_j \frac{\partial n_k}{\partial x_i} \frac{\partial n_k}{\partial x_j} \right) \\
 &\quad - 2q_o K_{22} e_{ijk} \frac{\partial n_k}{\partial x_j} + \varepsilon_o \Delta \varepsilon E_i E_j n_j
 \end{aligned} \tag{7.59}$$

In this representation, one must be careful that  $\vec{n}$  is a unit vector, i.e.,  $n_i n_i = 1$ . This issue can be taken care of by two methods: (1) the Lagrange multiplier method and (2) the renormalization method. In the first method, the Lagrange multiplier  $\lambda(n_i n_i - 1)$  should be added to the free energy density. In the second method, the values of the director components at step  $\tau+1$  are calculated by

$$n_i^{\tau+1}(l_x, l_y, l_z) = \frac{n_i^\tau(l_x, l_y, l_z) + \Delta n_i^{\tau+1}(l_x, l_y, l_z)}{\{[n_j^\tau(l_x, l_y, l_z) + \Delta n_j^{\tau+1}(l_x, l_y, l_z)] \cdot [n_j^\tau(l_x, l_y, l_z) + \Delta n_j^{\tau+1}(l_x, l_y, l_z)]\}^{1/2}} \tag{7.61}$$

If the anchoring of the liquid crystal at the cell surface is infinitely strong, then  $\vec{n}$  is fixed at the boundary. If the anchoring is weak, the surface energy must be considered in the minimization of the total free energy. Expressed in terms of the liquid crystal director, the surface energy is given by [17]

$$f_s = \frac{1}{2} W_{ij} n_i n_j \quad (7.62)$$

where  $W_{ij}$  is the anchoring tensor, which is symmetric. In the principal frame of the anchoring, the anchoring tensor is diagonalized. As an example, in a cell with homogeneous anchoring along the  $x$  axis and the cell normal direction along the  $z$  axis, the anchoring matrix is given by

$$\vec{W} = \begin{pmatrix} 0 & 0 & 0 \\ 0 & W_a & 0 \\ 0 & 0 & W_p \end{pmatrix} \quad (7.63)$$

where  $W_p$  and  $W_a$  are the polar and azimuthal anchoring strengths, respectively. In this representation, the same problem occurs as in the angle representation: an incorrect free energy may be numerically calculated when the liquid crystal directors at two neighboring lattice sites are anti-parallel. In that case, the numerical calculation will generate a large elastic energy, while the actual elastic energy is zero because  $\vec{n}$  and  $-\vec{n}$  are equivalent.

### 7.3.3 Tensor representation

In order to avoid the problem of incorrect calculation of the free energy when the liquid crystal directors at two neighboring lattice sites are anti-parallel, the tensor representation was introduced [5, 18, 19], where the orientation of the liquid crystal director is represented by the tensor defined by

$$\vec{Q} = \vec{n}\vec{n} - \frac{1}{3} \vec{I} \quad (7.64)$$

where  $\vec{I}$  is the identity tensor. Its components are given by

$$Q_{ij} = n_i n_j - \frac{1}{3} \delta_{ij} \quad (7.65)$$

where  $\delta_{ij}$  is the Kronecker delta. The elastic energy is calculated from  $\vec{Q}$ . When the liquid crystal directors at two neighboring lattice sites are anti-parallel, the  $\vec{Q}$  tensor is the same. The actual zero elastic energy is calculated. The elastic energy (Equation (7.43)) has four terms, and therefore four terms of the derivatives of  $\vec{Q}$  are needed:

$$G_1 = \frac{\partial Q_{jk}}{\partial x_l} \frac{\partial Q_{jk}}{\partial x_l} = \frac{\partial(n_j n_k)}{\partial x_l} \frac{\partial(n_j n_k)}{\partial x_l} = 2 \frac{\partial n_j}{\partial x_l} \frac{\partial n_j}{\partial x_l} \quad (7.66)$$

Note that  $\partial(n_j n_j)/\partial x_l = 0$ . From Equations (7.44) and (7.49) we have

$$\begin{aligned} \nabla \cdot (\vec{n} \nabla \cdot \vec{n} + \vec{n} \times \nabla \times \vec{n}) &= \frac{\partial}{\partial x_l} \left( n_l \frac{\partial n_k}{\partial x_k} - n_k \frac{\partial n_l}{\partial x_k} \right) = \frac{\partial n_l}{\partial x_l} \frac{\partial n_k}{\partial x_k} - \frac{\partial n_k}{\partial x_l} \frac{\partial n_l}{\partial x_k} \\ &+ n_l \frac{\partial^2 n_k}{\partial x_l \partial x_k} - n_k \frac{\partial^2 n_l}{\partial x_l \partial x_k} = \frac{\partial n_l}{\partial x_l} \frac{\partial n_k}{\partial x_k} - \frac{\partial n_k}{\partial x_l} \frac{\partial n_l}{\partial x_k} \end{aligned} \quad (7.67)$$

Substituting Equations (7.45), (7.47), and (7.66) into Equation (7.65), we have

$$\begin{aligned} G_1 &= 2[(\nabla \cdot \vec{n})^2 + (\nabla \times \vec{n})^2 - \nabla \cdot (\vec{n} \nabla \cdot \vec{n} + \vec{n} \times \nabla \times \vec{n})] \\ &= 2[(\nabla \cdot \vec{n})^2 + (\vec{n} \cdot \nabla \times \vec{n})^2 + (\vec{n} \times \nabla \times \vec{n})^2 - \nabla \cdot (\vec{n} \nabla \cdot \vec{n} + \vec{n} \times \nabla \times \vec{n})] \end{aligned} \quad (7.68)$$

The last term on the right hand side of this equation becomes a surface term when integrated over the volume and can usually be neglected:

$$\begin{aligned} G_2 &= \frac{\partial Q_{jk}}{\partial x_k} \frac{\partial Q_{jl}}{\partial x_l} = \frac{\partial(n_j n_k)}{\partial x_k} \frac{\partial(n_j n_l)}{\partial x_l} = \frac{\partial n_k}{\partial x_k} \frac{\partial n_l}{\partial x_l} + n_k n_l \frac{\partial n_j}{\partial x_k} \frac{\partial n_j}{\partial x_l} \\ &= (\nabla \cdot \vec{n})^2 + (\vec{n} \times \nabla \times \vec{n})^2 \end{aligned} \quad (7.69)$$

In obtaining this Equation (7.68), we used Equations (7.45) and (7.50):

$$G_4 = e_{jkl} Q_{jm} \frac{\partial Q_{km}}{\partial x_l} = e_{jkl} \left( n_j n_m - \frac{1}{3} \delta_{jm} \right) \frac{\partial(n_k n_m)}{\partial x_l} = e_{jkl} n_j \frac{\partial n_k}{\partial x_l} = -\vec{n} \times \nabla \times \vec{n} \quad (7.70)$$

$$\begin{aligned} G_6 &= Q_{jk} \frac{\partial Q_{lm}}{\partial x_j} \frac{\partial Q_{lm}}{\partial x_k} = \left( n_j n_k - \frac{1}{3} \delta_{jk} \right) \frac{\partial(n_l n_m)}{\partial x_j} \frac{\partial(n_l n_m)}{\partial x_k} \\ &= n_j n_k \frac{\partial(n_l n_m)}{\partial x_j} \frac{\partial(n_l n_m)}{\partial x_k} - \frac{1}{3} \frac{\partial(n_l n_m)}{\partial x_j} \frac{\partial(n_l n_m)}{\partial x_j} \\ &= 2n_j n_k \frac{\partial n_m}{\partial x_j} \frac{\partial n_m}{\partial x_k} - \frac{1}{3} \frac{\partial(n_l n_m)}{\partial x_j} \frac{\partial(n_l n_m)}{\partial x_j} = 2(\vec{n} \times \nabla \times \vec{n})^2 - \frac{1}{3} G_1 \end{aligned} \quad (7.71)$$

From Equations (7.67), (7.68), (7.69), and (7.70) we get the free energy density

$$\begin{aligned} f &= \frac{1}{12} (-K_{11} + 3K_{22} + K_{33}) G_1 + \frac{1}{2} (K_{11} - K_{22}) G_2 \\ &\quad + \frac{1}{4} (-K_{11} + K_{33}) G_6 - q_o K_{22} G_4 - \frac{1}{2} \epsilon_o \Delta \epsilon E_i E_j n_i n_j \end{aligned} \quad (7.72)$$

The relaxation method is used in the numerical calculation. The change of the director component  $n_i$  on lattice site  $(l_x, l_y, l_z)$  of the mesh at step  $\tau + 1$  is given by

$$\Delta n_i^{\tau+1}(l_x, l_y, l_z) = \alpha (\Delta x)^2 \left[ -\frac{\delta f^\tau}{\delta n_i}(l_x, l_y, l_z) \right] \quad (7.73)$$

The variation of the free energy with respect to  $n_i$  can be expressed in terms of the variation of the free energy with respect to  $Q_{jk}$ :

$$\frac{\delta f}{\delta n_i} = \frac{\delta f}{\delta Q_{jk}} \frac{\partial Q_{jk}}{\partial n_i} = \frac{\delta f}{\delta Q_{jk}} \frac{\partial(n_j n_k)}{\partial n_i} = \frac{\delta f}{\delta Q_{jk}} (n_j \delta_{ik} + n_k \delta_{ij}) = 2n_j \frac{\delta f}{\delta Q_{ji}} \quad (7.74)$$

$$\begin{aligned}
 H_1 &= \frac{\delta G_1}{\delta n_i} = 2n_j \frac{\delta G_1}{\delta Q_{ji}} = 2n_j \left[ \frac{\partial G_1}{\partial Q_{ji}} - \frac{\partial}{\partial x_l} \left( \frac{\partial G_1}{\partial Q_{ji,l}} \right) \right] \\
 &= -2n_j \frac{\partial}{\partial x_l} \left[ \frac{\partial (Q_{uv,w} Q_{uv,w})}{\partial Q_{ji,l}} \right] = -2n_j \frac{\partial (2Q_{uv,w} \delta_{ju} \delta_{iv} \delta_{lw})}{\partial x_l} = -4n_j \frac{\partial^2 Q_{ji}}{\partial x_l \partial x_l}
 \end{aligned} \quad (7.75)$$

$$H_2 = \frac{\delta G_2}{\delta n_i} = 2n_j \frac{\delta G_2}{\delta Q_{ji}} = -2n_j \left( \frac{\partial^2 Q_{jl}}{\partial x_i \partial x_l} + \frac{\partial^2 Q_{il}}{\partial x_j \partial x_l} \right) \quad (7.76)$$

$$H_4 = \frac{\delta G_4}{\delta n_i} = 2n_j \frac{\delta G_4}{\delta Q_{ji}} = -2n_j \left( e_{jkl} \frac{\partial Q_{li}}{\partial x_k} + e_{ikl} \frac{\partial Q_{lj}}{\partial x_k} \right) \quad (7.77)$$

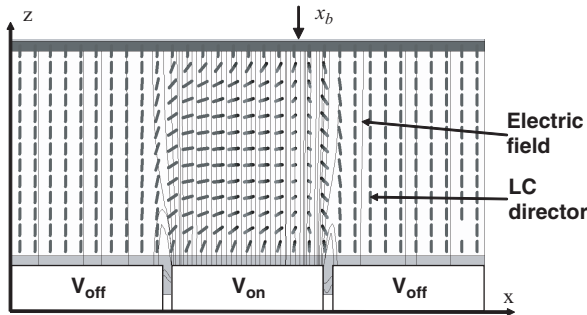
$$H_6 = \frac{\delta G_6}{\delta n_i} = 2n_j \frac{\delta G_6}{\delta Q_{ji}} = -2n_j \left( 2 \frac{\partial Q_{kl}}{\partial x_k} \frac{\partial Q_{ji}}{\partial x_l} + 2Q_{kl} \frac{\partial^2 Q_{ji}}{\partial x_l \partial x_k} - \frac{\partial Q_{kl}}{\partial x_i} \frac{\partial Q_{kl}}{\partial x_j} \right) \quad (7.78)$$

where  $Q_{jk,l} = \partial Q_{jk} / \partial x_l$ . Expressed in terms of  $H_1, H_2, H_4$ , and  $H_6$ , the change of the director component  $n_i$  at each lattice site is

$$\begin{aligned}
 \Delta n_i^{\tau+1} &= \alpha (\Delta x)^2 \left[ -\frac{1}{12} (-K_{11} + 3K_{22} + K_{33}) H_1^\tau - \frac{1}{2} (K_{11} - K_{22}) H_2^\tau \right. \\
 &\quad \left. - \frac{1}{4} (-K_{11} + K_{33}) H_6^\tau + K_{22} q_0 H_4^\tau + \Delta \varepsilon \varepsilon_0 (E_i E_j n_j) \right]
 \end{aligned} \quad (7.79)$$

Because  $\vec{n}$  is a unit vector, the director components must be renormalized by using Equation (7.60). In this representation, the problem of incorrect calculation of the free energy when the liquid crystal directors at two neighboring lattice sites are anti-parallel is avoided. A different problem, however, may exist when a real pi-wall defect is artificially removed [20]. Therefore the computer-simulated results should be carefully compared to the experimental results in order to prevent mistakes.

As an example, we consider a vertical alignment (VA) mode microdisplay [21, 22]. The pixel size is  $15 \mu\text{m}$  and the inter-pixel gap is  $0.9 \mu\text{m}$ . The cell thickness is  $2.3 \mu\text{m}$ . Homeotropic alignment layers are coated on the inner surface of the cell. The parameters of the liquid crystal are:  $K_{11} = 16.7 \times 10^{-12} \text{N}$ ,  $K_{22} = 7 \times 10^{-12} \text{N}$ ,  $K_{33} = 18.1 \times 10^{-12} \text{N}$ ,  $\varepsilon_{\parallel} = 3.6$ , and  $\varepsilon_{\perp} = 7.8$ . The voltage applied across the on-pixel is  $V_{on} = 5 \text{V}$  and the voltage applied across the off-pixel is  $V_{off} = 0.7 \text{V}$ . The simulated director configuration is shown in Figure 7.6. In the field-off state, the liquid crystal is aligned homeotropically.



**Figure 7.6** Simulated liquid crystal director configuration in the VA mode microdisplay

When a sufficiently high field is applied across the cell, the liquid crystal director is tilted toward the  $x$  direction because of the negative dielectric anisotropy. Because of the fringing effect, the electric field is not exactly in the  $z$  direction near the fringes of the pixel. The liquid crystal director is tilted in opposite directions at the two edges of the pixel; thus a defect wall is formed at the position  $x_b$ . If the liquid crystal director were confined in the  $x$ - $z$  plane, there would be a large splay and bend distortion. The figure shows that the liquid crystal director escapes in the  $y$  direction because of the small twist elastic constant.

## Homework Problems

- 7.1 In the display cell shown in Figure 7.3, calculate and plot the electric field in the cell. Also calculate the equal-potential lines for the following voltages: 2 V, 4 V, 6 V, and 8 V.
- 7.2 Use the angle representation and numerically calculate the tilt angle in the splay geometry as a function of the coordinate  $z$  at the following applied fields:  $E = 1.05E_c$ ,  $E = 1.3E_c$ ,  $E = 1.5E_c$ ,  $E = 2.0E_c$ , and  $E = 5.0E_c$ , where  $E_c$  is the threshold field of the Fredericksz transition. The cell thickness is  $5 \mu\text{m}$ . The elastic constants are  $K_{11} = 6.4 \times 10^{-12} \text{ N}$  and  $K_{33} = 10 \times 10^{-12} \text{ N}$ . Compare your results with Figure 5.4.
- 7.3  $90^\circ$  twisted nematic display. (1) Use the angle representation to numerically calculate the polar and azimuthal angles as a function of the coordinate  $z$  at the following applied voltages:  $V = 1.0 \text{ V}$ ,  $V = 1.2 \text{ V}$ ,  $V = 1.5 \text{ V}$ ,  $V = 2.0 \text{ V}$ , and  $V = 5.0 \text{ V}$ . The parameters of the cell and the liquid crystal are given in Figure 7.4. (2) Use the Jones matrix method to calculate the transmittance of the display as a function of applied voltage. The back polarizer is parallel to the liquid crystal director at the entrance plane and the front polarizer is parallel to the liquid crystal director at the exit plane. The refractive indices are  $n_e = 1.6$  and  $n_o = 1.5$ .
- 7.4 Use the tensor representation to numerically calculate the liquid crystal director configuration of a cholesteric liquid crystal in a hybrid cell. The cell thickness and length are  $L_z = 10 \mu\text{m}$  and  $L_x = 20 \mu\text{m}$ , respectively. The director is only a function of  $x$  (parallel to the cell surface) and  $z$  (perpendicular to the cell surface). On the top surface of the cell the liquid crystal is anchored homotropically, while at the bottom of the cell it is anchored homogeneously. The pitch  $P$  of the liquid crystal is  $5 \mu\text{m}$ . Initially the liquid crystal in the cell is in the isotropic state. The parameters of the liquid crystal are  $K_{11} = 6 \times 10^{-12} \text{ N}$ ,  $K_{22} = 3 \times 10^{-12} \text{ N}$ , and  $K_{33} = 10 \times 10^{-12} \text{ N}$ . Using periodic boundary conditions in the  $x$  direction, plot the director configuration in the  $x$ - $z$  plane.
- 7.5 Use the tensor representation to numerically calculate the liquid crystal director configuration of the cholesteric liquid crystal in the cell discussed in the previous problem. A voltage of 5 V is applied across the cell. The dielectric constants of the liquid crystals are  $\epsilon_{\perp} = 5$  and  $\epsilon_{\parallel} = 15$ . Using periodic boundary conditions in the  $x$  direction, plot the director configuration in the  $x$ - $z$  plane.

## References

- 1 J. E. Anderson, P. Watson, and P. J. Bos, *LC3D: liquid crystal display 3-D director simulator, software and technology guide* (Artech House, Reading, MA, 1999).
- 2 DIMOS, Autronic-Melchers GmbH, <http://www.autronic-melchers.com/index.html>.
- 3 LCD Master, [http://www.shinetech.jp.eng/index\\_e.html](http://www.shinetech.jp.eng/index_e.html).
- 4 Techwitz LCD, <http://www.sanayisystem.com/introduction.html>.
- 5 V. G. Chigrinov, H. S. Kwok, D. A. Yakpylev, G. V. Simonenko, and V. I. Tsoy, 'Invited paper, LCD optimization and modeling', *SID Symp. Dig.*, **28.1**, 982 (2004).
- 6 LCQuest, <http://www.eng.ox.ac.uk/lcquest/>.
- 7 Z. Ge, T. X. Wu, R. Lu, X. Zhu, Q. Hong, and S.-T. Wu, 'Comprehensive three-dimension dynamic modeling of liquid crystal devices using finite element method', *J. Disp. Technol.*, **1**, 194 (2005).
- 8 A. Taflove, *Computational electrodynamics: the finite-difference time domain method* (Reading, MA, Artech House, 1995).

- 9 J. Jin, *The finite element method in electromagnetics*, 2nd edn (Wiley-IEEE Press, Piscataway, NJ, 2002).
- 10 Y. W. Kwon and H. Bang, *The finite element method using MATLAB* (Boca Raton, FL CRC Press, 2000).
- 11 R. Barberi and G. Barbero, 'Variational calculus and simple applications of continuum theory', Chapter IX in *Liquid crystal materials*, ed. I. C. Khoo (Gordon and Breach, Amsterdam, 1991).
- 12 D. J. Griffiths, *Introduction to electrodynamics*, 2nd edn (Prentice Hall, Englewood Cliffs, NJ, 1989).
- 13 D. Jackson, *Classic electrodynamics*, 2nd edn (John Wiley & Sons, Inc., New York, 1975).
- 14 J. Mathews and R. L. Walker, *Mathematical methods of physics*, 2nd edn (W. A. Benjamin, Menlo Park, CA, 1970).
- 15 J. R. Reitz, F. J. Milford, and R. W. Christy, *Foundations of electromagnetic theory* (Addison-Wesley Reading, MA, 1993).
- 16 H. Mori, E. C. Gartland, Jr., J. R. Kelly, and P. J. Bos, 'Multidimensional director modeling using the Q tensor representation', *Jpn. J. Appl. Phys.*, **38**, 135 (1999).
- 17 S. V. Shiyankovskii, I. I. Smalyukh, and O. D. Lavrentovich, 'Computer simulations and fluorescence confocal polarizing microscopy of structures in cholesteric liquid crystals', in *Defects in liquid crystals: computer simulations, theory and experiments* (Kluwer Academic, Dordrecht, 2001).
- 18 D. W. Berreman and S. Meiboom, 'Tensor representation of Oseen-Frank strain energy in uniaxial cholesterics', *Phys. Rev. A*, **30**, 1955 (1984).
- 19 S. Dickmann, J. Eschler, O. Cossalter, and D. A. Mlynski, 'Simulation of LCDs including elastic anisotropy and inhomogeneous fields', *SID Symp. Dig. Tech. Pap.*, **24**, 638 (1993).
- 20 J. E. Anderson, P. Watson, and P. J. Bos, 'Comparisons of the vector and tensor method for simulating liquid crystal devices', *Liq. Cryst.*, **28**, 109 (2000).
- 21 K.-H. Fan-Chiang, X. Zhu, S.-T. Wu, and S.-H. Chen, 'Eliminating fringing field effects of vertical aligned liquid-crystal-on-silicon by using circularly polarized light', *SID Symp. Dig. Tech. Pap.*, **36**, 1290 (2005).
- 22 K.-H. Fan-Chiang, S.-T. Wu, and S.-H. Chen, 'Fringing-field effects on high-resolution liquid crystal microdisplays', *J. Disp. Techn.*, **1**, 309 (2005).



# 8

## Transmissive Liquid Crystal Displays

### 8.1 Introduction

Three types of liquid crystal displays (LCDs) have been developed: (1) transmissive, (2) reflective, and (3) transreflective. A transmissive LCD uses a backlight for illuminating the LCD panel which results in a high brightness and high contrast ratio. Some transmissive LCDs do not use phase compensation films or a multi-domain approach so that their viewing angle is limited and are more suitable for single viewer applications, such as notebook computers and games. With proper phase compensation, direct-view transmissive LCDs exhibit a wide viewing angle and have been used extensively for multiple viewers, such as desktop computers and televisions. Transmissive LCDs can also be used for projection displays, such as in data projectors. There, a high-power arc lamp or light-emitting diode (LED) arrays are used as the light source. To reduce the size of the optics and save on the cost of the projection system, the LCD panel is usually made small (less than 25 mm in the diagonal). Thus, polysilicon thin-film transistors (TFTs) are commonly used.

Similarly, reflective LCDs can be subdivided into direct-view and projection displays. In principle, a direct-view reflective LCD does not require a backlight so its weight is light and power consumption is low. A major drawback is poor readability under weak ambient light. Thus, a reflective LCD is more suitable for projection TVs employing liquid-crystal-on-silicon (LCoS) microdisplay panels. In a LCoS, the reflector employed is an aluminum metallic mirror. The viewing angle is less critical in projection displays than direct-view displays.

For outdoor applications, the displayed images of a transmissive LCD could be washed out by sunlight. A reflective LCD would be a better choice. However, such a reflective display is unreadable in dark ambient conditions. Transreflective LCDs integrate the features of a transmissive display and a reflective display. Thus, in dark ambient conditions the backlight is turned on and the display works primarily in the transmissive mode, while in bright ambient conditions, the backlight is switched off and only the reflective mode is operational.

Two monographs have been dedicated to projection displays [1] and reflective displays [2]. Therefore, in this chapter we will focus on mainstream TFT-addressed wide-view transmissive LCDs. We will start by introducing the twisted nematic (TN) mode, and then delve into in-plane switching (IPS) and multi-domain vertical alignment (MVA). Phase compensation methods for achieving wide viewing angles will be addressed.

## 8.2 Twisted Nematic Cells

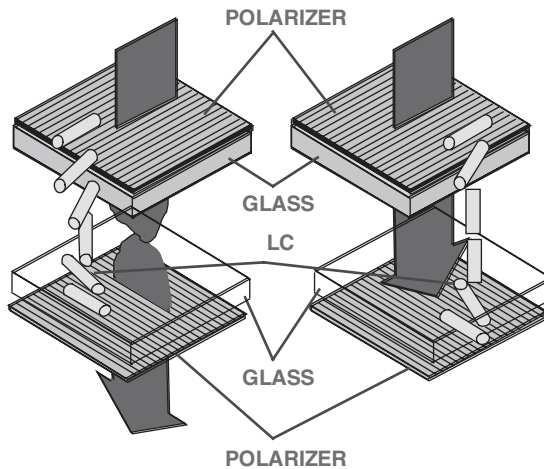
The 90° twisted nematic (TN) cell [3] has been used extensively for notebook computers where the viewing angle is not too critical. Figure 8.1 shows the LC director configurations of the normal-white TN cell in the voltage-off (left) and voltage-on (right) states.

In the voltage-off state, the top LC alignment is parallel to the optic axis of the top polarizer, while the bottom LC directors are rotated 90° and parallel to the optic axis of the bottom analyzer. When  $d\Delta n$  of the LC layer satisfies the Gooch–Tarry first minimum condition [4], the incoming linearly polarized light will follow closely the molecular twist and transmits through the crossed analyzer. In the voltage-on state, the LC directors are reoriented to be perpendicular to the substrates, excepting the boundary layers. The incoming light experiences little phase change and is absorbed by the analyzer, resulting in a dark state. The beauty of the TN cell is that the boundary layers are orthogonal so that their residual phase compensates for each other. As a result, the dark state occurs at a relatively low voltage.

### 8.2.1 Voltage-dependent transmittance

To compare different operating modes, let us focus on the normalized transmittance by ignoring the optical losses from polarizers and indium–tin–oxide (ITO) layers, and the interface reflections from substrates. The normalized transmittance ( $T_{\perp}$ ) of a TN cell can be described by the following Jones matrices as  $T_{\perp} = |M|^2$  [5]:

$$M = \begin{vmatrix} \cos \beta & \sin \beta \\ \sin \phi & \cos \phi \end{vmatrix} \begin{vmatrix} \cos \phi & -\sin \phi \\ \sin \phi & \cos \phi \end{vmatrix} \begin{vmatrix} \cos X - i \frac{\Gamma \sin X}{2X} & \phi \frac{\sin X}{X} \\ -\phi \frac{\sin X}{X} & \cos X + i \frac{\Gamma \sin X}{2X} \end{vmatrix} \begin{vmatrix} -\sin \beta \\ \cos \beta \end{vmatrix} \quad (8.1)$$



**Figure 8.1** LC and polarizer configurations of a 90° TN cell: left,  $V = 0$ ; right,  $V \gg V_{th}$

Here  $\beta$  is the angle between the polarization axis and the front LC director,  $\phi$  is the twist angle,  $X = \sqrt{\phi^2 + (\Gamma/2)^2}$ , and  $\Gamma = 2\pi d\Delta n/\lambda$ , where  $d$  is the cell gap. By simple algebraic calculations, the following analytical expression for  $|M|^2$  is derived:

$$|M|^2 = T_{\perp} = \left( \frac{\phi}{X} \cos \phi \sin X - \sin \phi \cos X \right)^2 + \left( \frac{\Gamma \sin X}{2X} \right)^2 \sin^2(\phi - 2\beta) \quad (8.2)$$

Equation (8.2) is a general formula describing the light transmittance of a TN cell (without voltage) as a function of twist angle, beta angle, and  $d\Delta n/\lambda$ . For a  $90^\circ$  TN cell,  $\phi = \pi/2$  and Equation (8.2) is simplified to

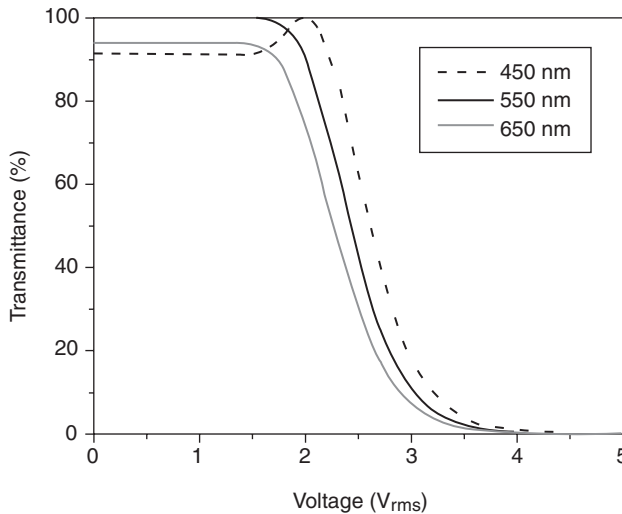
$$T_{\perp} = \cos^2 X + \left( \frac{\Gamma}{2X} \cos 2\beta \right)^2 \sin^2 X \quad (8.3)$$

Equation (8.3) has a special solution, i.e.,  $\cos^2 X = 1$ . When  $\cos X = \pm 1$  (i.e.,  $X = m\pi$ ,  $m$  an integer), then  $\sin X = 0$  and the second term in Equation (8.3) vanishes. Therefore,  $T_{\perp} = 1$ , independent of  $\beta$ . By setting  $X = m\pi$  and knowing that  $\Gamma = 2\pi d\Delta n/\lambda$ , the Gooch–Tarry condition is found as follows:

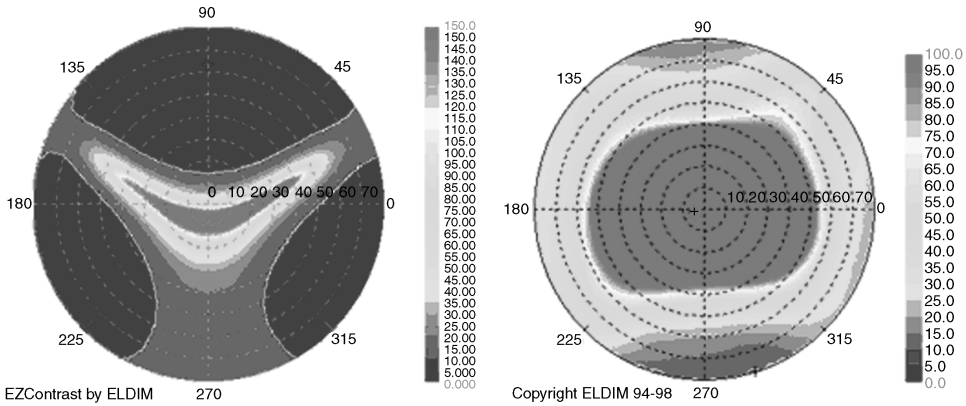
$$\frac{d\Delta n}{\lambda} = \sqrt{m^2 - \frac{1}{4}} \quad (8.4)$$

For the lowest order  $m = 1$ ,  $d\Delta n/\lambda = \sqrt{3}/2$ . This is the Gooch–Tarry first minimum condition for the  $90^\circ$  TN cell. For the second order,  $m = 2$  and  $d\Delta n = \sqrt{15}/2$ . The second minimum condition is used only for low-end displays such as wrist watches because a large cell gap is easier to fabricate and the utilized cyano-biphenyl LCs are less expensive. For notebook TFT LCDs, the first minimum is preferred because a rapid response time is required.

Figure 8.2 depicts the normalized light transmittance ( $T_{\perp}$ ) of a  $90^\circ$  TN cell at three primary wavelengths  $R = 650$ ,  $G = 550$ , and  $B = 450$  nm. Since the human eye is most sensitive to green, we normally optimize the cell design at  $\lambda = 550$  nm. From Equation (8.4), the first  $T_{\perp} = 1$  occurs at



**Figure 8.2** Voltage-dependent transmittance of a normal-white  $90^\circ$  TN cell.  $d\Delta n = 480$  nm



**Figure 8.3** Measured iso-contrast plots for TN LCDs without (left) and with (right) wide-view films. (Courtesy of Dr. H. Mori, Fuji Photo Film)

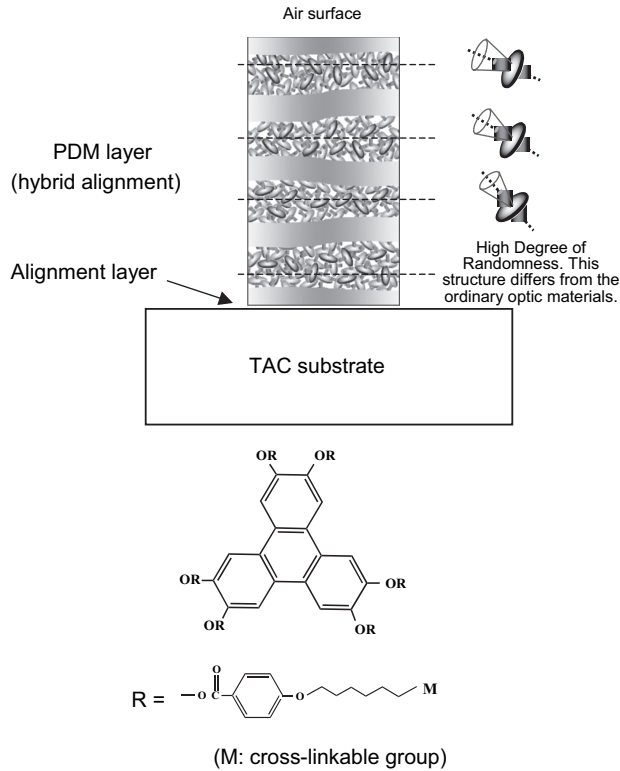
$d\Delta n \sim 480$  nm. The color dispersion (i.e., the wavelength dependency of the light transmittance) at  $\beta = 0$  is not too sensitive to  $d\Delta n/\lambda$  beyond the first minimum. Therefore, the TN cell can be treated as an achromatic half-wave plate. The response time depends on the cell gap and the  $\gamma_1/K_{22}$  of the LC mixture employed. For a  $4 \mu\text{m}$  cell gap, the optical response time is about 20–30 ms. At  $V = 5 V_{\text{rms}}$ , the contrast ratio (CR) reaches about 400:1. These performances, although not perfect, are acceptable for notebook computer applications. A major drawback of the TN cell is its narrow viewing angle and gray-scale inversion originating from the LC director’s tilt. Because of this tilt, the viewing angle in the vertical direction is narrow and asymmetric [6].

### 8.2.2 Film-compensated TN cells

Figure 8.3 (left) shows the simulated iso-contrast contour of a TN LCD [7]. In the normal viewing direction, the TN cell exhibits a good contrast ratio, but the contrast rapidly decreases in the upper direction and in the lower diagonal directions. In the lower direction, the contrast remains high, but gray-scale inversion is observed (not shown in Figure 8.3). The narrow viewing angle of a TN LCD is caused by several factors, e.g., the optical anisotropy of liquid crystals, the off-axis light leakage from crossed polarizers, the light scattering on the surface of polarizer or at the color filters, the collimation of backlight, and light diffraction from the cell structure.

In the on-state of a TN cell, the LC directors in the upper half are reoriented along the rubbing direction with almost no twist and that the lower half have a similar structure with the director plane orthogonal to that of the upper half. Thus, a uniform phase compensation film, such as a uniaxial  $a$  plate, cannot compensate the upper and lower parts simultaneously. Instead, a pair of wide-view films need to be used separately on both sides of the TN LC cell in order to compensate each of the half layers. Fuji Photo has skillfully developed discotic LC films for widening the viewing angle of TN cells. The molecular structures of the wide-view (WV) discotic material are shown in Figure 8.4.

Figure 8.4 shows the structure of the Fuji WV film. A discotic material (triphenylene derivatives) is coated on an alignment layer on a tri-acetyl cellulose (TAC) substrate. The discotic material has a hybrid alignment structure and three important features: (1) It has  $\pi$ -electrons spread in a disk-like shape, which gives rise to a high birefringence. (2) It takes on discotic nematic ( $N_D$ ) phase at a lower temperature than the temperature at which the TAC substrate starts to deform; this feature enables a uniform and monodomain film in a wide range of areas without defects. (3) It has cross-linkable groups at all of six side chains to make the obtained film durable.



**Figure 8.4** Structure of the WV film and the employed discotic compound. PDM represents polymerized discotic material

When heated, the discotic material takes on the  $N_D$  phase. The discotic material right next to the alignment layer has a high degree of randomness. In the vicinity of the alignment layer, the discotic molecules tend to align with the molecular plane almost parallel to the alignment layer surface and have few degrees of pretilt angle in the rubbing direction of the alignment layer surface. On the other hand, in the vicinity of the air surface the discotic molecules tend to align with the molecular plane almost perpendicular to the air surface. With the pinned alignment on both sides, the discotic material exhibits a hybrid alignment structure in the  $N_D$  phase. When cured by UV light, the discotic material is polymerized and the hybrid alignment structure of the polymerized discotic material (PDM) layer is fixed even after it is cooled down to room temperature. Each film has a hybrid alignment structure in which the director continuously changes in the PDM layer thickness direction without twist, while the direction of each discotic molecule fluctuates. This hybrid alignment structure consists of splay and bend deformations.

The azimuthal alignment direction of the PDM layer is parallel to the longitudinal direction of the film so that the WV film could be laminated on the polarizing film in a roll-to-roll process. Therefore, the WV film is used with the O mode in which the transmission axis of the polarizer is perpendicular to the adjacent rubbing direction of the TN cell. By contrast, the device configuration shown in Figure 8.1 is called E mode. The PDM layer exhibits a non-zero and asymmetric phase retardation value at all incident angles. This indicates that the PDM layer has an inhomogeneous alignment structure in the thickness direction. The TAC substrate also possesses a small birefringence which plays an important role in optical compensation. The ideal TAC substrates should be isotropic.

### 8.2.3 Viewing angle

Figure 8.3 compares the viewing angle of a TN LCD without and with a WV Fuji discotic compensation film. The viewing angle at a CR of 10:1 of the film-compensated TN LCD exceeds  $80^\circ$  in all azimuthal directions. The viewing angle is especially enlarged in the horizontal direction where both dark-state light leakage and yellowish color shift are reduced. The on-axis CR is also improved by 10%. The WV Fuji film remarkably improves the viewing angle of the TN LCDs without losing any light transmittance or deteriorating image quality. No change in the panel process is required because the conventional polarizer is simply replaced with a new polarizer laminated with the compensation film. The discotic film is also a cost-effective approach for obtaining a wide viewing angle compared to in-plane switching (IPS) and multi-domain vertical alignment (MVA) modes. These features enable TN LCDs to penetrate the larger sized LCD market segment, say the 20–25 inch diagonal. However, the reversed gray scale still exists in film-compensated TN LCDs, which ultimately limits their competitiveness with IPS and MVA LCDs for large-screen TVs.

## 8.3 IPS Mode

In the TN cell shown in Figure 8.1, the applied electric field is in the longitudinal direction. The tilted LC directors in the bulk cause different phase retardation as viewed from the right or left direction. This produces a narrow and asymmetric viewing angle in the vertical direction. To overcome the narrow viewing angle issue, an elegant driving scheme using a transverse electric field was proposed in the 1970s [8, 9] and implemented in TFT LCDs in the 1990s [10, 11]. The interdigital electrodes are arranged in the same substrate such that the generated fringing field is in the transverse plane. The LC directors are rotated in the plane. Thus, this driving scheme is often referred as the transverse field effect or IPS.

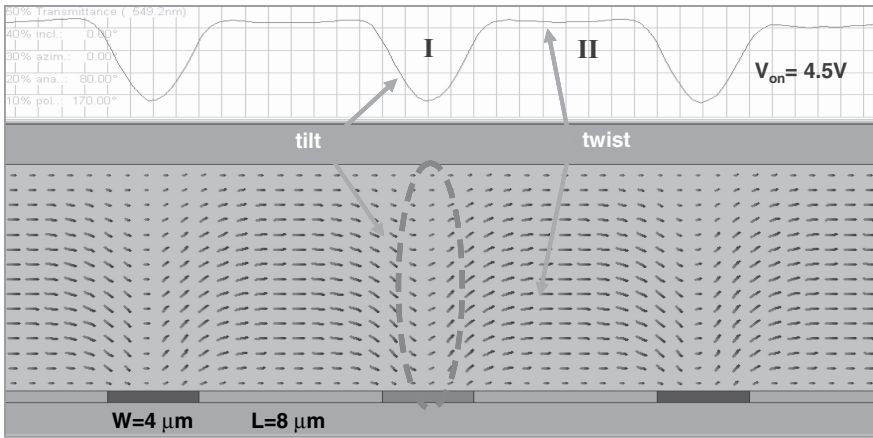
In an IPS mode, the interdigital electrodes are fabricated on the same substrate and the LC molecules are initially homogeneously aligned with a rubbing angle of  $\sim 10^\circ$  with respect to the striped electrodes. The transmission axis of the polarizer can be set to be parallel (E mode) or perpendicular (O mode) to the LC directors while the analyzer is crossed to the polarizer. The in-plane electric fields induced by the electrodes twist the LC directors, thus generating light transmission. However, due to the strong vertical electric field existing above the electrode surface, the LC directors in these regions mainly tilt rather than twist. As a result, the transmittance above the electrodes is greatly reduced. Overall, the conventional IPS mode has a light efficiency about 76% of that of a TN LCD mode, when a positive dielectric anisotropy ( $\Delta\epsilon$ ) LC material is used. Although using a negative  $\Delta\epsilon$  LC in the IPS mode could enhance the light efficiency to above 85%, the required on-state driving voltage is increased. For TFT LCDs, the preferred operating voltage is lower than  $5.5 V_{\text{rms}}$ .

### 8.3.1 Voltage-dependent transmittance

Figure 8.5 depicts the basic device structure of the IPS mode using a positive  $\Delta\epsilon$  LC [12, 13]. The front polarizer is parallel to the LC directors and the rear analyzer is crossed. In the voltage-off state, the incident light experiences no phase retardation so the outgoing beam remains linearly polarized and is absorbed by the crossed analyzer. In a voltage-on state, the fringing field reorients the LC directors and causes phase retardation of the incoming light and modulates the transmittance through the analyzer.

As shown in Figure 8.5, above the electrodes (region I) the electric field is unable to twist the LC directors. As a result, the light transmittance is lower than that in region II. The average transmittance is about 75% of the TN cell.

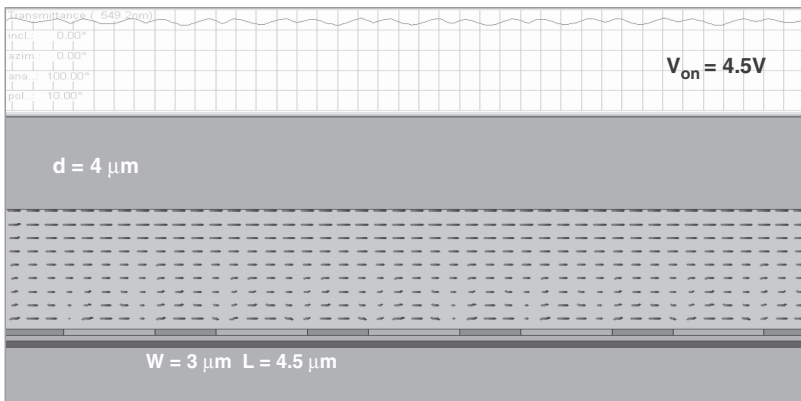
Based on the same operational principle, fringing field switching (FFS) [14] also utilizes the transverse electric field to switch the LC directors. The basic structure of FFS is similar to IPS except for the much smaller electrode gap ( $\ell \sim 0-1 \mu\text{m}$ ). In the IPS mode, the gap ( $\ell$ ) between the electrodes is larger than the



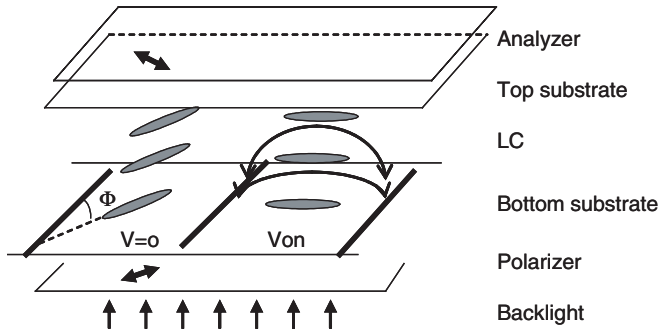
**Figure 8.5** Device structure, simulated on-state LC director distribution, and corresponding light transmittance of an IPS cell. Electrode width  $W = 4 \mu m$  and electrode gap  $L = 8 \mu m$

cell gap ( $d$ ). The horizontal component of the electric field is dominant between the electrodes. However, in the FFS mode where  $\ell < d$ , the fringing field exists above the electrodes. The fringing fields are able to twist the LC directors above the electrodes. Therefore, high light transmittance is obtained. In the FFS mode, both positive and negative  $\Delta\epsilon$  LC can be used [15]. The FFS mode using a negative  $\Delta\epsilon$  material can achieve 98% transmittance of that of a TN cell. The idea of using a positive  $\Delta\epsilon$  LC material in the FFS mode for achieving high transmittance ( $\sim 90\%$  of TN mode) has also been attempted [16]. Positive LCs usually exhibit a larger  $\Delta\epsilon$  and lower viscosity than their corresponding negative  $\Delta\epsilon$  LCs because their polar group(s) are along the principal molecular axis. However, the FFS mode employing a positive  $\Delta\epsilon$  LC would require high-resolution photolithography to fabricate  $1 \mu m$  electrode widths and increase the on-state voltage to  $\sim 6.5 V_{rms}$  in order to generate sufficient twist to the LC directors.

In the FFS mode, the negative  $\Delta\epsilon$  LC tends to have a higher on-state transmittance than the positive LC because its directors tend to align along the field so that it does not contribute to the phase retardation. Figure 8.6 shows a FFS structure with homogeneous alignment and a positive  $\Delta\epsilon$  LC mixture. The fringing field covers both electrodes and gaps. Unlike the IPS mode, there is no dead zone prohibiting



**Figure 8.6** Device structure, simulated on-state LC director distribution, and corresponding light transmittance of a FFS cell. Electrode width  $W = 3 \mu m$  and electrode gap  $L = 4.5 \mu m$



**Figure 8.7** Device configuration of a transmissive IPS cell. Left part,  $V = 0$ ; right part, voltage-on.  $\Phi$  = rubbing angle rubbing angle. Polarizer and analyzer are crossed

light transmittance. Thus, the light transmittance is improved. Both IPS and FFS modes are normally black under crossed-polarizer conditions. The transmittance of the FFS mode reaches  $\sim 95\%$  of the TN cell. The viewing characteristic of FFS is very similar to that of IPS; both are much wider than that of TN LCs [17].

### 8.3.2 Response time

Figure 8.7 shows the electrode configuration of the IPS mode under study. The electrode gap is  $\ell$  ( $\sim 10 \mu\text{m}$ ) and the width is  $\omega$  ( $\sim 5 \mu\text{m}$ ). When backflow and inertial effects are ignored, the dynamics of LC director rotation is described by the following Erickson–Leslie equation [4, 9]:

$$\gamma_1 \frac{\partial \phi}{\partial t} = K_{22} \frac{\partial^2 \phi}{\partial z^2} + \epsilon_o |\Delta \epsilon| E^2 \sin \phi \cos \phi \tag{8.5}$$

In Equation (8.5),  $\gamma_1$  is the rotational viscosity,  $K_{22}$  is the twist elastic constant,  $\Delta \epsilon$  is the dielectric anisotropy,  $E$  is the electric field strength, and  $\phi$  is the LC rotation angle. The homogeneous LC layers having cell gap  $d$  are along the  $z$  axis.

For simplicity, let us assume that the surface anchoring strength is so strong that the bottom and top boundary layers are fixed at  $\phi(0) = \phi(d) = \Phi$ , where  $\Phi$  is the LC alignment (or rubbing) angle with respect to the electrodes, as shown in Figure 8.7.

To solve the decay time, we set  $E = 0$  in Equation (8.5). After some algebra the decay time of the LC directors can be solved relatively easily. The decay time is independent of the initial rubbing angle  $\Phi$ :

$$\tau_{off} = \gamma_1 d^2 / \pi^2 K_{22} \tag{8.6}$$

From Equation (8.6), the LC director’s relaxation time is governed by the cell gap ( $d$ ) and the LC viscoelastic coefficient ( $\gamma_1/K_{22}$ ), and is independent of the rubbing angle. In a VA cell, the optical response time is about 50% of the LC director’s response time.

From Equation (8.5), the rise (or turn-on) time is more difficult to solve because it depends on the applied voltage and the initial rubbing angle. When the rubbing angle  $\Phi = 0$ , the LC directors are perpendicular to the electric field and the Freedericksz transition exists. Under these circumstances, the turn-on time can be solved [18]:

$$\tau_{on} = \frac{\gamma_1}{\epsilon_o |\Delta \epsilon| E^2 \frac{\sin(2\bar{x})}{2\bar{x}} - \frac{\pi^2}{d^2} K_{22}} \tag{8.7}$$



In Equation (8.7),  $\bar{x} = \int_0^{d/2} x dz$  and  $x = (\phi_m - \Phi) \sin(\pi z/d) e^{(t-\tau)/\tau}$ , where  $(\phi_m - \Phi)$  represents the twisted angle of the middle LC layer under the exerted electric field. In principle, Equation (8.7) is not limited to the small-signal regime. In the usual small-angle approximation (i.e., the electric field is only slightly above threshold),  $\bar{x} \ll 1$  and Equation (8.7) is reduced to the following commonly known equation:

$$\tau_{on} = \frac{\gamma_1}{\varepsilon_o |\Delta\varepsilon| E^2 - \frac{\pi^2}{d^2} K_{22}} \quad (8.8)$$

When the rubbing angle  $\Phi \neq 0$ ,  $\tau_{on}$  has the following complicated form:

$$\tau_{on} = \frac{\gamma_1}{\varepsilon_o |\Delta\varepsilon| E^2 \left( \cos(2\Phi) \frac{\sin(2\bar{x})}{2\bar{x}} + \sin(2\Phi) \frac{\cos(2\bar{x})}{2\bar{x}} \right) - \frac{\pi^2}{d^2} K_{22}} \quad (8.9)$$

At a given electric field,  $\bar{x}$  can be obtained from  $\phi_m$  which, in turn, is calculated from the following elliptical equation:

$$\frac{Ed}{2} \sqrt{\frac{\varepsilon_o |\Delta\varepsilon|}{K_2}} \sin \phi_m = \int_{\Phi}^{\phi_m} \frac{1}{\sqrt{1 - (\sin \phi / \sin \phi_m)^2}} d\phi \quad (8.10)$$

Strictly speaking, when the rubbing angle  $\Phi$  is not equal to zero the Freedericksz transition threshold is smeared. However, in normal-black IPS mode, the transmittance is proportional to the phase retardation  $\delta = 2\pi d \Delta n / \lambda$  of the LC cell as  $T \sim \sin^2(\delta/2)$ . In the small-voltage regime, the phase retardation is small and the transmittance exhibits a threshold-like transition.

This optical threshold voltage ( $V_{op}$ ) can be derived by assuming that the rise time is approaching infinity at  $V = V_{op}$ . Thus, the denominator in Equation (8.9) should vanish:

$$\varepsilon_o |\Delta\varepsilon| E^2 \left( \cos(2\Phi) \frac{\sin(2\bar{x})}{2\bar{x}} + \sin(2\Phi) \frac{\cos(2\bar{x})}{2\bar{x}} \right) - \frac{\pi^2}{d^2} K_{22} \rightarrow 0 \quad (8.11)$$

From Equation (8.11), the optical threshold voltage is derived as

$$V_{op} = E \cdot \ell = \frac{\pi \ell}{d} \sqrt{\frac{K_{22}}{\varepsilon_o |\Delta\varepsilon| \left( \cos(2\Phi) \frac{\sin(2\bar{x})}{2\bar{x}} + \sin(2\Phi) \frac{\cos(2\bar{x})}{2\bar{x}} \right)}} \quad (8.12)$$

From Equation (8.12), when  $\Phi = 0$  and  $\bar{x} \rightarrow 0$ , the optical threshold is reduced to the Freedericksz threshold. As the rubbing angle is increased, the optical threshold voltage is gradually decreased. At  $\Phi = 45^\circ$ , the optical threshold voltage reaches a minimum; however, the on-state voltage is also increased.

To compromise for the response time and operating voltage, a typical rubbing angle is set at  $\phi \sim 10^\circ$ . As the rubbing angle is increased by  $30^\circ$ , the rise time is reduced by two to three times, but the on-state voltage is slightly increased. An optimal rubbing angle is found to be around  $20\text{--}30^\circ$  [19].

### 8.3.3 Viewing angle

A common feature of IPS and FFS modes is that the LC cell is sandwiched between two crossed linear polarizers. At normal incidence, the LC layer in the voltage-off state does not modulate the polarization state of the incident linearly polarized light from the entrance polarizer. As a result, a good dark state is achieved since this linearly polarized light is completely absorbed by the crossed analyzer. However, at

oblique angles the incident light leaks through the crossed polarizers, especially at the bisectors. This light leakage stems from two factors. First, the absorption axes of the crossed polarizers are no longer orthogonal to each other under off-axis oblique view. As a result, the extinction ratio of these two crossed polarizers decreases and light leakage occurs. Secondly, in some cases, due to the effective birefringence effect of the LC layer, the obliquely incident linearly polarized light is modulated and it becomes elliptically polarized after traversing through the LC layer. Consequently, the analyzer cannot completely absorb the elliptically polarized light leading to light leakage off-axis. This light leakage in the dark state deteriorates the CR and thereby degrades the viewing angle performance.

To suppress the light leakage at oblique angles and further widen the viewing angle, several phase compensation schemes using uniaxial films [20–22] and biaxial films [23–25] have been proposed. Computer simulation and experimental results have been reported.

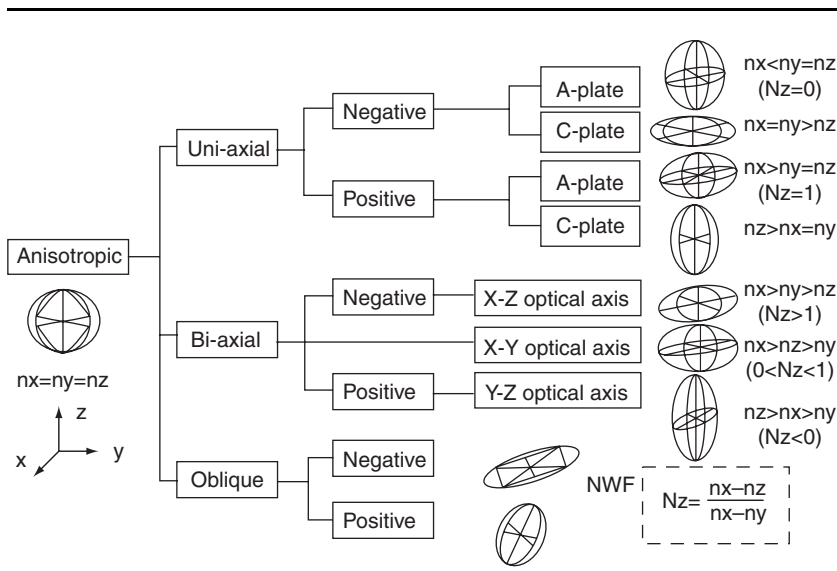
In this section, let us focus on the analytical solutions for the uniaxial film-compensated WV LCDs. With these analytical solutions, the interdependency between the LC cell and film parameters can be clearly revealed. More importantly, analytical solutions provide a clear physical description of the compensation mechanisms.

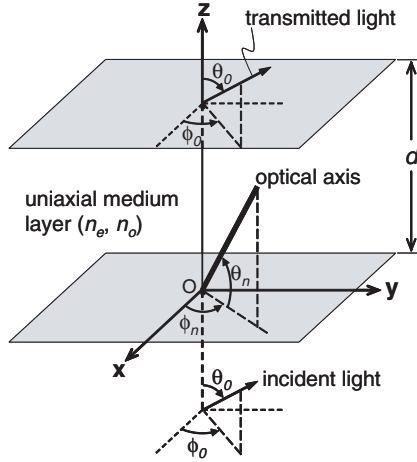
8.3.4 Classification of compensation films

Table 8.1 lists some commercially available compensation films, classified by their refractive indices. Different LC modes need different types of compensation films in order to obtain a satisfactory compensation effect. For example, the IPS mode may require a biaxial compensation film with  $n_x > n_z > n_y$ , [26] while the VA mode needs a compensation film with  $n_x > n_y > n_z$  [27]. Theoretical analyses on biaxial film-compensated LCDs are rather difficult. Here, we focus on uniaxial film-compensated WV LCDs.

Uniaxial film is an anisotropic birefringent film with only one optic axis. For simplicity, let us limit our discussions to those non-absorption uniaxial films only. From the viewpoint of optic axis orientation, uniaxial films can be classified into *a* film and *c* film. An *a* film’s optic axis is parallel to the film surface, while a *c* film’s optic axis is perpendicular to the film surface.

Table 8.1 Different types of compensation films used for WV LCDs





**Figure 8.8** Schematic view of arbitrary light impinging on a uniaxial medium

Both *a* film and *c* film can be further divided into positive or negative films depending on the relative values of the extraordinary refractive index  $n_e$  and the ordinary refractive index  $n_o$ . Table 8.1 lists all the types of compensation films and their refractive index relationship. In our analyses, we focus on uniaxial films. As a general rule, a positive uniaxial film means  $n_e > n_o$ , otherwise  $n_e < n_o$  for a negative uniaxial film.

**8.3.5 Phase retardation of uniaxial media at oblique angles**

Both uniaxial compensation film and the nematic LC layer can be treated as uniaxial media. When light propagates into a uniaxial film, generally two forward eigenwaves (one ordinary wave and one extraordinary wave) are evoked within the medium. After the light has passed through the uniaxial medium, phase retardation occurs between these two eigenwaves. Figure 8.8 shows an arbitrary oblique light with an incident angle  $\theta_0$  propagates in a uniaxial medium. Here, the *x*-*y* plane is chosen to be parallel to the medium layer surface and the *z* axis is along the surface normal. In such a coordinate system, the incident plane forms an angle  $\phi_0$  with respect to the *x* axis. The optic axis of the uniaxial medium is oriented at tilt angle  $\theta_n$  and azimuthal angle  $\phi_n$ , and the extraordinary and ordinary refractive indices of the uniaxial medium are  $n_e$  and  $n_o$ , respectively.

In general, the phase retardation of a uniaxial medium at oblique incidence can be expressed as [28]:

$$\Gamma = (k_{e,z} - k_{o,z})d \tag{8.13}$$

where *d* is the layer thickness of the uniaxial medium, and  $k_{e,z}$  and  $k_{o,z}$  are the *z* axis components of the wavevectors of the extraordinary and ordinary waves, respectively. From the Maxwell equations, these two *z* axis components of wavevectors  $k_{e,z}$  and  $k_{o,z}$  can be solved and are given by [29]:

$$k_{e,z} = \frac{2\pi}{\lambda} \left[ \frac{n_e n_o}{\epsilon_{zz}} \sqrt{\epsilon_{zz} - \left( 1 - \frac{n_e^2 - n_o^2}{n_e^2} \cos^2 \theta_n \sin^2 (\phi_n - \phi_0) \right) \sin^2 \theta_0 - \frac{\epsilon_{xz}}{\epsilon_{zz}} \sin \theta_0} \right] \tag{8.14}$$

and

$$k_{o,z} = \frac{2\pi}{\lambda} \sqrt{n_o^2 - \sin^2 \theta_0} \tag{8.15}$$

with  $\varepsilon_{xz} = (n_e^2 - n_o^2)\sin\theta_n \cos\theta_n \cos(\phi_n - \phi_0)$  and  $\varepsilon_{zz} = n_o^2 + (n_e^2 - n_o^2)\sin^2\theta_n$ . From Equations (8.13)–(8.15), one can easily obtain the phase retardation  $\Gamma$  of a general uniaxial medium at an arbitrary incident angle:

$$\Gamma = \frac{2\pi}{\lambda} d \left[ \frac{n_e n_o}{\varepsilon_{zz}} \sqrt{\varepsilon_{zz} - \left(1 - \frac{n_e^2 - n_o^2}{n_e^2} \cos^2\theta_n \sin^2(\phi_n - \phi_0)\right) \sin^2\theta_0} - \frac{\varepsilon_{xz}}{\varepsilon_{zz}} \sin\theta_0 - \sqrt{n_o^2 - \sin^2\theta_0} \right] \quad (8.16)$$

From Equation (8.16), the phase retardation  $\Gamma$  is dependent on the optical axes orientations  $\theta_n$  and  $\phi_n$  as well as the beam incident directions  $\theta_0$  and  $\phi_0$ .

In the uniaxial film-compensated LCDs, both  $a$  and  $c$  films are commonly used. In these two special cases, Equation (8.16) can be further simplified.

#### (1) Phase retardation of a film

For an  $a$  film, its optic axis lies in the plane parallel to the film surface, i.e.,  $\theta_n = 0^\circ$ . Consequently, the phase retardation of the  $a$  film at an arbitrary incident angle is given by

$$\Gamma_a = \frac{2\pi}{\lambda} d \left[ n_e \sqrt{1 - \frac{\sin^2\theta_0 \sin^2(\phi_n - \phi_0)}{n_e^2} - \frac{\sin^2\theta_0 \cos^2(\phi_n - \phi_0)}{n_o^2}} - n_o \sqrt{1 - \frac{\sin^2\theta_0}{n_o^2}} \right] \quad (8.17)$$

#### (2) Phase retardation of $c$ film

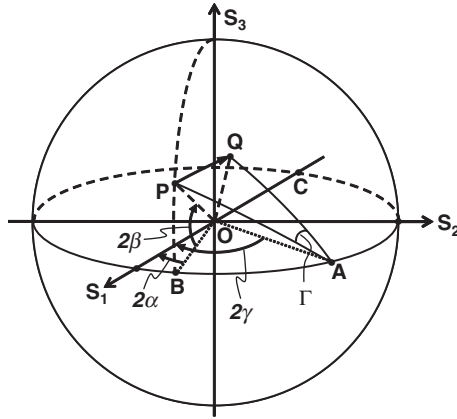
In a  $c$  film, its optic axis is perpendicular to the film surface, i.e.,  $\theta_n = 90^\circ$ . In this case, the phase retardation of the  $c$  film at any oblique incidence is

$$\Gamma_c = \frac{2\pi}{\lambda} n_o d \left( \sqrt{1 - \frac{\sin^2\theta_0}{n_e^2}} - \sqrt{1 - \frac{\sin^2\theta_0}{n_o^2}} \right) \quad (8.18)$$

From Equation (8.18),  $\Gamma_c$  is independent of the azimuthal angle ( $\phi_0$ ) of the incident light. This is because the  $c$  film's optic axis is perpendicular to its surface. Hence, the optical properties of a  $c$  film are axially symmetric around its optic axis.

### 8.3.6 Poincaré sphere representation

The Poincaré sphere representation is an elegant geometrical means for solving problems involving the propagation of polarized light through birefringent and optically active media [30]. For elliptically polarized light with long-axis azimuthal angle  $\alpha$  and ellipticity angle  $\beta$ , its polarization state can be represented by a point  $\mathbf{P}$  on the Poincaré sphere with longitude  $2\alpha$  and latitude  $2\beta$ , as Figure 8.9 shows. The radius of the sphere is one unit length. Here the long-axis azimuthal angle  $\alpha$  of the elliptically polarized light is with respect to the  $x$  axis. For a uniaxial film with its optic axis oriented at angle  $\gamma$  from the  $x$  axis, it can be represented by point  $\mathbf{A}$ , which is located at longitude  $2\gamma$  on the equator. Suppose the above-mentioned elliptically polarized light (point  $\mathbf{P}$ ) passes through the uniaxial film (point  $\mathbf{A}$ ). Then the overall effect on the Poincaré sphere is equivalent to rotating the  $\mathbf{AO}$  axis from point  $\mathbf{P}$  to point  $\mathbf{Q}$  by an angle  $\Gamma$ , which is determined by the phase retardation of the uniaxial film as expressed in Equation (8.16). From the definition of a spherical triangle, the spherical angle  $\mathbf{PAQ}$  is equal to the rotation angle  $\Gamma$ . It should be pointed out that if the uniaxial film has a positive birefringence ( $\Delta n = n_e - n_o > 0$ ), then the above-mentioned rotation from point  $\mathbf{P}$  to point  $\mathbf{Q}$  is clockwise; otherwise, the rotation is counterclockwise if the uniaxial layer has a negative birefringence ( $\Delta n < 0$ ).



**Figure 8.9** Schematic diagram of Poincaré sphere representation and the effect of uniaxial medium on the polarization state change of polarized incident light

For an *a* film, its optic axis lies in the plane parallel to the film surface. When an observer views the LCD panel from different azimuthal and polar angles, the effective optic axis on the wave plane will change with the viewing direction. As a result, its position on the equator of the Poincaré sphere will also change accordingly. On the other hand, a *c* film’s optic axis is perpendicular to the film surface. When an observer views the panel from different azimuthal and polar angles, the effective optic axis on the wave plane always forms 90° with respect to the horizontal reference. Therefore, its position on the Poincaré sphere is always the intersection of the equator and negative *S*<sub>1</sub> axis, which is denoted as point C in Figure 8.9.

**8.3.7 Light leakage of crossed polarizers at oblique view**

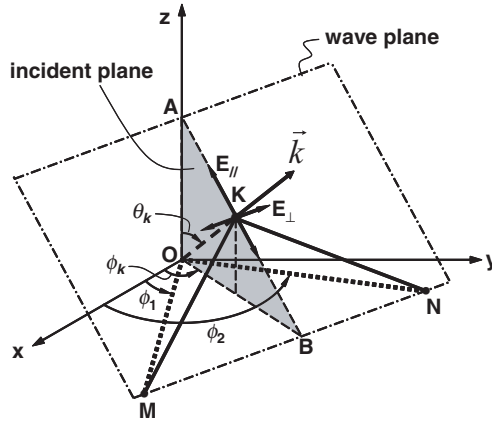
Considering a pair of crossed sheet polarizers with their absorption axes perpendicular to each other, the effective angle between their respective absorption axes varies with different viewing directions. Figure 8.10 shows the case when oblique light traverses through two sheet polarizers. The polarizer’s absorption axis **OM** makes an angle  $\phi_1$  with respect to the *x* axis in the *x*-*y* plane, while the analyzer’s absorption axis **ON** is oriented at angle  $\phi_2$ . The shaded triangle **OAB** in Figure 8.10 denotes the plane of incidence. The light beam, denoted by the wavevector **OK**, propagates at azimuthal angle  $\phi_k$  and polar angle  $\theta_k$  inside the sheet polarizer.

*(1) Effective polarizer angle on the wave plane*

Although these two linear polarizers form an angle  $(\phi_2 - \phi_1)$  in the *x*-*y* plane, their projections on the wave plane, however, form another angle **MKN**, as Figure 8.10 plots. Let us call this angle **MKN** the effective polarizer angle on the wave plane, which is expressed as  $\varphi$  hereafter. The extinction ratio of the crossed polarizers depends on this effective polarizer angle  $\varphi$  on the wave plane, rather than the absorption axes angle in the *x*-*y* plane.

Based on the dot product of vectors, the effective polarizer angle  $\varphi$  can be expressed as [31]:

$$\varphi = \cos^{-1} \left[ \frac{\cos(\phi_2 - \phi_1) - \sin^2 \theta_k \cos(\phi_1 - \phi_k) \cos(\phi_2 - \phi_k)}{\sqrt{1 - \sin^2 \theta_k \cos^2(\phi_1 - \phi_k)} \sqrt{1 - \sin^2 \theta_k \cos^2(\phi_2 - \phi_k)}} \right] \tag{8.19}$$



**Figure 8.10** Schematic view of the effective polarizer angle  $\varphi$  of two sheet polarizers on the wave plane of oblique incident light

where  $\phi_k = \phi_0$  and  $\theta_k = \sin^{-1}(\sin \theta_0/n_p)$ . Here  $n_p$  ( $\sim 1.5$ ) is the average real refractive index of the sheet polarizer, and  $\phi_0$  and  $\theta_0$  are the azimuthal and incident angles of the incident light measured in air, respectively. In a LCD employing crossed polarizers, the absorption axes of the polarizer and the analyzer are perpendicular to each other. If we set  $\phi_1 = 45^\circ$  and  $\phi_2 = -45^\circ$ , then the effective polarizer angle  $\varphi$  can be rewritten as

$$\varphi = \cos^{-1} \left[ \frac{-\sin^2 \theta_k \cos(\pi/4 - \phi_k) \cos(\pi/4 + \phi_k)}{\sqrt{1 - \sin^2 \theta_k \cos^2(\pi/4 - \phi_k)} \sqrt{1 - \sin^2 \theta_k \cos^2(\pi/4 + \phi_k)}} \right] \quad (8.20)$$

As quick verification, under normal view ( $\theta_k = 0^\circ$ ), the effective polarizer angle  $\varphi$  equals  $90^\circ$ , which is identical to the absorption axes angle in the  $x$ - $y$  plane, i.e.,  $\phi_2 - \phi_1 = 90^\circ$ .

To find the tendency of  $\varphi$  when the azimuthal angle  $\phi_0 (= \phi_k)$  changes, let us take the first-order derivative of  $\varphi$  with respect to  $\phi_k$  and obtain

$$\frac{\partial \varphi}{\partial \phi_k} = - \frac{\sin^2 \theta_k \cos \theta_k \sin 2\phi_k}{\cos^2 \theta_k + \frac{1}{4} \sin^4 \theta_k \cos^2 2\phi_k} \quad (8.21)$$

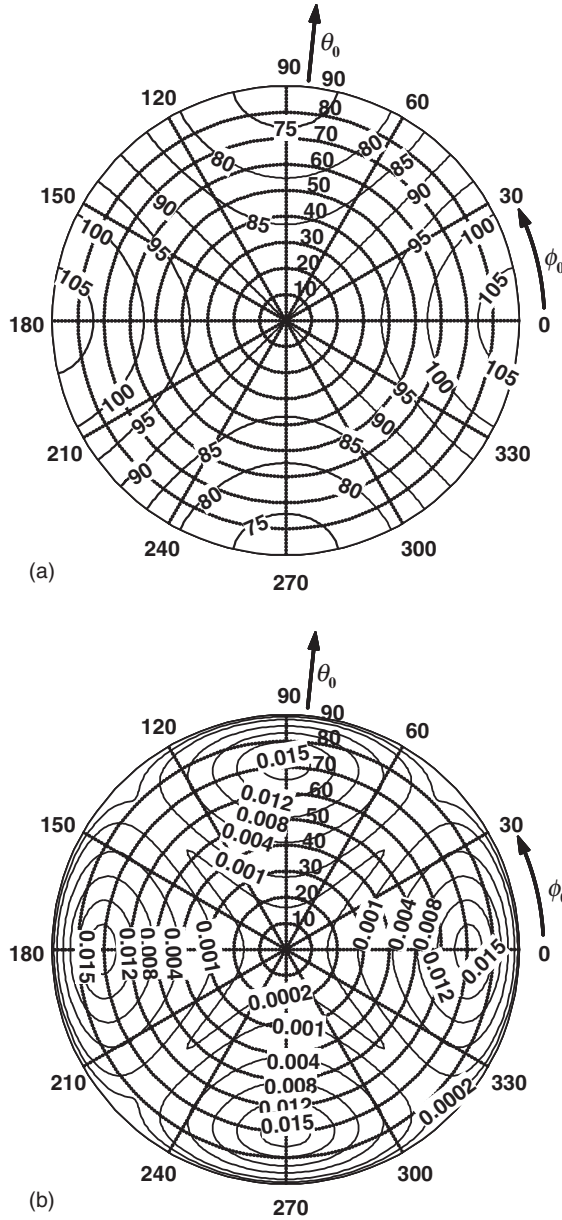
Apparently, when  $\phi_k = \phi_0 = 0^\circ, 90^\circ, 180^\circ$ , and  $270^\circ$ , the effective polarizer angle  $\varphi$  reaches extrema. The second-order derivative

$$\frac{\partial^2 \varphi}{\partial \phi_k^2} = - \frac{2\sin^2 \theta_k \cos \theta_k \cos 2\phi_k}{\cos^2 \theta_k + \frac{1}{4} \sin^4 \theta_k \cos^2 2\phi_k} - \frac{\sin^6 \theta_k \cos \theta_k \sin^2 2\phi_k \cos 2\phi_k}{(\cos^2 \theta_k + \frac{1}{4} \sin^4 \theta_k \cos^2 2\phi_k)^2} \quad (8.22)$$

further reveals that  $\varphi$  reaches maxima at  $\phi_k = \phi_0 = 0^\circ$  and  $180^\circ$  and minima at  $\phi_k = \phi_0 = 90^\circ$  and  $270^\circ$ . By substituting  $\phi_k = \phi_0 = 270^\circ$  into Equation (8.20), we derive the effective polarizer angle  $\varphi$  at the lower bisector viewing position:

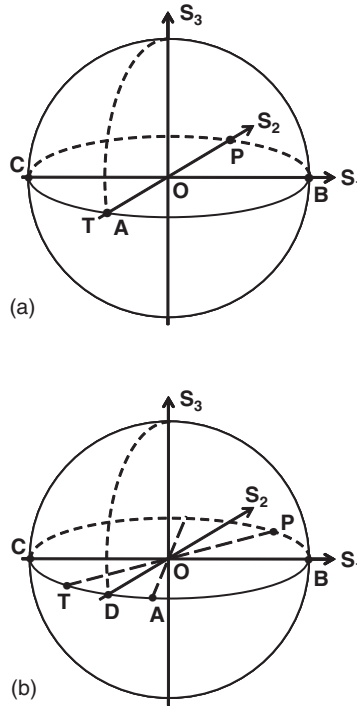
$$\varphi = \cos^{-1} \left( \frac{\sin^2 \theta_0/n_p^2}{2 - \sin^2 \theta_0/n_p^2} \right) \quad (8.23)$$

where  $\theta_0$  is the incident angle measured in air and  $n_p$  is the average real refractive index of the sheet polarizer.



**Figure 8.11** Dependence of (a) effective polarizer angle  $\varphi$  and (b) dark-state light leakage of crossed polarizers on the viewing azimuthal angle  $\phi_0$  and polar angle  $\theta_0$ . The absorption axes of the crossed polarizers are set at  $45^\circ$  and  $-45^\circ$ , respectively, and the incident light wavelength is  $\lambda = 550 \text{ nm}$

Figure 8.11(a) plots the dependence of effective polarizer angle  $\varphi$  on viewing polar angle  $\theta_0$  and azimuthal angle  $\phi_0$  as calculated from Equation (8.20). In the calculations, the average real refractive index of the sheet polarizer is taken to be  $n_p = 1.5$ . From Figure 8.11(a), at off-axis viewing directions, the effective polarizer angle  $\varphi$  deviates from  $90^\circ$ . Especially in all the bisector viewing directions, i.e.,  $\phi_0 = 0^\circ, 90^\circ, 180^\circ,$  and  $270^\circ$ , the effective polarizer angle  $\varphi$  deviates the farthest from  $90^\circ$  and reaches



**Figure 8.12** Demonstration of crossed polarizers on Poincaré sphere under (a) normal view and (b) oblique view at the lower bisector position  $\phi_0 = 270^\circ$ . Here the absorption axes of polarizer and analyzer are set at  $\phi_1 = 45^\circ$  and  $\phi_2 = -45^\circ$ , respectively

either maxima or minima. By contrast, in all on-axis viewing directions, i.e.,  $\phi_0 = 45^\circ, 135^\circ, 225^\circ$ , and  $315^\circ$ , the effective polarizer angle  $\varphi$  equals  $90^\circ$ , the same as the normal view.

The effective polarizer angle deviating from  $90^\circ$  at off-axis viewing directions causes dark-state light leakage which, in turn, degrades the device CR. As a typical example, Figure 8.11(b) shows the dark-state light leakage of crossed polarizers calculated by the extended Jones matrix method. In the calculation, both sheet polarizers are treated as anisotropic uniaxial media with complex refractive indices  $n_e = 1.5 + i0.0022$  and  $n_o = 1.5 + i0.000032$ . As Figure 8.11(b) shows, the light leakage reaches maxima at the bisector viewing directions, i.e.,  $\phi_0 = 0^\circ, 90^\circ, 180^\circ$ , and  $270^\circ$ .

(2) Crossed polarizers on Poincaré sphere

The dark-state light leakage of crossed polarizers can also be well explained on the Poincaré sphere, as shown in Figure 8.12(a) and (b). To facilitate the representation on the Poincaré sphere, we still set  $\phi_1 = 45^\circ$  and  $\phi_2 = -45^\circ$ , keeping the absorption axes of these two sheet polarizers perpendicular to each other in the  $x$ - $y$  plane. Figure 8.12(a) represents the view from the normal direction, while Figure 8.12(b) stands for an oblique view from the lower bisector, i.e.,  $\phi_0 = 270^\circ$ . In both figures, points  $P$  and  $A$  represent the effective absorption axis positions of polarizer and analyzer on the wave plane, respectively. The polarization state of the linearly polarized light after the polarizer, which is denoted by point  $T$ , is always orthogonal to the absorption axis of the polarizer on the wave plane. Therefore, on the Poincaré sphere, points  $T$  and  $P$  are always located on opposite sides along the diameter of the sphere.

As shown in Figure 8.12(a), under normal view the absorption axes of polarizer (point  $P$ ) and analyzer (point  $A$ ) are located at  $90^\circ$  and  $-90^\circ$  on the equator of the Poincaré sphere, respectively. Point  $T$ , the

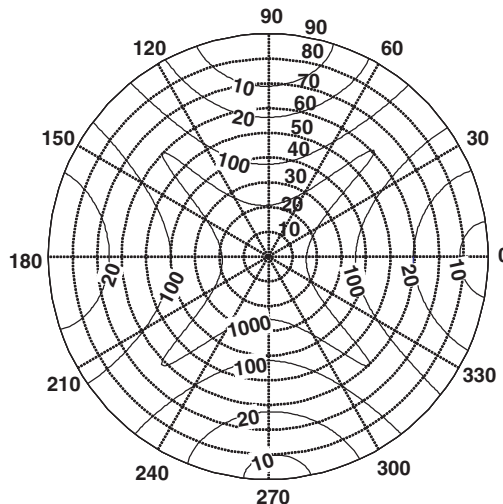


polarization state of the linearly polarized light after the polarizer, exactly overlaps point **A**, the absorption axis of the analyzer, resulting in complete light absorption and no light leakage from the normal viewing direction.

However, under oblique view from the lower bisector direction  $\phi_0 = 270^\circ$ , the effective absorption axis positions of both polarizer and analyzer move toward the horizontal reference. Accordingly, from the lower bisector viewing direction  $\phi_0 = 270^\circ$ , the effective polarizer angle  $\varphi$  becomes less than  $90^\circ$  as illustrated in Figure 8.11(a). As a result, on the Poincaré sphere, points **P** and **A** are no longer located on the  $S_2$  axis. Instead, point **P** is located between the  $S_1$  and  $S_2$  axes, while point **A** is located between the  $S_1$  and negative  $S_2$  axes, as Figure 8.12(b) shows. Moreover, point **P** is symmetric to point **A** about the  $S_1$  axis, and angle **POA** is twice the effective polarizer angle  $\varphi$ , i.e.  $\angle POA = 2\varphi$ . Meanwhile, point **T**, representing the polarization state of light after the polarizer, is on the other end of the diameter passing through point **P**. Therefore, point **T** also deviates from the negative  $S_2$  axis and is located symmetrically to point **A** with respect to the negative  $S_2$  axis. Because point **T** no longer overlaps with point **A**, light leakage occurs from the bisector viewing direction of the crossed polarizers.

It is easy to determine the relationship  $\angle TOA = \pi - 2\varphi$  from Figure 8.12(b). The larger the angle **TOA** is, the more severe the light leakage becomes. Since the effective polarizer angle  $\varphi$  deviates the farthest from  $90^\circ$  at all bisector viewing positions, the light leakage at bisectors is the severest, as depicted in Figure 8.11(b). If we can suppress the light leakage for all the bisector positions, the viewing angle of the LCD will be significantly enhanced. Thus, the goal of WV LCDs, which incorporate compensation films into the panel design, is to move point **T** to point **A** to minimize the light leakage from the analyzer. The introduced compensation film should improve the off-axis viewing performance but not affect the on-axis viewing performance.

In the following sections, let us analyze the compensation schemes of two uniaxial film-compensated WV LCDs and derive the analytical solutions for each scheme. In the WV LCDs with initially homogeneous alignment, such as IPS and FFS modes, let us assume that the stripe electrodes are in the bottom substrate and the electric fields are in the longitudinal direction. As the applied voltage exceeds the threshold voltage, i.e.,  $V > V_{th}$ , the LC directors are gradually twisted from the anchored bottom boundary layer to the middle and then twisted back from the middle to the top (unaffected) boundary layer. Although the FFS mode can achieve a higher optical efficiency than the IPS mode, their viewing angle performances are quite similar. For benchmarking, Figure 8.13 plots the calculated iso-contrast contours of an uncompensated IPS LCD. In the calculation throughout this section, unless



**Figure 8.13** Iso-contrast contour of an uncompensated IPS LCD at  $\lambda = 550$  nm

**Table 8.2** Parameters used in simulating the IPS LCD viewing angle performance

Parameters	Description	Values
$d_{LC}$	Cell gap	4 $\mu\text{m}$
$\theta_{pretilt}$	Surface tilt angle	1°
$n_{LC,e}$	$n_e$ of LC material	1.5649
$n_{LC,o}$	$n_o$ of LC material	1.4793
$n_{p,e}$	$n_e$ of sheet polarizer (complex)	1.5+i0.0022
$n_{p,o}$	$n_o$ of sheet polarizer (complex)	1.5+i0.000032
$n_{c^+e}$	$n_e$ of positive $c$ film	1.5110
$n_{c^+o}$	$n_o$ of positive $c$ film	1.5095
$n_{c^-e}$	$n_e$ of negative $c$ film	1.5095
$n_{c^-o}$	$n_o$ of negative $c$ film	1.5110
$n_{a^+e}$	$n_e$ of positive $a$ film	1.5110
$n_{a^+o}$	$n_o$ of positive $a$ film	1.5095
$n_{a^-e}$	$n_e$ of negative $a$ film	1.5095
$n_{a^-o}$	$n_o$ of negative $a$ film	1.5110
$\phi_1$	Absorption axis of polarizer	45°
$\phi_2$	Absorption axis of analyzer	-45° (or 135°)
$\lambda$	Wavelength of incident light	550 nm

otherwise stated, we assume that at bright state the middle layer LC directors are twisted by 45° with respect to both boundary layers. Other parameters employed in simulations are listed in Table 8.2.

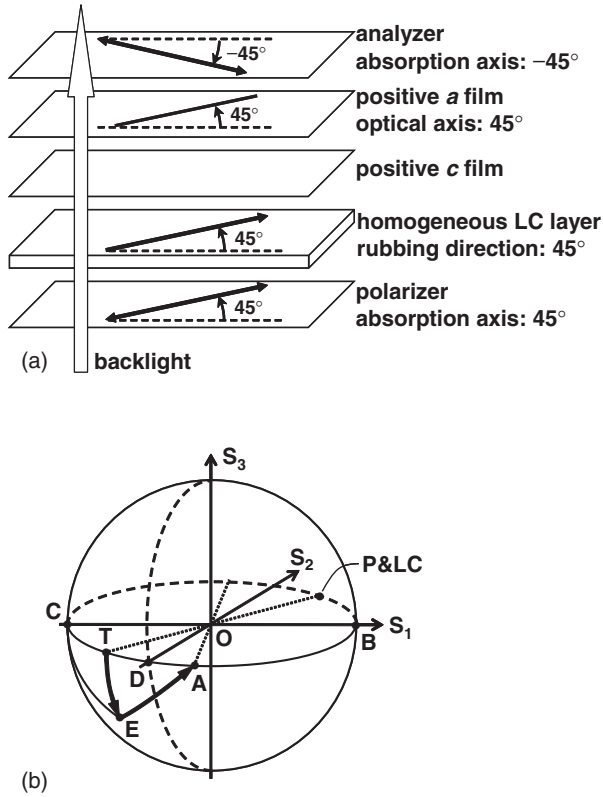
From Figure 8.13, without compensation films the IPS viewing angle at bisectors  $\phi_0 = 0^\circ, 90^\circ, 180^\circ,$  and  $270^\circ$  are relatively poor. At bisectors, the 10:1 CR only extends to  $\sim 70^\circ$  polar angle. This is due to the large dark-state light leakage at these bisector positions, as depicted in Figure 8.11(b).

In the following, we use the IPS LCD as an example to demonstrate two compensation schemes and provide for each scheme a comprehensive analytical solution. These compensation schemes are equally applicable to FFS LCDs.

**8.3.8 IPS with a positive a and a positive c film**

Figure 8.14(a) shows the device configuration of an IPS LCD using one positive  $a$  film and one positive  $c$  film for phase compensation. As shown in Figure 8.14(a), a positive  $c$  film and a positive  $a$  film are sandwiched between the analyzer and the homogeneous LC layer. More specifically, the positive  $a$  film, whose optic axis is oriented parallel to the absorption axis of the polarizer, is adjacent to the analyzer. Figure 8.14(b) explains the compensation principle on the Poincaré sphere when the observer views the panel from an oblique angle at the lower bisector position  $\phi_0 = 270^\circ$ .

The detailed compensation mechanism is explained as Figure 8.14(b) shows. When the unpolarized light from the backlight unit traverses the polarizer (point **P**), it becomes linearly polarized, and its polarization state is located at point **T**, which deviates from the absorption axis of the analyzer (point **A**). When such linearly polarized light (point **T**) passes through the homogenous LC layer, whose position on the Poincaré sphere overlaps with point **P**, the linear polarization state still remain the same (point **T**). Then, the linearly polarized light (point **T**) successively passes through the positive  $c$  film and the positive  $a$  film, whose effective optic axis positions on the Poincaré sphere are points **C** and **P**, respectively. When the linearly polarized light (point **T**) passes through the positive  $c$  film, its polarization state is rotated from point **T** to point **E** clockwise around the **CO** axis. This intermediate polarization state (point **E**), in general, is elliptical. By properly choosing the phase retardation values of



**Figure 8.14** (a) Device structure and (b) compensation principle of an IPS LCD with compensation of a positive *a* film and a positive *c* film

the positive *a* and *c* films, we can always fulfill the following goal: when the elliptically polarized light (point *E*) passes through the positive *a* film, the polarization state can be rotated clockwise around the **PO** axis so that point *E* is moved to point *A*. As a result, at  $V=0$  the light is completely absorbed by the analyzer (point *A*) leading to a good dark state even when viewed from an oblique angle at the bisectors.

To reach the above-mentioned objective, we can easily determine from Figure 8.14(b) that the following two requirements must be satisfied: (1) the arc  $\overline{TE}$  should be equal to the arc  $\overline{TA}$ , and (2) the arc  $\overline{TC}$  should be equal to the arc  $\overline{EC}$ . Besides, from Figure 8.14(b) we can also obtain  $\angle\text{POB} = \angle\text{AOB} = \varphi$ ,  $\overline{TA} = \pi - 2\varphi$ , and  $\overline{TC} = \varphi$ . Based on spherical trigonometry, we can find the following relationships from the spherical triangles **CTE** and **TEA**:

$$\angle\text{TCE} = 2\sin^{-1}(\text{ctg}\varphi) \tag{8.24a}$$

$$\angle\text{CTE} = \cos^{-1}(\text{ctg}^2\varphi) \tag{8.24b}$$

$$\angle\text{ATE} = \pi - \angle\text{CTE} \tag{8.24c}$$

where  $\varphi$ , determined by Equation (8.23), is the effective polarizer angle on the wave plane from the lower bisector viewing position  $\phi_0 = 270^\circ$ .

Since the required positive  $c$  film's phase retardation  $\Gamma_{c^+}$  equals the spherical angle  $\angle TCE$ , the required positive  $c$  film's thickness  $d_{c^+}$  can be derived from (8.18) and (8.24a) as

$$d_{c^+} = \lambda \frac{\sin^{-1}(\text{ctg}\varphi)/\pi}{n_{c^+,o} \left( \sqrt{1 - \frac{\sin^2\theta_0}{n_{c^+,e}^2}} - \sqrt{1 - \frac{\sin^2\theta_0}{n_{c^+,o}^2}} \right)} \quad (8.25)$$

On the other hand, the required positive  $a$  film's phase retardation  $\Gamma_{a^+}$  equals the spherical angle  $\angle ATE$ . Thus from (8.17), (8.24b), and (8.24c) we can derive the required positive  $a$  film's thickness  $d_{a^+}$  as

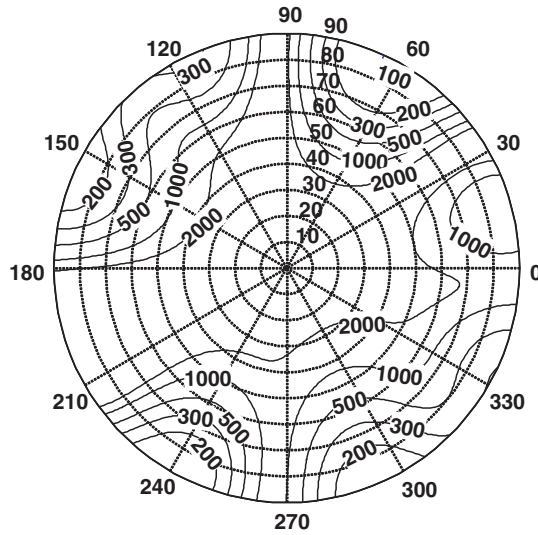
$$d_{a^+} = \lambda \frac{\frac{1}{2} - \cos^{-1}(\text{ctg}^2\varphi)/2\pi}{n_{a^+,e} \sqrt{1 - \frac{\sin^2\theta_0}{2n_{a^+,e}^2}} - \frac{\sin^2\theta_0}{2n_{a^+,o}^2} - n_{a^+,o} \sqrt{1 - \frac{\sin^2\theta_0}{n_{a^+,o}^2}}} \quad (8.26)$$

In the derivation of Equation (8.26), we substitute  $\phi_n = 45^\circ$  and  $\phi_0 = 270^\circ$  into Equation (8.17) because the positive  $a$  film's optic axis is oriented in the  $45^\circ$  direction, as Figure 8.14(a) shows, and the viewing direction is at the  $\phi_0 = 270^\circ$  azimuthal angle.

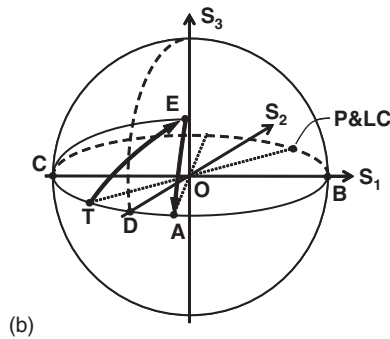
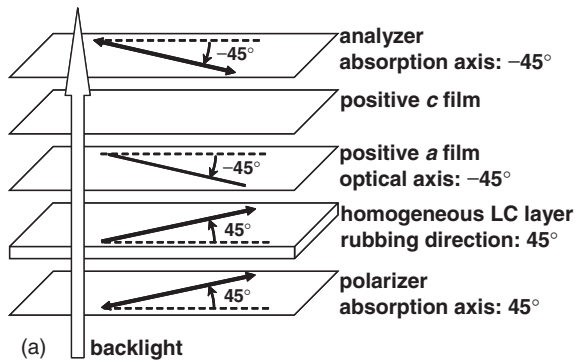
As we can see from Equations (8.23), (8.25), and (8.26), the required film thickness depends on the incident angle  $\theta_0$ , the film's refractive indices  $n_{c^+,e}$ ,  $n_{c^+,o}$ ,  $n_{a^+,e}$ , and  $n_{a^+,o}$ , and the polarizer's average real refractive index  $n_p$ . Therefore, once we know both the films' and polarizer's refractive indices, and the intended viewing angle (i.e., incident angle), we can determine the required film thickness from (8.23), (8.25), and (8.26). For instance, if we set  $\theta_0 = 70^\circ$  as the intended viewing angle where we would like to optimize our LCD designs, and use the parameters listed in Table 8.2, then we can calculate the required film thicknesses from Equations (8.25) and (8.26). The results are  $d_{c^+} = 60.09 \mu\text{m}$  and  $d_{a^+} = 92.59 \mu\text{m}$ . Based on these film thicknesses, Figure 8.15 depicts the calculated iso-contrast contour of an IPS LCD with one positive  $a$  film and one positive  $c$  film for phase compensation. Comparing Figure 8.15 to Figure 8.13, we can clearly see that the viewing angle performance at off-axis viewing directions, especially the bisector positions  $\phi_0 = 0^\circ, 90^\circ, 180^\circ$ , and  $270^\circ$ , is dramatically improved. Meanwhile, the CR at on-axis viewing directions  $\phi_0 = 45^\circ, 135^\circ, 225^\circ$ , and  $315^\circ$  remain unchanged.

This compensation scheme can also be modified by exchanging the positions of the positive  $c$  film and  $a$  film, as shown in Figure 8.16(a). Different from Figure 8.14(a), the positive  $a$  film is now adjacent to the LC layer and its optic axis is parallel to the absorption axis of the analyzer. The compensation principle is demonstrated in Figure 8.16(b). When the linearly polarized light (point **T**) passes through the positive  $a$  film, the polarization state is rotated clockwise around the **AO** axis so that point **T** is moved to point **E**. Now the intermediate state (point **E**) is located on the upper hemisphere. The role of the positive  $c$  film is to rotate point **E** to point **A** clockwise around the **CO** axis. Although the process of polarization state change is different, the required film thicknesses are still identical to those of the previous case as determined by Equations (8.25) and (8.27). The viewing angle is very similar to that shown in Figure 8.15.

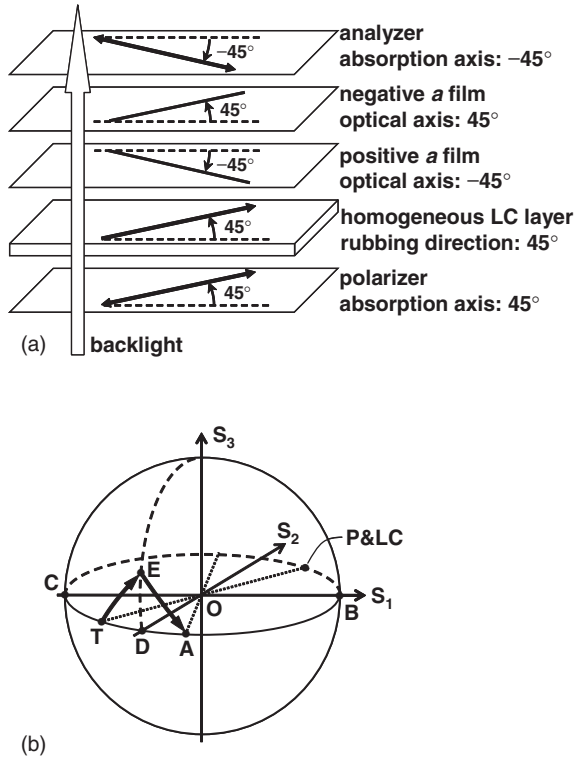
As shown in Figure 8.15, the viewing angle is not very symmetric, although the CR of this compensation scheme exceeds 100:1 at any viewing directions. This is because the intermediate state (point **E**) is not located on the great circle passing through the  $S_2$  and  $S_3$  axes, as shown in Figures 8.14(b) and 8.16(b). To get a more symmetric viewing angle, it is essential to locate the intermediate state on the great circle which passes through the  $S_2$  and  $S_3$  axes and bisects the arc  $\overline{TA}$ , as will be discussed in the following example.



**Figure 8.15** Iso-contrast contour of an IPS LCD with a positive  $a$  film ( $d_{a+} = 92.59 \mu\text{m}$ ) and a positive  $c$  film ( $d_{c+} = 60.09 \mu\text{m}$ ) under  $\lambda = 550 \text{ nm}$



**Figure 8.16** (a) Device structure and (b) compensation principle of an IPS LCD using one positive  $a$  film and one positive  $c$  film



**Figure 8.17** (a) Device structure and (b) compensation principle of an IPS LCD with compensation of one positive  $a$  film and one negative  $a$  film

### 8.3.9 IPS with a positive $a$ and a negative $a$ film

Figure 8.17(a) shows the device configuration of an IPS LCD with one positive  $a$  film and one negative  $a$  film [32,33]. As shown in the figure, a positive  $a$  film and a negative  $a$  film are sandwiched between the LC layer and the analyzer, with the positive  $a$  film adjacent to the LC layer. More specifically, the optic axis of the positive  $a$  film is parallel to the absorption axis of the analyzer, while the optic axis of the negative  $a$  film is parallel to the absorption axis of the polarizer. Figure 8.17(b) explains the compensation principle on the Poincaré sphere when the observer views the panel from an oblique angle at the lower bisector position, i.e.,  $\phi_0 = 270^\circ$ .

The detailed compensation mechanism is explained as Figure 8.17(b) demonstrates. When the unpolarized light from the backlight penetrates the polarizer (point  $P$ ), it becomes linearly polarized and its polarization state is located at point  $T$ , which deviates from the absorption axis of the analyzer (point  $A$ ). When such linearly polarized light (point  $T$ ) passes through the homogenous LC layer, whose position on the Poincaré sphere overlaps with point  $P$ , the linear polarization state remains the same (point  $T$ ). Then, the linearly polarized light (point  $T$ ) successively passes through the positive  $a$  film and the negative  $a$  film, whose positions on the Poincaré sphere are points  $A$  and  $P$ , respectively. When the linearly polarized light (point  $T$ ) passes through the positive  $a$  film, its polarization state is rotated clockwise from point  $T$  to point  $E$  around the  $AO$  axis. This intermediate polarization state (point  $E$ ), in general, is an elliptical polarization state. By properly choosing the phase retardation values of both positive  $a$  film and negative  $a$  film, we should be able to rotate point  $E$  to point  $A$  counterclockwise around the  $PO$  axis. As a result, in the voltage-off state the light is completely absorbed by the analyzer

(point **A**) and a very good dark state is achieved even when viewed from an oblique angle at the bisector positions.

To reach this objective, we can easily determine from Figure 8.17(b) that the following two requirements must be satisfied: (1) the arc  $\overline{\mathbf{EA}}$  should be equal to the arc  $\overline{\mathbf{TA}}$ ; and (2) the arc  $\overline{\mathbf{TA}}$  should be equal to the arc  $\overline{\mathbf{TE}}$ . In other words, the spherical triangle **ETA** should be an equilateral spherical triangle. In addition, from the Poincaré sphere we can also obtain  $\angle\mathbf{POB} = \angle\mathbf{AOB} = \varphi$  and  $\overline{\mathbf{TA}} = \pi - 2\varphi$ . Based on spherical trigonometry, the following relationship from the equilateral spherical triangle **ETA** can be derived:

$$\angle\mathbf{ETA} \equiv \angle\mathbf{EAT} = \cos^{-1}(-\text{ctg}\varphi \cdot \text{ctg}2\varphi) \tag{8.27}$$

where  $\varphi$ , determined by Equation (8.23), is the effective polarizer angle on the wave plane from the lower bisector viewing position, i.e.,  $\phi_0 = 270^\circ$ .

Since the required positive  $a$  film's phase retardation  $\Gamma_{a^+}$  equals the spherical angle **EAT**, the required positive  $a$  film's thickness  $d_{a^+}$  can be expressed from Equations (8.17) and (8.27) as

$$d_{a^+} = \lambda \frac{\cos^{-1}(-\text{ctg}\varphi \cdot \text{ctg}2\varphi)/2\pi}{n_{a^+,e} \sqrt{1 - \frac{\sin^2\theta_0}{2n_{a^+,e}^2} - \frac{\sin^2\theta_0}{2n_{a^+,o}^2}} - n_{a^+,o} \sqrt{1 - \frac{\sin^2\theta_0}{n_{a^+,o}^2}}} \tag{8.28}$$

In the derivation of Equation (8.28), we substitute  $\phi_n = -45^\circ$  and  $\phi_0 = 270^\circ$  into Equation (8.17) because the positive  $a$  film's optic axis is oriented in the  $-45^\circ$  direction, as Figure 8.17(a) shows, and the viewing direction is from the  $\phi_0 = 270^\circ$  azimuthal angle.

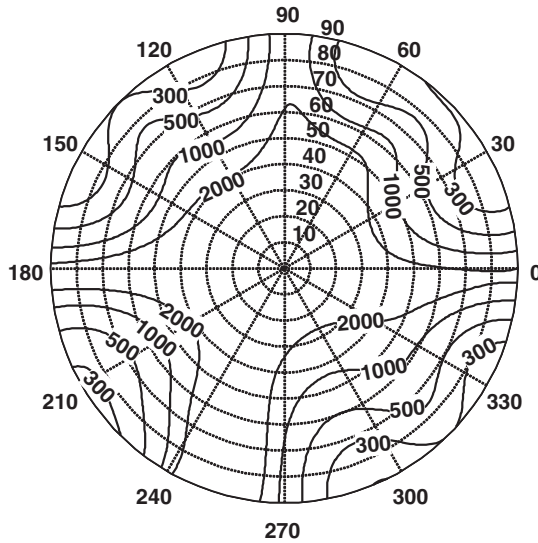
Similarly, the negative  $a$  film's phase retardation  $\Gamma_{a^-}$  is equal to the negative spherical angle **ETA**, i.e.,  $\Gamma_{a^-} = -\angle\mathbf{ETA}$ . Here the minus sign denotes that the phase retardation of the negative  $a$  film is negative and the rotation around the **PO** axis from point **E** to point **A** is counterclockwise. Thus, from Equations (8.17) and (8.27) we can obtain the negative  $a$  film's thickness  $d_{a^-}$  as

$$d_{a^-} = -\lambda \frac{\cos^{-1}(-\text{ctg}\varphi \cdot \text{ctg}2\varphi)/2\pi}{n_{a^-,e} \sqrt{1 - \frac{\sin^2\theta_0}{2n_{a^-,e}^2} - \frac{\sin^2\theta_0}{2n_{a^-,o}^2}} - n_{a^-,o} \sqrt{1 - \frac{\sin^2\theta_0}{n_{a^-,o}^2}}} \tag{8.29}$$

In the derivation of Equation (8.29), we substitute  $\phi_n = 45^\circ$  and  $\phi_0 = 270^\circ$  into Equation (8.17) because the negative  $a$  film's optic axis is oriented in the  $45^\circ$  direction, as Figure 8.17(a) shows, and the viewing direction is from the  $\phi_0 = 270^\circ$  azimuthal angle.

From Equations (8.23), (8.28), and (8.29), the required film thicknesses depend on the incident angle  $\theta_0$ , the film's refractive indices  $n_{a^+,e}$ ,  $n_{a^+,o}$ ,  $n_{a^-,e}$ , and  $n_{a^-,o}$ , and the polarizer's average real refractive index  $n_p$ . Therefore, once we know both the films' and polarizer's refractive indices as well as the intended viewing angle for LCD optimization, we can determine the required film thickness from Equations (8.23), (8.28), and (8.29). By using the parameters listed in Table 8.2 and choosing  $\theta_0 = 70^\circ$ , the required film thicknesses as calculated from Equations (8.28) and (8.29) are  $d_{a^+} = 61.38 \mu\text{m}$  and  $d_{a^-} = 61.37 \mu\text{m}$ . Based on these film thicknesses, Figure 8.18 plots the calculated iso-contrast contour of the IPS LCD with one positive  $a$  film and one negative  $a$  film. Comparing Figure 8.18 to Figure 8.13, we can see clearly that the viewing characteristic at off-axis directions, especially the bisector positions  $\phi_0 = 0^\circ, 90^\circ, 180^\circ$ , and  $270^\circ$ , is dramatically improved. In the meantime, the CR along the horizontal and vertical axes ( $\phi_0 = 45^\circ, 135^\circ, 225^\circ$ , and  $315^\circ$ ) remain unchanged.

The positions of the positive  $a$  film and the negative  $a$  film shown in Figure 8.17(a) are exchangeable. Simulation results indicate that the required film thicknesses remain the same. The Poincaré representation is still similar except that the intermediate polarization state (point **E**) is on the lower hemisphere.



**Figure 8.18** Iso-contrast contour of the IPS LCD with a positive  $a$  film ( $d_{a^+} = 61.38 \mu\text{m}$ ) and a negative  $a$  film ( $d_{a^-} = 61.37 \mu\text{m}$ ) under  $\lambda = 550 \text{ nm}$

The required film thickness  $d_{a^+}$  and  $d_{a^-}$  are still the same as obtained in Equations (8.28) and (8.29). And finally, the viewing angle performance is almost identical to that shown in Figure 8.18.

As shown in Figure 8.18, the CR exceeds 200:1 from all viewing directions. This viewing angle is more symmetric than that shown in Figure 8.15 using one positive  $a$  film and one positive  $c$  film for compensation. This is due to the fact that in this compensation scheme, the intermediate state (point **E**) is located on the great circle which passes through the  $S_2$  and  $S_3$  axes and bisects the arc **TA**. Another advantage of this compensation scheme is that it requires only uniaxial  $a$  films but does not require any  $c$  film or biaxial film. Since  $a$  film has a lower cost than  $c$  film and biaxial film, this compensation scheme has potentially low cost while providing excellent viewing characteristics.

### 8.3.10 Color shift

Color shift is another important issue for LCDs. In the IPS mode, a yellowish color shift occurs at the  $\phi = 45^\circ$  azimuthal angle and a bluish color shift occurs at  $\phi = -45^\circ$  due to the phase retardation difference. To suppress color shift, a chevron-shaped electrode similar to a two-domain structure has been proposed [34, 35]. Each pixel is divided into two domains where the LC directors face opposite directions and the color shift is compensated effectively.

## 8.4 VA Mode

Also called homeotropic alignment [36], VA is another common LC mode for direct-view transmissive and reflective projection displays. VA exhibits the highest CR among all the LC modes developed. Moreover, its CR is insensitive to the incident light wavelength, LC layer thickness, and operating temperature. Both projection [37, 38] and direct-view displays using homeotropic LC cells [39, 40] have been demonstrated. Besides the CR, the homeotropic cell also exhibits a faster response time than its corresponding homogeneous or TN cell. Two factors contributing to the faster response time are elastic

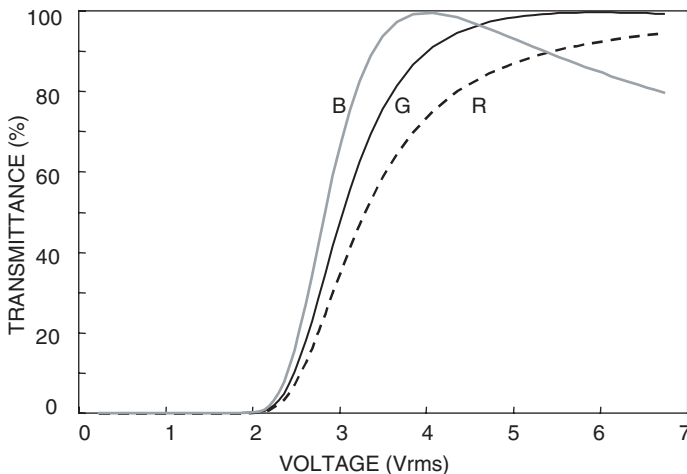


constant and cell gap. To achieve  $1\pi$  phase retardation for a transmissive display, the required  $d\Delta n$  for homogeneous and homeotropic cells is the same, i.e.,  $d\Delta n = \lambda/2$ . However, for a  $90^\circ$  TN cell, the required  $d\Delta n = 0.866\lambda$ . On the other hand, the governing elastic constant for homogeneous, twisted, and homeotropic cells are splay ( $K_{11}$ ), twist ( $K_{22}$ ), and bend ( $K_{33}$ ), respectively. From the elastic constant viewpoint, the order  $K_{33} > K_{11} > K_{22}$  holds for most LC mixtures. The response time of a LC layer is proportional to  $\gamma_1 d^2 / K\pi^2$ , where  $\gamma_1$  is the rotational viscosity and  $K$  is the corresponding elastic constant. Therefore, the homeotropic cell has a superior response time and CR among the three cells. This has been proven by some wide-angle direct-view displays employing the homeotropic cell [41, 42].

One requirement of a VA cell is in the need for high-resistivity LC mixtures having negative dielectric anisotropy. High resistivity is required for active matrix LCDs in order to avoid image flickering. Negative  $\Delta\epsilon$  is required for obtaining useful electro-optical effects. To obtain negative  $\Delta\epsilon$  LCs, the dipoles, in particular the fluoro groups, need to be in the lateral positions. Significant progress in material development has been achieved in the past decade. Nevertheless, the selection of negative  $\Delta\epsilon$  LC compounds is still far below that of positive ones. Furthermore, the lateral dipole groups often exhibit a higher viscosity than the axial compounds due to the larger moment of inertia.

#### 8.4.1 Voltage-dependent transmittance

Figure 8.19 shows the voltage-dependent optical transmittance of a VA cell with  $d\Delta n = 350$  nm between crossed polarizers. For computer calculations, a single domain VA cell employing a Merck high-resistivity MLC-6608 LC mixture is considered. Some physical properties of MLC-6608 can be summarized as follows:  $n_e = 1.558$ ,  $n_o = 1.476$  (at  $\lambda = 589$  nm and  $T = 20^\circ\text{C}$ ); clearing temperature  $T_c = 90^\circ\text{C}$ ; dielectric anisotropy  $\Delta\epsilon = -4.2$ ; and rotational viscosity  $\gamma_1 = 186$  mPa s at  $20^\circ\text{C}$ . In principle, to obtain 100% transmittance for a transmissive VA cell only requires  $d\Delta n \sim \lambda/2$ . Since the human eye is most sensitive to green ( $\lambda = 550$  nm), the required  $d\Delta n$  is around 275 nm. However, this is the minimum  $d\Delta n$  value required because under such conditions the 100% transmittance would occur at  $V \gg V_{th}$ . Due to the finite voltage swing from TFT (usually below  $6V_{rms}$ ), the required  $d\Delta n$  should be increased to  $\sim 0.6\lambda$ , i.e.,  $d\Delta n \sim 330$  nm.



**Figure 8.19** Voltage-dependent transmittance of a VA cell. LC: MLC-6608.  $d\Delta n = 350$  nm. R = 650 nm, G = 550 nm, and B = 450 nm

From Figure 8.19, an excellent dark state is observed at normal incidence. As the applied voltage exceeds the Freedericksz threshold voltage ( $V_{th} \sim 2.1 V_{rms}$ ), LC directors are reoriented by the applied electric field resulting in light transmission from the crossed analyzer. At  $\sim 6 V_{rms}$ , the normalized transmittance reaches 100% for the green light ( $\lambda = 550 \text{ nm}$ ).

### 8.4.2 Optical response time

When the backflow and inertial effects are ignored, the dynamics of the LC director reorientation is described by the following Erickson–Leslie equation [9,10]:

$$\begin{aligned} (K_{11} \cos^2 \phi + K_{33} \sin^2 \phi) \frac{\partial^2 \phi}{\partial z^2} + (K_{33} - K_{11}) \sin \phi \cos \phi \left( \frac{\partial \phi}{\partial z} \right)^2 \\ + \epsilon_o \Delta \epsilon E^2 \sin \phi \cos \phi = \gamma_1 \frac{\partial \phi}{\partial t} \end{aligned} \quad (8.30)$$

where  $\gamma_1$  is the rotational viscosity,  $K_{11}$  and  $K_{33}$  represent the splay and bend elastic constants, respectively,  $\epsilon_o \Delta \epsilon E^2$  is the electric field energy density,  $\Delta \epsilon$  is the LC dielectric anisotropy, and  $\phi$  is the tilt angle of the LC directors. In general, Equation (8.30) can only be solved numerically. However, when the tilt angle is small ( $\sin \phi \sim \phi$ ) and  $K_{33} \sim K_{11}$  (the so-called small-angle and single elastic constant approximation), the Erickson–Leslie equation is reduced to

$$K_{33} \frac{\partial^2 \phi}{\partial z^2} + \epsilon_o \Delta \epsilon E^2 \phi = \gamma_1 \frac{\partial \phi}{\partial t} \quad (8.31)$$

Under such circumstances, both rise time and decay time have simple analytical solutions [43]:

$$\begin{aligned} \tau_{rise} = \frac{1}{2} \frac{\tau_o}{\left| \left( \frac{V}{V_{th}} \right)^2 - 1 \right|} \\ \times \ln \left\{ \left[ \frac{\delta_o/2}{\sin^{-1}(\sqrt{0.1} \sin(\delta_o/2))} - 1 \right] \middle/ \left[ \frac{\delta_o/2}{\sin^{-1}(\sqrt{0.9} \sin(\delta_o/2))} - 1 \right] \right\} \end{aligned} \quad (8.32a)$$

$$\tau_{decay} = \frac{\tau_o}{2} \ln \left[ \frac{\sin^{-1}(\sqrt{0.9} \sin(\delta_o/2))}{\sin^{-1}(\sqrt{0.1} \sin(\delta_o/2))} \right] \quad (8.32b)$$

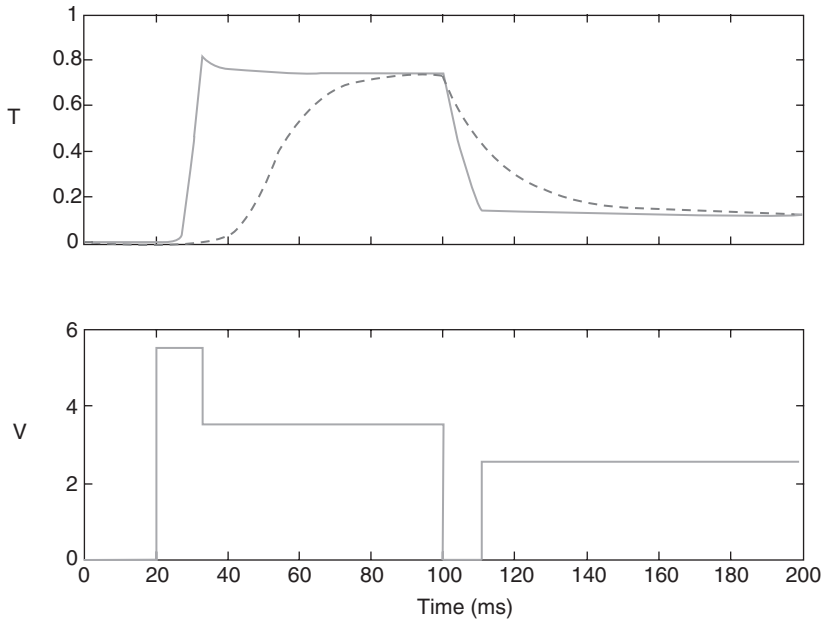
Here, both rise time and decay time are defined as transmittance (under crossed polarizers) changes from 10% to 90%. In these equations,  $\tau_o$  is the LC director reorientation time ( $1 \rightarrow 1/e$ ) and  $\delta_o$  is the net phase change from a bias voltage  $V = V_b$  to  $V = 0$ :

$$\tau_o = \frac{\gamma_1 d^2}{K_{33} \pi^2} \quad (8.33)$$

Equation (8.33) correlates the optical rise time and decay time to the LC director reorientation time ( $\tau_o$ ). Basically, it is a linear relationship except for the additional logarithmic term of the phase dependence.

### 8.4.3 Overdrive and undershoot voltage method

From Equation (8.32), the rise time depends on the applied voltage ( $V$ ), especially near the threshold region. Let us use a normal-black VA cell as an example. Typically, the cell is biased at a voltage ( $V_b$ )



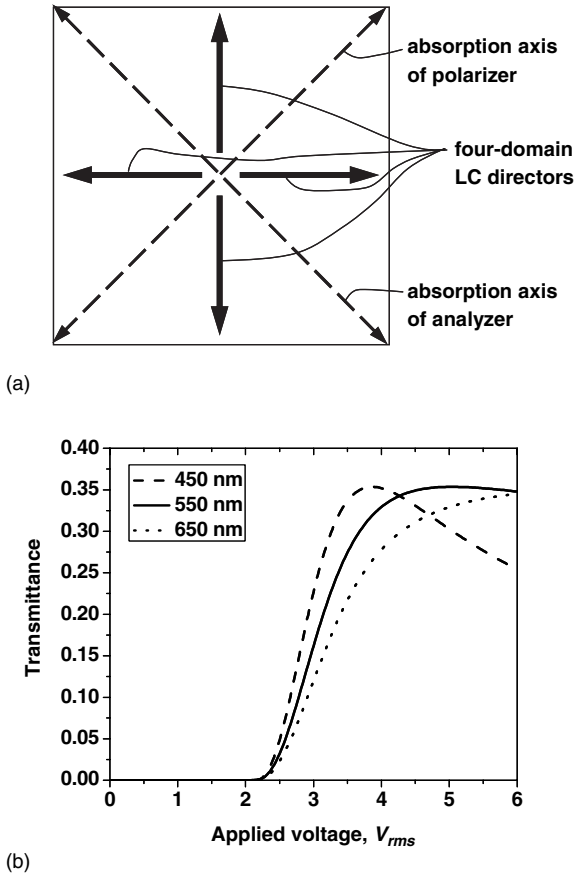
**Figure 8.20** The overdrive and undershoot voltage method for speeding up LC rise and decay times. Top traces are the optical response and bottom traces are the corresponding voltage waveforms. The dashed lines represent a normal driving and the solid lines are with overdrive and undershoot voltages

which is slightly below  $V_{th}$  in order to reduce the delay time incurred during the rise period and to keep a high CR. For some intermediate gray levels, the applied voltage is only slightly above  $V_{th}$ . Under such circumstances, the rise time would be very slow. To overcome this, we could apply a high voltage for a short period and then hold the transmittance at the desired gray level, as shown in Figure 8.20. This is the so-called overdrive voltage method [44]. Meanwhile, during the decay period, the voltage is turned off for a short period and then a small holding voltage is applied to keep the LC at the desired gray level. This is the undershoot effect [45]. With voltage overdrive and undershoot, the LC response time can be reduced by two to three times.

## 8.5 MVA Cells

Single domain VA has been used extensively in LCoS [46,47] for projection displays because of its excellent CR. However, for direct-view display the single domain VA has a relatively narrow viewing angle. To widen the viewing angle, MVA has been developed. Fujitsu has developed protrusion-type MVA [48,49] and Samsung has developed patterned vertical alignment (PVA) [50,51] using slits to generate fringing fields. The operating mechanisms are alike, but PVA does not require any physical protrusions so its CR is higher.

For simplicity, but without loss of generality, let us assume that in each pixel the LC directors form a four-domain orientation profile, as Figure 8.21(a) shows. Figure 8.21(b) depicts the calculated voltage-dependent transmittance curve of a typical MVA LCD using Merck MLC-6608 LC material whose parameters are listed in Table 8.3. Here, the absorption loss of polarizers has been taken into consideration. In film-compensated MVA cells, the refractive indices of the uniaxial films and polarizers are still the same as those listed in Table 8.2.

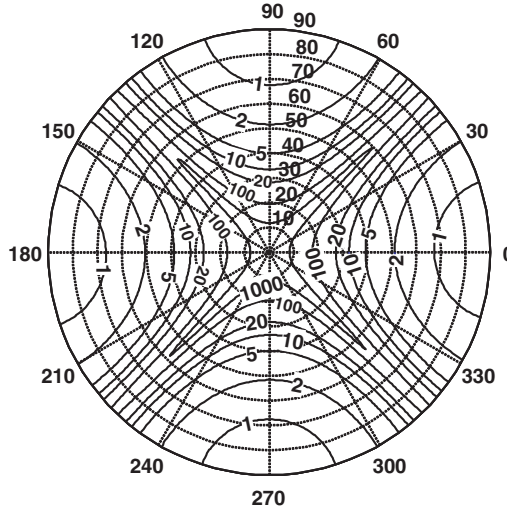


**Figure 8.21** (a) Schematic top view of the four-domain LC director distribution in the voltage-on state, and (b) the voltage-dependent transmittance curve of a MVA LCD

Figure 8.22 shows the calculated iso-contrast contour of the four-domain MVA LCD without film compensation. In the CR calculation, we first use continuum theory [52] to calculate the LC director distribution at  $V_{on} = 5 V_{rms}$  and  $V_{off} = 0$ , respectively, then use the extended Jones matrix to calculate the optical transmittance for each domain, and finally average up all four domains.

**Table 8.3** Parameters used in simulating the MVA LCD viewing angle performance

Parameters	Description	Values
$d_{LC}$	Cell gap	4.6 $\mu\text{m}$
$\theta_{pretilt}$	Surface tilt angle	89°
$n_{LC,e}$	$n_e$ of LC material MLC-6608	1.5606
$n_{LC,o}$	$n_o$ of LC material MLC-6608	1.4770
$\phi_1$	Absorption axis of polarizer	45°
$\phi_2$	Absorption axis of analyzer	-45° (or 135°)
$\lambda$	Wavelength of incident light	550 nm



**Figure 8.22** Simulated iso-contrast contour of a typical four-domain MVA LCD under  $\lambda = 550 \text{ nm}$

From Figure 8.22, without compensation films the viewing angle of the four-domain MVA cell at the bisector positions  $\phi_0 = 0^\circ, 90^\circ, 180^\circ,$  and  $270^\circ$  is very poor. At these bisectors, the 10:1 CR only extends to  $\sim 30^\circ$  polar angle. Two factors contribute to the narrow viewing angle: (1) the absorption axes of the crossed polarizers are no longer perpendicular to each other at off-axis oblique viewing directions; and (2) the vertically aligned LC layer behaves as a *c* film, which imposes a phase retardation on the obliquely incoming linearly polarized light and modulates its polarization state. The phase retardation  $\Gamma_{LC}$ , which is induced by the vertically aligned LC layer at oblique incident light, can be easily obtained from Equation (8.16) as

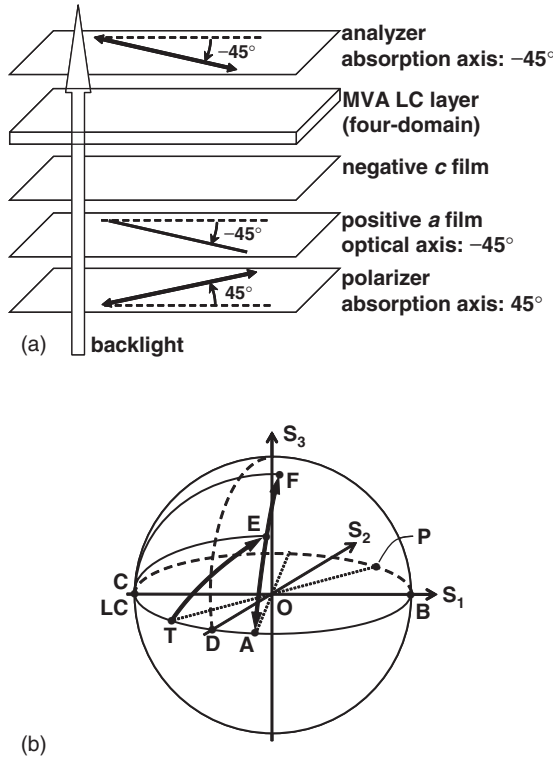
$$\Gamma_{LC} = \frac{2\pi}{\lambda} n_{LC,o} d_{LC} \left( \sqrt{1 - \frac{\sin^2 \theta_0}{n_{LC,e}^2}} - \sqrt{1 - \frac{\sin^2 \theta_0}{n_{LC,o}^2}} \right) \tag{8.34}$$

From Equation (8.34),  $\Gamma_{LC}$  depends on the incident angle  $\theta_0$ , the LC refractive indices  $n_{LC,e}$  and  $n_{LC,o}$ , and the LC layer’s thickness  $d_{LC}$ . As an example, at incident angle  $\theta_0 = 70^\circ$  the corresponding  $\Gamma_{LC}$ , calculated from the parameters listed in Table 8.3, is  $0.664\pi$  radians. Equation (8.34) will be frequently referred to in this section.

In the following, we use the four-domain MVA LCD as an example to demonstrate some uniaxial film compensation schemes and provide each scheme with a comprehensive analytical solution. All of these compensation schemes are equally applicable to PVA mode LCDs.

**8.5.1 MVA with a positive *a* and a negative *c* film**

Figure 8.23(a) shows the schematic device configuration of a MVA LCD with one positive *a* film and one negative *c* film. As shown in the figure, the positive *a* film and the negative *c* film are sandwiched between the polarizer and the MVA LC layer. More specifically, the optic axis of the positive *a* film is parallel to the absorption axis of the analyzer. Figure 8.23(b) explains the compensation principle on the Poincaré sphere when the observer views the panel from an oblique angle at the lower bisector position  $\phi_0 = 270^\circ$ .



**Figure 8.23** (a) Device structure and (b) compensation principle of a MVA LCD using one positive  $a$  film and one negative  $c$  film

The detailed compensation mechanism is explained using the Poincaré sphere shown in Figure 8.23(b). When the unpolarized light from the backlight source passes the polarizer (point  $P$ ), it becomes linearly polarized and its polarization state is located at point  $T$ , which deviates from the absorption axis of the analyzer (point  $A$ ). Then, such linearly polarized light (point  $T$ ) successively passes through the positive  $a$  film and the negative  $c$  film, whose positions on the Poincaré sphere are points  $A$  and  $C$ , respectively. When the linearly polarized light (point  $T$ ) passes through the positive  $a$  film, its polarization state is rotated clockwise from point  $T$  to point  $E$  around the  $AO$  axis. Point  $E$  is the first intermediate polarization state, which, in general, is elliptical. When this elliptically polarized light traverses the negative  $c$  film, its polarization state is rotated counterclockwise from point  $E$  to point  $F$  around the  $CO$  axis. Point  $F$  is the second intermediate polarization state, which is also elliptical. Then, this second intermediate elliptically polarized light passes through the unactivated MVA LC layer, whose position on the Poincaré sphere overlaps with point  $C$ . Let us assume that we can find the proper phase retardations of the positive  $a$  film and negative  $c$  film such that when the second intermediate elliptically polarized light passes through the unactivated MVA LC layer its polarization state is rotated clockwise from point  $F$  to point  $A$  around the  $CO$  axis. Consequently, at  $V = 0$  the light is completely absorbed by the analyzer (point  $A$ ) and a good dark state is achieved even when viewed from the oblique angle at the bisector positions.

To reach this objective, we can readily determine from Figure 8.23(b) that the following three requirements must be satisfied: (1) the arc  $\overline{EA}$  should be equal to the arc  $\overline{TA}$ ; (2) the arcs  $\overline{AC}$ ,  $\overline{EC}$ , and  $\overline{FC}$  all should be equal to each other; and (3) the spherical angle  $\overline{ACF}$  is the sum of the spherical angles  $\overline{ACE}$  and  $\overline{ECF}$ . Further, from Figure 8.23(b), we also find that  $\angle POB = \angle AOB = \varphi$ ,  $\overline{TA} = \pi - 2\varphi$ , and

$\overline{AC} = \pi - \varphi$ . Based on spherical trigonometry, we can derive the following relationships from the spherical triangles CAE and CAF:

$$\angle EAC = \cos^{-1}(-\text{ctg}^2 \varphi) \tag{8.35}$$

$$\angle ACE = 2 \sin^{-1}(\text{ctg} \varphi) \tag{8.36}$$

where  $\varphi$ , determined by Equation (8.23), is the effective polarizer angle on the wave plane from the lower bisector viewing position  $\phi_0 = 270^\circ$ .

Since the required positive  $a$  film's phase retardation  $\Gamma_{a^+}$  equals the spherical angle  $EAT (= \angle EAC)$ , the positive  $a$  film's thickness  $d_{a^+}$  is found from Equations (8.16) and (8.35) to be

$$d_{a^+} = \lambda \frac{\cos^{-1}(-\text{ctg}^2 \varphi)/2\pi}{n_{a^+,e} \sqrt{1 - \frac{\sin^2 \theta_0}{2n_{a^+,e}^2} - \frac{\sin^2 \theta_0}{2n_{a^+,o}^2}} - n_{a^+,o} \sqrt{1 - \frac{\sin^2 \theta_0}{n_{a^+,o}^2}}} \tag{8.37}$$

In the derivation of Equation (8.37), we substitute  $\phi_n = -45^\circ$  and  $\phi_0 = 270^\circ$  into Equation (8.16) because the positive  $a$  film's optic axis is oriented in the  $-45^\circ$  direction, as Fig 8.23(a) shows, and the viewing direction is from the  $\phi_0 = 270^\circ$  azimuthal angle.

On the other hand, the required negative  $c$  film's phase retardation  $\Gamma_{c^-}$  equals the negative spherical angle  $ECF$ , i.e.,  $\Gamma_{c^-} = -\angle ECF = \angle ACE - \angle ACF$ . The spherical angle  $ACF$  is equal to the unactivated MVA LC layer's phase retardation  $\Gamma_{LC}$  as shown in Equation (8.34). This is because the function of the unactivated MVA LC layer is to rotate clockwise around the  $CO$  axis from point  $F$  to point  $A$ . Thus, from Equations (8.18) and (8.36) we can obtain the required negative  $c$  film's thickness  $d_{c^-}$  as

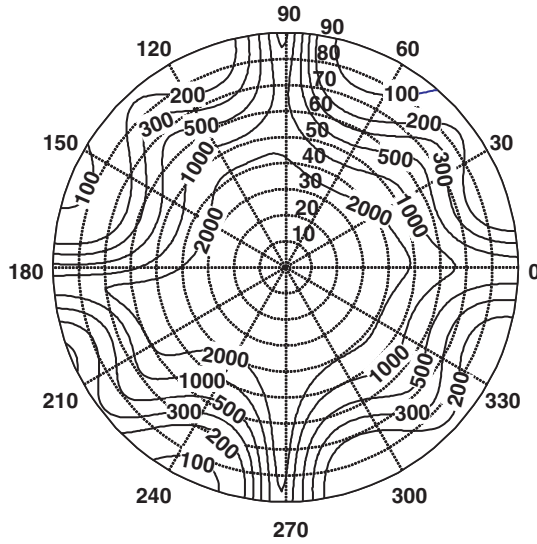
$$d_{c^-} = \lambda \frac{[2 \sin^{-1}(\text{ctg} \varphi) - \Gamma_{LC}]/2\pi}{n_{c^-,o} \left( \sqrt{1 - \frac{\sin^2 \theta_0}{n_{c^-,e}^2}} - \sqrt{1 - \frac{\sin^2 \theta_0}{n_{c^-,o}^2}} \right)} \tag{8.38}$$

where  $\Gamma_{LC}$  is given by Equation (8.34).

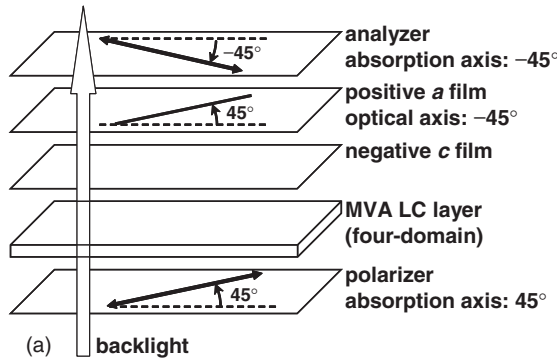
As we can see from Equations (8.23), (8.34), (8.37), and (8.38), for a given MVA LC cell, the required film thicknesses depend on the incident angle  $\theta_0$ , the film's refractive indices  $n_{c^-,e}$ ,  $n_{c^-,o}$ ,  $n_{a^+,e}$ , and  $n_{a^+,o}$ , and the polarizer's average real refractive index  $n_p$ . Therefore, once we know both the films' and polarizer's refractive indices as well as the intended viewing angle or incident angle for LCD optimization, we can determine the compensation films' thickness from Equations (8.23), (8.34), (8.37), and (8.38). For example, if we want to optimize the LCD viewing angle at  $\theta_0 = 70^\circ$ , then we can plug the parameters listed in Tables 8.2 and 8.3 into Equations (8.37) and (8.38) and find  $d_{a^+} = 92.59 \mu\text{m}$  and  $d_{c^-} = 186.08 \mu\text{m}$ . Based on the obtained film thicknesses, Figure 8.24 depicts the calculated iso-contrast contour of an MVA LCD compensated by one positive  $a$  film and one negative  $c$  film. Comparing Figure 8.24 to Figure 8.22, we can clearly see that the viewing angle performance at off-axis viewing directions, especially the bisector positions  $\phi_0 = 0^\circ, 90^\circ, 180^\circ$ , and  $270^\circ$ , is dramatically improved. In the meantime, the CR at on-axis viewing directions ( $\phi_0 = 45^\circ, 135^\circ, 225^\circ$ , and  $315^\circ$ ) remain the same.

This compensation scheme can be modified by exchanging the positions of the negative  $c$  film and the MVA LC layer. In other words, the incident light passes through the MVA LC layer first before it enters the negative  $c$  film. In this case, the required film thickness can still be determined by Equations (8.37) and (8.38), and the resultant viewing angle performance is nearly identical to Figure 8.24.

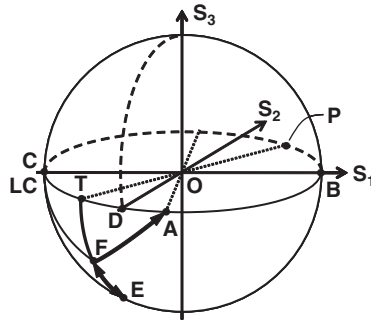
In addition, this compensation scheme can be further modified by placing the positive  $a$  film and negative  $c$  film between the MVA LC layer and the analyzer, as Figure 8.25(a) shows. Different from Figure 8.23(a), the positive  $a$  film is now adjacent to the analyzer and its optic axis is perpendicular to the



**Figure 8.24** Simulated iso-contrast contour of an MVA LCD with a positive  $a$  film ( $d_{a+} = 92.59 \mu\text{m}$ ) and a negative  $c$  film ( $d_{c-} = 186.08 \mu\text{m}$ ) under  $\lambda = 550 \text{ nm}$



(a)



(b)

**Figure 8.25** (a) An alternative device structure and (b) compensation principle of the MVA LCD using a negative  $c$  film and a positive  $a$  film



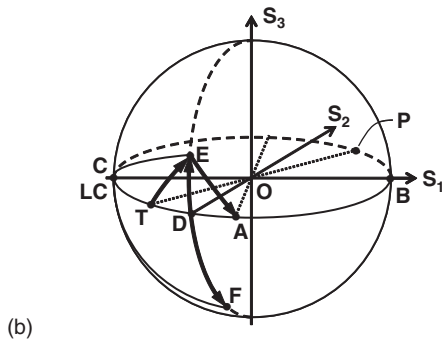
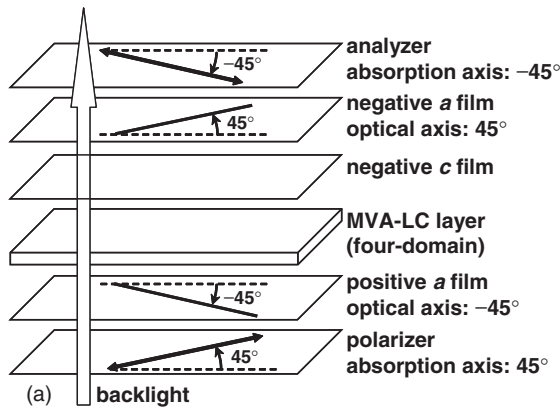
absorption axis of the analyzer. Figure 8.25(b) shows the compensation principle of the modified device. Following the same procedures, we can readily determine from Figure 8.25(b) that the required film thicknesses are identical to Equations (8.37) and (8.38). The resultant viewing angle is almost the same as that plotted in Figure 8.24.

As shown in Figure 8.24, with film compensation the 100:1 CR barely exceeds  $\sim 75^\circ$  polar angle. This viewing angle performance is not as good as that of the IPS LCDs described in Section 8.3. This is due to the fact that the intermediate states, points **E** and **F**, are not located on the great circle which passes through the  $S_2$  and  $S_3$  axes.

In the next example, we will describe a compensation scheme in which the intermediate states are located on the great circle passing through the  $S_2$  and  $S_3$  axes and bisecting the arc  $\overline{TA}$ .

**8.5.2 MVA with a positive a, a negative a, and a negative c film**

Figure 8.26(a) shows the schematic device configuration of a MVA LCD with one positive *a* film, one negative *a* film, and one negative *c* film. As shown in the figure, the positive *a* film is located between the polarizer and the MVA LC layer, while the negative *a* film and negative *c* film are sandwiched between the MVA LC layer and the analyzer. More specifically, the optic axis of the positive *a* film is parallel to the absorption axis of the analyzer, and the optic axis of the negative *a* film is parallel to the absorption axis of the polarizer. Figure 8.26(b) explains the compensation principle on the Poincaré sphere when the observer views the LCD panel from an oblique angle at the lower bisector position  $\phi_0 = 270^\circ$ .



**Figure 8.26** (a) Device structure and (b) compensation principle of an MVA LCD with one positive *a* film, one negative *a* film, and one negative *c* film

The detailed compensation mechanism is explained using Figure 8.26(b). When the unpolarized light from the backlight passes through the polarizer (point **P**), it becomes linearly polarized and its polarization state is located at point **T**, which deviates from the absorption axis of the analyzer (point **A**). Afterward, the linearly polarized light (point **T**) traverses the positive  $a$  film, whose position on the Poincaré sphere overlaps with point **A**, and its polarization state is rotated clockwise from point **T** to point **E** around the **AO** axis. Point **E** is the first intermediate elliptical polarization state.

To obtain a symmetric viewing angle, we intentionally locate the point **E** on the great circle passing through the  $S_2$  and  $S_3$  axes and bisecting the arc  $\overline{\mathbf{TA}}$ . Then this elliptically polarized light successively enters the unactivated MVA LC layer and the negative  $c$  film, whose positions on the Poincaré sphere are both at point **C**. When the elliptically polarized light passes through the unactivated MVA LC layer, its polarization state is rotated clockwise around the **CO** axis from point **E** to point **F**. Point **F** is the second intermediate elliptical polarization state, which is also located on the same great circle passing through the  $S_2$  and  $S_3$  axes. Then this second intermediate elliptically polarized light hits the negative  $c$  film. The phase retardation of the negative  $c$  film is designed such that when the second intermediate elliptically polarized light passes through the negative  $c$  film its polarization state will be rotated counterclockwise around the **CO** axis from point **F** back to point **E**. Now point **E** represents the third intermediate elliptical polarization state. After that, this third elliptically polarized light passes through the negative  $a$  film, whose position on the Poincaré sphere overlaps with point **P**. The phase retardation of the negative  $a$  film is properly chosen such that when the third intermediate elliptically polarized light (point **E**) passes through the negative  $a$  film its polarization state can be rotated counterclockwise around the **PO** axis from point **E** to point **A**. Consequently, the light is completely absorbed by the analyzer (point **A**) and a good dark state is achieved even when it is viewed from the bisector directions.

To determine each film's thickness, we find from Figure 8.26(b) that the following two requirements must be satisfied: (1) the arcs of  $\overline{\mathbf{EA}}$ ,  $\overline{\mathbf{ET}}$ , and  $\overline{\mathbf{TA}}$  should all be equal; and (2) the arc  $\overline{\mathbf{EF}}$  is located on the great circle passing through the  $S_2$  and  $S_3$  axes and bisecting the arc  $\overline{\mathbf{TA}}$ . That implies that the spherical triangle **ETA** is an equilateral spherical triangle. Furthermore, from Figure 8.24(b), we also obtain  $\angle \mathbf{POB} = \angle \mathbf{AOB} = \varphi$  and  $\mathbf{TA} = \pi - 2\varphi$ . Based on spherical trigonometry, we derive the following relationships from the equilateral spherical triangle **ETA**:

$$\angle \mathbf{EAT} = \angle \mathbf{ETA} = \cos^{-1}(-\text{ctg } \varphi \cdot \text{ctg } 2\varphi) \tag{8.39}$$

where  $\varphi$ , determined by Equation (8.23), is the effective polarizer angle on the wave plane as viewed from the lower bisector direction ( $\varphi_0 = 270^\circ$ ).

Since the required positive  $a$  film's phase retardation  $\Gamma_{a^+}$  equals the spherical angle **EAT**, the required positive  $a$  film's thickness  $d_{a^+}$  can be expressed from Equations (8.17) and (8.39) as

$$d_{a^+} = \lambda \frac{\cos^{-1}(-\text{ctg } \varphi \cdot \text{ctg } 2\varphi)/2\pi}{n_{a^+,e} \sqrt{1 - \frac{\sin^2 \theta_0}{2n_{a^+,e}^2} - \frac{\sin^2 \theta_0}{2n_{a^+,o}^2}} - n_{a^+,o} \sqrt{1 - \frac{\sin^2 \theta_0}{n_{a^+,o}^2}}} \tag{8.40}$$

In the process of deriving Equation (8.40), we substitute  $\phi_n = -45^\circ$  and  $\phi_0 = 270^\circ$  into Equation (8.16) because the positive  $a$  film's optical axis is oriented in the  $-45^\circ$  direction, as Figure 8.26(a) shows, and the viewing direction is from the  $\phi_0 = 270^\circ$  azimuthal angle.

Similarly, the required negative  $a$  film's phase retardation  $\Gamma_{a^-}$  is equal to the negative spherical angle **ETA**, i.e.,  $\Gamma_{a^-} = -\angle \mathbf{ETA}$ . Thus, from Equations (8.17) and (8.39) we derive the negative  $a$  film's thickness  $d_{a^-}$  as

$$d_{a^-} = -\lambda \frac{\cos^{-1}(-\text{ctg } \varphi \cdot \text{ctg } 2\varphi)/2\pi}{n_{a^-,e} \sqrt{1 - \frac{\sin^2 \theta_0}{2n_{a^-,e}^2} - \frac{\sin^2 \theta_0}{2n_{a^-,o}^2}} - n_{a^-,o} \sqrt{1 - \frac{\sin^2 \theta_0}{n_{a^-,o}^2}}} \tag{8.41}$$

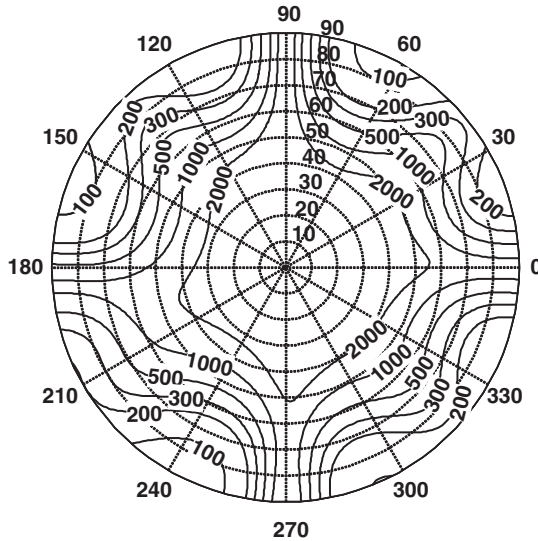
Here we substitute  $\phi_n = 45^\circ$  and  $\phi_0 = 270^\circ$  into Equation (8.17) because the negative  $a$  film's optical axis is oriented in the  $45^\circ$  direction, as Figure 8.26(a) shows, and the viewing direction is from the  $\phi_0 = 270^\circ$  azimuthal angle.

To obtain the negative  $c$  film's thickness, we need to find its phase retardation  $\Gamma_{c^-}$  first. From the compensation mechanism, it is easy to find that  $\Gamma_{c^-} = -\Gamma_{LC}$  since the unactivated MVA LC layer's role is to rotate clockwise around the **CO** axis from point **E** to point **F**. On the other hand, the negative  $c$  film's function is to rotate counterclockwise around the **CO** axis from point **F** back to point **E**. Therefore, from Equation (8.18) we derive the required negative  $c$  film's thickness  $d_{c^-}$  as

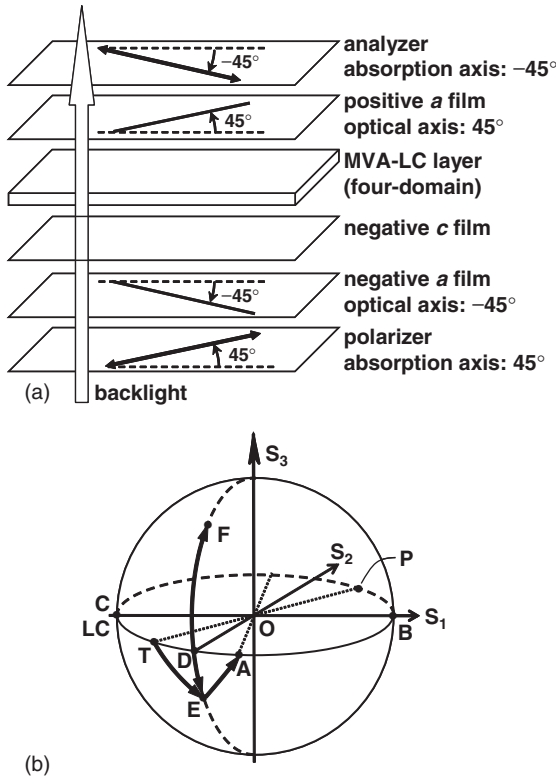
$$d_{c^-} = -\lambda \frac{\Gamma_{LC}/2\pi}{n_{c^-,o} \left( \sqrt{1 - \frac{\sin^2\theta_0}{n_{c^-,e}^2}} - \sqrt{1 - \frac{\sin^2\theta_0}{n_{c^-,o}^2}} \right)} \tag{8.42}$$

where  $\Gamma_{LC}$  is determined by Equation (8.34).

From Equations (8.23), (8.29), and (8.40)–(8.42), we find that for a given MVA LC cell the required film thicknesses depend on the incident angle  $\theta_0$ , the film's refractive indices  $n_{a^+,e}$ ,  $n_{a^+,o}$ ,  $n_{a^-,e}$ ,  $n_{a^-,o}$ ,  $n_{c^-,e}$ , and  $n_{c^-,o}$ , and the polarizer's average real refractive index  $n_p$ . Therefore, once we know the films' and polarizer's refractive indices and the intended viewing angle ( $\theta_0$ ) for optimizing the LCD panel, we can determine the compensation films' thickness from Equations (8.23), (8.29), and (8.40)–(8.42). For instance, if we choose  $\theta_0 = 70^\circ$  and use the parameters listed in Tables 8.2 and 8.3, then we can calculate the required film thicknesses from Equations (8.40)–(8.42). The results are  $d_{a^+} = 61.38 \mu\text{m}$ ,  $d_{a^-} = 61.37 \mu\text{m}$ , and  $d_{c^-} = 246.11 \mu\text{m}$ . Based on these film thicknesses, Figure 8.27 plots the simulated iso-contrast contour for an MVA LCD with one positive  $a$  film, one negative  $a$  film, and one negative  $c$  film. Comparing Figure 8.27 to Figure 8.24, we can clearly see that the viewing angle at off-axis viewing directions, especially the bisector positions ( $\phi_0 = 0^\circ, 90^\circ, 180^\circ,$  and  $270^\circ$ ), is dramatically improved. In the meantime, the CR at on-axis viewing directions, i.e.,  $\phi_0 = 45^\circ, 135^\circ, 225^\circ,$  and  $315^\circ$ , remain unchanged.



**Figure 8.27** Iso-contrast contour of an MVA LCD with one positive  $a$  film ( $d_{a^+} = 61.38 \mu\text{m}$ ), one negative  $a$  film ( $d_{a^-} = 61.37 \mu\text{m}$ ), and one negative  $c$  film ( $d_{c^-} = 246.11 \mu\text{m}$ ) under  $\lambda = 550 \text{ nm}$



**Figure 8.28** (a) An alternative device structure and (b) compensation principle of a MVA LCD with one positive *a* film, one negative *a* film, and one negative *c* film

This compensation scheme can be modified by exchanging the positions of the negative *c* film and the MVA LC layer while keeping both positive and negative *a* films unchanged. In other words, the incident light passes through the negative *c* film first before it enters the MVA LC layer. Under such circumstances, the required film thickness can still be found from Equations (8.40)–(8.42), and the resultant iso-contrast contour is nearly identical to Figure 8.27.

Another alternative is to exchange the positions of both the positive *a* film and the negative *a* film, as shown in Figure 8.28(a). Different from the device configuration sketched in Figure 8.26(a), the positive *a* film is now adjacent to the analyzer while the negative *a* film is adjacent to the polarizer. The corresponding compensation mechanism is illustrated in Figure 8.28(b). Following the same analysis as above, we can readily determine from Figure 8.28(b) that the required film thicknesses are identical to Equations (8.40)–(8.42). The resultant iso-contrast contour is almost the same as that shown in Figure 8.27.

From Figure 8.27, the 100:1 iso-contrast contours barely exceed  $\sim 75^\circ$  polar angle. Although the two intermediate polarization states, points **E** and **F**, are located on the great circle which passes through the  $S_2$  and  $S_3$  axes, these two intermediate states are not symmetrically located with respect to the plane of the equator.

Examples using more sophisticated compensation schemes can be found in Ref. 31. When more compensation films are used, there are more degrees of freedom to be used for optimization. However, the associated cost will increase.

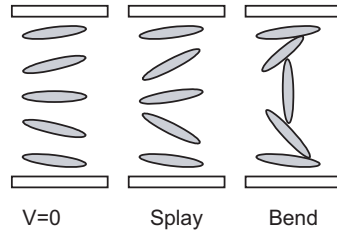


Figure 8.29 LC director configuration in a  $\pi$  cell

## 8.6 Optically Compensated Bend (OCB) Cell

The OCB mode utilizes a voltage-biased  $\pi$  cell compensated with phase retardation films. Its major advantages are two-fold: (1) a rapid response time; and (2) a symmetric and wide viewing angle. In a  $\pi$  cell [53], the pretilt angle in the alignment surfaces is in the opposite direction, as shown in Figure 8.29. The opposite pretilt angle exhibits two special features: (1) its viewing angle is symmetric; and (2) its bend director profile eliminates the backflow effect and, therefore, results in a rapid response time.

### 8.6.1 Voltage-dependent transmittance

Figure 8.30 plots the voltage-dependent transmittance curves of a uniaxial film-compensated bend cell. To make the splay-to-bend transition, a critical voltage ( $V_c \sim 1.0\text{--}1.5$  V) is biased to the  $\pi$  cell. Typically, the cell gap is around  $6\ \mu\text{m}$  and pretilt angle is  $7\text{--}10^\circ$  [54]. By adjusting the  $d\Delta n$  value of the compensation film, both normal-white and normal-black modes can be achieved [55]. Figure 8.30 shows the  $VT$  curves of a normal-white OCB at three primary wavelengths (R = 650, G = 550, B = 450 nm). The following parameters are used for simulations: LC  $d\Delta n = 436$  nm,  $\Delta\epsilon = 10$ , uniaxial  $a$  film  $d\Delta n = 53.3$  nm, and a pretilt angle of  $7^\circ$ . In reality, the uniaxial  $a$  film should be replaced by a biaxial film in order to widen the viewing angle. From Figure 8.30, a common dark state for RGB wavelengths appears at  $\sim 4.5$  V<sub>rms</sub>. Wavelength dispersion is a serious concern for any birefringence mode. To solve this

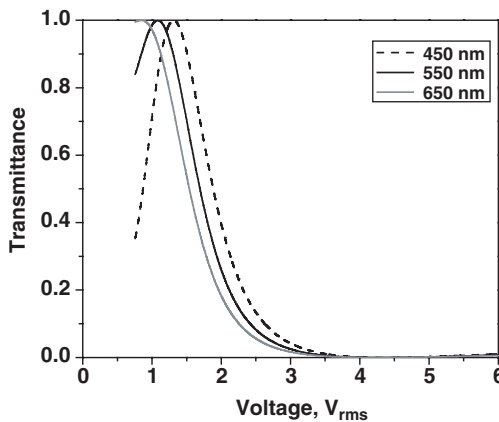


Figure 8.30 Voltage-dependent transmittance curves of a  $\pi$  cell.  $d\Delta n = 436$  nm, uniaxial film  $d\Delta n = 53.3$  nm, and its optic axis is perpendicular to that of the LC cell

problem, multiple cell gaps have to be used, i.e., the  $d\Delta n/\lambda$  values for all three primary wavelengths should be equal. For example, if  $d = 6 \mu\text{m}$  is used for green pixels, then the gaps for red and blue pixels should be 7.1 and 4.9  $\mu\text{m}$ , respectively. Here, the wavelength dispersion of the LC material is neglected [56]. Once these conditions are satisfied, the  $VT$  curves for R and B will overlap with that of G (dark solid line).

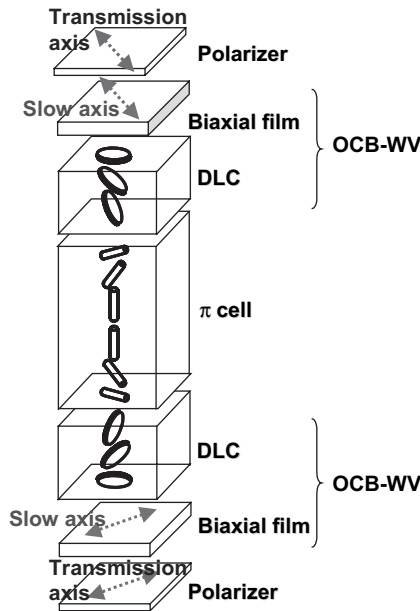
The fast response time of the OCB cell originates from three factors: the bias voltage effect (also known as the surface mode) [57], flow effect, and half-cell switching. The switching time between gray levels is less than 3 ms. A rapid response time is particularly important for LCD TV applications, especially at cold ambient conditions.

For other LCD modes, such as TN, MVA, and IPS, flow in the LC layer slows the rotational relaxation process of the director when the applied voltage is changed. For the  $\pi$  cell, on the other hand, there is no conflict between the torque exerted by the flow and the relaxation process of the director. The intrinsic wide viewing angle is due to the self-compensating structure. The retardation value stays almost the same even when the incident angle is changed in the director plane. However, retardation is not self-compensated at incidence out of the director plane. In addition, the on-axis CR of the  $\pi$  cell is low due to residual retardation even at a high applied voltage. To obtain a high on-axis CR and a wide viewing angle, an optical compensation film is required.

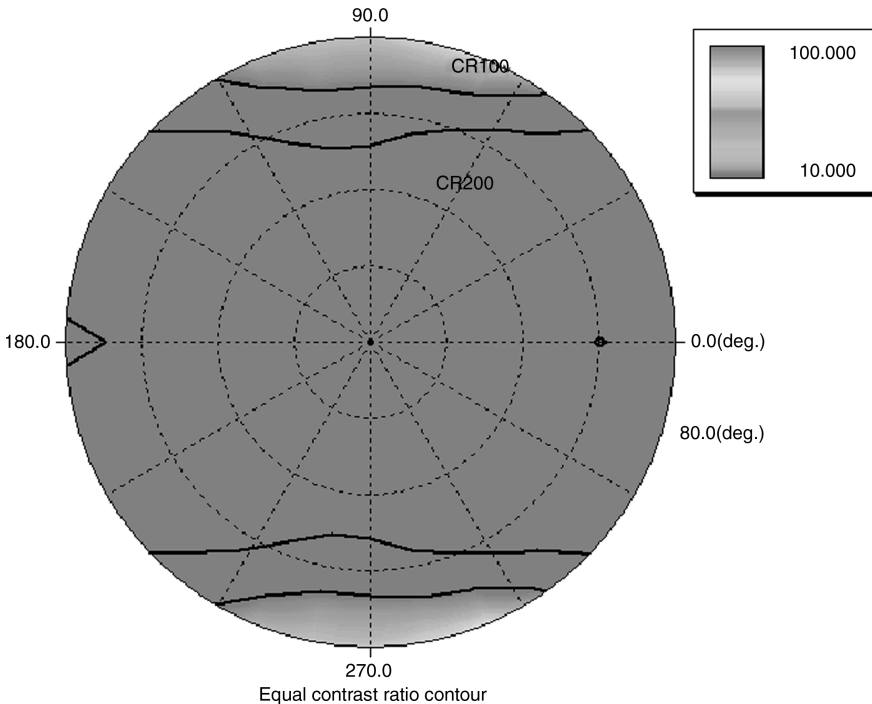
To obtain the bend alignment structure of the  $\pi$  cell, a voltage above the splay-to-bend transition voltage must be applied. The transition from splay to bend takes time, typically in the order of tens of seconds. The transition should be made faster than, say, 1 second.

**8.6.2 Compensation films for OCB**

To obtain a comparable viewing angle with VA and IPS, OCB requires more sophisticated optical compensation based on a discotic material [58]. Figure 8.31 shows the compensation schemes for a normal-white OCB mode. The fundamental idea is similar to that for TN mode. The retardation matching



**Figure 8.31** Idealized and simplified model of optical compensation for the  $\pi$  cell combined with the Fuji OCB films



**Figure 8.32** Simulated iso-contrast contour of Fuji film-compensated OCB cell

between the cell and the optical compensation film is especially important for the OCB mode, partially because the black state of the normal-white OCB cell has a finite residual retardation value that must be compensated by an optical film. For example, any retardation fluctuation of the cell or the film is easily noticeable. The OCB system requires a high level of uniformity and the cell parameters, as well as the film parameters, should be optimized in order to maximize the optical performance.

The polymer discotic material (PDM) developed by Fuji Photo Film has a hybrid alignment, which mimics half of the bend alignment structure of the OCB cell. Different from the discotic film developed for TN LCDs, the azimuthal alignment direction of the PDM layer is oriented at  $45^\circ$  with respect to the transmission axis of the polarizer, and the in-plane retardation of the PDM layer compensates for the in-plane retardation of the on-state OCB cell. The total in-plane retardation of the PDM layer should be the same as that of the on-state OCB cell so that the voltage-on state becomes black at a voltage lower than  $5 V_{rms}$ .

Figure 8.32 shows the simulated iso-contrast contour plot of the OCB panel. It is seen that OCB has a comparable viewing angle performance to VA and IPS. In addition to a faster response time, OCB has another advantage of less color shift at gray levels. Human skin especially looks good even at oblique incidence.

## Homework Problems

### 8.1 Twisted nematic cell

- (1) A student has prepared two identical TN cells except that one has a  $90^\circ$  twist angle and the other has  $80^\circ$ . How can the student distinguish which is which?

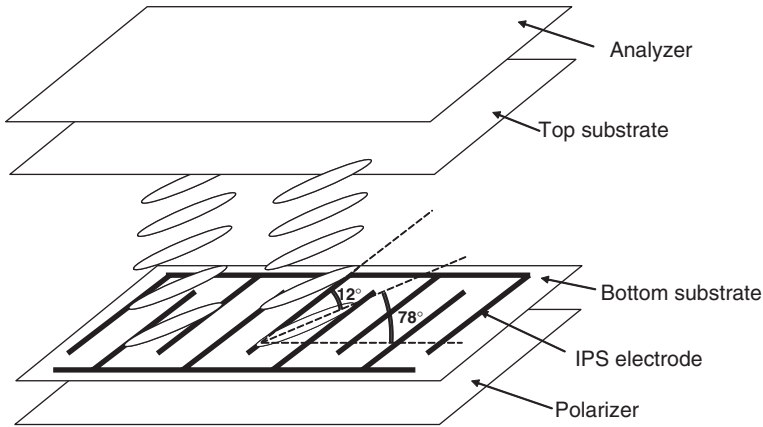


Figure 8.33

(2) A 90° TN cell is constructed using the following LC parameters:  $\Delta\epsilon = 8$ ,  $\Delta n = 0.1$  at  $\lambda = 550$  nm,  $K_{11} = 14$  pN,  $K_{22} = 7$  pN,  $K_{33} = 18$  pN, and  $\gamma_1 = 0.2$  Pa s. What is the required cell gap to satisfy the Gooch–Tarry first minimum condition? Estimate the optical decay time (100–10%) of the TN LC cell.

8.2 *In-plane-switching cell* Figure 8.33 shows the device configuration of a transmissive IPS LCD. The homogeneous alignment LC mixture is sandwiched between two substrates. The LC rubbing angle is 12° with respect to the IPS electrodes.

- (1) Draw the transmission axis of the polarizer and analyzer in the figure to obtain a normal-black mode.
- (2) If the LC mixture has birefringence  $\Delta n = 0.1$ , what is the required minimum cell gap for obtaining high transmittance?
- (3) Does the above IPS cell work well under normal-white conditions? Explain.
- (4) What are the pros and cons if we increase the rubbing angle to 30°?

8.3 *Homeotropic cell*

- (1) Can a homeotropic cell be used for normal-white LCD? Explain.

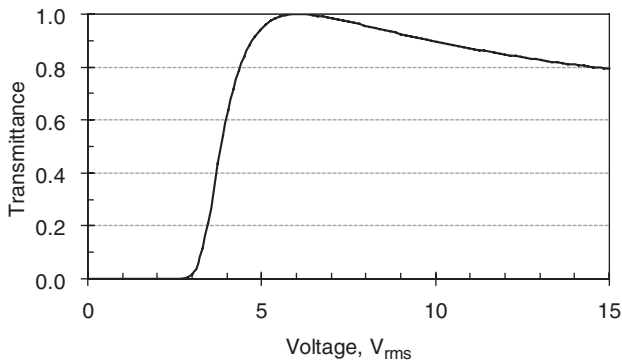


Figure 8.34



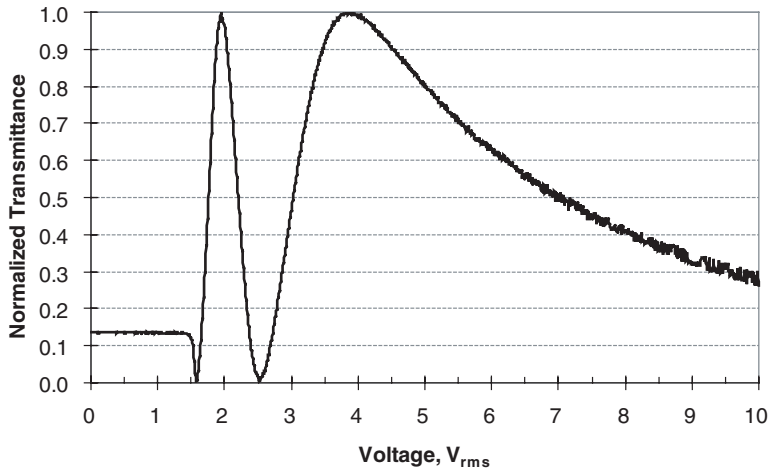


Figure 8.35

- (2) The voltage-dependent transmittance of a homeotropic cell, sandwiched between two crossed polarizers, is shown in Figure 8.34. Cell gap  $d = 5 \mu\text{m}$ ,  $\lambda = 633 \text{ nm}$ , and  $K_{33} = 15 \text{ pN}$ . Estimate the birefringence ( $\Delta n$ ) and dielectric anisotropy ( $\Delta\epsilon$ ) of the LC mixture.

8.4 *Homogeneous cell.* A homogeneous cell is useful as a tunable phase retardation plate. The chart in Figure 8.35 plots the voltage-dependent transmittance curve of a homogeneous LC cell at  $\lambda = 633 \text{ nm}$ . The polarizers are crossed and the angle between the front polarizer and the LC rubbing direction is  $45^\circ$ .

- (1) If the cell gap is  $d = 5 \mu\text{m}$ , what is the birefringence of the LC?
- (2) At what voltages is the output beam (before the analyzer) circularly polarized?
- (3) At what voltages is the output beam (before the analyzer) linearly polarized?
- (4) If you want to switch from circular to linear polarization, which voltages do you use in order to obtain the fastest response time?

## References

- 1 E. H. Stupp and M. Brennesholtz, *Projection Displays* (John Wiley & Sons, Inc., New York, 1998).
- 2 S. T. Wu and D. K. Yang, *Reflective Liquid Crystal Displays* (John Wiley & Sons, Inc., New York, 2001).
- 3 M. Schadt and W. Helfrich, 'Voltage-dependent optical activity of a twisted nematic liquid crystal', *Appl. Phys. Lett.*, **18**, 127 (1971).
- 4 C. H. Gooch and H. A. Tarry, 'The optical properties of twisted nematic liquid crystal structures with twisted angles  $\leq 90^\circ$ ', *J. Phys. D: Appl. Phys.*, **8**, 1575 (1975).
- 5 S. T. Wu and C. S. Wu, 'Mixed-mode twisted-nematic cell for transmissive liquid crystal display', *Displays*, **20**, 231 (1999).
- 6 H. Mori, Y. Itoh, Y. Nishiura, T. Nakamura, and Y. Shinagawa, 'Performance of a novel optical compensation film based on negative birefringence of discotic compound for wide-viewing-angle twisted-nematic liquid-crystal displays', *Jpn. J. Appl. Phys.*, **36**, 143 (1997).
- 7 H. Mori, 'The wide view film for enhancing the field of view of LCDs', *J. Disp. Technol.*, **1**, 179 (2005).
- 8 R. A. Soref, 'Transverse field effect in nematic liquid crystals', *Appl. Phys. Lett.*, **22**, 165 (1973).

- 9 R. A. Soref, 'Field effects in nematic liquid crystals obtained with interdigital electrodes', *J. Appl. Phys.*, **45**, 5466 (1974).
- 10 R. Kiefer, B. Weber, F. Windscheid, and G. Baur, 'In-plane switching of nematic liquid crystals', *Japan Displays '92*, 547 (1992).
- 11 M. Oh-e, M. Ohta, S. Arantani, and K. Kondo, 'Principles and characteristics of electro-optical behavior with in-plane switching mode', *Asia Display '95*, 577 (1995).
- 12 M. Oh-e, M. Yoneya, and K. Kondo, 'Switching of a negative and positive dielectric anisotropic liquid crystals by in-plane electric field', *J. Appl. Phys.*, **82**, 528 (1997).
- 13 M. Ohta, M. Oh-e, and K. Kondo, 'Development of super-TFT-LCDs with in-plane switching display mode', *Asia Display '95*, 707 (1995).
- 14 S. H. Lee, S. L. Lee, and H. Y. Kim, 'Electro-optic characteristics and switching principle of a nematic liquid crystal cell controlled by fringe-field switching', *Appl. Phys. Lett.*, **73**, 2881 (1998).
- 15 Y. M. Jeon, I. S. Song, S. H. Lee, H. Y. Kim, S. Y. Kim, and Y. J. Lim, 'Optimized electrode design to improve transmittance in the fringe-field switching liquid crystal cell', *SID Tech. Dig.*, **36**, 328 (2005).
- 16 Y. M. Jeon, I. S. Song, S. H. Lee, H. Y. Kim, S. Y. Kim, and Y. J. Lim, 'Optimized electrode design to improve transmittance in the fringe-field switching (FFS) liquid crystal cell', *SID Symp. Dig.*, **36**, 328, (2005).
- 17 K. H. Lee, S. H. Song, S. M. Yang, S. H. Park, J. K. Kim, J. K. Han, I. C. Park, and Y. J. Lim, 'CRT like characteristics of 32' WXGA TFT-LCD by true vision advanced FFS pixel concept', *SID Tech. Dig.*, **36**, 1742 (2005).
- 18 Y. Sun, Z. Zhang, H. Ma, X. Zhu, and S. T. Wu, 'Optimal rubbing angle for reflective in-plane-switching liquid crystal display', *Appl. Phys. Lett.*, **81**, 4907 (2002).
- 19 S. T. Wu, T. X. Wu, Q. Hong, X. Zhu, and R. Lu, 'Fast-response in-plane-switching pi-cell liquid crystal displays', US patent 6,987,549 B2 (Jan. 17, 2006).
- 20 J. Chen, K. H. Kim, J. J. Jyu, J. H. Souk, J. R. Kelly, and P. J. Bos, 'Optimum film compensation modes for TN and VA LCDs', *SID Tech. Dig.*, **29**, 315 (1998).
- 21 J. E. Anderson and P. J. Bos, 'Methods and concerns of compensating in-plane switching liquid crystal displays', *Jpn. J. Appl. Phys., Part 1*, **39**, 6388 (2000).
- 22 Q. Hong, T. X. Wu, X. Zhu, R. Lu, and S.-T. Wu, 'Extraordinarily high-contrast and wide-view liquid-crystal displays', *Appl. Phys. Lett.*, **86**, 121107 (2005).
- 23 Y. Saitoh, S. Kimura, K. Kusafuka, and H. Shimizu, 'Optimum film compensation of viewing angle of contrast in in-plane-switching-mode liquid crystal display', *Jpn. J. Appl. Phys., Part 1*, **37**, 4822, (1998).
- 24 T. Ishinabe, T. Miyashita, T. Uchida, and Y. Fujimura, 'A wide viewing angle polarizer and a quarter-wave plate with a wide wavelength range for extremely high quality LCDs', *Proceedings of the 21st International Display Research Conference (Asia Display/IDW'01)*, 485 (2001).
- 25 T. Ishinabe, T. Miyashita, and T. Uchida, 'Wide-viewing-angle polarizer with a large wavelength range', *Jpn. J. Appl. Phys., Part 1*, **41**, 4553 (2002).
- 26 F. Di Pasqual, H. Deng, F. A. Fernandez, S. E. Day, J. B. Davies, M. Johnson, A. A. Put, J. M. Eerenbeemd, J. Haaren, and J. Chapman, 'Theoretical and experimental study of nematic liquid crystal display cells using the in-plane-switching mode', *IEEE Trans. Electron Devices*, **46**, 661 (1999).
- 27 K. Ohmuro, S. Kataoka, T. Sasaki, and Y. Koite, 'Development of super-high-image-quality vertical-alignment-mode LC', *SID Tech. Dig.*, **26**, 845 (1997).
- 28 P. Yeh and C. Gu, *Optics of Liquid Crystal Displays* (John Wiley & Sons, Inc., New York, 1999).
- 29 A. Lien, 'A detail derivation of extended Jones matrix representation for twisted nematic liquid crystal displays', *Liq. Cryst.*, **22**, 171 (1997).
- 30 J. E. Bigelow and R. A. Kashnow, 'Poincaré sphere analysis of liquid crystal optics', *Appl. Opt.*, **16**, 2090 (1977).
- 31 X. Zhu, Z. Ge, and S. T. Wu, 'Analytical solutions for uniaxial film-compensated wide-view liquid crystal displays', *J. Disp. Technol.*, **2**, 3 (2006).
- 32 X. Zhu and S. T. Wu, 'Super wide view in-plane switching LCD with positive and negative uniaxial a-films compensation', *SID Dig. Tech. Pap.*, **34**, 1164 (2005).
- 33 R. Lu, X. Zhu, S. T. Wu, Q. Hong, and T. X. Wu, 'Ultrawide-view liquid crystal displays', *J. Disp. Technol.*, **1**, 3 (2005).

- 34 W. S. Asada, N. Kato, Y. Yamamoto, M. Tsukane, T. Tsurugi, K. Tsuda, and Y. Takubo, 'An advanced in-plane-switching mode TFT-LCD', *SID Tech. Dig.*, **28**, 929 (1997).
- 35 Y. Mishima, T. Nakayama, N. Suzuki, M. Ohta, S. Endoh, and Y. Iwakabe, 'Development of a 19 diagonal UXGA super TFT-LCM applied with super-IPS technology', *SID Tech. Dig.*, **31**, 260 (2000).
- 36 M. F. Schiekel and K. Fahrnschon, 'Deformation of nematic liquid crystals with vertical orientation in electric fields', *Appl. Phys. Lett.*, **19**, 391 (1971).
- 37 J. Grinberg, W. P. Bleha, A. D. Jacobson, A. M. Lackner, G. D. Myer, L. J. Miller, J. D. Margerum, L. M. Fraas, and D. D. Boswell, 'Photoactivated birefringence liquid crystal light valve for color symbology display', *IEEE Trans. Electron Devices*, **ED-22**, 775 (1975).
- 38 R. D. Sterling and W. P. Bleha, 'D-ILA technology for electronic cinema', *SID Tech. Dig.*, **31**, 310 (2000).
- 39 A. Takeda, S. Kataoka, T. Sasaki, H. Chida, H. Tsuda, K. Ohmuro, Y. Koike, T. Sasabayashi, and K. Okamoto, 'A super-high-image-quality multi-domain vertical alignment LCD by new rubbing-less technology', *SID Tech. Dig.*, **29**, 1077 (1997).
- 40 M. Oh-e, M. Yoneya, and K. Kondo, 'Switching of negative and positive dielectric anisotropic liquid crystals by in-plane electric fields', *J. Appl. Phys.*, **82**, 528 (1997).
- 41 C. K. Wei, Y. H. Lu, C. L. Kuo, C. Y. Liu, H. D. Liu, W. C. Chang, H. P. Huang, C. M. Cheng, and D. C. Yan, 'A wide-viewing angle polymer-stabilized homeotropically aligned LCD', *SID Tech. Dig.*, **29**, 1081 (1998).
- 42 Y. Kume, N. Yamada, S. Kozaki, H. Kisishita, F. Funada, and M. Hijiligawa, 'Advanced ASM mode: improvement of display performance by using a negative-dielectric liquid crystal', *SID Tech. Dig.*, **29**, 1089 (1998).
- 43 H. Wang, T. X. Wu, X. Zhu, and S. T. Wu, 'Correlations between liquid crystal director reorientation and optical response time of a homeotropic cell', *J. Appl. Phys.*, **95**, 5502 (2004).
- 44 S. T. Wu and C. S. Wu, 'Small angle relaxation of highly deformed nematic liquid crystals', *Appl. Phys. Lett.*, **53**, 1794 (1988).
- 45 S. T. Wu, 'A nematic liquid crystal modulator with response time less than 100  $\mu$ s at room temperature', *Appl. Phys. Lett.*, **57**, 986 (1990).
- 46 P. M. Alt, 'Single crystal silicon for high resolution displays', *Conference record of the International Display Research Conference.*, M19-28 (1997).
- 47 H. Kurogane, K. Doi, T. Nishihata, A. Honma, M. Furuya, S. Nakagaki, and I. Takanashi, 'Reflective AMLCD for projection displays', *SID Tech. Dig.*, **29**, 33 (1998).
- 48 K. Ohmuro, S. Kataoka, T. Sasaki, and Y. Koike, 'Development of super-high-image-quality vertical alignment-mode LCD', *SID Tech. Dig.*, **28**, 845 (1997).
- 49 A. Takeda, S. Kataoka, T. Sasaki, H. Chida, H. Tsuda, K. Ohmuro, Y. Koike, T. Sasabayashi, and K. Okamoto, 'A super high image quality multi-domain vertical alignment LCD by new rubbing-less technology', *SID Tech. Dig.*, **29**, 1077 (1998).
- 50 J. O. Kwag, K. C. Shin, J. S. Kim, S. G. Kim, and S. S. Kim, 'Implementation of new wide viewing angle mode for TFT-LCDs', *SID Tech. Dig.*, **31**, 256 (2000).
- 51 S. S. Kim, 'The world's largest (82-in) TFT LCD', *SID Tech. Dig.*, **36**, 1842 (2005).
- 52 P. G. de Gennes and J. Prost, *The Physics of Liquid Crystals*, 2nd edn (Oxford University Press, New York, 1995).
- 53 P. J. Bos and K. R. Koehler/Beran, 'The  $\pi$ -cell: a fast liquid crystal optical switching device', *Mol. Cryst. Liq. Cryst.*, **113**, 329 (1984).
- 54 T. Uchida, 'Field sequential full color LCD without color filter by using fast response LC cell', *The 5th International Display Workshops*, 151 (1998).
- 55 Y. Yamaguchi, T. Miyashita, and T. Uchida, 'Wide-viewing-angle display mode for the active-matrix LCD using bend-alignment liquid crystal cell', *SID Tech. Dig.*, **24**, 277 (1993).
- 56 S. T. Wu, 'Birefringence dispersion of liquid crystals', *Phys. Rev. A*, **33**, 1270 (1986).
- 57 J. L. Ferguson, 'Liquid crystal display with improved angle of view and response time', US patent 4,385,806 (1983).
- 58 Y. Ito, R. Matsubara, R. Nakamura, M. Nagai, S. Nakamura, H. Mori, and K. Miyahashi, 'OCB-WV film for fast-response-time and wide viewing angle LCD-TVs', *SID Tech. Dig.*, **36**, 986 (2005).

# 9

## Reflective and Transflective Liquid Crystal Displays

### 9.1 Introduction

As described in Chapter 8, transmissive liquid crystal displays (LCDs) have been widely used in laptop computers, desktop monitors, and high-definition televisions (HDTVs). The most commonly used transmissive  $90^\circ$  twisted nematic (TN) LCD [1] exhibits a high contrast ratio due to the self-phase compensation effect of the orthogonal boundary layers in the voltage-on state. However, its viewing angle is relatively narrow since the liquid crystal (LC) molecules are switched out of the plane and the oblique incident light experiences different phase retardations at different angles. For TV applications, a wide viewing angle is highly desirable. Currently, in-plane switching (IPS) [2] and multi-domain vertical alignment (MVA) [3] are the mainstream approaches for wide-view LCDs. A major drawback of the transmissive LCD is that its backlight source needs to be kept on all the time as long as the display is in use; therefore, the power consumption is relatively high. Moreover, the image of a transmissive LCD could be washed out by strong ambient light, e.g., direct sunlight because the panel's surface reflection from the direct sunlight is much brighter than the displayed images.

On the other hand, a reflective LCD has no built-in backlight unit; instead, it utilizes the ambient light for displaying images [4]. In comparison to transmissive LCDs, reflective LCDs have advantages in lower power consumption, lighter weight, and better outdoor readability. However, a reflective LCD relies on the ambient light and thus is inapplicable under low or dark ambient conditions.

In an attempt to overcome the above drawbacks and take advantage of both reflective and transmissive LCDs, transflective LCDs have been developed to use the ambient light when available and the backlight only when necessary [5]. A transflective LCD can display images in both transmissive mode (T mode) and reflective mode (R mode) simultaneously or independently. Since LC material itself does not emit light, the transflective LCD must rely on either ambient light or backlight to display images. Under bright ambient circumstances, the backlight can be turned off to save power and therefore the transflective LCD operates in the R mode only. Under dark ambient conditions, the backlight is turned on for illumination

and the transflective LCD works in the T mode. In the low- to medium-ambient surroundings, the backlight is still necessary. In this case, the transflective LCD runs in both T and R modes simultaneously. Therefore, the transflective LCD can accommodate a large dynamic range. Currently, the applications of transflective LCDs are mainly targeted at mobile display devices, such as cell phones, digital cameras, camcorders, personal digital assistants, pocket personal computers, global positioning systems, etc.

The major scientific and technological challenges for a transflective LCD are: reflector design, inequality in optical efficiency, color, and response time between the T mode and R mode. In this chapter, we first introduce the basic operational principles of reflective LCDs and then transreflectors and their underlying operating principles. Afterward, we analyze the factors affecting the image qualities. Finally, we describe the major problems with the current transflective LCD technologies and discuss potential solutions.

## 9.2 Reflective LCDs

Two types of reflective LCDs (R-LCDs) have been developed: direct-view and projection. Direct-view R-LCDs use ambient light for reading the displayed images, but projection R-LCDs use arc lamp or bright LEDs for projecting images onto a large screen. Direct-view R-LCDs are commonly used in games, signage, and some cell phones; projection R-LCDs are used in liquid-crystal-on-silicon (LCoS) rear projection TVs. Although the involved panel resolution and optical systems for direct-view and projection displays are different, their underlying LC operation modes are quite similar. Two monographs have been devoted to projection [6] and direct-view reflective LCDs [7]. In this section, we will only cover the background material for the introduction of transflective LCDs.

Figure 9.1 shows a typical R-LCD device structure. The linear polarizer and a broadband quarter-wave film form an equivalent ‘crossed’ polarizer. This is because the LC modes work better under crossed-polarizer conditions. The bumpy reflector not only reflects but also diffuses the ambient light to the observer. This is the most critical part in a R-LCD. The TFT is hidden beneath the bumpy reflector.

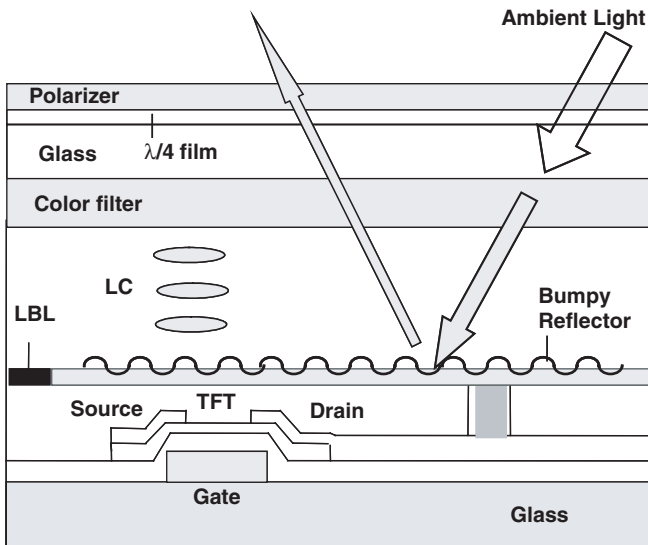


Figure 9.1 Device structure of a direct-view R-LCD

Thus, the R-LCD can have a large aperture ratio ( $\sim 90\%$ ). The light blocking layer (LBL) is used to absorb the scattered light from neighboring pixels.

Three popular LCD cells have been widely used for R-LCDs and transfective LCDs. They are the (1) vertical alignment (VA) cell, (2) film-compensated homogeneous cell, and (3) mixed-mode twisted nematic (MTN) cell. The VA and homogeneous cells utilize the phase retardation effect while the MTN cells use a combination of polarization rotation and birefringence effects. The VA cell has been described in detail in Section 8.4 for wide-view LCDs. For reflective LCDs, the cell gap is reduced to one-half of that of a transmissive LCD to account for the double pass of the incoming light. The voltage-dependent reflectance curves are basically the same as those shown in Figure 8.19 and will not be repeated in this chapter. The film-compensated VA cell is a favored choice for transfective LCDs because of its high contrast ratio and wide viewing angle. In the following two sections, we will briefly describe the film-compensated homogeneous cell and MTN cells.

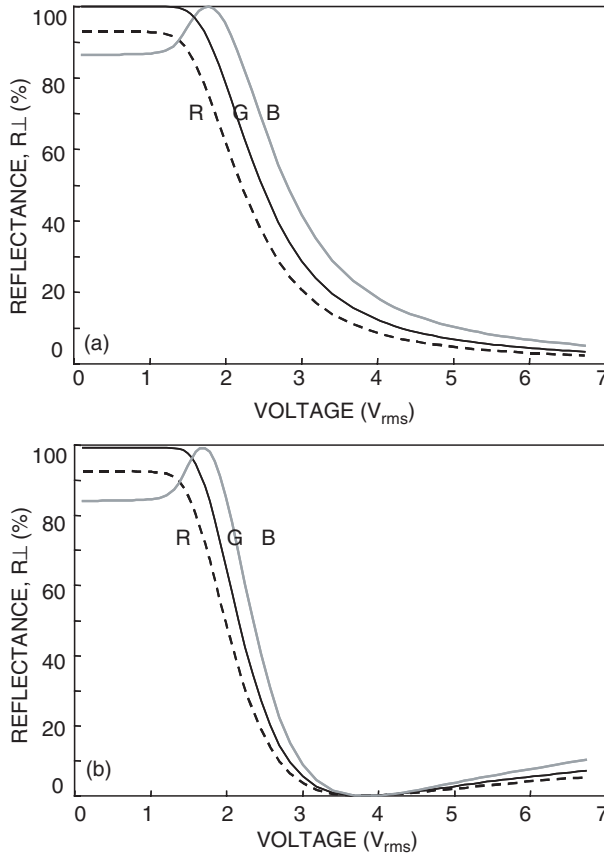
### 9.2.1 Film-compensated homogeneous cell

A homogeneous cell is not suitable for transmissive display because of its narrow viewing angle and lack of common dark state for RGB colors [8]. However, in a reflective display, the viewing angle is equivalent to a two-domain cell due to the mirror image effect [9]. For some handheld small-screen displays, the requirement for a wide viewing angle is not too demanding, so the homogeneous cell can still be useful. But for some high-end transfective LCDs intended for playing videos and movies, wide view is a necessity.

For a homogeneous cell, to obtain a common dark state for full-color display a phase compensation film has to be used in order to cancel the residual phase retardation of the cell resulting from boundary layers [10]. To design a homogeneous cell for reflective display, the required minimal  $d\Delta n$  value is  $\lambda/4$ ; that is to say, the LC cell functions like a quarter-wave plate. Using  $\lambda = 550$  nm, we find  $d\Delta n = 137.5$  nm. The cell gap and birefringence can be chosen independently, depending on the need. One could choose a thinner cell gap to obtain a faster response time or choose a lower birefringence LC mixture to maintain a reasonable cell gap for high-yield manufacturing. Other designs with  $d\Delta n = \lambda/2$  have been found to have a weak color dispersion [11].

For the purpose of illustrating the design procedures, let us use a Merck LC mixture MLC-6297-000 as an example. The LC and cell parameters are listed as follows: the angle between the front polarizer and cell rubbing direction  $\beta = 45^\circ$ , pretilt angle  $\alpha = 2^\circ$ , elastic constants  $K_{11} = 13.4$ ,  $K_{22} = 6.0$ , and  $K_{33} = 19.0$  pN, dielectric constants  $\epsilon_{\parallel} = 10.5$  and  $\Delta\epsilon = 6.9$ ,  $\Delta n = 0.125$ ,  $0.127$ , and  $0.129$  for R = 650, G = 550, and B = 450 nm.

Figure 9.2(a) depicts the voltage-dependent light reflectance of a homogeneous cell with  $d\Delta n = 137.5$  nm under crossed-polarizer conditions. For the purpose of comparing intrinsic LC performance, we only consider the normalized reflectance; the optical losses from the polarizer, substrate surfaces, indium-tin-oxide (ITO), and any other compensation film are neglected. From Figure 9.2(a), the bright-state intensity variation among RGB colors is within 10%. In the high-voltage regime, the reflectance is monotonously decreasing. However, it is difficult to obtain a common dark state for the RGB colors. A uniaxial phase compensation film (also called  $a$  film) is needed. Figure 9.2(b) plots the voltage-dependent reflectance of a homogeneous cell ( $d\Delta n = 184$  nm) compensated by an  $a$  film having  $(d\Delta n)_{\text{film}} = -48$  nm. A positive  $a$  film can be used as well, as long as its optic axis is perpendicular to the LC's rubbing direction. This normal-white mode has a relatively weak color dispersion and low dark-state voltage. In the high-voltage regime, the residual LC phase diminishes but the phase of the compensation film remains. As a result, some light leakage is observed. For display applications, the dark-state voltage can be controlled by the driving circuit. An important consideration whereas the width of the dark state so that when the temperature fluctuates the display contrast is not significantly affected. From simulations, a smaller  $d\Delta n$  value of the  $a$  film would lead to a broader dark state at a higher voltage. That means that the required voltage swing is larger.



**Figure 9.2** Voltage-dependent reflectance of (a) homogeneous cell with  $d\Delta n = 137.5$  nm, and (b) film-compensated homogeneous cell with  $d\Delta n = 184$  nm for the LC and  $d\Delta n = -48$  nm for the  $a$  film.

**9.2.2 MTN cell**

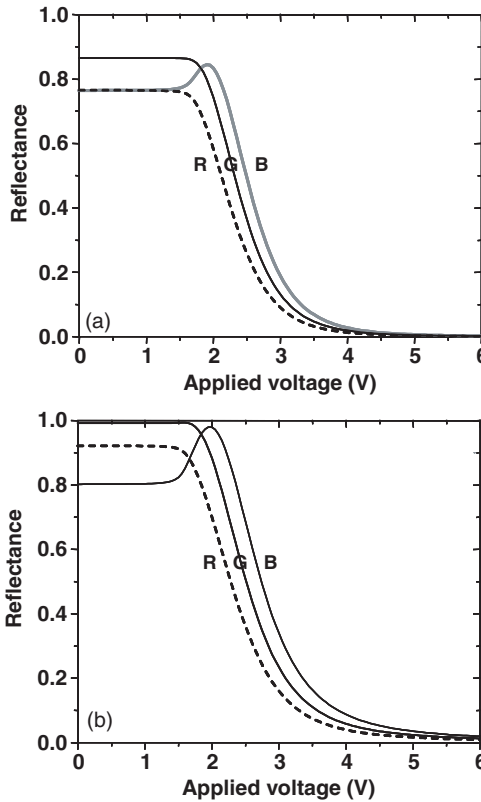
In the reflective cell shown in Figure 9.1, the incident light traverses the linear polarizer,  $\lambda/4$  film, and LC layer, and is reflected back by the imbedded mirror on the inner side of the rear substrate. In the voltage-off state, the normalized reflectance can be obtained by the Jones matrix method [12]:

$$R_{\perp} = \left( \Gamma \frac{\sin X}{X} \right)^2 \left( \sin 2\beta \cos X - \frac{\phi}{X} \cos 2\beta \sin X \right)^2 \tag{9.1}$$

Here,  $\Gamma = 2\pi d \Delta n / \lambda$ ,  $d$  is the cell gap,  $X = \sqrt{\phi^2 + (\Gamma/2)^2}$ ,  $\phi$  is the twist angle, and  $\beta$  is the angle between the polarization axis and the front LC director.

Several MTN modes with twist angle  $\phi$  varying from  $45^\circ$  to  $90^\circ$  have been used for direct-view and projection displays, depending on the desired contrast ratio and optical efficiency. In transflective LCDs, the  $75^\circ$  and  $90^\circ$  MTN cells are frequently used. Therefore, we only discuss these two modes here.

Figure 9.3(a) and (b) shows the voltage-dependent reflectance (VR) of the  $90^\circ$  and  $75^\circ$  MTN cells, respectively. For simulations, a Merck MLC-6694-000 ( $\Delta n = 0.0857$  at  $\lambda = 540$  nm) LC mixture and  $2^\circ$  pretilt angle are used. The  $90^\circ$  MTN cell has  $d\Delta n = 240$  nm and  $\beta = 20^\circ$  and the  $75^\circ$  MTN cell has



**Figure 9.3** Voltage-dependent reflectance of (a) 90° and (b) 75° MTN cells. The cell and LC material parameters are discussed in the text

$d\Delta n = 250$  nm and  $\beta = 15^\circ$ . Both MTN cells are broadband devices; this means that their VR curves are insensitive to the wavelength. During simulations, the following bandwidths are considered: R = 620–680 nm, G = 520–560 nm, and B = 420–480 nm. For each mode, the reflectance is calculated at every 10 nm and then averaged over the entire band.

From Figure 9.3, the 90° MTN cell exhibits a good dark state, similar to a transmissive TN cell because of the self-phase compensation effect of the orthogonal boundary layers. However, its maximum reflectance is only ~88%. On the other hand, the 75° MTN cell has nearly 100% reflectance, but its dark state has a slight light leakage. The contrast ratio at 5  $V_{rms}$  is around 100:1. This is because the boundary layers are not perfectly compensating each other.

For direct-view reflective displays, the outmost surface reflection (usually it is a plastic protective film without an anti-reflection coating) limits the device contrast ratio. Thus, the ~100:1 contrast ratio of the 75° MTN cell is still adequate. However, in projection displays the contrast ratio needs to exceed 1000:1. The 90° MTN and VA cells are better choices.

### 9.3 Transflector

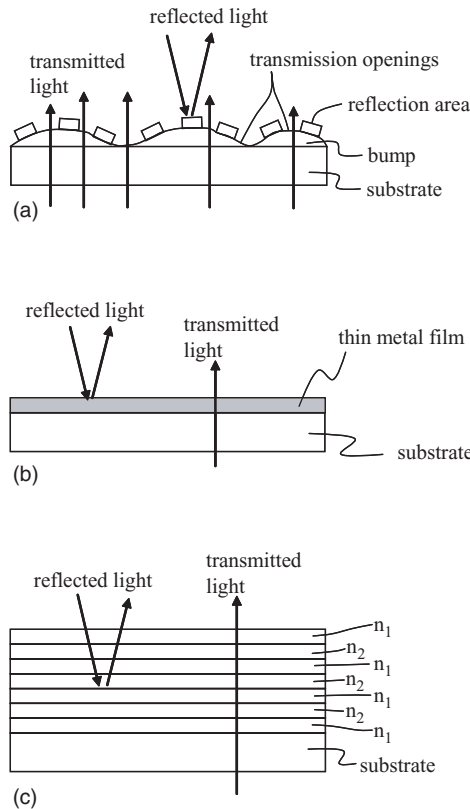
Since a transfective LCD should possess dual functions (transmission and reflection) simultaneously, a transflector is usually required between the LC layer and the backlight source. The main role of the transflector is to partially reflect the incident ambient light and to partially transmit the backlight to the



viewer. From a device structure viewpoint, the transflector can be classified into four major categories: (1) openings-on-metal transflector, (2) half-mirror metal transflector, (3) multilayer dielectric film transflector, and (4) orthogonal polarization transflector, as shown in Figure 9.4(a)–(c) and Figure 9.5(a)–(c).

### 9.3.1 Openings-on-metal transflector

Figure 9.4(a) shows the schematic structure of the openings-on-metal transflector proposed by Ketchpel and Barbara [13]. The typical manufacturing steps include first forming wavy bumps on the substrate, then coating a metal layer, such as silver or aluminum, on the bumps, and finally etching the metal layer according to the predetermined patterns. After etching, those etched areas become transparent so that the incident light can transmit through, while those unaffected areas are still covered by the metal layer and serve as reflectors. The wavy bumps function as diffusive reflectors to steer the incident ambient light away from surface specular reflection. Thus, the image contrast ratio is enhanced and the viewing angle widened in the R mode. Due to the simple manufacturing process, low cost, and stable performance, this type of transflector is by far the most popularly implemented in transflective LCD devices.



**Figure 9.4** Schematic illustration of the first three major types of transflectors: (a) openings-on-metal transflector, (b) half-mirror metal transflector, and (c) multilayer dielectric film transflector

### 9.3.2 Half-mirror metal translector

The half-mirror has been widely used in optical systems as a beam splitter. It was implemented in transfective LCDs by Borden [14] and Bigelow [15] with the basic structure shown in Figure 9.4(b). When depositing a very thin metallic film on a transparent substrate, one can control the reflectance and transmittance by adjusting the metal film thickness. The film thickness can vary, depending on the metallic material employed. Typically, the film thickness is around a few hundred angstroms. Since the transmittance/reflectance ratio of such a half-mirror translector is very sensitive to the metal film thickness, the manufacturing tolerance is very narrow and the volume production is difficult. Consequently, this kind of translector is not too popular in commercial products.

### 9.3.3 Multilayer dielectric film translector

Multilayer dielectric film is a well-developed technique in thin-film optics, but only very recently was it incorporated into transfective LCDs [16]. As illustrated in Figure 9.4(c), two dielectric inorganic materials with refractive indices  $n_1$  and  $n_2$  are periodically deposited as thin films on the substrate. By controlling the refractive index and thickness of each thin layer as well as the total number of layers, one can obtain the desired reflectivity and transmissivity. Similar to the half-mirror translector, the transmittance/reflectance ratio of the multilayer dielectric film is sensitive to each layer's thickness. In addition, to produce several layers successively increases the manufacturing cost. Therefore, the multilayer dielectric film translector is rarely used in current commercial transfective LCDs.

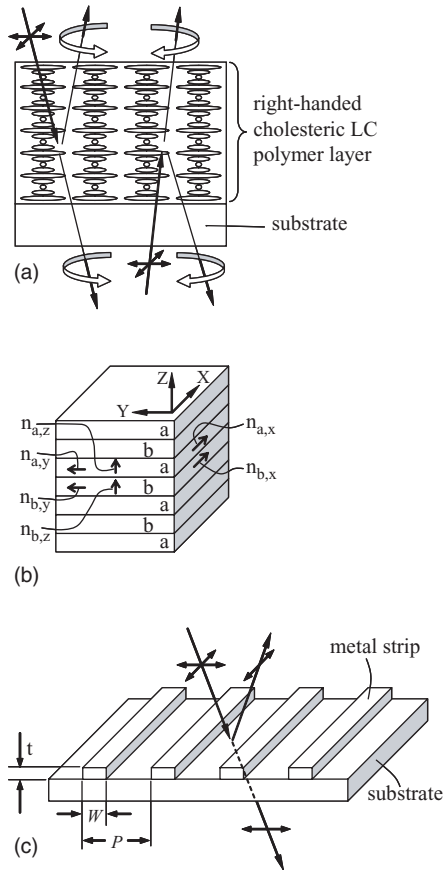
### 9.3.4 Orthogonal polarization transfectors

The orthogonal polarization translector has a special characteristic where the reflected and the transmitted polarized light from the translector have mutually orthogonal polarization states. For instance, if a translector reflects horizontal linearly (or right-handed circularly) polarized light, then it will transmit the complementary linearly (or left-handed circularly) polarized light. Figure 9.5(a)–(c) shows three such examples: the cholesteric reflector [17], birefringent interference polarizer [18], and wire grid polarizer (WGP) [19].

Cholesteric LC molecules are manifest as a planar texture with their helix perpendicular to the cell substrates when the boundary conditions on both substrates are tangential. If the incident wavelength is comparable to the product of the average refractive index and the cholesteric pitch, then the cholesteric LC layer exhibits a strong Bragg reflection [20]. Figure 9.5(a) shows the schematic configuration of a right-handed cholesteric reflector, where the cholesteric LC polymer layer is formed on a substrate. For incident unpolarized light, the right-handed circularly polarized light which has the same sense as the cholesteric helix is reflected, but the left-handed circularly polarized light is transmitted.

The birefringent–interference–polarizer translector consists of a multilayer birefringence stack with alternating low and high refractive indices, as shown in Figure 9.5(b). One way to produce such a translector is to stretch a multilayer stack in one or two dimensions. The multilayer stack consists of birefringent materials with low/high index pairs [21]. The resultant transfective polarizer exhibits a high reflectance for the light polarized along the stretching direction and, at the same time, a high transmittance for the light polarized perpendicular to the stretching direction. By controlling the three refractive indices of each layer,  $n_x$ ,  $n_y$ , and  $n_z$ , the desired polarizer behaviors can be obtained. For practical applications, an ideal reflective polarizer should have  $\sim 100\%$  reflectance along one axis (the so-called extinction axis) and  $0\%$  reflectance along the other (the so-called transmission axis) axis, at all the incident angles.

The WGP has been widely used for infrared spatial light modulators [22, 23]. It is constructed by depositing a series of parallel and elongated metal strips on a dielectric substrate, as Figure 9.5(c) shows. To operate in the visible spectral region, the pitch of metal strip  $P$  should be in the range of around 200 nm, which is approximately half of a blue wavelength [24]. In general, a WGP reflects light with its



**Figure 9.5** Schematic illustration of the three examples of orthogonal polarization transfectors: (a) cholesteric reflector, (b) birefringent interference polarizer, and (c) wire grid polarizer (WGP)

electric field vector parallel to the wires of the grid and transmits when it is perpendicular. In practice, the wire thickness  $t$ , wire width  $W$ , and grid pitch  $P$  play important roles in determining the extinction ratio and acceptance angle of the polarizer [25].

Unlike the first three transfectors discussed above, the entire area of the orthogonal polarization translector can be utilized for reflection and transmission simultaneously. Nevertheless, the transmitted light and reflected light possess an orthogonal polarization state so that the reflective and transmissive images exhibit a reversed contrast. Although an inversion driving scheme may correct such a reversed contrast problem [19], the displayed images are still unreadable in moderate brightness surroundings when both ambient light and backlight are in use. Furthermore, the birefringent interference polarizer is difficult to implement inside the LC cell. As a result, the undesirable parallax problem occurs. Thus, orthogonal polarization transfectors have not yet been widely adopted in high-end transfective LCDs.

### 9.4 Classification of Transflective LCDs

Based on the light modulation mechanisms, transflective LCDs can be classified into four categories: (1) absorption type, (2) scattering type, (3) reflection type, and (4) phase retardation type. The first three

categories do not modulate the phase of the incident light; rather, they absorb, scatter, or reflect. In these cases, one or no polarizer is preferred from the viewpoint of achieving high brightness. As for the phase retardation type, two polarizers are usually indispensable in order to make both transmissive and reflective modes work simultaneously.

#### 9.4.1 Absorption-type transreflective LCDs

To realize the absorption effect, a liquid crystal host is doped with a few percent (2–5 wt%) of dichroic dye. As the LC directors are reoriented by the electric field, the dye molecules follow. The dichroic dyes absorb light strongly (or weakly) when the incident light's polarization is parallel (or perpendicular) to the principal molecular axis. The ratio of these two absorption coefficients ( $\alpha_{\parallel}/\alpha_{\perp}$ ) is called the dichroic ratio, which significantly influences the contrast ratio of the display. Because of the dye's dichroism, the absorption of the LC cell is modulated by the electric field. This mechanism was first introduced in the nematic phase by Heilmeyer and Zanoni [26] and later in the cholesteric phase by White and Taylor [27]. In the twisted or helical LC structure, the guest–host display does not require a polarizer. A major technical challenge of guest–host displays is the tradeoff between reflectance/transmittance and contrast ratio. A typical contrast ratio for the guest–host LCD is  $\sim 5:1$  with  $\sim 40\text{--}50\%$  reflectance. The fairly low contrast ratio is limited by the dichroic ratio of the dye. Long-term stability of the dichroic dyes is another concern because of their strong absorption in the visible spectral region. So far, only a few guest–host LCDs have been commercialized.

##### (1) Nematic absorption transreflective display

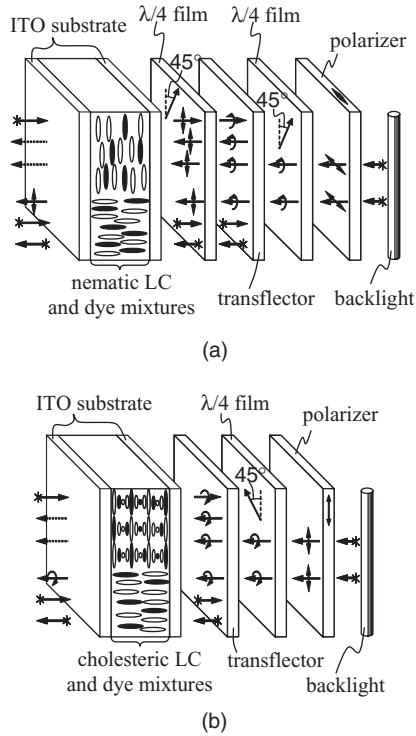
Figure 9.6(a) shows a transreflective LCD structure using a half-mirror metallic transreflector, two quarter-wave films, and nematic phase LC/dye mixtures [15]. In the figure, the upper half and lower half stand for the voltage-off and voltage-on states, respectively.

When there is no voltage applied, the LC/dye mixtures are homogeneously aligned by the anchoring energy of the cell. In the R mode, the unpolarized incident ambient light becomes linearly polarized after passing through the LC/dye layer. Then, its polarization state turns into right-handed circularly polarized light after traversing through the inner quarter-wave film. Upon reflection from the transreflector, its polarization state becomes left-handed circularly polarized due to a  $\pi$  phase change. When the left-handed circularly polarized light again passes through the inner quarter-wave film, it becomes linearly polarized with a polarization direction parallel to the LC alignment direction. As a result, the light is absorbed by the doped dye molecules and a dark state is achieved.

In the T mode, the unpolarized light from the backlight unit becomes linearly polarized after the polarizer. Then it changes to left-handed circularly polarized light after emerging from the outer quarter-wave film. After penetrating the transreflector, it still keeps the same left-handed circular polarization state. Thereafter, its travel path is identical to that of R mode. Finally, the light is absorbed by the dye molecules, resulting in a dark state.

In the voltage-on state, the LC and dye molecules are reoriented nearly perpendicular to the substrates, as illustrated in the lower half of Figure 9.6(a). Therefore, the light passing through it experiences little absorption so that no change in the polarization state occurs. In the R mode, the unpolarized ambient light passes through the LC/dye layer and the inner quarter-wave film successively without changing the polarization state. Upon reflection from the transreflector, it is still unpolarized light and goes all the way out of the transreflective LCD. Consequently, a bright state with little attenuation is achieved. In the T mode, the unpolarized backlight becomes linearly polarized after passing through the linear polarizer, the outer quarter-wave film, the transreflector, and the inner quarter-wave film, successively. Since the dye molecules are reoriented perpendicularly, the absorption loss is small. As a result, the linearly polarized light emerges from the transreflective LCD which leads to a bright state.

In the above-mentioned transreflective guest–host LCD, the inner quarter-wave film is put between the transreflector and the guest–host layer. There are two optional positions for the transreflector. If the



**Figure 9.6** Schematic configurations and operating principles of two absorption-type transflective LCDs with (a) nematic phase LC (host) and dye (guest) mixtures, and (b) cholesteric phase LC (host) and dye (guest) mixtures

transflector is located inside the LC cell, then the quarter-wave film should also be sandwiched inside the cell. Nevertheless, it is difficult to fabricate such a quarter-wave film and assemble it inside the cell. The final process of the cell is polyimide coating, baking, and rubbing. The post-baking temperature of polyimide is typically at  $\sim 250^{\circ}\text{C}$  for 1 h. The polymeric quarter-wave film may not be able to sustain such a high-temperature processing. Therefore, the external transflector is preferred. If the transflector is located outside the cell, then both the quarter-wave film and transflector can be laminated on the outer surface of the LC cell. In this case, however, a serious parallax problem would occur.

*(2) Cholesteric absorption transflective display*

To eliminate the quarter-wave film between the transflector and the LC layer, a transflective LCD design using a half-mirror metallic transflector and cholesteric LC/dye mixture has been proposed [28]. The device structure is illustrated in Figure 9.6(b). From Figure 9.6(b), only one quarter-wave film is employed, which is located between the transflector and the linear polarizer. Consequently, the quarter-wave film can be put outside of the cell, while the transflector can be sandwiched inside the cell. As a result, no parallax occurs. The upper and lower portions of this figure demonstrate the voltage-off and voltage-on states, respectively. In the voltage-off state, the LC/dye molecules render a right-handed planar texture with its helix perpendicular to the substrates. In the R mode, the unpolarized light is largely attenuated by the LC/dye layer and only weak light passes through it. Upon reflection from the transflector, it is further absorbed by the guest dye molecules, resulting in a dark state. In the T mode, the unpolarized backlight first becomes linearly polarized and then right-handed circularly polarized after

passing through the polarizer and, in turn, the quarter-wave film. The circularly polarized light is further attenuated after it penetrates the transflector. Such weak right-handed circularly polarized light is absorbed by the same handedness cholesteric LC/dye mixture, resulting in a dark state.

In the voltage-on state, both the LC and dye molecules are reoriented perpendicular to the substrates. As a result, little absorption occurs in the incident light. In the R mode, the unpolarized light is unaffected throughout the whole path, resulting in a very high reflectance. In the T mode, the unpolarized backlight becomes right-handed circularly polarized after passing through the polarizer, the quarter-wave film, and the transflector. It finally penetrates the LC/dye layer with little attenuation. Again, a bright state is obtained.

In the above-mentioned two absorption-type transflective LCDs, only one polarizer is employed instead of two. Therefore, the overall image in both T and R modes is relatively bright. However, due to the limited dichroic ratio of the dye molecules employed (~15:1), a typical contrast ratio of the guest–host LCD is around 5:1, which is inadequate for high-end full-color LCD applications [29]. Thus, the absorption-type transflective LCDs only occupy a small portion of the handheld LCD market.

9.4.2 Scattering-type transflective LCDs

Polymer-dispersed LC (PDLC) [30], polymer-stabilized cholesteric texture (PSCT) [31], and LC gels [32] all exhibit optical scattering characteristics and have wide applications in displays and optical devices. The LC gel-based reflective LCD can also be extended to transflective LCDs [33]. Figure 9.7 shows the schematic structure and operating principles of the LC gel-based transflective LCD. The device is composed of a LC gel cell, two quarter-wave films, a transflector, a polarizer, and a backlight. The cell was filled with a homogeneously aligned nematic LC and monomer mixture. After UV-induced polymerization, polymer networks are formed and the LC molecules are confined within the polymer networks.

When there is no voltage applied, the LC molecules exhibit a homogeneous alignment. Consequently, the LC gels are highly transparent for light traveling through, as illustrated in the upper portion of Figure 9.7. In the R mode, the unpolarized ambient light remains unpolarized all the way from entering to exiting the LC cell. As a result, a fairly bright state is obtained. In the T mode, the unpolarized backlight turns into a linearly polarized *p* wave after the polarizer. After passing the first quarter-wave film and penetrating the transflector, and the second quarter-wave film whose optic axis is orthogonal to that of

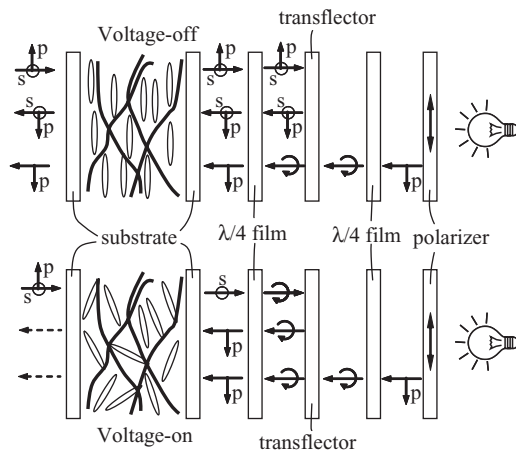


Figure 9.7 Schematic configuration and operating principles of scattering-type transflective LCD with homogeneously aligned LC gel

the first one, the  $p$  wave remains linearly polarized. Since the LC gel is highly transparent in the voltage-off state, the linearly polarized  $p$  wave finally comes out of the display panel, resulting in a bright output.

On the other hand, when the external applied voltage is high enough, the LC molecules deviate from the original homogeneous alignment by the exerted torque of the electric field. Therefore, microdomains are formed along the polymer chains such that the extraordinary ray, i.e., the linear polarization along the cell rubbing direction, is scattered, provided that the domain size is comparable to the incident light wavelength. In the meantime, the ordinary ray passes through the LC gels without being scattered. In the R mode, the unpolarized ambient light becomes a linearly polarized  $s$  wave after passing the activated LC cell since the  $p$  wave is scattered. After a round trip of passing the quarter-wave film, being reflected by the transflector, and passing the quarter-wave film again, the  $s$  wave is converted into a  $p$  wave. Due to the scattering of LC gels, this  $p$  wave is scattered again. Consequently, a scattering translucent state is achieved. In the T mode, the unpolarized backlight turns into a linearly polarized  $p$  wave after passing the polarizer, the second quarter-wave film, the transflector, and the first quarter-wave film, successively. Thereafter, similar to the case of the R mode, the  $p$  wave is scattered by the activated LC gels, resulting in a scattered translucent output.

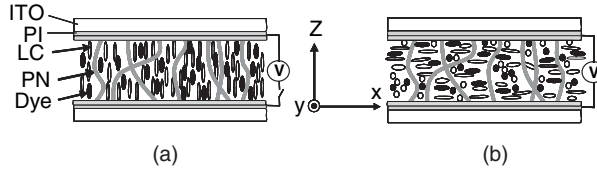
This scattering-type transflective LCD only needs one polarizer; therefore, it can achieve a very bright image. However, there are three major drawbacks in the above LC gel-based transflective LCD. First, the light-scattering mechanism usually leads to a translucent state rather than a black state. Therefore, the image contrast ratio is low and highly dependent on the viewing distance to the display panel. Although doping the LC gels with a small concentration of black dye can help to achieve a better dark state, the contrast ratio is still quite limited due to the limited dichroic ratio of the dye dopant. Secondly, the insertion of the first quarter-wave film will cause a similar parallax problem as in the absorption-type transflective LCD using cholesteric LCs. Thirdly, the required driving voltage is usually over 20 volts due to the polymer network constraint, which is beyond the capability of current TFTs developed for LCD applications. Therefore, these drawbacks hinder the scattering-type transflective LCD in wide-spread applications.

### 9.4.3 Scattering- and absorption-type transflective LCDs

White paper scatters and diffuses light in the bright state resulting in a wide viewing angle. When the paper is printed, the ink absorbs light and the printed areas become dark. To mimic the display shown in white paper, we can combine light-scattering and absorption mechanisms together in a dye-doped LC gel system [34].

Both dual-frequency LC and negative  $\Delta\epsilon$  LC gels have been demonstrated. Here, we only describe the dye-doped negative LC gel system because the TFT-grade negative  $\Delta\epsilon$  LC has been commonly employed in VA. For example, Merck ZLI-4788 has  $\Delta\epsilon = -5.7$  at  $f = 1$  kHz and  $\Delta n = 0.1647$  at  $\lambda = 589$  nm. To form a gel, one can mix ZLI-4788, a diacrylate monomer (bisphenol-A-dimethacrylate), and the dichroic dye S428 (Mitsui, Japan) at 90:5:5 wt% ratios. To make the device independent of polarization, the ITO glass substrates should have a polyimide (PI) coating, but *without* rubbing treatment. The PI layer provides VA for the LC molecules. The cell gap is controlled at about 5  $\mu\text{m}$ . To form a gel, the filled LC cell is cured by UV light ( $\lambda \sim 365$  nm,  $I \sim 15$  mW/cm<sup>2</sup>) at 13°C for 2 h. After photopolymerization, the formed chain-like polymer networks are along the cell gap ( $z$ ) direction because the LC directors are aligned perpendicular to the glass substrates during the UV curing process, as Figure 9.8(a) depicts.

Figure 9.8(a) and (b) illustrates the light modulation mechanisms of the dye-doped negative LC gel. At  $V = 0$ , the cell does not scatter light and the absorption is rather weak because the LC and dye molecules are aligned perpendicular to the substrate surfaces. At this stage, the display has the highest reflectance. When a high voltage at  $f = 1$  kHz is applied to the LC gel, the LCs and dye molecules are reoriented in the  $x$ - $y$  plane, as Figure 9.8(b) depicts. The polymer network scatters light strongly. Since the alignment layer has no rubbing treatment, the absorption has no preferred direction. Therefore,



**Figure 9.8** Operating principle of the dye-doped negative LC gel: (a) voltage-off state, and (b) voltage-on state. The PI has no rubbing treatment. PN: polymer network

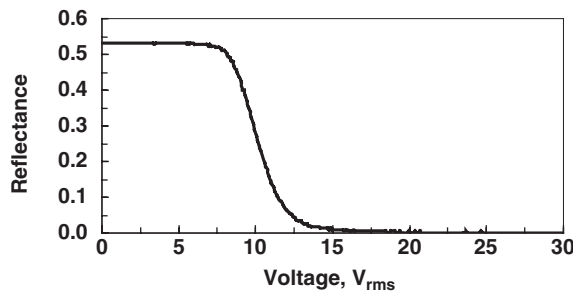
the display is polarization insensitive. Due to multiple scattering and absorption, a descent dark state can be obtained.

Figure 9.9 depicts the voltage-dependent reflectance of the dye-doped LC gel using a linearly polarized green diode laser ( $\lambda = 532 \text{ nm}$ ) instead of a white light source for characterizing the device performances because the guest–host system appears dark red rather than black. A dielectric mirror was placed behind the cell so that the laser beam passed through the cell twice. A large-area photodiode detector was placed at  $\sim 25 \text{ cm}$  (the normal distance for viewing a mobile display) behind the sample, which corresponds to  $\sim 2^\circ$  collection angle. The curve shown in Figure 9.9 is independent of the laser polarization. The maximum reflectance reaches  $\sim 52\%$  in the low-voltage regime and decreases gradually as  $V > V_{th}$  because the employed LC has a negative  $\Delta\epsilon$  and LC directors are homeotropically structured at  $V = 0$ . Because of the formed polymer networks, the threshold voltage is increased to  $\sim 7.5 \text{ V}_{\text{rms}}$ . At  $V = 20 \text{ V}_{\text{rms}}$ , the measured contrast ratio of the dye-doped negative LC gel exceeds  $\sim 200:1$ . In contrast, a typical guest–host LCD has a contrast ratio of about 5:1.

Response time is another important issue for guest–host displays. A typical response time for a guest–host display is around 50 ms because of the bulky dye molecules. Due to the polymer network, the response time of the dye-doped negative LC gel is rapid. The rise time is 1.0 ms and decay time is 4.5 ms when the applied voltage is switched between 0 and  $20 \text{ V}_{\text{rms}}$ . This dye-doped LC gel can also be configured in a polarizer-free transflective display using the dual cell gap approach.

#### 9.4.4 Reflection-type transflective LCDs

The cholesteric liquid crystal (CLC) layer exhibits a strong Bragg reflection with its reflection band centered at  $\lambda_o = nP_o$ , where  $n$  and  $P_o$  are the average refractive index and the cholesteric helix pitch, respectively. The reflection bandwidth  $\Delta\lambda_o = \Delta nP_o$  is proportional to the birefringence  $\Delta n$  of the CLC employed. Apparently, to cover the whole visible spectral range, a high-birefringence ( $\Delta n > 0.6$ ) CLC material is needed, assuming the pitch length is uniform [35]. Because the transmitted and reflected circular polarization states are orthogonal to each other, the CLC layer must rely on some additional elements to display a normal image without the reversed contrast ratio. By adopting an image-enhanced

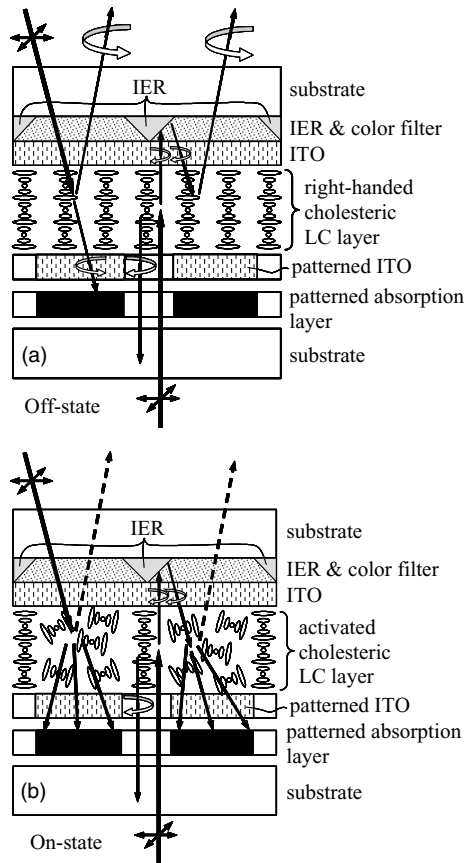


**Figure 9.9** Voltage-dependent reflectance of a dye-doped negative LC gel at  $f = 1 \text{ kHz}$ . Cell gap  $d = 5 \mu\text{m}$  and  $\lambda = 532 \text{ nm}$



reflector (IER) on the top substrate as well as a patterned ITO and a patterned absorption layer on the bottom substrate, the transflective cholesteric LCD can display an image without reversed contrast ratio, [36, 37] as shown in Figure 9.10(a) and (b). The opening areas of the patterned absorption layer on the bottom substrate match the IER on the top substrate. In addition, right above the patterned absorption layer and below the IER is the opening area of the patterned ITO layer. Therefore, the CLC molecules below the IER are not reoriented by the external electric filed.

In operation, when there is no voltage applied, the CLC layer exhibits a right-handed planar helix texture throughout the cell, as Figure 9.10(a) shows. In the R mode, when unpolarized ambient light enters the CLC cell, the left-handed circularly polarized light passes through the right-handed CLC layer and is absorbed by the patterned absorption layer. At the same time, the right-handed circularly polarized light is reflected by the same-sense CLC layer and the bright state results. In the T mode, when the unpolarized backlight enters the CLC layer, similarly, the right-handed circularly polarized light is reflected and it is either absorbed by the patterned absorption layer or recycled by the backlight unit. In the meantime, the left-handed circularly polarized light passes through the CLC layer and impinges onto the IER. Due to a  $\pi$  phase change upon reflection, it is converted to right-handed circularly polarized light, which is further reflected by the CLC layer to the reviewer. Consequently, a bright state occurs.



**Figure 9.10** Schematic configuration of reflection-type transflective cholesteric LCD and its operating principles at (a) off-state and (b) on-state

In the voltage-on state, the planar helix texture above the bottom-patterned ITO layer becomes a focal conic texture, while those LC molecules between the IER and the opening area of the bottom-patterned ITO layer are still unaffected, as shown in Figure 9.10(b). The focal conic texture, if the domain size is well controlled, exhibits a forward scattering for the incident light. In the R mode, the unpolarized incident ambient light is forward scattered by the focal conic textures. It is then absorbed by the patterned absorption layer, resulting in a dark state. In the T mode, the unpolarized light still experiences a right-handed planar helix texture before it reaches the IER on the top substrate. Thus, the right-handed polarized light is reflected back and it is either absorbed by the patterned absorption layer or recycled by the backlight unit. At the same time, the left-handed circularly polarized light passes through the planar texture and impinges onto the IER. Upon reflection, it turns into right-handed circularly polarized light. Then it is forward scattered by the focal conic texture and finally absorbed by the patterned absorption layer. As a result, a dark state is obtained.

In the above-mentioned transfective cholesteric LCD, no polarizer is employed. Therefore, its light efficiency is high. However, to produce the IER array on the top substrate increases the manufacturing complexity. In addition, the IER should be well aligned with the patterned absorption layer, otherwise light leakage will occur. More importantly, the forward scattering of the focal conic texture is incomplete. Some backward-scattered light causes a translucent dark state, which deteriorates the image contrast ratio. Therefore, the transfective cholesteric LCD is not yet popular for high-end LCD applications.

#### 9.4.5 Phase retardation type

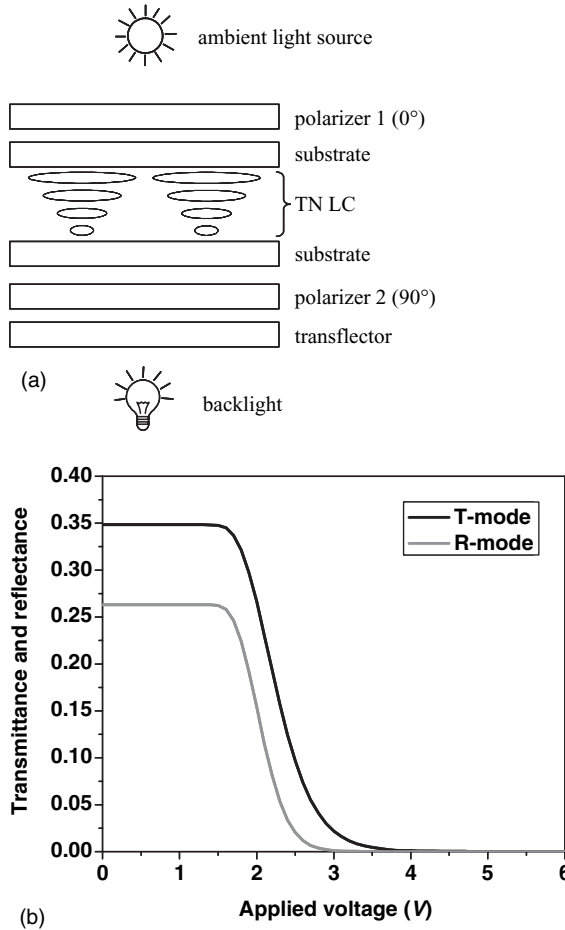
The operational principle of the phase retardation transfective LCDs, including homogeneous, VA, and TN cells, is based on the voltage-induced LC reorientation. Strictly speaking, the TN cells should belong to a polarization rotation effect. Since a transfective LCD consists of both T and R modes, two polarizers are usually required. Compared to the absorption, scattering, and reflection types, the phase retardation type of transfective LCDs has the advantages of higher contrast ratio, lower driving voltage, and better compatibility with the current volume manufacturing techniques. Therefore, the phase retardation type of transfective LCDs dominates in current commercial products, e.g., cellular phones and digital cameras.

In the following sections, we will describe the major transfective LCD approaches based on the phase retardation mechanism.

##### (1) Transfective TN and super-twisted nematic LCDs

The  $90^\circ$  TN cell can be used not only in transmissive and reflective LCDs [38], but also in transfective LCDs [39]. Figure 9.11(a) shows the device configuration of a transfective TN LCD. A  $90^\circ$  TN LC cell, which satisfies the Gooch–Tarry minima conditions [40], is sandwiched between two crossed polarizers. In addition, a translector is laminated on the outer side of the bottom polarizer and a backlight is intended for dark ambient conditions.

In the null voltage state, the LC directors exhibit a uniform twist throughout the cell from the lower substrate to the upper substrate. In the T mode, the incoming linearly polarized light which is generated by the bottom polarizer closely follows the twist profile of the LC molecules and continuously rotates  $90^\circ$  with respect to its original polarization state. This is known as the polarization rotation effect of the TN cell. Thus the linearly polarized light can pass through the top polarizer, resulting in a bright output known as a normal-white (NW) mode. In the R mode, the incoming linearly polarized light is rotated by  $90^\circ$  as it passes through the TN LC layer. It then penetrates the bottom polarizer and reaches the translector. A portion of the linearly polarized light is reflected back by the translector and passes through the bottom polarizer again. This linearly polarized light then follows the twisted LC molecules and its polarization axis is rotated by  $90^\circ$ , i.e., parallel to the transmission axis of the top polarizer. Accordingly, a bright state is achieved.



**Figure 9.11** Transfective TN LCDs: (a) schematic device configuration and (b) voltage-dependent transmittance and reflectance curves

In the voltage-on state, the bulk LC directors are reoriented substantially perpendicular to the substrate. The two boundary layers are orthogonal. The perpendicularly aligned bulk LC molecules do not modulate the polarization state of the incoming light. Meanwhile, these two orthogonal boundary layers compensate for each other. Consequently, the incoming linearly polarized light still keeps the same polarization state after it passes through the activated TN LC layer. In the T mode, the linearly polarized light which is generated by the bottom polarizer propagates all the way to the top polarizer without changing its polarization state. Therefore, it is blocked by the top polarizer, resulting in a dark state. In the R mode, the linearly polarized light produced by the top polarizer passes through the activated LC layer without changing its polarization state. Consequently, it is absorbed by the bottom polarizer and no light returns to the viewer's side. This is the dark state of the display.

To have a better understanding of the underlying operational principle and electro-optical (EO) performances, we carried out numerical simulations based on the extended Jones matrix method [41]. Hereafter, unless otherwise stated, we assume that (1) the LC material is MLC-6694-000 (from Merck); (2) the polarizer is a dichroic linear polarizer with complex refractive indices  $n_e = 1.5 + i \times 0.0022$  and  $n_o = 1.5 + i \times 0.000032$ ; (3) the transfecter does not depolarize the polarization state of the impinging

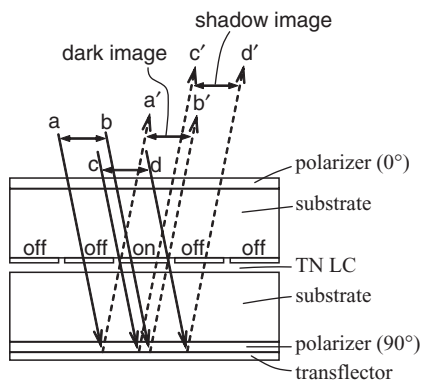
light upon reflection and transmission; (4) the transflector does not cause any light loss upon reflection and transmission; (5) the ambient light and backlight enter and exit from the panel in the normal direction; and (6) the light wavelength is  $\lambda = 550 \text{ nm}$ .

Figure 9.11(b) plots the voltage-dependent transmittance and reflectance curves of a typical transflective TN LCD. Here, twist angle  $\phi = 90^\circ$  and the first Gooch–Tarry minimum condition  $d\Delta n = 476 \text{ nm}$  is employed, where  $d$  is the cell gap and  $\Delta n$  is the LC birefringence. The gray scales of both the T and R modes overlap well with each other. This is because the reflection beam in the R mode experiences the bottom polarizer, LC layer, and the top polarizer successively in turn, as does the transmission beam in the T mode.

Compared to the conventional transmissive TN LCD, the above transflective TN LCD only requires one additional transflector between the bottom polarizer and the TN LC layer. Naturally, this transflective LCD device configuration can also be extended to a super-twisted nematic (STN) transflective LCD [42]. Different from the so-called polarization rotation effect in TN LCD, the STN LCD utilizes the birefringence effect of the STN LC layer [43]. Therefore, a larger twist angle ( $180^\circ$ – $270^\circ$ ), a thicker LC cell gap, and a different polarizer/analyzer configuration are required.

The above-mentioned TN and STN types of transflective LCDs have advantages in simple device structures and matched gray scales; however, their major drawbacks are in parallax and low reflectance.

Parallax is a deteriorated shadow image phenomenon in the oblique view of a reflective LCD [44]. Similarly, it also occurs in some transflective LCDs, such as the transflective TN and STN LCDs described above. Figure 9.12 demonstrates the cause of parallax in the R mode of a transflective TN LCD when the polarizer and transflector are laminated on the outer side of the bottom substrate. The switched-on pixel does not change the polarization state of the incident light because the LC molecules are reoriented perpendicular to the substrate. From the observer's side, when a pixel is switched on it appears dark, as designated by  $a'b'$  in the figure. The dark image  $a'b'$ , generated by the top polarizer, actually comes from the incident beam  $ab$ . Meanwhile, another incident beam  $cd$  passes through the activated pixel and does not change its linear polarization state as well. Therefore, it is absorbed by the bottom polarizer, resulting in no light reflection. Accordingly, a shadow image  $c'd'$  occurs from the observer's viewpoint. Different from the dark image  $a'b'$ , which is generated by the top polarizer, the shadow image  $c'd'$  is actually caused by the bottom polarizer. This is why the shadow image  $c'd'$  seems to appear under the dark image  $a'b'$ . Because the bottom polarizer and transflector are laminated outside the bottom substrate, the ambient light must traverse the bottom substrate before it is reflected back. Due to the thick bottom substrate, the reflection image beams  $a'b'$  and  $c'd'$  are shifted away from the pixel area that the incoming beams  $ab$  and  $cd$  propagate in, resulting in a shadow image phenomenon called parallax. Such a parallax



**Figure 9.12** Schematic view of the cause of parallax in the R mode of a transflective LCD with the polarizer and transflector laminated outside the bottom substrate

problem becomes more serious with the decrease of pixel size. Therefore, transflective TN and STN LCDs with these structures are not suitable for high-resolution full-color transflective LCD devices.

To overcome the parallax problem in transflective TN and STN LCDs, the bottom polarizer and translector must be located inside the LC cell. A burgeoning in-cell polarizer technology based on thin crystal film growth from aqueous lyotropic LC of supramolecules has attracted some attention in the transflective LCD industry [45]. By depositing both translector and polarizer inside the cell, the above-mentioned annoying parallax problem can be significantly reduced.

Nevertheless, transflective TN and STN LCDs still have another shortcoming, which is low reflectance in the R mode. As shown in Figure 9.11(b), although the gray scales of both modes overlap reasonably well with each other, the reflectance in the R mode is much lower than the transmittance in the T mode. This is because the light accumulatively passes through polarizers four times in the R mode but only twice in the T mode. Due to the absorption of polarizers, the light in the R mode suffers much more loss than that in the T mode. Accordingly, the reflectance of the R mode is reduced substantially.

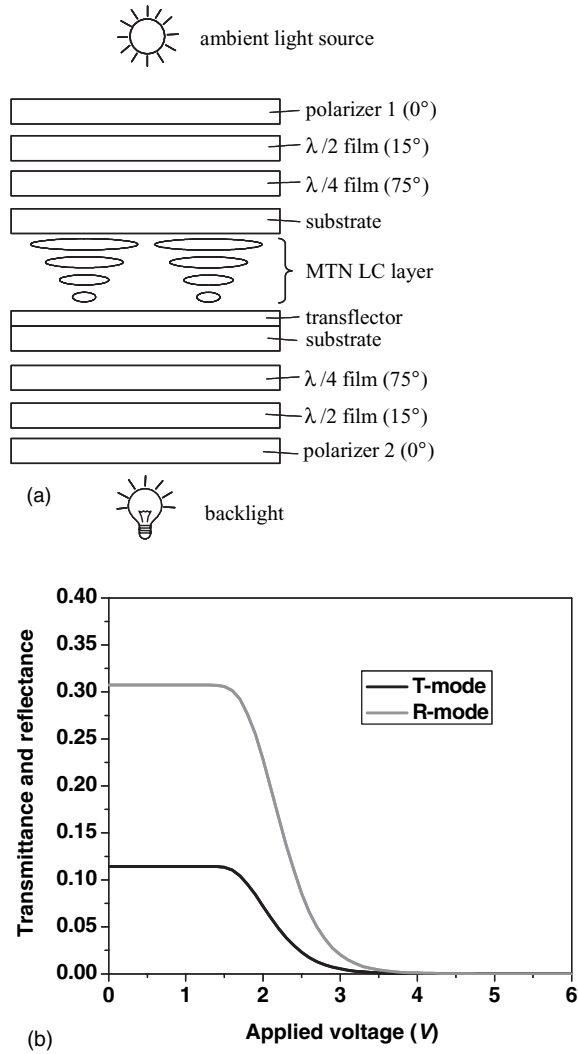
## (2) Transflective MTN LCDs

To overcome the parallax and low-reflectance problems of transflective TN and STN LCDs, the bottom polarizer for the R mode should be removed to the outer surface of the bottom substrate. Thus, the translector can be implemented on the inner side of the LC cell, acting as an internal translector. Under such a device configuration, the R mode operates as a single polarizer reflective LCD. More importantly, both ambient light and backlight pass through the polarizer twice; therefore, both T and R modes experience the same light absorption. Nevertheless, the conventional TN LC cell does not work well in the single polarizer reflective LCD. This is because, after the light travels a round trip in the LC layer, the light polarization state in the voltage-on state is identical to that in the voltage-off state.

By reducing the  $d\Delta n$  value of the TN LC layer to around one-half of that required in a conventional transmissive TN LCD, the MTN mode overcomes the problem mentioned above [46]. Unlike the TN LCD, the twist angle of the MTN mode can vary from  $0^\circ$  to  $90^\circ$  and its operating mechanism is based on the proper mixing of the polarization rotation and birefringence effects. Molsen and Tillin of Sharp Corp. incorporated the MTN mode into their transflective LCD design [47], as shown in Figure 9.13(a). Compared to the transflective TN LCD shown in Figure 9.11(a), this transflective MTN LCD exhibits two different features. First, the translector is located inside the LC cell; thus no parallax problem occurs. Secondly, a half-wave film and a quarter-wave film are inserted on each side of the MTN LC cell. These two films together with the adjacent linear polarizer function as a broadband circular polarizer over the whole visible spectral range [48]. Thereby, a good dark state can be guaranteed over the whole visible range for the R mode.

In the voltage-off state, the MTN LC layer is equivalent to a quarter-wave film. In the R mode, the incident unpolarized ambient light is converted into linearly polarized light after passing through the top polarizer. After penetrating the top two films and the MTN LC layer, the linearly polarized light still keeps its linear polarization except it has been rotated  $90^\circ$  from the original polarization direction. Upon reflection from the translector, it experiences the MTN LC layer and the top two films once again. Hence its polarization state is restored back to the original one, resulting in a bright output from the top polarizer. In the T mode, the unpolarized backlight turns into linearly polarized light after passing through the bottom polarizer. After it has passed through the bottom two films, penetrated the translector, and continued to traverse the MTN LC layer and the top two films, it becomes circularly polarized light. Finally, a partial transmittance is achieved from the top polarizer.

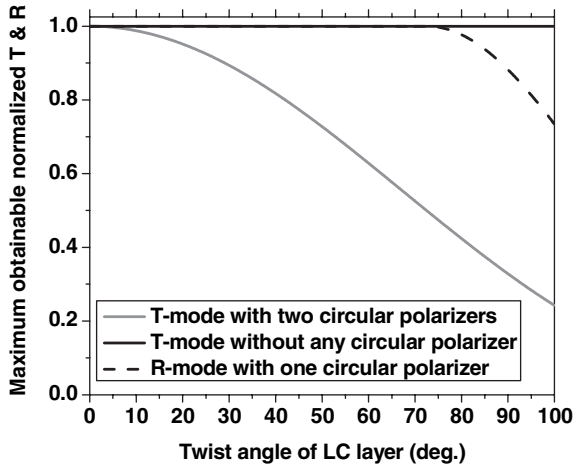
In the voltage-on state, the bulk LC directors are almost fully tilted up and the two unaffected boundary layers compensate each other in phase. Therefore, the LC layer does not affect the polarization state of the incident light. In the R mode, the linearly polarized light generated by the top polarizer turns into orthogonal linearly polarized light after a round trip in the top two films and the activated LC layer. Accordingly, this orthogonal linearly polarized light is blocked by the top polarizer, leading to a dark



**Figure 9.13** (a) Schematic device configuration and (b) voltage-dependent transmittance and reflectance curves of a transfective MTN LCD

state. In the T mode, the linearly polarized light, caused by the bottom polarizer, passes through the bottom two films, penetrates the transfective, then continues to pass through the activated LC layer and the top two films. Before it reaches the top polarizer, its linear polarization state is rotated by 90°, which is perpendicular to the transmission axis of the top polarizer, and the dark state results.

As an example, Figure 9.13(b) depicts the voltage-dependent transmittance and reflectance curves of a transfective MTN LCD with  $\phi = 90^\circ$  and  $d\Delta n = 240$  nm. Here both T and R modes operate in a NW mode. Generally speaking, for TN- or MTN-based LCDs, the NW display is preferred to as the normal-black (NB) state because the dark state of the NW mode is controlled by the on-state voltage. Thus, the dark state of the NW mode is insensitive to cell gap variation. A large cell gap tolerance is highly desirable for improving manufacturing yield.

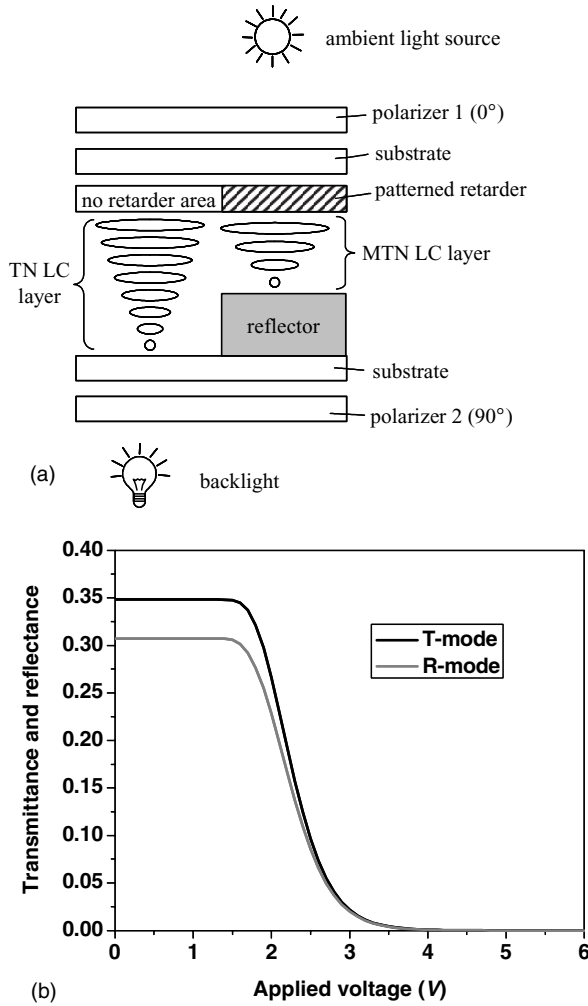


**Figure 9.14** The maximum obtainable normalized reflectance and transmittance in the transfective MTN LCD and the transfective TN LCD as a function of twist angle

By comparing Figure 9.13(b) to Figure 9.11(b), we can see two distinctions between the transfective MTN LCD and the transfective TN LCD. First, without the absorption from the bottom polarizer, the reflectance of the transfective MTN LCD is higher than that of the transfective TN LCD. Secondly, the transmittance of the transfective MTN LCD is much lower than that of the transfective TN LCD. This is because the maximum obtainable normalized transmittance is always less than 100% for a transmissive TN cell sandwiched between two circular polarizers [49]. Figure 9.14 shows the maximum obtainable normalized reflectance and transmittance in optimized transfective MTN and TN LCDs as a function of twist angle. Here, the normalized reflectance and transmittance represent the modulation efficiency of the polarization state; the light losses caused by the polarizers and reflector are all neglected. Due to the effect of the circular polarizer on both sides of the MTN cell, as long as the twist angle is larger than  $0^\circ$ , the maximum obtainable normalized transmittance gradually decreases in spite of the  $d\Delta n$  value of the MTN LC layer, as represented by the solid gray line in Figure 9.14. For instance, in the  $90^\circ$  MTN cell with a circular polarizer on both sides, the maximum obtainable normalized transmittance is  $\sim 33\%$ . On the other hand, the dark dashed line shows that the maximum obtainable normalized reflectance holds steadily at 100% until the twist angle reaches beyond  $73^\circ$ . In short, although the transfective MTN LCD overcomes the parallax problem, its maximum obtainable transmittance in the T mode is too low. A low transmittance demands a brighter backlight which, in turn, will consume more battery power and reduce its lifetime.

### (3) Patterned-retarder transfective LCDs

If we can remove both circular polarizers in the T mode, the maximum transmittance can be boosted to 100% for any twist angle from  $0^\circ$  to  $100^\circ$ , as designated by the solid dark line shown in Figure 9.14. Without the circular polarizers, the T mode operates in the same way as a conventional transmissive TN LCD. Philips Research Group proposed a dual-cell-gap transfective MTN/TN LCD using patterned phase retarders. Figure 9.15(a) shows the schematic device structure. Each pixel is divided into a transmission region and a reflective region by a derivative openings-on-metal type of translector. A patterned broadband phase retarder is deposited on the inner side of the top substrate. More specifically, the patterned phase retarder is located right above the reflection region, while no phase retarder exists above the transmission region. In addition, the cell gap in the transmission region is around twice that of the reflection region and the LC layer twists  $90^\circ$  in both regions. The patterned phase retarder actually



**Figure 9.15** (a) Schematic device configuration and (b) voltage-dependent transmittance and reflectance curves of the patterned-retarder transfective MTN/TN LCD

consists of a half-wave film and a quarter-wave film fabricated by wet coating techniques [50]. In the transmissive region, the cell is identical to the traditional transmissive TN LCD, while in the reflective region, it is a MTN mode. Figure 9.15(b) shows the voltage-dependent transmittance and reflectance curves with  $d\Delta n = 476 \text{ nm}$  in the transmission region and  $d\Delta n = 240 \text{ nm}$  in the reflective region. From the figure, both T and R modes have a very good gray-scale overlapping. Since the maximum normalized reflectance of the  $90^\circ$  MTN mode is around 88%, the reflectance is slightly lower than the transmittance.

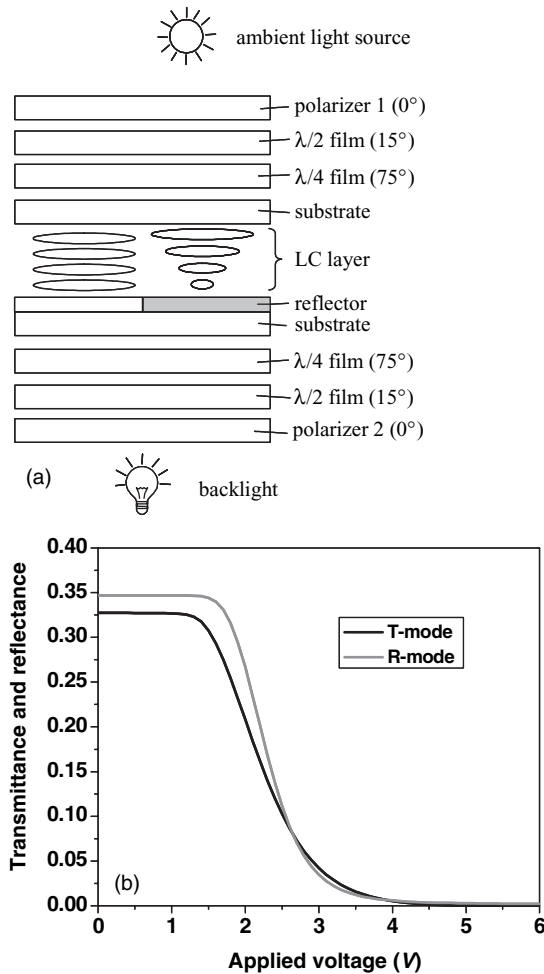
The patterned-retarder transfective MTN/TN LCD has advantages in the matched gray scale, high contrast ratio, and low color dispersion. However, under oblique incident angles, the ambient light might not pass through the patterned retarder; similarly, the backlight might pass through the patterned retarder. Thus, a deteriorated image may arise when viewed from an oblique angle. In addition, to fabricate such small-scale patterned phase retarders on a glass substrate and align them well with the transmission/reflection pixels is a challenging task.



(4) Transflective mixed-mode LCDs

To compensate for the intrinsic optical path differences between the transmission and reflection regions, Sharp Corp. proposed an approach to generate different director configurations simultaneously in both regions [51]. The different director configurations can be realized by such things as applying different alignment treatments, exerting different driving voltages, generating different electric fields, producing different cell gaps in both regions, and so on. Thus, the transmission region may, in principle, operate in a different LC mode from the reflection region, which leads to the name of transflective mixed-mode LCDs.

If two circular polarizers are indispensable in both sides of the cell, one solution to maximize the normalized transmittance is to decrease the LC twist angle to  $0^\circ$  in the transmission region while still maintaining a twist profile in the reflection region. Thus the transmission region can operate in electrically controlled birefringence (ECB) mode while the reflection region still runs in MTN mode. Figure 9.16(a) shows the device configuration of a transflective MTN/ECB LCD using the openings-on-



**Figure 9.16** (a) Schematic device configuration and (b) voltage-dependent transmittance and reflectance curves of a dual-rubbing transflective MTN/ECB LCD

metal translector [52]. The top substrate is uniformly rubbed while the bottom substrate has two rubbing directions: in the reflective region the LC layer twists  $75^\circ$ , and in the transmission region the LC layer has zero twist, i.e., homogenous alignment. Therefore, the reflective region works in the  $75^\circ$  MTN mode while the transmission region operates in the ECB mode. Coincidentally, their  $d\Delta n$  requirements are very close to each other; therefore, a single cell gap device configuration is adopted in both regions. Figure 9.16(b) plots the voltage-dependent transmittance and reflectance curves with  $d\Delta n = 278$  nm in both regions. Both T and R modes in the transfective MTN/ECB LCD almost simultaneously reach their maximum light efficiency through such a dual-rubbing process. Still, one might notice that the T mode has a slightly lower light efficiency than the R mode. This is because the  $d\Delta n$  requirement for both T and R modes is slightly different and a compromise is reached to optimize the R mode.

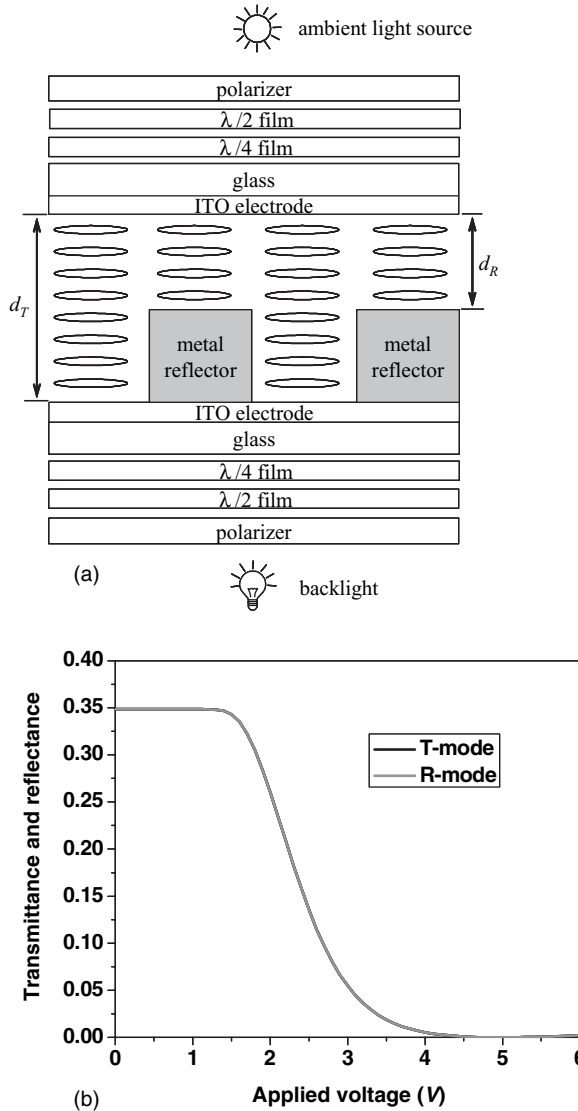
Besides the above-demonstrated dual-rubbing transfective MTN/ECB LCD, other similar dual-rubbing transfective mixed-mode LCDs are possible, such as the dual-rubbing transfective VA/HAN LCD [53] and the dual-rubbing transfective ECB/HAN LCD [54]. The common characteristic of these dual-rubbing transfective LCDs is that different rubbing directions or different alignment layers are required on at least one of the substrates. This leads to two obstacles for widespread applications. First of all, the dual-rubbing requirement induces a complicated manufacturing process and hence an increased cost. More seriously, the dual rubbing usually introduces a disclination line on the border of different rubbing regions, which lowers the image brightness and deteriorates the contrast ratio as well.

To avoid the dual-rubbing process while still maintaining a single cell gap device configuration, an alternative way to achieve different director configurations in both regions is to introduce different electric field intensities in both regions. For example, the transfective VA LCD utilizes periodically patterned electrodes to generate different LC tilt angle profiles in both regions [55]. Nevertheless, the metal reflector there is insulated from its surrounding ITO electrodes, which increases the manufacturing complexity. On the other hand, the patterned reflector is either connected to the common electrode or electrically floated, which results in either a dead zone in the reflection region or charge stability uncertainties. Another example is the transfective IPS LCD, which uses the different twist angle profiles along the horizontal direction of interdigitated electrodes for both transmission and reflection regions [56]. In this design, the in-cell retarder is used between the translector and LC layer. When there is no voltage applied, the LC layer is homogeneously aligned. The LC cell together with the in-cell retarder acts as a broadband quarter-wave film. Such a design has two shortcomings. First, unlike the conventional transmissive IPS LCD, the dark state here is very sensitive to the LC layer thickness. Secondly, the in-cell retarder is difficult to fabricate inside the cell.

## 9.5 Dual-cell-gap Transfective LCDs

Unless identical display modes are adopted in both T and R modes, there will always be some discrepancies between their voltage-dependent transmittance and reflectance curves. This is the reason that none of the above-mentioned transfective mixed-mode LCDs has perfectly matched voltage-dependent transmittance and reflectance curves. Different from the mixed display modes employed between transmission and reflection regions as described above, Sharp Corp. also introduced the dual-cell-gap concept for transfective LCDs [57].

Figure 9.17(a) shows the schematic device configuration of a dual-cell-gap transfective ECB LCD. Similar to the case of the dual-rubbing transfective MTN/ECB LCD, this dual-cell-gap transfective ECB LCD also uses a circular polarizer on both sides of the cell. The role of the circular polarizer is to make the display operate in a NW mode so that its dark state is not too sensitive to cell gap variation. Each pixel is divided into a transmission region with cell gap  $d_T$  and a reflection region with cell gap  $d_R$ . The LC directors are all homogeneously aligned within the cell; therefore, no dual-rubbing process is necessary and both regions operate identically in the ECB mode. Since the homogeneously aligned LC layer only imposes pure phase retardation on the incident polarized light,  $d_R$  is set to be around half of  $d_T$



**Figure 9.17** (a) Schematic device configuration and (b) voltage-dependent transmittance and reflectance curves of the dual-cell-gap transfective ECB LCD

to compensate for the optical path difference between ambient light and backlight. Figure 9.17(b) depicts the voltage-dependent transmittance and reflectance curves with  $d_R \Delta n = 168 \text{ nm}$  and  $d_T \Delta n = 336 \text{ nm}$ . As expected, both curves perfectly match each other and both modes reach the highest transmittance and reflectance simultaneously. Here  $d_R \Delta n$  and  $d_T \Delta n$  are designed to be slightly larger than  $\lambda/4$  and  $\lambda/2$ , respectively, in order to reduce the on-state voltage.

The downside of the dual-cell-gap approach is three-fold. First, due to the cell gap difference, the LC alignment is distorted near the boundaries of the transmissive and reflective pixels. This area should be

covered by black matrices in order to retain a good contrast ratio. Secondly, the thicker cell gap in the transmission region results in a slower response time than the reflective region. Fortunately, the dynamic response requirement in mobile applications is not as strict as those for video applications. This response time difference, although not perfect, is still tolerable. Thirdly, the view angle of the T mode is rather narrow because the LC directors are tilted up along one direction by the external electric field. By substituting the quarter-wave film with a biaxial film on each side of the cell, the viewing angle can be greatly improved [58]. Because the manufacturing process is compatible with the state-of-the-art LCD fabrication lines, the dual-cell-gap transfective ECB LCD is so far the mainstream approach for commercial transfective LCD products.

Besides the above dual-cell-gap transfective ECB LCD, others dual-cell-gap transfective LCDs are also proposed, such as the dual-cell-gap transfective VA LCD [59], dual-cell-gap transfective HAN LCD [60], and dual-cell-gap transfective FFS (Fringe-Field Switching) LCD [61, 62]. Similar to the dual-cell-gap transfective ECB LCD, both the dual-cell-gap transfective VA LCD and dual-cell-gap transfective HAN LCD also operate in ECB mode, although the initial LC alignment is different. On the other hand, in the dual-cell-gap transfective FFS LCD, LC molecules are switched in the plane parallel to the supporting substrates. Its dark state is achieved by a half-wave film and the initially homogeneously aligned LC layer. Consequently, the dark state is very sensitive to LC cell gap variation, which causes difficulties with maintaining a good dark state in both transmission and reflection regions due to the dual-cell-gap device configuration.

## 9.6 Single-cell-gap Transfective LCDs

Different from the dual-cell-gap transfective LCD, the single-cell-gap transfective LCD renders a uniform cell gap profile throughout the cell. Therefore, the dynamic responses of both T and R modes are close to each other. For instance, a single-cell-gap transfective LCD using an internal wire-grid polarizer has been proposed [63]. For the reflective mode, the imbedded wire grid polarizer serves as a polarization-dependent reflector for the ambient light. While for the transmissive mode, no achromatic quarter wave film is needed. This device can work as a normal-black mode by using a vertical-aligned cell or a normal-white mode by using a twisted-nematic cell. This device concept is fairly simple and has several outstanding performance characteristics. However, to implement the wire-grid polarizer in the inner surface of the bottom LC substrate could be a challenging task.

As a matter of fact, several transfective LCDs described in the above sections also belong to this single-cell-gap category, such as transfective TN and STN LCDs, transfective MTN LCDs, dual-rubbing transfective MTN/ECB LCDs, dual-rubbing transfective VA/HAN LCDs, dual-rubbing transfective ECB/HAN LCDs, transfective VA LCDs utilizing periodically patterned electrodes, and transfective IPS LCDs. Due to the fact that the ambient light travels twice while the backlight propagates only once in the LC layer, the light efficiency of both T and R modes cannot reach the maxima simultaneously unless mixed display modes are employed. This leads to the transfective mixed-mode LCDs as described in Figure 9.16. As discussed there, the transfective mixed-mode LCDs require either a dual-rubbing process or complicated electrode designs. Consequently such single-cell-gap transfective mixed-mode LCDs have not yet been commercialized.

## 9.7 Performance of Transfective LCDs

We have just described the basic operating principles of some main transfective LCDs. The simulation results are based on some ideal assumptions. It is understandable that many other factors can affect the display image qualities, such as color balance, image brightness, and viewing angle.

### 9.7.1 Color balance

Because the reflection beam passes through the color filter (CF) twice while the transmission beam only passes through once, generally speaking, the transflective LCD experiences unbalanced color between the T and R modes. To solve the color imbalance problem, different CF approaches have been developed. Sharp Corp. proposed a multi-thickness color filter (MT-CF) design for the transflective LCDs [64]. In this design, the CF thickness in the reflection region is around one-half of that in the transmission region. Because the ambient beam passes through the thinner CF twice, while the transmission beam passes through the thicker CF once, as a result these two beams experience almost the same spectral absorption. Therefore, such a CF thickness difference ensures almost identical color saturation between the transmission and reflection regions, resulting in a good color balance between T and R modes.

In addition to the MT-CF design, a pinhole-type CF design was also proposed by Sharp, in which the thicknesses of the CF in both regions are equal, but the CF in the reflection region is punched with some pinholes. Therefore, a portion of the ambient light does not 'see' the CF; instead, it passes through the pinholes directly. The problem of such a pinhole-type CF is its narrow color reproduction area because the ambient light spectrum is mixed with the RGB primary colors, which causes the color impurity.

An alternative approach to obtain the same color balance between the T and R modes is to fill the CF with some scattering materials in the reflection region [65]. The filled scattering materials serve two purposes. First, the equivalent CF thickness in the reflection region is decreased to around one-half of that in the transmission region. Secondly, the scattering materials can steer the reflection beam away from the specular reflection direction; therefore, a pure flat metal reflector can be used in the reflection region, which greatly simplifies the manufacturing process.

### 9.7.2 Image brightness

Image brightness is a very important feature for transflective LCDs. However, many factors decrease the overall image brightness. For instance, the red, green, and blue color filters have different light attenuation, which affects the overall brightness of the display panel. Furthermore, the reflection region of the openings-on-metal transflector, usually made from aluminum, has  $\sim 92\%$  reflectivity over the visible spectral region [66], which leads to a slightly lower light efficiency in the R mode.

In the case of the openings-on-metal transflector, the transflector area is intended for either the reflection or transmission region. To increase the backlight utilization efficiency while still keeping the ambient light efficiency unchanged, a transflective LCD design using a microtube array below the transmission pixels region has been proposed [67]. The microtube structure, which is similar to a funnel in shape, allows most of the backlight to enter from a larger lower aperture and to exit from a smaller upper aperture. Consequently, the backlight utilization efficiency can be greatly enhanced, provided that the transmission/reflection area ratio still remains unchanged. After optimization, the average backlight utilization efficiency is improved by  $\sim 81\%$ .

### 9.7.3 Viewing angle

Although the display panel size for most transflective LCDs is not too large, viewing angle is another important concern. The user of a cell phone would like to see clear images from every angle. The future cell phone will have expanded functions, such as videos and movies. The dual-cell-gap transflective ECB LCD has a relatively narrow viewing angle in the T mode, but by substituting the quarter-wave film with a biaxial film on each side of the cell, the viewing angle of the T mode can be greatly widened. In the R mode, surface reflection is the main factor deteriorating the image contrast ratio and viewing angle. To solve this problem, a bumpy reflector in the reflection region is commonly employed. The bumpy reflector serves two purposes: (1) to diffuse the reflected light which is critical for widening viewing

angle; and (2) to steer the reflected light away from the specular reflection so that the images are not overlapped with the surface reflections. To design bumpy reflectors [68], one needs to consider the fact that the incident beam and reflected beam might form different angles with respect to the panel normal. In optical modeling of the R mode, the asymmetric incident and exit angle features should be taken into consideration [69].

## Homework Problems

- 9.1 Let us design a normal-black reflective LCD using a  $45^\circ$  twisted nematic cell for projection displays. We want the display to be independent of beta angle ( $\beta$ ), the angle between the top LC rubbing direction and the incoming polarization axis. What is the required  $d\Delta n$  value at  $\lambda = 550$  nm?
- 9.2 In a transfective LCD, the reflective part usually has a lower contrast ratio and narrower viewing angle than the transmissive part. Why?
- 9.3 In most transfective LCDs, the reflective part usually has a broadband quarter-wave film. Explain why.
- 9.4 Sketch the device configuration of a transfective LCD using a double-cell-gap VA cell. The LC parameters are:  $\Delta n = 0.1$  ( $\lambda = 550$  nm),  $\Delta\epsilon = -4$ ,  $K_{11} = 10$  pN,  $K_{22} = 6$  pN,  $K_{33} = 20$  pN, and  $\gamma_1 = 0.1$  Pa s. (1) What are the cell gaps for the R and T regions? (2) Estimate the optical decay time. (3) Sketch the expected voltage-dependent transmittance and reflectance curves.
- 9.5 Sketch the device configuration of a transfective LCD using a double-cell-gap TN cell. The LC parameters are:  $\Delta n = 1.0$  ( $\lambda = 550$  nm),  $\Delta\epsilon = 10$ ,  $K_{11} = 10$  pN,  $K_{22} = 6$  pN,  $K_{33} = 20$  pN, and  $\gamma_1 = 0.1$  Pa s. (1) What are the cell gaps for the R and T regions? (2) Estimate the optical decay time. (3) Sketch the expected voltage-dependent transmittance and reflectance curves.
- 9.6 Given two linear sheet polarizers, a vertical aligned cell filled with a negative  $\Delta\epsilon$  LC, a wire grid polarizer (WGP), and a backlight, construct a normal-black transfective LCD. Assume the WGP can be deposited at any portion of the pixel. (1) Sketch the display configuration and show how it works. (2) Sketch the voltage-on state LC configuration and find the required  $d\Delta n$  value for achieving maximum reflectance.
- 9.7 Given two linear sheet polarizers, a  $90^\circ$  TN cell, a wire grid polarizer (WGP), and a backlight, construct a normal-white transfective LCD. Assume the WGP can be deposited at any portion of the pixel. (1) Sketch the display configuration and show how it works. (2) Sketch the voltage-off state LC configuration and find the required  $d\Delta n$  value for achieving maximum reflectance and transmittance.

## References

- 1 M. Schadt and W. Helfrich, 'Voltage-dependent optical activity of a twisted nematic liquid crystal', *Appl. Phys. Lett.*, **18**, 127 (1971).
- 2 M. Oh-e and K. Kondo, 'Electro-optical characteristics and switching behavior of the in-plane switching mode', *Appl. Phys. Lett.*, **67**, 3895 (1995).
- 3 K. Ohmuro, S. Kataoka, T. Sasaki, and Y. Koike, 'Development of super-high-image-quality vertical alignment mode LCD', *SID Tech. Dig.*, **28**, 845 (1997).
- 4 A. R. Kmetz, 'A single-polarizer twisted nematic display', *Proc. SID*, **21**, 63 (1980).
- 5 X. Zhu, Z. Ge, T. X. Wu, and S. T. Wu, 'Transflective liquid crystal displays', *J. Disp. Technol.*, **1**, 15 (2005).
- 6 E. H. Stupp and M. S. Brennesholtz, *Projection Displays* (John Wiley & Sons, Inc., New York, 1998).
- 7 S.-T. Wu and D.-K. Yang, *Reflective Liquid Crystal Displays* (John Wiley & Sons, Ltd, Chichester, 2001).
- 8 S. T. Wu and C. S. Wu, 'Optimization of film-compensated homogeneous cells for liquid crystal displays', *Liq. Cryst.*, **24**, 811 (1998).

- 9 C. L. Kuo, C. K. Wei, S. T. Wu, and C. S. Wu, 'Reflective display using mixed-mode twisted nematic liquid crystal cell', *Jpn. J. Appl. Phys.*, **36**, 1077 (1997).
- 10 S. T. Wu and C. S. Wu, 'Comparative studies of single-polarizer reflective liquid crystal displays', *J. SID*, **7**, 119 (1999).
- 11 T. H. Yoon, G. D. Lee, G. H. Kim, S. C. Kim, W. S. Park, J. C. Kim, and S. H. Lee, 'Reflective liquid crystal display using  $0^\circ$ -twisted half-wave cell', *SID Tech. Dig.*, **31**, 750 (2000).
- 12 S. T. Wu and C. S. Wu, 'Mixed twisted-nematic mode for reflective liquid crystal displays', *Appl. Phys. Lett.*, **68**, 1455 (1996).
- 13 R. D. Ketchpel and S. Barbara, 'Transflector', US patent 4,040,727 (Aug. 9, 1977).
- 14 H. C. Borden, Jr., 'Universal transmission reflectance mode liquid crystal display', US patent 3,748,018 (July 24, 1973).
- 15 J. E. Bigelow, 'Transflective liquid crystal display', US patent 4,093,356 (June 6, 1978).
- 16 H. Furuhashi, C. K. Wei, and C. W. Wu, 'Transflective liquid crystal display having dielectric multilayer in LCD cells', US patent 6,806,934 (Oct. 19, 2004).
- 17 D. R. Hall, 'Transflective LCD utilizing chiral liquid crystal filter/mirrors', US patent 5,841,494 (Nov. 24, 1998).
- 18 W. J. Schrenk, V. S. Chang, and J. A. Wheatley, 'Birefringent interference polarizer', US patent 5,612,820 (Mar. 18, 1997).
- 19 D. P. Hansen and J. E. Gunther, 'Dual mode reflective/transmissive liquid crystal display apparatus', US patent 5,986,730 (Nov. 16, 1999).
- 20 P. G. de Gennes and J. Prost, *The Physics of Liquid Crystals*, 2nd edn (Oxford University Press, New York, 1993).
- 21 J. Ouderkirk, S. Cobb, Jr., B. D. Cull, M. F. Weber, and D. L. Wortman, 'Transflective displays with reflective polarizing transflector', US patent 6,124,971 (Sept. 26, 2000).
- 22 M. Bass, E. W. Van Stryland, D. R. Williams, and W. L. Wolfe, *Handbook of Optics, Vol. II, Devices, Measurements, & Properties*, 2nd edn, 3.32–3.35 (McGraw-Hill, New York, 1995).
- 23 S. T. Wu, U. Efron, and L. D. Hess, 'Birefringence measurements of liquid crystals', *Appl. Opt.*, **23**, 3911 (1984).
- 24 R. T. Perkins, D. P. Hansen, E. W. Gardner, J. M. Thorne, and A. A. Robbins, 'Broadband wire grid polarizer for the visible spectrum', US patent 6,122,103 (Sept. 19, 2000).
- 25 X. J. Yu and H. S. Kwok, 'Optical wire-grid polarizers at oblique angles of incidence', *J. Appl. Phys.*, **93**, 4407 (2003).
- 26 G. H. Heilmeyer and L. A. Zanoni, 'Guest-host interactions in nematic liquid crystals. A new electro-optic effect', *Appl. Phys. Lett.*, **13**, 91 (1968).
- 27 D. L. White and G. N. Taylor, 'New absorptive mode reflective liquid-crystal display device', *J. Appl. Phys.*, **45**, 4718 (1974).
- 28 H. S. Cole, 'Transflective liquid crystal display', US patent 4,398,805 (Aug. 16, 1983).
- 29 S. Morozumi, K. Oguchi, R. Araki, T. Sonehara, and S. Aruga, 'Full-color TFT-LCD with phase-change guest-host mode', *SID Tech. Dig.*, **16**, 278 (1985).
- 30 J. W. Done, N. A. Vaz, B.-G. Wu, and S. Zumer, 'Field controlled light scattering from nematic microdroplets', *Appl. Phys. Lett.*, **48**, 269 (1986).
- 31 D. K. Yang, J. W. Doane, Z. Yaniv, and J. Glasser, 'Cholesteric reflective display: drive scheme and contrast', *Appl. Phys. Lett.*, **64**, 1905 (1994).
- 32 R. A. M. Hikmet, 'Electrically induced light scattering from anisotropic gels', *J. Appl. Phys.*, **68**, 4406 (1990).
- 33 H. Ren and S.-T. Wu, 'Anisotropic liquid crystal gels for switchable polarizers and displays', *Appl. Phys. Lett.*, **81**, 1432 (2002).
- 34 Y. H. Lin, H. Ren, S. Gauza, Y. H. Wu, X. Liang, and S. T. Wu, 'Reflective direct-view displays using dye-doped dual-frequency liquid crystal gel', *J. Disp. Technol.*, **1**, 230 (2005).
- 35 Q. Hong, T. X. Wu, and S. T. Wu, 'Optical wave propagation in a cholesteric liquid crystal using the finite element method', *Liq. Cryst.*, **30**, 367 (2003).
- 36 Y. P. Huang, X. Zhu, H. Ren, Q. Hong, T. X. Wu, S. T. Wu, S. H. Lin, and H. P. Shieh, 'Full-color transflective Ch-LCD with image-enhanced reflector', *SID Tech. Dig.*, **35**, 882 (2004).

- 37 Y. P. Huang, X. Zhu, H. Ren, Q. Hong, T. X. Wu, S. T. Wu, M. Z. Su, M. X. Chan, S. H. Lin, and H.-P. Shieh, 'Full-color transfective cholesteric LCD with image-enhanced reflector', *J. SID*, **12**, 417 (2004).
- 38 F. J. Kahn, 'Reflective mode, 40-character, alphanumeric twisted-nematic liquid crystal displays', *SID Tech. Dig.*, **9**, 74 (1978).
- 39 W. H. McKnight, L. B. Stotts, and M. A. Monahan, 'Transmissive and reflective liquid crystal display', US patent 4,315,258 (Feb. 9, 1982).
- 40 C. H. Gooch and H. A. Tarry, 'The optical properties of twisted nematic liquid crystal structures with twist angles  $\leq 90$  degrees', *J. Phys. D: Appl. Phys.*, **8**, 1575 (1975).
- 41 A. Lien, 'Extended Jones matrix representation for the twisted nematic liquid-crystal display at oblique incidence', *Appl. Phys. Lett.*, **57**, 2767 (1990).
- 42 K. Kawasaki, K. Yamada, R. Watanabe, and K. Mizunoya, 'High-display performance black and white supertwisted nematic LCD', *SID Tech. Dig.*, **18**, 391 (1987).
- 43 T. J. Scheffer and J. Nehring, 'A new, highly multiplexable liquid crystal display', *Appl. Phys. Lett.*, **45**, 1021 (1984).
- 44 T. Maeda, T. Matsushima, E. Okamoto, H. Wada, O. Okumura, and S. Iino, 'Reflective and transfective color LCDs with double polarizers', *J. SID*, **7**, 9 (1999).
- 45 T. Ohyama, Y. Ukai, L. Fennell, Y. Kato, H. G. Bae, and P. W. Sung, 'TN mode TFT-LCD with in-cell polarizer', *SID Tech. Dig.*, **35**, 1106 (2004).
- 46 S. T. Wu and C. S. Wu, 'Mixed-mode twisted nematic liquid crystal cells for reflective displays', *Appl. Phys. Lett.*, **68**, 1455 (1996).
- 47 H. Molsen and M. D. Tillin, 'Transfective liquid crystal displays', International patent application No. PCT/JP99/05210, International publication No. WO 00/17707 (Mar. 30, 2000).
- 48 S. Pancharatnam, 'Achromatic combinations of birefringent plates: Part I. An achromatic circular polarizer', *Proc. Indian Acad. Sci., Section A*, **41**, 130 (1955).
- 49 S. J. Roosendaal, B. M. I. van der Zande, A. C. Nieuwkerk, C. A. Renders, J. T. M. Osenga, C. Doornkamp, E. Peeters, J. Bruinink, J. A. M. M. van Haaren, and S. Takahashi, 'Novel high performance transfective LCD with a patterned retarder', *SID Tech. Dig.*, **34**, 78 (2003).
- 50 B. M. I. van der Zande, A. C. Nieuwkerk, M. van Deurzen, C. A. Renders, E. Peeters, and S. J. Roosendaal, 'Technologies towards patterned optical foils', *SID Tech. Dig.*, **34**, 194 (2003).
- 51 M. Okamoto, H. Hiraki, and S. Mitsui, 'Liquid crystal display', US patent 6,281,952 (Aug. 28, 2001).
- 52 T. Uesaka, E. Yoda, T. Ogasawara, and T. Toyooka, 'Optical design for wide-viewing-angle transfective TFT-LCDs with hybrid aligned nematic compensator', *Proceedings of the 9th International Display Workshops*, 417–420 (2002).
- 53 S. H. Lee, K. H. Park, J. S. Gwag, T. H. Yoon, and J. C. Kim, 'A multimode-type transfective liquid crystal display using the hybrid-aligned nematic and parallel-rubbed vertically aligned modes', *Jpn. J. Appl. Phys., Part 1*, **42**, 5127 (2003).
- 54 Y. J. Lim, J. H. Song, Y. B. Kim, and S. H. Lee, 'Single gap transfective liquid crystal display with dual orientation of liquid crystal', *Jpn. J. Appl. Phys., Part 2*, **43**, L972 (2004).
- 55 S. H. Lee, H. W. Do, G. D. Lee, T. H. Yoon, and J. C. Kim, 'A novel transfective liquid crystal display with a periodically patterned electrode', *Jpn. J. Appl. Phys., Part 2*, **42**, L1455 (2003).
- 56 J. H. Song and S. H. Lee, 'A single gap transfective display using in-plane switching mode', *Jpn. J. Appl. Phys., Part 2*, **43**, L1130 (2004).
- 57 M. Shimizu, Y. Itoh, and M. Kubo, 'Liquid crystal display device', US patent 6,341,002 (Jan. 22, 2002).
- 58 M. Shibazaki, Y. Ukawa, S. Takahashi, Y. Iefuji, and T. Nakagawa, 'Transfective LCD with low driving voltage and wide viewing angle', *SID Tech. Dig.*, **34**, 90 (2003).
- 59 H. D. Liu and S. C. Lin, 'A novel design wide view angle partially reflective super multi-domain homeotropically aligned LCD', *SID Tech. Dig.*, **23**, 558 (2002).
- 60 C. L. Yang, 'Electro-optics of a transfective liquid crystal display with hybrid-aligned liquid crystal texture', *Jpn. J. Appl. Phys., Part 1*, **43**, 4273 (2004).
- 61 T. B. Jung, J. C. Kim, and S. H. Lee, 'Wide-viewing-angle transfective display associated with a fringe-field driven homogeneously aligned nematic liquid crystal display', *Jpn. J. Appl. Phys., Part 2*, **42**, L464 (2003).



- 62 T. B. Jung, J. H. Song, D. S. Seo, and S. H. Lee, 'Viewing angle characteristics of transflective display in a homogeneously aligned liquid crystal cell driven by fringe-field', *Jpn. J. Appl. Phys., Part 2*, **43**, L1211 (2004).
- 63 Z. Ge, X. Zhu, and S. T. Wu, 'A transflective liquid crystal display using an internal wire grid polarizer', *J. Disp. Technol.*, **2**, 102 (2006).
- 64 K. Fujimori, Y. Narutaki, Y. Itoh, N. Kimura, S. Mizushima, Y. Ishii, and M. Hijikigawa, 'New color filter structures for transflective TFT-LCD', *SID Tech. Dig.*, **33**, 1382 (2002).
- 65 K. J. Kim, J. S. Lim, T. Y. Jung, C. Nam, and B. C. Ahn, 'A new transflective TFT-LCD with dual color filter', *Proceedings of the 9th International Display Workshops*, 433–436 (2002).
- 66 M. Bass, E. W. Van Stryland, D. R. Williams, and W. L. Wolfe, *Handbook of Optics, Vol. II, Devices, Measurements, & Properties*, 2nd edn Chapter 35 (McGraw-Hill, New York, 1995).
- 67 H. P. D. Shieh, Y. P. Huang, and K. W. Chien, 'Micro-optics for liquid crystal displays applications', *J. Disp. Technol.*, **1**, 62 (2005).
- 68 K. Nakamura, H. Nakamura, and N. Kimura, 'Development of high reflective TFT', *Sharp Tech. J.*, **69**, 33 (1997).
- 69 Z. Ge, T. X. Wu, X. Zhu, and S. T. Wu, 'Reflective liquid crystal displays with asymmetric incidence and exit angles', *J. Opt. Soc. Am. A*, **22**, 966 (2005).

# 10

## Liquid Crystal Display Matrices, Drive Schemes, and Bistable Displays

Liquid crystal displays are a dominant display technology. They are used in electronic watches, calculators, handheld devices such as cellular phones, head-mounted displays, laptop and desktop computers, direct-view and projection TVs, and electronic papers and books. They have the advantages of a flat panel, light weight, energy saving, and low drive voltage. In display applications, the liquid crystals modulate the light intensity because of their birefringence. Liquid crystals can also be reoriented by externally applied electric fields because of their dielectric anisotropies or ferroelectricity, which makes it possible to show spatial images when patterned electric fields are applied.

### **10.1 Segmented Displays**

In order for a liquid crystal display to display images, multiple elements are needed. The simplest multi-element displays are the segmented displays where each element has its own electrodes that are separated from the electrodes of other elements [1]. Voltages can be applied to each element independently. As an example, a segmented numerical liquid crystal display is shown in Figure 10.1. When a proper voltage is applied between the common electrode and a segmented electrode, an electric field is generated in the region between the electrodes and the liquid crystal in that region is switched to the field-on state. For example, when the voltage is applied to electrodes 1, 2, 4, 6, and 7, the numeral 5 is displayed. The segmented displays are also referred to as direct-drive displays. This type of display is only good for low-information-content displays because one electrode is needed for each element.

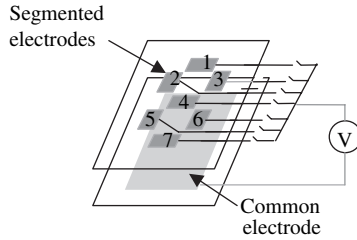


Figure 10.1 Schematic diagram of the segmented numerical liquid crystal display

### 10.2 Passive Matrix Displays and Drive Scheme

In order to display high-information-content images, an  $xy$  matrix must be used [1, 2]. There are striped electrodes on the substrates as shown in Figure 10.2. The overlapped region between a front electrode and a rear electrode is a display element referred to as a pixel. For a display consisting of  $N$  rows and  $M$  columns, there are  $N \times M$  elements, but there are only  $N + M$  electrodes. In the  $xy$  matrix, the structure of the electrode is greatly simplified. Driving the pixels, however, becomes complicated. It is impossible to apply a voltage to a pixel without affecting the other pixels in the matrix. For the purpose of simplicity, let us consider a  $2 \times 2$  matrix display as shown in Figure 10.3(a). The equivalent circuit is shown in Figure 10.3(b). The liquid crystals in the pixels can be regarded as capacitors. If we want to switch Pixel 11, we apply a voltage  $V$  to Column 1 and ground Row 1. The voltage across Pixel 11 is  $V$ . As can be seen from Figure 10.3(b), there is also a voltage  $V/3$  applied to the other three pixels, which may partially switch the pixels. This undesired voltage that is applied to the other pixels and partially switches them is referred to as *cross-talking*.

Now we consider how to address a  $N \times M$  ( $N$  rows and  $M$  columns)  $xy$  matrix display. The display is addressed one row at a time. The row electrodes are called scanning electrodes and the column electrodes are called signal electrodes or data electrodes. The state of the pixels is controlled by the voltages applied to the column electrodes. There are three issues that must be considered. The first issue is that there are voltages applied to the pixels on the rows not being addressed because of the column voltages. The second issue is that the voltages across the pixels on the row after addressing are not retained. The third issue is the frame time  $T_f$ . If the time interval to address a row is  $\Delta t$ , the frame time is  $T_f = N\Delta t$ . The frame time must be not only shorter than the response time ( $\sim 40$  ms) of the human eye, but also shorter than the relaxation time of the liquid crystal. When the frame time is shorter than the relaxation time of the liquid crystal, the state of the liquid crystal in a pixel is determined by the averaged (over the frame time) rms voltage applied across the pixel.

Let us consider a normal-black liquid crystal display. At zero volts, the transmittance of the liquid crystal display is zero and the display is black. At the voltage  $V_{on}$ , the display is switched to the bright state. A pixel of the display to be addressed in the bright state is called the *selected pixel* and a pixel to be addressed in the dark state is called the *non-selected pixel*. We consider a simple drive scheme.

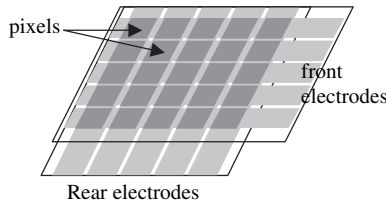


Figure 10.2 Schematic diagram of  $xy$  matrix

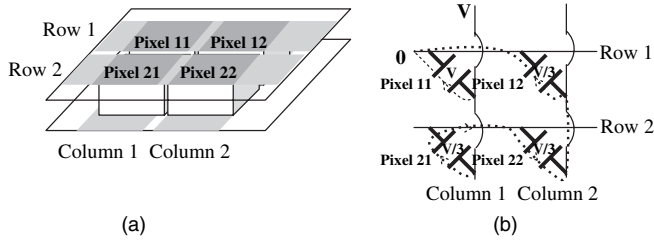


Figure 10.3 (a) Schematic diagram of a 2x2 matrix display. (b) The equivalent circuit

The column voltage to select the bright state is  $-V/b$  and the column voltage to select the black state is  $V/b$ , where  $b$  is a constant [2–4]. The row voltage to the row being addressed is  $(b - 1)V/b$  and the row voltage to the rows not being addressed is zero. For the selected pixel, the applied voltage is  $(b - 1)V/b - (-V/b) = V$  when being addressed and  $0 - (\pm V/b) = \mp V$  afterward. For the non-selected pixel, the applied voltage is  $(b - 1)V/b - V/b = (b - 2)V/b$  when being addressed and  $0 - (\pm V/b) = \mp V$  afterward. The rms voltage on the selected pixel is

$$\bar{V}_s = \left\{ \frac{1}{N} \left[ 1 \cdot V^2 + (N - 1) \left( \frac{V}{b} \right)^2 \right] \right\}^{1/2} \tag{10.1}$$

The rms voltage on the non-selected pixel is

$$\bar{V}_{ns} = \left\{ \frac{1}{N} \left[ 1 \cdot \left( \frac{b - 2}{b} V \right)^2 + (N - 1) \left( \frac{V}{b} \right)^2 \right] \right\}^{1/2} \tag{10.2}$$

The ratio between these two voltages is

$$R = \frac{\bar{V}_s}{\bar{V}_{ns}} = \left[ \frac{b^2 + (N - 1)}{(b - 2)^2 + (N - 1)} \right]^{1/2}$$

In order to optimize the performance of the display, the parameter  $b$  should be chosen to maximize  $R$ :

$$\frac{\partial R^2}{\partial b} = \frac{4[-b^2 + 2b + (N - 1)]}{(b - 2)^2 + (N - 1)} \equiv 0 \tag{10.3}$$

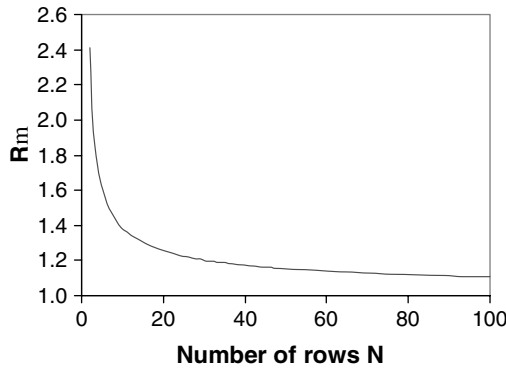
which gives

$$b = \sqrt{N} + 1 \tag{10.4}$$

The maximized ratio is

$$R_m = \left( \frac{\sqrt{N} + 1}{\sqrt{N} - 1} \right)^{1/2} \tag{10.5}$$

$R_m$  as a function of  $N$  is shown in Figure 10.4. The larger the number of rows is, the smaller the difference between the selected voltage and the non-selected voltage becomes.



**Figure 10.4** The ratio of the selected voltage and non-selected voltage as a function of the number of rows in the display

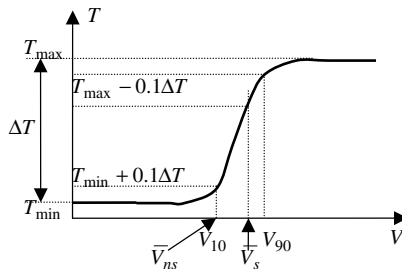
In passive matrix displays, the quality of the displayed images depends on the electro-optical response of the liquid crystal material. Consider a liquid crystal display whose voltage–transmittance curve is shown in Figure 10.5. In order to achieve high contrast, the non-selected voltage  $\bar{V}_{ns}$  should be set below  $V_{10}$  such that the transmittance of the black pixel is less than  $T_{\min} + 0.1\Delta T$ . The maximum selected voltage is  $\bar{V}_s = R_m \bar{V}_{ns}$ . If  $\bar{V}_s$  is lower than  $V_{90}$ , the transmittance of the bright pixel is lower than  $T_{\max} - 0.1\Delta T$ , which is clearly not good. Therefore the quality of the displayed images depends on the steepness of the voltage–transmittance curve of the liquid crystal and the number of rows of the display. The steepness of the voltage–transmittance curve can be characterized by the parameter  $\gamma$  defined by

$$\gamma = \frac{V_{90}}{V_{10}} \tag{10.6}$$

If  $\gamma \leq R_m$ , images with good contrast and high brightness can be displayed. In other words, for a given liquid crystal display,  $\gamma$  is fixed. The maximum number of rows the passive matrix display can have is given by

$$N_{\max} = \left( \frac{\gamma^2 + 1}{\gamma^2 - 1} \right)^2 \tag{10.7}$$

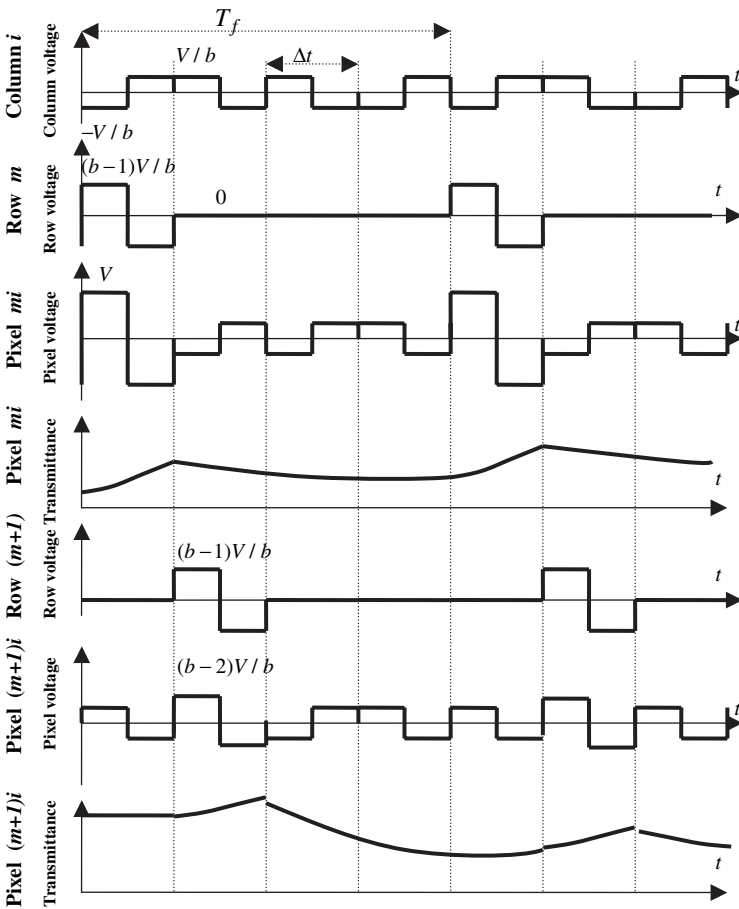
$1/N_{\max}$  is sometimes referred to as the duty ratio. For TN liquid crystal displays (LCDs),  $\gamma \sim 1.4$ ,  $N_{\max} \sim 9$ . This number of rows is only suitable for displays on simple calculators.



**Figure 10.5** The voltage–transmittance curve of the TN liquid crystal display

In order to increase the number of rows of TN LC passive matrix displays, the steepness of the voltage–transmittance curve must be increased. The steepness is measured by the difference between the saturation voltage  $V_s$  and the threshold voltage  $V_{th}$ . A smaller  $\Delta V = V_s - V_{th}$  generates steeper voltage–transmittance curves. The steepness can be achieved by the following methods [4]: (1) Increasing the twist angle, because the threshold voltage increases with the twist angle as shown in Figure 7.5. (2) Decreasing the pretilt angle, because the threshold voltage increases with decreasing pretilt angle as discussed in Chapter 5. (3) Decreasing the ratio between the cell thickness  $h$  and the pitch  $P$  of the LC, because the saturation voltage decreases with increasing pitch. The twist elastic energy is smaller for larger pitch. (4) Increasing  $K_{33}/K_{11}$ , because the threshold voltage increases with  $K_{33}$ . There is bend deformation in the field-activated states with small tilt angles but not in the saturated state. (5) decreasing  $K_{22}/K_{11}$ , because the saturation voltage decreases with  $K_{22}$ . (6) Decreasing  $\Delta\epsilon/\epsilon_{\perp}$ .

Usually AC voltage waves are used in addressing LCDs in which the LC molecules interact with applied electric fields through dielectric interaction. AC voltages can prevent the injection of ions into the LCS, which degrade the displays through long-term effects. The waveforms of the addressing voltages and the corresponding transmittance of the display are schematically shown in Figure 10.6



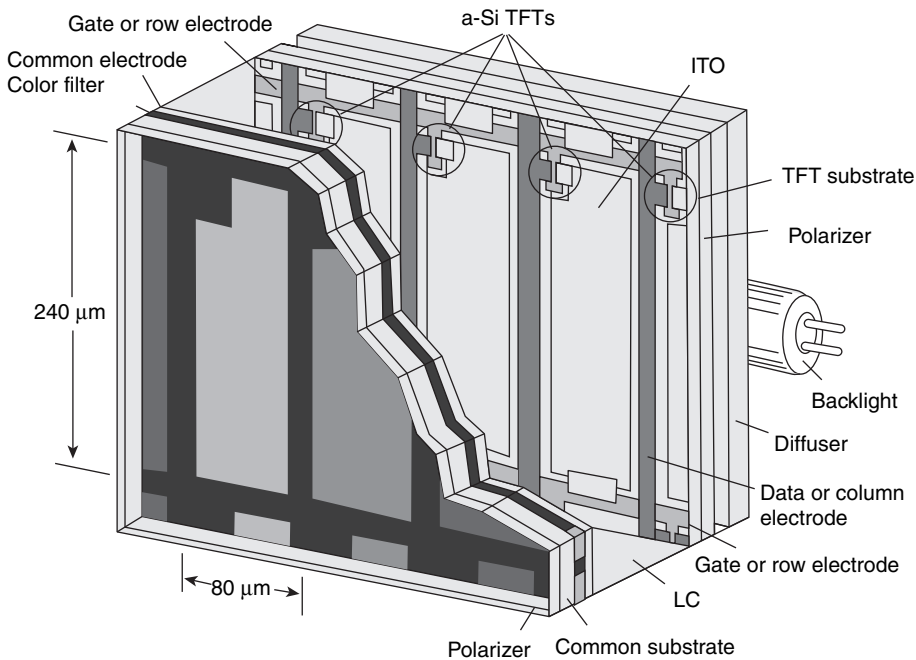
**Figure 10.6** Waveform of the column, row, and pixel voltages and the transmittance of the display under the pixel voltages

where the labeled voltages are the voltages of the first half of the voltage pulses [2]. If the column voltage is varied between  $-V/b$  and  $+V/b$ , gray-scale transmittances can be obtained.

### 10.3 Active Matrix Displays

Active matrix displays using thin-film transistors (TFTs) as electrical switches to control the transmission state of LC pixels offer excellent image quality and are commonly employed for direct-view displays [5, 6]. Figure 10.7 shows the device structure of a transmissive TFT LCD using amorphous silicon (a-Si) transistors for large-screen displays. Since LC do not emit light, a backlight is needed. A diffuser is used to homogenize the backlight. Since most LCDs require linearly polarized light for achieving high contrast ratio, two sheets of stretched dichroic polarizers are commonly used for large-screen direct-view displays. The first glass substrate contains TFT arrays which serve as light switches. Each display pixel is independently controlled by a TFT. Since a-Si exhibits photoelectric characteristics, TFTs need to be protected from backlight (by gate metal lines) and ambient light (by black matrices). Because of the black matrices, the actual aperture ratio (the transparent indium–tin–oxide electrode area) drops to 80–50%, depending on the device resolution and panel size. The LC layer is sandwiched between two substrates. The cell gap is usually controlled at around  $4\ \mu\text{m}$  for transmissive LCDs. The performance of the display such as light throughput, response time, and viewing angle are all determined by the LC mode employed.

For direct-view displays, such as notebook computers and desktop monitors, compact size and light weight are critically important. Under such circumstances, color filters are usually imbedded on the inner side of the second substrate. Some development efforts are attempting to integrate color filters on the TFT substrate. Three sub-pixels (red, green, and blue) form a color pixel. Each sub-pixel transmits only



**Figure 10.7** Device structure of a TFT LCD color pixel

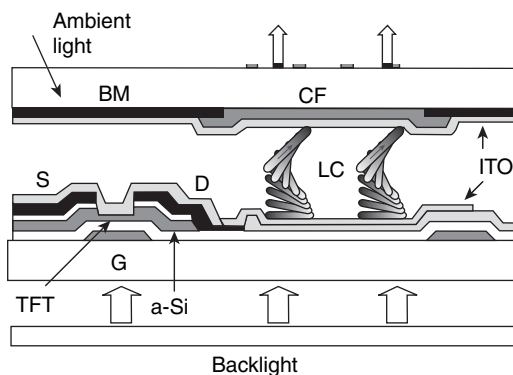
one color; the rest are absorbed. Thus, the transmittance of each color filter alone is less than 33%. The color filters are made of pigment materials, where transmittance at each color band is about 80–85%. Thus, the final transmittance of each color filter is  $\sim 27\%$ . Including polarizers, color filters, and TFT aperture ratio, the overall system optical efficiency is about 6–7% for a direct-view LCD panel. Low optical efficiency implies high power consumption. For portable displays, low power consumption is desirable because it lengthens the battery's operating hours. For LCD TVs, although the power consumption issue is not a burning issue at this stage, it will be addressed in due course.

For large-screen direct-view LCDs, a-Si TFT is a preferred choice because of its simpler manufacturing process and lower cost than poly-silicon (p-Si) TFT. However, the electron mobility of a-Si is about two orders of magnitude lower than that of p-Si, and the required pixel size is larger in order to maintain a good storage capacitance. A typical sub-pixel size for the a-Si TFT LCD is  $\sim 80 \mu\text{m} \times 240 \mu\text{m}$ . It takes three sub-pixels (RGB) to form a color pixel. Therefore, the pixel size of each color pixel is about  $240 \mu\text{m} \times 240 \mu\text{m}$ . On the other hand, p-Si has higher electron mobility than a-Si so its pixel size can be made smaller and its device resolution is therefore higher. This advantage is particularly important for small-screen LCDs where the aperture is an important issue.

### 10.3.1 TFT structure

The most commonly used TFT is the inverse-staggered (called bottom-gate) type, as shown in Figure 10.8. The ohmic layer ( $n^+$ a-Si) in the channel region can be etched either directly or by forming a protective film on the a-Si thin film. Each method has its own merits and demerits. The inverse-staggered structure offers a relatively simple fabrication process and its electron mobility is  $\sim 30\%$  larger than that of the staggered type. These advantages make the bottom-gate TFT structure a favored choice for TFT LCD applications.

Because a-Si is photosensitive, the a-Si TFT must be protected from incident backlight and ambient light, especially if the backlight is quite strong. Furthermore, the a-Si layer should be kept as thin as possible in order to minimize the photoinduced current, which would degrade the signal-to-noise ratio. In the bottom-gate TFTs, an opaque gate electrode is first formed at the TFT channel region, where it also serves as a light-shield layer for the backlight. On the color filter substrate, a black matrix shields the TFT from ambient light irradiation. In Figure 10.8, the drawing is not in scale: the TFT and black matrix parts should be much smaller than the transparent ITO part. A more realistic dimension is shown in Figure 10.7.



**Figure 10.8** The bottom-gate TFT structure. S stands for source, G for gate, D for drain, BM for black matrix, and CF for color filter



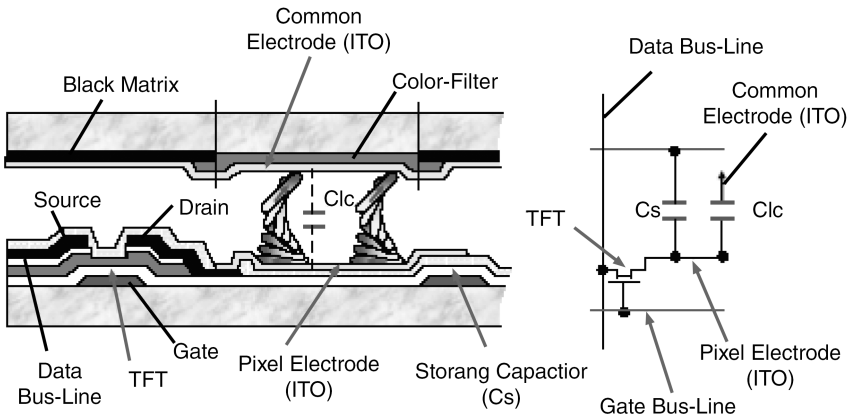


Figure 10.9 Equivalent circuit of a single pixel of TFT LCD

### 10.3.2 TFT operating principles

Figure 10.9 shows the equivalent circuit of a single pixel of a TFT LCD. Once the gate voltage exceeds a threshold, the TFT switch is open. The source (S) data voltage is transferred to the drain (D) which is connected to the bottom pixel electrode (ITO). The bottom pixel electrode and a gate line form a storage capacitor ( $C_s$ ) which plays an important role in holding the voltage. If the voltage across the LC layer is higher than the threshold voltage of the employed LC material, the LC directors will be reoriented by the voltage, resulting in light modulation of the backlight. The detailed transmission characteristics depend on whether the LC is in normal-white mode (TN) or normal-black mode (in-plane switching and multi-domain vertical alignment). In both situations, the polarizers are crossed.

DC voltage would induce undesirable electrochemical degradation in the organic LC molecules and should be avoided. Therefore, the polarity of the voltage has to be alternated every other frame. In normal operation, the gate voltage is set at 20V for the switch-on or at  $-5V$  for the switch-off state. Under these operating conditions, the a-Si TFT exhibits an on/off current ratio larger than  $10^6$ . Figure 10.10 illustrates the TFT operating principles.

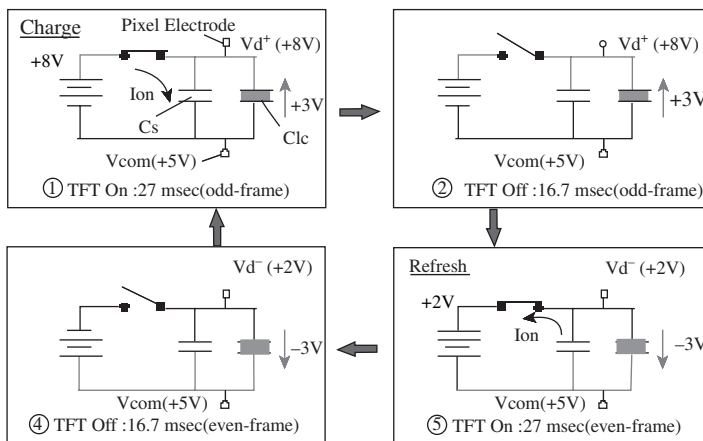


Figure 10.10 Keeping DC balance of the LC voltage

Let us assume that the common ITO electrode is biased at +5 V. For a given gray scale, the data voltage is at +8 V. When the gate is open, the TFT is turned on and the current flows through the channel and charges up the storage capacitor. The drain terminal has the same voltage as the data terminal, i.e.,  $V_d = +8$  V. Since the drain is connected to the bottom pixel electrode, the effective voltage across the LC cell is +3 V, as shown in the top left quadrant (defined as the first quadrant) of Figure 10.10. If the gate voltage is removed or below threshold, the TFT is turned off for a frame time which is 16.7 ms (60 Hz frame rate). In this period, the storage capacitor holds the charges so that the pixel voltage remains at +3 V. To balance the DC voltage, in the next frame the data voltage is reduced to +2 V, as shown in the third quadrant (clockwise). When the TFT is turned on, the voltage across the LC cell is reversed to -3 V, which is opposite to the +3 V shown in the previous frame. When the TFT is turned off as shown in the fourth quadrant, the storage capacitor holds the charges and the LC voltage remains at -3 V.

The LC reorientation dynamics depends on the square of the electric field, i.e., it is independent of the polarity of the electric field. However, if the LC is biased at a DC voltage for too long, then the ions will be swept to the polyimide alignment layer interface and stay there to form a thin layer to shield the voltage. The gray-scale voltage will be misrepresented. Therefore, to reduce the undesirable DC voltage effect, the polarity of the DC pulses needs to be alternated and a high-resistivity LC mixture needs to be employed.

### 10.4 Bistable Ferroelectric LCDs and Drive Scheme

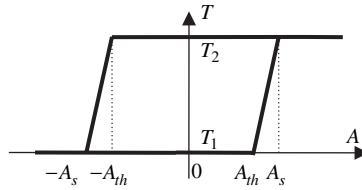
Multiplexibility of LC materials is necessary for their use in high-information-content displays. There are three ways to achieve this goal. The first one is to develop displays with a steep voltage–transmittance curve as discussed in the first section. The second way is to use active matrices where the voltage on a pixel can be controlled independently. The third way is to develop bistable LCS, the subject of the rest of this chapter.

As discussed in Chapter 4, surface-stabilized ferroelectric liquid crystals (SSFLCs) have two stable states at zero field. The two states have different planar orientational angles as shown in Figure 4.9. In the SSFLC display, the LC is sandwiched between two crossed polarizers. The transmission axis of the entrance polarizer is parallel to the orientation direction of one of the stable states, say state 1. The transmittance of state 1 is then zero. When the LC is in the other state, say state 2, the LC director makes an angle  $2\theta$  with the entrance polarizer, and the transmittance is  $T = \sin^2(4\theta)\sin^2(\pi\Delta nh/\lambda)$ , where  $2\theta$  is the cone angle. When  $2\theta$  is near  $\pi/4$  and  $\pi\Delta nh/\lambda$  is close to  $\pi/2$ , the transmittance of state 2 is one. The LC is switched between the two states by DC voltage pulses. When a voltage pulse with positive polarity is applied across the LC, say, the LC is switched into state 1. After the pulse, the LC remains in state 1. When a voltage pulse with negative polarity is applied, the LC is switched into state 2 and remains there afterward.

Experiments show that FLCs with high spontaneous polarizations respond accumulatively to voltage pulses [6–8]. The switching between the two stable states is determined by the ‘voltage–time–area’  $A$  defined by

$$A = \int_{t_1}^{t_2} V(t) dt$$

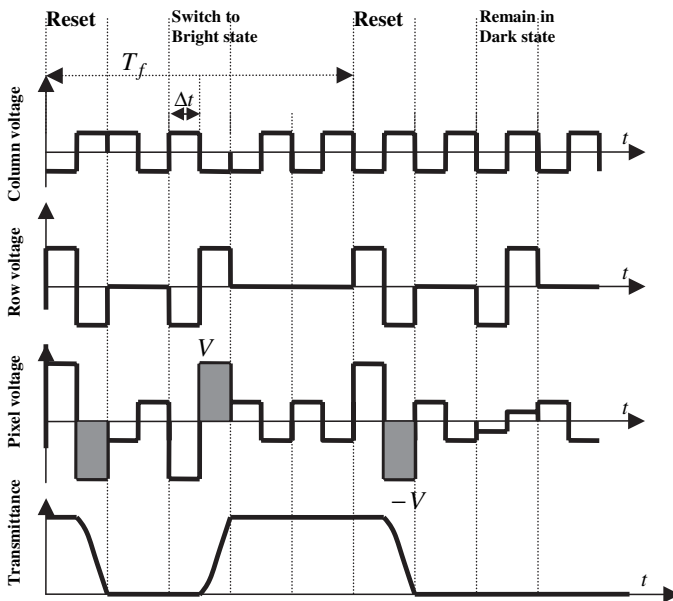
where the voltage is applied from time  $t_1$  to time  $t_2$ . When the voltage is applied sufficiently long or its amplitude is sufficiently high so that  $A$  is larger than a threshold  $A_{th}$ , the LC starts to transform from one state to the other as shown in Figure 10.11. If the FLC is initially in state 1 with low transmittance  $T_1$ , when the voltage–time–area is below the threshold  $A_{th}$ , the LC remains in state 1. When the voltage–time–area is increased above  $A_{th}$ , the LC starts to transform into state 2 and the



**Figure 10.11** Schematic diagram showing the transmittance of the SSFLC display as a function of voltage–area

transmittance increases. When the voltage–area is increased above  $A_s$ , the LC is completely switched to state 2, and the transmittance reaches the maximum value  $T_2$ . When the applied voltage is removed, the LC remains in state 2. When a voltage with negative polarity is applied, the voltage–time–area is negative. When the voltage–time–area is decreased below  $-A_{th}$ , the LC starts to transform back to state 1 and the transmittance begins to decrease. When the voltage–area is decreased below  $-A_s$ , the LC is completely switched back to state 1 and the transmittance decreases to the minimum value  $T_1$ .

A drive scheme for the SSFLC display is shown in Figure 10.12. At the beginning of each frame, the LC is reset to the dark state by applying a positive/negative (P/N) voltage pulse to all the rows. The column voltage to select the bright state is P/N and the column voltage to retain the dark state is negative/positive (N/P). A N/P voltage pulse is applied to the row being addressed. If the column voltage is P/N, the pixel voltage–time–area of the second half of the pulse is higher than  $A_s$ , and thus the bright state is selected. If the column voltage is N/P, the pixel voltage–time–area of the second half of the pulse is lower than  $A_{th}$ , and thus the dark state is retained. The voltage applied to



**Figure 10.12** Waveform of the column, row, and pixel voltages and the transmittance of the display under the pixel voltages

the rows not being addressed is zero. The voltage–time–areas of the voltages applied to the pixels on the rows not being addressed are higher than  $-A_{th}$  but less than  $A_{th}$ , and therefore their states do not change. AC voltage pulses are used to reduce undesired ionic effects.

## 10.5 Bistable Nematic Displays

### 10.5.1 Introduction

There are several types of bistable nematic LCDs which have good performance characteristics, namely twisted–untwisted bistable nematic LCDs [9–13], zenithal bistable nematic LCDs [14, 15], surface-induced bistable nematic LCDs [16–19], mechanically bistable nematic LCDs, and bistable STN LCDs [20–24]. A bistable nematic material has two bistable states with different optical properties. Once the LC is driven into a bistable state, it remains there. It can be used to make highly multiplexed displays on passive matrices. There is no limitation on the information content. Bistable nematic LCDs exhibit high contrast ratios and large viewing angles. The drawback is that most bistable nematic LCDs do not have gray-scale capability.

### 10.5.2 Twisted–untwisted bistable nematic LCDs

In the bistable twisted–untwisted nematic (BTN) (also called  $2\pi$  bistable) LCD, the two bistable states are selected by making use of the hydrodynamic motion of the LC as discussed in Chapter 5 [9, 11, 25]. Under one hydrodynamic condition, the LC is switched to one twisted state; under another hydrodynamic condition, the LC is switched to the other twisted state. An example is shown in Figure 10.13. One stable state is the  $0^\circ$  twist state shown by Figure 10.13(a) and the other stable state is the  $360^\circ$  state shown by Figure 10.13(c). Besides this particular design, there are other possible designs [26, 27]. Generally speaking, the twist angles of the two bistable states are  $\phi$  and  $\phi + 2\pi$  respectively.  $\phi$  is the angle between the alignment directions of the alignment layers on the bottom and top substrates of the cell. The angle  $\phi$  is usually in the region between  $-\pi/2$  and  $\pi/2$ . The twist angle difference between the two bistable states is  $2\pi$ .

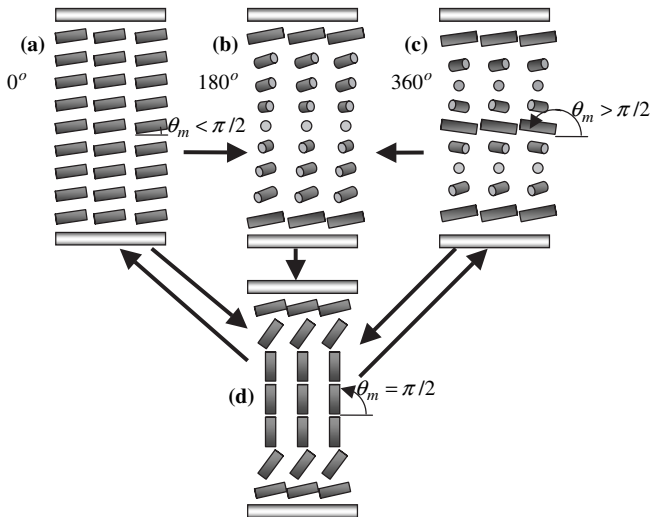


Figure 10.13 The LC director configurations of the states in the bistable TN LC

*(1) Bistability and switching mechanism*

We first consider the  $0^\circ/360^\circ$  BTN LC where the alignment directions on the two cell surfaces are parallel, as shown in Figure 10.13. Chiral dopants are added to the nematic LC to obtain the intrinsic pitch  $P$  such that  $h/P = 1/2$ , where  $h$  is the cell thickness. The real stable state is the  $180^\circ$  twist state, as shown in Figure 10.13(b); it has a free energy lower than both the  $0^\circ$  and  $360^\circ$  twist states. The  $0^\circ$  and  $360^\circ$  states are actually metastable.

The hydrodynamic effect is used to switch the LC between the bistable states in the BTNLC. As discussed in Chapter 5, the rotational motion of the LC director and the translational motions of the LC are coupled [28, 29]. On one hand, a rotation of the LC produces a viscous stress that results in a translational motion. On the other hand, a translational velocity gradient produces a viscous torque and affects the rotation of the director. In the BTN LC ( $\Delta\varepsilon > 0$ ), when an electric field slightly higher than the threshold  $V_{th}$  of the Freedericksz transition is applied, the LC is switched to the homeotropic state as shown in Figure 10.13(d). In this state, the LC is aligned homeotropically only in the middle of the cell and has no twisting. The LC near the surface of the cell has some twisting. Once the field is turned off, the LC relaxes into the  $0^\circ$  twist state, because the  $0^\circ$  twist state and the homeotropic state are topologically the same, while the  $180^\circ$  twist state is topologically different. If a very high field, higher than saturation voltage  $V_{sa}$ , is applied to the LC, the LC in most regions except very near the cell surfaces is aligned homeotropically and has low elastic energy. The LC director changes orientation rapidly in space near the surface and has a very high elastic energy. When the applied field is removed suddenly, in the region near the cell surface the LC director rotates very quickly because of the high elastic torque while the LC director in the middle rotates slowly because of the low elastic torque. Thus a translational motion is induced, which will affect the rotation of the LC in the middle in such a way that the tilt angle increases instead of decreasing. If the LC is a nematic LC without chiral agents, the opposite rotations of the director near the surface and the director in the middle produce a distortion of the director, which is not energetically favored. The angle of the director in the middle eventually decreases again, resulting in the backflow phenomenon [30–32]. If the LC has an intrinsic twist, the angle of the director in the middle can increase further and the LC is switched into the  $360^\circ$  twist state. In order for the angle of the LC in the middle to reach a value close to  $\pi$ , the LC must gain sufficient momentum at the beginning. If the initially applied voltage is not sufficiently high or a bias voltage is applied when the high voltage is turned off or the applied voltage is removed slowly, the LC in the middle cannot obtain a sufficiently high angular velocity to transform into the  $360^\circ$  twist state, and therefore the LC ends in the  $0^\circ$  twist state.

The parameters controlling the bistability are the angle  $\phi$  between the aligning directions of the alignment layers and intrinsic pitch  $P$  of the LC. So far bistability has been observed for  $-\pi/2 \leq \phi \leq \pi/2$ . The intrinsic pitch of the LC should be chosen heuristically in such a way that the  $(\phi + \pi)$  twist state has minimum free energy, i.e.,  $(\phi + \pi)$  is the intrinsic twist. Hence  $2\pi(h/P) = \phi + \pi$  [26].

The  $0^\circ/180^\circ$  BTN LC has also been reported [33,34]. In this LC, the two stable states are the  $0^\circ$  twisted and  $180^\circ$  twisted states. The chiral dopant concentration is chosen such that the two states have the same energy. The switching between the two states also makes use of the hydrodynamic effect. When a sufficiently high voltage is applied, the LC is switched to the homeotropic state. If the applied voltage is turned off slowly, the LC relaxes into the  $0^\circ$  twisted state. If the applied voltage is turned off abruptly, the LC relaxes into the  $180^\circ$  twisted state. With the employment of one tilted strong anchoring alignment layer and one weak planar anchoring alignment layer, the time interval of the addressing pulse can be reduced to microseconds.

*(2) Optical properties*

When a BTN display is optimized, the transmittance of one of the stable states should be zero and the transmittance of the other stable state should be one. The parameters of the display are the twist angles

$(\phi, 2\pi + \phi)$  of the stable states, the angle  $\alpha_i$  of the entrance polarizer, the angle  $\alpha_o$  of the exit polarizer, and the retardation  $\Gamma$  of the LC. As discussed in Chapter 3, the transmittance of a uniformly TN display in the geometry shown in Figure 3.3 is

$$\begin{aligned}
 T = & \cos^2(\alpha_o - \alpha_i - \Phi) - \sin^2 \Theta \sin[2(\alpha_o - \Phi)] \sin(2\alpha_i) \\
 & - \frac{\Phi^2}{\Theta^2} \sin^2 \Theta \cos[2(\alpha_o - \Phi)] \cos(2\alpha_i) - \frac{\Phi}{2\Theta} \sin(2\Theta) \sin[2(\alpha_o - \alpha_i - \Phi)]
 \end{aligned} \quad (10.8)$$

where  $\Phi$  is the twist angle,  $h$  is cell thickness,  $\Gamma = (2\pi/\lambda)(n_e - n_o)h$  is the total phase retardation angle, and  $\Theta = [\Phi^2 + (\Gamma/2)^2]^{1/2}$ . As an example, we consider how to choose the parameters for the  $(0^\circ, 360^\circ)$  BTN LC. Put the entrance polarizer at  $45^\circ$  with respect to the LC at the entrance plane, i.e.,  $\alpha_i = \pi/4$ . Put the exit polarizer at  $-45^\circ$  with respect to the LC at the entrance plane, i.e.,  $\alpha_o = -\pi/4$ . When the LC is in the state with a twist angle of  $0^\circ$ , namely  $\Phi = 0$ , the transmittance is

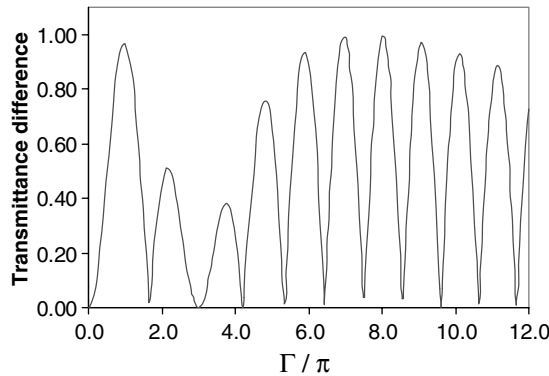
$$T(0^\circ) = \sin^2\left(\frac{\Gamma}{2}\right) \quad (10.9)$$

When the LC is in the state with a twist angle of  $360^\circ$ , namely  $\Phi = 2\pi$ , the transmittance is

$$T(360^\circ) = \sin^2 \left\{ \left[ (2\pi)^2 + \left(\frac{\Gamma}{2}\right)^2 \right]^{1/2} \right\} \quad (10.10)$$

In order to find the retardation  $\Gamma$  which maximizes the contrast, the difference of the transmittances is calculated and plotted as in Figure 10.14. Good performance is achieved when the transmittance difference is maximized. When the difference of the transmittances is maximized, the transmittances of the stable states and the corresponding retardation are as listed in Table 10.1. The good choices are: (1)  $\Gamma = 0.972\pi$ , which generates  $T(0^\circ) = 0.998$  and  $T(360^\circ) = 0.033$  [10]; (2)  $\Gamma = 6.924\pi$ , which generates  $T(0^\circ) = 0.986$  and  $T(360^\circ) = 0$ .

The angles of the polarizers as well as the twist angle  $\phi$  can also be varied to achieve good performance. For example, consider a  $(-90^\circ, 270^\circ)$  BTN LC where  $\phi = -90^\circ$ . The angles of



**Figure 10.14** Transmittance difference of the two stable states of the BTN LC vs. the retardation of the LC

**Table 10.1** Some of the retardations with which the performance of the BTN LC is optimized

$\Gamma/\pi$	$T(0^\circ)$	$T(360^\circ)$	$0^\circ$ Twist state	$360^\circ$ Twist state
0.972	0.998	0.033	Bright state	Dark state
2.000	0	0.491	Dark state	Bright state
4.000	0	0.267	Dark state	Bright state
6.000	0	0.894	Dark state	Bright state
6.924	0.986	0	Bright state	Dark state
8.000	0	0.993	Dark state	Bright state

the polarizers are  $-\alpha_i = \alpha_o = \pi/4$ . When the LC is in the  $-90^\circ$  twist state,  $\Phi = -\pi/2$ . The transmittance is

$$T(-90^\circ) = 1 - \sin^2 \left\{ \left[ \left( \frac{\pi}{2} \right)^2 + \left( \frac{\Gamma}{2} \right)^2 \right]^{1/2} \right\} = \cos^2 \left\{ \left[ \left( \frac{\pi}{2} \right)^2 + \left( \frac{\Gamma}{2} \right)^2 \right]^{1/2} \right\} \quad (10.11)$$

When the LC is in the  $270^\circ$  twist state,  $\Phi = 3\pi/2$ . The transmittance is

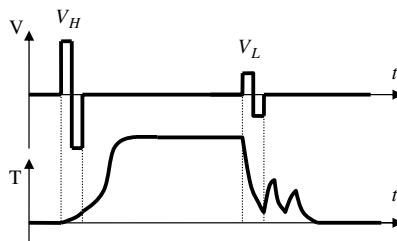
$$T(270^\circ) = 1 - \sin^2 \left\{ \left[ \left( \frac{3\pi}{2} \right)^2 + \left( \frac{\Gamma}{2} \right)^2 \right]^{1/2} \right\} = \cos^2 \left\{ \left[ \left( \frac{3\pi}{2} \right)^2 + \left( \frac{\Gamma}{2} \right)^2 \right]^{1/2} \right\} \quad (10.12)$$

When  $\Gamma = 2\sqrt{2}\pi$ ,  $T(-90^\circ) = 0$  and  $T(270^\circ) = 0.965$  [26]. With the help of the simplified Mueller matrix method and Poincaré sphere, a general condition for optimized performance can be derived. The optimization considered here is only for one wavelength. In reality, the transmission spectra of the two stable states are wavelength dependent because the phase retardation angle  $\Gamma$  is wavelength dependent. Therefore in designing BTN displays, the wavelength dispersion of the transmission spectra must be considered [35–39]. The BTN LC can also be used to make reflective displays [35].

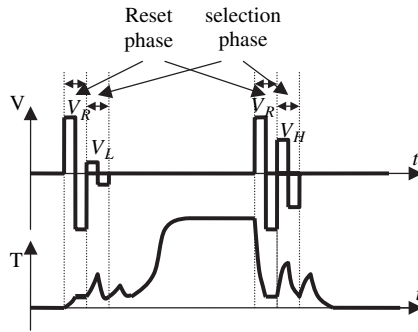
(3) Drive schemes

Bistability of a display material does not guarantee multiplexibility. Proper drive schemes must be designed in order to make multiplexed displays on a passive matrix. A good drive scheme should possess the properties of fast addressing speed, low drive voltage, no cross-talk, and simple waveform. According to the number of phases in the addressing, there are three major types of drive scheme for the BTN LC: (1) one-phase, (2) two-phase, and (3) three-phase drive schemes.

**(a) One-phase drive scheme** The one-phase drive scheme is shown schematically in Figure 10.15. The state of the LC is changed by one voltage pulse [10, 26, 40]. A low-voltage  $V_L$  addressing pulse



**Figure 10.15** Schematic diagram of the one-phase drive scheme and the response of the BTN LC



**Figure 10.16** Schematic diagram of the two-phase drive scheme and the response of the BTN LC

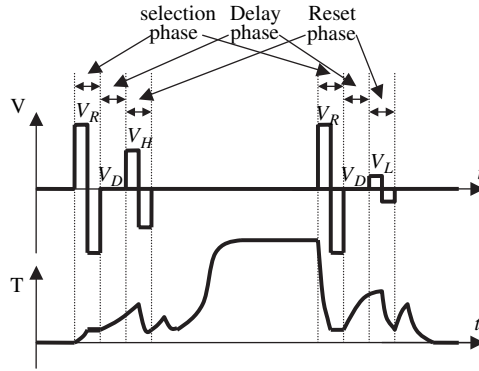
switches the material in to the low twisted state while a high-voltage  $V_H$  addressing pulse switches the material into the high twisted state. The low voltage is slightly higher than the threshold  $V_{th}$  of the Freedericksz transition. When the low voltage is applied, independent of the initial state of the LC, the LC is switched to a homeotropic state where the LC is aligned homeotropically only in a small region in the middle of the cell. When the low voltage is turned off, the LC relaxes into the low twisted state because it does not have sufficiently high potential. The high voltage is higher than the saturation voltage  $V_{sa}$ , which is much higher than the threshold of the Freedericksz transition. When the high voltage is applied, independent of the initial state, the LC is switched to a homeotropic state where the LC is aligned homeotropically in most regions of the cell except very close to the cell surfaces, and gains a high potential. When the high voltage is turned off, the LC relaxes into the high twisted state because of the hydrodynamic effect.

In addressing the display, the row voltage for the row being addressed is  $V_{rs} = (V_L + V_H)/2$ ; the row voltage for the row not being addressed is  $V_{rms} = 0$  V. The column voltage is  $V_{con} = -(V_H - V_L)/2$  to select the high twisting state and  $V_{coff} = (V_H - V_L)/2$  to select the low twisting state. The threshold of the Freedericksz transition of the LC must be higher than  $(V_H - V_L)/2$  in order to prevent cross-talk. The problem of this drive scheme is that the time interval to address one line is on the order of 10 ms, and thus the addressing speed is slow.

**(b) Two-phase drive scheme** The two-phase drive scheme is shown in Figure 10.16 [26]. In the reset phase, a high voltage  $V_R (> V_{sa})$  is applied to switch the LC to the homeotropic state. When the reset voltage is turned off, the LC begins to relax. In the selection phase, if the selection voltage  $V_S$  is the low voltage  $V_L$ , there is no hindrance to the rotation of the LC molecules in the middle of the cell; the tilt angle at the middle plane increases and the LC relaxes to the high twisted state. If the selection voltage  $V_S$  is the high voltage  $V_H$ , the applied voltage hinders the rotation of the LC molecules in the middle of the cell; the tilt angle at the middle plane decreases and the LC relaxes to the low twisted state. The time interval of the reset phase is on the order of 10 ms while the time interval of the selection phase is on the order of 1ms.  $(V_H - V_L)/2$  must be lower than the threshold of the Freedericksz transition of the LC in order to prevent cross-talk. Although the reset phase is long, multiple lines can be put into the reset phase such that the time is shared, which is known as the *pipeline algorithm*. Therefore the addressing speed of the two-phase drive scheme is faster than that of the one-phase drive scheme.

**(c) Three-phase drive scheme** The three-phase drive scheme is shown in Figure 10.17. It consists of three phases: reset, delay, and selection [41]. The physics behind this drive scheme is that at the beginning of the relaxation after the reset phase, the LC is allowed to relax freely, and the hydrodynamic effect can be controlled by a voltage in the late stage of the relaxation. Therefore the time interval of the selection phase is reduced. In the reset phase, the high voltage  $V_R (> V_{sa})$  switches the LC into the homeotropic texture. In the delay phase, the applied voltage  $V_D$  is zero and the LC starts to relax. In





**Figure 10.17** Schematic diagram of the three-phase drive scheme and the response of the BTN LC

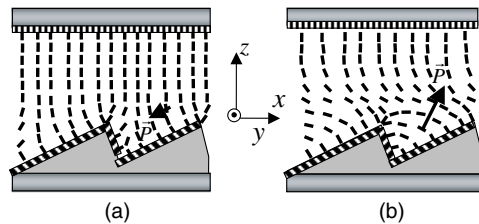
the selection phase, if the applied voltage  $V_S$  equals the high voltage  $V_H$ , the rotation of the LC molecules in the middle of the cell is hindered. After the selection phase, the liquid crystal is addressed to the low twisted state. If the applied voltage  $V_S$  equals the low voltage  $V_L$ , the rotation of the LC molecules in the middle of the cell is not hindered and the tilt angle increases. After the selection phase, the LC is addressed to the high twisted state.  $(V_H - V_L)/2$  must be lower than the threshold of the Freedericksz transition of the LC in order to prevent cross-talk. The time intervals of the reset and delay phases can be shared using the pipeline algorithm. The time interval of the selection phase can be as short as 100  $\mu$ s. Therefore the addressing speed is increased dramatically and video rate display becomes possible with this drive scheme.

**10.5.3 Surface-stabilized nematic LCDs**

In LCDs, the LC are usually sandwiched between two substrates. A certain alignment of the LC at the surface of the substrates is usually necessary in order for a display to operate properly. Bistable nematic LCs can be created by using surface alignment layers. They are divided into two categories: zenithal bistable TN and azimuthal TN.

*(1) Zenithal bistable TN LCs*

The zenithal (Z) bistable nematic LC was developed by Bryan-Brown *et al.*, using surface stabilization [15]. One substrate of the cell has an alignment layer with homeotropic anchoring and the other substrate is a one-dimensional grating as shown in Figure 10.18. The groove of the grating is along the y direction. The grooves are made from a photoresist. The non-symmetric profile of the grooves is obtained by using



**Figure 10.18** Schematic diagram of the LC director configurations of the two bistable states of the Z bistable nematic LC

UV light incident obliquely at  $60^\circ$  in the photolithography. A surfactant is coated on top of the grooves to obtain homeotropic anchoring.

The LC in the Z bistable cell has two stable states at zero field. One is the high-tilt state shown in Figure 10.18(a); the other is the low-tilt state shown in Figure 10.18(b). The flexoelectric effect plays an important role in switching the LC between the two stable states. As discussed in Chapter 4, the polarization produced by the flexoelectric effect is given by  $\vec{P} = e_1 \vec{n}(\nabla \cdot \vec{n}) + e_2(\nabla \times \vec{n}) \times \vec{n}$ . In the cell geometry shown in Figure 10.18, the LC director deformation occurs mainly near the grating surface; the bend deformation is dominant. The bending directions in the two states are different and therefore the induced polarization is upward in one of the states and downward in the other. The LC has a positive dielectric anisotropy. Besides the flexoelectric interaction, there is a dielectric interaction when a voltage is applied across the cell. When a sufficiently high voltage with one polarity is applied, the LC is switched to a homeotropic state with the LC near the grating substrate having a configuration similar to that in the high-tilt state; it relaxes into the high-tilt state after the applied voltage is removed. When a sufficiently high voltage with the opposite polarity is applied, the LC is switched to a homeotropic state with the LC near the grating substrate having a configuration similar to that in the low-tilt state; it relaxes into the low-tilt state after the applied voltage is removed.

In building a transmissive Z bistable display, crossed polarizers are used. The polarizers make an angle of  $45^\circ$  with the grating groove direction. Hence the plane containing the LC director makes an angle of  $45^\circ$  with the polarizers. The cell thickness and birefringence of the LC are chosen in such a way that the retardation of the low-tilt state is  $\pi$ , and therefore the transmittance of the low-tilt state is high. The retardation of the high-tilt state is small and therefore its transmittance is low. The Z bistable display can be addressed by DC voltage pulses. The width of the addressing voltage pulse is about  $10 \mu\text{s}$  for a field of about  $10 \text{ V}/\mu\text{m}$ , with which video rate is possible. The relaxation time from the field-on state to the low-tilt state is about 20ms and the relaxation time from the other field-on state to the low-tilt state is about 1ms. The material can also be used to make reflective displays with the retardation adjusted properly.

The Z bistable nematic LC can also be used to make displays by using a different geometry: the cell is made of the grating substrate and another substrate with a homogeneous anchoring [14, 42]. The aligning direction of the homogeneous anchoring makes an angle of  $90^\circ$  with respect to the LC director near the grating surface in the low-tilt state. Thus a hybrid TN LC is formed. In making a transmissive display, two crossed polarizers are used. The groove of the grating is arranged parallel to one of the polarizers. When the LC is in the low-tilt state, the material acts as a polarization guide and the transmittance of the display is high. When the LC is in the high-tilt state, the polarization of the incident light is rotated only slightly and therefore the transmittance is low. The selection of the states is made by using DC voltage pulses in the same way as already described. In this design, higher contrast is achieved. Furthermore, written images are retained at zero field even if the display is squeezed.

## (2) Azimuthal bistable nematic LCs

The alignment of a LC at the cell surface is due to the intermolecular interaction between the molecules of the alignment layer and the LC molecules as well as the geometrical shape of the surface of the alignment layer through the elastic energy of the LC. For an alignment layer having unidirectional grooves (grating), the LC is aligned along the groove direction. For an alignment layer having grooves in two perpendicular directions (bi-grating), two alignment directions can be created with properly controlled groove amplitude and pitch. The LC can be anchored along either direction. Thus two bistable orientation states can be achieved [43]. In order to be able to select the two states by applying a voltage in the cell normal direction, the pretilt angles of the two anchoring directions must be different.

Alignment layers with two anchoring directions and different pretilt angles can be produced by obliquely evaporating SiO on glass substrates twice. The blaze direction of the first evaporation is in the  $x$ - $z$  plane (with azimuthal angle  $\phi = 0^\circ$ ) and the blaze direction of the second evaporation is in the  $y$ - $z$  phase (with azimuthal angle  $\phi = 90^\circ$ ). The resulting alignment layer has two alignment directions: one has azimuthal angle  $\phi = 45^\circ$  and a non-zero pretilt angle, and the other has azimuthal angle  $\phi = -45^\circ$

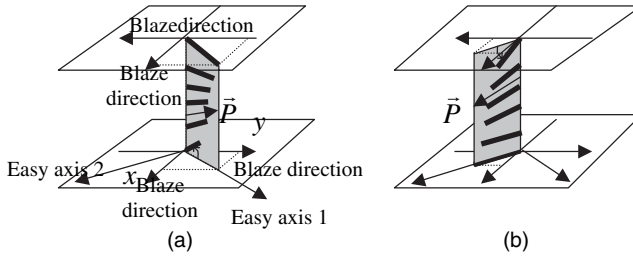


Figure 10.19 Schematic diagram of the azimuthal bistable nematic LC

and zero pretilt angle. In a cell with two such alignment layers on the two substrates, there are two stable states as shown in Figure 10.19. Because of the non-zero pretilt angle, there are splay deformations in the two bistable states, which induce flexoelectric polarizations. In the state shown in Figure 10.19(a), the flexoelectric polarization is upward, while in the state shown in Figure 10.19(b), the flexoelectric polarization is downward. Therefore these states can be selected by using DC voltages applied across the cell.

## 10.6 Bistable Cholesteric Reflective Displays

### 10.6.1 Introduction

Cholesteric (Ch) LC have a helical structure in which the LC director twists around a perpendicular axis named the helical axis [29]. The distance along the helical axis for the director to twist  $2\pi$  is called the pitch and is denoted by  $P_o$ . In this section we only discuss Ch LC with short pitches (in the visible and IR light regions). The optical properties of a Ch LC depend on the orientation of the helical axis with respect to the cell surface. There are four states as shown in Figure 10.20 [44]. When a Ch LC is in the planar state (also called planar texture) where the helical axis is perpendicular to the cell surface as shown in Figure 10.20(a), the material reflects light. A microphotograph of the planar state is shown in Figure 21(a). The dark lines are the disclination lines, called oily streaks [45–47], where the Ch layers are bent. When the LC is in the focal conic state (texture), the helical axis is more or less random throughout the cell as shown in Figure 20(b). It is a multi-domain structure and the material is scattering. A microphotograph of the focal conic state is shown in Figure 10.21(b), which is similar to the focal conic texture of smectic-A LC because the Ch LC can be regarded as a layered structure [46]. When an intermediate electric field is applied across the cell, the LC is switched to the fingerprint state (texture), and the helical axis is parallel to the cell surface as shown in Figure 10.20(c). A microphotograph of the fingerprint state is shown in Figure 10.21(c). When a sufficiently high field is applied across the cell, the

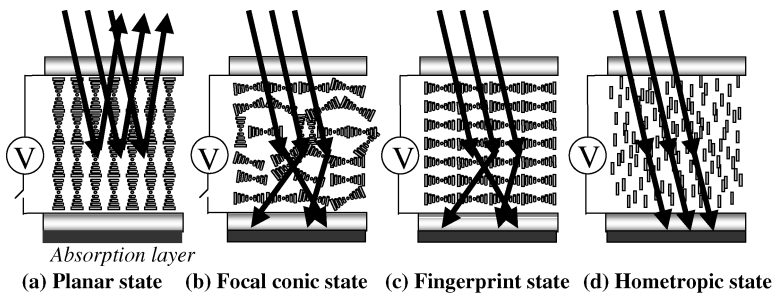
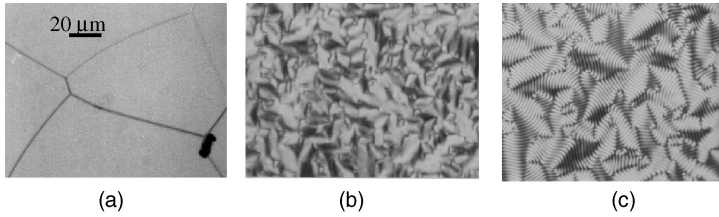


Figure 10.20 Schematic diagram of the Ch states



**Figure 10.21** Microphotographs of the Ch textures

LC ( $\Delta\epsilon > 0$ ) is switched to the homeotropic state where the helical structure is unwound with the LC director perpendicular to the cell surface as shown in Figure 10.20(d) [48]. The material is transparent in this state. When homeotropic alignment layers or weak homogeneous alignment layers are used (known as surface stabilization) or a small amount of polymer is dispersed in the LC (known as polymer stabilization), both the planar state and the focal conic state can be stable at zero field [49–54].

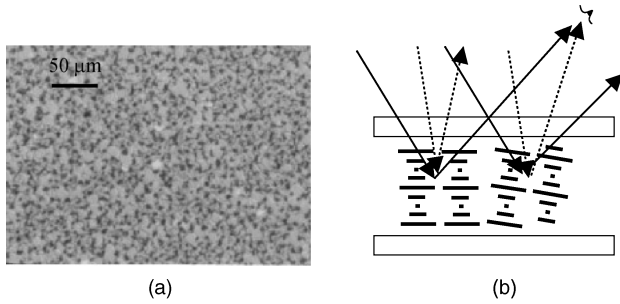
### 10.6.2 Optical properties of bistable Ch reflective displays

#### (1) Reflection

Bistable Ch reflective displays are operated between the reflecting planar state and the non-reflecting focal conic state. When a Ch LC is in the planar texture, the refractive index varies periodically in the cell normal direction. The refractive index oscillates between the ordinary refractive index  $n_o$  and the extraordinary refractive index  $n_e$ . The period is  $P_o/2$  because  $\vec{n}$  and  $-\vec{n}$  are equivalent. The LC exhibits Bragg reflection at the wavelength  $\lambda_o = 2\vec{n}(P_o/2) = \vec{n}P_o$  for normally incident light [28], where  $\vec{n} = (n_e + n_o)/2$  is the average refractive index. The reflection bandwidth is given by  $\Delta n P_o$ , where  $\Delta n = n_e - n_o$  is the birefringence. The reflected light is circularly polarized with the same handedness as the helical structure of the LC. If the (normally) incident light is unpolarized, then the maximum reflection from one Ch layer is 50%; 100% reflection can be achieved by stacking a layer of left-handed Ch LC and a layer of right-handed Ch LC. In bistable Ch reflective displays, a color absorption layer is coated on the bottom substrate. When the LC is in the planar state, the reflection of the display is the sum of the reflection from the LC and the reflection from the absorption layer. When the LC is in the focal conic state, the reflection of the display is only contributed by the reflection of the absorption layer. If the absorption layer is black and the LC reflects green light, the planar state appears green while the focal conic state is black [55]. If the absorption layer is blue and the LC reflects yellow light, the planar state appears white and the focal conic state appears blue [56].

#### (2) Viewing angle

When light is obliquely incident at an angle  $\theta$  on the Ch LC in the planar state, the central wavelength of the reflection band is shifted to  $\lambda = \vec{n}P_o \cos\theta$ . This shift of the reflection band is undesirable in display application if the LC is in the perfect planar state, because the color of the reflected light changes with viewing angle and the reflected light is only observed at the corresponding specular angle. This problem can be partially solved by dispersing a small amount of polymer in the LC or by using an alignment layer which gives weak homogeneous anchoring or homeotropic anchoring. The dispersed polymer and the alignment layer produce defects and create a poly-domain structure as shown in Figure 10.22(a). In this imperfect planar state, the helical axis of the domains is no longer exactly parallel to the cell normal but distributed around the normal. For incident light at one angle, light reflected from different domains is in different directions, as shown in Figure 10.22(b). Under room light condition where light is incident at all angles, at one viewing angle, light reflected from different domains has different colors. Because the



**Figure 10.22** (a) Microphotograph of the imperfect planar state. (b) The reflection from the imperfect planar state under room light conditions

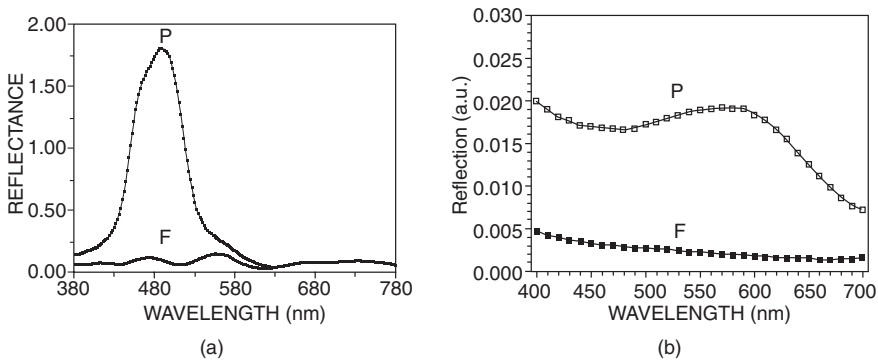
observed light is a mixture of different colors, the colors observed at different viewing angle are not much different. The poly-domain structure of the imperfect planar state and the isotropic incidence of room light are responsible for the large viewing angle of the Ch display [57].

(3) *Polymer-stabilized black–white Ch display*

The deviation of the helical axis from the cell normal direction in the poly-domain planar texture depends on the amount of the dispersed polymer. In the regular polymer-stabilized Ch display, the polymer concentration is low and the deviation is small. The reflection spectrum of the planar texture is not very wide as shown in Figure 10.23(a). The color of the reflected light is pure. The reflection spectra of surface-stabilized Ch displays are similar. The reflection of the focal conic texture is low as shown in Figure 10.23(a). If the polymer concentration is high, the deviation becomes large. When  $\bar{n}P_o$  equals the wavelength of red light, the reflection spectrum of the planar texture becomes very broad as shown in Figure 10.23(b). The planar texture has a white appearance. The display is called a polymer-stabilized black–white Ch display [58, 59]. In this display, the scattering of the focal conic texture is stronger than that of the focal conic texture of the regular polymer-stabilized Ch displays.

(4) *Gray scale*

The bistable Ch displays exhibit gray-scale memory states because of their multi-domain structure [55, 60, 61]. For each domain, it is bistable that it is either in the planar state or in the focal conic state. For



**Figure 10.23** The reflection spectra of the Cholesteric displays: P, planar texture; F, focal conic texture. (a) The regular polymer-stabilized Ch display. (b) The polymer-stabilized black–white display

different domains, the voltages to switch them from the planar state to the focal conic state are different. Once a domain is switched to the focal conic state, it remains there even after the applied voltage is turned off. If initially the LC is in the planar state, under a low applied voltage, few domains are switched to the focal conic state and the resulting reflectance is high; under a high applied voltage, many domains are switched to the focal conic state and the resulting reflectance is low. Therefore gray-scale reflectances are possible in bistable Ch reflective displays. The domain has a size around  $10\ \mu\text{m}$  and cannot be observed by the naked eye.

#### (5) Multiple color Ch displays

In a Ch display with a single layer of Ch LC, only a single color can be displayed. In order to make multiple color displays, Ch LCs with a variety of pitches must be used. This can be done either by stacking multiple layers of Ch LC with different pitches or by using one layer of Ch LC with different pitches partitioned in-plane.

Multiple color displays from one layer can be made from pixelation of colors. The displays have three alternating types of stripes of Ch LCs with three different pitches reflecting blue, green, and red light. Partition or other means of preventing interstripe diffusion must be used. Polymer walls, especially field-induced polymer walls, are good candidates. The different pitches can be achieved by two methods. In the first method, empty cells with partitions are filled with three Ch LCs with different pitches. The second method is photo color tuning [62, 63]. A photo-sensitive chiral dopant is added to the LC. The dopant undergoes a chemical reaction under UV irradiation and thus its chirality changes, and the pitch of the LC changes. After the display cells are filled with the mixture, the cells are irradiated by UV light with photomasks. By varying the irradiation time, different pitches are achieved. In this method, partitions are fabricated either before or after the photo color tuning. A polymer dispersing technique with large LC droplets can also be used with this method [64]. The major drawback of one-layer multiple color displays is that the reflection is low.

Multiple color displays from multiple layers are made by stacking three layers of Ch LCs with pitches reflecting blue, green, and red light [65–68]. Single layer displays with the three colors are fabricated first. Then they are laminated together. In order to decrease parallax, thin substrates, preferably substrates with a conducting coating on both sides, should be used to decrease the distance between the LC layers. Because of the scattering of the Ch LC, experiments show that the best stacking order from bottom to top is red, green, and blue.

### 10.6.3 Encapsulated Ch LCDs

When Ch LC are encapsulated in droplet form, the bistability can be preserved when the droplet size is much larger than the pitch [64]. There are two methods which are used to encapsulate Ch LCs: phase separation and emulsification. In the phase separation method [69], the Ch LCs is mixed with monomers or oligomers to make a homogeneous mixture. The mixture is coated on plastic substrates and then another substrate is laminated on. The monomers or oligomers are then polymerized to induce phase separation. The LC phase separates from the polymer to form droplets. In the emulsification method [70–73], the Ch LC, water, and a water-dissolvable polymer are placed in a container. The water dissolves the polymer to form a viscous solution, which does not dissolve the LC. When this system is stirred with a propeller blade at a sufficiently high speed, micron-size LC droplets are formed. The emulsion is then coated on a substrate and the water is allowed to evaporate. After the water evaporates, a second substrate is laminated to form the Ch display.

The encapsulated Ch LCs are suitable for flexible displays with plastic substrates. They have much higher viscosities than pure Ch LCs and can be coated on substrates in a roll-to-roll process [71, 72]. The polymers used for the encapsulation have good adhesion to the substrates and can make the materials self-adhesive to sustain the cell thickness. Furthermore, the encapsulated Ch LCs can no longer flow when squeezed, which solves the image-erasing problem in displays from pure Ch LCs where squeezing causes the LC to flow and to be switched to the planar state.

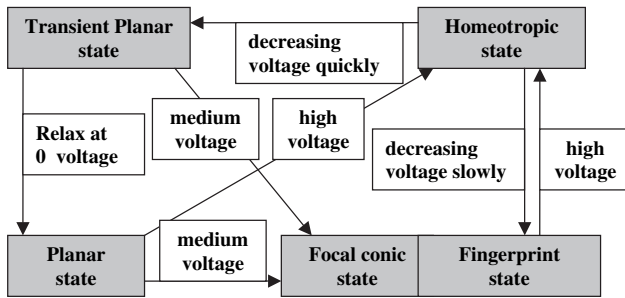


Figure 10.24 Schematic diagram showing the transitions among the Ch states

10.6.4 Transition between Ch states

The state of a Ch LC is mainly determined by surface anchoring, cell thickness, and applied fields. The LC can be switched from one state to another by applying electric fields. There are many possible transitions among the states as shown in Figure 10.24 [50, 54]. In order to design drive schemes for the bistable Ch reflective display, it is essential to understand the transitions. The Ch LC considered here have positive dielectric anisotropies unless otherwise specified.

(1) Transition between planar state and focal conic state

Under a given electric field and boundary conditions, a LC system is in a state with minimum free energy. In considering the state of the Ch LC in the bistable Ch display, the energies involved are the elastic energy of the deformation of the LC director, electric energy, and surface energy. In both the planar and focal conic states, the helical structure is preserved. In the planar state, the elastic energy is zero because there is no director deformation, while in the focal conic state, the elastic energy is positive because of the bend of the Ch layers. The electric energy is given by  $-(1/2)\Delta\epsilon\epsilon_o(\vec{E} \cdot \vec{n})^2$ , which depends on the orientation of the LC director. In the planar state, the electric energy is zero because the LC director  $\vec{n}$  is perpendicular to the field everywhere, while in the focal conic state, the electric energy is negative because the LC is parallel to the applied field in some regions. The elastic energy is against the planar–focal conic (P–F) transition while the electric energy favors the transition. When the applied field is sufficiently high, the planar state becomes unstable and the LC transforms from the planar to the focal conic state. There are two possible mechanisms for the transition from the planar to the focal conic state. One mechanism is the oily streaks as shown in Figure 10.25 [45, 47]. The oily streaks are bent Ch layers whose structure is shown in Figure 10.25(b). When the applied field is higher than a threshold  $E_{oily}$ , the

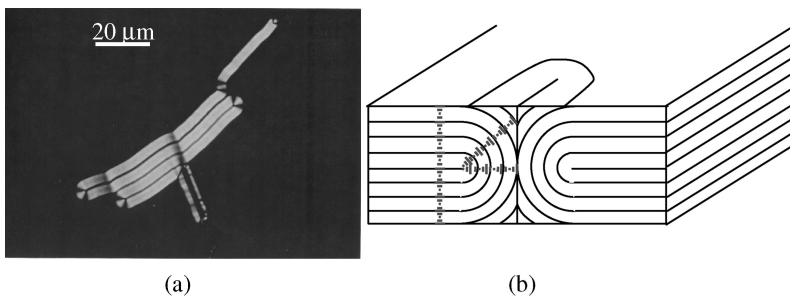
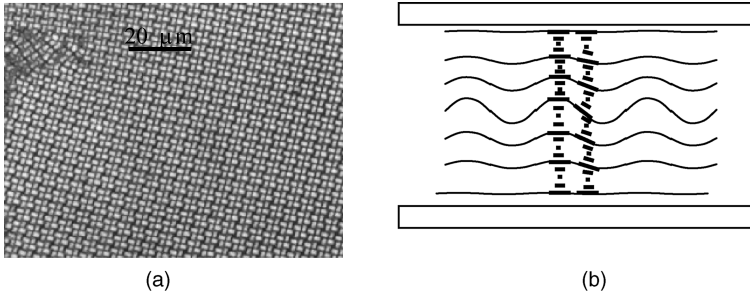


Figure 10.25 (a) Microphotograph of the oily streaks in the Ch LC. The bright finger is the oily streak. The dark background is the planar texture. (b) Schematic diagram showing the structure of the oily streak in cross-section



**Figure 10.26** (a) Microphotograph of Helfrich deformation. (b) Schematic diagram showing the structure of Helfrich deformation in a plane perpendicular to the cell surface

oily streaks nucleate from seeds such as impurities, guest particles, and surface irregularities; they grow with time until the whole system is switched into the focal conic state. The other mechanism is Helfrich deformation, as shown in Figure 10.26. Helfrich deformation is a 2-D undulation in the plane parallel to the cell surface [29, 45, 74, 75]. The structure of the LC in a vertical plane is shown in Figure 10.26(b). The wavelength of the undulation is  $\lambda = (2K_{33}/K_{22})^{1/4} (hP_o)^{1/2}$ . When the applied field is above a threshold  $E_{Helfrich}$ , the Ch layers start to undulate. Helfrich deformation is a homogeneous process and can take place simultaneously everywhere, and therefore it is much faster than the process of the oily streak. Once the applied field is above the threshold  $E_{Helfrich}$ , the amplitude of the undulation increases with increasing voltage, and eventually the amplitude diverges and the LC transforms into the focal conic state.

In bistable Ch reflective display applications, it is desirable that the threshold of the transition from the planar state to the focal conic state be high so that the Ch LC can remain in the planar state and the display does not exhibit flicker under addressing column voltage.

Once the Ch LC is in the focal conic state, it may remain there, depending on the surface anchoring condition. In bistable Ch reflective displays where either weak tangential or homeotropic alignment layers are used or polymers are dispersed in the LC, the LC remains in the focal conic state when the applied voltage is turned off. In order to switch the LC from the focal conic state back to the planar state, a high voltage must be applied to switch it to the homeotropic texture, then it relaxes back to the planar state after the high voltage is removed. This will be discussed in more detail later. If the cell has strong homogeneous alignment layers, the focal conic texture is not stable and the LC relaxes slowly back to the planar texture.

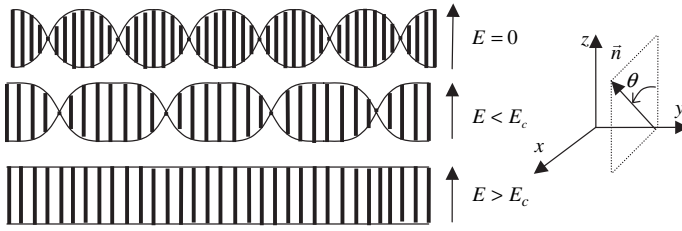
(2) Transition between the fingerprint state and homeotropic state

When the LC is in the focal conic state and the externally applied electric field is increased, more LC molecules are aligned parallel to the field. The LC is gradually switched to the fingerprint state. There is no sharp boundary between the focal conic state and the fingerprint state. When the applied field is increased further, the pitch of the LC becomes longer as shown in Figure 10.27. When the applied field is above a threshold  $E_c$ , the helical structure is unwound [29, 48], the pitch becomes infinitely long, and the LC is switched to the homeotropic state.

We first consider the unwinding of the helical structure. As the applied field is increased, the pi-walls (the narrow regions in which the LC director rotates by  $\pi$ ) are propelled apart horizontally and annihilated at the boundaries far away. In the fingerprint state, the LC director is given by  $n_x = \sin\theta(y)$ ,  $n_y = 0$ ,  $n_z = \cos\theta(y)$ . The free energy is given by

$$\begin{aligned}
 f &= \frac{1}{2} K_{22} [\vec{n} \cdot (\nabla \times \vec{n}) + q_o]^2 - \frac{1}{2} \Delta \epsilon \epsilon_o (\vec{n} \cdot \vec{E})^2 \\
 &= \frac{1}{2} K_{22} (\theta' - q_o)^2 + \frac{1}{2} \Delta \epsilon \epsilon_o E^2 \sin^2 \theta + \text{constant}
 \end{aligned}
 \tag{10.13}$$





**Figure 10.27** Schematic diagram showing the process of unwinding the helical structure in the fingerprint-homeotropic transition

where  $\theta' = \partial\theta/\partial y$ . The constant in this equation does not affect the director configuration and can be omitted. Using the dimensionless variables

$$\psi = f/K_{22}q_o^2, \quad \xi = q_o y, \quad e = E/E_o$$

where

$$E_o = \frac{\pi}{2}q_o \sqrt{\frac{K_{22}}{\epsilon_o \Delta \epsilon}} = \frac{\pi^2}{P_o} \sqrt{\frac{K_{22}}{\epsilon_o \Delta \epsilon}}$$

we have the dimensionless free energy density

$$\psi = \frac{1}{2} \left( \frac{d\theta}{d\xi} - 1 \right)^2 + \frac{1}{2} \left( \frac{\pi e}{2} \right)^2 \sin^2 \theta \tag{10.14}$$

Using the Euler-Lagrange equation to minimize the free energy, we obtain

$$\frac{d\theta}{d\xi} = \left[ \left( \frac{\pi e}{2} \sin \theta \right)^2 + A \right]^{1/2} \tag{10.15}$$

where  $A$  is the integration constant, which is field dependent. When  $e = 0$ ,  $d\theta/d\xi = 1$  then  $A = 1$ . When  $e \geq e_c = E_c/E_o$ ,  $d\theta/d\xi = 0$  and  $\theta = 0$ , hence. Thus, as the applied field is increased from 0 to  $e_c$ ,  $A$  changes from 1 to 0. The state normalized periodicity of the fingerprint state is  $(P/2)q_o$  and is given by

$$(P/2)q_o = \int_0^\pi \left[ A + \left( \frac{\pi e}{2} \sin \theta \right)^2 \right]^{-1/2} d\theta \tag{10.16}$$

By substituting Equation (10.15) into Equation (10.14), we have the free energy density

$$\psi = \frac{1}{2}(1 + A) - \frac{d\theta}{d\xi} + \left( \frac{\pi e}{2} \right)^2 \sin^2 \theta \tag{10.17}$$

The free energy density is a periodic function of  $\xi$  with the a period of  $(P/2)q_o$ . The averaged free energy density is given by

$$\begin{aligned}
 \bar{\psi} &= \frac{\int_0^{P/2} \left[ \frac{1}{2}(1+A) - \frac{d\theta}{d\xi} + \left( \frac{\pi e}{2} \sin \theta \right)^2 \right] d\xi}{(P/2)q_o} \\
 &= \frac{\int_0^{\pi} \left[ \frac{1}{2}(1+A) - \frac{d\theta}{d\xi} + \left( \frac{\pi e}{2} \sin \theta \right)^2 \right] \frac{d\xi}{d\theta} d\theta}{\int_0^{\pi} \left[ A + \left( \frac{\pi e}{2} \sin \theta \right)^2 \right]^{-1/2} d\theta} \\
 &= \frac{-\pi + \int_0^{\pi} \left\{ \int_0^{\pi} \left[ A + \left( \frac{\pi e}{2} \sin \theta \right)^2 \right]^{-1/2} + \frac{1}{2}(1-A) \left[ A + \left( \frac{\pi e}{2} \sin \theta \right)^2 \right]^{-1/2} \right\} d\theta}{\int_0^{\pi} \left[ A + \left( \frac{\pi e}{2} \sin \theta \right)^2 \right]^{-1/2} d\theta} \quad (10.18)
 \end{aligned}$$

Minimizing  $\bar{\psi}$  with respect to  $A$ ,  $\partial\bar{\psi}/\partial A = 0$ , which gives

$$\int_0^{\pi} \left[ A + \left( \frac{\pi e}{2} \sin \theta \right)^2 \right]^{1/2} d\theta = 2 \int_0^{\pi/2} \left[ A + \left( \frac{\pi e}{2} \sin \theta \right)^2 \right]^{1/2} d\theta = \pi \quad (10.19)$$

At any applied field  $e$ , the value of  $A$  can be found by solving Equation (10.19). Once the value of  $A$  is known, the helical pitch  $P$  can be calculated from Equation (10.16). At the threshold  $e_c$ ,  $A = 0$ . From Equation (10.19), we can obtain that  $e_c = 1$ . At this field, the pitch is

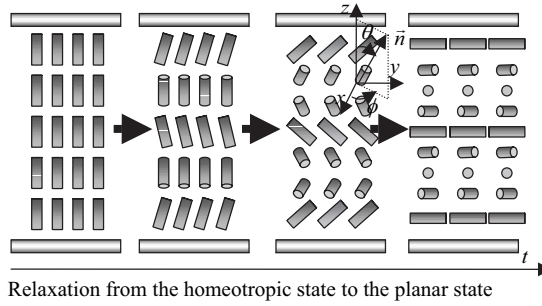
$$(P/2)q_o = \int_0^{\pi} \left[ A + \left( \frac{\pi e_c}{2} \sin \theta \right)^2 \right]^{-1/2} d\theta = \int_0^{\pi} \left( \frac{\pi}{2} \sin \theta \right)^{-1} d\theta = \infty$$

Therefore the critical field unwinding the helical structure is

$$E_c = E_o = \frac{\pi}{2} q_o \sqrt{\frac{K_{22}}{\epsilon_o \Delta \epsilon}} = \frac{\pi^2}{P_o} \sqrt{\frac{K_{22}}{\epsilon_o \Delta \epsilon}} \quad (10.20)$$

In reality, the pi-walls in the fingerprint–homeotropic transition are not parallel to each other. Instead, they form circles. The pi-wall circles shrink with increasing field. They annihilate at a threshold, which depends on the cell thickness and anchoring condition, slightly higher than  $E_c$ .

The fingerprint state homeotropic transition is reversible. The LC can transform directly from the homeotropic state back to the fingerprint. The transition is, however, a nucleation process and therefore is slow (on the order of 100 ms). There is also a hysteresis where the transition occurs only when the applied field is decreased below a threshold which is lower than the threshold to unwind the helical structure. If there are no nucleation seeds, the formation of helical structure in the middle of the homeotropic state



**Figure 10.28** Schematic diagram showing the rotation of the LC in the H-P relaxation mode

always causes the free energy to increase, i.e., there is an energy barrier against the homeotropic–fingerprint (H-F) transition. Experiments have shown that the threshold  $E_{HF}$  of the H-F transition is about  $0.9E_c$ . The hysteresis plays an important role in the dynamic drive scheme which will be discussed shortly.

(3) *Transition between the homeotropic state and the planar state*

For the LC in the homeotropic state, when the applied field is turned down, there are two relaxation modes. One is the H-F mode in which the LC relaxes into the fingerprint state (and then to the focal conic state) as discussed in the previous section. The other is the H-P mode in which the LC relaxes into the planar state [76, 77]. The rotation of the liquid crystal in the H-P mode is shown in Figure 10.28. The liquid crystal forms a conic helical structure with the helical axis in the cell normal direction. As the relaxation takes place, the polar angle  $\theta$  increases. When the polar angle  $\theta$  is zero, the LC is in the homeotropic state. When the polar angle is  $\pi/2$ , the LC is in the planar state.

We now consider the static conic helical structure. It is assumed that the polar angle  $\theta$  is a constant independent of  $z$  and the azimuthal angle  $\phi$  varies along  $z$  with a constant rate  $q$ , i.e., the twisting is uniform. The components of the director  $\vec{n}$  are given by  $n_x = \sin\theta\cos(qz)$ ,  $n_y = \sin\theta\sin(qz)$ , and  $n_z = \cos\theta$ . The free energy is given by

$$f = \frac{1}{2}K_{22}(q_0 - q\sin^2\theta)^2 + \frac{1}{2}K_{33}q^2\sin^2\theta\cos^2\theta + \frac{1}{2}\Delta\epsilon\epsilon_0 E^2\sin^2\theta \tag{10.21}$$

With the dimensionless variables  $K_3 = K_{33}/K_{22}$ ,  $\lambda = q/q_0$ ,  $\psi = f/K_{22}q_0^2$ , and  $e = E/E_c$ , the free energy becomes

$$\psi = \frac{1}{2}(1 - \lambda\sin^2\theta)^2 + \frac{1}{2}K_3\lambda^2\sin^2\theta\cos^2\theta + \frac{1}{2}\left(\frac{\pi}{2}e\right)^2\sin^2\theta \tag{10.22}$$

By minimizing  $\psi$  with respect to  $\lambda$ , we obtain

$$\lambda = \frac{1}{\sin^2\theta + K_3\cos^2\theta} \tag{10.23}$$

That is,

$$q = \frac{q_0}{\sin^2\theta + K_3\cos^2\theta}$$

When the polar angle  $\theta$  is very small,  $q = q_0/K_3 = K_{22}q_0/K_{33}$ , and the pitch is  $P = (K_{33}/K_{22})P_0$ . For most liquid crystals,  $K_{33}/K_{22} \approx 2$ . Hence the pitch  $p$  of the conic helical structure with small polar

angle is about twice the intrinsic pitch  $P_o$ . When the polar angle  $\theta$  is  $\pi/2$ ,  $q = q_o$ , i.e.,  $P = P_o$ . After the minimization with respect to  $\lambda$ , the free energy is

$$\psi = \frac{1}{2} + \frac{1}{2} \sin^2 \theta \left[ \left( \frac{\pi}{2} e \right)^2 - \frac{1}{K_3 + (1 - K_3) \sin^2 \theta} \right] \tag{10.24}$$

We then examine whether there is any stable conic helical structure. We minimize the free energy with respect to the polar angle  $\theta$ ,

$$\frac{\partial \psi}{\partial (\sin^2 \theta)} = \frac{1}{2} \left( \frac{\pi}{2} e \right)^2 - \frac{K_3}{2[K_3 + (1 - K_3) \sin^2 \theta]^2} \tag{10.25}$$

$$\frac{\partial^2 \psi}{\partial (\sin^2 \theta)^2} = \frac{K_3(1 - K_3)}{[K_3 + (1 - K_3) \sin^2 \theta]^3} \tag{10.26}$$

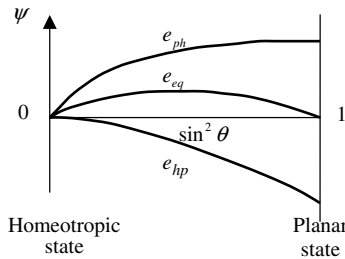
Because  $K_3 > 1$ , the second-order derivative is negative, and therefore there is no minimum free energy state in the region  $0 < \theta < \pi/2$ ; therefore there is no stable conic helical structure. The LC is either in the homeotropic state with  $\theta = 0$  or in the planar state with  $\theta = \pi/2$ . In Figure 10.29 the free energy of the conic helical structure given by Equation (10.24) is plotted as a function of  $\sin^2 \theta$  at three different fields;  $e_{eq} = 2/\pi$  is the field at which the planar state and the homeotropic state have the same free energy. At this field however, there is an energy barrier between the two states. When the applied field is increased from  $e_{eq}$ , the free energy of the homeotropic state becomes lower than that of the planar state, but the energy barrier persists. The energy barrier becomes lower with increasing field. When the field is sufficiently high, the energy barrier decreases to zero, and the planar state will become absolutely unstable. The critical field  $e_{ph} = (2/\pi)\sqrt{K_3}$  can be obtained from the equation

$$\left. \frac{\partial \psi}{\partial (\sin^2 \theta)} \right|_{\theta=\pi/2} = 0$$

The un-normalized critical field for the P-H transition is

$$E_{ph} = \frac{2}{\pi} \sqrt{\frac{K_{33}}{K_{22}}} E_c$$

For a LC with  $K_{33}/K_{22} = 2$ ,  $E_{hp} = 0.9E_c$ , which is slightly lower than the critical field  $E_c$  to unwind the helical structure in the fingerprint state. If the field is decreased from  $e_{eq}$ , the free energy of the planar



**Figure 10.29** The free energy of the conic helical structure as a function of the polar angle  $\theta$  at various applied fields

state becomes lower than that of the homeotropic state, but the energy barrier persists. The energy barrier becomes lower with decreasing field. When the field is sufficiently low, the energy barrier decreases to zero, and the homeotropic state will become absolutely unstable. The critical field  $e_{hp} = (2/\pi)/\sqrt{1/K_3}$  can be obtained from the equation

$$\left. \frac{\partial \psi}{\partial (\sin^2 \theta)} \right|_{\theta=0} = 0$$

The un-normalized critical field under which the H-P relaxation can occur is

$$E_{hp} = \frac{2}{\pi} \sqrt{\frac{K_{22}}{K_{33}}} E_c$$

For a liquid crystal with  $K_{33}/K_{22} = 2$ ,  $E_{hp} = 0.45E_c$ , which is much lower than the threshold  $E_{hf}$  for the H-F relaxation mode. Detailed dynamic studies show that in the H-P transition, the polar angle changes quickly but not the twisting rate. When the polar angle changes from 0 to  $\pi/2$ , the twisting rate is still around  $(K_{22}/K_{33})q_0$  which corresponds to the pitch  $(K_{33}/K_{22})P_o$ . This planar state with the pitch  $(K_{33}/K_{22})P_o$  is called the *transient planar state*. The transition from the homeotropic state to the transient planar state is a homogeneous transition with the transition time  $T_{hp} \approx \gamma P_o^2/K_{22}$ . For a LC with  $\gamma = 5 \times 10^{-2}$  NS/m<sup>2</sup>,  $K_{22} = 10^{-11}$  N, and  $P_o = 0.5 \mu\text{m}$ ,  $T_{hp} \sim 1$  ms. The transient planar state is unstable because its elastic energy is still high and the LC will relax through a nucleation process into the stable planar state with intrinsic pitch  $P_o$  [78]. The transition time is of the order of 100 ms.

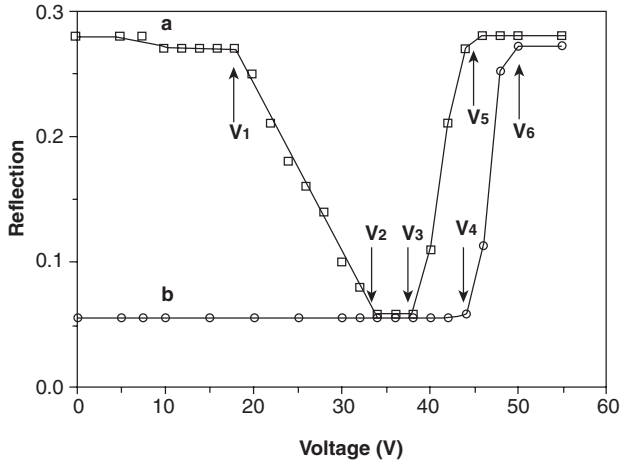
In summary, if the LC is in the homeotropic state and the applied field is reduced, there are two possible relaxation modes. If the applied field is reduced to the region  $E_{hp} < E < E_{hf}$ , the LC relaxes slowly into the fingerprint state and then to the focal conic state when the applied field is reduced further. If the applied field is reduced below  $E_{hp}$ , the LC relaxes quickly into the transient planar state and then to the stable planar state. In bistable Ch reflective displays, the way to switch the LC from the focal conic state to the planar state is by first applying a high field to switch it to the homeotropic state, and then turning off the field quickly to allow it to relax to the planar state.

### 10.6.5 Drive schemes for bistable Ch displays

As discussed in previous sections, Ch LC exhibit two bistable states at zero field: the reflecting planar state and the non-reflective focal conic state. They can be used to make multiplexed displays on passive matrices. In this section, we consider the drive schemes for the bistable Ch displays.

#### (1) Response of bistable Ch material to voltage pulses

In order to design drive schemes, we first must know the electro-optical response of the bistable Ch LC to voltage pulses. A typical response of a bistable Ch LC to a voltage pulse is shown in Figure 10.30 [51]. The horizontal axis is the amplitude of the voltage pulse. The vertical axis is the reflectance measured *not during the pulse but a few hundred milliseconds after the removal of the voltage pulse*, when the reflectance no longer changes. The response depends on the initial state of the Ch material. Curve a represents the response of the material initially in the planar state which is obtained by applying a voltage pulse higher than  $V_6$ . When the voltage of the pulse is below  $V_1 = 18$  V, the stability threshold voltage, the Ch material remains in the planar state during and after the pulse. When the voltage of the pulse is increased above  $V_1$ , some domains are switched into the focal conic state during the pulse and stay in the focal conic state after the pulse, and thus the reflectance after the pulse decreases. The higher the voltage of the pulse, more domains are switched to the focal conic state. When the voltage of the pulse reaches  $V_2 = 34$  V, all the domains are switched to the focal conic state and the minimum reflectance is reached. The region from  $V_1$  and  $V_2$  is the best region to achieve gray-scale reflectance. When the

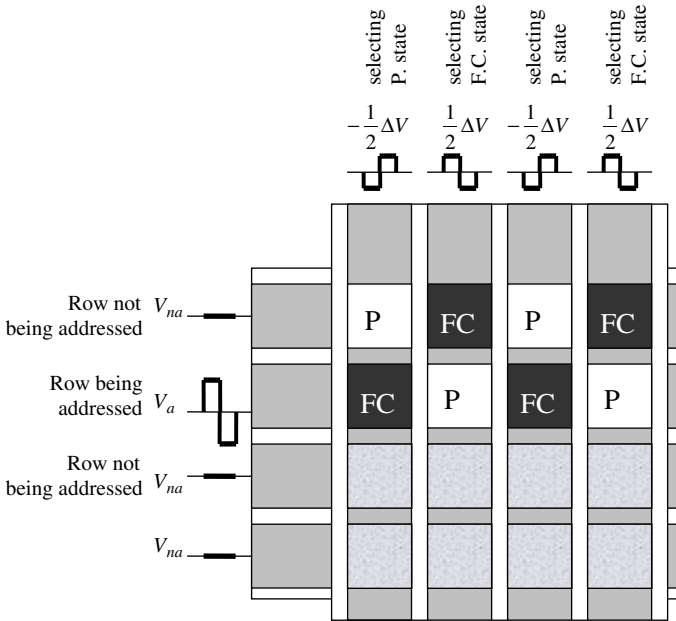


**Figure 10.30** The response of the bistable Ch LC to voltage pulses 40 ms wide: a, initially in the planar state; b, initially in the focal conic state

voltage of the pulse is increased above  $V_3 = 38$  V, some domains are switched to the homeotropic state and the remaining domains are switched to the focal conic state during the pulse. The domains switched to the homeotropic state relax to the planar state after the pulse, and therefore the reflectance increases again. When the voltage of the pulse is increased above  $V_5 = 46$  V, all domains are switched to the homeotropic state during the pulse and relax to the planar state after the pulse, and the maximum reflectance is obtained. Curve b represents the response of the material initially in the focal conic state which is obtained by applying an intermediate voltage pulse with a voltage, say,  $V_3$ . When the voltage of the pulse is below  $V_4 = 44$  V, the Ch material remains in the focal conic state during and after the pulse. When the voltage of the pulse is increased above  $V_4$ , some domains are switched to the homeotropic state and the remaining domains stay in the focal conic state during the pulse. The domains switched to the homeotropic state relax to the planar state after the removal of the pulse, and therefore the reflectance increases. When the voltage of the pulse is increased above  $V_6 = 52$  V, all the domains are switched to the homeotropic state during the pulse and relax to the planar state after the pulse, and the maximum reflectance is obtained.

### (2) Conventional drive scheme for bistable Ch displays

Because of the bistability and high stability threshold of Ch LC, they can be used to make multiplexed displays on a passive matrix. In the conventional drive scheme for the bistable Ch display, the display is addressed one line at a time [51, 54]. A high-voltage pulse switches the LC into the reflecting planar state and a low-voltage pulse switches the LC into the non-reflecting focal conic state. For the Ch LC whose response to a voltage pulse is shown in Figure 10.30, for the row being addressed, the applied voltage is  $V_a = (V_6 + V_3)/2 = 45$  V, as shown in Figure 10.31. The column voltage to select the planar state is  $-\frac{1}{2}\Delta V = -\frac{1}{2}(V_6 - V_3) = -7$  V (out of phase with respect to the row voltage). The voltage across the pixel to be addressed to the planar state is  $V_a - (-\frac{1}{2}\Delta V) = V_6$ . The column voltage to select the focal conic state is  $\frac{1}{2}\Delta V = \frac{1}{2}(V_6 - V_3) = +7$  V (in phase with respect to the row voltage). The voltage across the pixel to be addressed to the focal conic state is  $V_a - \frac{1}{2}\Delta V = V_3$ . If the column voltage is varied between  $-\frac{1}{2}\Delta V$  and  $\frac{1}{2}\Delta V$ , gray-scale reflectance can be obtained [79]. For the rows not being addressed, the applied voltage is  $V_{na} = 0$ . For the pixels on the row not being addressed, the absolute value of the voltage applied across them is  $|\frac{1}{2}\Delta V| = 7$  V, which is lower than the stability threshold voltage  $V_1 = 18$  V, as shown in Figure 10.30. Therefore the state of the Ch LC in these pixels remains

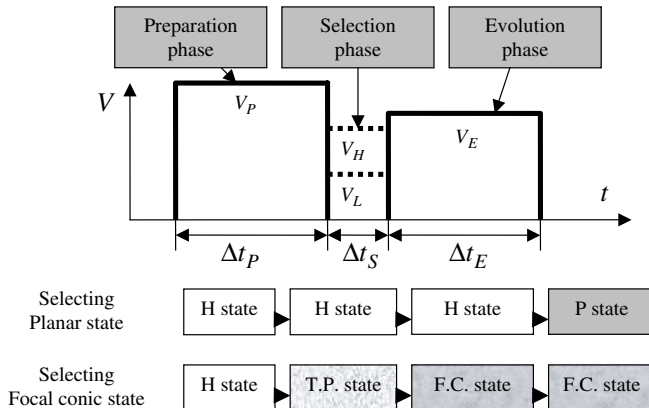


**Figure 10.31** Schematic diagram showing how the Ch display is addressed by the conventional drive scheme

unchanged. In this drive scheme, the time interval to address one line is usually a few tens of milliseconds. Therefore this drive scheme is only suitable for low-information-content displays.

(3) *Dynamic drive scheme for bistable Ch displays*

The dynamic drive scheme makes use of the dynamic process of the H-P transition and the hysteresis in the focal conic–homeotropic transition, and is much faster. The dynamic drive scheme consists of three phases: preparation, selection, and evolution, as shown in Figure 10.32 [54, 80]. In the



**Figure 10.32** Schematic diagram of the dynamic drive scheme for the Ch display

preparation (with the time interval  $\Delta t_P \sim 50$  ms), a high-voltage pulse is applied to switch the Ch LC into the homeotropic state. In the selection phase (with the time interval  $\Delta t_S \sim 1$  ms), if the applied voltage is  $V_H$ , which is higher than  $V_{hp}$ , the LC remains in the homeotropic state because of the high voltage and short time interval. If the applied voltage is  $V_L$ , which is lower than  $V_{hp}$ , the LC relaxes into the transient planar state. In the evolution phase (with the time interval  $\Delta t_E \sim 50$  ms), the applied voltage is between  $V_{hf}$  and  $V_c$ . If the LC is selected to remain in the homeotropic state in the selection phase, it remains in the homeotropic state in the evolution phase because the applied voltage is higher than the threshold voltage  $V_{hf}$  and thus the material cannot relax into the focal conic state [50, 81]. If the LC is selected to transform into the transient planar state in the selection phase, it is switched to the focal conic state but not the homeotropic state in the evolution phase because the transient planar state is unstable under the field and the applied voltage is lower than  $V_c$ . After the evolution phase, the applied voltage is reduced to zero. If the LC remains in the homeotropic state in the evolution phase, it relaxes to the planar state. If it is switched to the focal conic state in the evolution phase, it remains in the focal conic state. Although time intervals of the preparation and evolution phase are long, time can be shared by simultaneously putting multiple lines in the preparation and evolution phases. The time (frame time) needed to address a  $N$ -line display is  $\Delta t_P + N \times \Delta t_S + \Delta t_E$ , which is much shorter than the frame time of the conventional drive scheme. The addressing speed of the dynamic drive scheme is fast enough for electronic book and paper applications, where an updating rate of one page per second is required, but not fast enough for video rate applications.

## Homework Problems

- 10.1 *Multiplexed STN LCD on a passive matrix.* In order to have 100 rows, how steep must the voltage–transmittance curve be at least? Hint: find the  $\gamma$  value defined by Equation (10.6).
- 10.2 Consider a ( $0^\circ$ ,  $180^\circ$ ) bistable TN LC where the entrance polarizer is at  $45^\circ$  with respect to the LC at the entrance plane and the exit polarizer is at  $-45^\circ$  with respect to the LC at the entrance plane. Find the three values of the retardation with which the display has contrast ratios. Give the transmittances of the bright and dark states under those retardation values.
- 10.3 In the Helfrich deformation shown in Figure 10.26, the thickness of the cell is  $h$ . The cholesteric liquid crystal has pitch  $P$  and dielectric anisotropy  $\Delta\epsilon (> 0)$ . For small undulations, calculate the field threshold  $E_{Helfrich}$  and the wavelength  $\lambda$  of the undulations.
- 10.4 In the fingerprint–homeotropic transition shown in Figure 10.27, calculate the integration constant  $A$  and the normalized pitch  $P/P_o$  as a function of the normalized electric field  $E/E_C$ .

## References

- 1 A. R. Kmetz, ‘Matrix addressing of non-emissive displays’, in *Nonemissive electrooptical displays*, ed. A. R. Kmetz and F. K. von Willisen (Plenum, New York, 1976).
- 2 E. Kaneko, *Liquid crystal TV: principles and applications of liquid crystal displays*, (KTK Scientific Publishers, Tokyo, 1987).
- 3 P. M. Alt and P. Pleshko, ‘Scanning limitations of liquid crystal displays’, *IEEE Trans. Electron Devices*, **ED-21**, 146 (1974).
- 4 T. Scheffer and J. Nehring, ‘Twisted nematic and supertwisted nematic mode LCDs’, in *Liquid crystals - applications and uses*, Vol. 1, ed. B. Bahadur (World Scientific, Singapore, 1990)
- 5 F. C. Luo, ‘Active matrix LC Displays’, in *Liquid crystals - applications and uses*, Vol. 1, Chapter 15, ed. B. Bahadur (World Scientific, Singapore, 1990).
- 6 E. Lueder, *Liquid crystal displays: addressing schemes and electro-optical effects* (John Wiley & Sons, Ltd, Chichester, 2001).



- 7 J. W. Goodby, R. Blinc, N. A. Clark, S. T. Lagerwall, M. A. Osipov, S. A. Pikin, T. Sakurai, K. Yoshino, and B. Žekš, 'Ferroelectric liquid crystals: principle, properties and applications', in *Ferroelectricity and related phenomena*, Vol. 7 (Gordon and Breach, Amsterdam, 1991).
- 8 J. Dijon, 'Ferroelectric LCDs', in *Liquid crystals - applications and uses*, Vol. 1, Chapter 13, ed. B. Bahadur (World Scientific, Singapore, 1990).
- 9 D. W. Berreman and W. R. Heffner, 'New bistable cholesteric liquid-crystal display', *Appl. Phys. Lett.*, **37**, 109 (1980).
- 10 T. Tanaka, Y. Sato, A. Inoue, Y. Momose, H. Nomura, and S. Iino, 'A bistable twisted nematic (BTN) LCD driven by a passive-matrix addressing', *Proceedings of Asia Display* **95**, 259 (1995).
- 11 T. Tanaka, Y. Sato, T. Obikawa, H. Nomura, and S. Iino, 'Physical and electro-optical properties of bistable twisted nematic (BTN) LCD', Proceedings of the International Display Research Conference, M-64 (1997).
- 12 T.-Z. Qian, Z.-L. Xie, H.-S. Kwok, and P. Sheng, 'Dynamic flow and switching bistability in nematic liquid crystal cells', *Appl. Phys. Lett.*, **71**, 596 (1997).
- 13 Y. J. Kim, S. M. Park, I. Lee, S. W. Suh, and S. D. Lee, 'Numerical modeling and optical switching characteristics of a bistable TN-LCD', *Proceedings of EuroDisplay* **96**, 337 (1996).
- 14 G. P. Brown, 'Ultra low power bistable LCDs', Proceedings of the International Display Research Conference, 76 (2000).
- 15 G. P. Bryan-Brown, C. V. Brown, J. C. Jones, E. L. Wood, I. C. Sage, and P. Brett, 'Grating aligned bistable nematic device', *SID Symp. Dig. Tech. Pap.*, **28**, 37 (1997).
- 16 R. Barberi and G. Durand, 'Electrically controlled bistable surface switching in nematic liquid crystals', *Appl. Phys. Lett.*, **58**, 2907 (1991).
- 17 R. Barberi, M. Giocondo, and G. Durand, 'Flexoelectrically controlled bistable surface switching in nematic liquid crystals', *Appl. Phys. Lett.*, **60**, 1085 (1992).
- 18 R. Barberi, M. Giocondo, J. Li, and R. Bartolino, 'Fast bistable nematic display with gray scale', *Appl. Phys. Lett.*, **71**, 3495 (1997).
- 19 R. Barberi and G. Durand, 'Controlled textural bistability in nematic liquid crystals', in *Handbook of liquid crystal research*, ed. P. J. Collings and J. S. Patel (Oxford University Press, New York, 1997).
- 20 G. D. Boyd, J. Cheng, and P. D. T. Ngo, 'Liquid-crystal orientational bistability and nematic storage effects', *Appl. Phys. Lett.*, **36**, 556 (1980).
- 21 R. N. Thurston, J. Cheng, and G. D. Boyd, 'Mechanically bistable liquid crystal display structures', *IEEE Trans. Electron Devices*, **ED-27**, 2069 (1980).
- 22 J. Cheng and R. N. Thurston, 'The propagation of disclinations in bistable switching', *J. Appl. Phys.*, **52**, 2766 (1981).
- 23 P. A. Breddels and H. A. van Sprang, 'An analytical expression for the optical threshold in highly twisted nematic systems with nonzero tilt angles at the boundaries', *J. Appl. Phys.*, **58**, 2162 (1985).
- 24 H. A. van Sprang and P. Breddels, 'Numerical calculations of director patterns in highly twisted nematic configurations with nonzero pretilt angles', *J. Appl. Phys.*, **60**, 968 (1986).
- 25 J. C. Kim, G.-J. Choi, Y.-S. Kim, K. H. Kang, T.-H. Yoon, and K. G. Nam, 'Numerical modeling and optical switching characteristics of a bistable TN-LCD', *SID Symp. Dig. Tech. Pap.*, **28**, 33 (1997).
- 26 Z. L. Xie and H. S. Kwok, 'New bistable twisted nematic liquid crystal displays', *J. Appl. Phys. Lett.*, **84**, 77 (1998).
- 27 Z. L. Xie, Y. M. Dong, S. Y. Xu, H. J. Gao, and H. S. Kwok, ' $\pi/2$  and  $5\pi/2$  twisted bistable nematic liquid crystal display', *J. Appl. Phys.*, **87**, 2673 (2000).
- 28 W. H. de Jeu, *Physical properties of liquid crystalline materials* (Gordon and Breach, New York, 1980).
- 29 P. G. de Gennes and J. Prost, *The physics of liquid crystals* (Oxford University Press, New York, 1993).
- 30 D. W. Berreman, 'Liquid-crystal twist cell dynamics with backflow', *J. Appl. Phys.*, **46**, 3746 (1975).
- 31 C. Z. van Doorn, 'Dynamic behaviour of twisted nematic', *J. Appl. Phys.*, **46**, 3738 (1975).
- 32 J. Kelly, S. Jamal, and M. Cui, 'Simulation of the dynamics of twisted nematic devices including flow', *J. Appl. Phys.*, **86**, 4091 (1999).
- 33 I. Dozov, M. Nobili, and G. Durand, 'Fast bistable nematic display using monostable surface switching', *Appl. Phys. Lett.*, **70**, 1179 (1997).

- 34 P. Martinot-Lagrade, I. Dozov, E. Polossat, M. Giocondo, I. Lelidis, and G. Durand, 'Fast bistable nematic display using monostable surface anchoring switching', *SID Symp. Dig. Tech. Pap.*, **28**, 41 (1997).
- 35 S. T. Tang, H. W. Chiu, and H. S. Kwok, 'Optically optimized transmittive and reflective bistable twisted nematic liquid crystal display', *J. Appl. Phys.*, **87**, 632 (2000).
- 36 Z. L. Xie, H. J. Gao, S. Y. Xu, and S. H. Kwok, 'Optimization of reflective bistable nematic liquid crystal displays', *J. Appl. Phys.*, **86**, 2373 (1999).
- 37 H. Cheng and H. Gao, 'Optical properties of reflective bistable twisted nematic liquid crystal display', *J. Appl. Phys.*, **87**, 7476 (2000).
- 38 Z. L. Xie, H. J. Gao, B. Z. Chang, and S. Y. Xu, 'A new BTN LCD with high contrast ratio and large cell gap', *Proceedings of Asia Display* **98**, 303 (1998).
- 39 F. Zhou and D.-K. Yang, 'Analytical solution of film compensated bistable twisted nematic liquid crystal displays', *J. Disp. Technol.*, **1**, 217 (2005).
- 40 G.-D. Lee, K.-H. Park, K.-C. Chang, T.-H. Yoon, J. C. Kim, and E.-S. Lee, 'Optimization of drive scheme for matrix addressing of a bistable twisted nematic LCD', *Proceedings of Asia Display* **98**, 299 (1998).
- 41 T. Tanaka, T. Obikawa, Y. Sato, H. Nomura and S. Iino, 'An advanced driving method for bistable twisted nematic (BTN) LCD', *Proceedings of Asia Display* **98**, 295 (1998).
- 42 E. L. Wood, G. P. Bryan-Brown, P. Brett, A. Graham, J. C. Jones, and J. R. Hughes, 'Zenithal bistable device (ZBD) suitable for portable applications', *SID Symp. Dig. Tech. Pap.*, **31**, 124 (2000).
- 43 G. P. Bryan-Brown, M. J. Towler, M. S. Bancroft, and D. G. McDonnell, 'Bistable nematic alignment using bigratings', *Proceeding of the International Display Research Conference*, 209 (1994).
- 44 L. M. Blinov and V. G. Chigrinov, *Electrooptical effects in liquid crystal materials* (Springer-Verlag, New York, 1994).
- 45 S. Chandrasekhar, *Liquid crystals*, 2nd edn (Cambridge University Press, New York, 1997).
- 46 M. Kleman and O. D. Lavrentovich, *Soft matter physics: Introduction* (Springer-Verlag, New York, 2003).
- 47 O. D. Lavrentovich and D.-K. Yang, 'Cholesteric cellular patterns with electric-field -controlled line tension', *Phys. Rev. E*, **57**, *Rapid Commun.*, R6269 (1998).
- 48 R. B. Meyer, 'Distortion of a cholesteric structure by a magnetic field', *Appl. Phys. Lett.*, **14**, 208 (1969).
- 49 W. Greubel, U. Wolf, and H. Kruger, 'Electric field induced texture changes in certain nematic/cholesteric liquid crystal mixtures', *Mol. Cryst. Liq. Cryst.*, **24**, 103 (1973).
- 50 S.-T. Wu and D.-K. Yang, *Reactive liquid crystal displays* (John Wiley & Sons, Ltd, Chichester, 2001).
- 51 D.-K. Yang, and J. W. Doane, 'Cholesteric liquid crystal/polymer gel dispersions: reflective displays', *SID Symp. Dig. Tech. Pap.*, **23**, 759 (1992).
- 52 Z.-J. Lu, W. D. St. John, X.-Y. Huang, D.-K. Yang, and J. W. Doane, 'Surface modified reflective cholesteric displays', *SID Symp. Dig. Tech. Pap.*, **26**, 172 (1995).
- 53 D.-K. Yang, J. L. West, L. C. Chien, and J. W. Doane, 'Control of the reflectivity and bistability in displays based on cholesteric liquid crystals', *J. Appl. Phys.*, **76**, 1331 (1994).
- 54 D.-K. Yang, X. Y. Huang, and Y.-M. Zhu, 'Bistable cholesteric reflective displays: material and drive schemes', *Annu. Rev. Mater. Sci.*, **27**, 117 (1996).
- 55 J. W. Doane, D.-K. Yang, and Z. Yaniv, 'Front-lit flat panel display from polymer stabilized cholesteric textures', *Proceeding of Japan Display*, **92**, 73 (1992).
- 56 M. H. Lu, H. J. Yuan, and Z. Yaniv, 'Color reflective liquid crystal display', US patent 5,493,430, 1996.
- 57 D.-K. Yang, J. W. Doane, Z. Yaniv, and J. Glasser, 'Cholesteric reflective display: drive scheme and contrast', *Appl. Phys. Lett.*, **65**, 1905 (1994).
- 58 R. Q. Ma and D.-K. Yang, 'Polymer stabilized bistable black-white cholesteric reflective display', *SID Symp. Dig. Tech. Pap.*, **28**, 101 (1997).
- 59 R. Q. Ma and D.-K. Yang, 'Optimization of polymer stabilized bistable black-white cholesteric reflective display', *J. SID*, **7**, 61 (1999).
- 60 X.-Y. Huang, N. Miller, A. Khan, D. Davis, and J. W. Doane, 'Gray scale of bistable reflective cholesteric displays', *SID Symp. Dig. Tech. Pap.*, **29**, 810 (1998).
- 61 M. Xu and D.-K. Yang, 'Optical properties of the gray-scale states of cholesteric reflective displays', *SID Symp. Dig. Tech. Pap.*, **30**, 950 (1999).
- 62 L.-C. Chien, U. Muller, M.-F. Nabor, and J. W. Doane, 'Multicolor reflective cholesteric displays', *SID Symp. Dig. Tech. Pap.*, **26**, 169 (1995).

- 63 F. Vicentini and L.-C. Chien, 'Tunable chiral materials for multicolor reflective cholesteric displays', *Liq. Cryst.*, **24**, 483 (1998).
- 64 D.-K. Yang, Z. J. Lu, L. C. Chien, and J. W. Doane, 'Bistable polymer dispersed cholesteric reflective display', *SID Symp. Dig. Tech. Pap.*, **34**, 959 (2003).
- 65 K. Hashimoto, M. Okada, K. Nishiguchi, N. Masazumi, E. Yamakawa, and T. Taniguchi, 'Reflective color display using cholesteric liquid crystals', *SID Symp. Dig. Tech. Pap.*, **29**, 897 (1998).
- 66 D. Davis, A. Kahn, X.-Y. Huang, and J. W. Doane, 'Eight-color high-resolution reflective cholesteric LCDs', *SID Symp. Dig. Tech. Pap.*, **29**, 901 (1998).
- 67 J. L. West and V. Bodnar, 'Optimization of stacks of reflective cholesteric films for full color displays', *Proceedings of the 5th Asian Symposium on Information Display*, 29 (1999).
- 68 D. Davis, K. Hoke, A. Khan, C. Jones, X. Y. Huang, and J. W. Doane, 'Multiple color high resolution reflective cholesteric liquid crystal displays', *Proceedings of the International Display Research Conference*, 242 (1997).
- 69 T. Schneider, F. Nicholson, A. Kahn, and J. W. Doane, 'Flexible encapsulated cholesteric LCDs by polymerization induced phase separation', *SID Symp. Dig. Tech. Pap.*, **36**, 1568 (2005).
- 70 I. Shiyonovskaya, S. Green, G. Magyar, and J. W. Doane, 'Single substrate encapsulated cholesteric LCDs: coatable, drapable and foldable', *SID Symp. Dig. Tech. Pap.*, **36**, 1556 (2005).
- 71 S. W. Stephenson, D. M. Johnson, J. I. Kilburn, X.-D. Mi, C. M. Rankin, and R. G. Capurso, 'Development of a flexible electronic display using photographic technology', *SID Symp. Dig. Tech. Pap.*, **35**, 774 (2004).
- 72 G. T. McCollough, C. M. Johnson, and M. L. Weiner, 'Roll-to-roll manufacturing considerations for flexible, cholesteric liquid crystal (ChLC) display media', *SID Symp. Dig. Tech. Pap.*, **36**, 64 (2005).
- 73 N. Hiji, T. Kakinuma, M. Araki, and Y. Hikichi, 'Cholesteric liquid crystal micro-capsules with perpendicular alignment shell for photo-addressable electronic paper', *SID Symp. Dig. Tech. Pap.*, **36**, 1560 (2005).
- 74 W. Helfrich, 'Deformation of cholesteric liquid crystals with low threshold voltage', *Appl. Phys. Lett.*, **17**, 531 (1970).
- 75 J. P. Hurault, 'Static distortations of a cholesteric planar structure induced by magnetic or ac electric fields', *J. Chem. Phys.*, **59**, 2068 (1973).
- 76 D.-K. Yang and Z.-J. Lu, 'Switching mechanism of bistable cholesteric reflective displays', *SID Symp. Dig. Tech. Pap.*, **26**, 351 (1995).
- 77 M. Kawachi, O. Kogure, S. Yosji, and Y. Kato, 'Field-induced nematic-cholesteric relaxation in a small angle wedge', *Jpn. J. Appl. Phys.*, **14**, 1063 (1975).
- 78 P. Watson, J. E. Anderson, V. Sergan, and P. J. Bos, 'The transition mechanism of the transient planar to planar director configuration change in cholesteric liquid crystal displays', *Liq. Cryst.*, **26**, 1307 (1999).
- 79 J. Gandhi, D.-K. Yang, X.-Y. Huang, and N. Miller, 'Gray scale drive schemes for bistable cholesteric reflective displays', *Proceedings of Asia Display* **98**, 127 (1998).
- 80 X.-Y. Huang, D.-K. Yang, P. Bos, and J. W. Doane, 'Dynamic drive for bistable reflective cholesteric displays: a rapid addressing scheme', *SID Symp. Dig. Tech. Pap.*, **26**, 347 (1995).
- 81 X.-Y. Huang, D.-K. Yang, and J. W. Doane, 'Transient dielectric study of bistable reflective cholesteric displays and design of rapid drive scheme', *Appl. Phys. Lett.*, **69**, 1211 (1995).

# 11

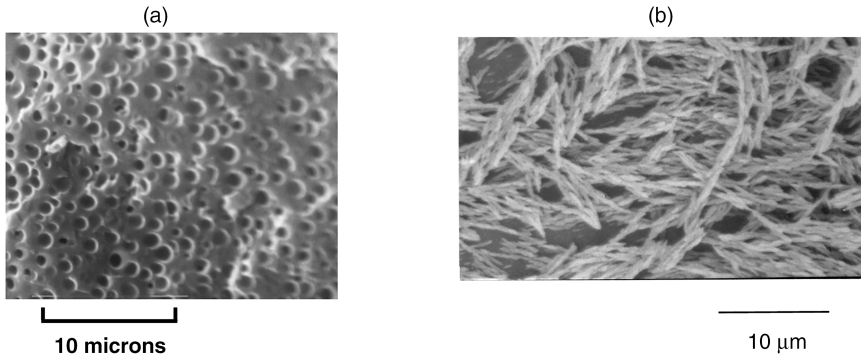
## Liquid Crystal/Polymer Composites

### 11.1 Introduction

Liquid crystal/polymer composites (LCPCs) are a relatively new class of materials for use in displays, light shutters, optical fiber telecommunications, and switchable windows [1–5]. They consist of low-molecular-weight liquid crystals and high-molecular-weight polymers, which are phase separated. According to the morphology, LCPCs can be divided into two sub-groups: polymer-dispersed liquid crystals (PDLCs) and polymer-stabilized liquid crystals (PSLCs). In a PDLC, the liquid crystal exists in the form of micron- and submicron-size droplets which are dispersed in the polymer binder. The concentration of the polymer is comparable to that of the liquid crystal. The polymer forms a continuous medium, but the liquid crystal droplets are isolated from one another. A scanning electron microscope (SEM) picture of a PDLC sample is shown in Figure 11.1(a). In a PSLC, the polymer forms a sponge-like structure. The concentration of the liquid crystal is much higher than that of the polymer. The liquid crystal forms a continuous medium. A SEM picture of a PSLC is shown in Figure 11.1(b). LCPCs can also be divided into two sub-groups according to the application: scattering device and non-scattering device. In a scattering device, the polymer produces or helps to produce a poly-domain structure of the liquid crystal in one field condition. The domain size is comparable to the wavelength of the light to be scattered. The material is highly scattering because of the large birefringence of the liquid crystal. In another field condition the liquid crystal is aligned unidirectionally along the applied field and the material becomes transparent. Two scattering devices from LCPCs are shown in Figure 11.2(a) and (b). In a non-scattering device, the liquid crystal is used to stabilize states of the liquid crystal.

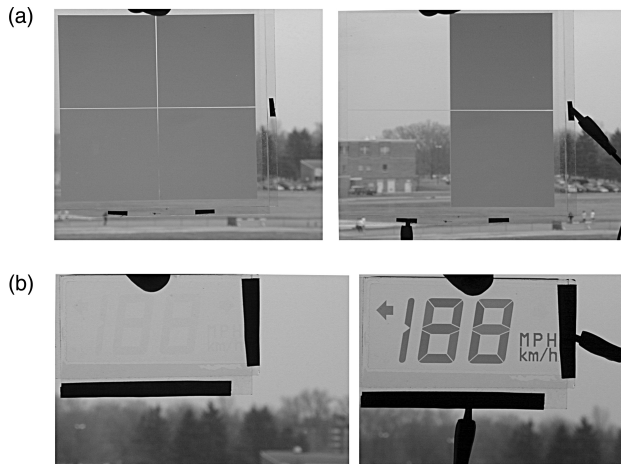
### 11.2 Phase Separation

LCPCs are phase-separated systems. In order to understand the phase separation involved, we will first discuss the basics of phase separation. Composites (or mixtures) have two or more components.



**Figure 11.1** (a) SEM picture of a PDLC. It was taken after the PDLC sample was fractured and the liquid crystal was extracted. The dark circles correspond to the liquid crystal droplets. (b) SEM picture of a PSLC. The picture was taken after the cell was split and the liquid crystal was extracted

They can be divided into two classes: homogeneous mixture and heterogeneous mixture. In a homogeneous mixture, the constituents are mixed on an atomic (or molecular) scale to form a single phase. Conversely, a heterogeneous mixture contains two or more distinct phases. Whether a composite forms a homogeneous single phase or phase separates to form a heterogeneous mixture is determined by the free energy. If the homogeneous mixture has a lower free energy than the heterogeneous mixture, the composite is in the homogeneous phase. If the heterogeneous mixture has a lower free energy than the homogeneous mixture, the composite is in the heterogeneous phase. The mixing free energy  $F_m$  is defined as the free energy  $F_{\text{homo}}$  of the homogeneous mixture minus the free energy  $F_{\text{hetero}}$  of the completely phase separated system, namely,  $F_m = F_{\text{homo}} - F_{\text{hetero}}$ . Phase separation depends on the details of the curve of the mixing free energy as a function of concentrations of the components.



**Figure 11.2** (a) Photo of the light shutter from polymer-stabilized cholesteric texture (PSCT) normal material. (b) Photo of the display from PSCT reverse-mode material

### 11.2.1 Binary mixture

The simplest mixture is a binary mixture that has two components A and B. In order to understand phase separation in this system, we consider its mixing free energy which is composed of two parts, mixing interaction energy  $U_m$  and mixing entropy  $S_m$ :

$$F_m = U_m - TS_m \quad (11.1)$$

where  $T$  is the temperature. The mixing interaction energy is the interaction energy of the homogeneous mixture minus the interaction energy of the completely phase-separated heterogeneous mixture. In the calculation of the mixing interaction energy, we assume that the molecules only interact with their nearest neighbor molecules. The interaction energies are  $u_{AA}$  for the interaction between A and A,  $u_{BB}$  for the interaction between B and B, and  $u_{AB}$  for the interaction between A and B. The total number of particles of the system is  $N$ , among which the total number of A particles is  $N_A$  and the total number of B particles is  $N_B$ . The molar fraction of component B is  $x_B = x = N_B/N$  and the molar fraction of component A is  $x_A = 1 - x = N_A/N$ . The number of nearest neighbors is  $P$ . In the homogeneous phase, among the nearest neighbors, the average number of A particles is  $(1 - x)P$  and the average number of B particles is  $xP$ . The total interaction energy of the homogeneous mixture is [6]

$$\begin{aligned} U_{\text{homo}} &= \frac{1}{2} \{ N_A [(1 - x)Pu_{AA} + xPu_{AB}] + N_B [(1 - x)Pu_{AB} + xPu_{BB}] \} \\ &= \frac{N}{2} P \{ (1 - x)[(1 - x)u_{AA} + xu_{AB}] + x[(1 - x)u_{AB} + xu_{BB}] \} \end{aligned} \quad (11.2)$$

where the factor 1/2 is used to take care of double counting the interaction energy. When the components are completely phase separated, the total interaction energy is

$$U_{\text{hetero}} = \frac{1}{2} N_A P u_{AA} + \frac{1}{2} N_B P u_{BB} = \frac{1}{2} NP [(1 - x)u_{AA} + xu_{BB}] \quad (11.3)$$

Therefore

$$U_m = U_{\text{homo}} - U_{\text{hetero}} = \frac{1}{2} PNx(1 - x)(2u_{AB} - u_{AA} - u_{BB}) \quad (11.4)$$

The average mixing interaction energy per particle is

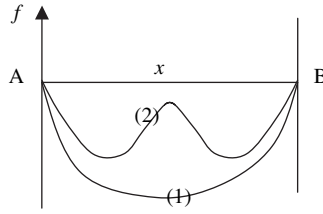
$$u_m = \frac{U_m}{N} = \frac{1}{2} Px(1 - x)(2u_{AB} - u_{AA} - u_{BB}) \quad (11.5)$$

Now we consider the mixing entropy. Imagine putting the  $N_A$  A particles and  $N_B$  B particles into a lattice with  $N = N_A + N_B$  lattice sites. The number of distinct states (arrangements of the particles) is [6]

$$G = \frac{N!}{N_A!N_B!} = \frac{N!}{(N - N_B)!N_B!} \quad (11.6)$$

When the system is completely phase separated, the number of states is close to one. Therefore the mixing entropy is

$$S_m = k_B \ln G - k_B \ln 1 = k_B [\ln N! - \ln N_B! - \ln(N - N_B)!] \quad (11.7)$$



**Figure 11.3** Schematic diagram showing the mixing free energy  $f$  as a function of the fraction  $x$  at two temperatures

For a macroscopic system,  $N \gg 1$ ,  $N_A \gg 1$ , and  $N_B \gg 1$ . Using the Sterling approximation that  $\ln N! = N(\ln N - 1)$ , Equation (11.7) becomes

$$S_m = -Nk_B[(1-x)\ln(1-x) + x\ln x] \quad (11.8)$$

The mixing entropy per particle is

$$s_m = -k_B(1-x)\ln(1-x) - k_Bx\ln x \quad (11.9)$$

The mixing free energy per particle is

$$f_m = u_m - Ts_m = ax(1-x) + k_B T[(1-x)\ln(1-x) - x\ln x] \quad (11.10)$$

where  $a = \frac{1}{2}P(2u_{AB} - u_{AA} - u_{BB})$ . In future discussions, the subscript  $m$  is omitted and when we say the free energy, we mean the mixing free energy. The entropic part of the mixing free energy is always negative and therefore always favors mixing. If the mixing interaction energy is negative, then the mixing free energy is negative and the system will be in the homogeneous phase. If the mixing interaction energy is positive, we have to look at the details of the  $f$  vs.  $x$  curve in order to see whether the system will phase separate or not. From Equation (11.10) we have

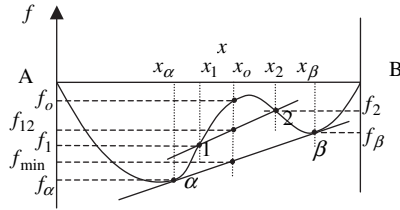
$$\frac{\partial^2 f}{\partial x^2} = -a + k_B T \left( \frac{1}{x} + \frac{1}{1-x} \right) \quad (11.11)$$

The second-order derivative has a minimum value at  $x = 0.5$ , which is  $(\partial^2 f / \partial x^2)_{\min} = -a + 4k_B T$ . When the temperature  $T$  is greater than  $a/4k_B$ , the second-order derivative is positive at any fraction  $x$ . The  $f$  vs.  $x$  curve is shown by curve (1) in Figure 11.3. The system is in the homogeneous phase. When the temperature  $T$  is less than  $a/4k_B$ ,  $\partial^2 f / \partial x^2 < 0$  in some region. The  $f$  vs.  $x$  curve is shown by curve (2). We will show that in this case the system phase separates into an A-rich phase (more A particles in the phase) and a B-rich phase (more B particle in the phase). We say the system is partially mixing.

Now we examine the partial mixing case in more detail. Consider a mixture with  $N$  particles and the fraction (of B particles)  $x_o$ . The number of A particles in the mixture is  $N_A = (1-x)N$  and the number of B particles in the mixture is  $N_B = xN$ . Its free energy per particle of the homogeneous mixture is  $f_o$  as shown in Figure 11.4. Assume that it phase separates into two new phases: phase 1 with the fraction  $x_1$  and phase 2 with the fraction  $x_2$ .  $N_1$  particles are in phase 1 and  $N_2$  particles are in phase 2. Because of the conservation of particles, we have

$$N_A = (1-x_o)N = (1-x_1)N_1 + (1-x_2)N_2 \quad (11.12)$$

$$N_B = x_o N = x_1 N_1 + x_2 N_2 \quad (11.13)$$



**Figure 11.4** Schematic diagram showing how the mixing free energy  $f$  changes in the phase separation

Solving these two equations, we have

$$N_1 = \frac{(x_2 - x_o)}{(x_2 - x_1)} N \quad (11.14)$$

$$N_2 = \frac{(x_o - x_1)}{(x_2 - x_1)} N \quad (11.15)$$

The average free energy per particle after phase separation is

$$f_{12} = \frac{1}{N} [N_1 f_1 + N_2 f_2] = f_1 + \frac{(x_2 - x_o)}{(x_2 - x_1)} (f_2 - f_1) \quad (11.16)$$

which is the free energy value of the intersection point of the straight line  $\overline{12}$  and the vertical line at  $x_o$ . It can be seen from the figure that  $f_{12}$  is lower than  $f_o$ . Therefore the phase separation can take place. It can also be seen that the free energy can even be lowered further if the mixture phase separates into phase  $\alpha$  and phase  $\beta$ . Points  $\alpha$  and  $\beta$  are the tangential points of the straight line  $\alpha\beta$  to the free energy curve [6]. Now the average free energy per particle after the mixture phase separating into phases  $\alpha$  and  $\beta$  is

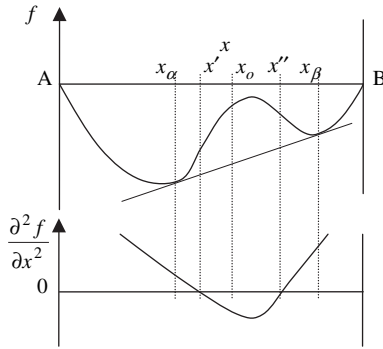
$$f_{\min} = f_\alpha + \frac{(x_\beta - x_o)}{(x_\beta - x_\alpha)} (f_\beta - f_\alpha) \quad (11.17)$$

Therefore, if  $x_\alpha < x < x_\beta$ , the single homogeneous phase is not stable and the mixture phase separates into phase  $\alpha$  and phase  $\beta$ . If  $0 < x < x_\alpha$  and  $x_\beta < x < 1$ , the free energy increases if the mixture phase separates, and therefore the mixture does not phase separate and the single homogeneous phase with the initial fraction is stable.

The criterion to determine partial phase separation is the second-order derivative of the free energy with respect to the concentration. If  $\partial^2 f / \partial x^2 > 0$  for any  $x$ , it is impossible to draw a straight line that is tangential to the free energy curve at two points, and there is no phase separation. If  $\partial^2 f / \partial x^2 < 0$  in some region, the free energy curve must have a local maximum at a fraction within this region, and it is possible to draw a straight line tangential to the free energy curve at  $x_\alpha$  and  $x_\beta$ . The single homogeneous phase is not stable in the region  $(x_\alpha, x_\beta)$  and phase separation will take place.

We next discuss how the mixing free energy changes as phase separation is taking place. Consider a composite with the initial fraction  $x_o$ ; before phase separation, the free energy is  $f_o = f(x_o)$ . As shown in Figure 11.5, if  $x_o$  is in the region  $(x_\alpha, x_\beta)$ , the homogeneous phase is not stable and the system phase separates into two phases: phase 1 with the fraction  $x_1 = x_o - \Delta x_1$  and phase 2 with the fraction  $x_2 = x_o + \Delta x_2$ . When the phase separation just begins to take place,  $\Delta x_1$  and  $\Delta x_2$  are





**Figure 11.5** Schematic diagram showing how the mixing free energy  $f$  changes as phase separation takes place

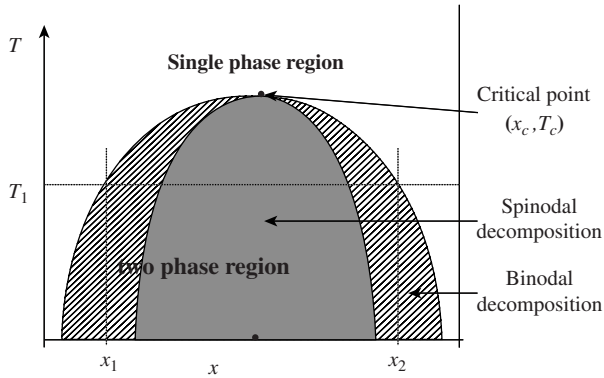
very small. Because of particle conservation, the percentage of the material in phase 1 is  $[\Delta x_2/(\Delta x_1 + \Delta x_2)]$  and the percentage of the material in phase 2 is  $[\Delta x_1/(\Delta x_1 + \Delta x_2)]$ . The change of the free energy is (keeping up to second-order terms)

$$\begin{aligned} \Delta f &= \frac{\Delta x_2}{(\Delta x_1 + \Delta x_2)} f(x_0 - \Delta x_1) + \frac{\Delta x_1}{(\Delta x_1 + \Delta x_2)} f(x_0 + \Delta x_2) - f(x_0) \\ \Delta f &= \frac{\Delta x_2}{(\Delta x_1 + \Delta x_2)} \left[ f(x_0) + \left. \frac{\partial f}{\partial x} \right|_{x_0} (-\Delta x_1) + \left. \frac{1}{2} \frac{\partial^2 f}{\partial x^2} \right|_{x_0} (-\Delta x_1)^2 \right] \\ &\quad + \frac{\Delta x_1}{(\Delta x_1 + \Delta x_2)} \left[ f(x_0) + \left. \frac{\partial f}{\partial x} \right|_{x_0} (\Delta x_2) + \left. \frac{1}{2} \frac{\partial^2 f}{\partial x^2} \right|_{x_0} (\Delta x_2)^2 \right] - f(x_0) \\ \Delta f &= \frac{1}{2} \Delta x_1 \Delta x_2 \left. \frac{\partial^2 f}{\partial x^2} \right|_{x_0} \end{aligned} \tag{11.18}$$

There are two types of phase separation in the region  $(x_\alpha, x_\beta)$ . When  $x' < x_0 < x''$ ,  $\partial^2 f / \partial x^2 < 0$ , the free energy decreases as phase separation takes place. The phase separation is known as the spinodal phase separation. When the phase separation occurs simultaneously throughout the system, it is referred to as the homogeneous transition. When  $x_\alpha < x_0 < x'$  or  $x'' < x_0 < x_\beta$ ,  $\partial^2 f / \partial x^2 > 0$ , the free energy increases in the initial stage of the phase separation process, which means there is an energy barrier against the transition. The phase separation is known as the binodal phase separation. When the deviation of the fractions of the phase-separated phases from the initial fraction is sufficiently large, the free energy will then decrease. In the phase separation, nucleation seeds are required to overcome the energy barrier, referred to as the nucleation transition.

### 11.2.2 Phase diagram and thermally induced phase separation

As mentioned earlier, the free energy of a binary mixture depends on the temperature. Therefore the phase separation also depends on the temperature. The phase diagram of a binary composite is shown in Figure 11.6. At low temperatures, the entropy term of the free energy does not contribute much to the free energy;  $\partial^2 f / \partial x^2 < 0$  for fraction  $x$  in some region. The free energy is lowered when the system phase separates into two phases. For example, when the temperature is  $T_1$ , the system phase separates into phase 1 with the fraction  $x_1$  and phase 2 with the fraction  $x_2$ . The fractions  $x_1$  and  $x_2$  are the values of the intersection points of the horizontal line at  $T_1$ , referred to as the *tie line*, with the



**Figure 11.6** Phase diagram of the binary composite

phase boundary of the two phase regions. As the temperature is increased, the entropy term plays a more important role which tends to make the system homogeneously mixing. The two-phase region becomes narrower. The summit point  $(x_c, T_c)$  of the phase boundary curve is the critical point. At this temperature, the minimum value of the second-order derivative becomes zero.

$$\frac{\partial^2 f}{\partial x^2} = 0 \quad (11.19)$$

Because the second-order derivative has a minimum value at the critical point, we have

$$\frac{\partial}{\partial x} \left( \frac{\partial^2 f}{\partial x^2} \right) = \frac{\partial^3 f}{\partial x^3} = 0 \quad (11.20)$$

Equation (11.20) gives the location where the second-order derivative has a minimum. Equation (11.19) means the minimum of the second-order derivative is zero. When the temperature is above  $T_c$ ,  $\partial^2 f / \partial x^2 > 0$  for any fraction  $x$ . The system is in a single phase where the components are homogeneously mixed. When the temperature is decreased from the single phase region into the two-phase region, the system transforms from single phase into two phases. This method can be used to produce phase separation in LCPCs, which is referred to as *thermally induced phase separation (TIPS)* [3, 7].

TIPS is used to make PDLCs. For example, 50% thermoplastic poly methyl methacrylate (PMMA) is mixed with 50% nematic liquid crystal E7 (from Merck). The glass transition temperature of PMMA is 105°C and the isotropic-nematic phase transition (the clearing point) temperature is 60.5°C. The materials can be uniformly mixed initially with the help of a common solvent, such as chloroform, in a bottle (more details will be given in the section on solvent-induced phase separation). Spacers can be added to help achieve uniform thickness of the PDLC film when the material is later sandwiched between two substrates. After mixing, the material is cast on a substrate and the solvent is allowed to evaporate in an open space. After evaporation of the chloroform, a cover glass is put on top of the PDLC. Pressure can be applied on the substrates to obtain uniform PDLC film thickness. At high temperature ( $> 70^\circ\text{C}$ ), the mixture is in a single homogeneous isotropic phase and the film appears clear. At room temperature, the liquid crystal phase separates from the thermoplastic to form droplets and the film is opaque. The droplet size can be controlled by the cooling rate with a smaller droplet formed at a faster cooling rate. TIPS is rarely used in manufacturing large-area PDLC films because it is difficult to achieve uniform thickness. It is, however, very useful in scientific investigations because PDLCs from thermal plastics can be

thermally cycled many times. Different droplet sizes can be obtained in one sample using different cooling rates. It should be noted that phase separation in LCPCs is complicated because of the involvement of mesophases.

11.2.3 Polymerization-induced phase separation

The mixing entropy given by Equation (11.9) is only valid when both components of the binary composite are small molecules. When one (or both) of the components is a polymer, the number of distinct states decreases because of the constraint that consecutive monomers in a polymer chain must be in the neighboring lattice sites. Therefore the mixing entropy decreases [8].

We consider a system consisting of a polymer and a solvent (a low-molecular-weight molecule such as liquid crystal). There are  $n$  polymer molecules and  $m$  solvent molecules. The degree of polymerization (number of monomers) of the polymer is  $x$ . One solvent molecule and one monomer of the polymer occupy the same volume. We calculate the number of distinct configurations of the system, from which the mixing entropy can be calculated. Imagine putting the polymer and solvent molecules into a lattice with  $N = nx + m$  lattice sites.  $Z$  is the number of nearest neighbors in the lattice. The polymer molecules are put into the lattice one by one. When the  $(i + 1)$ th polymer molecule is put into the lattice, the first monomer of the polymer can be put into one of the  $N - ix$  lattice sites, because  $ix$  lattice sites have been occupied by the first  $i$  polymer molecules. Therefore the number of ways to put the monomer into the lattice is  $N - ix$ . The second monomer can only be put into one of the  $Z$  nearest neighbor lattice sites of the first monomer as shown in Figure 11.7. These lattice sites, however, may have been occupied by the first  $i$  polymer molecules. The number of lattice sites occupied by the first  $i$  polymers and the first monomer of the  $(i + 1)$ th polymer is  $(ix + 1)$ . The probability that a lattice site is not occupied is  $(N - ix - 1)/N$ . Therefore the average number of ways to put the second monomer into the lattice is  $Z[(N - ix)/N]$ . The third monomer can only be placed on the nearest neighbor lattice sites of the second monomer. One of these nearest neighbor sites is occupied by the first monomer. Now the probability that a lattice site is not occupied is  $(N - ix - 2)/N$ . Therefore the number of ways to put the third monomer into the lattice is  $(Z - 1)[(N - ix - 2)/N]$ . In such a way the remaining monomers of the  $(i + 1)$ th polymer can be put into the lattice. The number of ways to put the  $(i + 1)$ th polymer into the lattice is

$$\begin{aligned} \Omega_{i+1} &= \frac{1}{2}[(N - ix)] \cdot \left[ Z \frac{(N - ix - 1)}{N} \right] \cdot \left[ (Z - 1) \frac{(N - ix - 2)}{N} \right] \dots \cdot \left\{ (Z - 1) \frac{[N - (i + 1)x + 1]}{N} \right\} \\ &= \frac{1}{2N} \left( \frac{Z - 1}{N} \right)^{x-2} \frac{(N - ix)!}{(N - ix - x)!} \end{aligned} \tag{11.21}$$

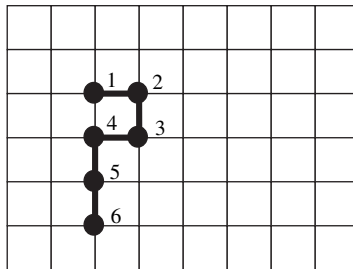


Figure 11.7 Schematic diagram showing how to put a polymer molecule into the lattice

where the factor  $1/2$  takes care of the fact that any of the two end monomers can be chosen as the first monomer. The number of ways to put the  $n$  polymer molecules into the lattice is

$$\begin{aligned}
 G &= \frac{1}{n!} \prod_{i=1}^n \Omega_i = \frac{1}{n!} \left[ \frac{Z}{2N} \cdot \left( \frac{Z-1}{N} \right)^{x-2} \right]^n \frac{N!}{(N-x)!} \cdot \frac{(N-x)!}{(N-2x)!} \cdot \frac{(N-2x)!}{(N-3x)!} \cdots \frac{[N-(n-1)x]!}{[N-nx]!} \\
 &= \frac{1}{n!} \left[ \frac{Z}{2N} \cdot \left( \frac{Z-1}{N} \right)^{x-2} \right]^n \frac{N!}{(N-nx)!} = \frac{1}{n!} \left[ \frac{Z}{2N} \cdot \left( \frac{Z-1}{N} \right)^{x-2} \right]^n \frac{N!}{m!} \\
 &= \frac{1}{n!} \left[ \frac{Z}{2N} \cdot \left( \frac{Z-1}{N} \right)^{x-2} \right]^n \frac{N!}{m!} \tag{11.22}
 \end{aligned}$$

where the factor  $1/n!$  takes care of the fact that the polymer molecules are not distinguishable. Because the solvent molecules are also not distinguishable, there is only one way to put them into the lattice sites not occupied by the polymer molecules. Therefore the number of distinct configurations is  $G$ . When the polymer and solvent are completely phase separated, the number of distinct configurations of the  $n$  polymer molecules is (equivalently, putting the polymer molecules into a lattice with  $nx$  lattice sites)

$$G_o = \frac{1}{n!} \left[ \frac{Z}{2(nx)} \cdot \left( \frac{Z-1}{nx} \right)^{x-2} \right]^n \frac{(nx)!}{0!} \tag{11.23}$$

The total mixing entropy is

$$\begin{aligned}
 \Delta S_m &= k_B \ln G - k_B \ln G_o \\
 &= k_B \ln \left[ \frac{N^{-n(x-1)} N!}{m!} \right] - k_B \ln [(nx)^{-n(x-1)} (nx)!] \\
 &= k_B \left[ -n \ln \left( \frac{nx}{N} \right) - m \ln \left( \frac{m}{N} \right) \right] \tag{11.24}
 \end{aligned}$$

The volume fractions of the polymer and solvent are  $\phi_n = nx/N = nx/(m+nx) \equiv \phi$  and  $\phi_m = m/N = m/(m+nx) = 1 - \phi$ , respectively. Therefore the total mixing entropy is [8–10]

$$\Delta S_m = -k_B N \left[ \frac{\phi}{x} \ln \phi + (1 - \phi) \ln(1 - \phi) \right] \tag{11.25}$$

The mixing entropy per particle is

$$\Delta s_m = -k_B \left[ \frac{\phi}{x} \ln \phi + (1 - \phi) \ln(1 - \phi) \right] \tag{11.26}$$

The mixing interaction energy per particle is (see Equation (11.5))

$$\Delta u_m = \frac{1}{2} Z \phi (1 - \phi) (2u_{nm} - u_{nn} - u_{mm}) \tag{11.27}$$

where  $u_{nm}$  is the interaction energy between two monomers,  $u_{mm}$  is the interaction energy between two solvent molecules, and  $u_{nm}$  is the interaction energy between a monomer and a solvent molecule. The

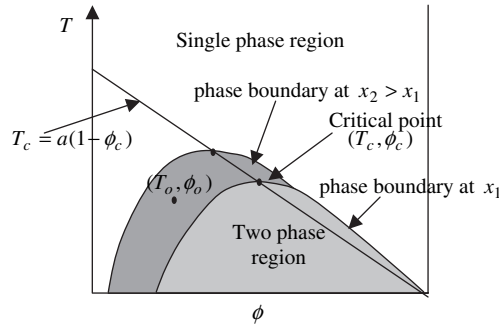


Figure 11.8 Phase diagram of the polymer/liquid crystal system

mixing free energy is

$$f = \Delta u_m - T\Delta s_m = k_B T \left[ \frac{Q}{T} \phi(1 - \phi) + (1 - \phi) \ln(1 - \phi) + \frac{\phi}{x} \ln \phi \right] \quad (11.28)$$

where  $Q = Z(2u_{nm} - u_{nn} - u_{mm})/2k_B$ . This equation is known as the Flory–Huggins equation. The phase diagram of a polymer/liquid crystal system is shown in Figure 11.8. At high temperatures, the entropy dominates in the free energy and the system is in a homogeneous phase. At low temperatures, the mixing entropy cannot compensate for the mixing interaction energy, and the system phase separates into two phases. The summit point of the phase boundary between the single phase region and the two-phase region is the critical point. Thus the critical point  $(T_c, \phi_c)$  is an indication of the phase boundary is. The critical point can be calculated by using Equations (11.19) and (11.20):

$$\left. \frac{\partial^2(f/k_B T)}{\partial \phi^2} \right|_{\phi_c, T_c} = \frac{1}{1 - \phi_c} + \frac{1}{x\phi_c} - 2\frac{Q}{T_c} = 0 \quad (11.29)$$

$$\left. \frac{\partial^3(f/k_B T)}{\partial \phi^3} \right|_{\phi_c, T_c} = \frac{1}{(1 - \phi_c)^2} - \frac{1}{x\phi_c^2} = 0 \quad (11.30)$$

From these two equations we have

$$\phi_c = \frac{1}{1 + \sqrt{x}} \quad (11.31)$$

$$T_c = 2Q \cdot \frac{x}{(1 + \sqrt{x})^2} \quad (11.32)$$

For large  $x (\gg 1)$ ,  $\phi_c = 1/\sqrt{x}$ ,  $T_c = 2Q(1 - 2\sqrt{x}) = 2Q(1 - 2\phi_c)$ . With increasing degree of polymerization  $x$ , the critical volume fraction of the polymer decreases and the critical temperature increases, which indicates that the phase boundary moves upward and the two-phase region becomes larger. For example, consider a system with polymer fraction  $\phi_o$  at temperature  $T_o$  as shown in Figure 11.8. Initially the degree of polymerization is  $x_1$  which is low. The mixing entropy is large. The system is in the homogeneous single phase. As the polymerization takes place, the degree of

polymerization increases, and the entropy decreases. The two-phase region expands. When the degree of polymerization becomes  $x_2$ , the point  $(T_o, \phi_o)$  is now in the two-phase region. The liquid crystal and the polymer phase separate. This method can be used to produce phase separation in LCPCs, and is referred to as *polymerization-induced phase separation* (PIPS) [7]. The size of the liquid crystal droplets formed in this method depends on the polymerization rate. Under a faster polymerization rate, smaller droplets are formed.

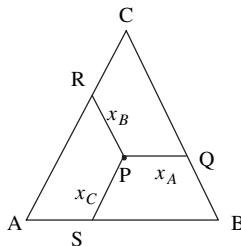
This method, especially with photopolymerization, is suitable for large-volume manufacture. In photopolymerization, monomers with acrylate or methylacrylate end groups, which have a double bond, are used. Some photo-initiators are also added. Upon absorbing a photon, the photo-initiator becomes a free radical which reacts with the acrylate group. The opened double bond reacts with another acrylate group. The chain reaction propagates until the opened double bond reacts with another free radical or open double bond, and then the polymerization stops. As an example, Norland 66 (which is a combination of acrylate monomers and photo-initiators) and E7 (EM Chemicals) are mixed in the ratio 1:1. The mixture is sandwiched between two substrates with electrodes and then cured under the irradiation of UV light of a few milliwatts per square centimeter. The polymerization rate is determined by the photo-initiator concentration and UV intensity. Smaller droplets are formed under higher UV irradiation or higher photo-initiator concentrations.

#### 11.2.4 Solvent-induced phase separation

It is difficult to mix liquid crystals directly with polymers because polymers are usually in solid state at room temperature. A solvent can be added to mix liquid crystals with polymers. We now consider phase separation in ternary mixtures with three components: liquid crystal (A), polymer (B), and solvent (C). We consider only the case where components A and B are immiscible in some region or fraction. Components A and C are miscible in any proportion and components B and C are also miscible in any proportion.

A ternary mixture is specified by the three fractions  $x_A$ ,  $x_B$ , and  $x_C$  of the three components A, B, and C. Because  $x_A + x_B + x_C = 1$ , only the fractions of two of the components have to be specified. Therefore a ternary mixture is represented by a point on a 2-D surface. The common way to represent ternary mixtures is the *equilateral triangle diagram*, as shown in Figure 11.9. The length of the three sides AB, BC, and AC of the triangle is one. The three corners A, B and C correspond to the three components. For a composite represented by a point P in the triangle, the fraction of a component is equal to the length of the line drawn from P to the side opposite to the corner representing the component, which is parallel to one of the sides from the corner. The fraction of A is  $PQ = x_A$ , the fraction of B is  $PR = x_B$  and the fraction of C is  $PS = x_C$ . It can be shown from geometry that  $x_A + x_B + x_C = 1$ . The equilateral triangle diagram has the following properties:

(1) All the points on a line drawn from one corner of the triangle to the opposite side represent the composites in which the relative fractions of the two components represented by the other two corners remain unchanged.



**Figure 11.9** Equilateral triangle representation of a ternary mixture

(2) When a mixture represented by point P phase separates into two phases represented by points U and V, the three points, P, U, and V, lie on a straight line and point P is between points U and V. The percentages of the material in the phases V and U are equal to  $PU/UV$  and  $PV/UV$ , respectively.

The mixing free energy of a ternary mixture is given by

$$f = \frac{1}{2}p[x_Ax_B(2u_{AB} - u_{AA} - u_{BB}) + x_Ax_C(2u_{AC} - u_{AA} - u_{CC}) + x_Bx_C(2u_{BC} - u_{BB} - u_{CC})] + k_B T[x_A \ln x_A + x_C \ln x_B + x_C \ln x_C] \tag{11.33}$$

where  $u_{AA}$  is the interaction energy between A and A,  $u_{BB}$  is the interaction energy between B and B,  $u_{CC}$  is the interaction energy between C and C,  $u_{AB}$  is the interaction energy between A and B,  $u_{AC}$  is the interaction energy between A and C,  $u_{BC}$  is the interaction energy between B and C, and  $p$  is the number of nearest neighbors. We consider the case where  $(2u_{AB} - u_{AA} - u_{BB}) > 0$ ,  $(2u_{AC} - u_{AA} - u_{CC}) < 0$ , and  $(2u_{BC} - u_{BB} - u_{CC}) < 0$ . When  $x_C$  is large,  $\Delta u_m < 0$ , the three components are homogeneously mixed. When  $x_C$  becomes small,  $\Delta u_m$  becomes positive. At sufficiently low temperatures, the system phase separates into two phases. The phase diagram is shown in Figure 11.10. For a composite, represented by point P, in the two-phase region, it will phase separate into two phases represented by points U and V which are the intersection points of a straight line, referred to as the tie line, with the phase boundary of the two-phase region. Point P lies on the straight line UV. UV is not necessarily parallel to AB and in this case the critical point T does not coincide with the summit point W. If the initial composite has a high fraction of the solvent, it is in the homogeneous single phase, say, it is represented by point I. When the solvent is allowed to evaporate, the point representing the composite moves along the straight line CI toward the side AB, because the ratio between the fractions of the liquid crystal and polymer is fixed. When the fraction of the solvent becomes sufficiently low, the representing point moves across the two-phase region boundary at point F into the two-phase region; the system will phase separate into two phases. This method is also used to make PDLCs and is referred to as *solvent-induced phase separation* (SIPS). The droplet size can be controlled by the solvent evaporation rate with smaller droplets formed at higher evaporation rates.

For example, 5% nematic liquid crystal E7 (Merck), 5% PMMA, and 90% chloroform are put into a closed bottle to mix. Then the homogeneous mixture, which is clear in appearance, is cast on a glass plate. The glass plate is put into a chamber with inject and vent holes. Air is blown into the chamber and then vented out at controlled rates. After a sufficient amount of chloroform has evaporated, the material changes to opaque when liquid crystal droplets begin to form. After all the chloroform has evaporated, another glass plate is put on top of the first glass plate to sandwich the PDLC. In practice, the SIPS method is rarely used, because it is difficult to control the solvent evaporation rate. This method is, however, very useful in preparing the initial mixtures for TIPS.

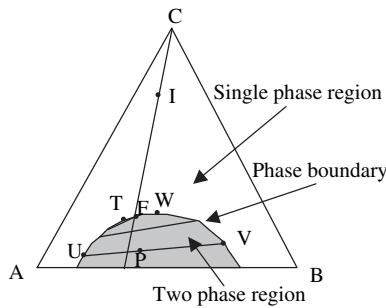


Figure 11.10 Phase diagram of the ternary mixture

11.2.5 Encapsulation

PDLCs formed by encapsulation are also called emulsion-based PDLCs [1, 11, 12]. In this method, a nematic liquid crystal, water, and a water-dissolvable polymer, such as polyvinyl alcohol, are put into a container. The water and the polymer dissolve each other to form a viscous solution. This aqueous solution does not dissolve the liquid crystal. When this system is stirred by a propeller blade at a sufficiently high speed, micron-size liquid crystal droplets are formed. Smaller liquid crystal droplets form at higher stirring speeds. Then the emulsion is coated on a substrate and the water is allowed to evaporate. After evaporation of the water, a second substrate is laminated to form PDLC devices.

11.3 Scattering Properties of LCPCs

The scattering of LCPCs is caused by the spatial variation of refractive index in the materials [13]. It is similar to the scattering of clouds in which water droplets are dispersed in air, or milk in which fat particles are dispersed in water. In PDLCs, the scattering is due to the refractive index mismatch between the liquid crystal and the polymer. In PSLCs, the scattering is due to the refractive index mismatch between the liquid crystal and the polymer network as well as that between liquid crystal domains. A precise calculation of the scattering of LCPCs is very difficult because of the birefringence of the liquid crystals, dispersion in domain size, and irregularity of domain shape. Here we will include only some qualitative discussion on the scattering.

11.3.1 Rayleigh-Gans scattering theory

When light is propagating in a medium, the electric field of the light induces a dipole moment at each point, which oscillates with the frequency of the light [13]. Each oscillating dipole radiates light in all directions, and the net electric field at any point is the vector sum of the fields produced by all the dipole radiators, as schematically shown in Figure 11.11.

The incident light is collimated and the electric field at the source point  $\vec{r}$  is

$$\vec{E}_{in}(\vec{r}, t) = \vec{E}_o e^{-i\vec{k}_o \cdot \vec{r} + i\omega t} \tag{11.34}$$

The total induced dipole moment in the volume element  $d^3r$  is given by

$$d\vec{P}(\vec{r}, t) = \vec{\alpha} \cdot \vec{E}_{in} = \vec{\alpha} \cdot \vec{E}_o e^{-i\vec{k}_o \cdot \vec{r} + i\omega t} \tag{11.35}$$

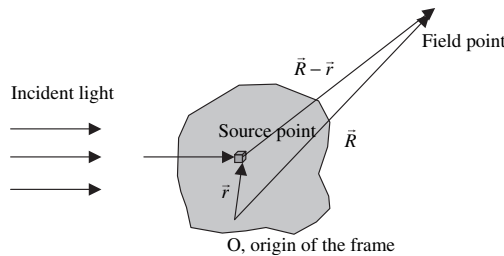
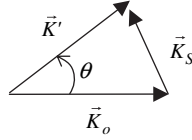


Figure 11.11 Schematic diagram showing the scattering of a medium





**Figure 11.12** Schematic diagram showing the wavevectors of the incident and scattered light

where  $\overleftrightarrow{\alpha}$  is the polarizability and  $\vec{K}_o$  is the wavevector of the incident light.  $\overleftrightarrow{\alpha}$  is related to the dielectric tensor by  $\overleftrightarrow{\alpha}(\vec{r}) = \epsilon_o[\overleftrightarrow{\epsilon}(\vec{r}) - \vec{I}]$ , where  $\vec{I}$  is the unit matrix.  $\vec{K}_o$  is related to the frequency  $\omega$  by  $\vec{K}_o = K_o \hat{k}_o = (\omega/C)\hat{k}_o = (2\pi/\lambda)\hat{k}_o$ , where  $C$  and  $\lambda$  are the speed and wavelength of light in vacuum, respectively, and  $\hat{k}_o$  is a unit vector along the incident direction. The wavevector of the scattered light is  $\vec{K}' = K_o \hat{k}'$ , as shown in Figure 11.12:

$$K_s = 2K_o \sin(\theta/2) \quad (11.36)$$

where  $\theta$  is the scattering angle.

The scattered field radiated by the dipole moment in the volume element  $d^3\vec{r}$  is given by

$$\begin{aligned} d\vec{E}_s(\vec{R}, t) &= \frac{\hat{k}' \times [\hat{k}' \times d\ddot{\vec{P}}(\vec{r}, t)]}{4\pi\epsilon_o C^2 |\vec{R} - \vec{r}|} e^{-i\vec{K}' \cdot (\vec{R} - \vec{r})} \\ &= \frac{\hat{k}' \times \{\hat{k}' \times [-\omega^2 \overleftrightarrow{\alpha}(\vec{r}) \cdot \vec{E}_o(\vec{r}, t) d^3 r]\}}{4\pi\epsilon_o C^2 |\vec{R} - \vec{r}|} e^{i\omega t - i\vec{K}_o \cdot \vec{r}} e^{-i\vec{K}' \cdot (\vec{R} - \vec{r})} \\ &= \frac{-\omega^2 \hat{k}' \times \{\hat{k}' \times [\overleftrightarrow{\alpha}(\vec{r}) \cdot \vec{E}_o]\}}{4\pi\epsilon_o C^2 |\vec{R} - \vec{r}|} e^{i\omega t - i(\vec{K}_o - \vec{K}') \cdot \vec{r} - i\vec{K}' \cdot \vec{R}} d^3 r \\ &= \frac{-\omega^2 \hat{k}' \times \{\hat{k}' \times [\overleftrightarrow{\alpha}(\vec{r}) \cdot \vec{E}_o]\}}{4\pi\epsilon_o C^2 |\vec{R} - \vec{r}|} e^{i\vec{K}_s \cdot \vec{r}} e^{i\omega t - i\vec{K}' \cdot \vec{R}} d^3 r \end{aligned} \quad (11.37)$$

For a far-field point,  $R \gg r$ ,  $|\vec{R} - \vec{r}| \approx R$ . Equation (11.37) becomes

$$d\vec{E}_s(\vec{R}, t) = \frac{-K_o^2 \hat{k}' \times \{\hat{k}' \times [\overleftrightarrow{\alpha}(\vec{r}) \cdot \vec{E}_o]\}}{4\pi\epsilon_o R} e^{i\vec{K}_s \cdot \vec{r}} e^{i\omega t - i\vec{K}' \cdot \vec{R}} d^3 r \quad (11.38)$$

The total scattered field is given by

$$\begin{aligned} \vec{E}_s(\vec{R}, t) &= -\frac{K_o^2}{4\pi\epsilon_o R} e^{i\omega t - i\vec{K}' \cdot \vec{R}} \int \hat{k}' \times \{\hat{k}' \times [\overleftrightarrow{\alpha}(\vec{r}) \cdot \vec{E}_o]\} e^{i\vec{K}_s \cdot \vec{r}} d^3 r \\ &= -\frac{\pi}{\epsilon_o R \lambda^2} V e^{i\omega t - i\vec{K}' \cdot \vec{R}} \hat{k}' \times \{\hat{k}' \times [\overleftrightarrow{\alpha}(\vec{K}_s) \cdot \vec{E}_o]\} \end{aligned} \quad (11.39)$$

where

$$\overleftrightarrow{\alpha}(\vec{K}_s) = \frac{1}{V} \int \overleftrightarrow{\alpha}(\vec{r}) e^{i\vec{K}_s \cdot \vec{r}} d^3 r$$

is the Fourier component of the polarizability and  $V$  is the volume of the scattering medium. The intensity of the scattered light is

$$I_S = |\vec{E}_s|^2 \propto \frac{1}{\lambda^4} \left| \frac{1}{4\pi\epsilon_o} \vec{\alpha}(\vec{K}_s) \right|^2 = \frac{1}{\lambda^4} \left| \frac{1}{4\pi} \vec{\epsilon}(\vec{K}_s) \right|^2 \quad (11.40)$$

The factor  $1/\lambda^4$  describes the wavelength dependence of the Rayleigh light scattering, which is responsible for the blue background of the sky: when sunlight propagates through the atmosphere, blue light is scattered more than red light by air density fluctuations. The factor  $|\vec{\epsilon}(\vec{K}_s)|$  describes the wavelength dependence of the light scattering due to the structure of the medium. If the medium consists of many domains with a linear size around  $D$ , the Fourier component of the refractive index peaks at  $2\pi/D$ , which means that light with wavelength around  $D$  is scattered strongly.

We define the coordinates for the incident light in such a way that the  $z$  axis is parallel to the incident direction and the  $x$  axis is in the plane defined by  $\vec{K}_o$  and  $\vec{K}'$  and the coordinates for the scattered light in such a way that the  $z'$  axis is parallel to the scattering direction and the  $x'$  axis is also in the plane defined by  $\vec{K}_o$  and  $\vec{K}'$ , as shown in Figure 11.13. If the incident field  $\vec{E}_o$  is linearly polarized in a direction making an angle  $\alpha$  with the  $x$  axis, in matrix form,

$$\vec{E}_o = \begin{pmatrix} E_{lo} \\ E_{ro} \end{pmatrix} = E_o \begin{pmatrix} \cos \alpha \\ \sin \alpha \end{pmatrix}$$

defined in frame  $xyz$ . The scattered field is

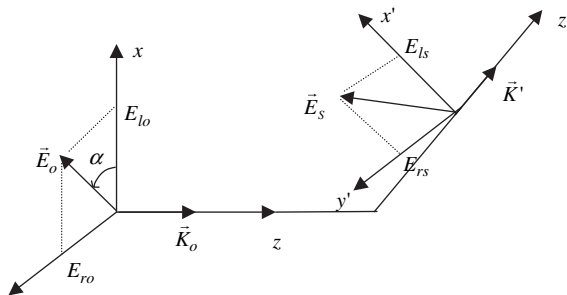
$$\vec{E}_s = \begin{pmatrix} E_{ls} \\ E_{rs} \end{pmatrix}$$

defined in frame  $x'y'z'$ . Rewriting Equation (11.39) in matrix form

$$\vec{E}_s = -\frac{K_o^2}{4\pi\epsilon_o R} V e^{-i\omega t + i\vec{K}' \cdot \vec{R}} \vec{k}' \times \{ \vec{k}' \times [ \vec{\alpha}(\vec{K}_s) \cdot \vec{E}_o ] \} \equiv \frac{1}{iK_o R} e^{-i\omega t + i\vec{K}' \cdot \vec{R}} \vec{S} \cdot \vec{E}_o \quad (11.41)$$

where

$$\vec{S} = \vec{S}(\theta, \alpha) = \begin{pmatrix} S_{ll} & S_{lr} \\ S_{rl} & S_{rr} \end{pmatrix}$$



**Figure 11.13** The coordinates for the incident and scattered light

is the scattering matrix. The two components of the differential scattering cross-section are

$$\left(\frac{d\sigma}{d\Omega}\right)_l = \frac{|E_{ls}|^2}{|E_o|^2} R^2 = \frac{1}{K_o^2} |S_{ll} \cos \alpha + S_{lr} \sin \alpha|^2 \quad (11.42)$$

$$\left(\frac{d\sigma}{d\Omega}\right)_r = \frac{|E_{rs}|^2}{|E_o|^2} R^2 = \frac{1}{K_o^2} |S_{lr} \cos \alpha + S_{rr} \sin \alpha|^2 \quad (11.43)$$

The total differential scattering section is

$$\frac{d\sigma}{d\Omega} = \left(\frac{d\sigma}{d\Omega}\right)_l + \left(\frac{d\sigma}{d\Omega}\right)_r$$

As an example, let us first consider the scattering of an isotropic spherical droplet with refractive index  $n$  and radius  $a$ . Then  $\vec{\alpha}(\vec{K}_s) \cdot \vec{E}_o = \alpha(\vec{K}_s) \vec{E}_o$  and

$$\begin{aligned} E_{ls} &= \hat{x}' \cdot \left\{ -i \frac{1}{4\pi\epsilon_o} K_o^3 V \alpha(\vec{K}_s) \hat{k}' \times [\hat{k}' \times \vec{E}_o] \right\} \\ &= -i \frac{1}{4\pi\epsilon_o} K_o^3 V \alpha(\vec{K}_s) \hat{x}' \cdot [\hat{k}' (\hat{k}' \cdot \vec{E}_o) - \vec{E}_o] \\ &= i \frac{1}{4\pi\epsilon_o} K_o^3 V \alpha(\vec{K}_s) \hat{x}' \cdot \vec{E}_o \\ &= i \frac{1}{4\pi\epsilon_o} K_o^3 V \alpha(\vec{K}_s) (\cos \theta \hat{x} + \cos \theta \hat{z}) \cdot (E_{lo} \hat{x} + E_{ro} \hat{y}) \\ &= i \frac{1}{4\pi\epsilon_o} K_o^3 V \alpha(\vec{K}_s) \cos \theta E_{lo} \end{aligned} \quad (11.44)$$

$$\begin{aligned} E_{ls} &= \hat{y}' \cdot \left( -i \frac{1}{4\pi\epsilon_o} K_o^3 V \alpha(\vec{K}_s) \hat{k}' \times [\hat{k}' \times \vec{E}_o] \right) \\ &= i \frac{1}{4\pi\epsilon_o} K_o^3 V \alpha(\vec{K}_s) \hat{y}' \cdot (E_{lo} \hat{x} + E_{ro} \hat{y}) \\ &= i \frac{1}{4\pi\epsilon_o} K_o^3 V \alpha(\vec{K}_s) E_{ro} \end{aligned} \quad (11.45)$$

Therefore the scattering matrix is

$$\vec{S} = i \frac{1}{4\pi\epsilon_o} K_o^3 V \alpha(\vec{K}_s) \begin{pmatrix} \cos \theta & 0 \\ 0 & 1 \end{pmatrix} \quad (11.46)$$

Now we calculate the Fourier component of the polarizability:

$$\begin{aligned} \alpha(\vec{K}_s) &= \frac{1}{V} \int_{\text{whole space}} \alpha(\vec{r}) e^{-i\vec{K}_s \cdot \vec{r}} d^3 r \\ &= \frac{1}{V} \int_{\text{inside droplet}} \alpha(\vec{r}) e^{-i\vec{K}_s \cdot \vec{r}} d^3 r + \frac{1}{V} \int_{\text{outside droplet}} \alpha(\vec{r}) e^{-i\vec{K}_s \cdot \vec{r}} d^3 r \\ &= \frac{1}{V} \int_{\text{whole space}} \alpha_{out} e^{-i\vec{K}_s \cdot \vec{r}} d^3 r + \frac{1}{V} \int_{\text{inside droplet}} (\alpha_{in} - \alpha_{out}) e^{-i\vec{K}_s \cdot \vec{r}} d^3 r \end{aligned}$$

The first integral is zero and  $\alpha_{in} = \varepsilon_o(\varepsilon - 1) = \varepsilon_o(n^2 - 1)$ . The medium outside the droplet is also isotropic with refractive index  $n_o$  and  $\alpha_{out} = \varepsilon_o(n_o^2 - 1)$ . Hence

$$\alpha(\vec{K}_s) = \frac{1}{V} \varepsilon_o (2\bar{n}\Delta n)^2 \int_{\text{inside droplet}} e^{-i\vec{K}_s \cdot \vec{r}} d^3 r \quad (11.47)$$

where  $\bar{n} = (n - n_o)$  and  $\Delta n = (n - n_o)$ . We define

$$Q(\theta) = \frac{1}{V} \int_{\text{inside droplet}} e^{-i\vec{K}_s \cdot \vec{r}} d^3 r$$

For the integration, we use polar coordinates with  $\vec{K}_s$  in the polar direction:

$$Q(\theta) = \frac{2\pi}{V} \int_0^\pi d\beta \int_0^a e^{-iK_s r \cos\beta} \sin\beta r^2 dr = \frac{4\pi}{VK_s^3} [\sin(aK_s) - aK_s \cos(aK_s)] \quad (11.48)$$

The differential scattering cross-section for unpolarized incident light is given by

$$\frac{d\sigma}{d\Omega} = \frac{K_o^6}{K_o^2} \frac{1}{16\pi^2} (2\bar{n}\Delta n)^2 (\cos^2\theta \langle \cos^2\alpha \rangle + \langle \sin^2\alpha \rangle) \left\{ \frac{4\pi}{K_s^3} [\sin(aK_s) - aK_s \cos(aK_s)] \right\}^2 \quad (11.49)$$

We know that  $K_s = 2K_o \sin(\theta/2)$ . Let  $A = aK_o$ . Then

$$\frac{d\sigma}{d\Omega} = \pi a^2 (2\bar{n}\Delta n)^2 \frac{(\cos^2\theta + 1)}{128\pi A^2} \left\{ \frac{\sin[2A \sin(\theta/2)] - 2A \sin(\theta/2) \cos[2A \sin(\theta/2)]}{\sin^3(\theta/2)} \right\}^2 \quad (11.50)$$

The light scattered in the forward direction is given by

$$\begin{aligned} \sigma_{\text{forward}} &= 2\pi \int_0^{\pi/2} \frac{d\sigma}{d\Omega} \sin\theta d\theta \\ &= \pi a^2 (2\bar{n}\Delta n)^2 \int_0^{\pi/2} \frac{(\cos^2\theta + 1)}{64A^2} \left\{ \frac{\sin[2A \sin(\theta/2)] - 2A \sin(\theta/2) \cos[2A \sin(\theta/2)]}{\sin^3(\theta/2)} \right\}^2 \sin\theta d\theta \end{aligned} \quad (11.51)$$

The light scattered in the backward direction is given by

$$\begin{aligned} \sigma_{\text{backward}} &= 2\pi \int_{\pi/2}^\pi \frac{d\sigma}{d\Omega} \sin\theta d\theta \\ &= \pi a^2 (2\bar{n}\Delta n)^2 \int_{\pi/2}^\pi \frac{(\cos^2\theta + 1)}{64A^2} \left\{ \frac{\sin[2A \sin(\theta/2)] - 2A \sin(\theta/2) \cos[2A \sin(\theta/2)]}{\sin^3(\theta/2)} \right\}^2 \sin\theta d\theta \end{aligned} \quad (11.52)$$

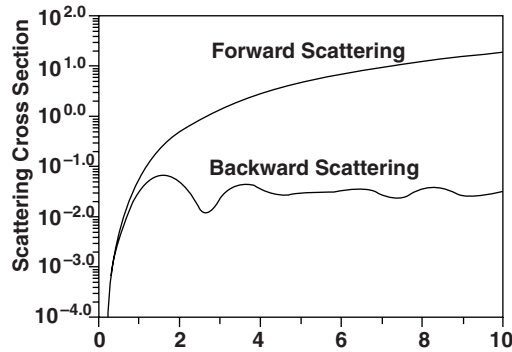


Figure 11.14 The scattering cross-sections vs.  $A$

The scattering cross-sections of the materials with  $n_o = 1.5$  and  $n = 1.7$  are plotted in Figure 11.14 where the unit of the vertical axis is  $\pi a^2$ . When the droplet size  $a$  is smaller than the wavelength  $\lambda$  ( $A = 2\pi a/\lambda$ ), the forward and backward scattering cross-sections are about the same. When the droplet size is larger than the wavelength, most of the scattered light is in the forward direction.

The scattering of liquid crystal droplets can be calculated in the same way except that dielectric tensor has to be used [14–16]. The calculation is more complicated and is not presented here. Readers interested in the detailed calculation of the scattering of PDLCs are referred to the papers published by Zumer, Kelly, and co-workers. The formulation presented in this section is called Rayleigh–Gans scattering and uses the following three assumptions: (1)  $|n/n_o - 1| \ll 1$ , therefore refraction at the droplet interface can be neglected; (2)  $2K_o a|n - n_o| \ll 1$ ; and (3)  $\sigma \ll 1$ , therefore there is no multiple scattering inside the droplet and the incident light intensity at any point inside the medium is the same.

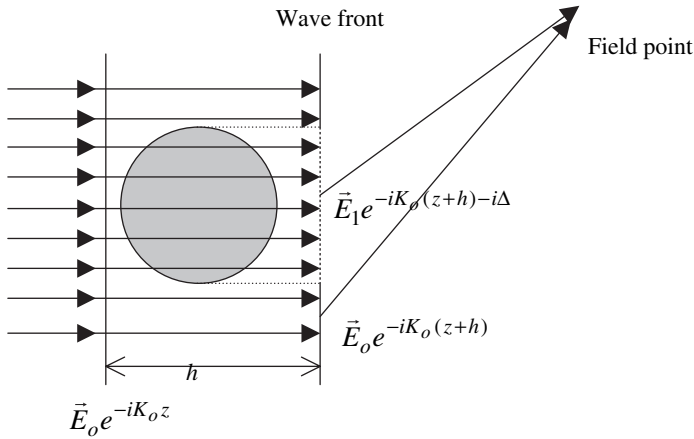
### 11.3.2 Anomalous diffraction scattering theory

As a matter of fact, in PDLCs, the droplet diameter is about  $1 \mu\text{m}$  and  $|n - n_o| \sim 0.2$ , so  $2K_o a|n - n_o| > 1$  for visible light. The assumptions for Rayleigh–Gans scattering do not hold. Hence Rayleigh–Gans scattering theory does not describe well the scattering of PDLCs. A better approach for PDLCs is the anomalous diffraction theory [17,18]. Here the assumptions are: (1)  $|n/n_o - 1| \ll 1$ , meaning that refraction at the droplet interface can be neglected; and (2)  $K_o a \gg 1$ , meaning that a light ray can be traced. In this theory, the light ray goes through the liquid crystal droplet without scattering, as shown in Figure 11.15. The phase and polarization state of the ray are calculated using the Jones matrix method. Consider a plane beyond the droplet which is perpendicular to the incident light propagation direction; the phase is no longer a constant on the plane but modified by the liquid crystal droplet. Take all the points on the plane as the centers of secondary spherical waves as in Huygen's principle. The scattered field is calculated by summing over all the fields of the secondary waves. One of the predictions of the theory is that the scattered light is concentrated in a cone of linear angle  $30^\circ$  in the forward direction, which agrees with experimental results.

When there are sufficient scattering objects in the medium, light will be scattered multiple times. Multiple scattering tends to make the scattering profile broader [19].

## 11.4 PDLCs

In PDLCs, the concentrations of polymer and liquid crystal are comparable. Liquid crystals form isolated droplets embedded in polymers. We will consider first the liquid crystal director



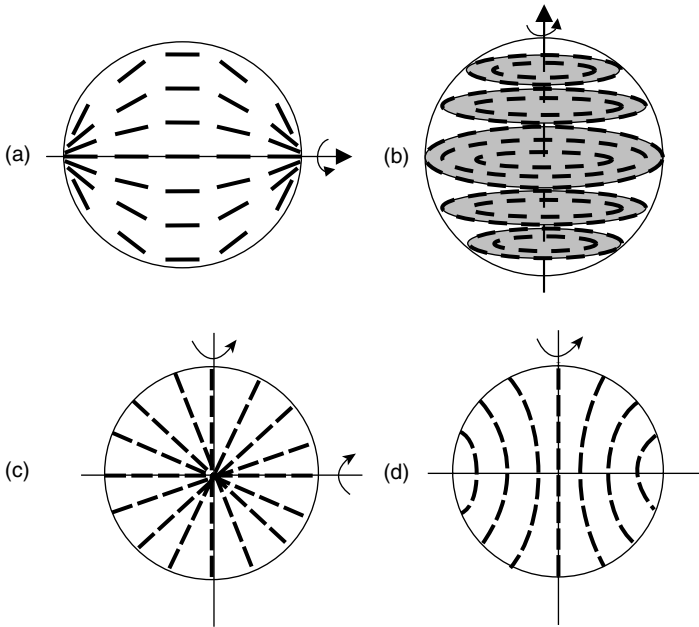
**Figure 11.15** Schematic diagram showing how the scattered field is calculated in the anomalous diffraction theory

configuration inside droplets, and then consider the electro-optical properties of PDLCs as well as their applications.

### 11.4.1 Liquid crystal droplet configurations in PDLCs

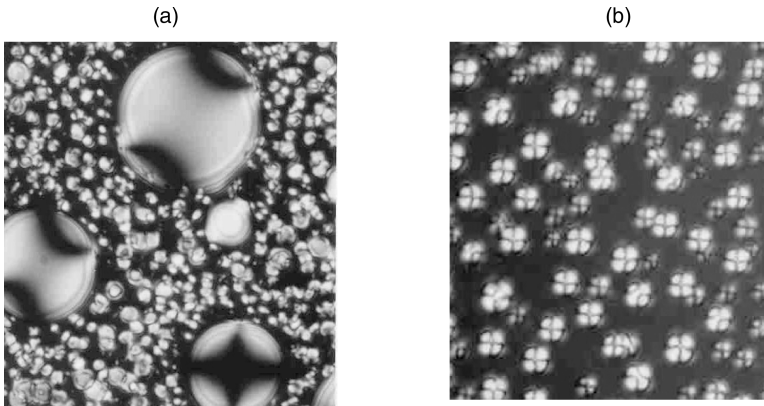
The liquid crystal dispersed in the polymer of a PDLC can be in one of the many possible liquid crystal phases such as nematic, cholesteric, smectic-A, and smectic-C\* [4]. The most common PDLC is polymer-dispersed nematic liquid crystal, which is the one we will discuss here. Inside a nematic droplet, the director configuration is determined by the droplet shape and size, the anchoring condition on the droplet surface and the externally applied field, as well as the elastic constants of the liquid crystal. There are four main types of nematic droplets as shown in Figure 11.16. When the anchoring condition is tangential, there are two types of droplets. One is the bipolar droplet as schematically shown in Figure 11.16(a) [20, 21], the other is the toroidal droplet as shown in Figure 11.16(b) [1,22]. When the anchoring condition is perpendicular, there are also two types of droplets. One is the radial droplet as shown in Figure 11.16(c) [23], the other is the axial droplet as shown in Figure 11.16(d) [23]. When a droplet is larger than 5 μm in diameter, it is possible to identify the droplet configuration using an optical microscope.

In the bipolar droplet, the rotational symmetry axis is referred to as the bipolar axis. The droplet director  $\vec{N}$  is defined as a unit vector along the bipolar axis. In the bipolar droplet with strong anchoring, there are two point defects at the ends of the diameter along the bipolar axis. The director field on a plane containing the bipolar axis is shown in Figure 11.16(a). The liquid crystal director is tangential to the circle along the circumference and parallel to the bipolar axis along the diameter. At other places inside the droplet, the director is oriented in such a way that the total free energy is minimized. There is a rotational symmetry of the director around the bipolar axis. A typical microphotograph of a sample with bipolar droplets under a microscope with crossed polarizers is shown in Figure 11.17(a). The dark brushes are the region where the liquid crystal director is parallel or perpendicular to the polarizers. The elastic deformations involved are splay and bend. When there is no externally applied field, the orientation of  $\vec{N}$  is arbitrary for perfect spherical droplets. In practice, the droplets are usually deformed. The deviation of the droplet from spherical shape results in a certain orientation of  $\vec{N}$  [24,25]. Preferred deformed bipolar droplets can be made by applying stresses or external fields during the formation of the droplets. When a sufficiently high external electric field is applied, the liquid crystal ( $\Delta\epsilon > 0$ ) is reoriented with the bipolar axis parallel to the field.



**Figure 11.16** Liquid crystal director configurations confined in droplets in PDLCs: (a) bipolar droplet, (b) toroidal droplet, (c) radial droplet, and (d) axial droplet

In the toroidal droplet, the liquid crystal director is aligned along concentric circles on planes perpendicular to a diameter, as shown in Figure 11.16(b). There is a line defect along the diameter of the droplet and rotational symmetry around the defect line. The bend elastic deformation is the only one involved. Toroidal droplets exist when the bend elastic constant is smaller than the splay elastic constant, otherwise the droplets take on the bipolar configuration. Toroidal droplets rarely exist because, for most liquid crystals, the bend elastic constant is usually larger than the splay elastic constant. Nevertheless, toroidal droplets have been reported [22]. When the droplet is sufficiently large



**Figure 11.17** Microphotographs of PDLCs: (a) bipolar droplet; (b) radial droplet

or an external field is applied, the director near the defect line will escape in a direction parallel to the symmetry axis so that the total free energy is reduced.

In the radial droplet, the director everywhere is along the radial direction [23], and there is a point defect in the center of the droplet. The director configuration on a plane cut through the droplet center is shown in Figure 11.16(c). There is rotational symmetry around any diameter of the droplet. A microphotograph of a sample with radial droplet under a microscope with crossed polarizers is shown in Figure 11.17(b). The dark cross is the region where the liquid crystal director is parallel or perpendicular to the polarizers. One striking feature of radial droplets is that they have only one texture which does not change when the sample is rotated with the microscope stage. Note that the dark cross at the center is narrow, because only in a small region is the director parallel to the propagation direction of the light. Splay elastic deformation is the only one present in the radial droplet.

In the axial droplet, there is line defect along the equator. The director on the plane perpendicular to the equator is shown in Figure 11.16(d) [21]. There is rotational symmetry around the diameter perpendicular to the plane of the equator. The texture of the axial droplet with symmetry axis parallel to the propagation direction of the light is similar to that of the radial droplet, except the dark cross at the center is wider, indicating that the director is aligned closer to the symmetry axis in the center. Both splay and bend elastic deformations exist in the axial droplet. The splay elastic energy of the axial droplet is lower than that of a radial droplet if all the material parameters and droplet size are identical. The axial droplet is more stable than the radial droplet if the anchoring is weak, or the droplet is small, or an external field is applied. If the liquid crystal is in the radial configuration at zero electric field, when a sufficiently high electric field is applied, it can be switched to the axial configuration with the symmetry axis parallel to the field.

Besides the four droplet configurations discussed above, other droplet configurations could exist under appropriate conditions. For example, there is the twisted bipolar droplet where the splay and bend elastic energy is reduced by introducing twist deformation. The point defect in the radial droplet could escape away the center in an effort to reduce the total free energy.

### 11.4.2 Switching PDLCs

Devices from PDLCs make use of two states of the liquid crystal droplets. One of the states is the field-off state in which either the droplet director orients randomly throughout the PDLCs or the liquid crystal director inside the droplet orients in all directions. The liquid crystal is in the directoral configuration in which the sum of the elastic and surface energies is minimized. The other state is the field-on state in which the droplet director is aligned uniformly along the applied field. If the droplets are bipolar droplets, in the field-off state, the bipolar axes (droplet director) of the droplets are oriented randomly throughout the cell; in the field-on state, the bipolar axes of the droplets are aligned along the applied field. If the droplets are axial droplets, in the field-off state, the symmetry axes (droplet director) of the droplets are oriented randomly throughout the cell; in the field-on state, the symmetry axes of the droplets are aligned parallel to the applied field. If the droplets are radial, in the field-off state, there is no droplet director; in the field-on state, they are switched to the axial droplet with symmetry axis parallel to the applied field. In order to have the transition from the first state to the second state in all those cases, the applied field must be sufficiently high so that the decrease of the electric energy can compensate for the increase of the elastic energy and surface energy. The threshold field, above which the applied field can produce the transition, depends on the following factors: (1) droplet size, (2) droplet shape, (3) anchoring condition, and (4) the material parameters, such as elastic constants and dielectric anisotropy, of the liquid crystal [3, 24, 25].

We discuss qualitatively the effects of droplet size on the drive voltage. Let us consider a PDLC with droplet size  $D$ . In the switching of a PDLC droplet, there are three energies involved: elastic energy, surface energy, and electric energy. The elastic energy density  $f_{elas}$  is proportional to  $K(1/D)^2$ , and the total elastic energy  $F_{elas}$  of the droplet is proportional to  $D^3 \cdot K(1/D)^2 = KD$ , where  $K$  is the elastic



constant. The surface energy density is proportional to the anchoring strength  $W$ . The surface extrapolation length is defined by  $d_e = K/W$ . The total surface energy of the droplet is proportional to  $WD^2 = KD^2/d_e = (D/d_e)KD$ . The total electric energy of the droplet is proportional to  $-\Delta\epsilon E^2 D^3$ . Depending on the droplet size and anchoring strength, there are three possible cases.

(1)  $D \gg d_e$ , corresponding to large droplet or strong anchoring

The liquid crystal on the surface of the droplet is oriented along the anchoring easy direction; the change of surface energy in the switching is negligible. Because the surface of the droplet is curved, the director inside the droplet cannot be uniform, and therefore elastic energy  $KD$  dominates. In the field-off state, the liquid crystal inside the droplet is in the state where the elastic energy is minimized. In the field-on state, the elastic energy is higher and the electric energy is lower. At the threshold field  $E_c$ , the decrease of the electric energy,  $-\Delta F_{electric}$ , can compensate for the increase of the elastic energy,  $\Delta F_{elastic}$ , namely

$$\Delta F_{elastic} = a_{elastic}KD \sim \Delta F_{electric} = a_{electric}\Delta\epsilon E_c^2 D^3 \quad (11.53)$$

where  $a_{elastic}$  and  $a_{electric}$  are constants. The threshold field is given by

$$E_c = \left( \frac{a_{elastic}}{a_{electric}\Delta\epsilon} \right)^{1/2} \frac{1}{D} \propto \frac{1}{D} \quad (11.54)$$

The threshold field is sometimes referred to as the switching field and the corresponding voltage is referred to as the switching voltage. When the droplet size is varied in a relatively small region, the switching field will change in such a way that  $E_c D$  remains fixed.

(2)  $D \ll d_e$ , corresponding to small droplet or weak anchoring

The liquid crystal inside the droplet is uniformly oriented along the direction  $\vec{N}$  at the sacrifice of the surface energy. The change of the elastic energy in the switching is small and negligible and the surface energy dominates. In the field-off state,  $\vec{N}$  is in the direction such that the surface energy is minimized. In the field-on state,  $\vec{N}$  reorients parallel to the applied field. The surface energy is higher and the electric energy is lower. At the threshold field  $E_c$ , the decrease of the electric energy,  $-\Delta F_{electric}$ , can compensate for the increase of the surface energy,  $\Delta F_{elastic}$ , namely

$$\Delta F_{surface} = a_{surface}WD^2 \sim \Delta F_{electric} = a_{electric}\Delta\epsilon E_c^2 D^3 \quad (11.55)$$

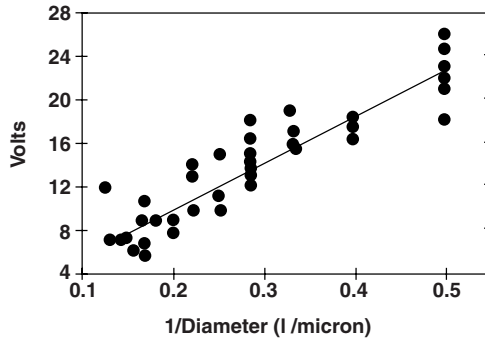
where  $a_{surface}$  is a constant. The threshold field is given by

$$E_c = \left( \frac{a_{surface}W}{a_{electric}\Delta\epsilon} \right)^{1/2} \frac{1}{\sqrt{D}} \propto \frac{1}{\sqrt{D}} \quad (11.56)$$

When the droplet size is varied in a relatively small region, the switching field will change in such a way that  $E_c \sqrt{D}$  remains fixed.

(3)  $D \sim d_e$ , corresponding to medium droplet size and medium anchoring strength

In this case, the liquid crystal in the bulk of the droplet is not aligned uniformly along one direction, nor is the liquid crystal on the surface of the droplet aligned along the anchoring easy direction.



**Figure 11.18** Drive voltage of the PDLC with strong anchoring as a function of the droplet sizes

Both elastic energy and surface energy are involved. At the threshold field, the decrease of the electric energy must compensate for the increase of the elastic energy and surface energy:

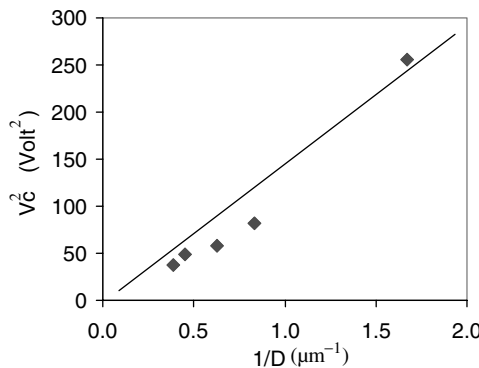
$$\Delta F_{surface} + \Delta F_{elastic} = a_{elastic}KD + a_{surface}WD^2 \sim \Delta F_{electric} = a_{electric}\Delta\epsilon E_c^2 D^3 \quad (11.57)$$

$$E_c = \left( \frac{a_{elastic}}{a_{electric}\Delta\epsilon} \frac{1}{D^2} + \frac{a_{surface}W}{a_{electric}\Delta\epsilon} \frac{1}{D} \right)^{1/2} \quad (11.58)$$

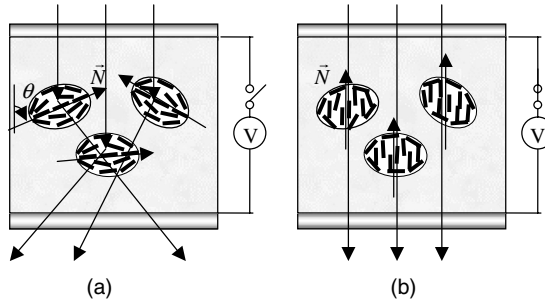
The droplet size dependence of the switching field can be used to obtain information on the droplet size and anchoring strength.

In PDLCs with strong anchoring, the drive voltage is usually high. Such an example is the PDLC made from PVA and ZLI2061 (from Merck) using the NCAP method [26]. The drive voltage  $V_d$  is approximately linearly proportional to  $1/D$ , as shown in Figure 11.18 where the cell thickness is 13  $\mu\text{m}$ .

In PDLCs with weak anchoring, the drive voltage is usually low. Such an example is the PDLC made from E7 (from Merck) and NOA65 (Norland Optical Adhesive) by photo-PIPS [27]. The cell thickness is 12  $\mu\text{m}$ . The square of the drive voltage  $V_d$  is approximately linearly proportional to  $1/D$ , as shown in Figure 11.19.



**Figure 11.19** Square of the drive voltage of the PDLC with weak anchoring as a function of the droplet size



**Figure 11.20** Orientation of liquid crystal inside the PDLC droplets in the field-off and field-on states

**11.4.3 Scattering PDLC devices**

We consider the working principle of scattering PDLC devices. As an example, we consider a PDLC with bipolar droplets. At zero field, the droplet director  $\vec{N}$  is oriented randomly throughout the cell as shown in Figure 11.20(a). For normal incident light with linear polarization in the plane defined by the propagation direction of the light and the bipolar axis, when it propagates through a droplet whose droplet director makes an angle  $\theta$  with the normal of the cell, it encounters a refractive index given approximately by

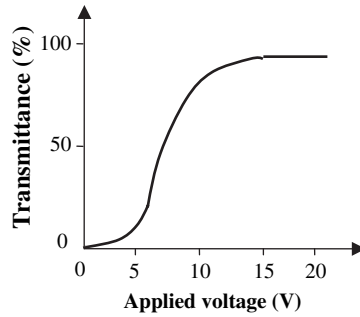
$$n(\theta) = \frac{n_{\parallel}n_{\perp}}{(n_{\parallel}^2\cos^2\theta + n_{\perp}^2\sin^2\theta)^{1/2}} \tag{11.59}$$

where  $n_{\parallel}$  and  $n_{\perp}$  are the refractive indices for light polarized parallel and perpendicular to the liquid crystal director, respectively. The (isotropic) polymer is chosen such that its refractive index  $n_p$  is the same as  $n_{\perp}$ . The light encounters a different refractive index when it propagates through the polymer and the liquid crystal droplet. Therefore the PDLC is a non-uniform optical medium and the light is scattered when it goes through the PDLC. When a sufficiently high electric voltage is applied across the PDLC cell, the droplets are reoriented with their droplet director  $\vec{N}$  parallel to the normal of the cell as shown in Fig 11.20(b).  $\theta = 0$  for all the droplets. Now, when the normal incident light propagates through the droplets, it encounters the refractive index  $n_{\perp}$  which is the same as the refractive index encountered when it propagates through the polymer. The PDLC is a uniform optical medium for the light. Therefore the light goes through the PDLC without scattering. The PDLC discussed here is a normal-mode light shutter in the sense that it is opaque in the field-off state and transparent in the field-on state.

A typical voltage–transmittance curve of PDLCs is shown in Figure 11.21 [28]. At 0 V, the material is in the scattering state and the transmittance is low. As the applied voltage is increased, the droplet director is aligned toward the cell normal direction and the transmittance increases. The drive voltage (at which the transmittance reaches 90% of the maximum value) is about 25 V. The maximum transmittance is about 90% (normalized to the transmittance of an empty cell).

The measured transmittance of PDLCs in the scattering state depends on the collection angle of the detection [29]. A typical scattering profile  $S(\theta)$  of PDLCs as a function of polar angle  $\theta$  defined with respect to the incident direction is shown in Figure 11.22 [30]. The scattering is independent of the azimuthal angle. The full width at half maximum (FWHM) of the scattering profile of the scattering state is about 30°. When the collection is  $2\delta$ , the measured light intensity is

$$I = \pi \int_{-\delta}^{+\delta} S(\theta)\sin\theta d\theta \tag{11.60}$$



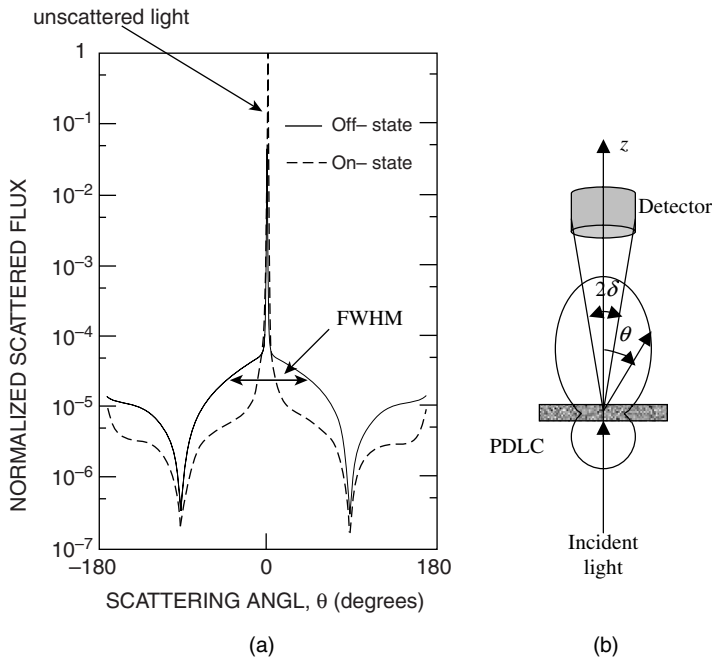
**Figure 11.21** Typical voltage–transmittance curve of PDLCs

The contrast ratio is

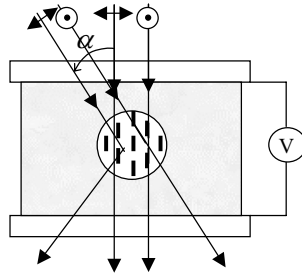
$$C = \frac{\int_{-\pi}^{+\pi} S(\theta) \sin \theta d\theta}{\int_{-\delta}^{+\delta} S(\theta) \sin \theta d\theta} \tag{11.61}$$

The larger the collection angle is, the more the scattered light will be collected, and thus the lower the contrast ratio is.

In the field-on state, the transmittance of the PDLC depends on the incident angle of light. For normally incident light, the refractive index encountered in the liquid crystal droplet is  $n_{\perp}$  which is



**Figure 11.22** (a) The scattering profile of the PDLC as a function of the polar angle  $\theta$  in the field-off and field-on states. (b) Measurement geometry

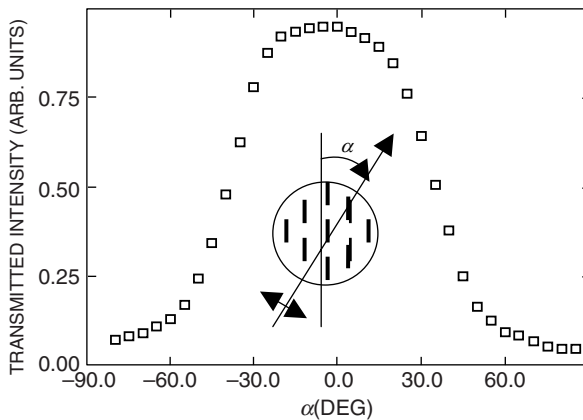


**Figure 11.23** Schematic diagram showing the scattering of the PDLC in the field-on state

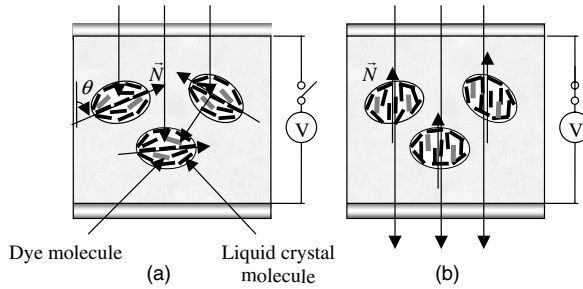
matched to that of the polymer, and therefore there is no scattering. For obliquely incident light as shown in Figure 11.23, if the polarization of the incident light is perpendicular to the incident plane, the light encounters the refractive index  $n_{\perp}$ , and therefore is not scattered. If the polarization is in the incident plane, when the incident angle is  $\alpha$ , the refractive index encountered is  $n(\alpha) = n_{\parallel}n_{\perp}/(n_{\parallel}^2\cos^2\alpha + n_{\perp}^2\sin^2\alpha)^{1/2}$ , which is different from the refractive index of the polymer, and therefore it is scattered. The larger the incident angle is, the more the refractive index encountered in the liquid crystal droplet is mismatched to the refractive index of the polymer, and the stronger the scattering is. The transmittance of the light with this polarization as a function of the incident angle  $\alpha$  is shown in Figure 11.24 [20]. The transmittance decreases by half when the incident angle is increased to  $30^{\circ}$ . If the incident light is unpolarized, the component with the parallel polarization is scattered at oblique angles, which makes the PDLC milky. This limitation on the viewing angle can be eliminated when a linear polarizer is laminated on the PDLC with the tradeoff that the on-state transmittance is decreased by half.

**11.4.4 Dichroic dye-doped PDLCs**

Dichroic dyes can be incorporated into PDLCs [31,32]. The dye molecules are usually elongated and have low molecular weight as liquid crystals and good solubility in the liquid crystal, but not in the



**Figure 11.24** Angular dependence of the transmittance of the PDLC in the on-state for incident light polarized in the incident plane



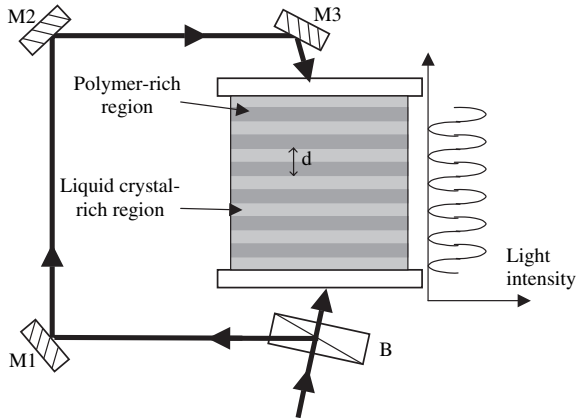
**Figure 11.25** Schematic diagram showing how the dichroic dye-doped PDLC works: (a) absorbing state; (b) transparent state

polymer. The dye and the liquid crystal phase separates from the polymer binder. The dye molecules are inside the droplet and can be switched. The used dye must be a positive type in the sense that the absorption transition dipole is along the long molecular axis. When the polarization of the incident light is parallel to the long axis of the dye molecules, the light is absorbed. When the polarization of the incident light is perpendicular to the long axis of the dye molecules, the light is not absorbed. In the field-off state, the dye molecules are randomly oriented with the droplets, as shown in Figure 11.25(a). When the cell is sufficiently thick, there are droplets oriented in every direction. The unpolarized incident light is absorbed. In the field-on state, the dye molecules are aligned in the cell normal direction with the liquid crystal, as shown in Figure 11.25(b). They are always perpendicular to the polarization of normally incident light. Therefore the light ideally passes through the cell without absorption. In practice, there is some absorption even in the field-on state, because of the thermal fluctuation of the dye molecules and the anchoring of the curved surface of the droplet.

There are a few points worth noting: (1) The dye molecules dissolved in the polymer do not change orientation under the applied field, and therefore tend to decrease the contrast of the PDLC. Therefore it is desirable that the solubility of the dye in the polymer is as low as possible. (2) Oblate droplet shape is desirable, because inside such a droplet, the dye molecules are oriented more in the plane parallel to the cell surface and absorb the light more strongly. (3) In the field-off state, the scattering of the material increases the optical path length of the light inside the cell, and therefore enhances the absorption. (4) Dye-doped PDLCs do not need polarizers, because of the random orientation of the droplets in the field-off state, which is an advantage over nematic dichroic dye displays. (5) Dye-doped PDLCs have gray levels, because as the applied field is increased, the droplets are gradually aligned toward the cell normal direction, which is an advantage over cholesteric dichroic dye displays.

#### 11.4.5 Holographic PDLCs

In PDLCs formed by PIPS, spatial variations in structure can be achieved when non-uniform polymerization conditions are introduced. Such an example is holographically formed PDLC [33–40]. The mixture of a liquid crystal and a photopolymerizable monomer is sandwiched between two glass substrates. A coherent laser light is used to initiate the polymerization. In the polymerization, the cell is irradiated by the laser light from both sides as shown in Figure 11.26. The two incident light rays interfere with each other inside the cell and form the intensity pattern as shown on the right side of the figure. In the region where the light intensity is high, more free radicals are produced, which initiates polymerization. When monomers migrate into that region, they will be likely to be polymerized and will not come out. The net effect is that monomers are attracted into the high-light-intensity regions to form the polymer and the liquid crystal molecules are pushed out. Thus alternating

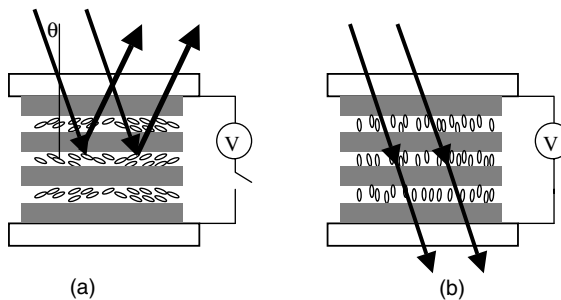


**Figure 11.26** Schematic diagram showing how the holographic PDLC is formed. B, beam splitter; M, mirror

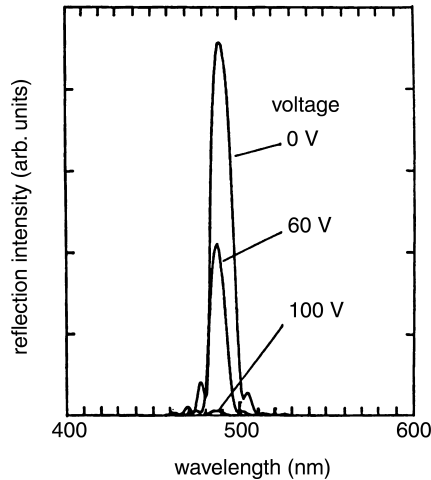
polymer-rich and liquid crystal-rich layers are formed. The period  $d$  (the thickness of one layer of polymer plus the thickness of one layer of liquid crystal) is determined by the wavelength and incident angle of the laser light.

The liquid crystal and polymer are chosen such that the ordinary refractive index  $n_o$  of the liquid crystal is equal to the refractive index  $n_p$  of the polymer. At zero field, the liquid crystal has a random orientation structure as shown in Figure 11.27(a), and the cell has a periodic refractive index. If the incident light satisfies the Bragg condition  $\lambda = d \cos \theta$ , it will be reflected. When a sufficiently high external electric field is applied across the cell, the liquid crystal ( $\Delta\epsilon > 0$ ) will be aligned perpendicular to the layers as shown in Figure 11.27(b). The incident light encounters the same refractive index in the polymer-rich layer and liquid crystal-rich layer, and passes through the material without reflection. Thus holographic PDLC can be used for switchable mirrors and reflective displays.

The spectral response of a holographic PDLC to applied electric fields is shown in Figure 11.28 where white incident light is used [37]. At 0V, due to the periodic refractive index, the cell has a high narrow reflection peak. When the applied voltage is increased, the liquid crystal is aligned toward the layer normal direction. The amplitude of the oscillation of the refractive index decreases and the reflection of the cell decreases. The drive voltage is approximately equal to the product of the field threshold of the Freedericksz transition of the liquid crystal layer and the cell thickness.



**Figure 11.27** Schematic diagram showing how the holographic PDLC is used for reflective displays



**Figure 11.28** Reflection spectra of the holographic PDLC under various applied voltages [37]

## 11.5 PSLCs

In PSLCs, the polymer concentration is usually less than 10%. The monomer used may be mesogenic with rigid cores similar to those of liquid crystal molecules [2, 41–44]. Before polymerization, the mixture of the monomer and the liquid crystal is in a liquid crystal phase. The polymerization environment is anisotropic due to the aligning effect of the liquid crystal on the monomer and the anisotropic diffusion of the monomer in the liquid crystal. Anisotropic fiber-like polymer networks are usually formed, which mimic the structure of the liquid crystal during polymerization. Because the liquid crystal and monomer are homogeneously mixed and in liquid crystal phase during polymerization, external fields and surface alignment techniques can be applied to create various polymer network structures. Therefore many fascinating structures can be achieved.

After polymerization, polymer networks tend to stabilize the state in which they are formed. In a PSLC, liquid crystal near the polymer network is aligned along the polymer network. The strength of the interaction between the liquid crystal and the polymer network is proportional to the surface area of the polymer network. The surface area of the polymer network can be increased by using higher polymer concentrations or producing smaller lateral size polymer networks.

### 11.5.1 Preparation of PSLCs

PSLCs are usually made from mixtures of liquid crystals and monomers. The monomer can be directly dissolved in the liquid crystal. Although any type of polymerization method can be used, photo-initiated polymerization is fast and is usually used. The monomer is usually acrylate or methyl acrylate because of its fast reaction rate. In order to form stable polymer networks, the functionality of the monomer must be larger than one. A small amount of photo-initiator is added to the mixture. The concentration of the photo-initiator is typically 1–5% of the monomer. When irradiated under UV light, the photo-initiator produces free radicals which react with the double bonds of the monomer and initiate the chain reaction of polymerization.

When the mixture of the liquid crystal, monomer, and photo-initiator is irradiated by UV light, the monomer is polymerized to form a polymer network. The UV intensity is usually a few milliwatts per square centimeter and the irradiation time is on the order of minutes. SEM [45,46], neutron scattering, confocal microscopy [47], birefringence study, and the Freedericksz transition technique have been used



to study the morphology of polymer networks in PSLCs [48,49]. The results suggest a bundle structure for the polymer networks. The lateral size of the bundle, as shown in Figure 11.1(b), is on the order of submicrons. The bundle consists of polymer fibrils with lateral size around a few nanometers and liquid crystals. The morphology of the polymer network is affected by the following factors: structure of the monomer, UV intensity, photo-initiator type and concentration, and the temperature. The lateral size of polymer networks is determined by the polymerization rate, mobility, and concentration of monomers [48]. Polymer networks with smaller lateral sizes are obtained with higher polymerization rates which can be achieved with higher UV intensities or high photo-initiator concentrations in photopolymerization. Polymer networks with smaller lateral sizes are also obtained with low mobility of monomers, which can be achieved with lower polymerization temperature. For example, 96.7% nematic liquid crystal E7, 3% monomer BAB6 {4,4'-bis[6-(acryloyloxy)-hexy]-1,1'-biphenylene}, and 0.3% benzoin methyl ether (BME) are mixed. The mixture is in nematic phase at room temperature. The viscosity of the mixture is comparable to that of the nematic liquid crystal and can be easily filled into cells in a vacuum chamber. The cells are then irradiated under UV light for the monomer to form a polymer network.

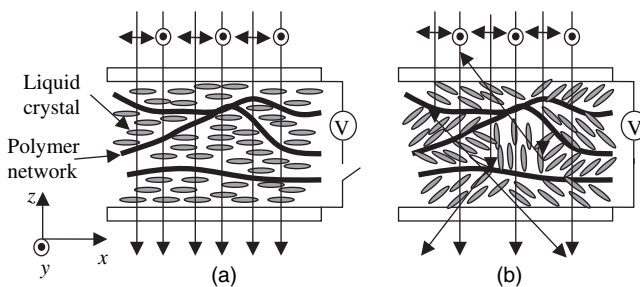
Monomers used in PSLCs preferably have a rigid core and flexible tails. They form anisotropic fibril-like networks. If the monomer does not have flexible tails, it forms a bead-like structure which is not stable under perturbations such as externally applied fields. If the monomer does not have a rigid core and is flexible, it can still form anisotropic networks.

### 11.5.2 Working modes of PSLCs

Polymer networks formed in liquid crystals are anisotropic and affect the orientation of liquid crystals. They tend to align the liquid crystal in the direction of the fibrils. They are used to stabilize desired liquid crystal configurations and control the electro-optical properties of liquid crystal devices. Polymer networks have been used to improve the performance, such as drive voltage and response times, of conventional liquid crystal devices such as TN and IPS displays.

#### (1) Polymer-stabilized nematic liquid crystals

**(a) Polymer-stabilized homogeneously aligned nematic liquid crystal light shutter** The polymer-stabilized homogeneously aligned nematic liquid crystal light shutter is made from a mixture of a nematic liquid crystal and diacrylate liquid crystal monomer [41, 50, 51]. Cells with anti-parallel homogeneous alignment layers are filled with the mixture and then photopolymerized in the nematic phase. The polymer network formed is parallel to the cell surface as is the liquid crystal. The nematic liquid crystal has a positive dielectric anisotropy. Figure 11.29 schematically shows how the shutter works. In Figure 11.29(a), when there is no applied voltage across the cell, the liquid crystal and the



**Figure 11.29** Schematic diagram showing how the polymer-stabilized homogeneously nematic liquid crystal light shutter works

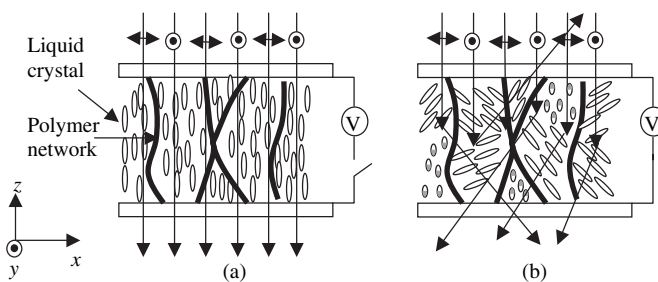
polymer network are homogeneously aligned in the  $x$  direction. When a light goes through the material, it encounters the same refractive index in the liquid crystal and polymer regions, and therefore it passes through the material without scattering. In Figure 11.29(b), the voltage applied across the cell intends to align the liquid crystal in the  $z$  direction while the polymer network tries to keep the liquid crystal in the  $x$  direction. As a result of the competition between the applied field and the polymer network, the liquid crystal is switched into a multi-domain structure. The liquid crystal molecules orient along the same direction within each domain but vary from domain to domain. The directions of the domains are random in the  $x$ - $z$  plane. For light polarized in the  $x$  direction, when it goes through the cell it encounters different refractive indices in different domains and therefore is scattered. For light polarized in the  $y$  direction, when it goes through the cell it always encounters the ordinary refractive index of the liquid crystal because the liquid crystal is oriented in the  $x$ - $z$  plane, and therefore it can pass through the cell without scattering. If the incident light is unpolarized, this shutter does not work well.

**(b) Polymer-stabilized homeotropic nematic liquid crystal light shutter** In order to overcome the problem where only one polarization component of unpolarized incident light is scattered in the polymer-stabilized homogeneously aligned nematic liquid crystal light shutter, the polymer-stabilized homeotropically aligned nematic liquid crystal was introduced [52]. The liquid crystal has a negative dielectric anisotropy ( $\Delta\epsilon < 0$ ). It is mixed with a small amount of diacrylate monomer and cells with homeotropic alignment layers are filled with it. The cells are irradiated by UV light for photopolymerization in the homeotropically aligned state. Thus the formed polymer network is perpendicular to the cell surface.

At zero field, the liquid crystal is in the uniform homeotropic state as shown in Figure 11.30(a); the material is a homogeneous optical medium. The light propagates through the material without scattering. When an electric field is applied, the liquid crystal molecules are tilted away from the field direction because of their negative dielectric anisotropy. The material is switched to a multi-domain structure as shown in Figure 11.30(b). When light propagates through the cell, it encounters different refractive indices in different domains because of the different tilts of the liquid crystal. The material is optically non-uniform and therefore it is scattering. When the liquid crystal molecules tilt, they tilt toward the  $x$  direction in some domains but toward the  $y$  direction in other domains. Therefore light polarized in both  $x$  and  $y$  directions is scattered. The polymer-stabilized homeotropically aligned nematic liquid crystal is a reverse-mode light shutter in the sense that it is transparent in the field-off state and scattering in the field-on state.

## (2) Polymer-stabilized cholesteric liquid crystals

Cholesteric liquid crystals (CLCs) have a helical structure where the liquid crystal director twists around a perpendicular axis, namely the helical axis. They exhibit three main textures (also referred to as states),



**Figure 11.30** Schematic diagram showing how the polymer-stabilized homeotropically nematic liquid crystal light shutter works

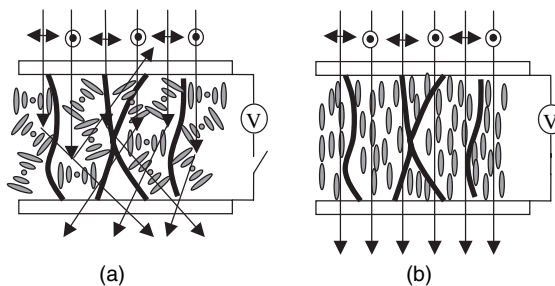
depending on the boundary condition and the applied field. When a CLC is in the planar texture (also referred to as Grandjean texture), the helical axis is perpendicular to the cell surface, and the material reflects light around the wavelength  $\bar{n}P$ , where  $\bar{n}$  is the average refractive index and  $P$  is the pitch of the liquid crystal. When the CLC is in the focal conic texture, the helical axis is more or less random throughout the cell, and the material is usually optically scattering. When a sufficiently high field is applied across the cell (along the cell normal direction), the CLC ( $\Delta\epsilon > 0$ ) is switched to the homeotropic texture where the helical structure is unwound and the liquid crystal director is aligned in the cell normal direction. The material is transparent. Polymer networks can be used to stabilize the planar texture or the focal conic texture at zero field.

**(a) Polymer-stabilized cholesteric texture normal-mode light shutter** The polymer-stabilized cholesteric texture (PSCT) normal-mode material is made from a mixture of CLC and a small amount of monomer [43,53]. The pitch of the liquid crystal is a few microns ( $\sim 0.5\text{--}5\ \mu\text{m}$ ). No special cell surface treatment is needed. The mixture is in the homeotropic texture in the presence of an external field when the monomers are polymerized. The polymer network formed is perpendicular to the cell surface as shown in Figure 11.31.

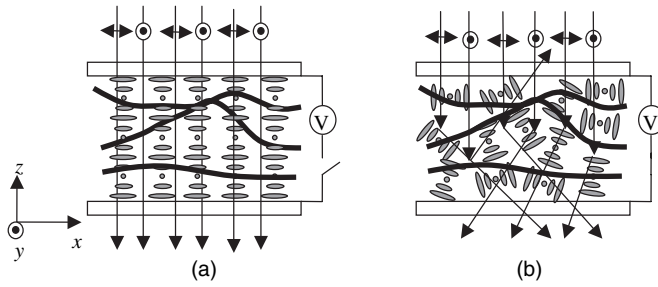
When the PSCT normal-mode light shutter is in a zero field state, the liquid crystal tends to have the helical structure, while the polymer network tends to keep the liquid crystal director parallel to it. The competition between these two factors results in the focal conic texture as shown in Figure 11.31(a). In this state, the material is optically scattering. When a sufficiently high electric field is applied across the cell, the liquid crystal ( $\Delta\epsilon > 0$ ) is switched to the homeotropic texture as shown in Figure 11.31(b), and therefore it becomes transparent. Because the concentration of the polymer is low and both the liquid crystal and the polymer are aligned in the cell normal direction, the PSCT normal-mode light shutter is transparent at any viewing angle. A photograph of a PSCT normal-mode light shutter is shown in Figure 11.2(a).

In order to scatter visible light strongly, the focal conic domain size has to be around the wavelength of the light. The main factors affecting the domain size are the pitch, polymer concentration, and curing UV intensity. The drive voltage is mainly determined by the pitch and the dielectric anisotropy of the liquid crystal. Faster responses can be achieved with shorter pitch CLCs. There is a hysteresis in the transition between the focal conic texture and the homeotropic texture, which also exists in pure CLCs.

**(b) PSCT reverse-mode light shutter** The PSCT reverse-mode light shutter is also made from a mixture of CLC ( $\Delta\epsilon > 0$ ) and a small amount of monomer. The pitch of the liquid crystal is a few microns ( $\sim 3\text{--}15\ \mu\text{m}$ ). A cell with homogeneous alignment layers is filled with the mixture. The mixture is in the planar texture at zero field because of the alignment layers. The monomers are polymerized in the planar texture. The polymer network formed is parallel to the cell surface [43, 53, 54].



**Figure 11.31** Schematic diagram showing how the PSCT normal-mode light shutter works

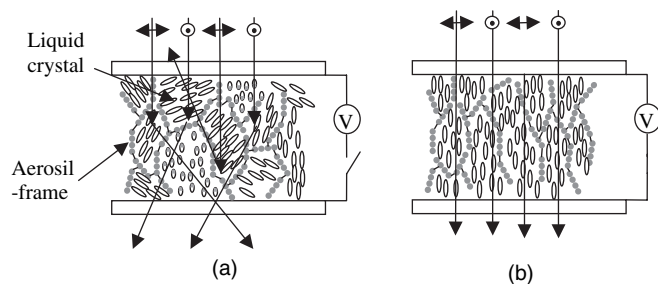


**Figure 11.32** Schematic diagram showing how the PSCT reverse-mode light shutter works

At zero field, the material is in the planar texture as shown in Figure 11.32(a). Because the pitch is in the IR region, the material is transparent to visible light. When an external field is applied across the cell, the field tends to align the liquid crystal in the cell normal direction while the polymer network tends to keep the liquid crystal in the planar texture. As a result of the competition between these two factors, the liquid crystal is switched to the poly-domain focal conic texture as shown in Figure 11.32(b), and the material becomes scattering. The polymer concentration must be sufficiently high and the polymerization rate should be low so that the polymer network is strong and not damaged (reoriented) under the applied field. A photograph of a PSCT reverse-mode light shutter is shown in Figure 11.2(b).

*(3) Aerosil-frame stabilized nematic liquid crystal*

Besides polymer networks, other networks can be used to stabilize liquid crystals [55–58]. One interesting example is the dispersion of nematic liquid crystal and silica particles. The volume fraction of the silica particles is a few percent. The silica particles of nanometer size form an aggregates via  $\equiv \text{Si}-\text{O}-\text{Si}$  moieties. The aggregates are linked to form aerosil-frame by hydrogen bonds between the  $\equiv \text{Si}-\text{OH}$  groups on the surface of the aggregates. The aerosil-frame creates a poly-domain structure as shown in Figure 11.33(a), and the material is scattering. When a sufficiently high field is applied, the liquid crystal ( $\Delta\epsilon > 0$ ) is aligned homeotropically as shown in Figure 11.33(b), and the material becomes transparent. The uniformly aligned liquid crystal exerts a torque on the aerosil-frame. A unique feature of the aerosil-frame is that the hydrogen bonds can be unlocked under stress, and the aerosil-frame broken. Then the  $\equiv \text{Si}-\text{OH}$  groups on the surface of the aggregates regroup to form hydrogen bonds again and the aggregates form a new frame which favors the homeotropic orientation of the liquid crystal. When the applied field is turned off, the material remains in the homeotropic state.



**Figure 11.33** Schematic diagram showing how the aerosil-frame stabilized nematic liquid crystal light shutter works

The aerosil-frame stabilized nematic liquid crystal material has a memory effect and is multi-stable. Two schemes can be employed to write the display made from the material. In the first scheme, a regular nematic liquid crystal with a positive dielectric anisotropy is used. The display is first switched to the transparent homeotropic state by applying a high voltage. It is then selectively addressed to the scattering state by using laser addressing. The laser irradiation heats the material locally to isotropic phase. When the material is quickly cooled to room temperature, the material ends in the scattering state. Thus images can be generated. In the second scheme, a dual-frequency nematic liquid crystal is used. When a low-frequency voltage is applied, the liquid crystal has a positive dielectric anisotropy and therefore is switched to the transparent state. When a high-frequency voltage is applied, the liquid crystal has a negative dielectric anisotropy and therefore is switched to the scattering state.

## 11.6 Displays from LCPCs

Scattering liquid crystal/polymer composites (LCPCs), besides being used for switchable privacy windows, can also be used to make displays. Without polarizers, they can only be used for reflective displays and projection displays because in both the transparent and scattering states most of the incident light still comes out in forward directions, except that in the scattering state, light is deviated from its original propagation direction. With polymerizers, they can be used for transmissive direct-view displays. These displays may not have the best optical performance, but they are compatible with flexible plastic substrates because of their adhesion to plastic substrates. They can be manufactured in a roll-to-roll process.

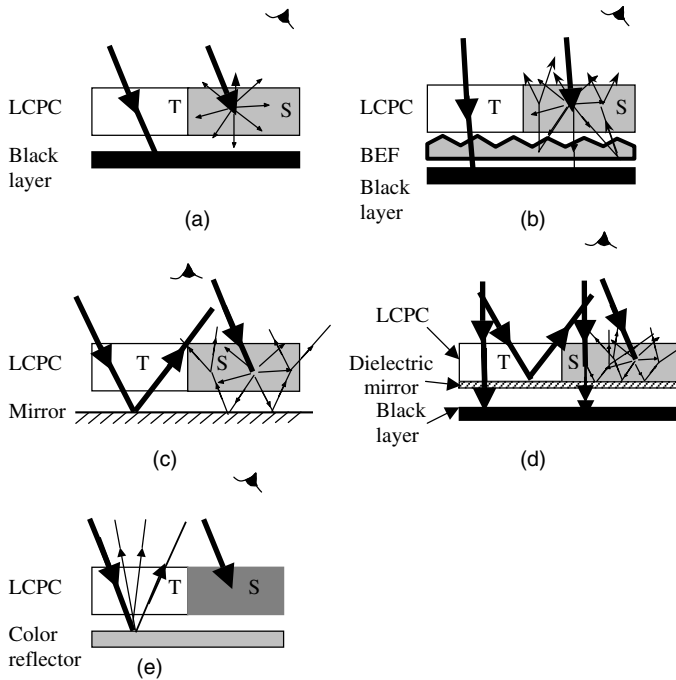
### 11.6.1 Reflective displays

There are several designs of scattering LCPCs for reflective displays. The simplest design is shown in Figure 11.34(a). The display consists of a layer of LCPC and a black absorbing layer [59]. When the LCPC in a pixel is in the transparent state, the incident light reaches the black layer and is absorbed, and the pixel appears black. When the LCPC is in the scattering state, some of the incident light is scattered backward and is observed by the reader's eyes, and the pixel appears gray–white. The problem of this design is that the reflectivity (the percentage of light scattered in the backward direction) is usually less than 25% [59].

One way to improve the reflectivity is to insert a brightness-enhancing film (BEF) [60,61], as shown in Figure 11.34(b), which transmits light with small incident angles (with respect to the film normal) but reflects light with large incident angles. When the LCPC in a pixel is in the transparent state, incident light with small incident angles goes through the LCPC and BEF, and reaches the black layer and is absorbed. When the LCPC is in the scattering state, incident light with small incident angles is scattered by the LCPC, and reaches the BEF with large incident angles and therefore is reflected back by the BEF. Therefore the reflectivity of the display is greatly increased. The tradeoff is that the contrast and viewing angle are decreased.

The third design is shown in Figure 11.34(c) where a mirror is used to replace the black layer. This display works well only when light is incident on it at one incident angle. When the LCPC in a pixel is in the transparent state, the light passes the LCPC, and is reflected by the mirror. The outgoing light is at the specular angle. If the reader looks at the display, not at the specular angle, the pixel has a black appearance. When the LCPC is in the scattering state, some of the incident light is scattered backward and the rest is scattered forward by the LCPC. The forward scattered light reaches the mirror and is reflected in all direction. Therefore the pixel has a white appearance. The reflectivity of the white is very high. The problem with this design is that the viewing angle is small.

The viewing angle can be improved by using a dielectric mirror as shown in Figure 11.34(d) [62]. The periodicity of the dielectric mirror is in the long-wavelength region. For normally incident light,



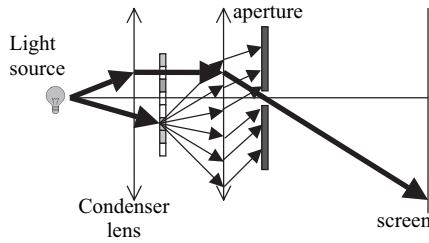
**Figure 11.34** Schematic structures of the reflective displays from scattering LCPCs: T, transparent state; S, scattering state

it only reflects long-wavelength light. For obliquely incident light, the reflection band is shifted to the short-wavelength region. The reader looks at the display in the normal direction. When the LCPC in a pixel is in the transparent state, light with small incident angles and short wavelength passes the LCPC and dielectric mirror and reaches the absorbing layer. The pixel has a black appearance. When the LCPC is in the scattering state, the incident light is scattered by the LCPC and reaches the dielectric mirror at large incident angle, and therefore is reflected. The pixel has a white appearance.

Black dichroic dye-doped LCPCs can also be used to make reflective displays [63]. Behind the LCPC film, there is a color reflector as shown in Figure 11.34(e). When the LCPC in a pixel is in the transparent state, light passes the LCPC and reaches the reflector and is reflected. The pixel shows the color of the reflector. When the LCPC is in the scattering absorbing state, the incident light is absorbed by the LCPC, and the pixel has a black appearance.

### 11.6.2 Projection displays

Scattering LCPCs can be used to make projection displays [29,64]. They do not need polarizers and therefore have high light efficiency. A simple projection display shown in Figure 11.35 is used to demonstrate the operating principle. The optical design is similar to that of a slide projector except that an additional aperture is placed at the focal plane of the objective lens. The condenser lens generates collimated light parallel to the principal axis. The objective lens produces an image on the screen of the display panel made from the LCPC. When the LCPC in a pixel (on-pixel) is in the transparent state, the collimated light passes the material without scattering, and then passes the aperture and reaches the screen. The corresponding area on the screen is bright. When the LCPC in

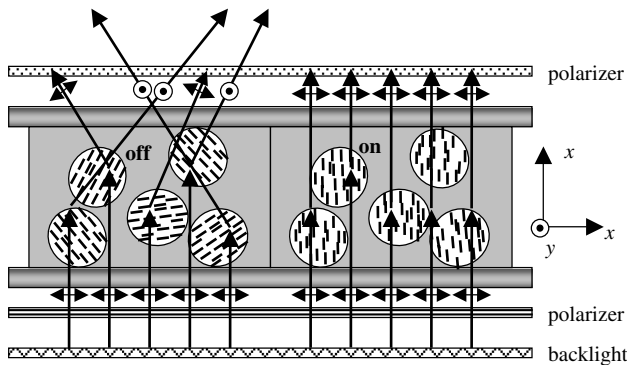


**Figure 11.35** Schematic diagram of the projection display from the scattering LCPC

a pixel is in the scattering state (off-pixel), the collimated incident light is scattered in all direction. Only a small part of the incident light can pass the aperture and reach the screen. The corresponding part on the screen is dark. In order to achieve high contrast, the aperture should be small so that little of the scattered light can go through it. The tradeoff with the small aperture is that light efficiency is low because incident light is never perfectly collimated if the light source is not a point light source but a filament of finite size. When the aperture is small and the incident light is not perfectly collimated, some light cannot pass the aperture and thus is lost even if a pixel is in the on-state.

**11.6.3 Transmissive direct-view displays**

Scattering LCPCs can also be used to make transmissive direct-view displays if polarizers are used. An example is shown in Figure 11.36 where a LCPC is sandwiched between two crossed polarizers along the *x* and *y* directions, respectively [65]. The light from the backlight becomes linearly polarized along the *x* direction after passing through the bottom polarizer. When the LCPC in a pixel (on-pixel) is in the scattering state, the linearly polarized incident light is depolarized with 50% light polarized along the *x* direction and 50% light polarized along the *y* direction. The light polarized along the *y* direction passes the top polarizer. The pixel is bright. When the LCPC in a pixel (off-pixel) is in the transparent state, the polarization of the incident light does not change when propagating through the material and the light is absorbed by the top polarizer. The pixel is dark. Besides its suitability for flexible displays, this display has a large viewing angle when compensated with a negative *c* plate. The drawback is that the maximum light efficiency is only 25%.



**Figure 11.36** Schematic diagram showing how the direct-view display from the scattering LCPC works

## Homework Problems

- 11.1 Consider a ternary mixture consisting of three different molecules A, B, and C. Their molar fractions are  $x_A$ ,  $x_B$ , and  $x_C$ , respectively, and  $x_A + x_B + x_C = 1$ . The intermolecular interaction energies are  $u_{AA}$  for the interaction between A and A,  $u_{BB}$  for the interaction between B and B,  $u_{CC}$  for the interaction between C and C,  $u_{AB}$  for the interaction between A and B,  $u_{AC}$  for the interaction between A and C, and  $u_{BC}$  for the interaction between B and C. Calculate the mixing interaction energy.
- 11.2 Consider a binary mixture consisting of A and B. The molar fraction of B is  $x$ . The interaction energies between them are:  $u_{AA} = -0.15$  eV,  $u_{BB} = -0.17$  eV, and  $u_{AB} = -0.13$  eV. The number  $P$  of nearest neighbors is 6. (1) Determine the phase diagram numerically. (2) Find the critical point  $(T_c, x_c)$  of the phase separation. (3) If the fraction of B in the homogeneous mixture is  $x_o = 0.3$ , at what temperature  $T_s$  will the system phase separate into two phases? (4) At temperature  $T = 800$  K, what are the fractions of B in the two-phase separated phases?
- 11.3 Consider a ternary mixture consisting of three types of molecules (A, B, C). The interaction energies between them are:  $u_{AA} = -0.15$  eV,  $u_{AB} = -0.05$  eV,  $u_{BB} = -0.15$  eV,  $u_{AC} = -0.20$  eV,  $u_{BC} = -0.175$  eV, and  $u_{CC} = -0.15$  eV. Consider only the interaction between nearest neighbors. The number of nearest neighbors is 6. The temperature is  $k_B T = 0.2$  eV. (1) Find the phase diagram represented in the equilateral triangle. (2) Determine the critical point. (3) For a mixture with molar fractions  $x_a = 0.4$ ,  $x_B = 0.45$ , and  $x_C = 0.15$ , will it phase separate? If it does, determine the fractions of the components in the two phases and the percentages of molecules in the two phases.
- 11.4 *Phase diagram of ternary mixture.* Consider a ternary mixture consisting of three types of molecules A, B, and C. A and C dissolve each other, B and C dissolve each other, but A and B do not dissolve each other. The interaction energies between them are  $u_{AA} = -0.15$  eV,  $u_{AB} = -0.05$  eV,  $u_{AC} = -0.20$  eV,  $u_{BB} = -0.14$  eV,  $u_{BC} = -0.175$  eV, and  $u_{CC} = -0.15$  eV. Consider only the interaction between nearest neighbors. The number of nearest neighbors is 6. The temperature is  $k_B T = 0.2$  eV. (1) Find the phase diagram represented in the equilateral triangle. (2) Determine the critical point. (3) If the initial mixture has the fractions  $x_a = 0.4$ ,  $x_B = 0.45$ , and  $x_C = 0.15$ , will it phase separate? If it does, determine the fractions of the three components in the two phases and the percentages of the molecules in the two phases.

The phase diagram of a ternary mixture at a given temperature is determined in the following way:

- (1) Choose an initial mixture with the fractions  $x_{Ao}, x_{Bo}, x_{Co}$  ( $= 1 - x_{Ao} - x_{Bo}$ ) which is a point on a straight line drawn from the corner corresponding to component C to the opposite side of the equilateral triangle. Calculate the average free energy per molecule  $f_h = f(x_{Ao}, x_{Bo})$  of the homogeneous single phase with the initial fractions.
- (2) Assume the initial mixture phase separates into two phases: phase 1 with fractions  $(x_{A1}, x_{B1}, x_{C1})$  and phase 2 with the fractions  $(x_{A2}, x_{B2}, x_{C2})$ . The percentage of molecules in phase 1 is  $w$  and the percentage of particles in phase 2 is  $(1 - w)$ . Because of particle conservation,  $x_{Ao} = wx_{A1} + (1 - w)x_{A2}$  and  $x_{Bo} = wx_{B1} + (1 - w)x_{B2}$ . Therefore among these variables  $x_{A1}, x_{B1}, x_{A2}, x_{B2}, w$ , only three are independent. Choose  $x_{A1}, x_{B1}, w$  as the independent variables, and then  $x_{C1} = 1 - x_{A1} - x_{B1}$ ,  $x_{A2} = (x_{Ao} - wx_{A1})/(1 - w)$ ,  $x_{B2} = (x_{Bo} - wx_{B1})/(1 - w)$ , and  $x_{C2} = (x_{Co} - wx_{C1})/(1 - w)$ . Note that  $0 \leq w \leq 1$ ,  $0 \leq x_{A1} \leq 1$ ,  $0 \leq x_{B1} \leq 1$ , and  $0 \leq x_{A1} + x_{B1} \leq 1$ . Find the average free energy per molecule  $f_i = wf(x_{A1}, x_{B1}) + (1 - w)f(x_{A2}, x_{B2})$  of the phase-separated system.
- (3) Find the  $x_{A1}, x_{B1}, w$  which give the minimum free energy  $f_{im}$ . If  $f_{im} < f_h$ , the system will phase separate into two phases corresponding to the fractions  $(x_{A1}, x_{B1}, x_{C1})$  and  $(x_{A2}, x_{B2}, x_{C2})$ . These two points are on the phase boundary curve. If  $f_{im} > f_h$ , then there is no phase separation.
- (4) Repeat the above steps with a different initial mixture. After a sufficiently large number of initial mixtures are tested, the points representing the phase-separated phases form the phase boundary.



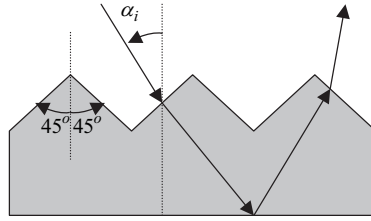


Figure 11.37

- 11.5 Consider the brightness-enhancing film shown in Figure 11.37. Calculate the incident angle region within which the incident light will be reflected from the bottom surface of the brightness-enhancing film by total internal reflection.
- 11.6 Calculate the director configuration inside a bipolar droplet with radius  $R = 5 \mu\text{m}$  under the following externally applied electric fields:  $0$ ,  $1 \text{ V}/\mu\text{m}$ ,  $10 \text{ V}/\mu\text{m}$ . The elastic constants are  $K_{11} = K_{33} = 10^{-11} \text{ N}$  and the dielectric anisotropy is  $\Delta\epsilon = 10$ . The electric field is applied along the bipolar axis.
- 11.7 The scattering profile of a PDLC in the scattering state is described by  $I(\theta) = (2/\pi)(1 + \cos \theta)$ , where  $\theta$  is the polar angle with the incident light direction. The incident light is collimated and normal to the cell surface. When the cell is in the transparent state, the light goes through the cell without scattering. The detector has a circular detection surface with a linear collection of  $10^\circ$ . What is the contrast ratio of the PDLC?

## References

- 1 P. S. Drzaic, 'Liquid crystal dispersions' (World Scientific, Singapore, 1995).
- 2 G. P. Crawford and S. Zumer, 'Liquid crystals in complex geometries' (Taylor & Francis, London, 1996).
- 3 J. W. Doane, 'Polymer dispersed liquid crystal displays', in 'Liquid crystals—applications and uses', Vol. 1, Chapter 14, ed. B. Bahadur (World Scientific, Singapore, 1990).
- 4 H.-S. Kitzerow, 'Polymer-dispersed liquid crystals, from the nematic curvilinear aligned phase to ferroelectric films', *Liq. Cryst.*, **16**, 1 (1994).
- 5 G. P. Crawford, J. W. Doane, and S. Zumer, 'Polymer dispersed liquid crystals: nematic droplets and related systems', in 'Handbook of liquid crystal research', Chapter 9, ed. P. J. Collings and J. S. Patel (Oxford University Press, New York, 1997).
- 6 C. Kittel and H. Kroemer, 'Thermal physics', 2nd edn (W. H. Freeman, San Francisco, 1980).
- 7 J. L. West, 'Phase separation of liquid crystals in polymers', *Mol. Cryst. Liq. Cryst.*, **157**, 427 (1988).
- 8 U. Eisele, 'Introduction to polymer physics' (Springer-Verlag, Berlin, 1990).
- 9 P. J. Flory, 'Thermodynamics of high polymer solutions', *J. Chem. Phys.*, **10**, 51 (1942).
- 10 M. L. Huggins, 'Thermodynamic properties of solutions of long-chain compounds', *Ann. New York Acad. Sci.*, **43**, 1 (1942).
- 11 J. L. Ferguson, 'Polymer encapsulated nematic liquid crystals for scattering and light control applications', *SID Symp. Dig. Tech. Pap.*, **16**, 68 (1985).
- 12 P. Becher, 'Emulsions, theory and practice', 3rd edn (Oxford University Press, Oxford, 2001).
- 13 H. C. van de Hulst, 'Light scattering by small particles' (Dover, New York, 1957).
- 14 S. Zumer and J. W. Doane, 'Light scattering from small nematic droplet', *Phys. Rev. A*, **34**, 3373 (1986).
- 15 G. P. Montgomery, Jr., 'Angle-dependent scattering of polarized light by polymer dispersed liquid-crystal films', *J. Opt. Soc. Am. B*, **5**, 774 (1988).
- 16 G. P. Montgomery, Jr., and N. Vaz, 'Light-scattering analysis of the temperature-dependent transmittance of a polymer-dispersed liquid-crystal film in its isotropic phase', *Phys. Rev. A*, **40**, 6580 (1989).

- 17 S. Zumer, 'Light scattering from nematic droplets: anomalous-diffraction approach', *Phys. Rev. A*, **37**, 4006 (1988).
- 18 J. R. Kelly, W. Wu, and P. Palffy-Muhoray, 'Wavelength dependence of scattering in PDLC film: droplet size effect', *Mol. Cryst. Liq. Cryst.*, **223**, 251 (1992).
- 19 J. R. Kelly and W. Wu, 'Multiple-scattering effects in polymer-dispersed liquid-crystals', *Liq. Cryst.*, **14**, 1683 (1993).
- 20 J. W. Doane, A. Golemme, J. L. West, J. B. Whitehead, Jr., and B.-G. Wu, 'Polymer dispersed liquid crystals for display application', *Mol. Cryst. Liq. Cryst.*, **165**, 511 (1988).
- 21 R. Ondris-Crawford, E. P. Boyko, B. G. Wagner, J. H. Erdmann, S. Zumer, and J. W. Doane, 'Microscope textures of nematic droplets in polymer dispersed liquid crystals', *J. Appl. Phys.*, **69**, 6380 (1991).
- 22 P. S. Drzaic, 'A new director alignment for droplets of nematic liquid crystal with low bend-to-splay ratio', *Mol. Cryst. Liq. Cryst.*, **154**, 289 (1988).
- 23 J. H. Erdmann, S. Zumer, and J. W. Doane, 'Configuration transition in a nematic liquid crystal confined to a small cavity', *Phys. Rev. Lett.*, **64**, 1907 (1990).
- 24 B. G. Wu, J. H. Erdmann, and J. W. Doane, 'Response times and voltages for PDLC light shutters', *Liq. Cryst.*, **5**, 1453 (1989).
- 25 H. Lin, H. Ding, and J. R. Kelly, 'The mechanism of switching a PDLC film', *Mol. Cryst. Liq. Cryst.*, **262**, 99 (1995).
- 26 P. S. Drzaic, 'Polymer dispersed nematic liquid crystal for large area displays and light valves', *J. Appl. Phys.*, **60**, 2142 (1986).
- 27 W. Wu, 'Single and multiple light scattering studies of PDLC films in the presence of electric fields', Dissertation (Kent State University, 1999).
- 28 J. W. Doane, N. A. Vaz, B.-G. Wu, and S. Zumer, 'Field controlled light scattering from nematic microdroplets', *Appl. Phys. Lett.*, **48**, 269 (1996).
- 29 A. Tomita and P. Jones, 'Projection displays using nematic dispersions', *SID Symp. Dig. Tech. Pap.*, **23**, 579 (1992).
- 30 N. A. Vaz, G. W. Smith, and G. P. Montgomery, Jr., 'A light control film composed of liquid crystal droplets dispersed in a UV-curable polymer', *Mol. Cryst. Liq. Cryst.*, **146**, 1 (1987).
- 31 P. S. Drzaic, 'Nematic droplet/polymer films for high-contrast colored reflective displays', *Display*, 2-13 (1991).
- 32 J. L. West and R. Ondris-Crawford, 'Characterization of polymer dispersed liquid crystal shutters by ultraviolet/visible and infrared absorption spectroscopy', *J. Appl. Phys.*, **70**, 3785 (1991).
- 33 R. L. Sutherland, 'Bragg scattering in permanent nonlinear-particle composite gratings', *J. Opt. Soc. Am. B*, **8**, 1516 (1991).
- 34 R. L. Sutherland, V. P. Tondiglia, and L. V. Natarajan, 'Electrically switchable volume gratings in polymer-dispersed liquid crystal', *Appl. Phys. Lett.*, **64**, 1074 (1994).
- 35 T. J. Bunning, L. V. Natarajan, V. P. Tondiglia *et al.*, 'Holographic polymer-dispersed liquid crystals (H-PDLCs)', *Annu. Rev. Mater. Sci.*, **30**, 83 (2000).
- 36 T. J. Bunning, L. V. Natarajan, V. P. Tondiglia *et al.*, 'Morphology of reflection holograms formed in situ using polymer-dispersed liquid crystals', *Polymer*, **14**, 3147 (1996).
- 37 K. Tanaka, K. Kato, S. Tsuru, and S. Sakai, 'Holographically formed liquid-crystal/polymer device for reflective color display', *J. SID*, **2**, 37 (1994).
- 38 G. P. Crawford, T. G. Fiske, and L. D. Silverstein, 'Reflective color LCDs based on H-PDLC and PSCT technologies', *SID Symp. Dig. Tech. Pap.*, **27**, 99 (1996).
- 39 M. J. Escuti, P. Kosssyrev, C. C. Bowley, S. Danworaphong, G. P. Crawford, T. G. Fiske, J. Colegrove, L. D. Silverstein, A. Lewis, and H. Yuan, 'Diffuse H-PDLC reflective displays: an enhanced viewing-angle approach', *SID Symp. Dig. Tech. Pap.*, **31**, 766 (2000).
- 40 C. C. Bowley, A. K. Fontecchio, and G. P. Crawford, 'Electro-optical investigations of H-PDLCs: the effect of monomer functionality on display performance', *SID Symp. Dig. Tech. Pap.*, **30**, 958 (1999).
- 41 R. A. M. Hikmet, 'Anisotropic gels obtained by photopolymerization in the liquid crystal state', in '*Liquid crystals in complex geometries*', ed. G. P. Crawford and S. Zumer 53-82 (Taylor & Francis, London, 1996).
- 42 D. J. Broer, 'Networks formed by photoinitiated chain cross-linking', in '*Liquid crystals in complex geometries*', ed. G. P. Crawford and S. Zumer 239-255 (Taylor & Francis, London, 1996).

- 43 D.-K. Yang, L.-C. Chien, and Y. K. Fung, 'Polymer stabilized cholesteric textures: materials and applications', in *'Liquid crystals in complex geometries'*, ed. G. P. Crawford and S. Zumer 103–143 (Taylor & Francis, London, 1996).
- 44 D. J. Broer, R. G. Gossink, and R. A. M. Hikmet, 'Oriented polymer networks obtained by photopolymerization of liquid crystal-crystalline monomers', *Angew. Makromol. Chem.*, **183**, 45 (1990).
- 45 Y. K. Fung, D.-K. Yang, Y. Sun, L. C. Chien, S. Zumer, and J. W. Doane, 'Polymer networks formed in liquid crystals', *Liq. Cryst.*, **19**, 797 (1995).
- 46 I. Dierking, L. L. Kosbar, A. C. Lowe, and G. A. Held, 'Two-stage switching behavior of polymer stabilized cholesteric textures', *J. Appl. Phys.*, **81**, 3007 (1997).
- 47 G. A. Held, L. L. Kosbar, I. Dierking, A. C. Lowe, G. Grinstein, V. Lee, and R. D. Miller, 'Confocal microscopy study of texture transitions in a polymer stabilized cholesteric liquid crystal', *Phys. Rev. Lett.*, **79**, 3443 (1997).
- 48 R. Q. Ma and D.-K. Yang, 'Freedericksz transition in polymer stabilized nematic liquid crystals', *Phys. Rev. E.*, **61**, 1576 (2000).
- 49 Y. K. Fung, A. Borstnik, S. Zumer, D.-K. Yang, and J. W. Doane, 'Pretransitional nematic ordering in liquid crystals with dispersed polymer networks', *Phys. Rev. E*, **55**, 1637 (1997).
- 50 R. A. M. Hikmet, 'Anisotropic gels and plasticised networks formed by liquid crystal molecules', *Liq. Cryst.*, **9**, 405 (1991).
- 51 R. A. M. Hikmet and H. M. J. Boots, 'Domain structure and switching behavior of anisotropic gels', *Phys. Rev. E*, **51**, 5824 (1995).
- 52 R. A. M. Hikmet, 'Electrically induced light scattering from anisotropic gels with negative dielectric anisotropy', *Mol. Cryst. Liq. Cryst.*, **213**, 117 (1992).
- 53 D.-K. Yang, L. C. Chien, and J. W. Doane, 'Cholesteric liquid crystal/polymer gel dispersion for haze-free light shutter', *Appl. Phys. Lett.*, **60**, 3102 (1992).
- 54 R. Q. Ma and D.-K. Yang, 'Polymer stabilized cholesteric texture reverse-mode light shutter: cell design', *J. SID*, **6**, 125 (1998).
- 55 M. Kreuzer and T. Tschudi, 'Erasable optical storage in bistable liquid crystal cells', *Mol. Cryst. Liq. Cryst.*, **223**, 219 (1992).
- 56 M. Kreuzer and H. Gottschling, and T. Tschudi, 'Structure from formation and self-organization phenomena in bistable optical elements', *Mol. Cryst. Liq. Cryst.*, **207**, 219 (1991).
- 57 M. Kreuzer, W. Balzer, and T. Tschudi, 'Formation of spatial structures in bistable optical elements containing nematic liquid crystals', *Mol. Cryst. Liq. Cryst.*, **198**, 231 (1991).
- 58 M. Kreuzer, H. Leigeber, R. Maurer, and A. Miller, 'Bacteriorhodopsin: a dynamic high resolution optical recording material for parallel optical information processing', *Proceedings of Japan Display '92*, 175 (1992).
- 59 P. Nolan, M. Tillin, D. Coates, E. Ginter, E. Lueder, and T. Kallfass, 'Reflective mode PDLC displays paper white display', *Proceedings of EuroDisplay '93*, 397 (1993).
- 60 J. D. LeGrange, T. M. Miller, P. Wiltzius, K. R. Amudson, J. Boo, A. van Blaaderer, M. Srinivasarao, and A. Kmetz, 'Brightness enhancement of reflective polymer-dispersed LCDs', *SID Symp. Dig. Tech. Pap.*, **26**, 275 (1995).
- 61 A. Kanemoto, Y. Matsuki, and Y. Takiguchi, 'Back scattering enhancement in polymer dispersed liquid crystal display with prism array sheet', *Proceedings of International Display Research Conference*, 183 (1994).
- 62 H. J. Cornelissen, J. H. M. Neijzen, F. A. M. A. Paulissen, and J. M. Schlangen, 'Reflective direct-view LCDs using polymer dispersed liquid crystal (PDLC) and dielectric reflectors', *Proceedings of the International Display Research Conference*, 144 (1997).
- 63 P. S. Drzaic, 'Light budget and optimization strategies for display applications of dichroic nematic droplet/polymer films', *Proc. SPIE*, **1455**, 255 (1991).
- 64 Y. Ooi, M. Sekine, S. Niiyama, Y. Hirai, M. Kunigita, T. Wakabayashi, M. Yuki, and T. Gunjima, 'LCPC project display system for HDTV', *Proceedings of Japan Display '92*, 113 (1992).
- 65 H. Yoshida, K. Nakamura, H. Tsuda, M. Ohashi, I. Tomita, and M. Okabe, 'Direct-view polymer-dispersed LCD with crossed Nicols and uniaxial film', *J. Soc. Inf. Disp.*, **2**, 135 (1994).

# Tunable Liquid Crystal Photonic Devices

## 12.1 Introduction

In addition to displays, liquid crystals have also been used extensively in tunable photonic devices, such as optical phased arrays for laser beam steering, variable optical attenuators (VOAs) for telecommunications, tunable-focus lenses for camera zoom lenses, liquid crystal-infiltrated photonic crystal fibers, [1, 2] diode laser-pumped dye-doped liquid crystal lasers, just to mention a few.

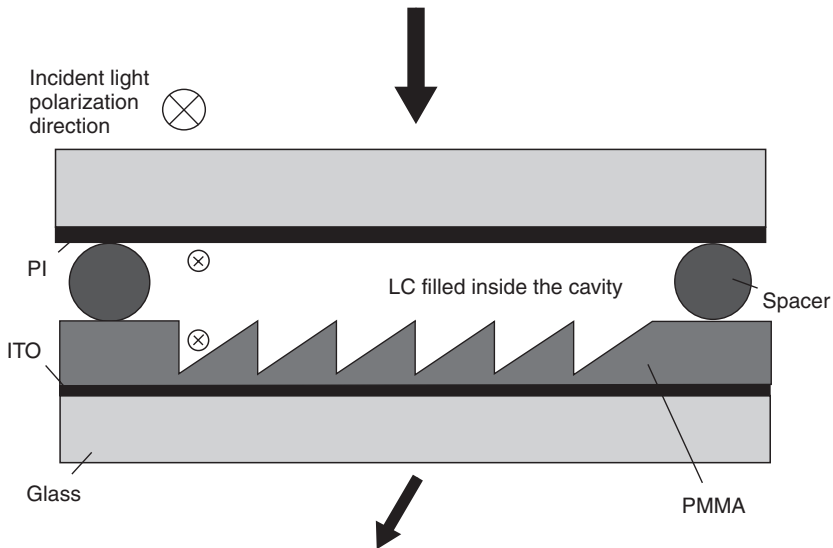
The performance criteria for displays and photonics are quite different. First, most displays such as computers and TVs are operating in the visible spectral region, but many photonic applications operate in the infrared. Laser beam steering for free-space communications operates at  $\lambda = 1.55 \mu\text{m}$ , for example. So do VOAs and photonic fibers. Secondly, most displays use amplitude modulation, but some photonics use phase modulation. For intensity modulation, the required phase retardation is  $1\pi$  at  $\lambda = 550 \text{ nm}$ , but for phase modulation, say beam steering, the minimum phase change is  $2\pi$  at  $\lambda = 1550 \text{ nm}$ . If we use the same LC material, then the required cell gap for a laser beam steerer is about six times thicker than that for a display device. A thicker cell gap implies a slower response time because the response time of a LC device is proportional to the cell gap squared. Thirdly, for display applications the 'detector' is the human eye, but for beam steering or fiber communications the detector is a solid state diode. The latter has a much faster response time than the former. Based on these three key performance factors, the technical challenge for a near-infrared phase modulator is at least one order of magnitude higher than for visible displays. Of course, most displays require a wide viewing angle, which is not so demanding in beam steering and VOA.

In this chapter, we select four topics to illustrate the potential applications of LCs in photonics and their technical challenges. The four representative subjects are: (1) laser beam steering, (2) VOAs, (3) tunable-focus lenses, and (4) polarization-independent LC devices.

## 12.2 Laser Beam Steering

Laser beam steering is an important subject for free-space communications, military applications, optical interconnects, projection displays, and other general industrial applications. The goal is to deliver and precisely control the laser beams to a desired location. The most common technique is to reflect the light by mechanically controlled mirrors. Because of the nature of mechanical movement, the speed of the system is limited. It is always desirable to develop compact and lightweight non-mechanical beam-steering devices to replace large and bulky mechanical systems. The other well-established beam-steering device is the acousto-optic modulator, which has a severely limited angular range. Many new solid state/micro-component technologies such as optical micro-electro-mechanical systems (MEMS), patterned liquid crystals, diffractive micro-optics, and photonic crystals have been investigated for building small, ultra-light, rapidly steered laser beam subsystems.

Two types of LC electro-optic beam-steering devices have been developed: diffractive [3] and prismatic types [4, 5]. A conventional simple grating structure produces several diffraction orders (first and higher orders). The theoretical diffraction efficiency of the first-order beam is about 34% [6]. The laser holographic blazing process shapes the grooves of the grating to concentrate the light to first order. The result is a much brighter spectrum. A well-designed LC prism grating can reach 100% diffraction efficiency for a first-order beam. A simple method for fabricating LC blazed gratings is to use a glass substrate with a sawtooth surface structure, as Figure 12.1 shows [7]. The LC layer thickness in this structure varies periodically and asymmetrically. The sawtooth substrate is a poly (methyl methacrylate) (PMMA) blazed grating made by electron beam lithography. The refractive index of PMMA is close to the ordinary index of the selected LC, but smaller than the extraordinary index. Therefore, in the voltage-off state, the in-plane distribution of the optical path length of the incident light has a sawtooth profile. The blazed grating is switched off when the applied voltage is sufficiently high.



**Figure 12.1** LC blazed-grating beam deflector using a glass substrate with a sawtooth surface structure: PI, polyimide; ITO, indium–tin–oxide; PMMA, poly methyl methacrylate

12.2.1 Optical phased array

The above surface relief grating causes distortion in LC alignment and might degrade the diffraction efficiency. It is better to use a sawtooth electric field to generate the LC blazed grating on a uniform LC layer, as shown in Figure 12.2. Several approaches have been reported to achieve the sawtooth electric field distribution, such as LC spatial light modulators, beam steerers with a stripe electrode [8, 9], and a combination of low- and high-resistive electrodes [10].

Figure 12.2 illustrates a transmission mode optical phased array (OPA) beam steerer composed of a one-dimensional (1-D) array of equal-spaced LC phase shifters [11]. The inner surface of the bottom transparent substrate is photolithographically patterned with transparent, conducting, striped electrodes having the desired spacing for the phase shifters in the array. The entire active aperture of the array is so patterned. The inner side of the top substrate is coated with a uniform, transparent, conducting ground electrode. On top of the electrodes, a thin SiO<sub>2</sub> layer is deposited to align LC molecules. For phase-only modulation, homogeneous alignment with a small ( $\sim 2-3^\circ$ ) pretilt angle is preferred. When the applied voltage between any given striped electrode and the underlying ground plane exceeds the Freedericksz transition threshold, a 1-D phase shifter in the LC volume underlying the patterned electrode is created.

The degree of nematic LC reorientation depends on the applied voltage [12]. Therefore, by controlling the applied voltage to each pixel, a stair-step blazed phase grating can be generated. Application of a periodic sequence of staircase voltage ramps of period  $\Lambda$  across the array aperture creates a corresponding periodic staircase profile of phase, as shown in the expanded portion of Figure 12.2. With properly weighted voltage steps, chosen to compensate for the non-linear phase-voltage profile of a typical LC, a linearly increasing phase profile can be produced. If the maximal phase shift on each staircase ramp of  $N$  voltage steps is  $2\pi(N - 1)/N$ , the periodic (modulo  $2\pi$ ) phase profile is equivalent to a single staircase phase ramp across the aperture. An electronically adjustable prism is simulated, and the beam is steered to a new direction  $\theta$  (relative to the phased array boresite) given by the general grating equation

$$\sin \theta + \sin \theta_{inc} = \lambda_o / \Lambda \tag{12.1}$$

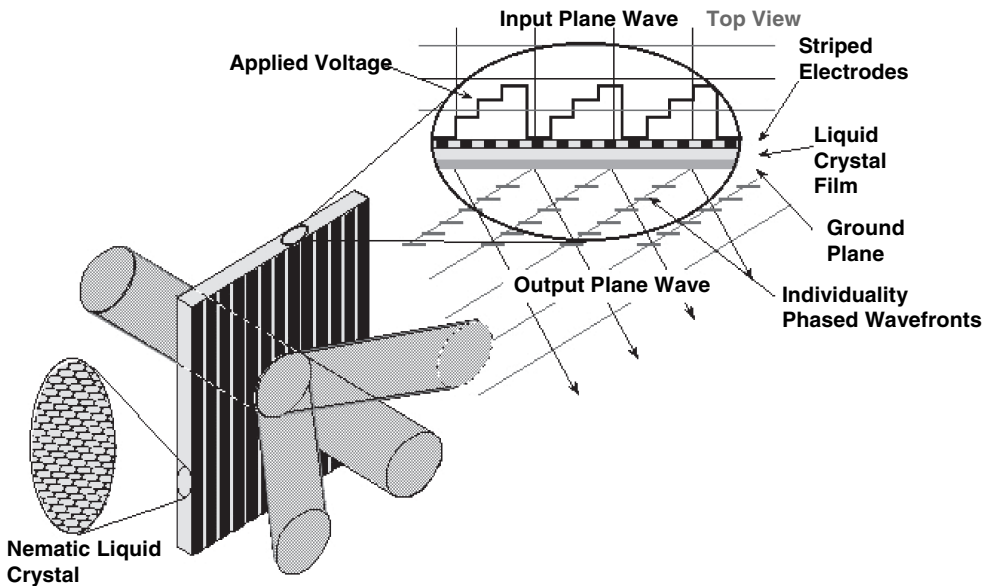
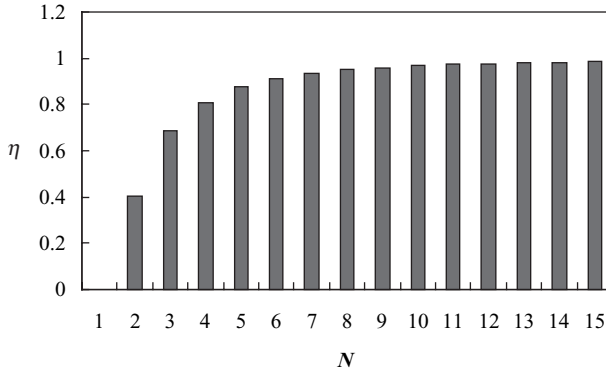


Figure 12.2 Schematic drawing of a 1-D optical phased array and a conceptual imposed phase shift



**Figure 12.3** Diffraction efficiency of a blazed grating as a function of the number of phase steps

where  $\theta_{inc}$  is the incident angle of the beam, and  $\Lambda$  is the period of the programmed grating. For a normally incident laser beam,  $\theta_{inc} = 0$  and Equation (12.1) is simplified. The steering direction depends on the periodicity (and sign) of the applied voltage ramp. The diffraction efficiency  $\eta$  of a grating with a stair-step blaze designed to maximize energy to first order is related to the number of steps  $N$  as [13]

$$\eta = [\sin(\pi/N)/(\pi/N)]^2 \tag{12.2}$$

Figure 12.3 plots the diffraction efficiency as a function of  $N$ . The efficiency grows rapidly with  $N$  and reaches  $\sim 95\%$  for an eight stair-step OPA. The remaining 5% is diffracted to higher orders, called sidelobes. Although increasing the number of stair steps would enhance the diffraction efficiency slightly, its fabrication complexity also increases. In practice, eight stair steps are normally used.

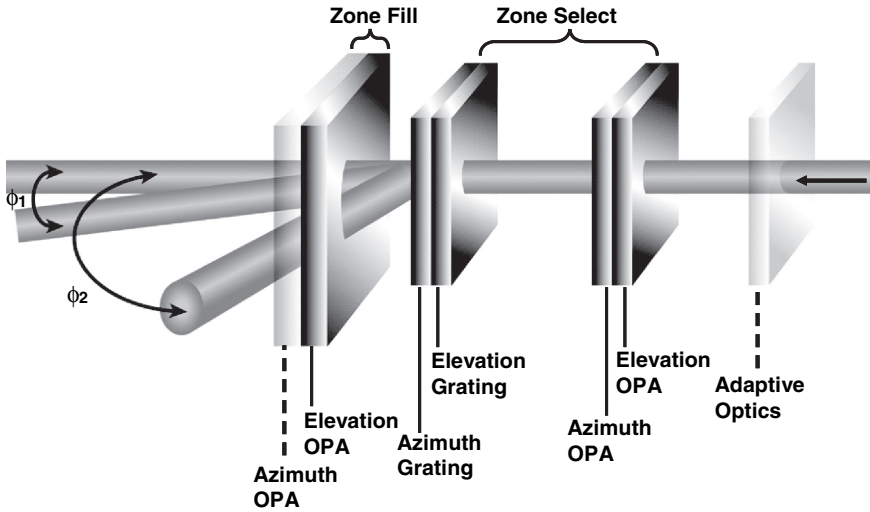
The OPA can be operated in reflective mode, provided that the bottom transparent electrode is replaced by a reflector. To achieve the same phase change, the required cell gap can be reduced by a half because of the double pass of the incident beam. As a result, the response time is four times faster.

Figure 12.4 shows a 2-D steering by cascading two 1-D steering arrays with crossed electrode patterns: one for azimuth (AZ) and one for elevation (EL). The cascading can use individual, discrete, steering devices. Relay lenses can be used to avoid beam walkoff between the devices, as is sometimes done with mechanical steerers [14]. However, the inherently thin ( $< 0.5$  mm) format of these LC cells has obviated the need for such relay lenses. The availability of both reflection- and transmission-mode variants facilitates the design of cascaded systems. An attractive prospect is the integration of AZ and EL steering units into a single thin cell, potentially conformal with an airframe. Current OPA designs are polarization dependent; they require the input beam to be linearly polarized along the direction of quiescent LC alignment for maximal efficiency. Later in this chapter, we will discuss two potential approaches that are polarization independent.

Since an OPA has a relatively small steering angle, to achieve large angle steering an auxiliary diffraction grating is needed. In Figure 12.4, the first two OPAs on the incident beam side and the double grating made of photothermal refractive glass [15, 16] form the large angle ( $\phi_2$ ) beam steerer for zone selection (also called coarse beam steerer). Once the laser beam is steered to a designated zone, the last two OPAs are used to fill the zone (also called fine beam steerer).

### 12.2.2 Prism-based beam steering

Figure 12.5 shows a prism-based beam-steering device using a birefringent prism with wedge angle  $\alpha$  and a switchable  $90^\circ$  TN cell as a polarization rotator. At  $V = 0$ , the TN cell rotates the input linearly polarized light by  $90^\circ$ , which acts as an extraordinary beam (refractive index  $n_e$ ) to the prism. The beam



**Figure 12.4** A 2-D beam steerer using zone select and zone fill OPAs in conjunction with two gratings

is deflected to an angle  $\theta_e$ . When the TN cell is activated, the LC directors are reoriented perpendicular to the substrate surfaces so that the polarization rotation effect vanishes. The polarization of the incident light is not affected by the TN cell. As a result, the outgoing light behaves like an ordinary beam (refractive index  $n_o$ ) to the prism and is deflected to an angle  $\theta_o$ .

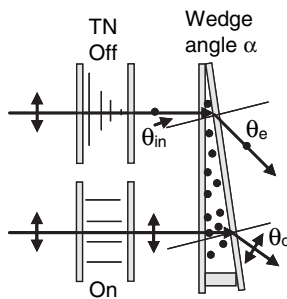
From Snell’s law, we can calculate the exit angles  $\theta_e$  and  $\theta_o$ :

$$n_e \sin \theta_{in} = \sin \theta_e \tag{12.3a}$$

$$n_o \sin \theta_{in} = \sin \theta_o \tag{12.3b}$$

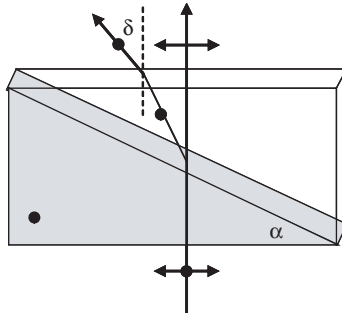
The difference between  $\theta_e$  and  $\theta_o$  is the steering angle. A prism with a larger birefringence would lead to a larger steering angle.

As shown in Figure 12.5, both beams walk off from the original beam path. To correct this walk-away phenomenon, a birefringent/isotropic bi-prism concept has been developed [17]. Figure 12.6 shows the device structure and operating mechanisms of the birefringent/isotropic bi-prism. The refractive index of



**Figure 12.5** The operating principles of a prism-type beam-steering device using a 90° TN cell as a polarization rotator





**Figure 12.6** Device structure of a birefringent/isotropic bi-prism beam steerer

the top isotropic prism is chosen to be equal to the  $n_o$  of the birefringent prism. Thus, the impinging ordinary ray is not deflected, while the extraordinary ray is deflected. Similarly, a  $90^\circ$  TN cell is used to control the input polarization. Following Snell's law, it is fairly easy to correlate the steering angle with the prism's wedge angle and the refractive indices of the birefringent prism as follows:

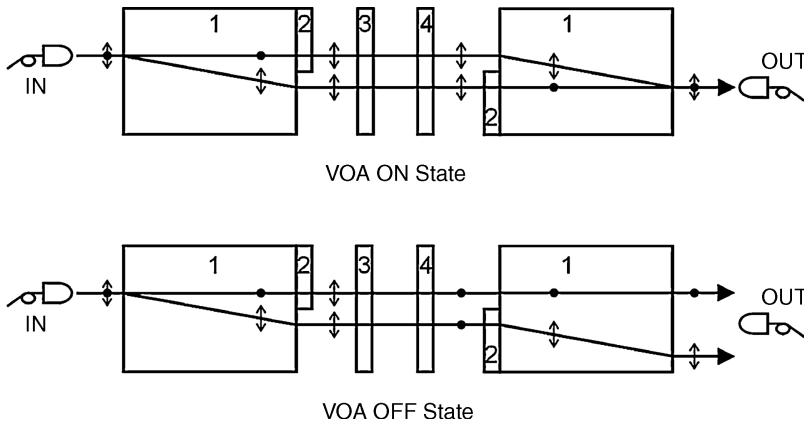
$$\delta = \sin^{-1} \{ n_o \sin [ (\sin^{-1} ((n_e/n_o) \sin \alpha)) - \alpha ] \} \quad (12.4)$$

Let us assume that the refractive indices of the birefringent prism (it can be a crystal or LC) are  $n_e = 1.7$  and  $n_o = 1.5$ . Then, in order to get a  $1^\circ$  steering angle, the required prism angle should be  $5^\circ$ . By stacking  $N$  basic units whose  $\alpha$  values are in binary sequence, we can obtain  $2^N$  beam steering positions [18].

### 12.3 VOAs

LC-based VOAs have been developed for fiber optic communications at  $\lambda = 1.55 \mu\text{m}$  because of their low cost, low loss, and low power consumption [19–21]. For most telecommunications applications, a fast response time and a large dynamic range ( $>30$  dB) are required. Two types of LC VOAs have been developed, namely nematic and ferroelectric liquid crystal (FLC). Ferroelectric liquid crystal (FLC) is attractive for its microsecond response time, but there are several issues to be solved: (1) it is a bistable device; (2) its ultra-thin cell gap ( $d < 2 \mu\text{m}$ ); (3) residual DC voltage; (4) mechanical robustness; and (5) long-term reliability. Because FLC is a bistable device, to obtain gray scales a pulse width modulation method has to be implemented. The thin-cell requirement lowers the manufacturing yield and the residual DC voltage causes gray-scale instability. Moreover, the molecular alignment in a FLC cell is sensitive to mechanical disturbance. On the other hand, nematic VOA is easy to fabricate and it has natural gray scales. The major disadvantage is a slow response time. To achieve a fast response time, a small cell gap [23], a high-temperature effect [24, 25], dual-frequency LC materials [26–28], a voltage effect [29], and a polymer-network LC [30] have been investigated. A typical nematic LC-based VOA has a response time of approximately 5–15 ms, which is still slower than a mechanical shutter whose response time is approximately 1 ms. To outperform the mechanical shutter, the nematic VOA should have a sub-millisecond response time at room temperature while maintaining a wide dynamic range and low operating voltage ( $\leq 20 V_{\text{rms}}$ ).

In Chapter 6, we introduced dual-frequency liquid crystal (DFLC) materials and the operating mechanisms for achieving fast response times. In this section, we will demonstrate a fast-response and wide-dynamic-range nematic VOA using a high-birefringence and low-viscosity DFLC together with the overdrive and undershoot voltage method described in Chapter 8. To achieve a submillisecond response time at room temperature ( $T \sim 21^\circ\text{C}$ ), we use a low-frequency ( $f = 1 \text{ kHz}$ ) overdrive voltage



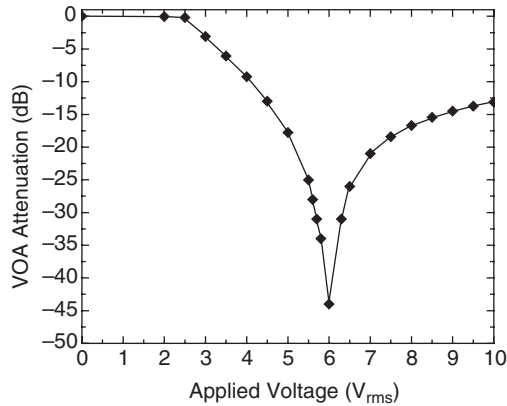
**Figure 12.7** Schematic diagram of DFLC-based VOA, where ‘1’, ‘2’, ‘3’, and ‘4’ represent a polarization beam displacer, half-wave plate, master LC cell, and compensation cell, respectively

to decrease rise time and a high-frequency ( $f = 30$  kHz) undershoot voltage to accelerate the decay process. The measured dynamic range exceeds 40 dB at  $\lambda = 1.55\mu\text{m}$ .

Figure 12.7 shows a schematic diagram of the LC-based VOA, where two polarization beam displacers and a LC cell are sandwiched between two identical fiber collimators with an 80 mm working distance. The light from the input fiber is collimated by the first gradient index (GRIN) lens collimator. When the light is incident on the first polarization beam displacer (PBD), a calcite crystal, (10 mm thick with  $45^\circ$  a cut), it is separated into an ordinary beam and an extraordinary beam. A quartz half-wave plate (HWP) is laminated to the calcite beam displacer to rotate the polarization state of the top beam. Therefore, both beams have the same polarization before entering the LC cell which is a  $3.7\mu\text{m}$  homogeneous cell with its rubbing direction oriented at  $45^\circ$  to the input light polarization. Its phase retardation ( $\delta = 2\pi d\Delta n/\lambda$ ) is approximately  $1.2\pi$  at  $\lambda = 1.55\mu\text{m}$ . To ensure a high transmittance at  $V = 0$ , an identical LC cell, i.e., with the same cell gap, LC material, and alignment but with no voltage applied, is placed behind the master LC cell to act as a phase compensation cell. The rubbing direction of the compensation cell is orthogonal to that of the master cell so that the net phase retardation at  $V = 0$  is zero. This master compensation cell configuration exhibits an excellent wavelength tolerance [31]. Under such circumstances, the top and bottom beams are recombined by the second PBD and HWP and then coupled into the collecting fiber collimator, as shown in the upper part of Figure 12.7. This is the high-transmittance state of the VOA. To make the device compact, the compensation LC cell can be replaced with a polymeric film, which is used in display devices to increase the viewing angle [32].

When a proper voltage is applied to the master LC cell to make a  $\pi$  phase change, the incident beams cannot retain their original polarizations. As a result, they are separated by the second beam displacer. No light is coupled into the collecting fiber collimator and the off-state results, as shown in Figure 12.7. By tuning the master cell voltage, different gray scales can be obtained. If the LC cell gaps are all uniform, then the VOA should have no polarization-dependent loss (PDL) and no polarization mode dispersion (PMD).

The VOA performance is mainly determined by the LC material employed. To achieve a fast response time, a DFLC mixture is chosen for the demonstration. The key feature of a DFLC is that it exhibits a crossover frequency ( $f_c$ ). In the  $f < f_c$  region, the dielectric anisotropy ( $\Delta\epsilon$ ) is positive, while in the  $f > f_c$  region  $\Delta\epsilon$  becomes negative. In the low-frequency region, the electric field-induced torque reorients the LC molecules along the field direction. This leads to the rapid rise time. During the relaxation period, a high-frequency electric field is applied to the cell. Because  $\Delta\epsilon$  is negative, the high-frequency electric field helps to accelerate the relaxation of the LC molecules to their original positions. As a result, a rapid decay time is achieved.



**Figure 12.8** Measured VOA attenuation on a dB scale as a function of applied voltage. The VOA is addressed by a 1 kHz square-wave AC source

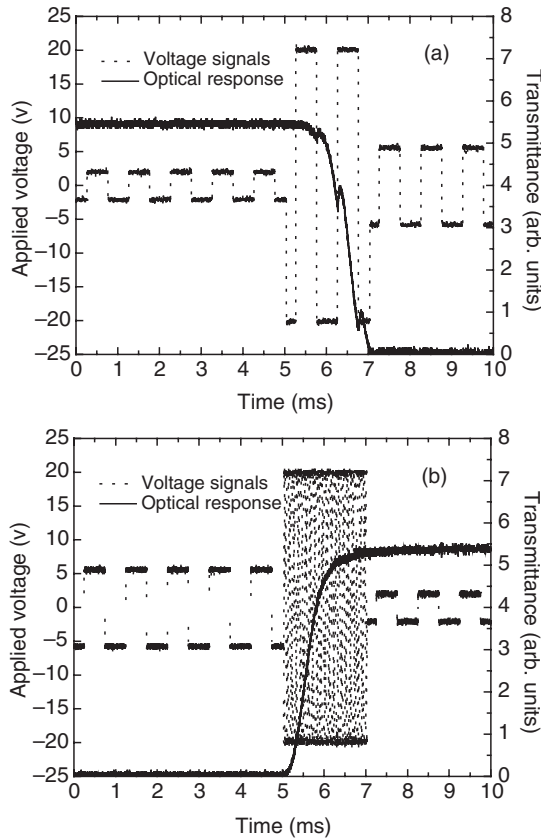
Most of the commercially available DFCL mixtures have a low birefringence, high viscosity, and small  $|\Delta\epsilon|$  values. Due to their low birefringence, a thick LC layer is required, particularly for the 1.55  $\mu\text{m}$  infrared wavelength. The thick LC layer leads to a slow response time and a high operating voltage. To overcome these drawbacks, the UCF Group developed a high-birefringence and low-viscosity DFCL mixture using 30% biphenyl esters and 70% lateral difluoro tolans [33]. The physical properties of the DFCL mixture at room temperature ( $T = 21^\circ\text{C}$ ) are summarized as follows: crossover frequency  $f_c \approx 4$  kHz;  $\Delta n = n_e - n_o = 0.25$  at  $\lambda = 1.55$   $\mu\text{m}$ ;  $\Delta\epsilon = 4.73$  at  $f = 1$  kHz; and  $\Delta\epsilon = -3.93$  at  $f = 30$  kHz.

For VOA demonstration, an Ando AQ4321D tunable laser operated at  $\lambda = 1.55$   $\mu\text{m}$  is used as a light source. The output fiber is connected to an Ando AQ8201-21 power monitor for measuring transmittance. A computer-controlled LabVIEW system is used for data recording and processing. The insertion loss of the DFCL VOA at  $V = 0$  is about  $-2.0$  dB (without connector). The PDL remains less than 0.1 dB over the whole ITU (International Telecommunication Union) C-band (1.53–1.57  $\mu\text{m}$ ), as expected. Although the measured insertion loss is still not sufficiently low, the actual fiber-to-fiber coupling loss is only  $\sim 0.8$  dB when taking into account the  $\sim 1.2$  dB propagation loss which is mainly contributed by the uncoated LC cells.

Figure 12.8 plots the measured voltage-dependent VOA attenuation. The VOA is addressed by square waves at  $f = 1$  kHz. Because of the positive  $\Delta\epsilon$  in the low-frequency region, the LC directors are reoriented along the electric field direction as the voltage exceeds  $2.5 V_{rms}$  (threshold voltage). At  $V = 6 V_{rms}$ , which corresponds to a  $\pi$  phase change, an off-state with  $-43$  dB attenuation is achieved. As shown in Figure 12.8, this off-state is quite stable. Within  $\pm 0.3 V_{rms}$  voltage variation, the measured attenuation remains at over  $-30$  dB, which is important if this VOA is to be used as a light switch or wavelength blocker. As the applied voltage exceeds  $6 V_{rms}$ , the net phase change due to the orthogonal master and compensation cells deviates from  $1\pi$  so that the optimal off-state condition is no longer satisfied. As a result, the VOA attenuation gradually decreases.

Figure 12.9 shows the turn-on and turn-off times of the DFCL cell with the overdrive and undershoot voltages applied during the rise and decay periods. The commercial LC VOA is normally driven by a 20 V AC voltage source. For a fair comparison, the overdriving voltage of the DFCL cell is also limited to  $20 V_{rms}$ . Figure 12.9(a) shows the applied waveforms and the corresponding optical signals. The  $20 V_{rms}$  low-frequency voltage burst is applied for 2 ms between the  $2 V_{rms}$  bias and  $6 V_{rms}$  holding voltages. The turn-on time (90–10%) is 0.73 ms for the 3.7  $\mu\text{m}$  DFCL cell.

During the relaxation process, the constant bias voltage exerts a torque to resist LC molecules returning to their original positions. To overcome this bottleneck, a high-frequency ( $f = 30$  kHz)



**Figure 12.9** Rise (a) and decay (b) time of the DFCLC VOA using overdrive and undershoot voltages and corresponding optical responses.  $\lambda = 1.55 \mu\text{m}$

voltage is imposed before applying the bias voltage, as depicted in Figure 12.9(b). This is known as the undershoot effect. The decay time (10–90%) is suppressed to 0.78 ms, which is approximately an order of magnitude faster than that of a commercial LC VOA.

The response times shown above are all between the VOA's 'on-' and 'off-' states. However, the dual-frequency overdrive and undershoot can also apply to the fast gray-scale transition between two arbitrary attenuation states. A high-voltage (e.g.,  $20 V_{\text{rms}}$ ) burst of suitable frequency and duration may be inserted between the initial and target states to accelerate the LC director's rise or decay.

## 12.4 Tunable-focus Lenses

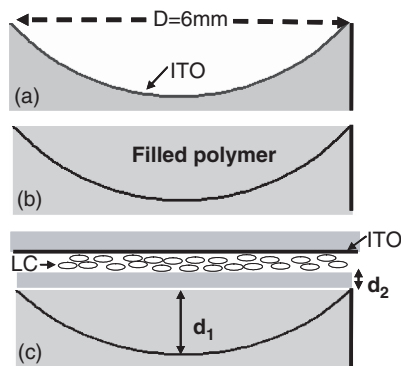
A mechanical zoom lens typically consists of two groups of lenses. By adjusting the distance between these lens groups, the effective focal length of the zoom lens can be turned mechanically. It would be ideal if these lenses were replaced by a single tunable-focus LC lens. To make a LC lens, the gradient refractive index profile has to be created. Generally speaking, there are three approaches to generate the desired gradient refractive index: (1) homogeneous LC layer with inhomogeneous electric field, (2) inhomogeneous LC layer with homogeneous electric field, and (3) inhomogeneous LC layer with inhomogeneous electric field. To achieve these goals, various efforts such as surface relief profile

[34–36], line or hole-patterned electrode [37–40], Fresnel zone type [41, 42], modal control [43], as well as the polymer network LC technique [44, 45] have been attempted. Among these approaches, the surface relief lens which combines a passive solid state lens and a LC modulator possesses some attractive features, e.g., simple fabrication, single electrode, and an easy-to-realize spherical phase profile within the LC layer. However, an LC lens with curved inner surfaces will scatter light due to the poor molecular alignment. Moreover, its tunable-focus range is rather limited.

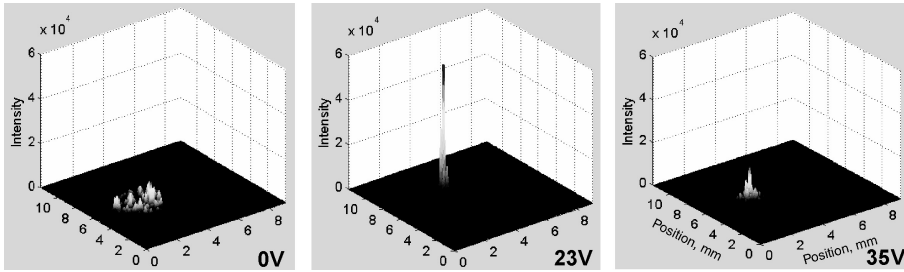
#### 12.4.1 Tunable-focus spherical lens

In this section, we use an example to illustrate the fabrication procedure and operating principle of a tunable-focus spherical lens. Unlike the surface relief LC lens, the present lens has planar substrates and a uniform LC layer. To create an inhomogeneous electric field, one of the flat substrates has an imbedded spherical electrode and the other has a planar electrode. The electric field from the spherical and planar electrodes induces a centro-symmetric gradient refractive index distribution within the LC layer which, in turn, causes the focusing effect. The electric field strength will affect the LC alignment and then change the refractive index profile. As a result, the focal length can be tuned by the applied voltage. Unlike the non-uniform LC layer approach, this lens exhibits a uniform optical response across the lens aperture due to the homogeneous cell gap. No light scattering or diffraction occurs because of the homogeneous LC alignment and continuous electrode. Both positive and negative lenses can be realized by simply reversing the shape of the spherical electrode.

Figure 12.10 illustrates the fabrication procedures of such a positive spherical LC lens. The concave surface of the bottom glass substrate is coated with a transparent ITO electrode, as shown in Figure 12.10(a). Next, the sag area is matched by a convex glass lens with the same curvature or filled with a polymer having the same refractive index as the employed glass substrate to form a planar substrate, as shown in Figure 12.10(b). In this case, let us assume that the sag area is filled with a UV curable prepolymer. The glass substrate which is in contact with the prepolymer has  $d_2 = 0.55$  mm but no ITO electrode. When the prepolymer is cured by UV light, the lens and the LC cell are attached together. The inner surfaces of the LC cell are coated with polyimide alignment layers and rubbed in the anti-parallel direction. The pretilt angle is  $\sim 3^\circ$ . The empty LC mixture is filled with a high-birefringence LC mixture and a homogeneous alignment is induced by the buffed polyimide layers, as shown in Figure 12.10(c).



**Figure 12.10** Fabrication process of a spherical LC lens: (a) deposit ITO on a concave glass lens, (b) fill the sag area with polymer, and (c) assemble the LC lens cell with another flat glass substrate. (Reprinted with permission from H. Ren *et al.*, ‘Tunable-focus flat liquid crystal spherical lens’, *Applied Physics Letters*, June 7, 2004, Volume 84, Issue 23, pp. 4789, Figure 1, © 2004, American Institute of Physics)

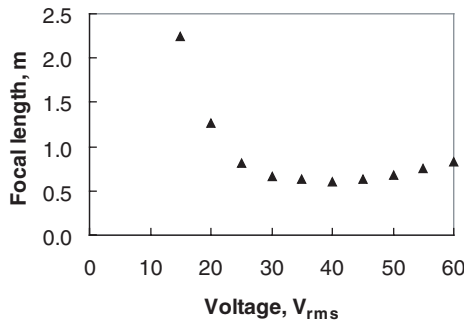


**Figure 12.11** CCD images of the measured He-Ne laser beam intensity profile at  $V = 0, 23,$  and  $35 V_{\text{rms}}$ , respectively. (Reprinted with permission from H. Ren *et al.*, ‘Tunable-focus flat liquid crystal spherical lens’, *Applied Physics Letters*, June 7, 2004, Volume 84, Issue 23, pp. 4789, Figure 3, © 2004, American Institute of Physics)

In Figure 12.10, the concave glass lens has a radius  $R = -9.30$  mm, aperture  $D = 6$  mm, and sag  $d_1 = 0.34$  mm (BK7 glass,  $n_g = 1.517$ ). The refractive index of the filled polymer NOA65 ( $n_p \sim 1.524$ , Norland Optical Adhesive) will affect the initial focal length of the LC lens. If  $n_p \approx n_g$ , then the LC device will not focus light in the voltage-off state, but if  $n_p$  is much smaller than  $n_g$ , then the device will have an initial focus. To reduce the cell gap for keeping a reasonably fast response time, a high-birefringence LC mixture designated as UCF-2 ( $\Delta n = 0.4$  at  $\lambda = 633$  nm [46]) is used. The cell gap is  $40 \mu\text{m}$ .

Figure 12.11 shows the CCD images of the lens at three voltage states:  $V = 0, 23,$  and  $35 V_{\text{rms}}$ . At  $V = 0$ , the observed He-Ne laser beam is not very uniform due to its Gaussian intensity distribution. The peak intensity is  $\sim 6 \times 10^3$  arbitrary units. As the voltage reaches  $23 V_{\text{rms}}$ , the focusing effect manifests. The measured intensity at the CCD focal plane exceeds  $6.5 \times 10^4$  arbitrary units. As the voltage is further increased, the peak intensity of the outgoing beam tends to decrease. At  $V = 35 V_{\text{rms}}$ , the peak intensity drops to  $1.7 \times 10^4$  arbitrary units. This is because the LC directors in the bulk have been reoriented by the electric field and the curvature of the refractive index profile is gradually flattened. As a result, the focal length of the lens increases and the measured light intensity at the CCD focal plane decreases.

Figure 12.12 plots the voltage-dependent focal length of the flat LC spherical lens. At  $V = 0$ , the LC directors are aligned homogeneously due to the surface anchoring effect of the substrates. Thus, no



**Figure 12.12** Voltage-dependent focal length of the flat LC spherical lens. Lens aperture  $D = 6$  mm, LC (UCF-2) cell gap  $d = 40 \mu\text{m}$ , and  $\lambda = 633$  nm. (Reprinted with permission from H. Ren *et al.*, ‘Tunable-focus flat liquid crystal spherical lens’, *Applied Physics Letters*, June 7, 2004, Volume 84, Issue 23, pp. 4789, Figure 5, 2004, American Institute of Physics)

focusing effect occurs or the focal point is at infinity. As the voltage increases, the focal length is reduced because of the established gradient refractive index. At  $V \sim 40 V_{\text{rms}}$ , the focal length reaches a minimum ( $f \sim 60 \text{ cm}$ ). Further increasing the voltage will cause the focal length to bounce back, but at a different rate. The response time of the lens is around 1–2 s at room temperature. This is somewhat too slow. For practical applications, the switching time should be less than 5 ms to avoid image blurring during focus change.

The focal length of an LC lens can be calculated using the Fresnel approximation:

$$f = \frac{r^2}{2\delta n d_{LC}} \tag{12.5}$$

where  $r = D/2$  ( $D$  is the lens aperture),  $d_{LC}$  is the LC layer thickness, and  $\delta n$  is the refractive index difference between the lens center and border.

From Figure 12.10,  $\delta n$  is determined by the electric field difference between the lens center and the border. When a voltage  $V$  is applied to the lens cell, the electric field in the center ( $E_{\text{Center}}$ ) and at the border ( $E_{\text{Border}}$ ) is expressed as follows:

$$E_{\text{Center}} = \frac{V/\epsilon_{LC}}{\frac{d_{LC}}{\epsilon_{LC}} + \frac{d_2}{\epsilon_2} + \frac{d_1}{\epsilon_1}} \tag{12.6}$$

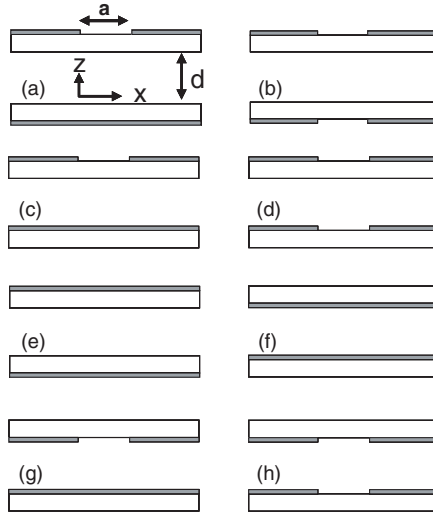
$$E_{\text{Border}} = \frac{V/\epsilon_{LC}}{\frac{d_{LC}}{\epsilon_{LC}} + \frac{d_2}{\epsilon_2}} \tag{12.7}$$

where  $\epsilon_{LC}$ ,  $\epsilon_2$ , and  $\epsilon_1$  represent the dielectric constant of the LC, medium 2, and medium 1, respectively. In an ideal case, the glass substrate which is closer to the spherical electrode should be eliminated, i.e.,  $d_2 \sim 0$ . In such conditions, the electric field shielding effect resulting from the glass substrate is minimized and the required operating voltage is lowered. From Equation (12.5), the shortest focal length occurs when  $\delta n = \nabla n$ , i.e., the LC directors in the border are completely reoriented by the electric field while those in the center are not yet reoriented due to the weaker electric field.

Can the above-mentioned flat spherical lens be used for eyeglasses? For an eyeglass, the aperture ( $D$ ) needs to be at least 3 cm and the focal length should be around 25 cm. From Equation (12.5), if we use a LC material with  $\delta n \sim 0.4$ , the required cell gap is  $\sim 1.1 \text{ mm}$ . For such a thick LC cell, the response time would be very sluggish. Moreover, the LC inside the cell will probably not align well so that light scattering will occur. Thus, the lens design shown in Figure 12.10 may not be practical for large-aperture eyeglasses. It is more realistic for a millimeter-sized lens aperture.

### 12.4.2 Tunable-focus cylindrical lens

A cylindrical lens focuses light in one dimension. It can be used for stretching an image, focusing light into a slit, converging light for a line scan detector, or correcting a low-order aberration. In a solid cylindrical lens, its focal length is fixed. To get a variable focal length, a group of lenses, e.g., mechanical zoom lenses, is often necessary. This, however, makes the optical system bulky and costly. An alternative approach for obtaining a variable focal length is through the use of LC-based cylindrical lenses for which several methods have been considered and proposed [47–49]. Among them, lenses with slit electrodes are particularly interesting due to their simple fabrication, simple operation, and the possibility of widening the aperture size.



**Figure 12.13** The eight possible electrode configurations considered for making a cylindrical LC lens:  $a$  = slit width and  $d$  = cell gap. The rubbing direction is along the  $y$  axis and the polarization of the incident light is along the rubbing direction

Figure 12.13 shows eight possible electrode configurations for generating electric fields to create cylindrical lenses [50]. However, configurations E and F are not suitable for forming lenses due to the lack of an inhomogeneous electric field. The structures in G and H are more suitable for making cylindrical microlens arrays than a single large-aperture lens due to their narrow electrode gaps. The aperture size of a micro-sized cylindrical LC lens is usually in the 100  $\mu\text{m}$  range. Thus, its application is therefore limited to microlenses or microlens arrays.

In order to have a large aperture size, four possible configurations have been considered as shown in A to D. In configuration A, a slit electrode is coated on the outer surface of the top substrate, whereas a continuous electrode is coated on the outer surface of the bottom substrate. In configuration B, a slit electrode is coated on the outer surface of both the top and bottom substrates. The two slits are parallel and symmetrical. In configuration C, a slit electrode is coated on the outer surface of the top substrate, whereas a continuous electrode is coated on the inner surface of the bottom substrate. In configuration D, a slit electrode is coated on the outer surface of the top substrate, whereas another slit electrode is coated on the inner surface of the bottom substrate. The two slits are also parallel and symmetrical. Each of the LC cells has the same cell gap  $d = 40 \mu\text{m}$ . The slit spacing, called the aperture width, of the slit electrode is  $a = 2 \text{ mm}$ . The inner surfaces of both the top and bottom substrates are coated with polyimide and buffed in anti-parallel directions along the slit direction. This rubbing direction is helpful to avoid disclination lines during device operation. In the interest of using a thinner cell gap, a high-birefringence and low-viscosity LC mixture should be used.

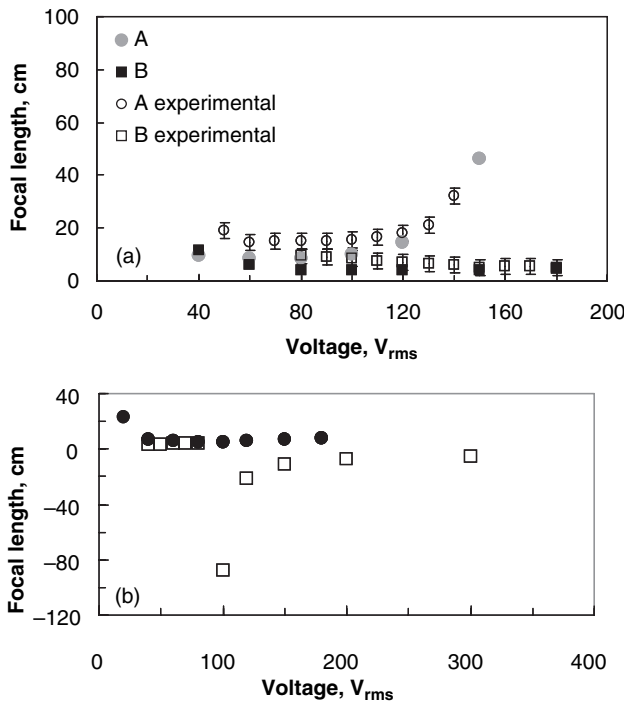
To optimize the lens design, we need to know the LC director profiles of the above four device configurations. Several commercial computer programs are available and can be used to calculate the LC director's distribution. The parameters used in the simulations are listed as follows:  $\epsilon_{\parallel} = 14.9$ ,  $\epsilon_{\perp} = 3.3$ ,  $K_{11} = 20.3 \text{ pN}$ ,  $K_{33} = 33.8 \text{ pN}$ ,  $n_e = 1.9653$ , and  $n_o = 1.5253$ . First, we need to calculate the effective extraordinary refractive index ( $n_{eff}$ ). The LC director profile for every LC layer can be extracted using the following equation:

$$\frac{1}{n_{eff}(\theta(V))^2} = \frac{\sin^2\theta(V)}{n_o^2} + \frac{\cos^2\theta(V)}{n_e^2} \tag{12.8}$$



where  $\theta(V)$  is the tilt angle of the LC layer at a given applied voltage  $V$ . Second, we need to calculate the refractive index differences  $dn(V) = n_{eff}(\theta(V)) - n_o$  in each of the LC layers and then average them. The effective focal length  $f$  of a cylindrical LC lens is related to the lens radius ( $r$ ), wavelength ( $\lambda$ ), and phase difference ( $\Delta\delta = 2\pi d\Delta n/\lambda$ ) between the center and edge of the aperture as  $f = \pi \cdot r^2 / (\lambda \cdot \Delta\delta)$ .

Figure 12.14(a) shows the calculated and measured voltage-dependent focal length of two cylindrical LC lenses: configurations A and B. The agreement between the simulated and measured results is reasonably good. From the simulation results, we find that configuration B has the best positive refractive index profile and the shortest focal length. Configuration A has a severe image aberration problem and longer focal length ( $>15$  cm) due to the broader and shallower refractive index profile as compared to B. For configuration C (Figure 12.14(b)), the simulated minimum focal length occurs at  $V \sim 60 V_{rms}$ , which is consistent with the experimental results reported by Ren *et al.* [49]. For configuration D, if the aperture size is maintained at 2 mm then the fringing field-induced refractive index profile is far from the ideal parabolic shape so that the image quality is poor. In order to maintain a parabolic refractive index profile, the aperture size needs to be reduced to 1.2 mm. Under such circumstances, the simulation results indicate that both positive and negative lenses can be obtained depending on the applied voltage. When  $V < 100 V_{rms}$ , the lens has a positive focal length but becomes negative as  $V > 100 V_{rms}$ . The minimum focal length for the positive lens is  $\sim 3$  cm and the maximum focal length for the negative lens is  $\sim -5$  cm.



**Figure 12.14** The voltage-dependent focal length of cylindrical LC lenses: (a) simulation and experimental results for configurations A and B, (b) simulation results for configurations C and D. The solid circles in (b) are for configuration C and the open squares are for configuration D with reduced aperture size  $a = 1.2$  mm

### 12.4.3 Switchable positive and negative microlens

The microlens array is a useful component for optical interconnections, optical fiber switches, shutters of optical super-resolution devices, light deflection devices, and imaging processing. In 3-D display systems based on integral photography, the microlens array with dynamically variable image planes is useful for enhancing the resolution of real and virtual images and for increasing the depth perception of images [51]. To display 3-D images, a lens with variable focal length is highly desirable. In conventional devices, this is commonly done by moving the lens array along the optic axis. This kind of system leads to a bulky device and requires extra mechanical elements for movement. The variable-focus lenses can be obtained by changing the shape of the lens [52] or creating a gradient refractive index profile in the materials with uniform thickness, as discussed in this chapter. For a LC microlens, a spatial distribution of refractive index can be induced and varied continuously by the applied voltage instead of mechanical movement. Thus, the switching time is greatly reduced.

As shown in Equation (12.6), the focal length of a LC lens depends on the lens radius, LC layer thickness, and its gradient refractive index. Normally, a lens can have either a positive or negative focal length. In this section, a LC microlens array whose focal length can be switched from positive to negative or vice versa by the applied voltage is introduced.

Figure 12.15 illustrates the structure of a microlens array. To make the focal length electrically tunable, the convex surface of the top BK-7 glass substrate is coated with a thin ITO electrode and then flattened by a polymer film. For phase-only modulation, homogeneous LC alignment should be used. Thus, the polymer surface and the bottom ITO glass substrate with a thin polyimide alignment layer are rubbed in anti-parallel directions. The cell gap is controlled at  $18\ \mu\text{m}$  by Mylar spacers and hermetically sealed using UV-curable glue. To achieve a fast response time, a DFCLC is used. The physical properties of the DFCLC mixture are summarized as follows: crossover frequency  $f_c \sim 5\ \text{kHz}$ ,  $\Delta n \sim 0.285$  (at  $\lambda = 633\ \text{nm}$  and  $T = 22^\circ\text{C}$ ), and dielectric anisotropy  $\Delta\epsilon = 4.73$  at  $f = 1\ \text{kHz}$  and  $\Delta\epsilon = -3.93$  at  $50\ \text{kHz}$ .

As depicted in Figure 12.15, the top flattened substrate and the LC layer work together as a zoom lens. The refractive index of the filled polymer NOA-76 ( $n_p \sim 1.51$ ,  $\epsilon = 3.33$ ) plays an important role in affecting the initial focal length of the microlens. If the filled polymer has a similar refractive index to that of the top glass substrate (BK7,  $n_g = 1.517$ ), i.e.,  $n_p \approx n_g$ , then the whole structure will have a uniform refractive index and does not focus light in the voltage-off state. If the polymer has a different refractive index from glass, i.e.,  $n_p \neq n_g$ , then the microlens will have an initial focus  $f_s$  at  $V = 0$ . In Figure 12.15, each single, convex, glass microlens has radius  $R = 450\ \mu\text{m}$ , aperture  $D = 500\ \mu\text{m}$ , and height  $d_1 = 76\ \mu\text{m}$ . The extra polymer layer has thickness  $d_2 = 81\ \mu\text{m}$ . As a result, the microlens has a positive focal length ( $f_s = 4.26\ \text{cm}$ ) at  $V = 0$ . As the applied voltage increases, the LC directors are

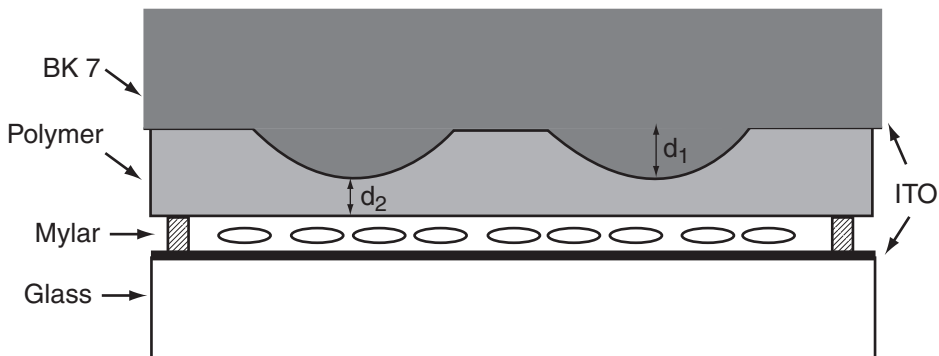
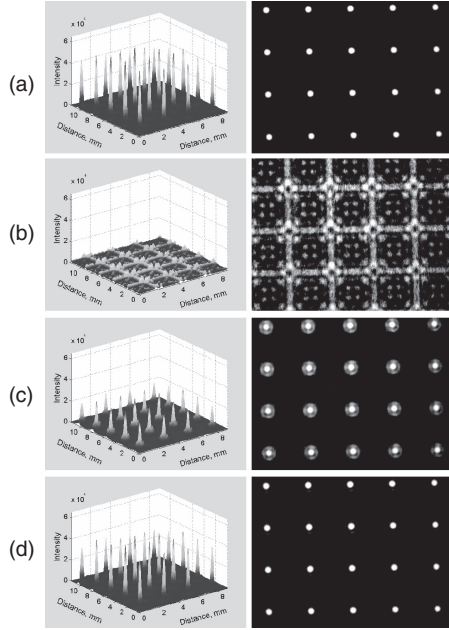


Figure 12.15 Device structure of a DFCLC microlens array



**Figure 12.16** CCD images of the DFLC microlens array (right) and the corresponding 3-D light intensity profiles (left) at (a) 0, (b)  $50V_{\text{rms}}$ , (c)  $150V_{\text{rms}}$ , and (d)  $200V_{\text{rms}}$

reoriented by the electric field. The voltage-induced refractive index change within the LC layer leads to a tunable-focus microlens array. The resultant focal length of the microlens array can be positive or negative depending on the applied voltage.

Figure 12.16 shows the CCD images of the microlens at  $V = 0, 50, 150,$  and  $200 V_{\text{rms}}$ . At  $V = 0$ , the focusing effect is caused by the top substrate only, as shown in Figure 12.16(a). When the applied voltage exceeds a threshold, the LC directors are reoriented. The gradient refractive index is formed because of the inhomogeneous electric field as Figure 12.15 depicts. The LC layer adds a diverging effect to the whole rooming lens system. As  $V > 30 V_{\text{rms}}$ , the focal length of the whole system becomes negative. At  $50 V_{\text{rms}}$ , the beam diverges to the edges of each single microlens, as shown in Figure 12.16(b). In the high-voltage regime, the LC directors are all reoriented perpendicular to the substrates. The gradient refractive index profile is gradually flattened and erased. The diverging effect of the LC lens weakens and the microlens becomes a converging lens again, as shown in Figure 12.16(c) and (d).

To explain this focal length transition phenomenon quantitatively, we need to calculate the voltage-induced LC director reorientation numerically. First, we calculate the voltage-dependent refractive index change for a symmetric, uniform LC layer and use that to predict the voltage-dependent focal length. The LC directors are reoriented along the electric field ( $\vec{E}$ ) direction in order to minimize the free energy. The free energy associated with the elastic forces can be described in terms of three elastic constants. The free energy of the nematic LC directors in the static electric field  $\vec{E}$  is generally expressed by [53]

$$\vec{F} = \frac{1}{2}k_{11}(\nabla \cdot \vec{n})^2 + \frac{1}{2}k_{22}(\vec{n} \cdot \nabla \times \vec{n})^2 + \frac{1}{2}k_{33}(\vec{n} \times \nabla \times \vec{n})^2 - \frac{1}{2}[\varepsilon_{\perp} \vec{E}^2 + \Delta\varepsilon(\vec{n} \cdot \vec{E})^2] \quad (12.9)$$

where  $\vec{n} = (n_x, n_y, n_z)$  is the LC director vector,  $k_{11}$ ,  $k_{22}$ , and  $k_{33}$  are the elastic constants associated with splay, twist, and bend deformations, and  $\Delta\varepsilon$  and  $\varepsilon_{\perp}$  are the dielectric anisotropy and dielectric constant

in the perpendicular direction of the LC, respectively. The LC director reorientation is calculated by a standard 1-D finite-element method.

The tilt angle profile  $\theta(z)$  can be used to calculate the average refractive index,  $\langle n \rangle$ , of the liquid crystal at different applied voltages. For a given tilt angle the refractive index is given by the index ellipsoid equation [54]

$$n(z) = \frac{n_e n_o}{\sqrt{n_o^2 \cos^2 \theta(z) + n_e^2 \sin^2 \theta(z)}} = \frac{n_e n_o}{\sqrt{n_o^2 + (n_e^2 - n_o^2) \sin^2 \theta(z)}} \quad (12.10)$$

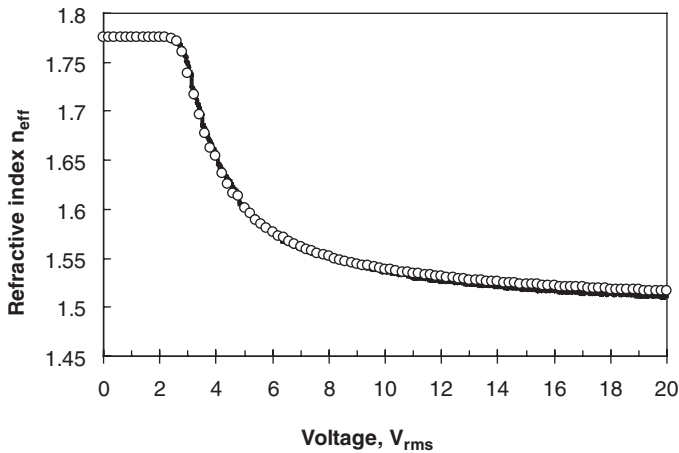
The tilt angle profile  $\theta(z)$  is used in Equation (12.10) to calculate the optical path,  $\bar{n}d$ , when light goes through the cell. Using the above equations and DFLC parameters ( $k_{11} = 33.5$  pN,  $k_{33} = 35$  pN,  $\varepsilon_{\perp} = 7.44$ ,  $\varepsilon_{\parallel} = 12.17$ ,  $n_o = 1.490$ ,  $n_e = 1.775$ , and with a pretilt angle of  $2^\circ$ ), the voltage-dependent average effective refractive index can be calculated, as plotted in Figure 12.17. The solid line and open circles represent the experimental and simulation results, respectively, at  $\lambda = 633$  nm. The agreement is very good.

When a voltage  $V$  is applied to the LC microlens array, the electric field at the center ( $E_{Center}$ ) and at the border ( $E_{Border}$ ) of each microlens is expressed as [55]

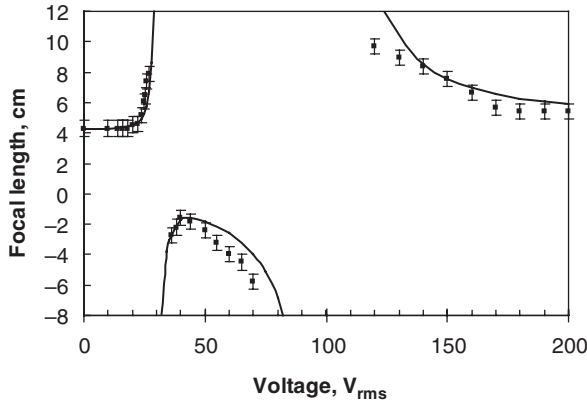
$$E_{Center} = \frac{V/\varepsilon_{LC}}{\frac{d_{LC}}{\varepsilon_{LC}} + \frac{d_2}{\varepsilon_p}} \quad (12.11)$$

$$E_{Border} = \frac{V/\varepsilon_{LC}}{\frac{d_{LC}}{\varepsilon_{LC}} + \frac{d_1 + d_2}{\varepsilon_p}} \quad (12.12)$$

where  $d_1$  represents the microlens thickness and  $d_2$  the thickness of the polymer layer shown in Figure 12.15,  $d_{LC}$  is the LC layer thickness, and  $\varepsilon_{LC}$  and  $\varepsilon_p$  represent the dielectric constant of the LC and polymer, respectively. At  $V = 0$ ,  $\varepsilon_{LC} = \varepsilon_{\perp}$ . As  $V > V_{th}$ , the effective  $\varepsilon_{LC}$  will change and affect the electric field distribution through the cell. Finally, the equilibrium state is achieved. By using the final voltage distribution, the LC tilt angle, average effective birefringence, and the phase difference between the center and borders of each microlens can be calculated.



**Figure 12.17** Voltage-dependent average refractive index of DFLC used in the experiment. Solid line and open circles represent the experimental and simulation results, respectively.  $\lambda = 633$  nm



**Figure 12.18** Voltage-dependent focal length of the DFLC microlens array. LC cell gap  $d = 18 \mu\text{m}$ , diameter of microlens  $D = 500 \mu\text{m}$ ,  $\lambda = 633 \text{ nm}$

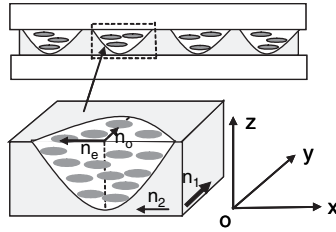
From the Fresnel approximation, the focal length of an LC lens is related to the lens radius  $r$  and  $\delta n = \hat{n}_{Center} - \hat{n}_{Border}$  which is the refractive index difference between the lens center and borders, as described in Equation (12.5).

Figure 12.18 plots the measured (points) and simulated (lines) voltage-dependent focal length of the microlens [56]. At  $V = 0$ , LC directors are aligned homogeneously and no focusing effect occurs in the LC layer. The system shows the initial focus contributed solely by the top glass microlens array. As the voltage increases, the LC layer behaves like a diverging lens so that the combined focal length increases accordingly. At  $V \sim 30 V_{rms}$ , the microlens begins to behave like a diverging lens. At  $\sim 40 V_{rms}$ , the microlens reaches the shortest negative focal length. Further increasing the voltage would reorient all the LC directors perpendicular to the substrates and reduce the phase difference. The microlens becomes a converging lens again and gradually approaches the initial focal length but at a different rate. The simulation results agree with experiment quite well in the lower voltage regime ( $< 40 V_{rms}$ ) but in the higher voltage regime (between 40 and  $130 V_{rms}$ ) the fitting deviates somewhat. This is because, in the simulations, the anchoring energy at the boundaries is assumed to be infinite, which means that the LC directors near the substrates will not be reoriented at all by the electric field. But in reality, the LC directors near the substrates will still be reoriented slightly by the strong electric field at a high voltage. Therefore, in the high-voltage regime the measured focus change is faster than that simulated. Above  $140 V_{rms}$ , the LC directors are reoriented nearly perpendicular to the substrates in both experimental data and simulation results. Therefore, the measured focal length agrees well with the simulated values in the high-voltage regime.

A key consideration for using DFLC material is to obtain a fast response time. Using 1 kHz and 50 kHz driving frequencies to switch the microlens array between 0 and  $200 V_{rms}$ , the rise time is 3.9 ms and decay time is 5.4 ms for the  $18 \mu\text{m}$  cell gap. Compared to a nominal nematic LC, the response time is hundreds of milliseconds. The high driving voltage ( $200 V_{rms}$ ) results from the small dielectric anisotropy of DFLC at low and high frequencies. To lower the operating voltage, we can either reduce the  $d_2$  shown in Figure 12.15 or increase the dielectric constant of the filled polymer.

#### 12.4.4 Hermaphroditic LC microlens

Most of the LC lenses are polarization sensitive. When the incoming light polarization is parallel to the LC alignment direction, i.e., extraordinary ray, the focal length of the LC lens can be tuned continually



**Figure 12.19** Side view of the hermaphroditic LC microlens array.  $n_1$  and  $n_2$  are the refractive indices of the molded microlens along the  $y$  and  $x$  axis, respectively.  $n_o$  and  $n_e$  are the ordinary and extraordinary refractive indices of the LC material. (Reproduced with permission from H. Ren *et al.* ‘Hermaphroditic liquid-crystal microlens’, *Optical Letters*, Volume 30, pp. 376–378 (Feb. 15, 2005), Figure 1, © 2005, Optical Society of America)

within a finite range which depends on the LC birefringence. However, for the ordinary ray (i.e., the incident light polarization is perpendicular to the LC directors), the focal length of the LC lens does not change with voltage. Both positive and negative lenses can be designed according to need, but once the lens is designed it exhibits either a positive or a negative lens. Although under some special operating conditions the central part of a positive LC lens could exhibit a negative focusing property [57], the surrounding part remains positive. This volcano type of LC lens has severe index distortion.

Figure 12.19 shows the side view of a hermaphroditic microlens which could exhibit either a positive or a negative focal length depending on the input light polarization [58]. Unlike a conventional LC lens whose focal length is tunable by the applied voltage, the hermaphroditic LC microlens changes focal length according to the angle between the polarization axis and the LC directors. For the extraordinary ray, the focal length is positive, while for the ordinary ray the focal length becomes negative. By changing the relative angle between the incident light polarization and the LC directors, the focal length of the LC lens can be varied. This polarization rotation can be achieved manually or by an electrically controlled  $90^\circ$  TN cell. The switching time is about 10–20 ms, depending on the LC cell gap and material employed.

In Figure 12.19 the flat lens is composed of a plano-convex LC lens and a plano-concave molded polymeric lens (shaded areas). The LC directors in the plano-convex lens are aligned along the  $x$  axis. The ordinary and extraordinary refractive indices ( $n_o$  and  $n_e$ ) are along the  $y$  and  $x$  axis, respectively. On the other hand, the plano-concave lens is made of UV-cured polymer/LC composite on a polyimide surface whose rubbing direction is along the  $y$  axis. Thus, its refractive indices are also anisotropic:  $n_1 > n_2$ . The LC material chosen for this lens satisfies the following relationship:  $n_e \sim n_1 > n_2 \sim n_o$ . When the incident light passes through the convex and concave lenses from the  $z$  axis with its polarization at an angle  $\theta$  with respect to the  $x$  axis, the focal length of the microlens can be expressed as

$$f = R / (n_{LC} - n_{mold}) \tag{12.13}$$

Here,  $R$  is the radius of curvature of the lens surface and  $n_{LC}$  and  $n_{mold}$  denote the effective refractive index of the LC and the molded polymeric lens, respectively. Both  $n_{LC}$  and  $n_{mold}$  are dependent on  $\theta$  as

$$n_{LC} = \frac{n_o \cdot n_e}{\sqrt{(n_o^2 \cos^2 \theta + n_e^2 \sin^2 \theta)}} \tag{12.14}$$

$$n_{mold} = \frac{n_1 \cdot n_2}{\sqrt{(n_1^2 \cos^2 \theta + n_2^2 \sin^2 \theta)}} \tag{12.15}$$

From these equations, when  $\theta = 0$ , the focal length of the lens is  $f_1 = R/(n_e - n_2)$ . In this case, the focal length  $f_1$  is positive. If  $\theta = 90^\circ$ , then the focal length of the lens is  $f_2 = R/(n_o - n_1)$ . Because  $n_o < n_1$ , the focal length  $f_2$  is negative. When  $n_{LC} \sim n_{mold}$ , the focal length of the lens approaches infinity. By tuning the incident light polarization axis gradually from 0 to  $90^\circ$ , the focal length changes from positive to negative.

## 12.5 Polarization-independent LC Devices

Most LC devices operate under linearly polarized light in order to achieve high contrast ratio. The use of a polarizer reduces the optical efficiency dramatically. The maximum transmittance of a pair of polarizers is only about 38%. Polarization-independent LC devices for phase or amplitude modulation are highly desirable.

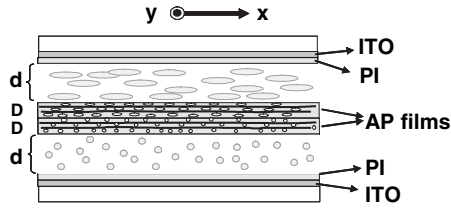
Phase-only modulation [59] plays an important role in adaptive optics, optical cross-connect switching, laser beam steering, and low-cost electro-optic sensors. Several interesting applications using phase modulators have been identified, e.g., tunable-focus lenses [60], gratings and prisms [61], and spatial light modulators [62]. LC-based phase modulators offer several advantages: low cost, light weight, low power consumption, and no mechanical moving parts. Several LC-based phase modulators have been developed, e.g., homogeneous LC [63], polymer network LC (PNLC) [64], and sheared PNLC [65, 66]. The homogeneous cell is attractive for its large phase shift and low operating voltage ( $<10 V_{rms}$ ). However, it is polarization dependent and the response time is relatively slow. A PNLC cell significantly reduces the response time but its operating voltage is increased. To obtain a  $2\pi$  phase change in a transmissive PNLC cell, the required voltage is  $\sim 90 V_{rms}$  for a  $12 \mu m$  E44 cell, which corresponds to  $\sim 7 V/\mu m$ . To achieve a larger phase change by increasing the cell gap would result in substantial light scattering and a higher voltage. The sheared PNLC cell does not require alignment layers but it needs a shearing force to stress the LC directors and to suppress light scattering. Its response time is also in the submillisecond regime but its operating voltage is also relatively high. A common drawback of these three approaches is that they are polarization sensitive. For laser applications, the incident light polarization may not always be parallel to the LC directors to ensure a phase-only modulation. Thus, it is highly desirable to develop polarization-independent phase modulators.

Several approaches for obtaining polarization-independent LC phase modulation have been developed, e.g., the  $90^\circ$  TN cell operated at a voltage about three times higher than the threshold voltage [67, 68], nanoscale polymer-dispersed liquid crystal (nano-PDLC) [69], voltage-biased PDLC [70], and voltage-biased polymer-stabilized cholesteric texture (PSCT) [71]. A common problem with these approaches is that their phase change is relatively small and operating voltage is quite high. For instance, the nano-PDLC is scattering free, polarization independent, and has a submillisecond response time. However, its phase shift is small and its operating voltage is around  $15\text{--}20 V_{rms}/\mu m$ . Increasing the cell gap would enhance the phase change, but the operating voltage would increase further. The voltage-biased micro-sized PDLC and PSCT are also polarization independent; however, their residual phase is still small ( $\sim 0.1\pi$  at  $\lambda = 633 \text{ nm}$ ) so that their applications are limited to micro-photonic devices, such as tunable-focus microlens arrays.

In the following sections, we introduce two polarization-independent LC phase modulators: (1) a double-layered structure with two ultra-thin anisotropic polymer films as cell separators, and (2) a double-layered LC gel without any separator.

### 12.5.1 Double-layered homogeneous LC cells

The double-layered structure has been proposed for guest–host LC displays [72, 73]. The conventional approach uses a thin glass ( $\sim 0.3 \text{ mm}$ ) or Mylar film ( $\sim 0.1 \text{ mm}$ ) to separate the two orthogonal LC layers. In the former case, an ITO glass substrate is used as a middle substrate. To overcome the electric field



**Figure 12.20** The structure of a polarization-independent phase modulator: AP, anisotropic polymer. (Reproduced with permission from Y. H. Lin *et al.*, ‘Polarization-independent liquid crystal phase modulator using a thin polymer-separated double-layered structure’, *Optical Express*, Volume 13, pp. 8746–8752 (Oct. 31, 2005), Figure 1, © 2005, Optical Society of America)

shielding effect, both sides of the ITO layers should be pixilated and connected via feed-through holes, and then coated with a thin polyimide layer which is rubbed in the orthogonal direction to match the LC alignment. This approach is difficult for high-resolution devices because of the complicated pixel structures and precision registration between the passive ITO pixels in the middle substrate and the active elements. To reduce the parallax incurred by the middle glass substrate and to enable high resolution, a thin Mylar film has been considered. However, the Mylar film cannot align the LC molecules because the post-baking temperature ( $\sim 250^\circ\text{C}$ ) of polyimide is higher than the glass transition temperature of the Mylar film.

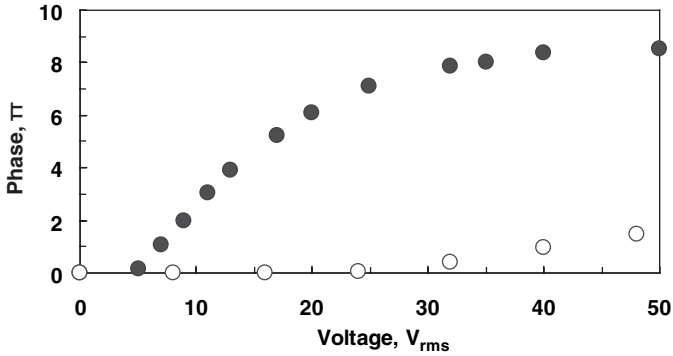
In this section, we introduce an anisotropic polymer film [74] which is thin, optically anisotropic, and possesses alignment capability. Figure 12.20 shows the schematic design of a double-layered polarization-independent phase modulator. The cell consists of two glass substrates which are overcoated with thin ( $\sim 80\text{ nm}$ ), mechanically buffed polyimide layers, two anisotropic polymer films, and two LC layers. The top and bottom LC directors are oriented orthogonal to each other. To achieve orthogonal homogeneous LC layers, the principal axes of these two anisotropic polymer films are also arranged to be orthogonal to each other.

The anisotropic film is made of Merck E7 nematic LC mixture, photo-initiator IRG184, and an LC monomer RM-257 (4-(3-Acryloyloxypropyloxy)-benzoic acid 2-methyl-1,4-phenylene ester) at 19:1:80 wt% ratios. The LC/monomer mixture was injected into a homogeneous cell with a  $23\ \mu\text{m}$  cell gap which was controlled by the Mylar stripes and then the cell was exposed to UV light at an intensity  $I = 10\ \text{mW}/\text{cm}^2$  for  $\sim 30\ \text{min}$  at  $90^\circ\text{C}$ . After UV exposure, the two substrates of the homogeneous cell were peeled off and a solidified anisotropic film of  $23\ \mu\text{m}$  thickness was obtained. The anisotropic polymer film is fully transparent. A large film can be sliced into two identical films. These two films are then stacked together in orthogonal directions. The LC mixture employed is also E7. The empty cell was filled with the LC by the one-drop-fill method. The cell gap of each LC layer was controlled by a Mylar film to be  $d \sim 12\ \mu\text{m}$ . The total dimension of the cell is around  $25\ \text{mm}$  by  $25\ \text{mm}$ .

To characterize the phase shift of the double-layered LC cell, a Mach–Zehnder interferometer and an unpolarized He–Ne laser ( $\lambda = 633\ \text{nm}$ ) were used. Figure 12.21 plots the measured voltage-dependent phase shift of the double-layered E7 LC cell (solid circles). The threshold voltage is  $\sim 5\ V_{\text{rms}}$ . For reference, the threshold voltage of the single E7 cell without any middle substrate is  $\sim 0.95\ V_{\text{rms}}$ . The increased threshold voltage originates from the dielectric shielding effect of the two middle polymeric layers. In the interferometer, the measured phase shift is referenced to that at  $V = 0$ . The total phase shift reaches  $\sim 8.1\pi$  at  $V = 40\ V_{\text{rms}}$ . This total phase shift is independent of the incident light polarization. Also included in Figure 12.21 are the simulated results (open circles) of a similar double-layered structure using a glass separator  $0.3\ \text{mm}$  thick. Because of the electric field screening effect, the required voltage to reach a  $2\pi$  phase change is beyond  $50\ V_{\text{rms}}$ .

The obtainable phase shift of the described double-layered structure is much larger and the operating voltage is much lower than those of nano-PDLC, PDLC, and PSCT. To further lower the operating





**Figure 12.21** Voltage-dependent phase shift of the polarization-independent LC phase modulator at  $\lambda = 633$  nm. Solid circles represent the measured data using two anisotropic polymeric films while open circles are the simulated results of the double-layered structure using a glass separator 0.3 mm thick. (Reproduced with permission from Y. H. Lin *et al.*, ‘Polarization-independent liquid crystal phase modulator using a thin polymer-separated double-layered structure’, *Optical Express*, Volume 13, pp. 8746–8752 (Oct. 31, 2005), Figure 5, © 2005, Optical Society of America)

voltage of the double-layered structure, we can reduce the thickness of the anisotropic polymer films, but the tradeoff is that a thinner polymer film may degrade the uniformity of the cell.

The response time of the double-layered LC cell is  $\sim 300$  ms at  $T \sim 23^\circ\text{C}$ . The slow response time originates from the thick LC layers ( $d \sim 12$   $\mu\text{m}$ ) and high viscosity of the E7 LC employed. To reduce the response time, a high- $\Delta n$  and low-viscosity LC should be used [75]. A high- $\Delta n$  LC enables a thinner cell gap to be used, which is helpful for reducing the response time.

The thickness of the polymer film is 23  $\mu\text{m}$ , which is larger than that of the LC layer (12  $\mu\text{m}$ ). The flexibility and hardness can be controlled by the fabrication process, such as UV curing conditions and LC concentration. Although the anisotropic films are thin, their deformation during operation should not be a problem because the films are still sandwiched by two glass substrates. Therefore, the mechanical stability of the system is not a concern.

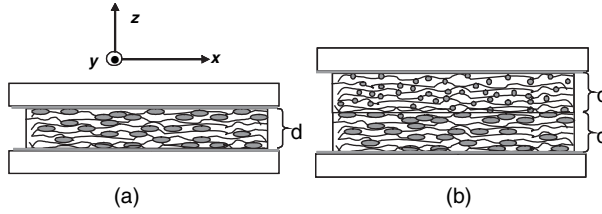
### 12.5.2 Double-layered LC gels

To achieve a fast response time, another polarization-independent phase modulator using two thin stratified LC gels has been developed [76]. The two homogeneously aligned gel films are identical, but stacked in orthogonal directions. Because of the high LC concentration and uniform molecular alignment, the LC gel possesses a large phase change ( $> 1\pi$ ). Meanwhile, because of the relatively high monomer concentration (28 wt%) the formed LC domains are in the submicron range. Therefore, the response time of the LC gel is around 0.5 ms.

In a LC gel, the homogeneously aligned LC is stabilized by dense polymer networks, as shown in Figure 12.22(a). The phase shift along the  $z$  axis can be expressed as

$$\Delta\delta_{Gel}(V) = \frac{2\pi dc[n_e - n_{eff}(V)]}{\lambda} \quad (12.16)$$

where  $d$  is the cell gap,  $c$  is the LC concentration,  $\lambda$  is the incident wavelength,  $n_e$  and  $n_{eff}(V)$  are the extraordinary and effective refractive indices of the LC, respectively. As  $V \rightarrow \infty$ ,  $n_{eff} \rightarrow n_o$ , where  $n_o$  is the ordinary refractive index of the LC. From Figure 12.22(a), the homogeneous LC gel is polarization dependent. To make it polarization independent, two identical homogeneous LC gels are stacked in orthogonal directions, as shown in Figure 12.22(b).



**Figure 12.22** A homogeneous LC gel: (a) single layer and (b) two orthogonal layers. (Reprinted with permission from H. Ren *et al.*, ‘Polarization-independent and fast-response phase modulators using double-layered liquid crystal gels’, *Applied Physics Letters*, February 6, 2006, Volume 88, pp. 061123, Figure 1, © 2006, America Institute of Physics)

As the voltage increases, the phase change occurs because of the electric field-induced LC director reorientation. At a very high voltage, the voltage-induced phase shift is reduced to

$$\Delta\delta_{Gel}(V \rightarrow \infty) = \frac{2\pi dc\Delta n}{\lambda} \quad (12.17)$$

where  $\Delta n = n_e - n_o$  is the LC birefringence. In comparison, the LC droplets in a nano- or voltage-biased PDLC cell are almost randomly orientated. Thus, the phase shift is

$$\Delta\delta_{PDLC}(V) = \frac{2\pi d'c'[\bar{n} - n_{eff}(V)]}{\lambda} \quad (12.18)$$

where  $\bar{n} = (2n_o + n_e)/3$  is the average refractive index of the LC at  $V=0$ , and  $d'$  and  $c'$  are the cell gap and LC concentration, respectively. As  $V \rightarrow \infty$ ,  $n_{eff} \rightarrow n_o$ , and the phase shift is reduced to

$$\Delta\delta_{PDLC}(V \rightarrow \infty) = \frac{2\pi d'c'\Delta n}{3\lambda} \quad (12.19)$$

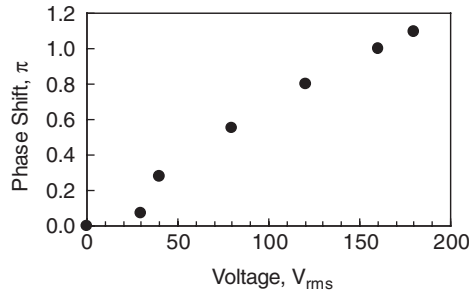
To fairly compare the phase change of the orthogonal LC gel films with the nano-PDLC, let us use the same LC material. To achieve polarization independence, the LC gel needs two orthogonal layers, but nano-PDLC only needs one. Thus,  $d' = 2d$ . However, the LC concentration in the gel is two times higher than that in nano-PDLC, i.e.,  $c = 2c'$ . From Equation (12.17) and Equation (12.19), we find

$$\frac{\Delta\delta_{Gel}(V \rightarrow \infty)}{\Delta\delta_{PDLC}(V \rightarrow \infty)} = 3 \quad (12.20)$$

From Equation (12.20), the phase shift of the LC gel is three times higher than that of nano-PDLC.

The LC gel is made by mixing 28 wt% of photocurable rod-like LC diacrylate monomer (RM257) in a nematic LC (E48:  $n_o = 1.523$ ,  $\Delta n = 0.231$  at  $\lambda = 589$  nm). The mixture was injected into an empty cell in the nematic state. The inner surfaces of the ITO-glass substrates were coated with a thin polyimide layer and then rubbed in anti-parallel directions. The filled cell was exposed to UV light ( $\lambda \sim 365$  nm,  $I \sim 10$  mW/cm<sup>2</sup>) for 30 min. The cell gap was controlled at 8  $\mu$ m by spacer balls.

After UV exposure, the cell is highly transparent. To peel off the gel, the top glass substrate is cleaved off. The stratified gel remains on the bottom substrate surface without LC leakage. From microscopic inspection, the LC gel is indeed aligned homogeneously without being damaged during cell cleaving. To assemble a double-layered structure, the LC gel was cut in half, stacked together at orthogonal directions, and then covered with another top ITO substrate, as Figure 12.22(b) depicts. Similarly,



**Figure 12.23** Measured phase shift of a 16  $\mu\text{m}$  double-layered LC gel at different voltages.  $\lambda = 633\text{ nm}$ . (Reprinted with permission from H. Ren *et al.*, ‘Polarization-independent and fast-response phase modulators using double-layered liquid crystal gels’, *Applied Physics Letters*, February 6, 2006, Volume 88, pp. 061123, Figure 3, © 2006, America Institute of Physics)

the phase change is monitored by a Mach–Zehnder interferometer using an unpolarized He–Ne laser beam. When an AC voltage ( $f = 1\text{ kHz}$ ) was applied to the LC gel, the interference fringes moved as recorded by a digital CCD camera.

Figure 12.23 shows the voltage-dependent phase shift of a 16  $\mu\text{m}$  double-layered LC gel at  $\lambda = 633\text{ nm}$ . The threshold voltage is  $\sim 30\text{ V}_{rms}$ . This high threshold originates from the dense polymer networks. Beyond this threshold, the phase change increases almost linearly with the applied voltage. The estimated total phase change from an 8  $\mu\text{m}$  LC gel which contains  $\sim 80\text{ wt\%}$  E48 should be  $\sim 2\pi$  for a linearly polarized He–Ne laser ( $\lambda = 633\text{ nm}$ ). Therefore, the applied voltage has not reached the saturation regime.

The rise time of the LC gel is  $\sim 200\ \mu\text{s}$  and decay time is  $\sim 500\ \mu\text{s}$  at room temperature ( $\sim 22^\circ\text{C}$ ). Such a fast response time results from the small LC domain sizes and polymer stabilization. Due to the relatively high monomer concentration (28 wt%), the formed polymer networks are quite dense so that the formed LC domains are of submicron size. Similar to a nano-PDLC, the contact interfaces between the polymer networks and the LC molecules are large. As a result, the anchoring force of polymer networks exerted on the LC is very strong. This is the primary reason for the observed fast response time and high threshold voltage.

To get a  $2\pi$  phase change for laser beam steering and other photonic applications, the LC gel can be operated in reflective mode without increasing the operating voltage. For practical applications, the operating voltage of the LC gel is still too high ( $11\text{ V}_{rms}/\mu\text{m}$ ). To increase the phase change and reduce the operating voltage, a high- $\Delta n$  and high- $\Delta\epsilon$  LC material should be considered as well as optimizing the LC and monomer concentration. A high- $\Delta n$  LC also enables a thinner gel to be used, which, in turn, helps reduce the operating voltage. A high- $\Delta\epsilon$  LC lowers the threshold and operating voltages simultaneously. Increasing the LC concentration will boost the phase change and reduce the operating voltage. However, the gel may become too soft to stand alone. Its response time will also increase slightly.

## Homework Problems

- 12.1 Use Figure 12.6 to derive Equation (12.4) and explain how to obtain a large steering angle.
- 12.2 A student wants to design a polarization-independent tunable-focus microlens using a  $90^\circ$  TN cell. The LC mixture employed has the following properties:  $\Delta\epsilon = 12$ ,  $\Delta n = 0.5$  at  $\lambda = 550\text{ nm}$ ,  $K_{11} = 10\text{ pN}$ ,  $K_{22} = 6\text{ pN}$ ,  $K_{33} = 20\text{ pN}$ , and  $\gamma_1 = 0.2\text{ Pa s}$ . If the microlens diameter is  $200\ \mu\text{m}$ , what is the maximum tunable range of the focal length at  $\lambda = 550\text{ nm}$ ?

- 12.3 Nanosized polymer-dispersed liquid crystal (nano-PDLC), voltage-biased PDLC, double-layered homogeneous LC, and double-layered LC gels are all polarization independent. Compare their pros and cons.
- 12.4 A  $90^\circ$  TN cell is filled with a LC whose physical properties are listed as follows:  $\Delta\epsilon = 10$ ,  $\Delta n = 0.1$  at  $\lambda = 550$  nm,  $K_{11} = 14$  pN,  $K_{22} = 7$  pN,  $K_{33} = 18$  pN, and  $\gamma_1 = 0.2$  Pa s.
- (1) Under what conditions can the TN cell be used as a polarization-independent phase modulator?
  - (2) Explain why this phase modulator is polarization independent.

## References

- 1 T. T. Alkeskjold, J. Lagsgaard, A. Bjarklev, D. D. Hermann, J. Broeng, J. Li, and S. T. Wu, 'All-optical modulation in dye-doped nematic liquid crystal photonic bandgap fibers', *Opt. Express*, **12**, 5857 (2004).
- 2 F. Du, Y. Q. Lu, and S. T. Wu, 'Electrically tunable liquid crystal photonic crystal fiber', *Appl. Phys. Lett.*, **85**, 2181 (2004).
- 3 J. Borel, J. C. Deutsch, G. Labrunie, and J. Robert, 'Liquid crystal diffraction grating', US patent 3,843,231 (1974).
- 4 W. Kulchke, K. Kosanke, E. Max, M. A. Habberger, T. J. Harris, and H. Fleisher, 'Digital light deflector', *Appl. Opt.*, **5**, 1657 (1966).
- 5 H. Meyer, D. Riekman, K. P. Schmidt, U. J. Cschmidt, M. Rahlff, E. Schroder, and W. Thust, 'Design and performance of a 20-stage digital light beam deflector', *Appl. Opt.*, **11**, 1732 (1972).
- 6 T. K. Gaylord and M. G. Moharam, 'Planar dielectric grating diffraction theories', *Appl. Phys. B-Photophys. Laser Chem.*, **28**, 1 (1982).
- 7 X. Wang, D. Wilson, R. Muller, P. Maker, and D. Psaltis, 'Liquid-crystal blazed-grating beam deflector', *Appl. Opt.*, **39**, 6545 (2000).
- 8 D. P. Resler, D. S. Hobbs, R. C. Sharp, L. J. Friedman, and T. A. Dorschner, 'High-efficiency liquid-crystal optical phased-array beam steering', *Opt. Lett.*, **21**, 689 (1996).
- 9 C. M. Titus, J. R. Kelly, E. C. Gartland, S. V. Shiyonovskii, J. A. Anderson, and P. J. Bos, 'Asymmetric transmissive behavior of liquid-crystal diffraction gratings', *Opt. Lett.*, **26**, 1188 (2001).
- 10 W. Klaus, M. Ide, S. Morokawa, M. Tsuchiya, and T. Kamiya, 'Angle-independent beam steering using a liquid crystal grating with multi-resistive electrodes', *Opt. Commun.*, **138**, 151 (1997).
- 11 P. F. McManamon, T. A. Dorschner, D. L. Corkum, L. J. Friedman, D. S. Hobbs, M. Holz, S. Liberman, H. Q. Nguyen, D. P. Resler, R. C. Sharp, and E. A. Watson, 'Optical phased array technology', *Proc. IEEE*, **84**, 268 (1996).
- 12 S. T. Wu, U. Efron, and L. D. Hess, 'Birefringence measurement of liquid crystals', *Appl. Opt.*, **23**, 3911 (1984).
- 13 K. Rastani, A. Marrakchi, S. F. Habiby, W. M. Hubbard, H. Gilchrist, and R. E. Nahory, 'Binary phase Fresnel lenses for generation of 2-dimensional beam arrays', *Appl. Opt.*, **30**, 1347 (1991).
- 14 L. Beiser, 'Laser beam information scanning and recording', in *Laser Scanning and Recording Vol. 378*, 3 (Bellingham, WA, SPIE, 1985).
- 15 L. B. Glebov, 'Volume hologram recording in inorganic glasses', *Glass Sci. Technol., Suppl. C1*, **75**, 73 (2002).
- 16 O. M. Efimov, L. B. Glebov, L. N. Glebova, K. C. Richardson, and V. I. Smimov, 'High-efficiency Bragg gratings in photothermorefractive glass', *Appl. Opt.*, **38**, 619 (1999).
- 17 C. M. Titus, P. J. Bos, and O. D. Lavrentovich, 'Efficient accurate liquid crystal digital light deflector', *Proc. SPIE*, **3633**, 244 (1999).
- 18 O. Pishnyak, L. Kreminska, O. D. Lavrentovich, J. J. Pouch, F. A. Miranda, and B. K. Winker, 'Liquid crystal digital beam steering device based on decoupled birefringent deflector and polarization rotator', *Mol. Cryst. Liq. Cryst.*, **433**, 279 (2005).
- 19 C. Mao, M. Xu, W. Feng, T. Huang, K. Wu, and J. Wu, 'Liquid crystal applications in telecommunication', *Proc. SPIE*, **5003**, 121 (2003).
- 20 L. Eldada, 'Optical communication components', *Rev. Sci. Instrum.*, **75**, 575 (2004).

- 21 J. J. Pan, H. Wu, W. Wang, X. Qiu, and J. Jiang, *Proceedings of the National Fiber Optics Engineers Conference*, Telcordia, Orlando, FL, 943 (2003).
- 22 N. A. Riza and S. F. Yuan, 'Reconfigurable wavelength add-drop filtering based on a Banyan network topology and ferroelectric liquid crystal fiber-optic switches', *J. Lightwave Technol.*, **17**, 1575 (1999).
- 23 S. T. Wu and U. Efron, 'Optical properties of thin nematic liquid crystal cells', *Appl. Phys. Lett.*, **48**, 624 (1986).
- 24 V. V. Belyaev, S. Ivanov, and M. F. Grebenkin, 'Temperature dependence of rotational viscosity of nematic liquid crystals', *Sov. Phys. Crystallogr.*, **30**, 674 (1985).
- 25 S. T. Wu, U. Efron, and A. M. Lackner, 'Optimal operating temperature of liquid crystal modulators', *Appl. Opt.*, **26**, 3411 (1987).
- 26 H. K. Bucher, R. T. Klingbiel, and J. P. VanMeter, 'Frequency-addressed liquid crystal field effect', *Appl. Phys. Lett.*, **25**, 186 (1974).
- 27 M. Schadt, 'Low-frequency dielectric relaxation in nematics and dual-frequency addressing of field effects', *Mol. Cryst. Liq. Cryst.*, **89**, 77 (1982).
- 28 M. Xu and D. K. Yang, 'Dual frequency cholesteric light shutters', *Appl. Phys. Lett.*, **70**, 720 (1997).
- 29 S. T. Wu, 'A nematic liquid crystal modulator with response time less than 100  $\mu$ s at room temperature', *Appl. Phys. Lett.*, **57**, 986 (1990).
- 30 Y. Q. Lu, F. Du, Y. H. Lin, and S. T. Wu, 'Variable optical attenuator based on polymer stabilized twisted nematic liquid crystal', *Opt. Express*, **12**, 1221 (2004).
- 31 S. T. Wu, 'Dual parallel-aligned cells for high speed liquid crystal displays', *J. Appl. Phys.*, **73**, 2080 (1993).
- 32 S.-T. Wu and D.-K. Yang, *Reflective Liquid Crystal Displays* (John Wiley & Sons, Ltd Chichester, 2001).
- 33 X. Liang, Y. Q. Lu, Y. H. Wu, F. Du, H. Y. Wang, and S. T. Wu, 'Dual-frequency addressed variable optical attenuator with submillisecond response time', *Jpn. J. Appl. Phys.*, **44**, 1292 (2005).
- 34 S. Sato, 'Liquid-crystal lens-cells with variable focal length', *Jpn. J. Appl. Phys.*, **18**, 1679 (1979).
- 35 B. Wang, M. Ye, M. Honma, T. Nose, and S. Sato, 'Liquid crystal lens with spherical electrode', *Jpn. J. Appl. Phys.*, **41**, L1232 (2002).
- 36 H. S. Ji, J. H. Kim, and S. Kumar, 'Electrically controllable microlens array fabricated by anisotropic phase separation from liquid-crystal and polymer composite materials', *Opt. Lett.*, **28**, 1147 (2003).
- 37 T. Nose and S. Sato, 'A liquid-crystal microlens obtained with a non-uniform electric-field', *Liq. Cryst.*, **5**, 1425 (1989).
- 38 M. Ye and S. Sato, 'Optical properties of liquid crystal lens of any size', *Jpn. J. Appl. Phys.*, **41**, L571 (2002).
- 39 N. A. Riza and M. C. DeJule, '3-terminal adaptive nematic liquid-crystal lens device', *Opt. Lett.*, **19**, 1013 (1994).
- 40 W. W. Chan and S. T. Kowel, 'Imaging performance of the liquid-crystal-adaptive lens with conductive ladder meshing', *Appl. Opt.*, **36**, 8958 (1997).
- 41 J. S. Patel and K. Rastani, 'Electrically controlled polarization-independent liquid-crystal Fresnel lens arrays', *Opt. Lett.*, **16**, 532 (1991).
- 42 H. Ren, Y. H. Fan, and S. T. Wu, 'Tunable Fresnel lens using nanoscale polymer-dispersed liquid crystals', *Appl. Phys. Lett.*, **83**, 1515 (2003).
- 43 A. F. Naumov, M. Yu. Loktev, I. R. Guralnik, and G. Vdovin, 'Liquid-crystal adaptive lenses with modal control', *Opt. Lett.*, **23**, 992 (1998).
- 44 H. Ren and S. T. Wu, 'Tunable electronic lens using a gradient polymer network liquid crystal', *Appl. Phys. Lett.*, **82**, 22 (2003).
- 45 V. V. Presnyakov, K. E. Asatryan, and T. V. Galstian, 'Polymer-stabilized liquid crystal for tunable microlens applications', *Opt. Express*, **10**, 865 (2002).
- 46 S. Gauza, H. Wang, C. H. Wen, S. T. Wu, A. J. Seed, and R. Dabrowski, 'High birefringence isothiocyanato tolane liquid crystals', *Jpn. J. Appl. Phys.*, **42**, 3463 (2003).
- 47 S. T. Kowel, D. S. Cleverly, and P. G. Kornreich, 'Focusing by electrical modulation of refraction in a liquid-crystal cell', *Appl. Opt.*, **23**, 278 (1984).

- 48 T. Nose, Y. Yamada, and S. Sato, 'Improvement of optical properties and beam steering functions in a liquid crystal microlens with an extra controlling electrode by a planar structure', *Jpn. J. Appl. Phys.*, **39**, 6383 (2000).
- 49 H. Ren, Y. H. Fan, S. Gauza, and S. T. Wu, 'Tunable-focus cylindrical liquid crystal lens', *Jpn. J. Appl. Phys.*, **43**, 652 (2004).
- 50 Y. H. Lin et al., 'Tunable-focus cylindrical liquid crystal lenses', *Jpn. J. Appl. Phys.*, **44**, 243 (2005).
- 51 B. Lee, S. Jung, S. W. Min, and J. H. Park, 'Three-dimensional display by use of integral photography with dynamically variable image planes', *Opt. Lett.*, **26**, 1481 (2001).
- 52 H. Ren and S. T. Wu, 'Variable-focus liquid lens by changing aperture', *Appl. Phys. Lett.*, **86**, 211107 (2005).
- 53 P. G. de Gennes and J. Prost, *The Physics of Liquid Crystals* (Clarendon Press, Oxford, 1993).
- 54 M. Born and E. Wolf, *Principles of Optics* (Pergamon, Oxford, 1993).
- 55 H. Ren, Y. H. Fan, S. Gauza, and S. T. Wu, 'Tunable-focus flat liquid crystal spherical lens', *Appl. Phys. Lett.*, **84**, 4789 (2004).
- 56 Y. H. Fan, H. Ren, X. Liang, H. Wang, and S. T. Wu, 'Liquid crystal microlens arrays with switchable positive and negative focal lengths', *J. Disp. Technol.*, **1**, 151 (2005).
- 57 S. Yanase, K. Ouchi, and S. Sato, 'Molecular orientation analysis of a design concept for optical properties of liquid crystal microlenses', *Jpn. J. Appl. Phys.*, **40**, 6514 (2001).
- 58 H. Ren, J. R. Wu, Y. H. Fan, Y. H. Lin, and S. T. Wu, 'Hermaphroditic liquid-crystal microlens', *Opt. Lett.*, **30**, 376 (2005).
- 59 P. F. McManamon, T. A. Dorschner, D. L. Corkum, L. J. Friedman, D. S. Hobbs, M. Holz, S. Liberman, H. Q. Nguyen, D. P. Resler, R. C. Sharp, and E. A. Watson, 'Optical phased arrays technology', *Proc. IEEE*, **84**, 268 (1996).
- 60 H. Ren, Y. H. Fan, S. Gauza, and S. T. Wu, 'Tunable-focus flat liquid crystal spherical lens', *Appl. Phys. Lett.*, **84**, 4789 (2004).
- 61 H. Ren, Y. H. Fan, and S. T. Wu, 'Prism grating using polymer stabilized nematic liquid crystal', *Appl. Phys. Lett.*, **82**, 3168 (2003).
- 62 U. Efron, *Spatial Light Modulators* (Marcel Dekker, New York, 1994).
- 63 V. Freedericksz and V. Zolina, 'Forces causing the orientation of an anisotropic liquid', *Trans. Faraday Soc.*, **29**, 919 (1933).
- 64 Y. H. Fan, Y. H. Lin, H. Ren, S. Gauza, and S. T. Wu, 'Fast-response and scattering-free polymer network liquid crystals', *Appl. Phys. Lett.*, **84**, 1233 (2004).
- 65 Y. H. Wu, Y. H. Lin, Y. Q. Lu, H. Ren, Y. H. Fan, J. R. Wu, and S. T. Wu, 'Submillisecond response variable optical attenuator based on sheared polymer network liquid crystal', *Opt. Express*, **12**, 6377 (2004).
- 66 J. L. West, G. Zhang, and A. Glushchenko, 'Fast birefringent mode stressed liquid crystal', *Appl. Phys. Lett.*, **86**, 031111 (2005).
- 67 J. S. Patel, 'Polarization insensitive tunable liquid-crystal etalon filter', *Appl. Phys. Lett.*, **59**, 1314 (1991).
- 68 Y. Huang, T. X. Wu, and S. T. Wu, 'Simulations of liquid-crystal Fabry-Perot etalons by an improved 4x4 matrix method', *J. Appl. Phys.*, **93**, 2490 (2003).
- 69 R. L. Sutherland, V. P. Tondiglia, L. V. Natarajan, T. J. Bunning, and W. W. Adams, 'Electrically switchable volume gratings in polymer-dispersed liquid crystals', *Appl. Phys. Lett.*, **64**, 1074 (1994).
- 70 H. Ren, Y. H. Lin, Y. H. Fan, and S. T. Wu, 'Polarization-independent phase modulation using a polymer-dispersed liquid crystal', *Appl. Phys. Lett.*, **86**, 141110 (2005).
- 71 Y. H. Lin, H. Ren, Y. H. Fan, Y. H. Wu, and S. T. Wu, 'Polarization-independent and fast-response phase modulation using a normal-mode polymer-stabilized cholesteric texture', *J. Appl. Phys.*, **98**, 043112 (2005).
- 72 T. Uchida, H. Seki, C. Shishido, and M. Wada, 'Bright dichroic guest-host LCDs without a polarizer', *Proc. SID*, **22**, 41 (1981).
- 73 M. Hasegawa, C. Hellermark, A. Nishikai, Y. Taira, and A. C. Lowe, 'Reflective stacked crossed guest-host display with a planarized inner diffuser', *SID Tech. Dig.*, **31**, 128 (2000).

## **374 TUNABLE LIQUID CRYSTAL PHOTONIC DEVICES**

- 74 Y. H. Lin, H. Ren, Y. H. Wu, Y. Zhao, J. Fang, Z. Ge, and S. T. Wu, 'Polarization-independent liquid crystal phase modulator using a thin polymer-separated double-layered structure', *Opt. Express*, **13**, 8746 (2005).
- 75 S. Gauza, H. Wang, C. H. Wen, S. T. Wu, A. Seed, and R. Dabrowski, 'High birefringence isothiocyanato tolane liquid crystals', *Jpn. J. Appl. Phys.*, **42**, 3463 (2003).
- 76 H. Ren, Y. H. Lin, and S. T. Wu, 'Polarization-independent and fast-response phase modulators using double-layered liquid crystal gels', *Appl. Phys. Lett.*, **88**, 061123 (2006).

# Index

- A-plate, 70
- Absorption, 30, 55, 57, 88, 157, 159, 160, 208,  
211–216, 218, 220, 225, 227, 231, 232,  
250–257, 260, 262, 268, 291, 333, 345
- Active matrix, 223, 278, 303
- Alignment, 16, 33–37, 55, 70, 77, 103, 104, 113,  
115, 116, 120, 131, 135–138, 142, 154, 155, 159,  
166, 169, 170, 195, 200, 202–206, 215, 222,  
225, 235–237, 241, 243, 245, 251, 253, 254,  
264–267, 280, 281, 283, 284, 288–291, 295, 305,  
306, 335–338, 345
- Amorphous, 278
  - Thin-film-transistors, 278
  - TN, 277, 280
  - Cell, 278
- Analytic representation, 42
- Anchoring, 33–35, 37, 77, 113–115, 120, 129, 131,  
132, 135, 137, 139–144, 155, 188, 193, 206, 251,  
284, 288, 289, 291, 294, 295, 297, 305, 325,  
327–329, 333
- Anomalous diffraction scattering theory, 324
- Axial droplet, 325, 327
- Axially symmetric-aligned microcell, 210
- Azimuthal bistable nematic, 289
  
- Backflow, 150, 154, 156, 206, 224, 284, 304
- Bend, 19, 20, 23, 113, 114, 116, 131, 135, 136,  
145, 166, 169, 188, 196, 203, 223, 224,  
235–237, 277, 289, 294, 325–327,  
345
  - elastic constant, 19, 20, 22, 30, 115, 124, 145, 152,  
166, 169, 170, 196, 206, 223, 326
  - geometry, 131, 135, 137, 140, 142, 144
  - deformation, 113, 114
- Berreman 4x4 matrix, 95
- Binary mixture, 35, 309, 312, 343
- Binodal decomposition, 313
- Bipolar droplet, 325, 327, 330, 344
- Birefringence, 3, 4, 30, 70, 74, 115, 159–163, 166, 167,  
172, 174, 175, 202, 208, 210, 235, 238, 239,  
245, 249, 255, 259, 260, 264, 273, 289, 291, 307,  
319, 335
  - Birefringence effect, 208, 245, 259, 260
- Bistable, 115, 120, 124, 125, 156, 273, 281, 283, 284,  
288–295, 300–302, 304–306, 346
  - Nematic, 283, 288, 304, 305, 346
  - Cholesteric, 156, 290, 292, 304–306
- Boltzmann distribution, 5, 16
  
- C-plate, 208
- Calamitic, 1
- Cayley-Hamilton theory, 78, 98
- Cell gap, 120, 142, 145, 157, 159–161, 170, 171,  
201, 202, 206, 223, 235, 236, 238, 239, 245,  
254, 255, 259, 261, 262, 264–267, 269, 278, 305
- Cell gap tolerance, 261
- Chiral-homeotropic cell, 238
- Cholesteric, 4, 21–24, 36, 57, 65, 66, 68, 69, 71, 80, 92,  
95, 101–105, 116, 118, 119, 125, 156, 196, 197,  
249–257, 267, 290, 292, 303–306, 325, 333,  
337, 338, 346
  - Cholesteric display, 292, 305, 306
  - Cholesteric phase, 4, 23, 118, 119, 251, 252
- Circular polarization, 43, 45, 81, 83, 84, 91, 251, 255



## 376 INDEX

- Cole-Kashnow cell
- Color, 24, 202, 204, 222, 237, 244, 245, 253, 260, 263, 267, 268, 278, 279, 291–293, 305, 306, 341, 345
- Filter, 268, 278, 279
- Compensation Films, 57, 70, 76, 199, 208, 209, 215, 216, 227, 229, 234, 236
- Uniaxial, 70, 209
- biaxial, 208
- twisted, 77, 124, 138, 200, 237, 283
- discotic, 1
- Computer simulation, 197, 208
- Contrast ratio, 157, 199, 202, 243, 245–248, 251, 253–257, 263, 265, 267–269, 278, 283, 303, 305, 331, 344
- Cross-talking, 274
- Dichroic ratio, 251, 253, 254
- Dielectric constant, 26, 33, 41, 53, 58, 108, 157, 166, 185
- Dillectric permittivity, 25
- Dipole moment, 1, 10, 11, 24–26, 30, 31, 33, 35, 113, 122, 166, 167, 319
- Discotic, 1, 4, 202–204, 236, 237
- Double cell, 269
- Dual frequency, 340
- Duty ratio, 276
- Dye, 251–255, 332, 333, 341
- Dye-doped PDLC, 332, 333, 341
- Eigen mode, 47–49, 51–54, 56–58, 60, 61, 63–67, 69, 81
- Eigen vector, 54, 74
- Electric field, 25–27, 30, 31, 36, 39, 41–43, 45, 47, 49, 53, 58, 61, 65–67, 69, 73, 75, 82–85, 87, 95, 107–109, 112, 113, 115–117, 120–124, 127, 131, 135, 137–139, 158, 171, 179–181, 183–185, 196, 204–207, 215, 224, 250, 251, 254, 264, 265, 267, 273, 277, 281, 284, 290, 294, 295, 303, 305, 306, 319, 325, 327, 334, 337, 338, 344, 345
- Electric displacement, 26, 39, 41, 51, 180, 185
- Electrophoretic display, 303
- Elastic constant, 19, 20, 22, 30, 36, 115, 124, 145, 152, 157, 166, 169, 170, 196, 206, 223, 224, 245, 325–327, 344
- Ellipticity, 45, 85, 86, 89–91, 210
- Ellipticity angle, 45, 86, 89, 91, 210
- Elliptical polarization, 43, 45, 91, 92, 220, 232
- Energy flux, 42, 52, 53
- Enthalpy, 7
- Entropy, 4–7, 9, 17, 35, 182, 309, 310, 312–317
- Euler-Lagrange equation, 129, 141, 142, 155, 296
- Ferro-electric, 120–122, 273
- Field-induce order, 108, 109, 124
- Film compensation, 71, 226, 227, 231
- Finite difference method, 184
- Figure-of-merit, 170
- Flexoelectric, 112–117, 124, 125, 289, 290
- Focal conic state, 290–295, 298, 300, 301, 303
- Fringing field, 197, 204, 205, 225
- Freedericksz transition, 114, 127, 131, 143, 144, 150, 188, 196, 206, 207, 284, 287, 346
- Gibbs free energy, 8, 9, 180, 181, 183
- Gooch-Tarry first minimum, 200, 201, 238
- Guest-host display, 251, 255
- Grating light valve
- Gray scale, 122, 202, 204, 278, 281, 283, 292, 293, 300, 301, 304–306
- Helfrich deformation, 295, 303
- Heilmeyer-Zanoni cell, 251
- Helmholtz free energy, 7–9
- Holographic, 334, 345
- Color filter, 202, 244, 256, 268, 278, 279
- PDLC, 333, 334, 345
- Reflector, 244, 256, 263, 264, 268, 341, 350
- Homeotropic cell, 222, 223, 238, 239
- Homeotropic state, 71, 113, 154, 284, 287, 289, 291, 295, 297–301, 303, 337, 339, 340
- Homogeneous cell, 239, 245, 246
- Hysteresis, 297, 302, 338
- In-plane electrophoretic display, 204
- In-plane switching, 167, 200, 204, 243, 280
- Interferometric modulation, 347
- Iso-contrast, 202, 215, 218, 219, 221, 222, 226, 227, 229, 230, 233, 234, 237
- Jones Matrix, 73, 74, 76, 77, 86, 94, 104, 105, 196, 214, 226, 246, 258, 324
- Jones vector, 73–78, 81, 85, 88
- Lamp, 161, 199, 244
- Lagrange multiplier, 50, 129, 183, 192
- Landau-de Gennes theory, 12, 16, 35, 108
- Lasing, 68, 69, 71
- Leslie viscosity coefficient, 150
- Light control film, 345
- Linear polarization, 42, 91, 92, 115, 216, 220, 239, 254, 259–261, 330
- Liquid crystal, 1–4, 10–12, 14, 16–18, 20–25, 27, 28, 30, 31, 33–37, 39, 42, 55, 57, 58, 63, 65, 66, 68–71, 73, 76, 77, 80–82, 92, 93, 95, 98, 101, 103–105, 107–109, 112–125, 127, 129, 131, 133, 135–157, 176, 177, 179–191, 193, 195–197, 199,

- 202, 241, 243, 251, 255, 270, 273, 274, 276, 281, 288, 298, 300, 303–307, 313, 314, 316–319, 324–328, 330, 332–340, 344–346
- On silicon, 244
- High  $\Delta n$ , 334
- STN, 108, 336, 346
- TN, 3, 70, 77, 81, 82, 108, 154, 202, 245, 277, 283, 288, 303, 308, 318, 336, 338, 341, 346
- Magnetic induction, 39
- Magnetic field, 10, 24, 39, 52, 53, 67, 95, 97, 305
- Magnetic susceptibility, 24, 25, 27
- Maier-Saupe theory, 16, 18, 20, 35
- Mauguin condition, 62, 80
- Meuller matrix, 82, 86, 92, 94
- Mirror image, 21, 245
- Mixed-mode TN, 245
- Mueller Matrix, 82, 86–88, 90, 92, 94, 104, 286
- Multi-domain, 199, 200, 204, 243, 280, 290, 292, 337
  - TN, 200, 204
  - VA, 200, 204, 225, 236, 280
- Navier-Stokes equation, 146
- Negative birefringence film, 210
- Negative dielectric, 113, 136, 167, 174, 196, 223, 337, 340, 346
- Nematic, 2–4, 10–12, 14–16, 18, 22, 27, 33, 35–37, 69, 70, 74, 77, 104, 105, 107–109, 111, 112, 115–117, 122, 124, 125, 131, 138, 145, 147, 155, 156, 159, 160, 164, 167, 169, 176, 179, 188, 196, 200, 202, 209, 237, 240, 243, 245, 251–253, 269, 283, 284, 303–306, 313, 318, 319, 325, 333, 336, 337, 339, 340, 344–346
- Oblique angle, 208, 209, 216, 217, 220, 227, 228, 231, 263, 332
- Oily streak, 290, 294, 295
- Order parameter, 10–18, 20, 25, 30, 33, 35, 108, 109, 111, 112, 119, 124, 159, 166, 169
- Oseen-Frank energy, 20
- Over relaxation method, 188
- Passive matrix, 274, 276, 277, 286, 301, 303
- Patterned vertical alignment, 225
- Phase compensation, 199, 200, 202, 208, 216, 218, 245, 247
- Phase-only, 349, 361, 366
- Phase retardation, 74, 79, 157, 203–205, 207, 209, 210, 216, 218, 220–223, 227–229, 232, 235, 239, 243, 245, 257, 265, 285, 286
- Phase separation, 293, 306–309, 311–314, 317, 318, 343, 344
- Pi cell, 240
- Planar state, 101, 104, 290–295, 298–301, 303
- Plane polarized light, 43
- Poincaré sphere, 88, 90, 210, 214
- Polymer-dispersed liquid crystal, 344, 345
- Polymer-stabilized, 171, 253
- Polymerization induced phase separation, 306, 314, 317
- Poynting vector, 42, 52, 53, 70
- Pretilt angle, 70, 142, 143, 188, 203, 235, 246, 277, 289, 290, 304
- Polarization, 2, 10, 11, 25, 27, 30, 31, 33, 36, 42, 43, 45–47, 49, 57, 58, 60, 61, 63–66, 69–71, 73–76, 80–84, 86, 88–92, 103–105, 107, 113, 115–123, 167, 201, 207, 210, 211, 214–218, 220, 221, 227, 228, 232, 234, 239, 245, 246, 249–251, 254, 255, 257–261, 269, 289, 290, 324, 330, 332, 333, 337, 342
- Polarization rotation, 245, 257, 259, 260
- Polarizer, 55, 56, 70, 76, 82, 84, 85, 87, 94, 104, 105, 120, 136, 171, 196, 200, 202–204, 206, 207, 211–218, 220, 221, 227, 229, 231–234, 237–239, 244–246, 249–255, 257–262, 265, 269, 281, 285, 303, 332, 342
- Projection display, 161, 199, 200, 222, 225, 244, 246, 247, 269, 340, 341, 345
- Protrusion, 225
- Radial droplet, 325, 327
- Rayleigh-Gans scattering, 319, 324
- Reflector, 199, 244, 249, 250, 256, 262, 265, 268, 341
- Refractive index, 16, 23, 25, 27, 30, 41, 47–49, 53, 54, 56, 64–66, 70, 81, 99, 103, 104, 115, 158, 162–165, 171–174, 209, 212, 213, 218, 229, 233, 249, 255, 291, 319, 321, 330, 332, 334, 337, 338
- Relaxation method, 186, 188, 191, 194
- Resistivity, 166, 167, 223, 281
- Response time, 122, 124, 145, 157, 166, 168, 169, 171, 201, 202, 206, 207, 222–225, 235–237, 239, 244, 245, 255, 267, 274, 278, 336, 345
- Resolution, 197, 205, 244, 260, 278, 279, 306, 346
- Scattering profile, 324, 330, 344
- Screen, 204, 244, 245, 278, 279, 341, 342
- Scavenger
- Self-phase compensation, 247
- Smectic-A, 3, 22–24, 118, 119, 122, 124, 290, 325
  - Chiral smectic-A, 122
- Smectic-C, 3, 118–120, 122, 123, 325
  - Chiral smetic C, 118
- Solvent induced phase separation, 313, 317
- Solubility, 332, 333

## 378 INDEX

- Super-cooling, 15, 16
- Super-heating, 15, 16
- SpectraVue™
- Stokes vector, 83–87, 89–95, 104
- Surface stabilization, 288, 291
- Super twisted nematic, 189, 257, 259
  
- Temperature effect, 159, 161
- Ternary mixture, 317, 318, 343
- Tensor representation, 193, 196, 197
- Thermally induced phases separation, 312, 313
- Threshold voltage, 133, 157, 166, 169, 188, 207, 215, 224, 255, 277, 280, 301, 303, 306
- Tolane, 167, 172
- Toriodal droplet, 325, 326
- Transmissive display, 199, 223, 245, 289
- Transverse field, 204
- Transient planar state, 300, 303
  
- Twist angle, 62, 77, 80, 93, 124, 138, 144, 155, 188, 201, 237, 246, 259, 260, 262, 264, 265, 277, 283, 285
- Twisted nematic, 77, 104, 105, 138, 155, 156, 167, 188, 196, 200, 245, 269, 283, 303–305
  
- Uniaxial, 3, 10, 12, 24, 25, 53, 55–57, 70, 73, 74, 76, 77, 90, 98, 101, 105, 107, 112, 116, 117, 179, 208–211, 214, 215, 225, 227, 235, 240, 245, 346
  
- Vector representation, 190
- Viewing angle, 57, 76, 157, 199, 200, 202, 204, 207, 208, 215, 216, 218, 221, 222, 225–227, 229, 231–233, 235–237, 243, 245, 248, 254, 267–269, 278, 283, 291, 292, 332, 338, 340, 342
- Viscosity, 2, 3, 30, 117, 121–123, 140, 144–150, 157, 166–170, 205, 206, 223, 224, 336
  
- Zenithal bistable nematic, 283